Final Technical Report

on

Nonlocal Theory for Fracturing of Quasi-Brittle Materials

Grant AFOSR 91-0140

1/15/91 – 1/14/94

Principal Investigator:

ZDENĚK P. BAŽANT

Walter P. Murphy Professor of
Civil Engineering and Materials Science
Northwestern University, Evanston, IL 60208

UNCLASSIFIED

SECURITY CLASSIFICATION OF THIS PAGE

REPORT DOCUMENTATION PAGE

1a. REPORT SECURITY CLASSIFICATION: Unclassified	1b RESTRICTIVE MARKINGS
2a. SECURITY CLASSIFICATION AUTHORITY	3. DISTRIBUTION / AVAILABILITY OF REPORT: Approved for public release, distribution unlimited
2b. DECLASSIFICATION / DOWNGRADING SCHEDULE	
4. PERFORMING ORGANIZATION REPORT NUMBER(S): 0650-350-C457 (AR1)	5. MONITORING ORGANIZATION REPORT NUMBER(S): 60208 AFOSR-TR- 94 0204
6a. NAME OF PERFORMING ORGANIZATION: Northwestern University; 6b. OFFICE SYMBOL (If applicable)	7a. NAME OF MONITORING ORGANIZATION: AFOSR / NA
6c. ADDRESS (City, State, and ZIP Code): Technological Institute, 2145 Sheridan Road, Evanston, IL 60208-3109	7b. ADDRESS (City, State, and ZIP Code): AFOSR/NA, Bolling AFB DC 20332-6448
8a. NAME OF FUNDING / SPONSORING ORGANIZATION: AFOSR / NA; 8b. OFFICE SYMBOL (If applicable): NA	9. PROCUREMENT INSTRUMENT IDENTIFICATION NUMBER: AFOSR-91-0140
8c. ADDRESS (City, State, and ZIP Code): Bldg. 410, Room A237, Bolling A.F.B., Washington, DC 20332-6448	10. SOURCE OF FUNDING NUMBERS: PROGRAM ELEMENT NO. 61102F; PROJECT NO. 2302; TASK NO. DS; WORK UNIT ACCESSION NO.

11. TITLE (Include Security Classification)

NONLOCAL THEORY FOR FRACTURING OF QUASIBRITTLE MATERIALS

12. PERSONAL AUTHOR(S)
Zdenek P. Bazant, Walter P. Murphy of Civil Engrg. & Materials Science, Northwestern Univ.

13a. TYPE OF REPORT	13b. TIME COVERED	14. DATE OF REPORT (Year, Month, Day)	15. PAGE COUNT
Final Report	FROM 1/15/91 TO 1/14/94	March 1, 1994	210

16. SUPPLEMENTARY NOTATION

17. COSATI CODES			18. SUBJECT TERMS (Continue on reverse if necessary and identify by block number)
FIELD	GROUP	SUB-GROUP	QUASIBRITTLE MATERIAL, MICROMECHANISMS

19. ABSTRACT (Continue on reverse if necessary and identify by block number)

The failure of quasibrittle materials, which include concrete, rock, high-performance ceramics and fiber composites, cannot be treated according to the classical theories of plasticity or fracture mechanics because growth of zones of strain softening damage due to cracking must be considered. The mathematical treatment involves difficulties with spurious excessive localization. To remedy them, the nonlocal continuum concept was previously introduced, however, without theoretical foundation. The principal objective of the research has been to formulate the nonlocal damage concept on the basis of micromechanics of systems of growing and interacting cracks. This has led to a new model in which the nonlocal interactions are based on a smeared crack influence function, are tensorial and directional, and exhibit a power-type long-range decay. An iterative method for solving a Fredholm integral equation for the crack interactions in a finite element code has also been formulated. Advances have further been made in several related problems of micro-macro correlation. The applicability limits of the classical Weibull theory of random microstrength have been identified and a nonlocal probabilistic generalization derived. The time dependence and rate effect in damage evolution have been described on the basis of the activation theory for bond ruptures. The problems of scaling and size effect associated with damage have been analyzed, both theoretically and experimentally (with tests on concretes, fiber composites and rocks). Using discrete element method, the relations of the macrofracture characteristics to the statistics of the microstrength and microductility have been established. The results provide a deeper understanding of the evolution of damage, especially in high performance materials.

DISTRIBUTION / AVAILABILITY OF ABSTRACT: ☒ UNCLASSIFIED/UNLIMITED ☐ SAME AS RPT. ☐ DTIC USERS	21. ABSTRACT SECURITY CLASSIFICATION
22a NAME OF RESPONSIBLE INDIVIDUAL: DR WALTER JONES	22b TELEPHONE (Include Area Code) / 22c OFFICE SYMBOL: AFOSR/NA

DD FORM 1473, 84 MAR — 83 APR edition may be used until exhausted. All other editions are obsolete

SECURITY CLASSIFICATION OF THIS PAGE

UNCLASSIFIED

Final Technical Report

on

Nonlocal Theory for Fracturing of Quasi-Brittle Materials

Grant AFOSR 91-0140

1/15/91 – 1/14/94

Principal Investigator:

ZDENĚK P. BAŽANT

Walter P. Murphy Professor of
Civil Engineering and Materials Science
Northwestern University, Evanston, IL 60208

Contents

I State of Knowledge at the Start of Project

By 1990, the time of the writing of the proposal for this grant, some aspects of failure of quasi-brittle materials were already understood. But the continuum description of solids with statistically nonuniform crack arrays was not understood. The mathematical approaches were semi-empirical, phenomenological and descriptive rather than predictive. The lacked theoretical foundation in micromechanics.

a) Initial Nonlocal Damage Concept and Localization Limiter

Quasibrittle materials are characterized by development of large zones of distributed cracking damage before the final fracture. Prior to 1976, the distributed damage was simply ignored and structures were analyzed according to elasticity with a strength (or allowable stress) limit, plastic limit analysis, or fracture mechanics of distinct cracks. In the 1970's, various constitutive models with the so-called strain softening (that is, a decrease of stress with increasing strain) were proposed to handle distributed cracking. Examples were the continuum damage mechanics, endochronic theory, or plasticity with a degrading yield limit.

It was soon realized, however, that strain softening has a basic fault: the material is inherently unstable. This leads to spurious excessive localization of damage. In finite element analysis, this is manifested by the so-called spurious mesh sensitivity, which is caused by the fact that the damage front tends to localize into the smallest volume possible. This causes that, upon refining the element size to zero, the energy required to fail the structure tends also to zero, which is of course physically impossible. At the beginning of 1980's, it was proposed to cope with these problems by introducing some sort of a localization limiter. This concept was formulated first in the form of the so-called crack band model, and then in the more general form of a nonlocal damage continuum (to be distinguished from the classical nonlocal concept of Eringen, which dealt with nonlocal elasticity).

In the nonlocal formulation, the increments of damage (or cracking strain) were calculated from the average strain taken over the neighborhood of a given point. The size of this neighborhood had to be specified. This was done by introducing a material property called the characteristic length. The volume over which the averaging was carried out was called the characteristic volume.

The nonlocal approach did overcome the aforementioned mathematical difficulties. The boundary value problem with strain softening was regularized, the paradoxical phenomenon of imaginary wave speed (non-existence of wave propagation) was eliminated, excessive (unrestricted) damage localization was prevented and, in finite element calculations, the spurious mesh sensitivity was avoided. It was also demonstrated that the finite element calculations could be made to match many experimental results quite well.

The critical test results were those concerned with the size effect, that is, the dependence of the nominal strength (maximum load divided by characteristic structure dimension and thickness) on the characteristic dimension (size) of the structure. Individually, these results were described quite successfully with the nonlocal damage concepts.

In particular, the finite element results were shown to agree with the approximate size effect law representing a transition from plastic limit analysis at very small structure sizes to linear elastic fracture mechanics at very large structure sizes. The largest amount of test results were gathered for concrete, but many test results were also assembled for rock, and some for ice and wood. It was also shown that from the measurements of the size effect is should be possible to calibrate the nonlocal continuum models, and particularly to determine the characteristic length of the material.

However, a fundamental problem was recognized at the end of the 1980's: The nonlocal concept was purely empirical. Although it was felt it had to do with the coarseness of the microstructure and with the size and spacing of the microcracks, no physically based micromechanical theory for the nonlocal continuum concept was available. The spatial averaging was entirely a phenomenological concept. It was not known what the tensorial and directional character of the averaging should be. So it was taken simply as scalar and directionally isotropic, for no other reason than lack of knowledge.

By fitting of numerous test data with finite element codes, it was also discovered that different types of problems required using different characteristic lengths, for the same material. Thus, the nonlocal models did not have predictive capability, except for each narrow range of problems for which they were calibrated. Also, the size effect and scaling laws were tied to a particular geometry and could not be translated from one type of structure to another.

It thus became obvious that a serious micromechanical analysis had to be undertaken to put the nonlocal continuum concept on a sound physical foundation. To do that was taken in 1990 as the principal objective of the proposal for the present project.

With regard to the size effect, another gap was in the role of interfacial slip and interfacial fracture, for example along the interfaces of fibers and matrix in composites. A further gap was the nonexistence of broad-range experimental data on the size effect in geometrically scaled specimens of fiber composites. Only such results can clearly reveal the inapplicability of strength theories or plastic-type limit analysis.

Furthermore, the test results were limited to tensile dominated failures. There was scarcely any information on the role of distributed cracking and the inherent size effect in compression failure of quasi-brittle materials.

b) Weibull's Theory of Random Strength

There were also misconceptions. There was a competing and much older theory of the size effect, proposed by Weibull in 1939. This theory, in which the size effect was explained by the randomness of the material strength, ignored the large stress redistributions that are caused by damage growth prior to failure. It also ignored the fact that the release of stored energy from the structure, which is larger in a larger structure, is itself a source of a strong deterministic size effect.

It thus became clear that Weibull's statistical theory of size effect could apply only to those structures which fail at the initiation of macroscopic cracking, that is at the moment the microscopic flaws cease to be microscopic. This approximation is of course

good enough for many structures, particularly metallic structures, which typically fail (or must be considered to fail) when a crack exceeds about 1% of the cross section dimension, for which the stress redistributions and energy release aspects are still macroscopically insignificant. However, such a situation is blatantly untrue for concrete. Reinforced concrete structures typically develop, in a stable manner, large cracks, typically reaching over 50 to 90% of the cross section dimension. Likewise, design of good composites or toughened ceramics requires that there is large stable crack growth before the maximum load is reached.

The assumptions of Weibull's theory also do not hold for fiber composites and modern toughened ceramics. In fact, the basic principle in designing stronger and tougher composites and ceramics is to force the damage to remain broadly distributed, thus blunting and shielding potential large cracks—in other words, achieve concrete-like behavior.

c) Rate Effect and Fatigue

Another crucial aspect was insufficiently understood and unquantified—the rate effect or time dependence in the development of distributed damage. It was obvious that time plays at least some role in every type of failure. But physically justified formulations for distributed damage were lacking.

Numerical analysts recognized in the early 1980's that introduction of rate dependence in the failure development has the effect of regularizing the boundary value problem of strain softening and preventing spurious mesh sensitivity. Later, however, it was found that the regularization, which precluded waves of imaginary velocity, is short-lived. Spurious excessive damage localization and spurious mesh sensitivity develop gradually in time. The problem is not regularized asymptotically, for infinite times. This showed that despite of taking time dependence in the evolution of damage into consideration, it was still necessary to use some sort of a nonlocal model, with a characteristic length. Various ways of throwing viscosity into the stress-strain relations of plasticity with a degrading yield limit or other constitutive models were attempted and showed some desirable features. But there was no physical foundation, no true predictive capability.

Related to the time effect is fatigue. The fatigue behavior of quasi-brittle materials is quite different from metals. They are less sensitive to fatigue, by virtue of blunting and shielding of potential distinct cracks by large damage zones. But fatigue cannot be ignored. Yet it was not known how the concept of distributed damage, and the fact that it inevitably involves a size effect, should impinge on fatigue.

d) Micromechanics of Crack Systems

Finally, as for micromechanics of crack systems, major advances have of course been achieved between 1975 and 1990. However, they were limited to the elastic properties of bodies with macroscopically uniform random systems of distributed cracks or various types of oriented systems. They did not clarify the effect of growth of cracks during loading, nor the effect of spatial localization of the cracks, which makes the macroscopic fields nonuniform.

For example, the well-known solutions of Budianski and O'Connel, or Budianski and Hoenig, Kachanov, Ju and others, considered only cracks of fixed length (i.e., not allowed to grow), distributed spatially uniformly over an infinite body. These solutions used various homogenization methods such as the methods of periodic cells, the self-consistent method of Hill, the Mori-Tanaka method and other methods for composites, in order to determine the macroscopic tensor of effective elastic moduli. In the diagram of stress versus strain, this meant that these previous solutions provided only the secant elastic moduli. They were incapable of providing information on the tangent elastic moduli, which can yield a negative softening slope (corresponding to a non-positive definite material stiffness matrix).

Thus, there was a serious gap of knowledge: How should the difference between the secant elastic moduli and the tangent elastic moduli, caused by the growth of cracks during loading, be determined?. This difference determines the inelastic stress increments — the basic characteristic of the macroscopic stress-strain relation for damage.

As for crack interactions, they were taken into account in some of the solutions, however, only for the case of spatially uniformly distributed cracks. In that case the interactions are simple: they basically cancel each other. The crack interactions in large crack systems that become macroscopically nonuniform, that is, localize, were not considered in previous studies. Yet, these are essential for the properties limiting localization of damage.

Making progress in the foregoing gaps of knowledge, with a thrust on the *micro-macro*, was adopted as the goal of the present project.

II Objective of Research Effort

The basic overall objective of the research effort was to develop fundamental understanding of the macro-micro correlation in the phenomena of distributed damage. In detail, the objectives (which were slightly updated as the research was advancing), were as follows:

1. Principal Objective:

(a) Analyze interactions among growing cracks in large microcrack systems and deduce a continuum approximation of the discrete relations for the interacting cracks.

2. Further Objectives:

(b) Formulate compression failure of a quasi-brittle material as the propagation of a band of splitting microcracks.

(c) Determine the macroscopic consequences of softening slip or interface fracture between fiber and matrix in composites.

(d) Analyze the effect of inclusions such as aggregate pieces or fibers (in the transverse cross section of a composite) on the microcrack interactions.

(e) Determine the consequences of the rate-process theory for bond ruptures, governed by activation energy and Maxwell energy distribution, for the macroscopic rate-dependent damage or fracture model.

(f) Analyze the effect of distributed cracking in a boundary layer, affecting the strength and size effect in the bending of beams or plates.

(g) Identify in mathematical terms the limitations of Weibull probabilistic theory of size effect and damage for the case of quasi-brittle materials, determine the macroscopic consequences for a probabilistic failure theory, and deduce a rational nonlocal generalization of the Weibull concept.

(h) Determine the size effect in fatigue of a quasi-brittle material, caused by the existence of a large zone of distributed cracking.

III Summary of Accomplishments

1. Principal Accomplishment

The principal accomplishment of the project has been the development of a nonlocal damage model based on micromechanics of crack interactions, described in [1] and applied to localization analysis in [2] (the idea first presented in [34]).[1]

Compared to the situation before, this model appears to represent a major breakthrough in the continuum modeling of distributed damage. The model considers not only stationary cracks but cracks that grow with the process of loading. It relates the growth of these cracks to the macroscopic continuum stress-strain relation for cracking damage with strain softening (such as continuum damage mechanics, or plasticity with degrading yield limit).

The model is based on the discrete matrix relations for the superposition method for interacting cracks, and utilizes its simplified version due to Kachanov. The classical homogenization methods could not be used (as they apply only to macroscopically uniform states of deformation and stress, while main concern is the localizing, nonuniform, and nonhomogeneous states). So, a new concept for the micro-macro transition had to be formulated: Find a continuum field equation whose possible discrete approximation coincides with the matrix equation governing a system of interacting microcracks. Such a discrete approximation can be obtained for nonuniform states, which makes the continuum transition possible.

The result is a new type of nonlocal continuum, described by a Fredholm integral equation for the unknown nonlocal inelastic stress increments. In contrast to the previous, heuristic nonlocal formulations, there are two spatial integrals instead of one. One integral, which is similar to that used in the previous formulations, ensues from the fact that crack interactions are governed by the average stress over the crack length (rather than the

[1] The references are listed at the end and the main ones are attached.

value of the macroscopic stress field at the crack center). This integral can be regarded as a short-range averaging of the inelastic macro-stresses.

The second integral describes long-range crack interactions. Its kernel is a crack influence function which has directional and tensorial properties, in contrast to the previous nonlocal formulations. This influence function is a second-rank tensor and varies with a directional angle, i.e., is anisotropic. Thus it exhibits sectors of shielding and amplification (which were missing from previous formulations).

A rather interesting property came out theoretically: for long distances of two interacting cracks, the influence function decays as the inverse square of distance in two dimensions and as the inverse cube of distance in three dimensions. This decay is of course similar to long-range interactions in many other physical laws (although in previous formulations the kernel of the spatial integral was assumed to decay as an exponential). This type of decay implies some interesting properties: The influence function is not integrable over an infinite space or infinite plane. This means that it is impossible to cause a homogeneous growth of strain softening damage over an infinite space.

Effective application in finite element codes is made possible by formulating the solution of the discretized integral equation in terms of the Gauss-Seidel iterative method. The advantage is that this type of solution can be conveniently combined with the normal iterations of each loading step in a nonlinear finite element code. This greatly simplifies the handling of the nonlinearity, by allowing the nonlocal inelastic stress increments to be calculated from the local once explicitly. The calculation of the nonlocal inelastic stress increments involves evaluation of an integral over the finite elements of the structure, which contains the crack influence function. For the crack influence function, simplified closed-form expressions which have asymptotically exact properties for an infinite space as well as for close-range interactions, are derived.

An appealing feature of the new nonlocal formulation is that the constitutive law becomes strictly local. This avoids difficulties with the unloading criterion or with the continuity condition of plasticity, which were encountered in previous nonlocal formulations in which the nonlocal spatial integral was part of the constitutive law.

The aforementioned superposition method for interacting cracks is based on decomposing a loading step, for example in a finite element program, into two substeps: In the first step, the cracks are imagined to be temporarily frozen (or glued), that is, prevented from opening and growing. In the second substeps, these cracks are imagined unfrozen or unglued. This means that the stress increments transmitted across the previously frozen cracks must be applied as loads on the crack surfaces, in two opposite directions.

The properties of this new, micromechanically justified nonlocal formulation have been studied by analyzing localization of strain-softening damage into a planar band [2]. To some extent, they have been explored in finite element calculations (however, this work is still continuing and a paper has not yet been written). It is found that the new nonlocal model predicts localization to begin as soon as the local constitutive law deviates from linearity, which can be already before the peak of the stress-strain diagram. This is a major difference from the previous models, which indicated localization to occur only after a certain negative post-peak slope has been exceeded and allowed no localization in

the pre-peak hardening regime. It was also shown that bifurcations of the equilibrium path can occur, according to the new formulation, even in the regime of local hardening, and even in the absence of geometric nonlinearities of buckling.

Although some new interesting questions have arisen and further studies will be necessary, the development of the new nonlocal model appears to represent a major advance in the understanding and description of the micro-macro correlation of the processes involved in distributed softening damage due to cracking.

2 Further Accomplishments

2.1 Distributed damage, interface fracture and size effect in aerospace fiber composites.

The damage in fiber composites, which are important for aerospace applications, has some particular characteristics due to the anisotropic nature of the material and the role played by interface fracture. For this reason, tests of geometrically similar notched specimens of isotropic and cross-ply laminates of carbon fiber-epoxy composites, made from unidirectionally reinforced plies, were tested for the size effect [3]. As might have been expected from the distributed nature of damage, the size effect is found to be quite significant and follows approximately the general size effect law for quasi-brittle materials. The size effect tests yield the basic fracture characteristics, particularly the fracture energy of the material and the effective length of the fracture process zone (which is related to the characteristic length of the nonlocal continuum). These results mean that the aerospace composites should be analyzed as quasi-brittle materials and that size effects due to distributed damage should be taken into account.

Furthermore, a simplified analytical solution has been obtained for the pullout of a fiber from a matrix [4, 19]. It was assumed that the interface stress-slip relationship exhibits post-peak softening and terminates with a final frictional plateau. This assumption is commonly made in the analysis of interface behavior in composites, both for fibers in laminates and for reinforcing bars in concrete. It turned out [4] that the softening interface slip alone produces a size effect, again approximately following the size effect law for quasi-brittle materials. From this size effect, the interface stress-slip characteristics can be identified more easily than from other methods. This is made possible by the simplicity of the analytical solution, which can be inverted [4].

To exploit this solution, further tests have been conducted on pullout of reinforcing bars from concrete [5]. In contrast to previous pullout tests, the specimens have been engineered in such a way that the failure would occur due to interface slip exclusively, with no cracking around the bar. From such tests [5], the interface stress-slip softening characteristics have been identified. This is a new method of identifying the interface properties from experiments. In the limit for very large sizes, obtained by extrapolation of the test results, the theory makes it also possible to determine the interface fracture energy.

2.2 *Propagation of a band of splitting microcracks as a mechanism of compression failure*

In a homogeneous field of uniaxial compressive stress, cracks parallel to the stress vector release no energy. Yet they are typically seen to form in that manner. Obviously there must be other mechanisms which provide transverse tensile stresses on the microscale. These are no doubt the inhomogeneity of the material and local buckling of damaged material on the microscale.

A theory of compression failure due to the propagation of a band of splitting microcracks has been formulated, taking into account local buckling of microslabs of the material between adjacent splitting cracks [6]. This concept has been applied to the analysis of failure of circular cavities in a compressive stress field—a problem of importance in many applications such as boreholes in rock or openings in structural parts. It was shown that in contrast to the strength-based analysis of compression failures (or plastic limit analysis), the theory always exhibits a size effect. In the simplest form, the size effect for the failure stress of a circular opening decreases as the inverse 2/5 power of the opening diameter [6]. The theory has also been applied to the calculation of size effect in the failure of concrete columns (which would similarly be applicable to the failure of rock walls). The failure mechanism, according to experiments, has been considered to involve a push-out of a triangular region limited by an inclined band of splitting microcracks [7]. The predicted size effect was confirmed experimentally [8] by size effect tests of reduced-scale reinforced concrete columns. (The current methods, embodied in standards, do not consider any size effect in compression failures of concrete.)

The foregoing models consider interacting cracks in a homogeneous material. This is good enough for graphite epoxy or similar composites, but is a simplification in the case of concrete, due to the presence of inclusions in the form of hard aggregate pieces. Therefore, the problem of a body containing both microcracks and inclusions has been analyzed [9]. The analysis has been numerical, using the superposition method for cracks systems, which was extended to inclusions. It was shown that the inclusions play a significant role, but they do not alter the qualitative nature of crack interactions. The main role of aggregate is to decide the dominant spacing of the microcracks.

2.3 *Identification of macro-fracture characteristics by random particle simulation of microstructure*

The quasi-brittle material behavior can be easily simulated by random particle systems (discrete element method) in which the interparticle force-displacement relationship exhibits softening. Such a particle system can approximate the microstructure of a material such as concrete or fiber composite in the transverse cross section. An efficient numerical scheme has been developed and used to study the correlation of the macroscopic fracture characteristics to the characteristics of the microstructure, particularly the mean and coefficient of variation of interparticle strength, and the mean and coefficient of variation of microductility (displacement at which the interparticle force is reduced to zero). It was shown that the macrofracture characteristics can be identified by simulating geomet-

rically similar specimens of different sizes and exploiting the calculated size effect [10]. Furthermore, it was shown that regular lattices of particles always exhibit directional bias for fracture, even if the strength values are randomized. A method to efficiently generate random particle systems of prescribed particle size distribution has been formulated [10].

2.4 Nonlocal generalization of probabilistic Weibull theory of random strength

For reasons mentioned before, Weibull probabilistic theory of random strength has been generalized to a nonlocal form that can be applied to quasi-brittle materials [11, 12]. The classical assumption that the material failure probability is determined, according to Weibull probability distribution, by the local tensile stress has been replaced by the assumption that it is determined by the average of strain in the neighborhood of a given point.

It was found that, for small structure sizes, this leads to the same size effect as the classical Weibull theory, but for large structure sizes the size effect is different and approaches the deterministic size effect of linear elastic fracture mechanics. The approach to a deterministic size effect for large sizes is explained by the fact that the size of the fracture process zone tends to be independent of the structure size when the specimens are large.

2.6 Rate effect in evolution of damage and fracture

For reasons explained in Section I, modeling of the rate effect and understanding of its micromechanics is of paramount importance. In order to eliminate the difficult and complicating effects of wave propagation, tests have been conducted in the static range, at loading rates varied over 5 orders of magnitude [13, 14]. The interrelationship of the loading rate effect and size effect has been experimentally studied for rocks [15] (whose behavior is similar to ceramics) and concrete.

Aside from the well-known dependence of strength and fracture energy on the loading rate, several new effects have been found. The fracture specimens of concrete in the post-peak range exhibit load relaxation, but those of rock do not [13–15]. This means that creep of concrete plays a role in the rate effect. Loading concrete at a faster rate causes a shift of the size effect closer to linear elastic fracture mechanics, that is, toward a more brittle behavior. The slower the loading, the higher the brittleness [13–15], which at first seemed surprising. This is micromechanically explained by relaxation of the stress in the vicinity of the fracture or damage front, which occurs in concrete due to creep (but not in rocks, in which this phenomenon is not observed). Another new phenomenon that came out from experiments was the reversal of softening response to hardening response by a sudden increase of the loading rate [16]. This is a dramatic effect which can cause that the second peak is even higher than the previous peak under the previous loading rate [16].

These phenomena have first been modeled by a simple rate-dependent generalization of the R-curve approach to quasi-brittle fracture, in which the creep in the specimen was also taken into account [17]. To obtain a more realistic model based on micromechanics,

the rupture of bonds in the fracture process zone was analyzed according to the rate-process theory for thermally activated processes governed by activation energy [13, 18]. Based on Maxwell distribution of kinetic energies of atoms or molecules, a rate-dependent generalization of the stress-displacement relationship of the cohesive crack model has been obtained (an equivalent form for the crack band model for distributed cracking then also follows). This rate-dependent formulation was also applied in a crack-band finite element analysis of concrete, and it was shown that the aforementioned experimentally observed phenomena can be simulated [18]. The generalization of the cohesive crack model to rate dependence has been formulated in a general way on the basis of compliance influence functions (Green's functions) [20]. Finally, it was shown that the size effect curves according to the cohesive crack model can be directly calculated based on eigenvalue analysis of the maximum load, making integration of the solution for the increase of the load from zero to the maximum unnecessary. It was shown that the structure size for which a given relative crack length corresponds to the maximum load is an eigenvalue of a certain integral equation [20].

As an alternative to the cohesive crack model, a novel approach to simulating fracture with a crack-tip blunting zone has been formulated by assuming that the cohesive crack is a superposition of infinitely many linear elastic cracks with infinitely densely distributed tips and with infinitely small stress intensity factors [21]. This approach is sometimes advantageous, since it allows exploiting the known solutions of linear elastic fracture mechanics. The rate effect and creep have also been incorporated in this approach. It was shown that fracture simulation by such a model can reproduce the size effect observed in quasi-brittle materials as well as the effects of loading rate [21].

2.7 Fatigue aspects of quasi-brittle fracture

Tests of size effect under fatigue loading have been conducted for geometrically similar specimens of different sizes, using both normal and high-strength concretes [22, 23]. It was found that fatigue failures also exhibit a size effect, but of a type that deviates from the well known Paris law for the growth of cracks under cyclic loading, which is known to apply to metals. The size effect is again found to be transitional, approaching Paris law for very large sizes. It was also shown that for high-strength concretes the fatigue behavior is more brittle, with a stronger size effect than for normal concretes.

2.8 Boundary-layer size effect

As pointed out in Section I, in some situations quasi-brittle structures fail at the initiation of fracture growth from the surface. In that case, the microcracking is not yet localized at the moment of failure, but it still engenders size effect. This type of size effect is of a different nature. A simple analytical formulation for this type of size effect, as manifested in the tests of modulus of rupture for bending, has been formulated and calibrated by test results [24].

2.9 Refinements of microplane model for strain-softening constitutive relations

This constitutive model for damage, developed under a previous AFOSR grant, was further extended and refined. A new concept of geometric damage was formulated [25]. This made it possible to separate the effect of a reduction of the effective load-bearing cross section on planes of various orientations within the material from the stress-strain relationship for the true stress (stress in the undamaged part of the cross section). This analysis also provided a rational expression for the damage tensor, as a fourth-rank tensor. Compression failures and cyclic loading failures of concrete have been simulated by extensions of this model [26, 27].

2.10 Analysis of bifurcations that lead to localization of damage

It was shown that, in direct tensile tests, the tensile strain-softening damage due to cracking leads to a bifurcation of the equilibrium path such that the specimen must flex to the side [28, 29].

2.11 Some further related works

Several other studies of localization, nonlocal damage, size effect and other aspects related to the present project have also been carried out [30–40].

Concluding Remarks

The foregoing diverse results complement the principal accomplishment outlined in Section 1. Their common theme is the micro-macro correlation of damage and fracture. Several types of phenomena arise on the microscale, including microcracking, influence of inclusions, rate effects in the microcrack growth, probabilistic aspects of the microstructure, etc. They all need to be taken into account in order to obtain a fully realistic model based on micromechanics.

IV. Professional Personnel Associated with the Research Effort

1. Personnel

1. Zdeněk P. Bažant (Principal Investigator)
2. Issac Daniel (Faculty Advisor)
3. William F. Schell (M.S., June 1992)
4. Stephen Beissel (M.S., June 1992)
5. Milan Jirásek (Ph.D., June 1993)

6. Ravindra Gettu (Ph.D., June 1992)
7. Yunping Xi (Ph.D., June 1992)
8. Zhengzhi Li (Graduate Research Assistant)
9. Joško Ožbolt (Post-Doctoral Research Associate)
10. Ignacio Carol (Post-Doctoral Research Associate)
11. Mohammad T. Kazemi (Ph.D., June 1991)
12. Gilles Pijaudier-Cabot (Visiting Post-Doctoral Research Associate from E.N.S. de Cachan, France)
13. Mazen R. Tabbara (Post-Doctoral Research Associate)
14. Zhishen Wu (Visiting Post-Doctoral Research Associate from Nagoya University, Japan)
15. Yuan-Neng Li (Post Doctoral Research Associate)
16. Michael Thoma (Visiting Research Associate from Universität Münich, Germany)
17. Rodrigue Desmorat (Visiting Research Associate from E.N.S. de Cachan, France)

2. Theses:

Ph.D.

1. Mohammed T. Kazemi, *Fracture Characteristics of Quasi-brittle Materials from the Size Effect Method and Implications in Design*, 1990.
2. Ravindra Gettu, *Concrete and Rock Fracture and the Influence of Loading Rate*, 1992.
3. Yunping Xi, *Analysis of concrete creep, shrinkage and fracture by deterministic and probabilistic methods*, 1992.
4. Milan Jirásek, *Modeling of Fracture and Damage in Quasibrittle Materials*, 1993.

M.S.

1. William F. Schell, *Fatigue Fracture of High Strength Concrete Under High Frequency Loading*, 1991.
2. Stephen Beissel, *Numerical Analysis of Nonlinear and Time-Dependent Fracture by Means of the Smeared-Tip Superposition Method*, 1990.

V. List of Publications

1. Principal Publications

[1] Bažant, Z.P. (1994). "Nonlocal damage concept based on micromechanics of crack interactions." *ASCE J. of Engrg. Mech.*, 120—in press.

[2] Jirásek, M. and Bažant, Z.P. (1994). "Localization analysis of nonlocal model based on crack interactions." *ASCE J. of Engrg. Mech.*—in press.

[3] Bažant, Z.P., Li, Z., and Daniel, I. (1994). "Size effect and fracture characteristics of fiber composite laminates." Report, Northwestern University, to be submitted to ASCE *J. of Engrg. Mech.*

[4] Bažant, Z.P., and Desmorat, R. (1994). "Size effect in fiber or bar pullout with interface fracture and softening slip." Report, Northwestern University, *J. of Engrg. Mech.*, ASCE — in press.

2. Further Publications

[5] Bažant, Z.P., Li, Z., and Thoma, M. (1994). "Identification of stress-slip law for fiber or bar pullout from size effect tests." Report, Northwestern University, submitted to ASME *J. of Appl. Mech.*

[6] Bažant, Lin, F.-B., Z.P., and Lippmann, H. (1993). "Fracture energy release and size effect in borehole breakout." *Int. Journal for Numerical and Analytical Methods in Geomechanics*, 17, 1–14.

[7] Bažant, Z.P. (1994). "Size effect in tensile and compressive quasibrittle failures." Proc., *JCI International Workshop on Size Effect*, Sendai, ed. by H. Mihashi, Tohoku University, Nov. 1993, 141–160.

[8] Bažant, Z.P., and Kwon, Y.W. (1992). "Size effect in strength of reinforced concrete columns." Fracture Mechanics of Concrete Structures (Proc. *Int. Conf. on Fracture Mechanics of Concrete Structures*, Breckenridge, Colorado, June), ed. by Z.P. Bažant, Elsevier Applied Science, London, 556–560.

[9] Pijaudier-Cabot, G., and Bažant, Z.P. (1991). "Cracks interacting with particles or fibers in composite materials." *J. of Engineering Mechanics* ASCE 117(7), 1611–1630.

[10] Jirásek, M., and Bažant, Z.P. (1993). "Macroscopic fracture characteristics of random particle systems," submitted to *Int. J. of Fracture.*

[11] Bažant, Z.P., Xi, Y., and Reid, S.G. (1991). "Statistical size effect in quasi-brittle structures: I. Is Weibull theory applicable?" ASCE *J. of Engineering Mechanics* 117(11), 2609–2622.

[12] Bažant, Z.P., and Xi, Y. (1991). "Statistical size effect in quasi-brittle structures: II. Nonlocal theory." ASCE *J. of Engineering Mechanics* 117(11), 2623–2640.

[13] Bažant, Z.P. (1993). "Current status and advances in the theory of creep and interaction with fracture." Proc., *5th International RILEM Symposium (ConCreep 5)*, held at U.P.C., Barcelona, September, ed. by Z.P. Bažant and I. Carol, E & FN Spon, London, 291–307.

[14] Bažant, Z.P., Bai, S.-P., and Gettu, R. (1993). "Fracture of rock: Effect of loading rate." *Engineering Fracture Mechanics*, 45(3), 393–398.

[15] Bažant, Z.P., and Gettu, R. (1992). "Rate effects and load relaxation in static fracture of concrete." *ACI Materials Journal*, 89(5), 456–468.

[16] Bažant, Z.P., Gu, W.-H., and Faber, K.T. (1993). "Softening reversal and other effects of a change in loading rate on fracture of concrete." Structural Engrg. Report No. 93-7/B667s, Northwestern University; also *ACI Materials J.* — in press.

[17] Bažant, Z.P., and Jirásek, M. (1993). "R-curve modeling of rate and size effects in quasibrittle fracture." *Int. Journal of Fracture*, 62, 355–373.

[18] Wu, Z.-S., and Bažant, (1993). "Finite element modeling of rate effect in concrete fracture with influence of creep." Proc., *5th International RILEM Symposium (ConCreep 5)*, held at U.P.C., Barcelona, September, ed. by Z.P. Bažant and I. Carol, E & FN Spon, London, 427–432.

[19] Bažant, Z.P., and Desmorat, R. (1994). "Softening slip and size effect in bond fracture." Proc., *ACI Symposium*, Vancouver, Marhc 1993; also *J. of Engrg. Mech.* ASCE 120(3), 593–617.

[20] Li, Y.-N., and Bažant, Z.P. (1993). "Eigenvalue analysis of size effect for cohesive crack model." Structural Engrg. Report No. 93-8/420s, Northwestern University, *Int. J. of Fracture*—in press.

[21] Bažant, Z.P., and Beissel, S. (1993). "Smeared tip superposition method for fracture with bridging stresses, rate effect and creep." submitted to *Int. J. of Fracture*—in press.

[22] Bažant, Z.P., and Xu, K. (1991). "Size effect in fatigue fracture of concrete." *ACI Materials J.* 88 (4) 390–399.

[23] Bažant, Z.P., and Schell, W.F. (1993). "Fatigue fracture of high-strength concrete and size effect." *ACI Materials Journal*, 90(5), 472–478.

[24] Bažant, Z.P., and Li, Z. (1993). "Modulus of rupture: Size effect due to fracture initiation in boundary layer." Structural Engrg. Report No. 93-5/457m, Northwestern University; also *J. of Engrg. Mech.*, ASCE—in press.

[25] Carol, I., Bažant, Z.P., and Prat, P.C. (1991). "Geometric damage tensor based on microplane model." *J. of Engineering Mechanics* 117(10), 2429–2448.

[26] Bažant, Z.P., and Ožbolt, J. (1992). "Compression failure of quasi-brittle material: Nonlocal microplane model." *J. of Engineering Mechanics*, ASCE 118(3), 540–556.

[27] Ožbolt, J., and Bažant, Z.P. (1992). "Microplane model for cyclic triaxial behavior of concrete." *J. of Engineering Mechanics*, ASCE 118(7), 1365–1386.

[28] Bažant, Z.P., and Cedolin, L. (1993). "Why direct tension specimens break flexing to the side." *J. of Struct. Engrg.*, ASCE, 119(4), 1101–1113.

[29] Bažant, Z.P., and Cedolin, L. (1992). "Why direct tension specimens flex and break at midlength." *Fracture Mechanics of Concrete Structures*, (Proc. Int. Conf. on Fracture Mechanics of Concrete Structures, Breckenridge, Colorado, June), ed. by Z.P. Bažant, Elsevier Applied Science, London, 443–448.

[30] Pijaudier-Cabot, G., Bažant, Z.P., and Benallal, A. (1992). "Localization limiting properties of nonlocal damage models." *Damage Mechanics and Localization* (Proc. Winter Annual Meeting of ASME, Anaheim, November), ed. by J.W. Ju and K. C. Valanis, Am. Soc. of Mech. Engrgs., New York, 125–134.

[31] Bažant, Z.P., and Gopalaratnam, V.S. (1992). "Fracture mechanics of concrete: An aperçu of basic concepts and models." *Fracture Mechanics of Concrete Structures*, (Proc. Int. Conf. on Fracture Mechanics of Concrete Structures, Breckenridge, Colorado, June), ed. by Z.P. Bažant, Elsevier Applied Science, London, 145-154.

[32] Bažant, Z.P., and Jirásek, M. (1992). "R-curve modeling of rate effect in static fracture and its interference with size effect." *Fracture Mechanics of Concrete Structures*, (Proc. Int. Conf. on Fracture Mechanics of Concrete Structures, Breckenridge, Colorado, June), ed. by Z.P. Bažant, Elsevier Applied Science, London, 918–923.

[33] Carol, I., Bažant, Z.P., Prat, P.C. (1992). "Microplane-type constitutive models for distributed damage and localized cracking in concrete structures." *Fracture Mechanics of Concrete Structures*, (Proc. Int. Conf. on Fracture Mechanics of Concrete Structures, Breckenridge, Colorado, June), ed. by Z.P. Bažant, Elsevier Applied Science, London, 299–304.

[34] Bažant, Z.P. (1992). "New concept of nonlocal continuum damage: crack influence function." *Macroscopic Behavior of Heterogenous Materials from the Microstructure* (Proc. Winter Annual Meeting of ASME, Anaheim, November), ed. by S. Torquato and D. Krajcinovic, Am. Soc. of Mech. Engrgs., New York, 153–160.

[35] Bažant, Z.P. (1991). "Fracture mechanics of quasi-brittle structures: Recent advances." (Proc., *11th International Conference on Structural Mechanics in Reactor Technology*, Tokyo, August), ed. by H. Shibata, Vol. H, Paper H04/1, pp. 97–107.

[36] Bažant, Z.P., and Kazemi, M.T. (1991). "Size dependence of concrete fracture energy determined by RILEM work-of-fracture method." *International J. of Fracture* 51, 121–138.

[37] Carol, I., Prat, P.C., and Bažant, Z.P. (1992). "New explicit microplane model

for concrete: Theoretical aspects and numerical implementation." *Int. J. Solids Structures* 29(9), 1173–1191.

[38] Bažant, Z.P., and Tabbara, M.R. (1992). "Bifurcation and stability of structures with interacting propagating cracks." *Int. J. of Fracture* 53, 273–289.

[39] Bažant, Z.P. (1991). "Why continuum damage is nonlocal: Micromechanics arguments." *Journal of Engineering Mechanics* ASCE 117(5), 1070–1087.

[40] Bažant, Z. P. and Kazemi, M. T. (1990). "Size effect in fracture of ceramics and its use to determine fracture energy and effective process zone length." *J. of American Ceramic Society* 73(7), 1841–1853.

[41] Bažant, Z.P., and Jirásek, M. (1993). "Effects of crack growth rate and creep in static fracture of concrete." Proc., *12th Int. Conf. on Struct. Mech. in Reactor Tech. (SMiRT)*, held at Stuttgart University, August, ed. by K. Kussmaul, Elsevier Science Publishers, Vol. A. Supplement, 175–180.

3. Papers Presented at Conferences and Seminars

3.1 Principal, Keynote or Distinguished Lectures

[1] Fracture and size effects in quasi-brittle structures, 2nd International Torroja Lecture (presented after being awarded the Gold Medal of the Building Research Institute of Spain), National Council for Scientific Research, Madrid, Spain, Jan. 21, 1991.

[2] Size effects of fracture and localization: aperçu of recent advances and their extension to simultaneous fatigue and rate sensitivity, Int. Conference on Fracture Processes in Brittle Disordered Materials (org. by J. van Mier), Noordwijk, the Netherlands, June 20, 1991.

[3] Fracture mechanics of concrete: an aperçu of basic conceptual models (co-author V.S. Gopalaratnam), First Int. Conference on Fracture Mechanics of Concrete Structures(FraMCoS 1), Breckenridge, Colorado, June 1, 1992.

[4] Fracture size effect and concrete design code (closing lecture), Comett "Fracture of Concrete", Madrid, Spain, November 27, 1992.

[5] Time-dependence on fracture and fatigue in concrete and rock, Medal Lecture (lecture in Czech, presented after the conferral of the Medal of Merit for Advances in Mechanics), Annual Meeting, Czech Society for Mechanics, held at Techn. Univ. Prague, February 1, 1993.

[6] Interaction of creep and fracture of concrete, Proc., *5th International RILEM Symposium (ConCreep 5)*, held at U.P.C., Barcelona, September 6, 1994.

3.2 Invited Conference Lectures

[7] Fracture mechanics of concrete, U.S.-Japan Workshop on Finite Element Analysis of Reinforced Concrete Structures (org. by C. Meyer), Columbia University, New York, June 3, 1991.

[8] Fracture mechanics of quasi-brittle structures: recent advances, 11th Int. Conference on Structural Mechanics in Reactor Technology (SMiRT 11), Keio Plaza Hotel, Tokyo, Aug. 20, 1991.

[9] Rate and size effects in concrete failure: implications for dams, Int. Conference on Dam Fracture, University of Colorado, Boulder, September 12, 1991.

[10] Microplane model for damage in concrete, Scandanavian Workshop on Materials Models for Fracture and Damage in CR.C. Structures, Hotel Actif, (org. by P. Bergan), Det Norske Veritas, Oslo, Norway, February 14, 1992.

[11] Fracture models for concrete and size effect, ibid, February 15, 1992.

[12] New concept of nonlocal continuum damage: Crack influence function, Symposium on Macroscopic Behavior of Heterogenous Materials from the Microstructure, 113th ASME Winter Annual Meeting, Hilton, Anaheim, California, November 12, 1992.

[13] Micromechanics-based continuum model for fracture of damaging materials (with M. Jirásek), Symposium on Material Mechanics, ASCE-ASME-SES Joint Mechanics Conference (MEET '93), University of Virginia, Charlottesville, VA, June 9, 1993.

3.3 Invited Colloquium Lectures and Seminars at Universities and Laboratories

[14] Size effect in failure of quasi-brittle structures, Polytecnic University of Catalonia, International Center of Numerical Methods in Engineering, Barcelona, Jan. 17, 1991.

[15] Nonlocal generalization of Weibull statistical theory of size effect in quasi-brittle structures, Dept. of Mechanics, Faculty of Mechanical Engineering, Technical University, Munich, Jan. 29, 1991.

[16] Micromechanics arguments for nonlocality of continuum damage, Institut für Werkstoffe im Bauwesen, Stuttgart University, Feb. 1, 1991.

[17] Recent advances in deterministic and statistical theories of size effect in structures with damage and localization (presented in French), Laboratory of Mechanics, E,N.S., Paris, Cachan, Feb. 7, 1991.

[18] Size effect in failure of quasi-brittle structures, Institute of Mechanics, Faculty of Civil Engineering, Technical University, Vienna, Austria, Feb. 13, 1991.

[19] Size effect in failure of quasi-brittle structures (presented in Czech), Czech Technical

University at Prague, Faculty of Civil Engineering, Czechoslovakia, Feb. 19, 1991.

[20] Size effects and brittle fracture of concrete and concrete structures, Special lecture at Institution of Structural Engineers, London, U.K., Feb. 21, 1991.

[21] Should fracture mechanics size effects be introduced into concrete design codes? Dept. of Civil and Mineral Engineering, University of Minnesota, Minneapolis, MN, March 1, 1991.

[22] Nonlocal statistical size effect in structures with large stable crack growth, Constructed Facilities Division Seminar, Dept. of Civil Engineering, MIT, Boston, March 21, 1991.

[23] Size effect in failure of structures exhibiting stable fracture growth, Materials and Structures Seminar, Dept. of Civil and Environmental Engineering, University of Western Michigan, Ann Arbor, MI, May 16, 1991.

[24] Size effect in failure of quasi-brittle structures, Faculty of Engineering Science Seminar Series, the University of Western Ontario, London, Ontario, Canada, May 17, 1991.

[25] Fracture mechanics of concrete structures and size effect, Dept. of Civil and Environmental Engineering, Politecnic University, New York, June 6, 1991.

[26] Fracture of brittle materials, guest lecture of Graduiertenkolleges, Institute for Structural Design and Construction, Suttgart University, Germany, June 25, 1991.

[27] Instabilities and bifurcations caused by localization of damage or fracture, Institute of Mechanics, Dept. of Mechanical Engineering, T.H. Darmstadt, July 8, 1991.

[28] Size effect in brittle failure of concrete structures, Shimizu Institute of Technology, Shimizu Corp., Tokyo, Aug. 21, 1991.

[29] Size effect in failure of quasi-brittle structures – energy release and nonlocal theory, National Chung-Hsing University, Tai-Chung, Taiwan, Aug. 23, 1991.

[30] Consequences of fracture mechanics for future design practice and codes for reinforced concrete structures, a lecture for practicing engineers sponsored by the Chinese Institute of Civil and Hydraulic Engineering and the Chinese Society of Structural Engineering, Dept. of Civil Engineering, National Taiwan University, Taipei, Aug. 26, 1991.

[31] Nonlocal generalization of Weibull statistical strength theory, Center for Earthquake Engineering Research, National Taiwan University, Taipei, Aug. 27, 1991.

[32] Should design codes consider fracture mechanics size effect? Korea Insitute of Construction Technology (co-sponsored by Korean Concrete Institute, KCI), Seoul, Korea, Aug. 29, 1991.

[33] Nonlocal generalization of Weibull statistical theory and nonlocal finite element codes, Structural Engineering Dept., Korea Atomic Energy Research Institute,

Taejun, Korea, Aug. 30, 1991.

[34] Critique and nonlocal generalization of Weibull-type random strength theories for quasi-brittle structures, Colloquia on Modern Topics in Mechanics, Northwestern University, October 18, 1991.

[35] Deterministic and statistical size effects and critique of Weibull-type theories of random strength, Solid Mechanics Seminar, Arizona State University, Tempe, November 1, 1991.

[36] Scaling laws and nonlocal concepts in mechanics of fracture and damage, Dept. of Mechanics, Technical University, Budapest, Hungary, August 31, 1992.

[37] Recent results on scaling laws for fracture and damage and nonlocal continuum models (presented in Czech), Institute of Theoretical and Applied Mechanics (UTAM), Prague, Czech Republic, September 3, 1992.

[38] Size effects in brittle failure of concrete and reinforced concrete structures, SEAOI (Structural Engineers Association of Illinois) Dinner Meeting, Chicago, November 3, 1992.

[39] New nonlocal damage concept based on micromechanics of crack interactions, University of Southern California, Los Angeles, November 10, 1992.

[40] Scaling laws and nonlocal concepts for mechanics of damage, Rensselaer Polytechic Institute, Troy, NY, January 14, 1993.

[41-45] Stability, localization and scaling problems in the theory of damage and fracture, Series of five seminars, Politecnico di Milano, Italy, February 2, 4, 9, and 12, 1993.

[46] Scaling laws, nonlocal concepts and micromechanics of quasibrittle materials, Universita di Pavia, Italy, February 11, 1993.

[47] Stability, localization and scaling problems in the theory of damage and fracture (presented in French), Dept. of Civil Engineering, INSA, Lyon, France, February 17, 1993.

[48] Scaling laws and nonlocal concepts for mechanics of damage, M.I.T., Cambridge, MA, March 17, 1993.

[49] Scaling laws and nonlocal concepts in mechanics of damage and fracture (presented in French), Ecole Polytechnique, Montreal, Quebec, Canada, April 29, 1993.

[50] Scaling laws and nonlocal concepts in mechanics of quasibrittle materials (presented in French), University of Sherbrooke, Quebec, Canada, May 5, 1993.

3.4 Contribtued Conference Lectures

[51] Fracture mechanics size effect in concrete structures, 9th Structures Congress ASCE, Indianapolis, IN, April 29, 1991.

[52] Nonlocality of continuum approximation of microcracked materials, ASCE Engineering Mechanics Specialty Conference on Mechanics Computing in 1990's and Beyond, Columbus, OH, May 21, 1991.

[53] Numerical analysis of fracture and damage localization (co-authored by G. Gioia and S. Beissel), 1st U.S. National Congress on Computational Mechanics, Hyatt Regency, Chicago, July 22, 1991.

[54] Nonlocal generalization of Weibull theory for random strength of concrete structures (co-authored by Y. Xi), 11th Int. Conference on Structural Mechanics in Reactor Technology (SMiRT I), Tokyo, Aug. 20, 1991.

[55] Symmetry breaking bifurcations in strain sofening damage: Tensile buckling and shear bending (co-authors: L. Cedolin and J. Ožbolt), 28th Annual Meeting, Society of Engineering Science, University of Florida, Gainesville, November 6, 1991.

[56] Nonlinear analysis of strain-softening damage under monotonic and cyclic load (co-authors J. Ožbolt and R. Eligehausen), 9th Engineering Mechanics Conferences of ASCE, Texas A & M University, College Station, Texas, May 26, 1992.

[57] Markov model for random growth of crack with R-curve (co-author Y. Xi), First Int. Conference on Fracture Mechanics of Concrete Structures (FraMCoS 1), Breckenridge, Colorado, June 1, 1992.

[58] Microplane-type constitutive models for distributed damage and localized cracking in concrete structures (presented by co-author I. Carol), ibid, June 3, 1992.

[59] Size effect in strength of reinforced concrete columns (co-author Y.-W. Kwon), ibid, June 4, 1992.

[60] Instabilities and bifurcations due to strain-softening damage and fracture (co-authors L. Cedolin and J. Ožbolt), 18th Int. Congress of Theoretical and Applied Mechanics, Haifa, Israel, August 25, 1992.

[61] Size effect due to fracture behavior and its impact on design code, ACI Fall Convention, San Juan, Puerto Rico, October 29, 1992.

[62] Discrete element modeling of fracture and size effect in quasibrittle materials (with M. Jirásek), Second Int. Conference on Discrete Element Methods (DEM), M.I.T., Cambridge, MA, March 18, 1993.

[63] Fracture of random quasibrittle materials: Markov process and Weibull-type models (with Y. Xi), 6th International Conference on Structural Safety and Reliability (ICOSSAR), Innsbruck, Austria, August 11, 1993.

Appendix 1.

Copies of Transparencies from a Lecture Explaining the Principal Accomplishment

(Section III-1, Ref. [1], [2], [34])

CONTINUUM MODEL FOR DAMAGE LOCALIZATION IN SOLIDS WITH INTERACTING MICROCRACKS

OUTLINE

1. Historical Overview, Problem Statement
2. New Nonlocal Model Based on Crack Interactions
3. Properties of Smoothed Crack Influence Function
4. Localization in a Layer
5. Size Effect and Applications in Finite Element Analysis with Microplane Model

STRAIN-SOFTENING

OBSERVATIONS

Acoustic emissions

Distributed cracking:

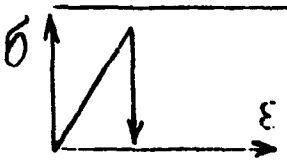

Rashid 1967

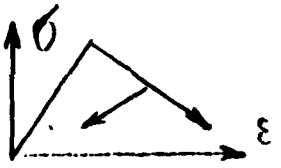

Scanlan 1972

1973

At first — controversial ... dismissed for violation of Drucker's postulate, Hadamard's condition (wave velocity real)

PROBLEMS:

— Mesh objectivity (spurious mesh sensitivity)

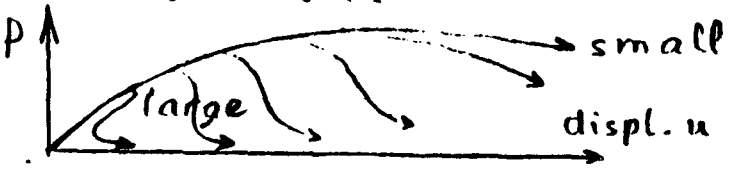

— Energy dissipation converges to zero

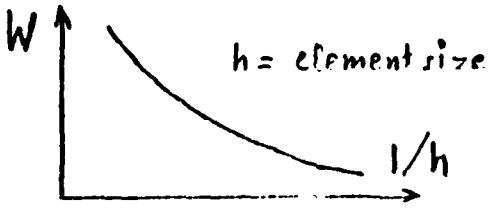

— Spurious localization of damage to a zero volume

— Loss of ellipticity of static problem
" hyperbolicity of wave problem

Same kind of problem occurs for: Nonassociated flow rule (lack of normality)

a) **False remedy** (sidetracking the problem)
— continuum damage mechanics

$\sigma = (1 - \omega)\, T$
$T = f(\varepsilon)$
"true" stress

ω 

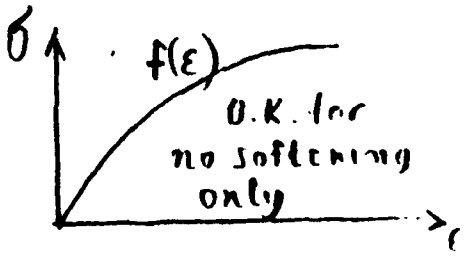

b) **Partial remedy:** Regularization by means of
VISCOSITY (artificial or real)
— does not work asymptotically
for $t \to \infty$

c) The only **general remedy**
— some type of **NONLOCAL** concept

1. Limit the crack band width, h_{min} (or element size)

... crack band model
1976, 1979, 1983

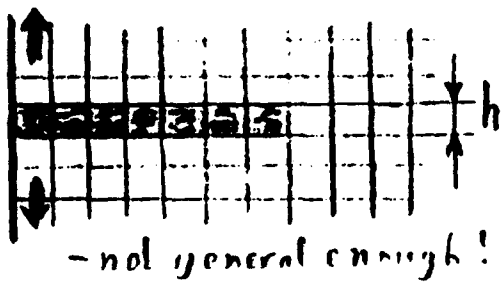

2. Nonlocal continuum damage
1984, 1987

a) Averaging model (1984) (Nonlocal integral)
b) Gradient models (micropolar plasticity, etc.)
— related (result of Taylor series expansion)

Physical Justification of Nonlocality?

— microcracks - but how?
— inclusions, grains? - No

CURRENT STATUS OF MICROMECHANICS OF SOFTENING DAMAGE DUE TO MICROCRACKING OF MATERIALS

Stage 1. Effective (*Secant*) Elastic Moduli of Microcracked Solid

– easier, nearly all the studies have so far been limited to this (see e.g. a review by M. Kachanov, Appl. Mech. Rev. 45(8), 1992, 304-335), but is less important.

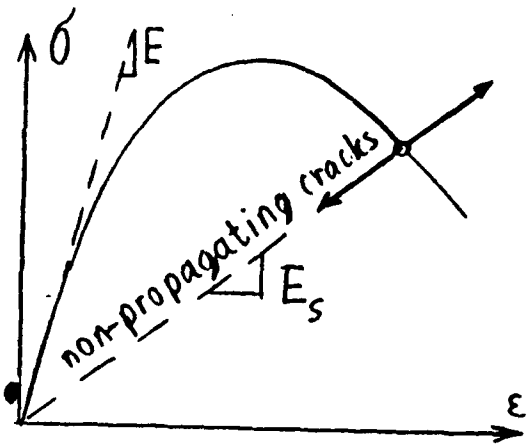

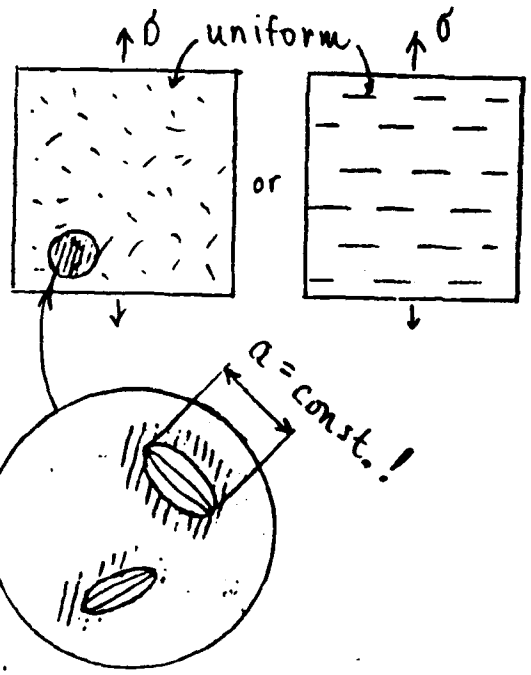

TOPICS STUDIED:

Crack density tensor – anisotropy due to cracks – crack friction and slip – fluid-filled cracks – interacting but statistically uniformly distributed cracks (no localization) – (secant) elastic moduli with or without crack interactions – self-consistent method, Mori-Tanaka method, method of effective field – differential scheme – periodic crack arrays of various geometries, with shielding and amplification configurations – variational bounds on effective moduli.

ASSUMED THAT:

1. Cracks do not propagate during deformation increment.
2. Cracks remain statistically uniform on the macroscale.

LIMITATION:

– This can yield only the secant moduli E_s (but one needs mainly the tangent moduli E_t).

Stage 2. Tangent Elastic Moduli at *Propagating* Microcracks

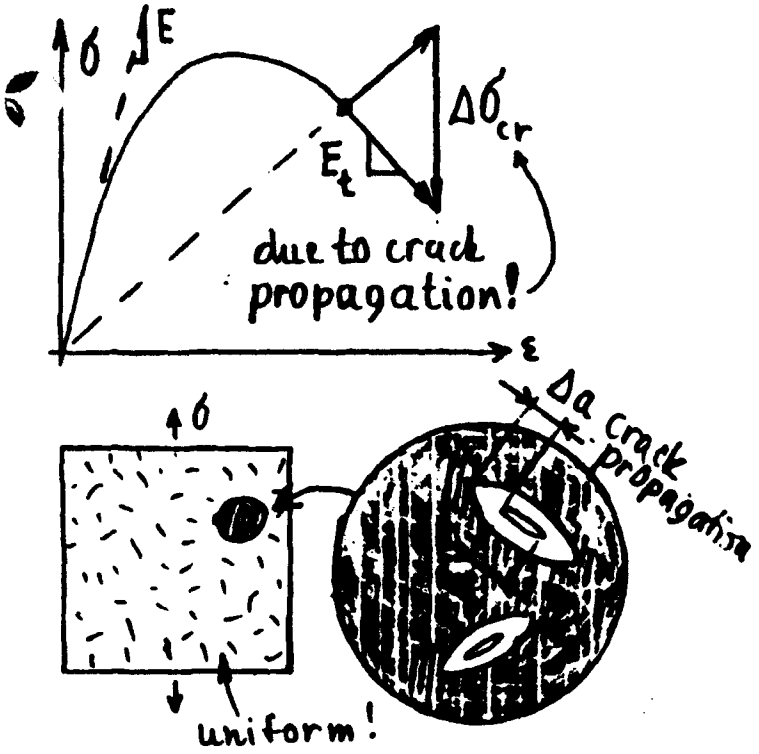

- hardier, studied very little but is much more important.

ASSUMED:
Cracks do not localize due to crack interactions.

- yields only the local moduli, without the effect of crack interactions.

Stage 3. Tangent Stiffness at Propagating Interacting Microcracks with Localization

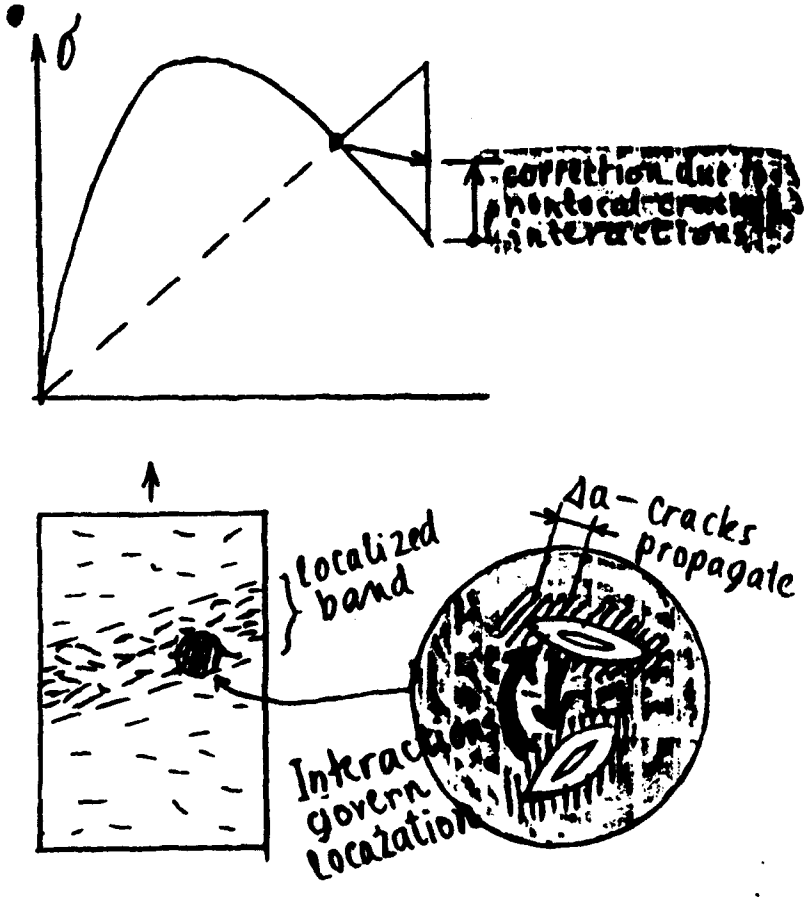

- very hard, not studied so far
but required for realistic solution!

Interactions of propagating cracks cause a change of stiffness from its local value to a certain nonlocal value governing localization of cracking.

LOCAL AND NONLOCAL MACROSCOPIC STRESS-STRAIN RELATIONS

a) Local form:

$$\Delta\sigma = E : (\Delta\epsilon - \Delta\epsilon'') = E : \Delta\epsilon - \Delta S \qquad (1)$$

$$\Delta\sigma = E : \Delta\epsilon - \Delta S \qquad (2)$$

where ΔS = inelastic stress increment tensor

b) Previous nonlocal damage model (Pijaudier-Cabot & Bažant):

$$\Delta\sigma = E : \Delta\epsilon - \Delta\bar{S} \qquad (3)$$

$\Delta\bar{S}$ is the nonlocal inelastic stress increment, defined by spatial averaging:

$$\boxed{\Delta\bar{S}(x) = \int_V \alpha(x,\xi)\Delta S(\xi)\, \mathrm{d}V(\xi)} \qquad (4)$$

$$\int_V \alpha(x,\xi)\, \mathrm{d}V(\xi) = 1 \qquad (5)$$

kernel $\alpha(x,\xi)$ = nonlocal weight function of mean 1 (normalized).

NONLOCALITY CAUSED BY INTERACTION OF GROWING MICROCRACKS: Two substeps:

I. Cracks frozen, stresses due to loads solved.

II. Cracks unfrozen, stresses due to crack tractions solved.

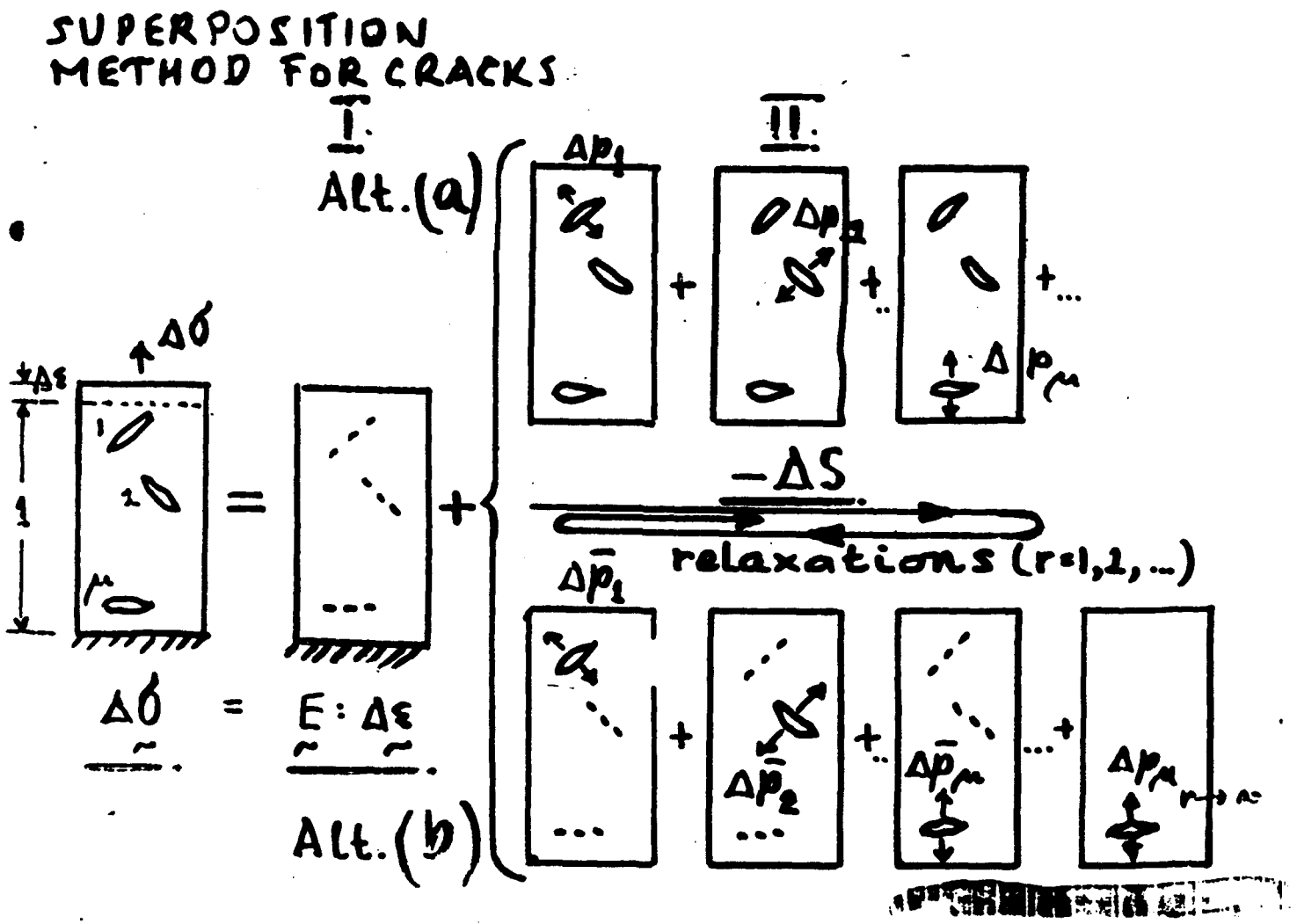

Normal surface traction due to unfreezing of a crack:

$$\Delta p_\mu = n_\mu \Delta S_\mu n_\mu \qquad (6)$$

Superposition method (Collins 1963, Datsyshin and Savruk 1973, Gross 1982, Chudnovsky and Kachanov 1983, Chudnovsky et al. 1987, Chen 1984, and Horii and Nemat-Nasser 1985)—Kachanov's (1987) simplification:

$$\boxed{\Delta \bar{p}_\mu = \langle \Delta p_\mu \rangle + \sum_{\nu=1}^{N} \Lambda_{\mu\nu} \Delta \bar{p}_\nu} \qquad \nu = 1, \ldots N \qquad (7)$$

in which $\langle .. \rangle$ = averaging operator over crack surface; $\Lambda_{\mu\nu}$ = crack influence coefficients.

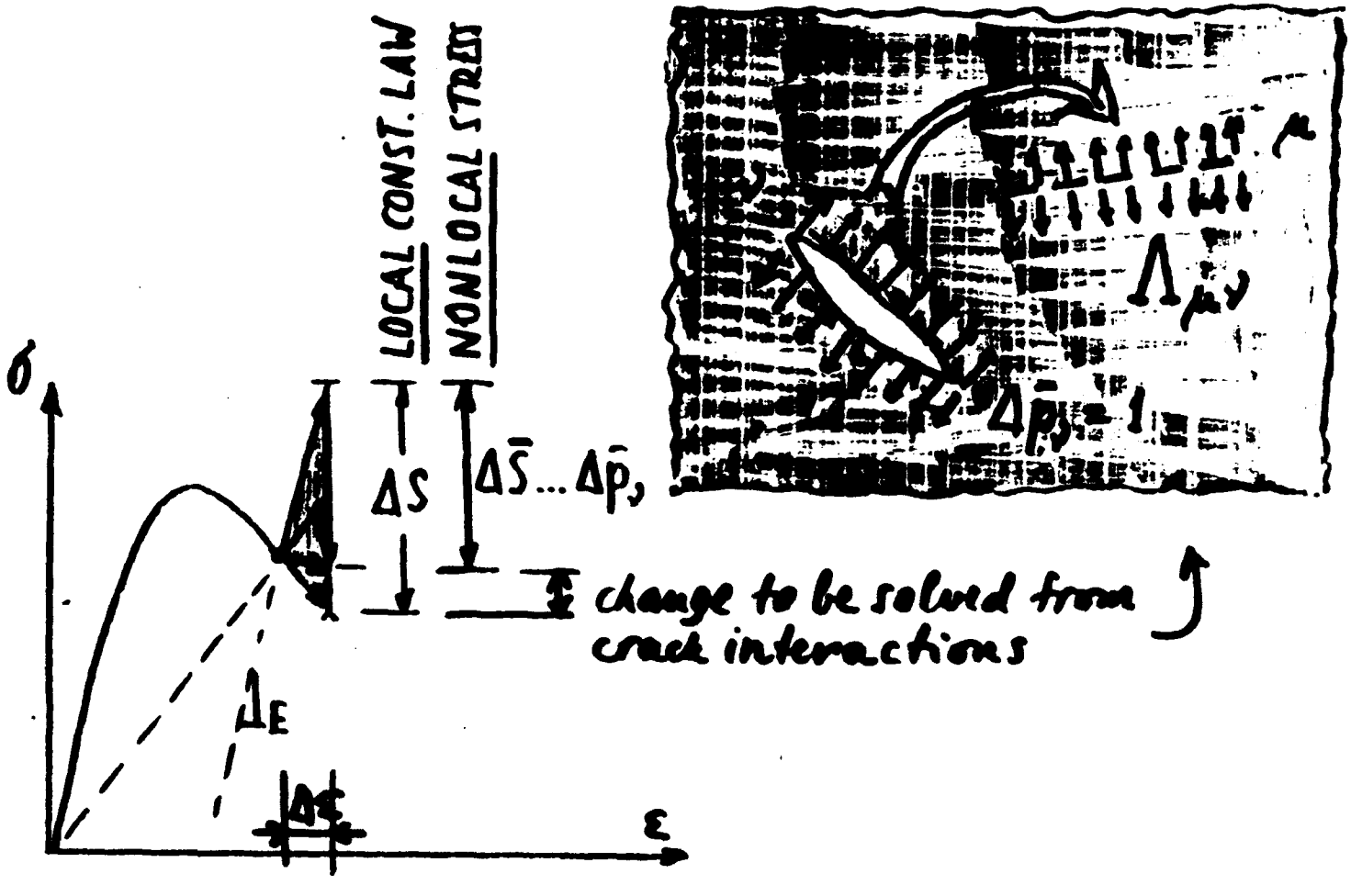

Simplifying hypothesis: Consider at each point only the dominant microcrack orientation, coinciding with the maximum principal inelastic macro-stress $\Delta\overline{S}^{(1)}$ (i.e., Mode I). Denote:

$$\Delta\overline{S}_{\mu}^{(1)} = \Delta(n_{\mu}\overline{S}_{\mu}n_{\mu}) = [n_{\mu}\overline{S}_{\mu}n_{\mu}]_{\text{new}} - [n_{\mu}\overline{S}_{\mu}n_{\mu}]_{\text{old}} \quad (8)$$

In terms of macro-stresses:

$$\boxed{\Delta\overline{S}_{\mu}^{(1)} - \sum_{\nu=1}^{N}\Lambda_{\mu\nu}\Delta\overline{S}_{\nu}^{(1)} = \langle\Delta S_{\mu}^{(1)}\rangle} \quad (9)$$

① ②

NONLOCAL CON TINUUM—Fredholm integral equation:

$$\boxed{\Delta\bar{S}^{(1)}(x) - \underbrace{\int_V \Lambda(x,\xi)\Delta\bar{S}^{(1)}(\xi)\mathrm{d}V(\xi)}_{①} = \underbrace{\langle\Delta S^{(1)}(x)\rangle}_{②}} \quad (10)$$

where : $\langle\Delta S^{(1)}(x)\rangle = \int_V \Delta S^{(1)}(\xi)\alpha(x,\xi)\mathrm{d}V(\xi)$ (11)

$\Lambda(x_\mu, \xi_\nu)$ = crack influence function.

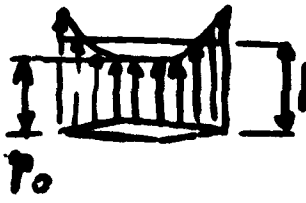

.... coupled with stiffness equations (equil.) of FEM

① ⟨... ⟩ Short-range averaging, with weights $\int \alpha\, dV = 1$

② New - Long-range crack interactions, $\int \Lambda\, dV = 0$

- Directional, tensorial

Note:- The continuum is not obtained by homogenization.

Rather: Seek continuum equation whose discrete form is the matrix crack interaction equation

- The constitutive law is only LOCAL !

Gauss-Seidel Iteration Method (discrete):

$$\underbrace{\Delta\bar{S}_\mu^{(1)[r+1]}}_{(r+1)^{st}} = \langle \Delta S_\mu^{(1)} \rangle + \sum_{\nu=1}^{N} \Lambda_{\mu\nu} \underbrace{\Delta\bar{S}_\nu^{(1)[r]}}_{r^{th}\ \text{iteration}} \quad (\mu = 1, 2, \ldots N) \tag{14}$$

$\langle \Delta S_\mu^{(1)} \rangle$: LOCAL (fixed)

Method of successive approximations (continuum):

$$\underbrace{\Delta\bar{S}^{(1)}(x)}_{\text{new}} \leftarrow \langle \Delta S^{(1)}(x) \rangle + \int_V \Lambda(x,\xi) \underbrace{\Delta\bar{S}^{(1)}(\xi)}_{\text{old}}\, dV(\xi) \tag{15}$$

IDEA: Combine it with the iterations in each load step of a finite element code.

Alternative Forms:

Define: $\{\langle S_\mu \rangle\} = [\alpha_{\mu\nu}]\{S_\nu\}$ (averaging)

$$\{\Delta\bar{S}_\mu^{(1)}\} = [C_{\mu\nu}]\{\Delta S_\nu^{(1)}\}$$

where $[C_{\mu\nu}] = [\delta_{\mu\lambda} - \Lambda_{\mu\lambda}]^{-1}[\alpha_{\lambda\nu}]$

Continuum counterpart:

$$\Delta\bar{S}^{(1)}(\underset{\sim}{x}) = \int_V C(\underset{\sim}{x}, \underset{\sim}{\xi})\, \Delta S^{(1)}(\underset{\sim}{\xi})\, dV(\underset{\sim}{\xi})$$

CRACK INFLUENCE FUNCTION $\Lambda(\underset{\sim}{x}, \underset{\sim}{\xi})$

- statistical concept

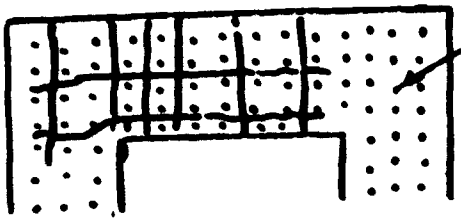

numerical integration points of finite elements
— sampling points for the cracks

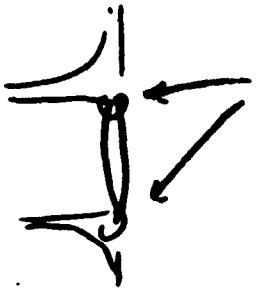

crack tips or microcracks cannot be distinguished

Locally statistically homogeneous field of cracks

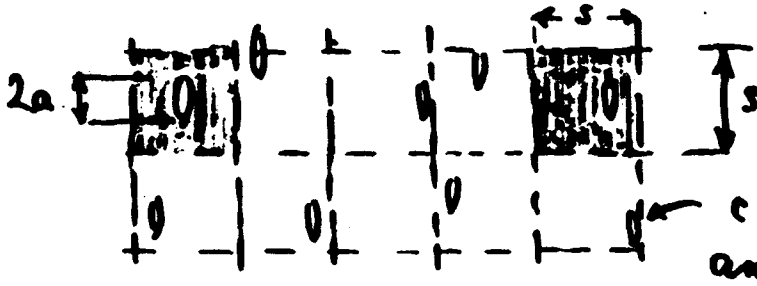

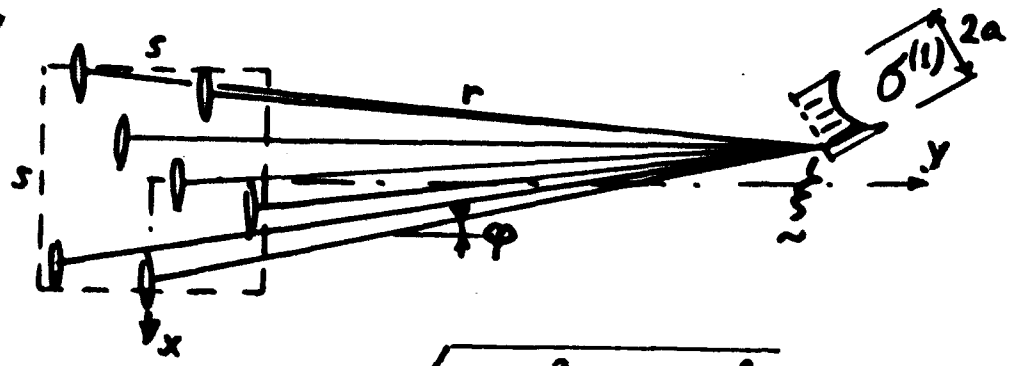

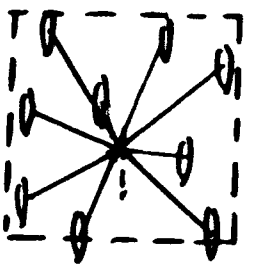

$$r = \sqrt{(x-\xi)^2 + (y-\eta)^2} \qquad \varphi = \arctan\frac{y-\eta}{x-\xi} \qquad \vec{r} = (\vec{\xi} - \vec{x})$$

$$A(\underset{\sim}{0}, \underset{\sim}{\xi}) = \left\langle E\left[\sigma^{(1)}(\xi_1 - x_1, \xi_2 - x_2)\right]\right\rangle$$

average over length $2a$ of target crack

math. expectation — center of source crack lies anywhere in cell $s \times s$

$$= \frac{1}{2a}\int_{-a}^{a} \frac{1}{s^2}\int_{-s/2}^{s/2}\int_{-s/2}^{s/2} \sigma^{(1)}(\xi_1 - x_1, \xi_2 - x_2)\, dx_1 dx_2\, da'$$

Westergaard's solution (for crack pressure $\sigma = 1$ in inf. body)

Complex potential: $Z = \dfrac{z}{\sqrt{z^2 - a^2}} \qquad z = re^{i\varphi}$

$$\sigma_{xx} = \operatorname{Re} Z - y \operatorname{Im}\frac{dZ}{dz} - 1$$

$$\sigma_{yy} = \operatorname{Re} Z + y \operatorname{Im}\frac{dZ}{dz} - 1$$

$$\tau_{xy} = y \operatorname{Re}\frac{dZ}{dz}$$

Kernel: CRACK INFLUENCE FUNCTION $\Lambda(\underset{\sim}{\xi}, \underset{\sim}{x})$

- directional (anisotropic), with amplification and shielding sectors
- tensorial

2D

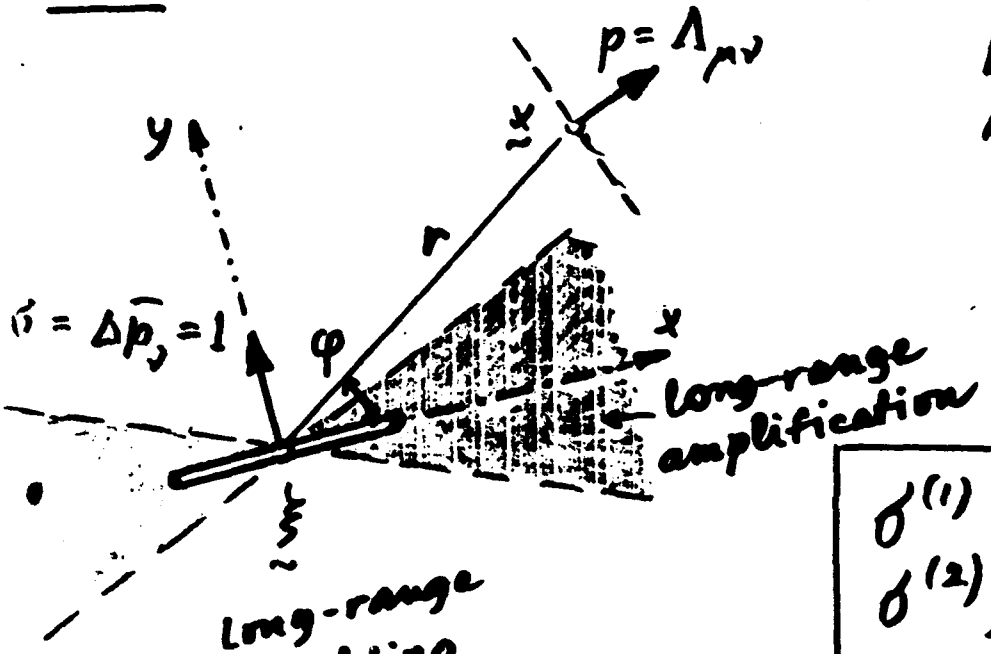

Long-Range Asymptotic Field

At x:

$$\left.\begin{matrix}\sigma^{(1)} \\ \sigma^{(2)}\end{matrix}\right\} = \sigma k(r)\left(\frac{\cos 2\varphi}{2} \pm \sin\varphi\right)$$

$$\tan 2\varphi^{(1)} = -\cot 3\varphi$$

Distinguish ① ② ③

$$k(r) = r^{-2}$$

① Macro-Mode I

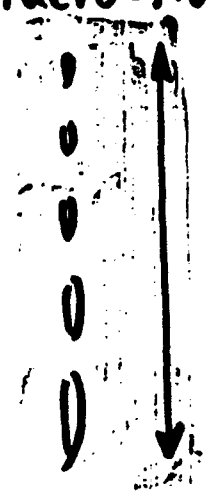

Amplification sector → long distance interaction

② Macro-Mode II, III
— weaker distance interaction

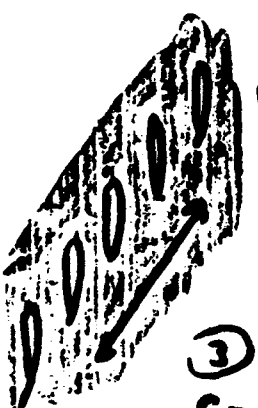

③ Compression Splitting: Shielding sector → short distance interaction only

CRACK INFLUENCE FUNCTION IN TWO DIMENSIONS:

separated form

$$\Lambda(\underset{\sim}{x},\underset{\sim}{\xi}) = -\frac{k(r)}{2\ell^2}\left[\cos 2\theta + \cos 2\psi + \cos 2(\theta+\psi)\right] \quad (16)$$

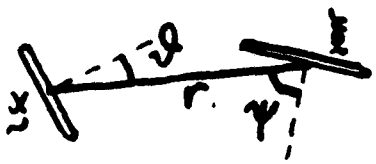

where $$k(r) = \left(\frac{\kappa \ell r}{r^2+\ell^2}\right)^2 \quad (17)$$

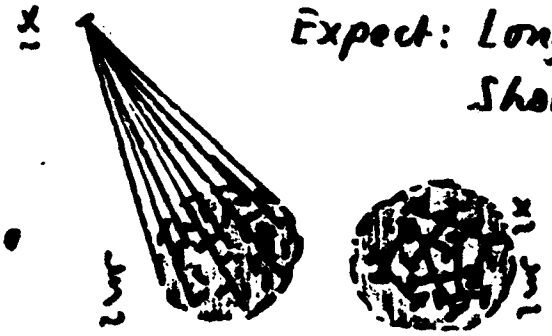

Expect: Long-range interactions will be preserved
Short-range interactions will cancel each other

$k(r) \sim r^{-2}$ ... asymptote for $r \gg \ell$

$k(r) = 0$ ... asymptote for $r \ll \ell$

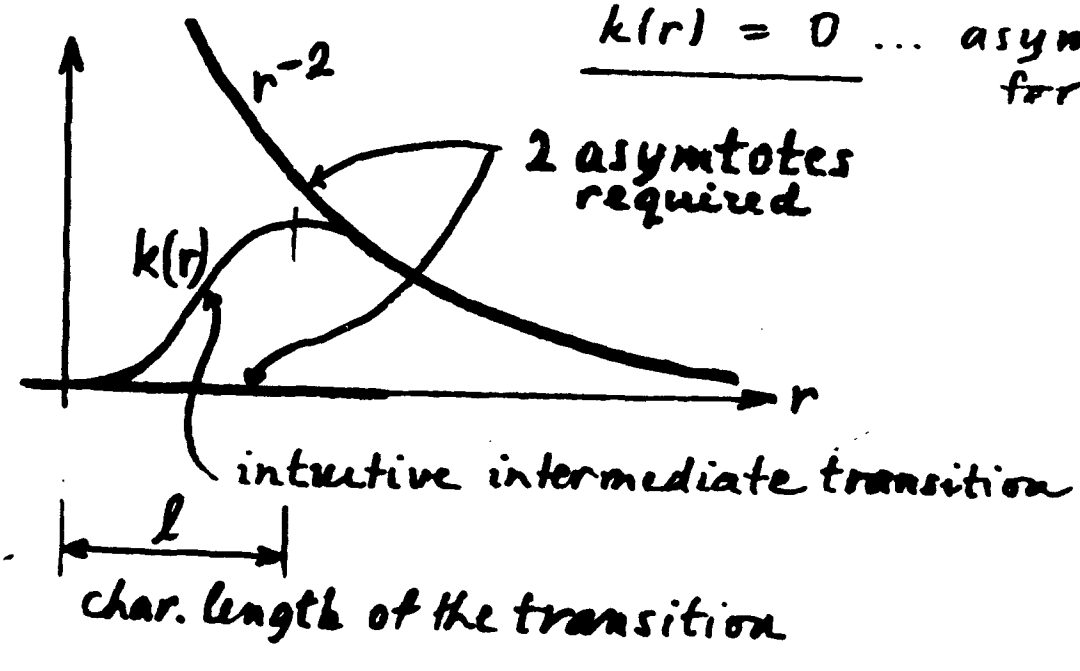

3D-Stress Field of a Penny-Shaped Crack

(after Fabrikant)

$$\sigma_{xx} = \frac{\sigma_1 + \mathrm{Re}\,\sigma_2}{2}, \qquad \sigma_{yy} = \frac{\sigma_1 - \mathrm{Re}\,\sigma_2}{2}, \qquad \tau_{xy} = \frac{\mathrm{Im}\,\sigma_2}{2}$$

$$\tau_{xz} = \mathrm{Re}\,\tau_z, \qquad \tau_{yz} = \mathrm{Im}\,\tau_z$$

$$\sigma_z = \frac{2\sigma}{\pi}(B - D), \qquad \sigma_1 = \frac{2\sigma}{\pi}[(1+2\nu)B + D]$$

$$\sigma_2 = e^{2i\phi}\,\frac{2\sigma}{\pi}\,\frac{a l_1^2 l_3}{l_2^2 l_4^2}\left(1 - 2\nu + \frac{z^2[a^2(6l_2^2 - 2l_1^2 + \rho^2) - 5l_2^4]}{l_4^4 l_3^2}\right)$$

$$\tau_z = -e^{i\phi}\,\frac{2\sigma}{\pi}\,\frac{z l_1[a^2(4l_2^2 - 5\rho^2) + l_1^4]l_3}{l_2 l_4^6}$$

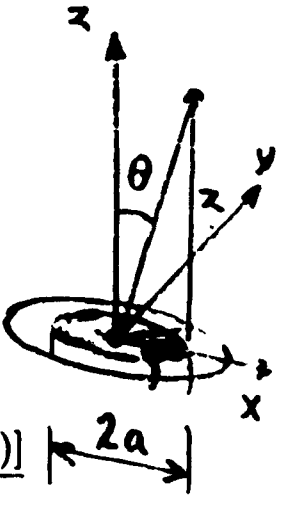

$$B = \frac{a l_3}{l_4^2} - \arcsin\frac{a}{l_2}, \qquad D = \frac{a z^2[l_1^4 + a^2(2a^2 + 2z^2 - 3\rho^2)]}{l_4^6 l_3}$$

$$l_1 = \frac{L_2 - L_1}{2}, \qquad l_2 = \frac{L_2 + L_1}{2}, \qquad l_3 = \sqrt{l_2^2 - a^2}, \qquad l_4 = \sqrt{l_2^2 - l_1^2}$$

$$L_1 = \sqrt{(a-\rho)^2 + z^2}, \qquad L_2 = \sqrt{(a+\rho)^2 + z^2}$$

LONG-RANGE ASYMPTOTIC FIELD

$$\sigma_{\rho\rho} = \sigma k(r)\left[(1+2\nu)\left(\sin^2\theta - \frac{2}{3}\right) + (1 - 2\nu - 5\cos^2\theta)\sin^2\theta\right]$$

$$\sigma_{\phi\phi} = \sigma k(r)\left[(1+2\nu)\left(\sin^2\theta - \frac{2}{3}\right) - (1 - 2\nu - 5\cos^2\theta)\sin^2\theta\right]$$

$$\sigma_{zz} = \sigma k(r)\left(\sin^2\theta - \frac{2}{3}\right)$$

$$\sigma_{\rho z} = -\sigma k(r)\sin 2\theta\,(4 - 5\sin^2\theta), \qquad \sigma_{\rho\phi} = \sigma_{\phi z} = 0$$

$k(r) = a^3/(\pi r^3)$

→ replace by:

(same asymptotic form, but usable for close range)

$$k(r) = \frac{1}{\pi}\left(\frac{\kappa l r}{r^2 + l^2}\right)^3$$

For cracking in all directions:

k l refer to I J cartesian coordinates

$$\Delta\overline{S}_{IJ}(x) \leftarrow \langle \Delta S_{IJ}(x) \rangle + \int_V \sum_{i=1}^{3} R^{(i)}_{IJkl}(\xi) L^{(i)}_{kl}(x,\xi) \Delta\overline{S}^{(i)}(\xi) \mathrm{d}V(\xi) \quad (12)$$

Admissibility of uniform stress fields requires (for 2D):

$$\int_V^{\odot} \Lambda(x,\xi)\mathrm{d}V(\xi) = \lim_{R\to\infty} \int_0^R \left(\int_0^{2\pi} \Lambda(x,\xi) r \mathrm{d}\phi \right) \mathrm{d}r = 0 \quad (13)$$

first angular then radial integration path

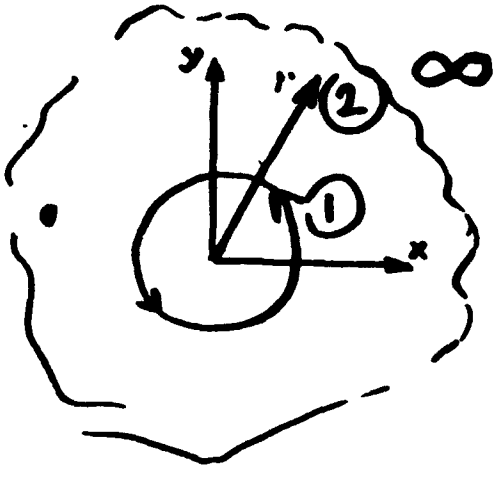

Consequence:

Softening damage cannot be made to increase uniformly over an infinite body (by mechanical means). It must localize!

NEW NONLOCAL DAMAGE CONCEPT: MICROMECHANICS OF CRACK INTERACTIONS

1. Macroscopically nonuniform (statistically nonhomogeneous) system of interacting and growing microcracks- Kachanov's simplification of superposition method.

2. Continuum counterpart: Fredholm integral equation for nonlocal inelastic stress increments, with two integrals.

   - Saint-Venant principle: short-range averaging.
   - Kernel = long-range crack influence function: 1) zero mean, 2) second-rank tensor, 3) directional dependence, 3) shielding and amplification sectors.
   - Long range decay as r^{-2} in 2D, r^{-3} in 3D; ∞–space: uniform cracking is nonintegrable!

3. Gauss-Seidel iteration: Nonlocal inelastic stress increments in finite element code solved by iterations in load steps.

4. Constitutive law *local* → no problem with unloading criterion and continuity condition!

5. Localization into a band within a layer: 1) bifurcates well before load-deflection peak, 2) load-deflection peak occurs before stress-strain peak.

6. Nonlocal microplane analysis of fractures dominated by: mode I, shear & compression—*same* characteristic length.

Appendix 2.

Reprints of Selected Publications

AFOSR Project on Micromechanics of Nonlocal Damage

ASCE Journal of Engineering Mechanics 120 (1994), No.3 (March)—in press.

NONLOCAL DAMAGE CONCEPT BASED ON MICROMECHANICS OF CRACK INTERACTIONS

ZDENĚK P. BAŽANT

Walter P. Murphy Professor of Civil Engineering

Report No. 92-7/C457n

Department of Civil Engineering

Northwestern University

Evanston, Illinois 60208, USA

July 17, 1992

Revised April 28, 1993

NONLOCAL DAMAGE CONCEPT BASED ON MICROMECHANICS OF CRACK INTERACTIONS

ZDENĚK P. BAŽANT[1], FELLOW, ASCE

ABSTRACT: A nonlocal continuum model for strain-softening damage is derived by micromechanics analysis of a macroscopically nonhomogeneous (nonuniform) system of interacting and growing microcracks, using Kachanov's simplified version of the superposition method. The continuum model is obtained by seeking a continuum field equation whose possible discrete approximation coincides with the matrix equation governing a system of interacting microcracks. The result is a Fredholm integral equation for the unknown nonlocal inelastic stress increments, which involves two spatial integrals. One integral, which ensues from the fact that crack interactions are governed by the average stress over the crack length rather than the crack center stress, represents short-range averaging of inelastic macro-stresses. The kernel of the second integral is the long-range crack influence function which is a second-rank tensor and varies with directional angle (i.e., is anisotropic), exhibiting sectors of shielding and amplification. For long distances r, the weight function decays as r^{-2} in two dimensions and as r^{-3} in three dimensions. Application of the Gauss-Seidel iteration method, which can conveniently be combined with iterations in each loading step of a nonlinear finite element code, simplifies the handling of the nonlocality by allowing the nonlocal inelastic stress increments to be calculated from the local ones explicitly. This involves evaluation of an integral containing the crack influence function, for which closed-form expressions are derived. Because the constitutive law is strictly local, no difficulties arise with the unloading criterion or the continuity condition of plasticity.

INTRODUCTION

The nonlocal continuum—a concept introduced in elasticity by Eringen (1965, 1966), Kröner (1967) and others (see Bažant, 1986)—is a continuum in which the stress at a given point depends not only on the strain at that point but on the deformation of a certain neighborhood. As is now generally accepted, finite element analysis of distributed strain-softening damage, including its final localization into sharp fracture, requires the use of some type of nonlocal continuum (Bažant, 1984; Bažant, Belytschko and Chang, 1984; Bažant, 1986). An effective type is the nonlocal damage concept, in which the local damage or fracturing strain figuring in the incremental stress-strain relation is replaced by its spatial average (Pijaudier-Cabot and Bažant, 1987; Bažant and Pijaudier Cabot, 1988; Bažant and Lin, 1988a,b; Bažant and Ožbolt, 1990, 1992a, 1992b).

[1]Walter P. Murphy Professor of Civil Engineering, Northwestern University, Evanston, Illinois 60208

The argument for the nonlocal damage concept has been mainly computational—the need to limit localization of strain-softening damage to zones of nonzero volume. The physical explanation, on the other hand, has been mainly phenomenologic and empirical. Intuitively, it has been expected that the main source of nonlocality must be the interactions among adjacent microcracks. Certain micromechanics arguments based on a system of microcracks have been shown to lead to the nonlocal damage concept (Bažant, 1987, 1991). However, interpretation of these arguments for the purpose of finite element analysis has not been clear. The interactions among the microcracks with simultaneous crack growth during the loading steps have not been taken into account, and the form of the spatial integral characterizing the nonlocal continuum has not been physically justified. The crack interactions have recently been analyzed by Pijaudier-Cabot and Bažant (1991), and Bažant and Tabbara (1992). However, the problem of determining the nonlocal continuum approximation has not been addressed in that context. It will be in this paper (the contents of which have been summarized at a recent conference; Bažant1992).

A special case of nonlocal continuum models for strain softening, which will not be studied here, are the gradient models, which can be obtained from a Taylor series expansion of the nonlocal spatial integral (Bažant, 1984). Much attention has recently been devoted to gradient-dependent plasticity of micropolar (or Cosserat) type (de Borst, 1990, 1991; de Borst and Sluys, 1991; Mühlhaus and Aifantis, 1991; Vardoulakis, 1989; Sluys, 1992; and Dietsche and Willam, 1992). These models, however, have so far been justified by the need to regularize the boundary value problem, while a physical justification from micromechanics is still lacking. Some microstructural physical arguments for micropolarity have been offered for sand, but they have been vague and inconclusive.

Important contributions to micromechanics of cracking and damage have been made by Kachanov (1985, 1990), Chudnovsky et al. (1987), Ju and Lee (1991), Lee and Ju (1991), Ju (1990, 1991), Krajcinovic and Fonseka (1981), Benveniste et al. (1989) and others; see also the review in Bažant (1986). Most studies have so far been limited to the special problem of determining the effective elastic moduli of randomly microcracked solids that are on the macroscale in a statistically homogeneous state (for an excellent review, see Kachanov, 1992). For this special problem, it has been possible to apply the homogenization methods for composites, such as Hill's self-consistent model, methods of periodic cells, methods of composite cylinders or composite spheres, variationally-based bounds such as Hashin-Shtrickman bounds, statistical models for macro-homogeneous crack arrays, etc.

However, homogenization is not the principal, most difficult issue. Rather, it is the continuum smearing of damage that is spatially nonuniform (statistically nonhomogeneous). The smearing must preserve the essential interactions of cracks or other micro-defects that govern localization

of strain. This issue cannot be handled by homogenization methods because they apply only to macroscopically uniform fields. A different type of continuum model is required to handle localization. Such a model will be proposed in this paper.

Numerical studies with a finite element program are beyond the scope of this paper, but are already in progress (in collaboration with J. Ożbolt, using the microplane constitutive law). The results indicate that structural failures dominated by tension, shear or compression can all be modeled using the same nonlocal material characteristics, especially the same characteristic length. This has not been possible with the previous nonlocal models.

LOCAL AND NONLOCAL MACROSCOPIC STRESS-STRAIN RELATIONS

Finite element analysis of inelastic solids is generally carried out in small loading steps. For each of them the local constitutive law may be written in the incremental form

$$\Delta\boldsymbol{\sigma} = \boldsymbol{E} : (\Delta\boldsymbol{\epsilon} - \Delta\boldsymbol{\epsilon}'') = \boldsymbol{E} : \Delta\boldsymbol{\epsilon} - \Delta\boldsymbol{S} \tag{1}$$

Here $\Delta\boldsymbol{\sigma}, \Delta\boldsymbol{\epsilon}$ = increments of the stress and strain tensors, $\boldsymbol{E}$ = fourth-rank tensor of elastic moduli of uncracked material, $\Delta\boldsymbol{\epsilon}''$ = inelastic strain increment tensor, and $\Delta\boldsymbol{S}$ = inelastic stress increment tensor. In a nonlocal continuum formulation, Eq. (1) is replaced by

$$\Delta\boldsymbol{\sigma} = \boldsymbol{E} : \Delta\boldsymbol{\epsilon} - \Delta\overline{\boldsymbol{S}} \tag{2}$$

$\Delta\overline{\boldsymbol{S}}$ is the nonlocal inelastic stress increment tensor, which has been defined in recent works by the spatial averaging integral:

$$\Delta\overline{\boldsymbol{S}}(\boldsymbol{x}) = \int_V \alpha(\boldsymbol{x},\boldsymbol{\xi})\Delta\boldsymbol{S}(\boldsymbol{\xi})\, \mathrm{d}V(\boldsymbol{\xi}) \tag{3}$$

V = volume of the body; $\boldsymbol{x}, \boldsymbol{\xi}$ = coordinate vectors; and $\alpha(\boldsymbol{x},\boldsymbol{\xi})$ = given nonlocal weight function. When $\Delta\boldsymbol{S}(\boldsymbol{x})$ is a uniform field, $\Delta\overline{\boldsymbol{S}}(\boldsymbol{x}) = \Delta\boldsymbol{S}(\boldsymbol{x})$ must represent a possible solution. Hence the normalizing condition

$$\int_V \alpha(\boldsymbol{x},\boldsymbol{\xi})\, \mathrm{d}V(\boldsymbol{\xi}) = 1 \tag{4}$$

NONLOCALITY CAUSED BY INTERACTION OF GROWING MICROCRACKS

The main source of post-peak strain-softening is the gradual spread of distributed microcracking. Accordingly, consider an increment of prescribed loads or boundary displacements for an elastic solid that contains, at the beginning of the load step, many microcracks numbered as $\mu = 1, \ldots N$. On the macroscale, the microcracks are considered to be smeared, as required by a continuum model. Exploiting the principle of superposition, we may decompose the loading step into two substeps:

I. In the first substep, the cracks (already opened) are imagined temporarily "*frozen*" (or "filled with a glue"), that is, they can neither grow and open wider nor close and shorten. Also, no new cracks can nucleate. The stress increments, caused by strain increments $\Delta\epsilon$ and transmitted across the temporarily frozen (or glued) cracks (I in Fig. 2), are then simply given by $\boldsymbol{E} : \Delta\epsilon$. This is represented by the line segment $\overline{13}$ (Fig. 1) having the slope of the initial elastic modulus E.

II. In the second substep, the prescribed boundary displacements and loads are held constant, the cracks are "unfrozen" (or "unglued"), and the stresses transmitted across the cracks are relaxed. This is equivalent to applying pressures (surface tractions) on the crack faces (II in Fig. 2). In response to this pressure, the cracks are now allowed to open wider and grow (remaining critical according to the crack propagation criterion), or to close and shorten. Also, new cracks are now allowed to nucleate.

If no cracks grew or closed (nor new cracks nucleated), the unfreezing (or unglueing) at prescribed increments of loads or boundary displacements that cause macro-strain increment $\Delta\epsilon$ would engender the stress drop $\overline{34}$ down to point 4 on the secant line $\overline{01}$ (Fig. 1). The change of state of the solid would then be calculated by applying the opposite of this stress drop onto the crack surfaces. However, when the cracks propagate (and new cracks nucleate), a larger stress drop defined by the local strain-softening constitutive law and represented by the segment $\Delta S = \overline{32}$ in Fig. 1 takes place. Thus, the normal surface tractions

$$\Delta p_\mu = \boldsymbol{n}_\mu \Delta \boldsymbol{S}_\mu \boldsymbol{n}_\mu \tag{5}$$

representing the normal component of tensor $\Delta \boldsymbol{S}_\mu$, must be considered in the second substep as loads Δp_μ that are applied onto the crack surfaces (Fig. 2), the unit normals of which are denoted as $\boldsymbol{n}_\mu$ (a product with no product sign denotes here a product of tensors contracted on one index; often it is written as the dot product, but here we omit the dot). Note also that for mode II or III cracks, a similar equation could in general be written for the tangential tractions on the crack faces.

Now we introduce two simplifying hypotheses:

1. Although the stress transmitted across each temporarily frozen crack varies along the crack, we consider only its average, i.e., Δp_μ is constant along each crack (Fig. 3a). This approximation, which is crucial for our formulation, was introduced by Kachanov (1985, 1987). He discovered by numerical calculations that the error is negligible except for the rare case when the distance between two crack tips is at least an order of magnitude less than their size.

2. We consider only Mode I crack openings, i.e. neglect the shear modes (modes II and III). This is often justified, for instance in materials such as concrete, by a high surface roughness which prevents any significant relative slip of the microcrack faces (the mode II or III relative displacements that can occur on a macroscopic crack are mainly the result of Mode I openings of microcracks that are inclined with respect to the macrocrack).

A simple-minded kind of superposition method would be to unfreeze all the cracks, load by pressure only one crack at a time, and then superpose all the cases (Fig. 2a). In this approach, the pressure on each crack, Δp_μ, would be known. But one would still have to solve a body with many cracks.

A better kind of superposition method is that adopted by Kachanov (1985, 1987), which was also used by Datsyshin and Savruk (1973), Gross (1982), Chudnovsky and Kachanov (1983), Chudnovsky et al. (1987), Chen (1984), and Horii and Nemat-Nasser(1985), and in a displacement version was introduced already by Collins, 1963. In this kind of superposition, one needs to have the solution of the given body for the case of only *one* crack, with all the other cracks considered frozen (Fig. 2a). The cost to pay for this advantage is that the pressures to be applied at the cracks are unknown in advance and must be solved. By virtue of Kachanov's approximation, we apply this kind of superposition to the average crack pressures only. The opening and the stress intensity factor of crack μ are approximately characterized by the uniform (average) crack pressure $\Delta\bar{p}_\mu$ that acts on a *single* crack within the given solid that has elastic moduli $\boldsymbol{E}$ and contains no other crack. This pressure is solved from the superposition relation:

$$\Delta\bar{p}_\mu = \langle \Delta p_\mu \rangle + \sum_{\nu=1}^{N} \Lambda_{\mu\nu} \Delta\bar{p}_\nu \qquad \mu = 1, ...N \tag{6}$$

$\langle ... \rangle$ is the averaging operator over the crack length; $\Lambda_{\mu\nu}$ are the crack influence coefficients representing the average pressure (Fig. 3a) at the frozen crack μ caused by a unit uniform pressure applied on unfrozen crack ν, with all the other cracks being frozen (Fig. 3b); and $\Lambda_{\mu\mu} = 0$ because the summation in (6) must skip $\nu = \mu$. The reason for the notation for $\Delta\bar{p}_\mu$ with an overbar instead of the operator $\langle ... \rangle$ is that the unknown crack pressure is uniform and thus its distribution over the crack area never needs to be calculated and no averaging of pressure actually needs to be carried out.

Note that the exact solution requires considering pressures $\Delta p_\mu(x')$ and $\Delta\bar{p}_\mu(x')$ that vary with coordinate x' along each crack. In numerical analysis, the crack must then be subdivided into many intervals. This could hardly be reflected on the macroscopic continuum level, but is doubtless unimportant at that level.

Substituting (5) into (6), we obtain

$$\Delta(\boldsymbol{n}_\mu \overline{\boldsymbol{S}}_\mu \boldsymbol{n}_\mu) = \langle \Delta(\boldsymbol{n}_\mu \boldsymbol{S}_\mu \boldsymbol{n}_\mu) \rangle + \sum_{\nu=1}^{N} \Lambda_{\mu\nu} \Delta(\boldsymbol{n}_\nu \overline{\boldsymbol{S}}_\nu \boldsymbol{n}_\nu) \tag{7}$$

The values of $\Delta\overline{\boldsymbol{S}}_\mu$ are graphically represented in Fig. 1 by the segment $\Delta\overline{S} = \overline{35}$. This segment can be smaller or larger than segment $\overline{32}$.

Now we adopt a third simplifying hypothesis: In each loading step, the influence of the microcracks at macro-continuum point of coordinate vector $\boldsymbol{\xi}$ upon the microcracks at macro-continuum point of coordinate vector $\boldsymbol{x}$ is determined only by the dominant microcrack orientation. This orientation is normal to the unit vector $\boldsymbol{n}_\mu$ of the maximum principal inelastic macro-stress tensor $\Delta\overline{\boldsymbol{S}}^{(1)}$ at the location of the center of microcrack μ. We use the definition:

$$\Delta\overline{S}_\mu^{(1)} = \Delta(\boldsymbol{n}_\mu \overline{\boldsymbol{S}}_\mu \boldsymbol{n}_\mu) = [\boldsymbol{n}_\mu \overline{\boldsymbol{S}}_\mu \boldsymbol{n}_\mu]_{\text{new}} - [\boldsymbol{n}_\mu \overline{\boldsymbol{S}}_\mu \boldsymbol{n}_\mu]_{\text{old}} \tag{8}$$

The subscripts 'new' and 'old' denote the values at the beginning and end of the loading step, respectively. According to this hypothesis, the dominant crack orientation generally rotates from one loading step to the next. Eq. (7) may now be written as:

$$\Delta\overline{S}_\mu^{(1)} - \sum_{\nu=1}^{N} \Lambda_{\mu\nu} \Delta\overline{S}_\nu^{(1)} = \langle \Delta S_\mu^{(1)} \rangle \tag{9}$$

Alternatively, one might assume $\boldsymbol{n}_\mu$ to approximately coincide with the direction of the maximum principal strain. Such an approximation is simpler to use in finite element programs. It might be realistic enough, especially when the elastic strains are relatively small.

When the principal directions of the inelastic stress tensor $\boldsymbol{S}$ do not rotate, the increment operators Δ can of course be moved inside each product in (7), i.e. $\Delta(\boldsymbol{n}_\mu \overline{\boldsymbol{S}}_\mu \boldsymbol{n}_\mu) = \boldsymbol{n}_\mu \Delta\overline{\boldsymbol{S}}_\mu \boldsymbol{n}_\mu$, etc. One might wonder whether this should not be done even when these directions rotate (i.e. when $\boldsymbol{n}_\mu$ varies), which would correspond to crack orientations being fixed when the cracks begin to form. But according to the experience with the so-called rotating crack model, empirically verified for concrete, it is more realistic to assume that the orientation of the dominant cracks rotates with the principal direction of $\boldsymbol{S}$.

It might seem we should have taken in the foregoing equations only the positive part of ΔS_μ. But this is not necessary since the unloading criterion prevents ΔS_μ from being negative.

FIELD EQUATION FOR NONLOCAL CONTINUUM

Now comes the most difficult step. We need to determine the nonlocal field equation for the macroscopic continuum which represents the continuum counterpart of (9). The homogenization

theories as known are inapplicable, because they apply only to macroscopically uniform fields while the nonuniformity of the macroscopic field is the most important aspect for handling localization problems. The following simple concept is proposed:

The continuum field equation we seek is an equation whose discrete approximation can be written in the form of the matrix crack interaction relation (9).

This concept leads us to propose the following field equation for the continuum approximation of microcrack interactions:

$$\Delta\overline{S}^{(1)}(\boldsymbol{x}) - \int_V \Lambda(\boldsymbol{x},\boldsymbol{\xi})\Delta\overline{S}^{(1)}(\boldsymbol{\xi})\mathrm{d}V(\boldsymbol{\xi}) = \langle\Delta S^{(1)}(\boldsymbol{x})\rangle \tag{10}$$

because an approximation of the integral by a sum over the continuum variable values at the crack centers yields (9). Here we denoted $\Lambda(\boldsymbol{x}_\mu,\boldsymbol{\xi}_\nu) = \mathcal{E}(\Lambda_{\mu\nu})/V_c$ = crack influence function, V_c is a constant that may be interpreted roughly as the volume per crack, and $\mathcal{E}$ is a statistical averaging operator which yields the average (moving average) over a certain appropriate neighborhood of point $\boldsymbol{x}$ or $\boldsymbol{\xi}$. Such statistical averaging is implied in the macro-continuum smoothing and is inevitable because in a random crack array the characteristics of the individual cracks must be expected to exhibit enormous random scatter.

It must be admitted that the sum in (9) is an unorthodox approximation of the integral from (10) because the values of the continuum variable are not sampled at certain predetermined points such as the chosen mesh nodes but are distributed at random, that is, at the microcrack centers. Another point to note is that (9) is only one of various possible discrete approximations of (10). Since this approximation is not unique, the uniqueness of (10) as a continuum approximation is not proven. Therefore, acceptability of (10) will also depend on computational experience (which has so far been favorable).

When (10) is approximated by finite elements, it is again converted to a matrix form similar to (9). However, the sum then runs over the integration points of the finite elements. This means the crack pressures (or openings) that are translated into the inelastic stress increments are only sampled at these integration points, in the sense of their density, instead of being represented individually as in (9). Obviously, such a sampling can preserve only the long-range interactions of the cracks and the averaging. The individual short-range crack interactions will be lost, but they are so random and vast in number that aspiring to represent them in any detail would be futile anyway.

For macroscopic continuum smearing, the averaging operator $\langle\ldots\rangle$ over the crack length now needs reinterpretation. Because of the randomness of the microcrack distribution, the macro-continuum variable at point $\boldsymbol{x}$ should represent the spatial average of the effects of all the possible

microcrack realizations within a neighborhood of point x whose size is roughly equal to the spacing ℓ of the dominant microcracks (which is in concrete approximately determined by the spacing of the largest aggregates); hence,

$$\langle \Delta S^{(1)}(x) \rangle = \int_V \Delta S^{(1)}(\xi) \alpha(x, \xi) \mathrm{d}V(\xi) \tag{11}$$

The weight function $\alpha(x, \xi)$ is analogous to that in (3). It should vanish everywhere outside a domain of a diameter roughly equal to ℓ. For computational reasons, it seems preferable that α have a smooth bell shape. Because of randomness of the microcrack distribution, function $\alpha(x, \xi)$ may be considered as rotationally symmetric (i.e., same in all directions, or isotropic). Strictly speaking, the macroscopic averaging domain could be a line segment in the direction of the dominant microcrack (that is, normal to $\Delta S^{(1)}(x)$), or an elongated roughly elliptical domain. However, using a line segment seems insufficient for preventing damage localization into a line in the case of a homogeneous uniaxial tension field, and it would also be at variance with the energy release argument for nonlocality of damage presented in Bažant (1987, 1991).

Equation (10) represents a Fredholm integral equation (i.e., an integral equation of the second kind with a square-integrable kernel) for the unknown $\Delta \overline{S}^{(1)}(x)$, which corresponds in Fig. 1 to the segment $\overline{35}$. The inelastic strain increment tensors $\Delta S^{(1)}(x)$ on the right-hand side, which correspond in Fig. 1 to the segment $\overline{32}$, are calculated from the strain increments using the given local constitutive law (for example the microplane model, continuum damage theory, plastic-fracturing theory, or plasticity with yield limit degradation).

SOME ALTERNATIVE FORMS AND PROPERTIES OF THE CONTINUUM MODEL

The solution of (10) can be written as:

$$\Delta \overline{S}^{(1)}(x) = \langle \Delta S^{(1)}(x) \rangle - \int_V K(x, \xi) \langle \Delta S^{(1)}(\xi) \rangle \mathrm{d}V(\xi) \tag{12}$$

in which function $K(x, \xi)$ is the resolvent of the kernel $\Lambda(x, \xi)$. (This resolvent could be calculated numerically in advance of the nonlocal finite element analysis, but it would not allow a simple physical interpretation and a closed-form expression.) With the notation

$$\Psi_{\mu\nu} = \delta_{\mu\nu} - \Lambda_{\mu\nu} \tag{13}$$

where $\delta_{\mu\nu}$ = Kronecker delta, Eq. (9) can be transformed to

$$\sum_\nu \Psi_{\mu\nu} \Delta \overline{S}_\nu^{(1)} = \langle \Delta S_\mu^{(1)} \rangle \tag{14}$$

The macro-continuum counterpart of this discrete matrix relation is

$$\int_V \Psi(\boldsymbol{x},\boldsymbol{\xi})\Delta\overline{S}^{(1)}(\boldsymbol{\xi})\mathrm{d}V(\boldsymbol{\xi}) = \langle\Delta S^{(1)}(\boldsymbol{x})\rangle = \int_V \Delta S^{(1)}(\boldsymbol{\xi})\alpha(\boldsymbol{x},\boldsymbol{\xi})\mathrm{d}V(\boldsymbol{\xi}) \tag{15}$$

which represents an integral equation of the first kind for the unknown function $\Delta\overline{S}^{(1)}(\boldsymbol{\xi})$. Obviously,

$$\Psi(\boldsymbol{x},\boldsymbol{\xi}) = \delta(\boldsymbol{x}-\boldsymbol{\xi}) - \Lambda(\boldsymbol{x},\boldsymbol{\xi}) \tag{16}$$

where $\delta(\boldsymbol{x}-\boldsymbol{\xi})$ = Dirac delta function in two or three dimensions; indeed, substitution of this expression into Eq. (15) yields Eq. (10).

Defining the inverse square matrix:

$$[B_{\mu\nu}] = [\Psi_{\mu\nu}]^{-1} \tag{17}$$

we may write the solution of the equation system (14) as

$$\Delta\overline{S}^{(1)}_{\mu} = \sum_{\nu} B_{\mu\nu}\langle\Delta S^{(1)}_{\nu}\rangle = \sum_{\lambda} C_{\mu\lambda}\Delta S^{(1)}_{\lambda}, \quad C_{\mu\lambda} = \sum_{\nu} B_{\mu\nu}\alpha_{\nu\lambda}. \tag{18}$$

with $\alpha_{\nu\lambda} = \alpha(\boldsymbol{x}_\nu,\boldsymbol{\xi}_\lambda)$. The macro-continuum counterpart of the last equation is

$$\Delta\overline{S}^{(1)}(\boldsymbol{x}) = \int_V B(\boldsymbol{x},\boldsymbol{\xi})\langle\Delta S^{(1)}(\boldsymbol{\xi})\rangle\mathrm{d}V(\boldsymbol{\xi}) = \int_V C(\boldsymbol{x},\boldsymbol{\xi})\Delta S^{(1)}(\boldsymbol{\xi})\mathrm{d}V(\boldsymbol{\xi}) \tag{19}$$

where $B(\boldsymbol{x}_\mu,\boldsymbol{\xi}_\nu) = \mathcal{E}(B_{\mu\nu})/V_c$ and $C(\boldsymbol{x},\boldsymbol{\xi}) = \int_V B(\boldsymbol{x},\boldsymbol{\xi})\alpha(\boldsymbol{\xi},\boldsymbol{x})\mathrm{d}V(\boldsymbol{\xi})$. The kernel $B(\boldsymbol{x},\boldsymbol{\xi})$ represents the resolvent of the kernel $\Psi(\boldsymbol{x},\boldsymbol{\xi})$ of (15). Furthermore,

$$B(\boldsymbol{x},\boldsymbol{\xi}) = \delta(\boldsymbol{x}-\boldsymbol{\xi}) - K(\boldsymbol{x},\boldsymbol{\xi}) \tag{20}$$

because substitution of this equation into Eq. (19) furnishes Eq. (12). With (19) we have reduced the nonlocal formulation to the same form as (3) for the previous nonlocal damage formulation (Pijaudier-Cabot and Bažant, 1987; Bažant and Pijaudier-Cabot, 1989; Bažant and Ožbolt, 1990, 1991, 1992). However, the presence of the Dirac delta function in the last equation makes Eq. (19) inconvenient for computations. Aside from that, it seems inconvenient to calculate in finite element codes function $B(\boldsymbol{x},\boldsymbol{\xi})$. Another difference is that the weight function (i.e., the kernel) is anisotropic (and, in the present simplification, associated solely with the principal inelastic stresses).

Note also that if we would set $\Lambda(\boldsymbol{x},\boldsymbol{\xi}) = 0$, the present model would become identical to the aforementioned previous nonlocal damage model. But this would not be realistic. The interactions characterized by $\Lambda(\boldsymbol{x},\boldsymbol{\xi})$ appear to be essential.

Because the nonlocal integral in (22) is additive to the local stress ΔS, the present nonlocal model can be imagined as an overlay of two solids that are forced to have equal displacements at all points: (i) The given solid with all the damage due to cracks, but local behavior (no crack interactions); and (ii) an overlaid solid that describes crack interactions only. The nonlocal stress $\Delta\overline{S}$ represents the sum of the stresses from both solids. It is the stress that is to be used in formulating the differential equilibrium equations for the solid.

For the sake of simplicity, we have so far assumed that the influence of point $\boldsymbol{\xi}$ on point $\boldsymbol{x}$ depends only on the orientation of the maximum principal inelastic stress at $\boldsymbol{\xi}$. Since at $\boldsymbol{\xi}$ there might be cracks normal to all the three principal stresses (denoted now by superscripts $i = 1, 2, 3$ in parentheses), it might be more realistic to consider that each of them separately influences point $\boldsymbol{x}$. In that case, Eqs. (9) and (10) can be generalized as follows:

$$\Delta\overline{S}_{\mu}^{(i)} - \sum_{\nu=1}^{N}\sum_{j=1}^{3}\Lambda_{\mu\nu}^{(ij)}\Delta\overline{S}_{\nu}^{(j)} = \langle\Delta S_{\mu}^{(i)}\rangle \tag{21}$$

$$\Delta\overline{S}^{(i)}(\boldsymbol{x}) - \int_V \sum_{j=1}^{3}\Lambda^{(ij)}(\boldsymbol{x},\boldsymbol{\xi})\Delta\overline{S}^{(j)}(\boldsymbol{\xi})\mathrm{d}V(\boldsymbol{\xi}) = \langle\Delta S^{(i)}(\boldsymbol{x})\rangle \qquad (j = 1, 2, 3) \tag{22}$$

Similar generalizations can be made in the subsequent equations, too. Note that when the body is infinite, all the summations or integrations in this paper are assumed to follow a special path labeled by $\odot$, which will be defined in the next section.

The heterogeneity of the material, such as the aggregate in concrete, is not specifically taken into account in our equations. Although the heterogeneity obviously must influence the nonlocal properties (e.g. Pijaudier-Cabot and Bažant, 1991), this influence is probably secondary to that of microcracking. The reason is that the pre-peak (hardening) inelastic behavior, in which microcracking is much less pronounced than after the peak while the heterogeneity is the same, can be adequately described by a local continuum. The main effect of heterogeneity (such as the aggregates in concrete, or grains in ceramics) is indirect; it determines the spacing, orientations and configurations of the microcracks.

ADMISSIBILITY OF UNIFORM INELASTIC STRESS FIELDS

In the previous nonlocal formulations, the requirement that a field of uniform inelastic stress and damage must represent at least one possible solution led to the normalizing condition (4). Similarly, we must now require that the homogeneous stress field $\Delta\overline{S}^{(1)} = \langle\Delta S^{(1)}\rangle$ satisfy (9) and (10) identically. This yields the conditions that the integral of $\Lambda(\boldsymbol{x},\boldsymbol{\xi})$ or the sum of $\Lambda_{\mu\nu}$ over an infinite body vanish. However, the asymptotic behavior of $\Lambda(\boldsymbol{x},\boldsymbol{\xi})$ for $r \to \infty$ which will be discussed later causes this integral or sum to be divergent. Therefore, the conditions must be imposed in a

special form—the integral in polar coordinates is required to vanish only for a special path, labeled by $\odot$, in which the angular integration is completed before the limit $r \to \infty$ is calculated, that is,

$$\int_V^{\odot} \Lambda(\boldsymbol{x},\boldsymbol{\xi})\mathrm{d}V(\boldsymbol{\xi}) = \lim_{R\to\infty}\int_0^R \left(\int_0^{2\pi} \Lambda(\boldsymbol{x},\boldsymbol{\xi})r\mathrm{d}\phi\right)\mathrm{d}r \;=\; 0 \text{ (for 2D)}$$

$$\int_V^{\odot} \Lambda(\boldsymbol{x},\boldsymbol{\xi})\mathrm{d}V(\boldsymbol{\xi}) = \lim_{R\to\infty}\int_0^R \left(\int_0^{2\pi}\int_0^{\pi} \Lambda(\boldsymbol{x},\boldsymbol{\xi})r^2\sin\theta\mathrm{d}\theta\mathrm{d}\phi\right)\mathrm{d}r \;=\; 0 \text{ (for 3D)} \qquad (23)$$

r,ϕ are polar coordinates, r,θ,ϕ are spherical coordinates. Furthermore, labeling again by $\odot$ a similar summation path (or sequence) over all the cracks ν in an infinite body, the following discrete condition needs to be also imposed:

$$\sum_{\nu}^{\odot} \Lambda_{\mu\nu} = 0 \qquad (24)$$

This condition applies only to an array of infinitely many microcracks that are, on the macroscale, perfectly random and distributed statistically uniformly over an infinite body (or are periodic). By the same reasoning, for an infinite body we must also have

$$\int_V^{\odot} K(\boldsymbol{x},\boldsymbol{\xi})\mathrm{d}V(\boldsymbol{\xi}) = 0 \qquad (25)$$

$$\int_V^{\odot} \Psi(\boldsymbol{x},\boldsymbol{\xi})\mathrm{d}V(\boldsymbol{\xi}) = \int_V^{\odot} B(\boldsymbol{x},\boldsymbol{\xi})\mathrm{d}V(\boldsymbol{\xi}) = \int_V^{\odot} C(\boldsymbol{x},\boldsymbol{\xi})\mathrm{d}V(\boldsymbol{\xi}) = 1; \qquad (26)$$

and in the discrete form

$$\sum_{\nu}^{\odot} \Psi_{\mu\nu} = \sum_{\nu}^{\odot} \alpha_{\mu\nu} = \sum_{\nu}^{\odot} B_{\mu\nu} = \sum_{\nu}^{\odot} C_{\mu\nu} = 1 \qquad (27)$$

For integration paths in which the radial integration up to $r \to \infty$ is carried out before the angular integration, the foregoing integrals and sums are divergent.

GAUSS-SEIDEL ITERATION APPLIED TO NONLOCAL AVERAGING

For the purpose of finite element analysis, we will now assume that subscripts μ and ν label the numerical integration points of finite elements, rather than the individual microcracks. This means that the microcracks are represented by their mean statistical characteristics sampled only at the numerical integration points.

In finite element programs, nonlinearity is typically handled by iterations of the loading steps. Let us, therefore, examine the iterative solution of (9) or (14), which represents a system of N linear algebraic equations for N unknowns $\Delta\overline{S}_{\mu}^{(1)}$ if $\Delta S_{\mu}^{(1)}$ are given. The matrix of $\Psi_{\mu\nu}$ is in general nonsymmetric (because the influence of a large crack on a small crack is not the same as the influence of a small crack on a large crack). This nonsymmetry seems disturbing until one realizes

that this is so only because of our choice of variables $\Delta\overline{S}_\nu^{(1)}$ and $\langle\Delta S_\mu^{(1)}\rangle$, which do not represent thermodynamically conjugate pairs of generalized forces and generalized displacements. If $\langle\Delta S_\mu^{(1)}\rangle$ were expressed in terms of the average crack openings $\overline{w}_\nu$, then the equation system resulting from (9) or (14) would have a matrix which would have to be symmetric (because of Betti's theorem), and also positive definite (if the body is stable). These are the attributes mathematically required for convergence of the iterative solution by Gauss-Seidel method (e.g., Rektorys, 1969; Collatz, 1960; Korn and Korn, 1968; Varga, 1962; Fox, 1965; Strang, 1980). Aside from that, convergence of the iterative solution of (9) or (14) must also be expected on physical grounds (because it is mechanically equivalent to the relaxation method, which always converges for stable elastic systems).

In the r-th iteration, the new, improved values of the unknowns, labeled by superscripts $[r+1]$, are calculated from the previous values, labeled by superscript $[r]$, either according to the recursive relations:

$$\Delta\overline{p}_\mu^{[r+1]} = \langle\Delta p_\mu\rangle + \sum_{\nu=1}^{N}\Lambda_{\mu\nu}\Delta\overline{p}_\nu^{[r]} \tag{28}$$

$$\Delta\overline{S}_\mu^{(1)[r+1]} = \langle\Delta S_\mu^{(1)}\rangle + \sum_{\nu=1}^{N}\Lambda_{\mu\nu}\Delta\overline{S}_\nu^{(1)[r]} \qquad (\mu = 1,2,...N) \tag{29}$$

or according to the recursive relations:

$$\Delta\overline{p}_\mu^{[r+1]} = \langle\Delta p_\mu\rangle + \sum_{\nu=1}^{\mu-1}\Lambda_{\mu\nu}\Delta\overline{p}_\nu^{[r+1]} + \sum_{\nu=\mu+1}^{N}\Lambda_{\mu\nu}\Delta\overline{p}_\nu^{[r]} \qquad (\mu = 1,2,...N) \tag{30}$$

$$\Delta\overline{S}_\mu^{(1)[r+1]} = \langle\Delta S_\mu^{(1)}\rangle + \sum_{\nu=1}^{\mu-1}\Lambda_{\mu\nu}\Delta\overline{S}_\nu^{(1)[r+1]} + \sum_{\nu=\mu+1}^{N}\Lambda_{\mu\nu}\Delta\overline{S}_\nu^{(1)[r]} \qquad (\mu = 1,2,...N) \tag{31}$$

Equation (29), also known as the Gauss method or Jacobi method, is normally slightly less efficient than (31), in which the latest approximations are always used. The values of $\Delta S_\mu^{(1)}$ may be used as the initial values of $\Delta\overline{S}_\mu^{(1)[r]}$ in the first iteration.

It is possible to derive Eq. (28) more directly, rather than from (6). To this end, we note that the sequence of iterations is identical to a solution by the relaxation method in which one crack after another is relaxed (i.e. its pressure reduced to zero) while all the other cracks are frozen (which is a problem with one crack only), as illustrated in Fig. 2b. Each relaxation produces pressure on the previously relaxed cracks. After relaxing, one by one, all the cracks, the cycle through all the cracks is repeated again and again. This kind of relaxations is known in mechanics to converge in general (this was numerically demonstrated for a system of cracks and inclusions by Pijaudier-Cabot and Bažant, 1991). The solution to which the relaxation process converges is obviously that defined by Eq. (9). Note also that this relaxation argument in fact represents a simple way to prove the superposition equation (6).

For structural engineers, it is interesting to note the similarity with the Cross method (moment distribution method) for elastic frames. Relaxing the pressure at one crack while all the other microcracks are frozen (glued) is analogous to relaxing one joint in a frame while all the other joints are held fixed. Repeating this for each joint, and then repeating the cycles of such relaxations of all the joints, eventually converges to the exact solution of the frame.

The macro-continuum counterpart of the Gauss-Seidel iterative method, which converges to the solution of the Fredholm integral equation (10), is analogous to (29) and is given by the following relation for successive approximations (iterations):

$$\Delta\overline{S}^{(1)[r+1]}(\boldsymbol{x}) = \langle \Delta S^{(1)}(\boldsymbol{x}) \rangle + \int_V \Lambda(\boldsymbol{x},\boldsymbol{\xi}) \Delta\overline{S}^{(1)[r]}(\boldsymbol{\xi})\, dV(\boldsymbol{\xi}) \tag{32}$$

The discrete approximation of the last relation is the equation that ought to be used in finite element programs with iterations in each step. We see that the form of averaging is different from that currently used, given by (3). There are now two additive spatial integrals, one for close-range averaging of the inelastic stresses from the local constitutive relation and one for long-range crack interactions based on the latest iterates of the inelastic stresses.

In programming, the old iterates need not be stored in the computer memory. So the subscripts $[r]$ and $[r+1]$ may be dropped and equations (31) and (32) and may be replaced by the following assignment statements:

$$\Delta\overline{S}_\mu^{(1)} \leftarrow \langle \Delta S_\mu^{(1)} \rangle + \sum_{\nu=1}^{N} \Lambda_{\mu\nu} \Delta\overline{S}_\nu^{(1)} \qquad (\mu = 1, 2, \ldots N) \tag{33}$$

$$\Delta\overline{S}^{(1)}(\boldsymbol{x}) \leftarrow \langle \Delta S^{(1)}(\boldsymbol{x}) \rangle + \int_V \Lambda(\boldsymbol{x},\boldsymbol{\xi}) \Delta\overline{S}^{(1)}(\boldsymbol{\xi})\, dV(\boldsymbol{\xi}) \tag{34}$$

A strict implementation of Gauss-Seidel iterations suggests programming one iteration loop for (33) to be contained within another loop for the iterations of the loading step in which the displacement and strain increments in the structure are solved. However, one common iteration loop, which is computationally much more efficient, can serve both purposes. Then, of course, the iteration solution is not exactly the Gauss-Seidel method because the strains are also being updated during each iteration. There is already some computational experience showing that convergence can still be achieved.

The common iteration loop has the advantage that it permits the use of the explicit load-step algorithm for structural analysis. In a loading step of this algorithm, one evaluates in each iteration at each integration point the elastic stress increments $\boldsymbol{E} : \Delta\epsilon$ and the local inelastic stress increments ΔS from fixed strains $\Delta\epsilon$; then one uses (33) to calculate from ΔS the nonlocal inelastic stress increments $\Delta\overline{S}$ for all the integration points, and solves new nodal displacements and strains

by elastic structural analysis.

CRACK INFLUENCE FUNCTION

Cracks Far from Boundary in Two-Dimensional Body

By virtue of applying the Gauss-Seidel iterative method, coefficients $\Lambda_{\mu\nu}$ can be obtained from the stress field of only *one* pressurized crack in the given elastic solid. In practice, this solid is finite, and then $\Lambda_{\mu\nu}$ should in principle be calculated taking into account the geometry of the body. This means that for every different body shape and size and every different crack location, a new set of coefficients $\Lambda_{\mu\nu}$ would have to be calculated. This would be a preposterous task.

A simplification is suggested, however, by the decay of stresses with the distance from a pressurized crack. For practical purposes, the distance of most cracks from the boundary is such that the interference of the boundary with the stress field of the crack is negligible. So, except for points near the boundary, this field can be approximately calculated as if the crack were embedded in an infinite elastic solid.

For the purpose of macro-continuum representation, some aspects of the stress field in an infinite body underlying the crack influence function Λ must be preserved while others must be simplified. Preserved must be the long-range asymptotic form of this field, because the long-range contributions to the integral that come from the neighborhood of a remote point ξ come to point x from nearly the same direction and nearly the same distance (Fig. 3c). How to handle the close-range fields of the microcracks is a much more difficult question. Certain aspects must obviously be simplified: First, it is impossible to represent on the macro-scale the microcracks as finite in size, having (in two dimensions) two distinct crack tips, and second, the singularities of the stress fields near the crack tips must be smeared at the macro-level as a nonsingular, bounded field. The first condition is met by taking the long-range asymptotic field of a crack in infinite elastic solid. This is easy to derive, as follows.

Consider now a crack in an infinite solid, subjected to uniform pressure σ (Fig. 3b,e). According to Westergaard's solution (e.g. Broek, 1987; Hellan, 1984),

$$\sigma_{xx} = \mathrm{Re}Z - y\,\mathrm{Im}\;Z' - \sigma, \qquad \sigma_{yy} = \mathrm{Re}Z + y\,\mathrm{Im}\;Z' - \sigma, \qquad \tau_{xy} = -y\,\mathrm{Re}\;Z' \tag{35}$$

in which σ_{xx} and σ_{yy} are the normal stresses, τ_{xy} is the shear stress, and

$$Z = \sigma z\,(z^2 - a^2)^{-1/2}; \qquad z = r\,e^{i\phi} \tag{36}$$

Here $2a$ = crack length, $i^2 = -1$, $Z' = dZ/dz$, and r, ϕ = polar coordinates with origin at the crack

center and angle ϕ measured from the crack direction x. For $r \gg a$ we have the approximation:

$$Z = \sigma\left(1 - \frac{a^2}{r^2\, e^{2i\phi}}\right)^{-1/2} = \sigma\left(1 + \frac{a^2}{2r^2} e^{-2i\phi} + ...\right) = \sigma\left(1 + \frac{a^2}{2z^2} + ...\right) \tag{37}$$

From this, we calculate

$$\begin{aligned} \text{Re } Z &= \sigma\left(1 + \frac{a^2}{2r^2}\cos 2\phi + ...\right), \qquad Z' = \sigma(-a^2 z^{-3} + ...) \\ y \text{ Im } Z' &= \sigma a^2 r \sin\phi \text{ Im } (-r^{-3} e^{-3i\phi}) = -\sigma a^2 r^{-2} \sin\phi(-\sin 3\phi) \end{aligned} \tag{38}$$

Substituting this into (35) and using the formulas for products of trigonometric functions, we get the following simple result for the long-range ($r \gg a$) asymptotic field:

$$\begin{aligned} \sigma_{xx} &= \sigma k(r)\frac{\cos 4\phi}{2}, \qquad \sigma_{yy} = \sigma k(r)\left(\cos 2\phi - \frac{\cos 4\phi}{2}\right) \\ \tau_{xy} &= \sigma k(r)\frac{\sin 4\phi - \sin 2\phi}{2} \end{aligned} \tag{39}$$

where $k(r) = a^2/r^2$. Subscripts x, y refer to cartesian coordinates with origin at point ξ coinciding with the crack center and axis y normal to the crack; σ_{xx} and σ_{yy} are the normal stresses, τ_{xy} is the shear stress; and ϕ are polar coordinates with origin at the crack center, with the polar angle ϕ measured from axis x. The principal stresses $\sigma^{(1)}$ and $\sigma^{(2)}$ and the first principal stress direction $\phi^{(1)}$ are given by:

$$\sigma^{(1)} = \sigma k(r)\left(\frac{\cos 2\phi}{2} + \sin\phi\right), \qquad \sigma^{(2)} = \sigma k(r)\left(\frac{\cos 2\phi}{2} - \sin\phi\right) \tag{40}$$

$$\tan 2\phi^{(1)} = -\cot 3\phi$$

The foregoing expressions describe the long-range form of function $\Lambda(x, \xi)$. It does not matter that they have a r^{-2} singularity at the crack center, because they are invalid for not too large r. Note that the average of each expression over the circle r = constant is zero, which is in fact a necessary property.

Function $\Lambda(x, \xi)$ can also be easily determined for small r. As intuitively suggested by Fig. 3d, the short-range interactions go in all directions and should cancel each other. That this is indeed so is confirmed by Kachanov's (1992) numerical studies of interactions of randomly generated crack systems that are uniform over a large body. He found that for such systems the classical assumption of noninteracting cracks is very good, which means that all the interactions mutually cancel. It follows that for $r \to 0$, the function $\Lambda(x, \xi)$ should approach the asymptote $\Lambda = 0$ (Fig. 3g).

For intermediate r, calculation of $\Lambda(x, \xi)$ would need to take into account statistical interactions, which seems very difficult. Therefore, we propose to use a smooth empirical function that approaches for $r \to \infty$ and for $r \to 0$ the two asymptotic curves we established, as shown in Fig.

3g. We also know the function must be bounded. The simplest expression to have these properties, which replaces a^2/r^2 in the foregoing expressions, is

$$k(r) = \left(\frac{\kappa \ell r}{r^2 + \ell^2} \right)^2 \tag{41}$$

Here ℓ is an empirical constant that represents the distance to the peak in Fig. 3g. It may be identified with what has been called the *characteristic length* of the nonlocal continuum. Probably its value reflects the dominant spacing of the microcracks, which in turn is determined by size and spacing of the dominant inhomogeneities such as aggregates in concrete, or grain or crystal size in ice, ceramics and rocks. It may perhaps be taken equal to the larger of the crack size and the maximum inhomogeneity (aggregate) size. κ is an empirical constant such that $\kappa\ell$ roughly represents the average or effective crack size a for the macro-continuum (in theory, it seems this value should be increased during the loading process since the cracks grow).

In the formalism we introduced previously, $\Lambda(\boldsymbol{x}, \boldsymbol{\xi})$ is a scalar. All the information on the relative crack orientations is embedded in the values of this function. The principal stress direction at point $\boldsymbol{\xi}$, which can be regarded as the dominant crack direction at that location (Fig. 3e), is all the directional information needed to calculate the stress components at point $\boldsymbol{x}$; see (40), in which $r = \|\boldsymbol{x} - \boldsymbol{\xi}\|$ = distance between points $\boldsymbol{x}$ and $\boldsymbol{\xi}$. The value of $\Lambda(\boldsymbol{x}, \boldsymbol{\xi})$, needed for (32) or (9), may be determined as the projection of the stress tensor produced at point $\boldsymbol{x}$ onto the principal inelastic stress direction at that point. According to Mohr circle: $2\Lambda(\boldsymbol{x}, \boldsymbol{\xi}) = (\sigma_{xx} + \sigma_{yy}) + (\sigma_{xx} - \sigma_{yy}) \cos 2(\psi - \theta) - 2\tau_{xy} \sin 2(\psi - \theta)$ in which θ, ψ = angles of the principal inelastic stress directions at points $\boldsymbol{\xi}, \boldsymbol{x}$, respectively, with the line connecting these two points (i.e. with the vector $\boldsymbol{x} - \boldsymbol{\xi}$). Substituting here for σ_{xx}, etc., the expressions from (39), one obtains a trigonometric expression which (as Planas, 1992, pointed out), can be brought by trigonometric transformations to the form:

$$\Lambda(\boldsymbol{x}, \boldsymbol{\xi}) = -\frac{k(r)}{2\ell^2} [\, \cos 2\theta + \cos 2\psi + \cos 2(\theta + \psi) \,] \tag{42}$$

where $\theta = 90° - \phi$. Note that the function $\Lambda(\boldsymbol{x}, \boldsymbol{\xi})$ is symmetric. This is of course a necessary consequence of the fact that the body is elastic.

Two properties contrasting with the previous nonlocal formulations should be noted: (1) the crack influence function is not axisymmetric (isotropic) but depends on the polar angle (i.e. is anisotropic), and (2) it exhibits a shielding sector and an amplification sector. We may define the amplification sector as the sector in which σ_{yy} (the same stress component as that applied at the crack faces) is positive, and the shielding sector as the sector in which σ_{yy} is negative. The amplification sector $\sigma_{yy} \geq 0$ is, according to (39), given by $\phi \leq \phi_b$ where

$$\phi_b = 55.740° \tag{43}$$

The sector in which the volumetric stress $\sigma_{xx}+\sigma_{yy}$ (first stress invariant) is positive is $\phi \leq 45°$. The sector in which $\sigma_{xx} \geq 0$ is $\phi \leq 22.5°$ and $\phi \geq 67.5°$. The sector in which $2\,\tau_{\max} = \sigma_{xx} - \sigma_{yy} \geq 0$ is $\phi \leq 45°$. The maximum principal stress $\sigma^{(1)}$ is positive for all angles ϕ, and the minimum principal stress $\sigma^{(2)}$ is positive for $\phi < 21.471°$.

The consequence of the anisotropic nature of the crack influence function is that interactions between adjacent cracks depend on the direction of damage propagation with respect to the orientation of the maximum principal inelastic stress. In a cracking band that is macroscopically of mode I (Fig. 4a), propagating in the dominant direction of the microcracks, the microcracks assist each other in growing because they lie in each other's amplification sectors. In a cracking band that is macroscopically of mode II (Fig. 4b), the microcracks are mutually in the transition between their amplification and shielding sectors, and thus interact little. Under compression, a band of axial splitting cracks may propagate sideways (Fig. 4c), and in that case the microcracks inhibit each other's growth because they lie in each other's shielding sectors. Different interactions of this kind probably explain why good fitting of test data with the previous nonlocal microplane model required using a different material characteristic length for different type of problems (e.g., mode I fracture specimens versus diagonal shear failure of reinforced beam).

Cracks Far from Boundary in Three-Dimensional Body

The case of three dimensions (3D) is not difficult when the cracks are penny-shaped and the boundary is remote. The stresses around such cracks have been expressed as integrals of Bessel functions (Sneddon and Lowengrub, 1969; Kassir and Sih, 1975), which are cumbersome for calculations. Recently, however, Fabrikant (1990) ingeniously derived the following closed-form expressions:

$$\begin{aligned} \sigma_{xx} &= \frac{\sigma_1 + \mathrm{Re}\,\sigma_2}{2}, \qquad \sigma_{yy} = \frac{\sigma_1 - \mathrm{Re}\,\sigma_2}{2}, \qquad \tau_{xy} = \frac{\mathrm{Im}\,\sigma_z}{2} \\ \tau_{xz} &= \mathrm{Re}\,\tau_z, \qquad \tau_{yz} = \mathrm{Im}\,\tau_z \end{aligned} \tag{44}$$

in which

$$\begin{aligned} \sigma_z &= \frac{2\sigma}{\pi}(B - D), \qquad \sigma_1 = \frac{2\sigma}{\pi}[(1+2\nu)B + D] \\ \sigma_2 &= e^{2i\phi}\,\frac{2\sigma}{\pi}\,\frac{a l_1^2 l_3}{l_2^2 l_4^2}\left(1 - 2\nu + \frac{z^2[a^2(6l_2^2 - 2l_1^2 + \rho^2) - 5l_2^4]}{l_4^4 l_3^2}\right) \\ \tau_z &= -e^{i\phi}\,\frac{2\sigma}{\pi}\,\frac{z l_1[a^2(4l_2^2 - 5\rho^2) + l_1^4] l_3}{l_2 l_4^6} \\ B &= \frac{a l_3}{l_4^2} - \arcsin\frac{a}{l_2}, \qquad D = \frac{a z^2[l_1^4 + a^2(2a^2 + 2z^2 - 3\rho^2)]}{l_4^6 l_3} \\ l_1 &= \frac{L_2 - L_1}{2}, \quad l_2 = \frac{L_2 + L_1}{2}, \quad l_3 = \sqrt{l_2^2 - a^2}, \quad l_4 = \sqrt{l_2^2 - l_1^2} \\ L_1 &= \sqrt{(a-\rho)^2 + z^2}, \qquad L_2 = \sqrt{(a+\rho)^2 + z^2} \end{aligned} \tag{45}$$

in which a = crack radius (Fig. 3f); r, θ, ϕ are the spherical coordinates attached to cartesian coordinates x, y, z at point ξ, with angle θ measured from axis z which is normal to the crack at point ξ; r = distance between points x and ξ; and ρ, ϕ, z are the cylindrical coordinates with origin at the crack center and ρ, ϕ as polar coordinates in the crack plane, angle ϕ being measured from axis x.

Since the long-range asymptotic form of the foregoing stress field has not been given, we need to derive it. For this purpose, one needs to note that, for large r, $L_1 \approx r - a\sin\theta, L_2 \approx r + a\sin\theta$ (see the meaning of L_1 and L_2 in Fig. 3f), $l_1 \approx a\sin\theta, l_2 \approx r$ and, for $r \gg a$, $\arcsin(a/l_2) \approx [1 + (a^2/6l_2^2)]a/l_2$, $\sqrt{l_2^2 - a^2} \approx r[1 - (a^2/2r^2)]$. The result is the following long-range asymptotic field:

$$\begin{aligned}
\sigma_{\rho\rho} &= \sigma k(r)\left[(1+2\nu)\left(\sin^2\theta - \frac{2}{3}\right) + (1 - 2\nu - 5\cos^2\theta)\sin^2\theta\right] \\
\sigma_{\phi\phi} &= \sigma k(r)\left[(1+2\nu)\left(\sin^2\theta - \frac{2}{3}\right) - (1 - 2\nu - 5\cos^2\theta)\sin^2\theta\right] \\
\sigma_{zz} &= \sigma k(r)\left(\sin^2\theta - \frac{2}{3}\right) \\
\sigma_{\rho z} &= -\sigma k(r)\sin 2\theta\,(4 - 5\sin^2\theta), \qquad \sigma_{\rho\phi} = \sigma_{\phi z} = 0
\end{aligned} \tag{46}$$

in which, for three dimensions, $k(r) = a^3/(\pi r^3)$. For the same reasons as those that led to Eq. (41), this expression may be replaced by

$$k(r) = \frac{1}{\pi}\left(\frac{\kappa\ell r}{r^2 + \ell^2}\right)^3 \tag{47}$$

The crack influence function based on (46) satisfies again the condition that its spatial average over every surface r = constant be zero.

It is important to note that, asymptotically for large distances r, the crack influence function in three dimensions decays as r^{-3}, whereas in two dimensions it decays as r^{-2}. Again, in contrast to the previous formulations, the weight function (crack influence function) is not axisymmetric (isotropic) but depends on the polar or spherical angles (i.e. is anisotropic).

Note again that one can distinguish a shielding sector and an amplification sector. According to the change of sign of σ_{zz} in

Eq. (46), the boundary of these sectors is given by the angle

$$\theta_b = \arcsin\sqrt{2/3} = 54.736^\circ \tag{48}$$

or $90^\circ - \theta_b = 35.264^\circ$. Thus, the amplification sector $\theta \geq \theta_b$ is significantly narrower in three than in two dimensions.

In the case of a field translationally symmetric in z, one might wonder whether integration over z might yield the two-dimensional crack influence function. However, this cannot occur because the two-dimensional crack influence function corresponds in three dimensions to a field of strip cracks aligned in th z direction, which cannot yield the same properties as the penny-shaped cracks.

Cracks Near Boundary

When the boundary is near, the crack influence function should be obtained by solving the stress field of a pressurized crack located at a certain distance d from the boundary; Fig. 4d. Obviously, the function will depend on d as a parameter, i.e., $\Lambda(\boldsymbol{x}, \boldsymbol{\xi}, d)$. Functions Λ will be different for a free boundary, fixed boundary (Fig. 4e), sliding boundary, and elastically supported boundary or interface with another solid. When the crack is near a boundary corner (Fig. 4f), Λ represents the solution of the stress field of a pressurized crack in the wedge, and will depend on the distances form both boundary planes of the wedge. These solutions will be much more complicated than for a crack in infinite body, and simplifications will be needed. On the other hand, because of the statistical nature of the crack system, exact solutions of these problems are not needed. Only their essential feature are.

A crude but simple approach to the boundary effect is to consider the same weight function as for an infinite solid, protruding outside the given finite body. In the previous nonlocal formulations, based on the idea of spatial averaging, the same weight function as for the infinite solid has been used in the spatial integral and the weight function has simply been scaled up (renormalized), so that the integral of the weight function over the reduced domain would remain 1. In the present formulation, such scaling would have to be applied to all the weight functions whose integral should be 1, i.e. α, ψ, B, C. For those weight functions whose integral should vanish, a different scaling would be needed to take the proximity of the boundary into account; for example, the values at the boundary should be scaled up so that the spatial integral would always vanish, as indicated in (23). As a reasonable simplification, this might perhaps be done by replacing the $\Lambda_{\mu\nu}$ values for the integration points $\boldsymbol{\xi}_\nu$ of the boundary finite elements by $k_b \Lambda_{\mu\nu}$ where the multiplicative factor k_b is determined from the condition that $\sum_{\nu=1}^{N} \Lambda_{\mu\nu} = 0$ (with the summation carried over all the points in the given finite body);

$$k_b = - \sum_{\text{interior } \nu} \Lambda_{\mu\nu} \Big/ \sum_{\text{boundary } \nu} \Lambda_{\mu\nu} \tag{49}$$

LONG-RANGE DECAY AND INTEGRABILITY

Consider now an infinite two-dimensional elastic solid in which the stress, strain and cracking are

macroscopically uniform. All the microcracks are of the same size a, and the area per crack is s^2. The stress σ applied on each microcrack is the same. From (39) we calculate the contribution to the nonlocal integral from domain V_1 outside of a circle of radius R_1 that is sufficiently large for permitting the approximation $k(r) \approx a^2/r^2$;

$$\int_{V_1}^{\odot} (\sigma_{xx} + \sigma_{yy}) \mathrm{d}V = \lim_{R \to \infty} \int_{r=R_1}^{R} \int_{\phi=0}^{2\pi} \frac{\sigma a^2 \cos 2\phi}{2r^2} \frac{r \mathrm{d}\phi \mathrm{d}r}{s^2} = \frac{\sigma a^2}{2s^2} \int_{r=R_1}^{\infty} \int_{\phi=0}^{2\pi} \frac{\cos 2\phi}{r} \mathrm{d}\phi \mathrm{d}r \qquad (50)$$

Now an important observation, to which we already alluded: The last expression is an improper integral which is divergent (because it is divergent when the integrand is replaced by its absolute value; see e.g. Rektorys, 1969). This also means that the value of the integral depends on the integration path. For some path the integral may be convergent, and that path, shown in (50), has been labeled by $\odot$. So we must conclude that a homogeneous ΔS field, that is, a field of uniform length increment of all the cracks in an infinite body that is initially in a statistically uniform state, is impossible.

But this is not all that surprising. As is known from analysis of bifurcation and stable equilibrium path, strain-softening damage (which is due to microcrack growth) must localize (e.g. Bažant and Cedolin, 1991). So in practice the domain of the integrals such as the last one must not be infinite in two directions. It can only be finite or infinite in one direction only, as is the case for a localization band. The basic reason for this situation is that the asymptotic decay r^{-2}, which we have obtained, is relatively weak—much weaker than the exponential decay assumed in previous works (for an exponential decay, the integration domain could be infinite in all directions without causing this kind of problem).

A similar analysis of uniform damage can be carried out for an infinite three-dimensional solid, and the conclusion is that the integration domain, that is, the zone of growing microcracks, can only be finite or infinite in two directions only (a localization layer), but not in three.

A similar divergence of the integral over infinite space has been known to occur in other problems of physics, for example, in calculation of the stresses from periodically distributed inclusions, or the light received from infinitely many statistically uniformly distributed stars. For a perspicacious mathematical study of this type of problem, see Furuhashi, Kinoshita and Mura (1981).

GENERAL FORMULATION: TENSORIAL CRACK INFLUENCE FUNCTION

In Eq. 10, the principal stress orientations at points $\boldsymbol{x}$ and $\boldsymbol{\xi}$ are reflected in the values of the scalar function $\Lambda(\boldsymbol{x}, \boldsymbol{\xi})$. For the purpose of general analysis, however, it seems more convenient to use a tensorial crack influence function referred to common structural cartesian coordinates $X \equiv X_1, Y \equiv X_2, Z \equiv X_3$, and transform all the inelastic stress tensor components to X, Y, Z.

The local cartesian coordinates $x \equiv x_1, y \equiv x_2, z \equiv x_3$ at point ξ are chosen so that axis y coincide with the direction of the maximum principal value of the inelastic stress tensor $\overline{S}(\xi)$, and axes x and z coincide with the other two principal directions (Fig. 4). Equations (33) and (34) may be rewritten in common structural coordinates as follows:

$$\Delta\overline{S}_{\mu IJ} \leftarrow \langle \Delta S_{\mu IJ} \rangle + \sum_{\nu=1}^{N} \sum_{i=1}^{3} R^{(i)}_{\nu IJkl} \Lambda^{(i)}_{\mu\nu kl} \Delta\overline{S}^{(i)}_{\nu} \qquad (\mu = 1,2,...N; i = 1,2,3) \tag{51}$$

$$\Delta\overline{S}_{IJ}(x) \leftarrow \langle \Delta S_{IJ}(x) \rangle + \int_V \sum_{i=1}^{3} R^{(i)}_{IJkl}(\xi) \Lambda^{(i)}_{kl}(x,\xi) \Delta\overline{S}^{(i)}(\xi) dV(\xi) \qquad (i = 1,2,3) \tag{52}$$

in which, similarly to (22), we included the influence of the dominant cracks normal to all the principal stress direction at each point; $R^{(i)}_{IJkl}(\xi)$ or $R^{(i)}_{\nu IJkl} = c_{kI}c_{lJ}$ = fourth-rank coordinate rotation tensor (programmed as a square matrix when the stress tensors are programmed as column matrices) at point ξ or ξ_μ; c_{kI}, c_{lJ} = coefficients of rotation transformation of coordinate axes (direction cosines of new axes) from local coordinates x_i at point ξ (having in general a different orientation at each ξ) to common structural coordinates X_I ($c_{kI} = \cos(x_k, X_I), X_I = c_{kI}x_k, \sigma_{IJ} = c_{kI}c_{lJ}\sigma_{kl}$) ; subscripts I, J or k, l refer to cartesian components in the common structural coordinates or in the local coordinates at ξ; and $\Lambda^{(i)}_{\mu\nu kl}$ or $\Lambda^{(i)}_{kl}(x,\xi)$ = components of a tensorial discrete or continuous nonlocal weight function (crack influence function, replacing the scalar function Λ), which are equal to ℓ^{-2} times the cartesian stress components σ_{kl} for $\sigma = 1$ as defined by (39) for two dimensions, or ℓ^{-3} times such cartesian components as defined by (46) for three dimensions (with $r = \|x - \xi\|$).

CONSTITUTIVE RELATION AND GRADIENT APPROXIMATION

As is clear from the foregoing exposition, the constitutive relation is defined only locally. It yields the inelastic stress increment $\langle \Delta S^{(1)}(x) \rangle$, illustrated by segment $\overline{32}$ shown in Fig. 1. This contrasts with the previous nonlocal formulations, in which the nonlocal inelastic strain, stress or damage was part of the constitutive relation. This caused conceptual difficulties as well as continuity problems with formulating the unloading criterion. Furthermore, in the case of nonlocal plasticity, this also caused difficulties with the consistency condition for the subsequent loading surfaces.

Here these difficulties do not arise, because the nonlocal spatial integral is separate from the constitutive relation. Thus the unloading criterion can, and must, be defined strictly locally. If plasticity is used to define the local stress-strain relation, the consistency condition of plasticity is also local.

Recently there has been much interest in limiting localization of cracking by means of the so-

called gradient models. These models can be looked at as approximations of the nonlocal integral-type models, and can be obtained by expanding the nonlocal integral in Taylor series (Bažant, 1984). Unlike the present model, there have been only scant and vague attempts at physical justifications for the gradient models, especially for aggregate-matrix composites such as concrete. It seems that the physical justification for the gradient models of such materials must come indirectly, through the integral-type model. However, if that is the case, the present conclusions signal a problem. If the spatial integral in (10) were expanded into Taylor series and truncated, the long-range decay of the type r^{-2} or r^{-3} could not be preserved. Yet it seems that this decay is for microcrack systems important. If so, then the gradient approximations are physically unjustified.

CONCLUSIONS

1. The inelastic stress increments correspond to the stresses that the load increment would produce on the cracks if they were temporarily "frozen" (or "glued"), i.e., prevented from opening and growing. The nonlocality arises from two sources: (1) *crack interactions*, which means that application of the pressure on the crack surfaces that corresponds to the "unfreezing" (or "unglueing") of one crack produces stresses on all the other frozen cracks; and (2) averaging of the stresses due to unfreezing over the crack surface, which is needed because crack interactions depend primarily on the stress average over the crack surface (or the stress resultant) rather than the stress at the crack center. The crack interactions (source 1) can be solved by Kachanov's (1987) simplified version of the superposition method, in which only the average crack pressures are considered.

2. The resulting nonlocal continuum model involves two spatial integrals: One integral, which corresponds to source (1) and has been absent from previous nonlocal models, is long-range and has a weight function whose spatial integral is 0; it represents interactions with remote cracks and is based on the long-range asymptotic form of the stress field caused by pressurizing one crack while all the other cracks are frozen. Another integral, corresponding to source (2), is short-range, involves a weight function whose spatial integral is 1, and represents spatial averaging of the local inelastic stresses over a domain whose diameter is roughly equal to the spacing of major microcracks (which is roughly equal to the spacing of large aggregates in concrete).

3. As an approach to continuum smoothing when the macroscopic field is nonuniform, one may seek a continuum field equation whose possible discrete approximation coincides with the matrix equation governing a system of interacting microcracks.

4. The long-range asymptotic weight function of the nonlocal integral representing crack interactions (source 1) has a separated form which is calculated as the remote stress field of a crack in infinite body. It decays with distance r from the crack as r^{-2} in two dimensions and r^{-3} in

three dimensions. This long-range decay is much weaker than assumed in previous nonlocal models. In consequence, the long-range integral diverges when the damage growth in an infinite body is assumed to be uniform. This means that only the localized growth of damage zones can be modeled.

5. In contrast to the previous nonlocal formulations, the weight function (crack influence function) in the long-range integral is a tensor and is not axisymmetric (isotropic). Rather, it depends on the polar or spherical angle (i.e. is anisotropic), exhibiting sectors of shielding and amplification.

6. When an iterative solution of crack interactions according to the Gauss-Seidel iterative method is considered, the long-range nonlocal integral based on the crack influence function yields the nonlocal inelastic stress increments explicitly. This explicit form is suitable for iterative solutions of the loading steps in nonlinear finite element programs. The nonlocal inelastic stress increments represent a solution of a tensorial Fredholm integral equation in space, to which the iterations converge.

7. The constitutive law, in this new formulation, is strictly local. This is a major advantage, eliminating difficulties with formulating the unloading criterion and the continuity condition, experienced in the previous nonlocal models in which nonlocal inelastic stresses or strains have been part of the constitutive relation.

ACKNOWLEDGMENT.—Financial support under AFOSR Grant 91-0140 to Northwestern University is gratefully acknowledged. Supplementary support for the analysis of cracking damage in concrete was received from the Center for Advanced Cement Based Materials at Northwestern University. The general approach was conceived during a visiting appointment at Lehrstuhl für Mechanik (director Prof. Horst Lippmann), Technische Universität München, supported under Humboldt Award of Senior U.S. Scientist. Stimulating discussions by graduate research assistant Milan Jirásek, as well as visiting scholars Joško Ožbolt (research engineer on leave from Stuttgart University) and Jaime Planas (professor of materials science on leave from Technical University, Madrid), are appreciated. Thanks for illuminating comments are due to Toshio Mura and John Dundurs, professors at Northwestern University.

REFERENCES

Bažant, Z. P., Belytschko, T. B., and Chang, T.-P. (1984). "Continuum model for strain softening," *J. of Engng. Mechanics* ASCE, 110, 1666–1692.

Bažant, Z. P., (1984). "Imbricate continuum and its variational derivation," *J. of Engng. Mech. ASCE*, 110, 1693–1712.

Bažant, Z.P. (1986). "Mechanics of distributed cracking," *Appl. Mech. Reviews ASME*, 39, 675–

705.

Bažant, Z. P. (1987). "Why continuum damage is nonlocal: justification by quasi-periodic microcrack array," *Mechanics Research Communications*, 14 (5/6), 407–419.

Bažant, Z.P. (1991). "Why continuum damage is nonlocal: micromechanics arguments." *Journal of Engineering Mechanics* ASCE 117(5), 1070–1087.

Bažant, Z. P., and Pijaudier-Cabot, G. (1988). "Nonlocal continuum damage, localization instability and convergence," *ASME J. of Applied Mechanics*, 55, 287-293.

Bažant, Z. P., and Lin, F.-B. (1988a). "Nonlocal smeared cracking model for concrete fracture," *J. of Struct. Engng. ASCE* 114 (11), 2493–2510.

Bažant, Z. P., and Lin, F. -B. (1988b). "Nonlocal yield limit degradation," *International J. for Numerical Methods in Engineering*, 26, 1805–1823.

Bažant, Z. P., and Ožbolt, J. (1990)."Nonlocal microplane model for fracture, damage, and size effect in structures," *ASCE J. of Engng. Mech.* 116(11), 2484–2504.

Bažant, Z. P., and Ožbolt, J. (1992a)."Compression failure of quasibrittle material: Nonlocal microplane model", *ASCE J. of Engrg. Mechanics* 118 (3), March, 540–556.

Ožbolt, J., and Bažant(1992b). "Microplane model for cyclic triaxial behavior of concrete." *J. of Engineering Mechanics* 118(7), 1365–1386.

Bažant, Z.P., and Tabbara, M.R. (1992), "Bifurcation and stability of structures with interacting propagating cracks", *Int. J. of Fracture* 53, 273–289.

Bažant, Z.P. (1992). "New concept of nonlocal continuum damage: Crack influence function", in *Macroscopic Behavior of Heterogeneous Materials from Microstructure*, AMD–Vol.147 (ASME Winter Annual Meeting, Anaheim), ed. by S. Torquato and D. Krajcinovic, ASME, New York, 153–160.

Benveniste, Y., Dvorak, G.J., Zarzour, J., and Wung, E.C.J. (1989), "On interacting cracks and complex configurations in linear elastic media", *Int. J. of Solids and Structures* 25 (11), 1279–1293.

Broek, D. (1987). *Elementary engineering fracture mechanics*, Martinus Nijhoff, Doordrecht–Boston (p. 77).

Collatz, L. (1960). *The numerical treatment of differential equations*, Springer, Berlin.

Collins, W.D. (1963). *Proc. of the Royal Society* A274, 1359, 507–526.

Chudnovsky, A., and Kachanov, M. (1983). *Int. J. of Engrg. Science* 21 (8), 1009–1018.

Chudnovsky, A., Dolgopolsky, A., and Kachanov, M. (1987). "Elastic interaction of a crack with a microcrack array (parts I& II)", *Int. J. of Solids and Structures* 23, 1–21.

Datsyschin, A.P., and Savruk, M.P. (1973). *J. of Appl. Math. and Mech. (PMM)*, 326–332.

de Borst, R. (1990). "Simulation of localisation using Cosserat theory", *Proc., Int. Conf. on Computer-Aided Analysis and Design of Concrete Stuctures* (held at Zell-am-See, Austria), ed. by N. Bićanić and H.A. Mang, Pineridge Press, Swansea, 931-944.

de Borst, R. (1991). Simulation of strain localisation: A reappraisal of the Cosserat continuum, *Eng. Comp.* 8, 317-332.

de Borst, R. and Sluys, L.J. (1991). "Localisation in a Cosserat continuum under static and dynamic loading conditions", *Comp. Meth. Appl. Mech. Eng.* 90, 805-827.

Dietsche, A., and Willam, L.J. (1992). "Localization analysis of elasto-plastic Cosserat continua", in *Damage and Localization*, AMD-Vol.142 (Winter Annual Meeting, Anaheim), ed. by J.W. Ju and K.C. Valanis, ASME, New York, 25–40.

Eringen, A.C. (1965). "Theory of micropolar continuum", *Proc., Ninth Midwestern Mechanics Conference*, Univ. of Wisconsin, Madison, 23–40.

Eringen, A.C. (1966). "A unified theory of thermomechanical materials", *Int. J. of Engrg. Science* 4, 179–202.

Fabrikant, V.I. (1990). "Complete solutions to some mixed boundary value problems in elasticity", in *Advances in Applied Mechanics* 27, 153–223, ed. by J. Hutchinson and T. Wu, Academic Press.

Fox, L. (1965). *An introduction to numerical linear algebra*, Oxford University Press, New York.

Furuhashi, R., Kinoshita, N., and Mura, T. (1981)."Periodic distributions of inclusions", *Int. J. of Engrg. Science* 19, 231–236.

Gross, D. (1982), *Ingenieur-Archiv* 51, 301–310.

Hellan, K. (1984). *Introduction to fracture mechanics*, McGraw-Hill, New York (p. 234).

Horii, H., and Nemat-Nasser, S. (1985). "Elastic fields of interacting inhomogeneities", *Int. J. of Solids and Structures* 21, 731–745.

Ju, J.W. (1991). "On two-dimensional self-consistent micromechanical damage models for brittle solids", *Int. J. of Solids and Structures* 27 (22), 227–258.

Ju, J.W. (1990). "Isotropic and anisotropic damage variables in continuum damage mechanics", *ASCE J. of Engrg. Mechanics* 116 (12), 2764–2770.

Ju, J.W., and Lee, X. (1991). "Micromechanical damage models for brittle solids. Part I: Tensile Loadings", *ASCE J. of Engrg. Mechanics* 117 (7), 1495–1594.

Kachanov, M. (1985). "A simple technique of stress analysis in elastic solids with many cracks", *Int. J. of Fracture*, 28, R11–R19.

Kachanov, M. (1987). "Elastic solids with many cracks: A simple method of analysis", *Int. J. of Solids and Structures* 23, 23–43.

Kachanov, M., and Laures, J.-P. (1989). "Three-dimensional problems of strongly interacting arbitrarily located penny-shaped cracks", *Int. J. of Fracture* 41, 289–313.

Kachanov, M. (1980). "A continuum model of medium with cracks", *ASCE J. of Engrg. Mechanics* 106, 1039–1051.

Kachanov, M. (1992). "Effective elastic properties of cracked solids", *Appl. Mech. Reviews* 45 (8), 304-335.

Kassir, M.K., and Sih, G.C. (1975), *Three-dimensional crack problems*, Noordhoff International Publishing, Leyden, Netherlands.

Korn, G.A., and Korn, T.M. (1968). "Mathematical handbook for scientists and engineers", 2nd ed., McGraw Hill, New York (ch. 20).

Krajcinovic, D. and Fonseka, G.U. (1981), "The continuous damage theory of brittle materials (1 & 2)", *ASME J. of Applied Mechanics* 48, 809–824.

Kröner, E. (1967), "Elasticity theory of materials with long-range cohesive forces", *Int. J. of Solids and Structures* 3, 731–742.

Lee, X., and Ju, J.W. (1991). "Micromechanical damage models for brittle solids. Part II: Compressive Loadings", *ASCE J. of Engrg. Mechanics* 117 (7), 1515–1536.

Mühlhaus, H.-B., and Aifantis, E.C. (1991). "A variational principle for gradient plasticity", *Int. J. of Solids and Structures* 28, 845-858.

Pijaudier-Cabot, G., and Bažant, Z. P. (1987). "Nonlocal damage theory," *J. of Engng. Mechanics ASCE*, 113, (10), 1512–1533.

Pijaudier-Cabot, G., and Bažant (1991). "Cracks interacting with particles or fibers in composite materials." *Journal of Engineering Mechanics* ASCE 117(7), 1611–1630.

Planas, J. (1992). Privately communicated comment on a draft of this paper, Northwestern University, July 13.

Rektorys, K. (1969). *Survey of Applicable Mathematics*, Iliffe Books Ltd., London.

Sluys, L.J. (1992). "Wave propagation, localisation and dispersion in softening solids", Doctoral Thesis, Technical University Delft, Netherlands.

Sneddon, I.N., and Lowengrub, M. (1969). *Crack problems in the classical theory of elasticity*, John Wiley & Sons, New York.

Strang, G. (1980). *Linear algebra and its applications*, 2nd ed., Academic Press, New York.

Varga, R.S. (1962). *Matrix iterative analysis*, Prentice Hall.

Vardoulakis, I. (1989). "Shear banding and liquefaction in granular materials on the basis of Cosserat continuum theory", Ingenieur-Archiv 59, 106-113.

FIGURE CAPTIONS

Fig. 1 Local and Nonlocal Inelastic Stress Increments During the Loading Step.

Fig. 2 Superposition Method for a Solid with Many Cracks (a, b — two alternatives).

Fig. 3 Crack Interactions of Various Types, Their Radial and Angular Dependences, and Coordinates.

Fig. 4 Cracks Near Boundary and Crack Bands.

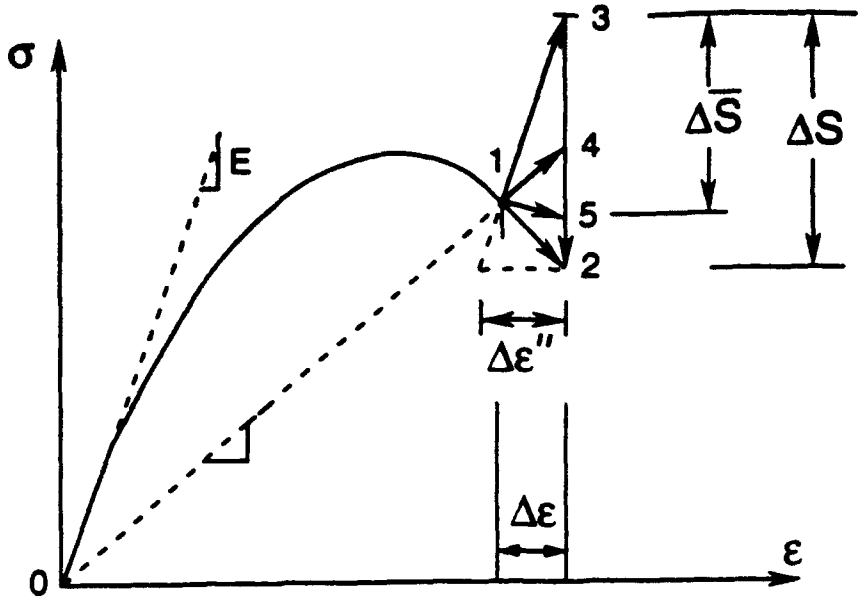
σ
E
3
4
1
5
2
ΔS̄
ΔS
Δε″
Δε
0
ε

Fig. 1

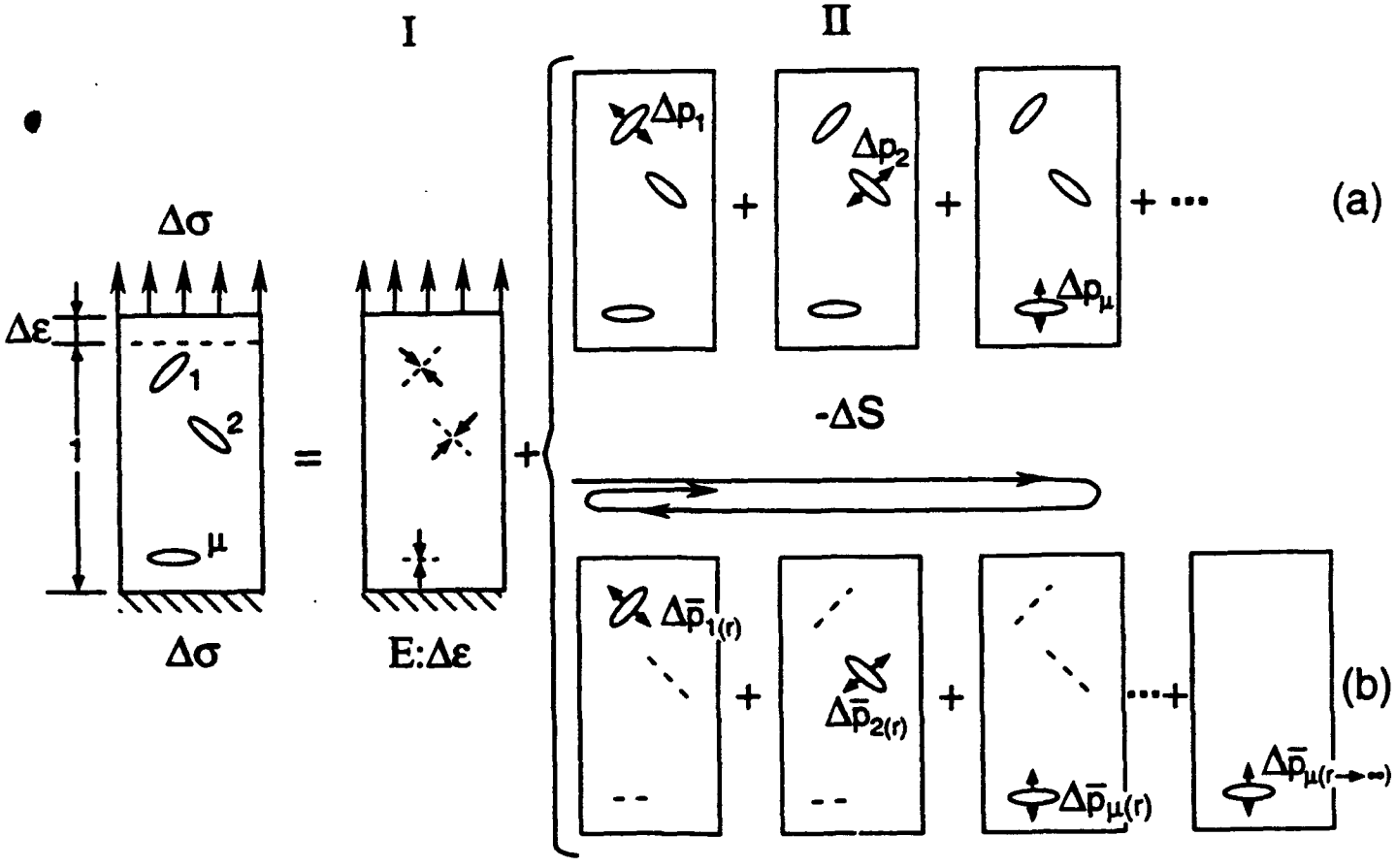
I
II
Δσ
Δε
1
1
2
μ
=
+
Δσ
E:Δε
Δp1
Δp2
Δpμ
+
+
+ ···
(a)
-ΔS
Δp̄1(r)
Δp̄2(r)
Δp̄μ(r)
···+
Δp̄μ(r→∞)
(b)

Fig. 2

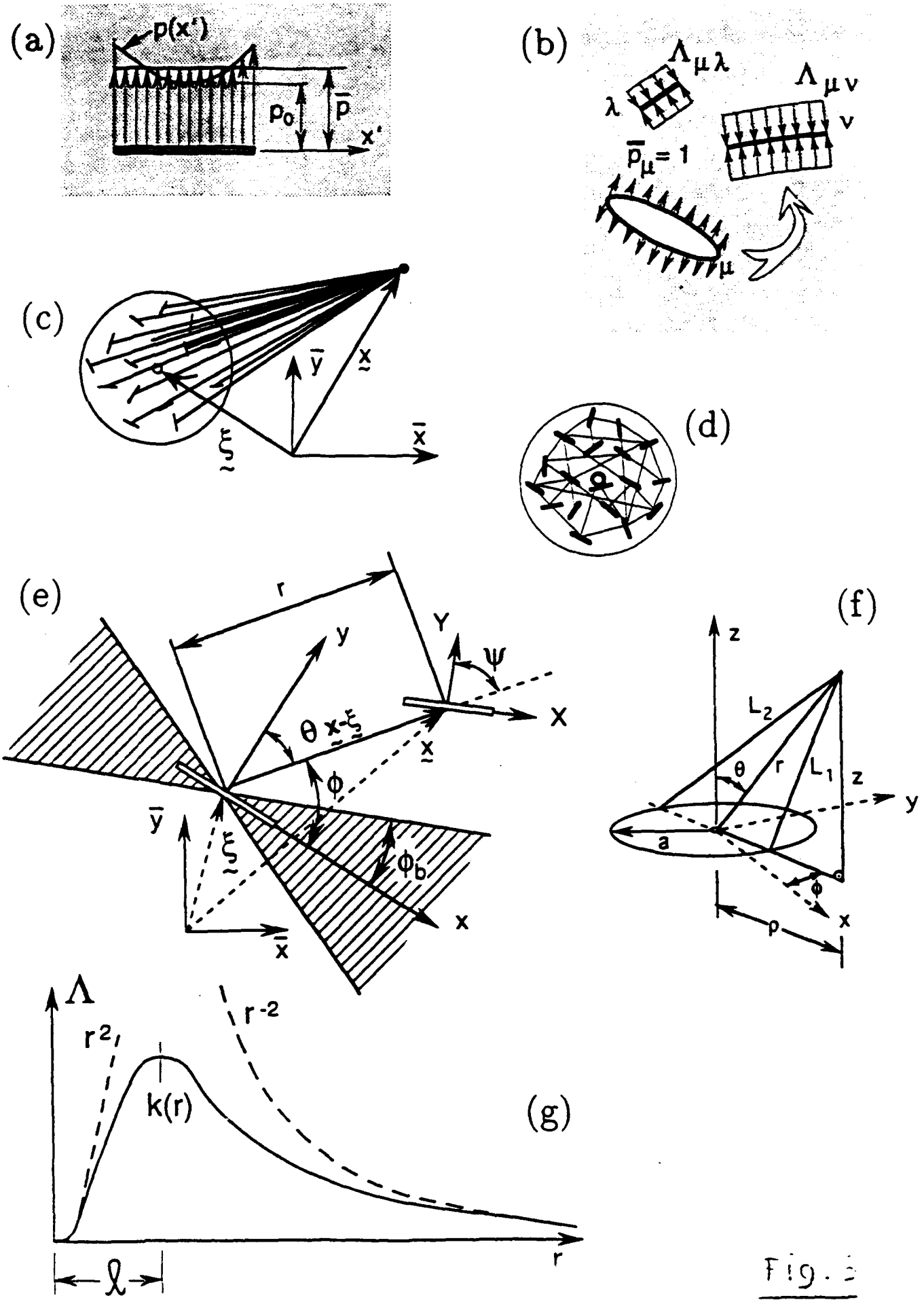
(a)
p(x')
p_0
$\bar{p}$
x'
(b)
$\Lambda_{\mu\lambda}$
$\Lambda_{\mu\nu}$
λ
ν
$\bar{p}_\mu = 1$
μ
(c)
$\bar{y}$
$\underset{\sim}{x}$
$\bar{x}$
$\underset{\sim}{\xi}$
(d)
(e)
r
y
Y
ψ
X
$\theta_{\underset{\sim}{x}-\underset{\sim}{\xi}}$
$\underset{\sim}{x}$
ϕ
$\bar{y}$
$\underset{\sim}{\xi}$
ϕ_b
x
$\bar{x}$
(f)
z
L_2
θ
r
L_1
z
y
a
ϕ
x
ρ
Λ
r^2
r^{-2}
k(r)
(g)
r
ℓ

Fig. 3

NONLOCAL DAMAGE THEORY BASED ON MICROMECHANICS OF CRACK INTERACTIONS[1]

By ZDENĚK P. BAŽANT[2], F.ASCE

Errata and Addendum

Errata:

- In the sentence preceding (12), replace the word 'subscript' by the word 'superscript'.
- In equation (35b), replace σ_{xx} by σ_{yy}.
- In the last sentence of the second paragraph after (40), replace $r \rightarrow \infty$ by $r \rightarrow 0$.

Addendum: A rigorous mathematical definition of the continuum crack influence function Λ has not been given in the paper. It can be given as folows. Function $\Lambda(0,\xi)$ represents the influence of a source crack at $x = 0$ on a target crack at ξ. At the macro-continuum point $x = 0$ there may or may not be a crack. To idealize the random two-dimensional arrangement of cracks, we may imagine that the center of the source crack influencing some target crack can occur randomly, with equal probability, anywhere within the square $s \times s$ centered at point $x = 0$; s represents the typical spacing of the dominant cracks of length $2a$ near point $x = 0$ (in a material such as concrete, $s \approx$ spacing of the largest aggregate pieces. The macroscopic crack influence function can describe the influence of the source crack only in the average sense. Therefore, $\Lambda(0,\xi)$ is defined as the mathematical expectation, $\mathcal{E}$, with regard to all the possible realizations of the source crack center within the square $s \times s$; $\Lambda(0,\xi) = \langle \mathcal{E}[\sigma^{(1)}(\xi - x, \eta - y)] \rangle$ where the operator $\langle \quad \rangle$ represents averaging over length $2a$ of the target crack at ξ, and $(\xi - x, \eta - y) = r =$ vector from the center $x = (x,y)$ of a source crack to the center $\xi = (\xi,\eta)$ of the target crack. In detail, chosing axis y to be normal to the source crack, we have

$$\Lambda(0,\xi) = \frac{1}{2a}\int_{-a}^{a}\frac{1}{s^2}\int_{-s/2}^{s/2}\int_{-s/2}^{s/2}\sigma^{(1)}(\xi - x, \eta - y)\,dx\,dy\,da' \tag{53}$$

where $\sigma^{(1)}$ is the principal str[illegible] $\xi = (\xi,\eta)$ caused by a unit uniform pressure applied on the faces of a crack of length $2a$ centered at $x = (x,y)$, as given by equation (40). The last integral, gives the precise mathematical definition of Λ. However, the integral seems difficult to evaluate and unnecessarily complicated. The simple approximation given in the paper on the basis of the asymptotic properties of this integral appears to be preferable for practical computations.

---

[1] *J. of Engrg. Mech. ASCE*, 120 (3), March 1994, .

[2] Walter P. Murphy Professor of Civil Engineering and Materials Science, Northwestern University, Evanston, Illinois 60208.

LOCALIZATION ANALYSIS OF NONLOCAL MODEL BASED ON CRACK INTERACTIONS

MILAN JIRÁSEK[1] AND ZDENĚK P. BAŽANT[2], FELLOW ASCE

ABSTRACT.— The conventional nonlocal model, often used as a localization limiter for continuum-based constitutive laws with strain-softening, has been based on an isotropic averaging function. It has recently been shown that this type of nonlocal averaging leads to a model which cannot satisfactorily reproduce experimental results for very different test geometries without modifying the value of the characteristic length depending on geometry. A micromechanically based enrichment of the nonlocal operator by a term taking into account the directional dependence of crack interactions can be expected to improve the performance of the nonlocal model. The aim of this paper is to examine this new model in the context of a simple localization problem reducible to a one-dimensional description. Strain localization in an infinite layer under plane stress is studied using both the old and the new nonlocal formulations. The importance of a renormalization of the averaging function in the proximity of a boundary is demonstrated and the differences between the localization sensitivity of the old and new model are pointed out. In addition to the detection of bifurcations from an initially uniform state, the stable branch of the load-displacement diagram is followed using an incremental procedure.

Introduction

As is now widely accepted, continuum modeling of progressive cracking in quasibrittle materials such as concrete, rock, tough ceramics or ice, requires constitutive models that exhibit strain-softening. In the context of standard local constitutive models (in which the stress-strain relationship at one point is not influenced by the evolution of stress and strain at other points), the presence of strain-softening leads to serious theoretical as well as numerical deficiencies. The governing differential equations lose ellipticity (in a static formulation) or hyperbolicity (in a dynamic formulation) and the problem ceases to be well-posed. These deficiencies manifest themselves in numerical calculations by spurious mesh sensitivity—strain usually

[1]Postdoctoral Research Fellow, Northwestern University, Evanston, Illinois 60208; currently Assistant Professor, Faculty of Civil Engrg., Czech Technical University, Thákurova 7, 166 29 Prague, Czech Republic.

[2]Walter P. Murphy Professor of Civil Engineering, Northwestern University, Evanston, Illinois 60208.

localizes into a narrow band whose width depends on the size of finite elements in the mesh and converges to zero as the mesh is refined. The corresponding load-displacement diagram always exhibits snapback for a sufficiently fine mesh and the total energy dissipated by fracture converges to zero.

To remedy the situation, a device called the *localization limiter* must be introduced to enforce a finite width of the localization band and a finite energy dissipation. The localization width is closely related to the so-called characteristic length of the material determined by the microstructure, e.g., by the size of inhomogeneities.

Several types of localization limiters have been proposed. A wide class of localization limiters is represented by the *nonlocal continuum* concept, which was introduced into continuum mechanics by Eringen (1965, 1966), Kröner (1967), Eringen and Edelen (1972) and others, and was proposed as a localization limiter by Bažant, Belytschko and Chang (1984). An effective nonlocal damage model was developed by Pijaudier-Cabot and Bažant (1987) and Bažant and Lin (1988). It bears some resemblance to the crack band model (Bažant and Oh, 1983) and to the mesh-dependent softening modulus of Pietruszczak and Mróz (1981). A differential form of the nonlocal concept (Bažant, 1984) was exploited in various gradient-dependent models (Schreyer and Chen, 1986; Lasry and Belytschko, 1988; de Borst and Mühlhaus, 1991). A more refined limiter of this type is the *micropolar continuum* (Cosserat and Cosserat, 1909), which was extended to strain-softening problems by Mühlhaus and Vardoulakis (1987). A computational model for the elastoplastic Cosserat continuum was formulated by de Borst and Sluys (1991). *Viscoplastic regularization* (Needleman, 1987) limits localization by adding rate-dependent terms to the constitutive equations.

New Approach to Nonlocal Averaging

One of the most powerful and computationally effective localization limiters is the concept of nonlocal averaging, first used in strain-softening analysis by Bažant (1984) and Bažant, Belytschko and Chang (1984).

The original version of the nonlocal approach, which was dealing with nonlocal total strain, led to certain numerical difficulties and resulted into a cumbersome imbricate structure of the finite element approximation. A substantial increase of computational efficiency was achieved by later improvements based on the idea that only the quantities directly associated with strain-softening, such as the damage, the damage energy release rate or the accumulated plastic strain, should be treated as nonlocal, while the elastic part of the behavior should remain local. Nonlocal versions of several constitutive models were successfully implemented into finite element codes and applied to a variety of problems by Bažant and Pijaudier-Cabot (1988), Bažant and Lin (1988) and Bažant and Ožbolt (1990). The nonlocal version

(Bažant and Ožbolt, 1990) of the microplane model (Bažant and Prat, 1988) proved to be particularly efficient for the computer analysis of structures made of quasibrittle materials such as concrete. However, it also became clear that the classical nonlocal concept based on an isotropic weight function has its limitations and does not allow formulating a model universally applicable to the same material under different loading conditions. More specifically, it turned out that the values of the characteristic length required to fit experimental data for very different test geometries are significantly different and therefore cannot be regarded as a true material parameter. Moreover, the physical meaning of nonlocal averaging was not clear and theoretically supported, and so the nonlocal concept appeared as an artifice dictated merely by the need to regularize the governing differential equations.

To overcome these difficulties, a micromechanically based derivation of the nonlocal operator has recently been presented (Bažant, 1992). This led to certain modifications of the original approach. Both the original and the new approaches start from the incremental form of a local constitutive law

$$\Delta\sigma = \mathbf{C}_t : \Delta\epsilon \tag{1}$$

where $\Delta\sigma, \Delta\epsilon$ are the increments of the stress and strain tensor and $\mathbf{C}_t$ is the fourth-rank tangential stiffness tensor of the material. The total stress increment is decomposed into the elastic and inelastic part:

$$\Delta\sigma = \mathbf{C}_u : (\Delta\epsilon - \Delta\epsilon'') = \mathbf{C}_u : \Delta\epsilon - \Delta\mathbf{S} \tag{2}$$

Here, $\mathbf{C}_u$ denotes the stiffness tensor for unloading, $\Delta\epsilon''$ is the increment of the inelastic strain tensor and $\Delta\mathbf{S}$ the increment of the local inelastic stress tensor. Equations (1) and (2) can be combined to yield the law relating the local inelastic stress increment to the strain increment:

$$\Delta\mathbf{S} = (\mathbf{C}_u - \mathbf{C}_t) : \Delta\epsilon \tag{3}$$

In the nonlocal formulation, the elastic stress increment remains unchanged while the inelastic stress increment $\Delta\mathbf{S}$ is replaced by its nonlocal value $\Delta\bar{\mathbf{S}}$. The constitutive law is now given by

$$\Delta\sigma = \mathbf{C}_u : \Delta\epsilon - \Delta\bar{\mathbf{S}} \tag{4}$$

where the nonlocal inelastic stress increment is to be computed by applying a certain nonlocal operator on the local inelastic stress increment derived from the strain increment according to (3). In the previously used nonlocal formulation, this operator represents weighted averaging over a certain neighborhood:

$$\Delta\bar{\mathbf{S}}(\mathbf{x}) = \int_V \Phi(\mathbf{x}, \xi)\Delta\mathbf{S}(\xi)d\xi \tag{5}$$

The scalar weight function $\Phi(\mathbf{x}, \xi)$ depends only on the distance $r = \|\mathbf{x} - \xi\|$ between the "source point" ξ and the "effect point" $\mathbf{x}$, and on a parameter called the characteristic length l of the nonlocal continuum. The usual form of $\Phi(\mathbf{x}, \xi)$ has been either a Gaussian distribution function or a bell-shaped function with a compact support $\Phi(\mathbf{x}, \xi) = \Phi_0[1 - (r/l)^2]^2 (r \leq l)$ where Φ_0 is a normalizing factor such that $\int_{-\infty}^{\infty} \Phi(\mathbf{x}, \xi) d\xi = 1$.

Based on analysis of the equations describing the interaction among microcracks in an elastic medium, the following generalization of the nonlocal concept has recently been derived (Bažant, 1992):

$$\Delta \bar{S}^{(i)}(\mathbf{x}) = \int_V \Phi(\mathbf{x}, \xi) \Delta S^{(i)}(\xi) d\xi + \int_V \sum_{j=1}^{3} \Lambda^{(ij)}(\mathbf{x}, \xi) \Delta \bar{S}^{(j)}(\xi) d\xi \tag{6}$$

where $\Delta S^{(i)}, i = 1, 2, 3$, are the increments of the principal inelastic stresses and $\Lambda^{(ij)}(\mathbf{x}, \xi)$ is the so-called crack influence function. Superscripts $^{(ij)}$ at $\Lambda^{(ij)}$ indicate that the value of this function depends not only on the locations of the source point and the effect point, but also on the orientation of the principal directions at these points. Analysis of the stress fields in two- and three-dimensional infinite bodies with a single crack provides us with the asymptotic form of the crack influence function and shows that this function is decaying as r^{-2} in two dimensions and r^{-3} in three dimensions, in contrast to the much faster decay of the aforementioned averaging function $\Phi(\mathbf{x}, \xi)$. Furthermore, the crack influence function is not isotropic, i.e. it cannot be reduced to a function of the distance r only. The behavior of Λ for small values of r is a statistical problem, cannot be easily derived, and has to be reasonably approximated. The following form of the crack influence function for two-dimensional problems has been derived after certain simplifications (Bažant, 1992):

$$\Lambda(\mathbf{x}, \xi) = -\frac{k(r)}{2l^2}[\cos 2\theta + \cos 2\psi + \cos 2(\theta + \psi)] \tag{7}$$

where

$$k(r) = \left(\frac{\kappa l r}{r^2 + l^2}\right)^2 \tag{8}$$

The angles θ and ψ characterize the orientations of two interacting cracks as shown in Fig. 1a, and κ is a nondimensional parameter roughly equal to the ratio of the average crack size and the characteristic length. The orientations θ and ψ depend on stress state at each point.

A substantial simplification of Equation (6) can be obtained by taking into account only the interactions between dominant cracks forming in the planes perpendicular to the maximum principal stress;

$$\Delta \bar{S}^{(1)}(\mathbf{x}) = \int_V \Phi(\mathbf{x}, \xi) \Delta S^{(1)}(\xi) d\xi + \int_V \Lambda^{(11)}(\mathbf{x}, \xi) \Delta \bar{S}^{(1)}(\xi) d\xi \tag{9}$$

The superscripts $^{(1)}$ and $^{(11)}$ will further be omitted to simplify the notation. Note that in the continuum description a crack is considered at every point. This is of course only the continuum smearing. The cracks are in reality discrete (in more detail, see Bažant, 1992).

Simplified One-Dimensional Problem

Behavior of the new nonlocal model in general multidimensional problems can hardly be treated analytically. It is feasible after implementation in a finite element program, but this will be the subject of another paper (Ožbolt and Bažant). The present paper will focus on the basic properties of the new model, which must be examined first. The most basic property is one-dimensional localization of damage into a straight band, taking place inside an infinite layer of thickness L (Fig. 1b). For the case of a local continuum in which the localization limiter is introduced as a lower limit on the band width, as in the crack band model, this problem was treated in Bažant (1988a) and Bažant and Lin (1989) (see also Bažant and Cedolin, 1991, Sec. 13.3). To make use of the simple expression for the crack influence function $\Lambda(\mathbf{x}, \xi)$ in two dimensions (in contrast to the much more complicated form for a 3-D continuum), we will consider a plane stress situation—the dimension of the layer in the z-direction is assumed to be so small that the corresponding normal stress σ_z is negligible. On the other hand, the dimension of the layer in the y-direction is very large and the corresponding normal strain ϵ_y is negligible. The layer is loaded by enforcing a uniform displacement in the x-direction at one of the fixed boundaries, which causes an increase of strain ϵ_x and a change of stress σ_x. To simplify the notation, the subscripts at σ_x and ϵ_x as well as at the corresponding stiffness coefficients will be dropped. The stiffness coefficients C_u, C_t and C_s (to be defined later) are to be understood as the components C_{1111} (or C_{xx}) of the stiffness tensors $\mathbf{C}_u$, $\mathbf{C}_t$, $\mathbf{C}_s$, resp., in a local constitutive law describing a plane stress problem.

As the shear strains and stresses are zero, equilibrium in the x-direction requires σ_x to be constant, but ϵ_x can in general vary as a function of x. Of course, for a local continuum with a one-to-one relationship between stress and strain, ϵ_x would have to be a constant, too, but the existence of a softening part in the stress-strain law can lead to strain localization and loss of uniqueness. In a local formulation, localization would occur right at peak stress and there would be no lower limit on the width of the possible localization band. As will be shown later, in the present nonlocal formulation the strain can cease to be constant even before the peak stress, but a true localization band forms only after the peak and its width cannot decrease below a certain minimum depending on the ratio of the layer width and the characteristic length of the model, as well as on the tangential modulus.

With the assumption that all the quantities depend only on one spatial variable

x and that the total stress (and thus also the stress increment) is independent of x, we can set $y = 0$ in the basic equations (3), (4) and (9) and rewrite them as

$$\Delta S(x) = [C_u(x) - C_t(x)]\Delta\epsilon(x) \tag{10}$$

$$\Delta\sigma = C_u(x)\Delta\epsilon(x) - \Delta\bar{S}(x) \tag{11}$$

$$\begin{aligned}\Delta\bar{S}(x) &= \int_{-\infty}^{\infty}\int_{-\infty}^{\infty}\Phi(x,0,\xi,\eta)\Delta S(\xi)d\xi d\eta + \int_{-\infty}^{\infty}\int_{-\infty}^{\infty}\Lambda(x,0,\xi,\eta)\Delta\bar{S}(\xi)d\xi d\eta = \\ &= \int_{-\infty}^{\infty}\hat{\Phi}(x,\xi)\Delta S(\xi)d\xi + \int_{-\infty}^{\infty}\hat{\Lambda}(x,\xi)\Delta\bar{S}(\xi)d\xi \end{aligned} \tag{12}$$

where

$$\hat{\Phi}(x,\xi) = \int_{-\infty}^{\infty}\Phi(x,0,\xi,\eta)d\eta, \qquad \hat{\Lambda}(x,\xi) = \int_{-\infty}^{\infty}\Lambda(x,0,\xi,\eta)d\eta \tag{13}$$

The term that is additional in (9) compared to (5) should vanish in a state of uniform strain when the local and nonlocal inelastic stresses are identical. It might therefore be expected that $\hat{\Lambda}\int_{-\infty}^{\infty}\hat{\Lambda}(\mathbf{x},\xi)d\xi = 0$ for any value of $\mathbf{x}$. If the integral is formally transformed to polar coordinates, the integrand is given by a product of a periodic function of the angular coordinate with zero mean and another function of the radius, and on this basis the foregoing condition seems to be satisfied. A careful examination of the definition of $\Lambda(\mathbf{x},\xi)$ however reveals that for large values of r, Λ behaves asymptotically as r^{-2} in two dimensions and r^{-3} in three dimensions, and so the integral $\int_{\infty}^{\infty}\int_{\infty}^{\infty}\Lambda(x,y,\xi,\eta)d\eta d\xi$ is not absolutely convergent. Such a problem with integrability is common to many physical problems formulated in an infinite domain and is not easy to overcome. Fortunately it disappears when dealing with real-life finite bodies or with semiinfinite bodies bounded at least in some direction. This is also the case for the layer studied in this chapter. The limits of integration in the x-direction are finite and, with this modification, the integral converges but is not equal to zero.

In the simple situation considered, the directions of the maximum principal inelastic stress at all points are aligned (Fig. 1b), which implies that $\theta = \psi$. With the notation $\zeta = (x - \xi)/l$, the one-dimensional crack influence function can be expressed as

$$\hat{\Lambda}(x,\xi) = \frac{\pi\kappa^2}{l}\left[\frac{4\zeta^6 + 6\zeta^4 + 1.5\zeta^2 + 0.25}{(1+\zeta^2)^{3/2}} - 4|\zeta|^3\right] \tag{14}$$

A surprising fact is that the resulting function is positive for all values of its arguments (Fig. 1c), which contradicts the intuitively expected property $\int_{-\infty}^{\infty}\hat{\Lambda}(x,\xi)d\xi = 0$. This is a consequence of the lack of absolute integrability of the original two-dimensional crack influence function. By some tedious algebraic manipulations it can be shown that the function in the brackets in (14) decays for large ζ as $\frac{1}{2}\zeta^{-3} + O(\zeta^{-5})$, and so the one-dimensional crack influence function is integrable.

Bifurcation Analysis of Post-Peak Behavior

Formulation of the Problem

Having developed the basic framework of a one-dimensional localization problem, we now focus on the analysis of a possible bifurcation of the equilibrium path after reaching the peak stress and entering the softening regime. The local stress-strain law is assumed to be linear up to the peak, with a constant slope C_0, and then to start decaying with an initial slope C_s.

Up to the peak, the tangential stiffness C_t and the unloading stiffness C_u are identical and equal to C_0, and thus the local inelastic stress increments given by (10) vanish at all points of the layer. The basic equation (12) has a trivial solution $\Delta\bar{S}(x) = 0$ and (11) then implies $\Delta\epsilon(x) = \Delta\sigma/C_0 = \text{const.}$, which means that the strains remain uniform up to the peak. The picture dramatically changes after the peak stress is reached. A part of the layer can experience further strain increase accompanied by softening while the rest unloads in an elastic way. The unloading modulus C_u is still equal to C_0 at all points of the layer, but the tangential modulus C_t remains equal to C_0 only in the unloading part (denoted by U) and jumps to C_s in the softening region (denoted by S). Equations (10) and (11) can be substituted into (12) to get a single integral equation for the unknown strain increment $\Delta\epsilon(x)$:

$$\begin{aligned} C_0\Delta\epsilon(x) - \Delta\sigma &= \int_{-\infty}^{\infty} \hat{\Phi}(x,\xi)(C_0 - C_t(\xi))\Delta\epsilon(\xi)d\xi \\ &\quad + \int_{-\infty}^{\infty} \hat{\Lambda}(x,\xi)(C_0\Delta\epsilon(\xi) - \Delta\sigma)d\xi \end{aligned} \tag{15}$$

So far, we have kept the integration limits at minus and plus infinity. The region outside the layer can be thought of to be fixed to perfectly rigid clamps which represent a continuation of the body. So it seems to be natural to set the corresponding strain and stress increments equal to zero. Moreover, the difference $C_0 - C_t(\xi)$ is zero for ξ lying in the unloading region U and the integrand in the first integral vanishes outside the softening region S. After dividing by C_0 and rearranging, equation (15) reads

$$\mu \int_S \hat{\Phi}(x,\xi)\Delta\epsilon(\xi)d\xi + \int_0^L \hat{\Lambda}(x,\xi)\Delta\epsilon(\xi)d\xi - \Delta\epsilon(x) = \frac{\Delta\sigma}{C_0}(\lambda(x) - 1) \tag{16}$$

where $\mu = 1 - C_s/C_0$, $\lambda(x) = \int_0^L \hat{\Lambda}(x,\xi)d\xi$. The parameter μ characterizes the local constitutive law. It is always positive; its values between 0 and 1 indicate hardening, $\mu = 1$ corresponds to a horizontal yield plateau, and $\mu > 1$ to softening. On the other hand, the type of the global load-displacement diagram is determined by the sign of the stress increment $\Delta\sigma$. Naturally, $\Delta\sigma > 0$ means global hardening,

$\Delta\sigma < 0$ global softening and $\Delta\sigma = 0$ implies a horizontal yield plateau in the load-displacement diagram.

In addition to equation (16), an acceptable solution of the problem must satisfy the loading-unloading criterion

$$\Delta\epsilon(x) \geq 0 \text{ if } x \in S, \qquad \Delta\epsilon(x) \leq 0 \text{ if } x \in U \tag{17}$$

This additional condition is exploited to determine the extent of the softening and unloading region.

When studying the bifurcation problem, the increments of stress and strain are infinitesimal and $\Delta\epsilon(x)$ can change proportionally to $\Delta\sigma$. As this study focuses primarily on the softening behavior, we can look for a strain increment per a unit stress decrement and normalize it by the initial elastic modulus C_0 to get a nondimensional quantity $e(x) = -C_0\Delta\epsilon(x)/\Delta\sigma$. In terms of this unknown function, equation (16) can be rewritten as

$$\mu \int_S \hat{\Phi}(x,\xi)e(\xi)d\xi + \int_0^L \hat{\Lambda}(x,\xi)e(\xi)d\xi - e(x) = 1 - \lambda(x) \tag{18}$$

If we look for solutions that cane exhibit global hardening, we can replace the definition of $e(x)$ by $e(x) = C_0\Delta\epsilon(x)/\Delta\sigma$ and the right hand side of (18) changes its sign. Finally, the case of no stress change (resulting into a plateau in the load-displacement diagram) can be treated by setting $e(x) = \Delta\epsilon(x)$ and replacing the right hand side of (18) by zero. The loading-unloading condition is the same for all the above-mentioned cases:

$$e(x) \geq 0 \text{ if } x \in S, \qquad e(x) \leq 0 \text{ if } x \in U \tag{19}$$

Discretization of the Problem

To solve equation (18) numerically, one can look for the values $e_0, e_1, e_2, \ldots e_N$ of the unknown function $e(x)$ at a finite number of points $x_0 = 0, x_1, x_2, \ldots x_N = L$. The unknowns can be collected to form a vector (column matrix), $\mathbf{e}$. After approximating the integrals by sums, the integral equation (18) can be replaced by a matrix equation

$$(\mu\mathbf{F} + \mathbf{L} - \mathbf{I})\mathbf{e} = \mathbf{i} - \mathbf{l} \tag{20}$$

where $\mathbf{F}$ and $\mathbf{L}$ are square matrices, $\mathbf{l}$ is a vector, $\mathbf{I}$ stands for the unit square matrix and $\mathbf{i}$ for the vector with all components equal to 1. The matrix counterpart of the loading-unloading criterion (17) is then

$$\mathbf{Se} \geq \mathbf{0}, \qquad \mathbf{Ue} \leq \mathbf{0} \tag{21}$$

where the diagonal incidence matrices $\mathbf{S}$ and $\mathbf{U} = \mathbf{I} - \mathbf{S}$ have zero and unit diagonal elements indicating whether the corresponding point lies in the softening or unloading region. To evaluate the vector $\mathbf{l}$ and the matrices $\mathbf{F}$ and $\mathbf{L}$ in (20), a numerical quadrature rule must be applied to the integrals in (18).

Solution Strategies

As the solution of (20) is subject to (21), it must be constructed in an iterative way. In a parameter study, when one wants to explore the effect of μ on the post-peak behavior, the softening region S can be chosen in advance and one can then look for the corresponding value of μ:

1. Given S and U, compute the matrices $\mathbf{L}$ and $\mathbf{F}$ and the vector $\mathbf{l}$.
2. Make an initial estimate of the parameter μ.
3. Assemble $(\mu\mathbf{F} + \mathbf{L} - \mathbf{I})$ and $\mathbf{i} - \mathbf{l}$.
4. Solve the system of linear equations (20).
5. Check if the solution $\mathbf{e}$ satisfies conditions (21). If it does, output the solution and stop. If it does not, modify μ and go to step 3.

It can be expected that softening will tend to concentrate in a band either inside the layer or at its boundary. The former situation can be denoted as U-S-U (unloading band – softening band – unloading band), the latter by S-U (softening band – unloading band). Another possibility is that all the material softens (denoted simply by S) or that there ex: t several separate localization bands, e.g. S-U-S or S-U-S-U.

Method of Analysis and Solution for Old Nonlocal Model

Now we need to explain how to construct an admissible solution for a given value of parameter μ, discuss the meaning of the eigenvalues and the character of the solutions for different localization modes. The computational procedure can be best illustrated by a simple example. The parameter κ is first set to zero, which means that the two-dimensional crack influence function $\Lambda(\mathbf{x}, \xi)$ defined by (7), (8), as well as its one-dimensional counterpart $\Lambda(x, \xi)$ defined by (14), is identically zero and the old nonlocal formulation is recovered. The matrix $\mathbf{L}$ and vector $\mathbf{l}$ then disappear from the equations and (20) takes a special, simpler form

$$(\mu\mathbf{F} - \mathbf{I})\mathbf{e} = \mathbf{i} \tag{22}$$

Fig. 2a shows the strain increment profiles for an assumed localization pattern U-S-U with the total length of the layer $L = 20l$ and the assumed length of the softening

region $h = 10l$. The profiles were constructed for a sequence of μ values between 0.99 and 1.03 and the loading-unloading criterion was tested for each of them. A solution satisfies the loading-unloading criterion if it is positive for $x/l \in (5, 15)$ and negative everywhere else. Fig. 2a indicates that for $\mu = 0.99$ and $\mu = 1.00$, the solution is negative over the whole layer and it decreases as μ grows. Between $\mu = 1.00$ and $\mu = 1.01$, the solution jumps to large positive values and then decreases again. The interval on which it is positive shrinks and at $\mu = 1.02$ it only slightly exceeds the assumed softening interval $S = (5, 15)$. When μ reaches 1.03, the interval with positive strain increments is already inside S. As this transition is continuous, there must be a value of μ between 1.02 and 1.03 for which the loading-unloading criterion is exactly satisfied. If a function $f(\mu)$ is defined by assigning to each μ the value of the strain increment at $x = 5$, a necessary condition to satisfy the loading-unloading criterion is $f(\mu) = 0$. This nonlinear equation can be solved by one of the standard techniques, e.g. by the secant method or by the Newton method. In the latter case, the derivative of f is computed numerically using a difference formula. The graph of $f(\mu)$ is shown in Fig. 2b and it is clear that once the interval containing the root and no singularities is located, the iteration process converges without any problems.

The singular points of $f(\mu)$ correspond to the values of μ for which the coefficient matrix $(\mu\mathbf{F} - \mathbf{I})$ is singular, or, equivalently, to the eigenvalues of $\mathbf{F}^{-1}$. When increasing μ from zero, the first singular value is reached approximately at $\tilde{\mu}_1 = 1.006$. At this point, the strain increments jump from large negative to large positive values (see Fig. 2a). For $\mu < \tilde{\mu}_1$, the function $f(\mu)$ has only negative values and the corresponding solutions are not admissible. The first root of $f(\mu)$ can be found at $\mu_1 = 1.0237$ and the corresponding solution is really admissible (it satisfies the loading-unloading criterion). After the second singular value $\tilde{\mu}_2$ is passed, another root can be detected at $\mu_2 = 1.0990$, but the corresponding solution drops below zero in a small interval in the middle of the softening band and therefore is not admissible.

The iterative procedure can be repeated for different sizes of the softening region and each of the calculations yields one possible post-peak branch for a particular value of the parameter μ. Several such solutions are depicted in Fig. 3a. More localized solutions require a higher value of μ, i.e. a steeper slope of the descending part of the local constitutive law. Solutions with a larger softening zone are possible for smaller values of μ, however, μ must always be larger than 1, which means that the local law must exhibit softening (and not hardening or a horizontal plateau).

Other sets of solutions can be constructed for other localization patterns. It turns out, however, that, for the old nonlocal model with $\kappa = 0$, the solutions are invariant with respect to a shift along the x-axis and therefore the S-U localization profiles have the same shape as the U-S-U profiles and are only shifted to the boundary. Similarly, the S-U-S profiles can be obtained by moving two identical

U-S-U profiles to both boundaries (Fig. 3b). This seems to be a deficiency, because the presence of boundaries would no doubt affect the shape of the localization profiles and the corresponding values of μ. The behavior of the present model can be understood if one realizes that the softening region is not affected by anything outside it, because the local inelastic stress increments in the unloading region are zero and thus they do not contribute to the nonlocal inelastic stress increments, which can be evaluated from the strain displacements in the softening zone only. That is why the position of the softening region does not make any difference and the only important thing is its length. At the same time, the strain increment profiles evaluated under the assumption of loading only (the S type of localization pattern) are highly nonuniform, with strain concentration in the middle of the layer (Fig. 3c). This means that the boundaries repel strain localization.

Renormalized Averaging Function

The picture substantially changes if the averaging function $\Phi(x, \xi)$ is renormalized in the vicinity of the boundaries. The normalizing condition $\int_{-\infty}^{\infty} \Phi(x, \xi)\, d\xi = 1$ ensures that a uniform local quantity in an infinite body leads to a uniform nonlocal quantity with the same value. If this property is to be preserved in a finite body, the integration domain must be changed to the domain of the body V and, instead of the original averaging function in an infinite body $\Phi(\mathbf{x}, \xi) = \Phi_0[1 - (r/l)^2]^2$, a normalized function

$$\Phi_n(\mathbf{x}, \xi) = \frac{\Phi(\mathbf{x}, \xi)}{\int_V \Phi(\mathbf{x}, \xi) d\xi} \tag{23}$$

must be used.

When the normalized averaging function is implemented, the model is able to exactly reproduce uniform strain increments and also the shape of the S-U and S-U-S localization patterns becomes more reasonable (Fig. 3d,e). This formulation is therefore adopted for the subsequent development.

Due to renormalization, the matrix $\mathbf{F}$ assembled under the assumption of loading everywhere has the property that the sum of its elements in every row is equal to 1 (this is the discrete analog of the integral normalizing condition). This can be written as $\mathbf{Fi} = \mathbf{i}$ where $\mathbf{i}$ is the previously defined vector with all components equal to 1. As of course also $\mathbf{Ii} = \mathbf{i}$, equation (22) has a solution $\mathbf{e} = \mathbf{i}/(\mu - 1)$ for any $\mu \neq 1$. If $\mu > 1$, this solution is admissible and it represents uniform strain increment profiles associated with stress decrements. The corresponding post-peak branch in the global load-displacement diagram has the same slope as the post-peak branch in the local constitutive law. If $\mu < 1$, the solution is not admissible under the assumption that stress decreases, however, it is admissible if one assumes that stress increases. Again, the slope of the global load-displacement diagram is the same as the slope of the local constitutive law (both are positive and hardening

occurs). The transition from hardening to softening is given by $\mu = 1$ when the coefficient matrix in (22) becomes singular. But this is perfectly consistent with the fact that the unknown function $e(x)$ defined by $e(x) = -C_0\Delta\epsilon(x)/\Delta\sigma$ can be introduced only if the stress change is not zero. If $\Delta\sigma = 0$, equation (22) can be used only if $e(x)$ is replaced directly by $\Delta\epsilon(x)$ and the right hand side is set to zero. The homogeneous set of equations with the singular coefficient matrix $\mathbf{F} - \mathbf{I}$ has infinitely many solutions, all of them multiples of the eigenvector $\mathbf{i}$. The physical meaning is that for a local constitutive law with a horizontal plateau, the strain increments are uniform and arbitrarily large while the stress does not change at all.

Besides the uniform solution, several other admissible solutions may exist for the same value of the parameter μ, i.e. for the same post-peak slope of the local constitutive law. It can be proven (Bažant, 1988b) that the branch that will be actually followed by the real system is the one with the steepest descent. All other branches are unstable in the sense that they can never be followed spontaneously, unless an additional restriction is imposed on the system (despite the fact that the points on these branches might be stable states). Stability of different branches of the global response existing for a given local constitutive law can be evaluated by introducing a parameter related to the post-peak slope of the load-displacement diagram. To avoid difficulties with a discontinuity at snapback, the negative inverse value of the post-peak slope is used as such parameter rather than the slope itself. It is convenient to introduce a nondimensional compliance parameter

$$s = -\frac{C_0\Delta\bar{\epsilon}}{\Delta\sigma} = -\frac{C_0}{L\Delta\sigma}\int_0^L \Delta\epsilon(x)dx = \frac{1}{L}\int_0^L e(x)dx \tag{24}$$

whose values are positive for post-peak softening and negative if snapback occurs; $s = 0$ corresponds to a vertical drop in the global load-displacement diagram indicating a loss of stability under displacement control.

It follows from the definition of the compliance parameter s that the actual branch is that which minimizes s. To study the effect of μ on the localization pattern and on the post-peak slope, the compliance parameter was evaluated for various types of solutions and plotted against μ. Fig. 4 shows such a plot for $\kappa = 0, L = 20l$ and a renormalized averaging function Φ_n. It is clear that the pattern S-U dominates in all situations covered by this plot. This means that the strain tends to localize into a band at one boundary (the S-U pattern) rather than into a band in the middle (the U-S-U pattern) or into two symmetric bands at both boundaries (the S-U-S pattern). The decrease of s with an increasing μ indicates that the post-peak slope of the load-displacement diagram is getting steeper as the slope of the local constitutive law becomes steeper. At $\mu = 1.14$, s becomes negative, which corresponds to the occurrence of a snapback. Beyond this limit, the test cannot be performed in a stable manner by controlling only the relative displacement of the boundaries.

It is interesting to check whether localization would occur for all values of $\mu > 1$, i.e., whenever the local constitutive law exhibits softening. It turns out that the localization threshold lies slightly above 1. This threshold is determined by the solution of the S-U type with the maximum possible localization width $h = L = 20l$. At this extreme width, the S-U localization pattern is in fact identical with the S pattern denoting loading only. However, the corresponding solutions are distinct, because the S solutions are uniform while the S-U solution must satisfy the degenerated loading-unloading condition $\Delta\epsilon(L) = 0$ (the unloading region U shrinks to one point). As the matrix $\mathbf{F}$ is uniquely determined by the assumption of loading everywhere, the governing equation

$$(\mu\mathbf{F} - \mathbf{I})\mathbf{e} = \mathbf{i} \tag{25}$$

is the same for both cases. To get two distinct solutions, the coefficient matrix $\mu\mathbf{F} - \mathbf{I}$ must be singular and μ is therefore the reciprocal of an eigenvalue of $\mathbf{F}$. As explained before, the matrix $\mathbf{F}$ assembled under the assumption of loading only has always $\tilde{\phi}_1 = 1$ as its eigenvalue (and it turns out to be the largest eigenvalue). The corresponding $\tilde{\mu}_1 = 1/\tilde{\phi}_1$ is also equal to 1 but then equation (25) has no solution. This means that for a local constitutive law with a horizontal plateau, the global response does not exhibit softening. The second largest eigenvalue $\tilde{\phi}_2$ of $\mathbf{F}$ is smaller than 1 and its inverse value $\tilde{\mu}_2 = 1/\tilde{\phi}_2$ is the critical value of μ for which localization starts. As $\det(\tilde{\mu}_2\mathbf{F} - \mathbf{I}) = 0$, solutions of (25) can be written as

$$\mathbf{e} = \frac{1}{\tilde{\mu}_2 - 1}\mathbf{i} + \alpha\tilde{\mathbf{e}}_2 \tag{26}$$

where $\tilde{\mathbf{e}}_2$ is the eigenvector of $\mathbf{F}$ corresponding to the eigenvalue $\tilde{\phi}_2$ and α is an arbitrary constant. Only solutions with all components nonnegative are admissible and the one with the last component equal to 0 is the initial solution of the S-U type. When μ is increased, the softening band S ceases to extend over the whole layer and starts shrinking.

A similar analysis has been performed for other widths of the layer and the effect of the layer width L as an additional parameter has been investigated. As expected, narrow layers are less susceptible to localization than wide ones, and higher values of μ are needed to produce results similar to those for wide layers. Three important characteristics of the localization sensitivity can be defined:

- $\tilde{\mu}_1 = 1$ ... transition from global softening to global hardening,
- $\tilde{\mu}_2$ ... onset of localization,
- μ_s ... snapback, loss of stability.

The values of $\tilde{\mu}_1$, $\tilde{\mu}_2$ can be determined by an eigenvalue analysis of the matrix $\mathbf{F}$ while μ_s must be solved for by iteratively looking for the value of μ causing the

compliance parameter s to be zero. The characteristic values $\tilde{\mu}_1, \tilde{\mu}_2, \mu_s$ are plotted against the ratio L/l in Fig. 5. Depending on the layer width and the slope of the local constitutive law, four types of behavior can be distinguished and graphically represented as four regions in Fig. 5:

- A - global hardening,
- B - global softening without localization, strain increments remain uniform,
- C - localization into a softening band, stable during displacement control,
- D - snapback in the global load-displacement diagram immediately after peak.

Analysis of the New Model

So far, all analyses and considerations have been concerned with the old localization model characterized by the absence of the additional term based on the crack influence function. How will the results be affected by the presence of this term in the integral equation (16) or its matrix counterpart (20)? The first striking difference is that uniform strain increments are no longer possible. This can be easily proven by substituting $\Delta\epsilon(x) = \Delta\epsilon = \text{const.}$ into (16), which leads to

$$(\mu - 1)\Delta\epsilon + \frac{\Delta\sigma}{C_0} = \lambda(x)\left(\frac{\Delta\sigma}{C_0} - \Delta\epsilon\right) \tag{27}$$

As the function $\lambda(x)$ is not constant (due to boundary effect), this equation can be satisfied only if the expression $\Delta\sigma/C_0 - \Delta\epsilon$ (multiplying $\lambda(x)$ on the right hand side) is zero, but then (27) reduces to $\mu\Delta\epsilon = 0$, which can hold only if $\mu = 0$ or $\Delta\epsilon = 0$. The latter case represents no change at all and can be excluded. Uniform strain increments are therefore possible only if $\mu = 0$, which happens if the local constitutive law has a linear elastic part. As soon as any nonlinearity occurs, strain increments become nonuniform. Fig. 6a shows several solutions derived under the assumption of loading only for $\kappa = 0.1$ and μ ranging from 0.979 to 0.985 while Fig. 6b shows such solutions for μ ranging from 1.002 to 1.008.

Again, the roots of the characteristic equation

$$\det(\mu\mathbf{F} + \mathbf{L} - \mathbf{I}) = 0 \tag{28}$$

mark important points where the number of admissible solutions or the character of the solution change. The first characteristic value $\tilde{\mu}_1$ corresponds to the transition from global hardening to global softening. Between $\tilde{\mu}_1$ and $\tilde{\mu}_2$, there is only one admissible solution for each value of μ. This solution is nonuniform but all the points are softening. At $\tilde{\mu}_2$, solutions of the S-U type start existing and as their compliance parameter s is smaller than that of the S type solutions, the actual response follows

the localized branch. In contrast to the old nonlocal model with $\kappa = 0$, the S type solution ceases to be admissible at some value of μ and it changes into a U-S-U solution. However, the S type solution is "reborn" at the third characteristic value $\tilde{\mu}_3$ along with an S-U-S solution and at some higher value of μ it changes its character again. The compliance parameter is plotted against the parameter μ for the most important localization patterns in Fig. 7. The figure reveals that the actual solution is of the S-U type for all values of $\mu > \tilde{\mu}_1$. This was the case for the old nonlocal model, too, but an important difference can be noticed: The generalized nonlocal model allows strain localization even for $\mu < 1$, i.e. even when the local constitutive law exhibits hardening rather than softening. The hardening slope must, however, be sufficiently small. This is demonstrated in Fig. 8 (similar to Fig. 5 for the old model), showing the four different regions as discussed at the end of the preceding subsection.

Incremental Analysis of the Loading Process

Formulation of the Problem

The previous section was devoted to the analysis of the initial directions of the post-peak branches, assuming a linear behavior up to the peak. Let us proceed to a more complicated problem—an incremental analysis of the entire stable post-peak branch, i.e. the branch starting with the lowest value of the compliance parameter defined previously. Recall that the basic integral equation (18) was derived under the assumption that the unloading modulus $C_u(x)$ be everywhere equal to the initial modulus C_0 and the tangential modulus $C_t(x)$ be equal to the softening modulus C_s in the softening region S and to the initial modulus C_0 in the unloading region U. But this is the case only in a uniform state with no damage. After a finite nonuniform increment is applied, the values of $C_u(x)$ and $C_t(x)$ in general change, except for one situation—the bilinear local constitutive law with unloading as in plasticity (by which we mean unloading with the initial slope C_0). In this special case, strain increments grow proportionally to the decreasing stress until the local stress drops down to zero at the first point of the body. All the other local constitutive laws require a generalization of equation (18).

The derivation can follow the same line as for the bifurcation analysis but the moduli must be treated as functions rather than constants. Introducing two auxiliary functions

$$\mu(x) = \frac{C_u(x) - C_t(x)}{C_0}, \qquad \nu(x) = \frac{C_u(x)}{C_0} \tag{29}$$

the integral equation governing the problem under consideration can be derived:

$$\int_S \hat{\Phi}(x,\xi)\mu(\xi)e(\xi)d\xi + \int_0^L \hat{\Lambda}(x,\xi)\nu(\xi)e(\xi)d\xi - \nu(\xi)e(x) = 1 - \lambda(x) \qquad (30)$$

The matrix counterpart of (30) can be written in a form similar to (20):

$$(\mathbf{F}_\mu + \mathbf{L}_\nu - \mathbf{N}_\nu)\mathbf{e} = \mathbf{i} - \mathbf{l} \qquad (31)$$

Subscripts $_\mu$ and $_\nu$ emphasize that the matrices depend on the current values of the functions $\mu(x), \nu(x)$, which are in turn determined by the total strain profile $\epsilon(x)$, the profile of the maximum previously reached strain $\epsilon_{max}(x)$ and the local constitutive law. Note that ?? is a generalized form of (20) but describes the problem on a different level — as an evolution equation characterizing an entire branch of the equilibrium path rather than a bifurcation from a given state.

Bilinear Local Constitutive Law

As an example, consider a bilinear local constitutive law with damage (unloading to the origin); Fig. 9a. Let ϵ_p be the strain at peak stress and ϵ_f the strain at complete failure. Given the current strain ϵ and the maximum previously reached strain ϵ_{max}, the parameters μ, ν at the given material point can be evaluated as follows:

1) Virgin loading ($\epsilon_{max} < \epsilon_p$): $\mu = 0, \qquad \nu = 1$

2) Softening ($\epsilon_p \le \epsilon_{max} < \epsilon_f$): $\mu = \frac{\epsilon_f \epsilon_p}{\epsilon_f - \epsilon_p}\frac{1}{\epsilon_{max}}, \qquad \nu = \frac{\epsilon_p}{\epsilon_f - \epsilon_p}\left(\frac{\epsilon_f}{\epsilon_{max}} - 1\right)$

3) Complete fracture ($\epsilon_f \le \epsilon_{max}$): $\mu = 0, \qquad \nu = 0$

Note that the unloading region is excluded from the integral containing $\mu(x)$ and therefore it is not necessary to make a difference between softening and unloading-reloading after previous damage (ν is the same for both cases).

Typical load-displacement diagrams start by a linear elastic part which exactly corresponds to the local constitutive law, because in the absence of inelastic stress increments, the local and nonlocal stress is the same. The load-displacement diagram bifurcates right at peak and, according to the results presented in the previous section, the actual branch is that which represents localization into a softening band at one boundary. As the loading continues, the localization band becomes narrower (Fig. 9d) and the load-displacement diagram becomes steeper (Fig. 10) until a snap-back occurs.

The global response was followed up to the snapback or even beyond it for layers of different sizes and for local constitutive laws with different post-peak slopes. As expected, the global response is more brittle for steeper local post-peak slopes characterized by the ratio C_s/C_0 (Fig. 10a) and for larger relative sizes L/l (Fig. 10b).

Nonlinear Local Constitutive Laws

All the load-displacement diagrams constructed in the previous subsection tend to snap back, even for small sizes and for small post-peak slopes in the local constitutive law. The reason is that, as the strain increases, the tangential modulus $C_t = C_s$ remains constant while the unloading modulus C_u decreases to zero and so the parameter $1 - C_t/C_u$ grows without any bounds. To model long tails in the load-displacement diagram with a progressively decreasing slope, the local constitutive law must exhibit a similar type of behavior. One of the simplest examples is given by a law linear up to the peak with a subsequent exponential decay (Fig. 9d):

$$\sigma = f\frac{\epsilon}{\epsilon_p} \text{ if } \epsilon \leq \epsilon_p, \qquad \sigma = f \exp\left[-k\left(\frac{\epsilon}{\epsilon_p} - 1\right)\right] \text{ if } \epsilon \geq \epsilon_p \tag{32}$$

where k is a nondimensional constant controlling the initial post-peak slope. Large values of k indicate a steep post-peak slope. Unloading is assumed to follow the initial slope. This type of a local constitutive law results into a progressive increase of the width of the localization band (Fig. 9e) and the corresponding global load-displacement diagrams are quite reasonable (Fig. 11a).

As the most complex example, let us consider a case when the local constitutive law is nonlinear even before the peak stress. A simple law of this type is given by (Fig. 9c):

$$\sigma = C_0\epsilon \exp\left(-\frac{\epsilon}{\epsilon_p}\right) \tag{33}$$

This can be again combined either with unloading to the origin (damage) or unloading with the initial slope (plasticity). The former case is studied here. The incremental solution must begin with zero stress and displacement, and the normalized load-displacement diagram starts slightly deviating from the local constitutive law even in the pre-peak range (Fig. 11b). The evolution of the total strain profiles is depicted in (Fig. 9e) (for the law with damage). It is clear that, in the pre-peak range, the strain at all the points is increasing but not uniformly. Soon after the peak stress, the solution bifurcates to a stable branch corresponding to localization in a band at one boundary. The width of the localization band then progressively increases.

Conclusions

The performance of a new nonlocal model recently proposed by Bažant (1992) has been tested on the problem of strain localization in a semiinfinite layer, which can be reduced to an integral equation for a single unknown function of one variable,

with an additional loading-unloading condition. The following conclusions about the localization properties of the model can be drawn:

1. The conventional nonlocal model with an isotropic averaging function without renormalization cannot capture strain localization at the boundaries. Localized strain profiles are invariant with respect to a shift and not affected by the proximity of the boundary.

2. With a renormalized averaging function, the conventional nonlocal model leads to uniform strain increments in the hardening regime and in the softening regime with a very small post-peak slope. The strain increments localize into a band at one boundary if the post-peak slope of the local constitutive law exceeds a certain minimum value, which depends on the size of the layer. Large post-peak slopes of the local constitutive law result into a snapback.

3. The new nonlocal model, which contains an integral describing the effect of orientation-dependent crack interactions leads to nonuniform strain profiles as soon as the local constitutive law deviates from linearity. The global load-displacement diagram can start softening even before the peak in the local constitutive law is reached. Similarly, the solution can bifurcate already in the (locally) hardening regime.

4. The present method of analysis has been used to trace the entire loading process and study the evolution of the localized strain profiles. Several local constitutive laws leading to reasonable shapes of the load-displacement diagram have been presented.

Acknowledgment

Financial support under AFOSR Grant 91-0140 to Northwestern University is gratefully acknowledged. The development of the crack influence function was partially supported by the Center for Advanced Cement-Based Materials at Northwestern University.

References

Bažant, Z. P. (1984). Imbricate continuum and its variational derivation. *Journal of Engineering Mechanics ASCE* **110**: 1693-1712.

Bažant, Z. P. (1988a). Softening instability: Part I—Localization into a planar band. *Journal of Applied Mechanics ASME* **55**: 523-529.

Bažant, Z. P. (1988b). Stable states and paths of structures with plasticity or damage. *Journal of Engineering Mechanics ASCE* **114**: 2013-2034.

Bažant, Z. P. (1992). *New nonlocal damage concept based on micromechanics of crack interactions.* Report No. 92-7/C457n, Evanston: Northwestern University; also *J. of Engrg. Mech. ASCE* **120**, (1994), March – in press.

Bažant, Z. P., Belytschko, T. B. and Chang, T.-P. (1984). Continuum model for strain softening. *Journal of Engineering Mechanics ASCE* **110**: 1666-1692.

Bažant, Z. P., and Cedolin L. (1991). *Stability of structures: Elastic, inelastic, fracture and damage theories.* New York, N.Y.: Oxford University Press.

Bažant, Z. P. and Lin, F.-B. (1988). Nonlocal yield-limit degradation. *International Journal for Numerical Methods in Engineering* **26**: 1805-1823.

Bažant, Z. P. and Lin, F.-B. (1989). Stability against localization of softening into ellipsoids and bands: parameter study. *International Journal of Solids and Structures* **25**: 1483-1498.

Bažant, Z. P. and Oh, B.-H. (1983). Crack band theory for fracture of concrete. *Matériaux et Constructions* **16**: 155-177.

Bažant, Z. P. and Ožbolt, J. (1990). Nonlocal microplane model for fracture, damage, and size effect in structures. *Journal of Engineering Mechanics ASCE* **116**: 2485-2505.

Bažant, Z. P. and Pijaudier-Cabot, G. (1988). Nonlocal continuum damage, localization instability and convergence. *Journal of Applied Mechanics ASME* **55**: 287-293.

Bažant, Z. P. and Prat, P. (1988). Microplane model for brittle plastic material: I. Theory, II. Verification. *Journal of Engineering Mechanics ASCE* **114**: 1672-1702.

Cosserat, E. and Cosserat, F. (1909). *Théorie des corps déformables*, Paris: Hermann.

de Borst, R. and Mühlhaus, H. B. (1991). Continuum models for discontinuous media. *Symposium on Fracture Mechanics of Brittle Disordered Materials* 19-21, Noordwijk: RILEM.

de Borst, R. and Sluys, L. J. (1991). Localization in a Cosserat continuum under static and dynamic loading conditions. *Computational Methods in Applied Mechanics and Engineering* **90**: 805-827.

Eringen, A. C. (1965). Theory of micropolar continuum. *Proc. Ninth Midwestern Mechanics Conference* 23-40, University of Wisconsin, Madison.

Eringen, A. C. (1966). A unified theory of thermomechanical materials. *International Journal of Engineering Science* **4**: 179-202.

Eringen, A. C. and Edelen, D. G. B. (1972). On nonlocal elasticity. *International Journal of Engineering and Science* **10**: 233-248.

Kröner, E. (1967). Elasticity theory of materials with long-range cohesive forces. *International Journal of Solids and Structures* **3**: 731-742.

Lasry, D. and Belytschko, T. (1988). Localization limiters in transient problems. *International Journal of Solids and Structures* **24**: 581-597.

Mühlhaus, H. B. and Vardoulakis, I. (1987). The thickness of shear band in granular materials. *Géotechnique* **37**: 271-283.

Needleman, A. (1987). Material rate dependence and mesh sensitivity in localization problems. *Computational Methods in Applied Mechanics and Engineering* **67**: 68-85.

Pietruszczak, S. T. and Mróz, Z. (1981). Finite element of strain-softening metals. *International Journal for Numerical Methods in Engineering* **10**: 327-334.

Pijaudier-Cabot, G. and Bažant, Z. P. (1987). Nonlocal damage theory. *Journal of Engineering Mechanics ASCE* **113**: 1512-1533.

Schreyer, H. and Chen, Z. (1986). One-dimensional softening with localization. *Journal of Applied Mechanics* **53**: 791-797.

Figure 1: a) Orientation angles θ and ψ, b) geometry of the infinite layer, c) one-dimensional crack influence function $\Lambda(r)$, d) nonlocal averaging function $\Phi(r)$.

Figure 2: a) Solutions for different values of μ, b) graph of the function $f(\mu)$

Figure 3: Admissible solutions: a) U-S-U, b) S-U-S, c) S, d) S-U with renormalization, e) S-U-S with renormalization

Figure 4: Compliance parameter for different localization patterns

Figure 5: Critical values of μ depending on the layer width: a) global picture, b) magnified

Figure 6: Nonuniform solutions of the S type

Figure 7: Compliance parameter for different localization patterns

Figure 8: Critical values of μ depending on the layer width

Figure 9: a) Bilinear law, b) linear-exponential law, c) exponential law, evolution of the total strain profile for d) bilinear law, e) linear-exponential law, f) exponential law

Figure 10: Load-displacement diagrams a) for different local post-peak slopes, b) for different sizes

Figure 11: Load-displacement diagram: a) linear-exponential law, b) exponential law

Fig. 1

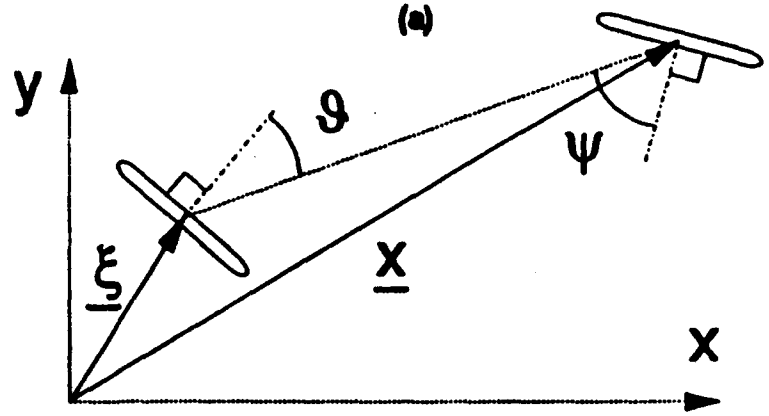
(a)
y
ϑ
ψ
ξ
X
X

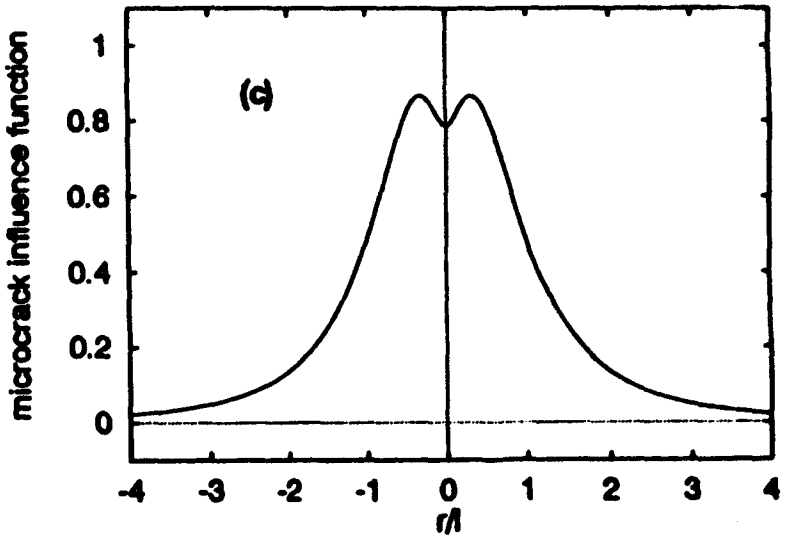
(c)
microcrack influence function
1
0.8
0.6
0.4
0.2
0
-4
-3
-2
-1
0
1
2
3
4
r/l

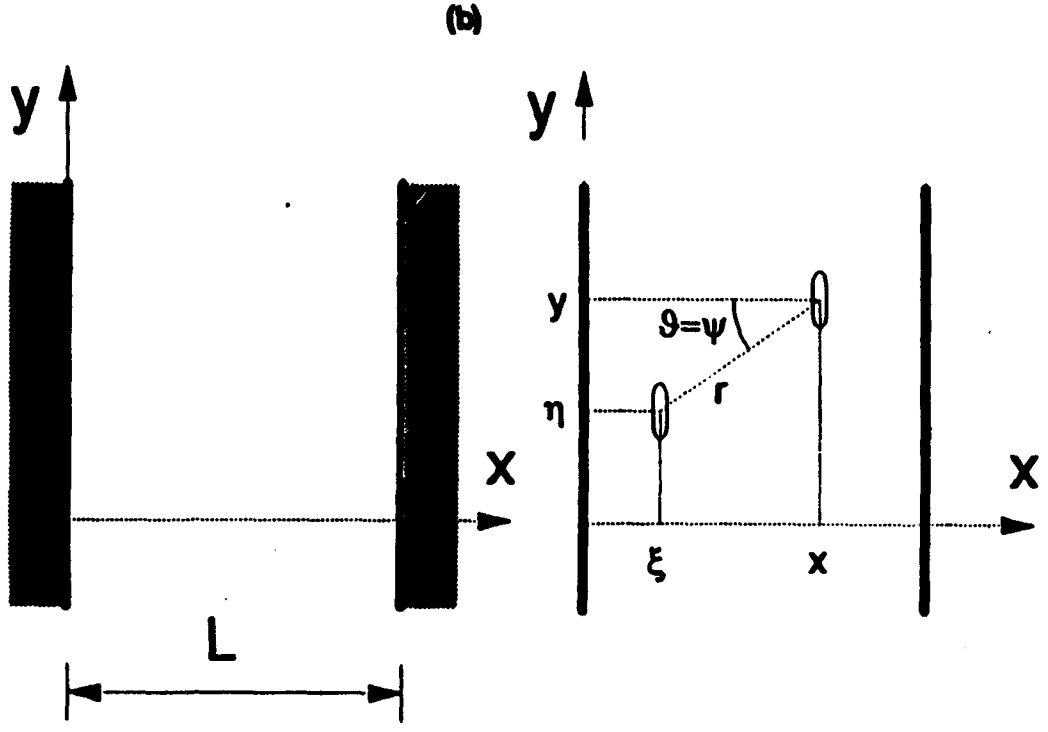
(b)
y
X
L
y
y
ϑ=ψ
η
r
X
ξ
x

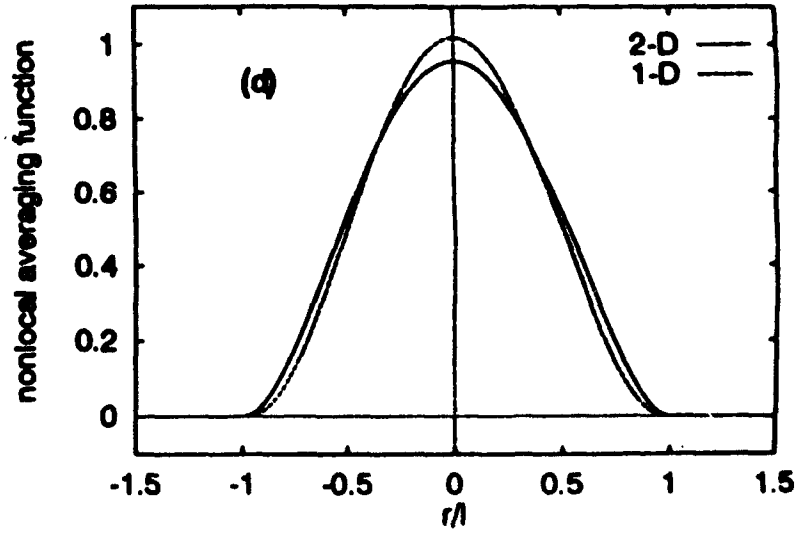
(d)
2-D
1-D
nonlocal averaging function
1
0.8
0.6
0.4
0.2
0
-1.5
-1
-0.5
0
0.5
1
1.5
r/l

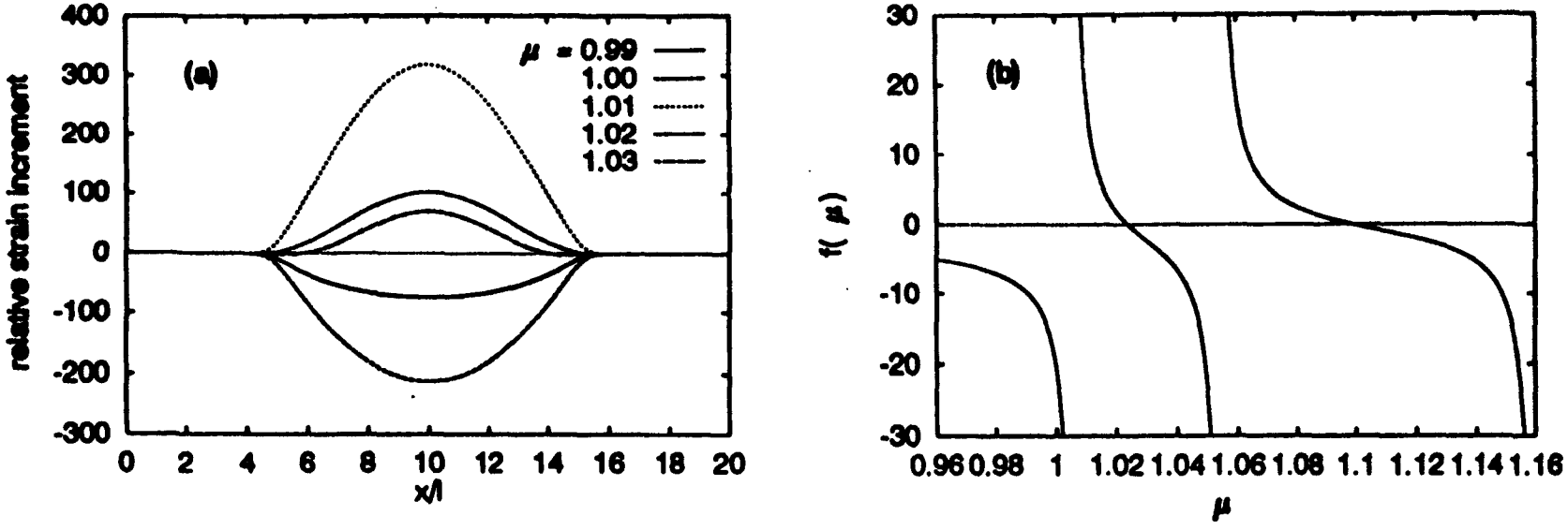
(a)
μ = 0.99
1.00
1.01
1.02
1.03
relative strain increment
x/l
400
300
200
100
0
-100
-200
-300
0 2 4 6 8 10 12 14 16 18 20
(b)
f(μ)
μ
30
20
10
0
-10
-20
-30
0.96 0.98 1 1.02 1.04 1.06 1.08 1.1 1.12 1.14 1.16

Fig. 2

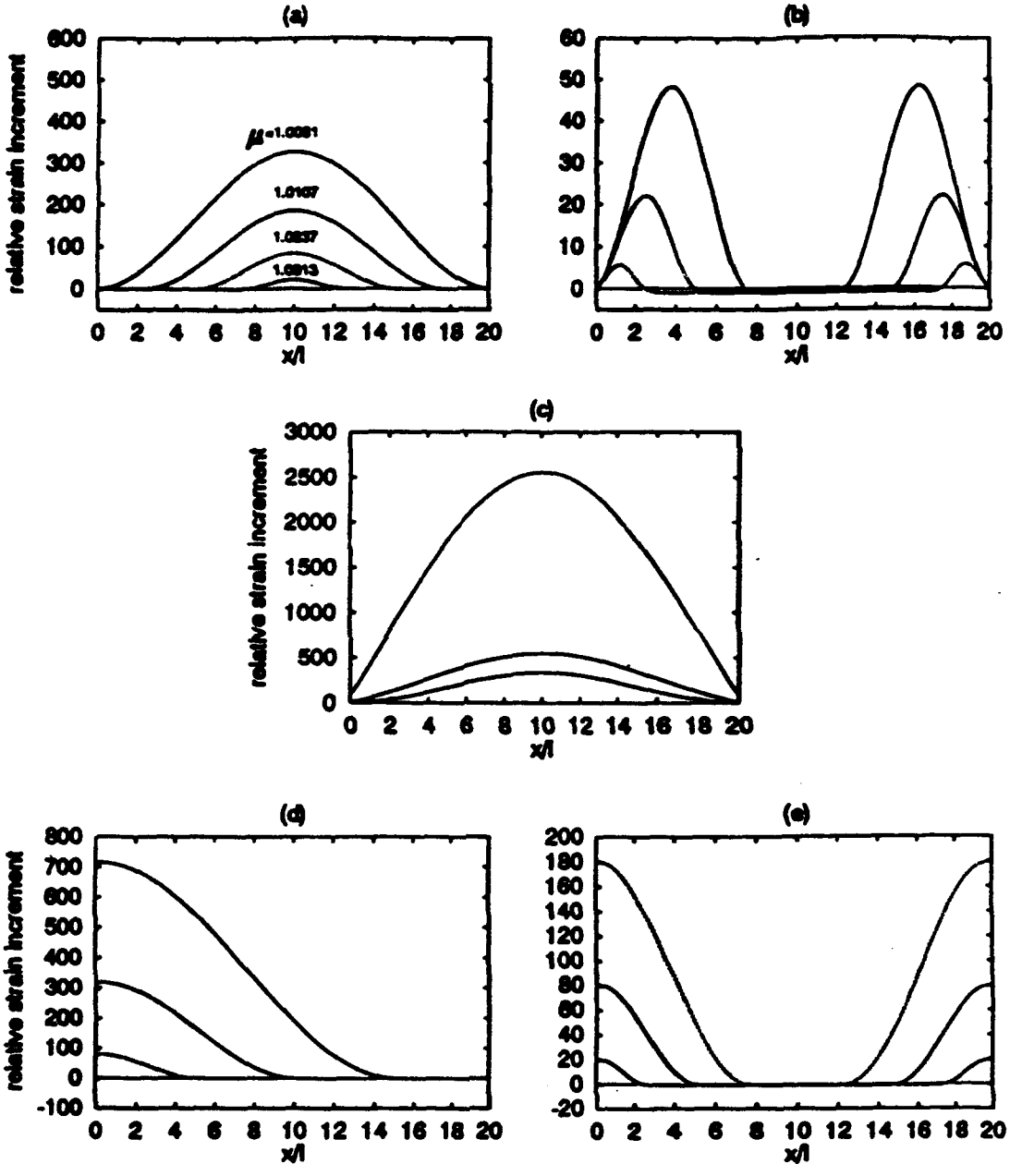
(a)
(b)
(c)
(d)
(e)
relative strain increment
x/l
μ=1.0081
1.0107
1.0037
1.0013

Figure 3

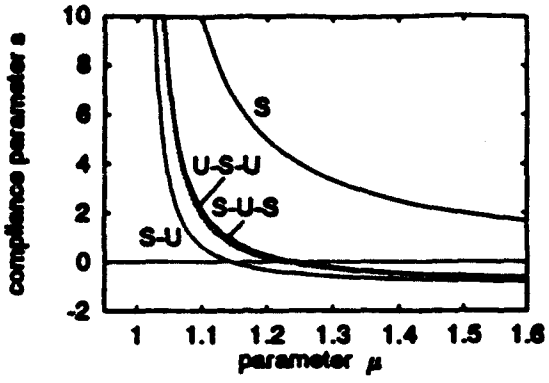

Figure 4

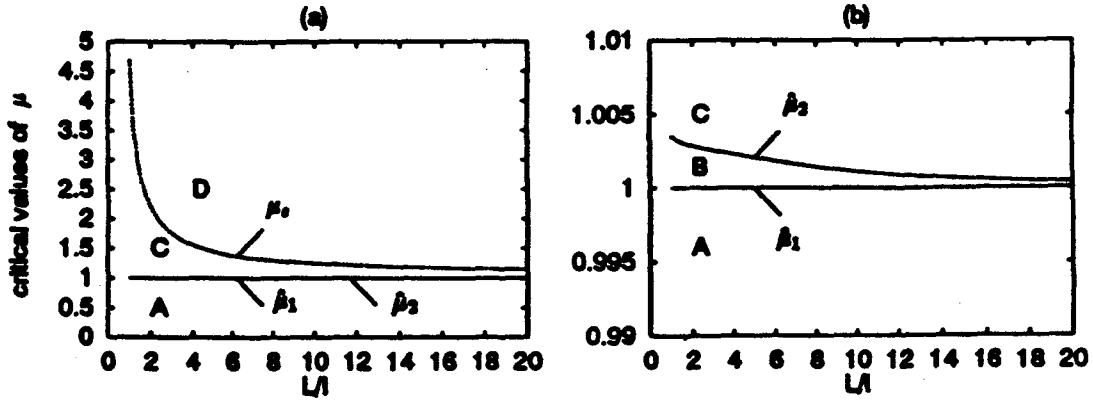

Figure 5

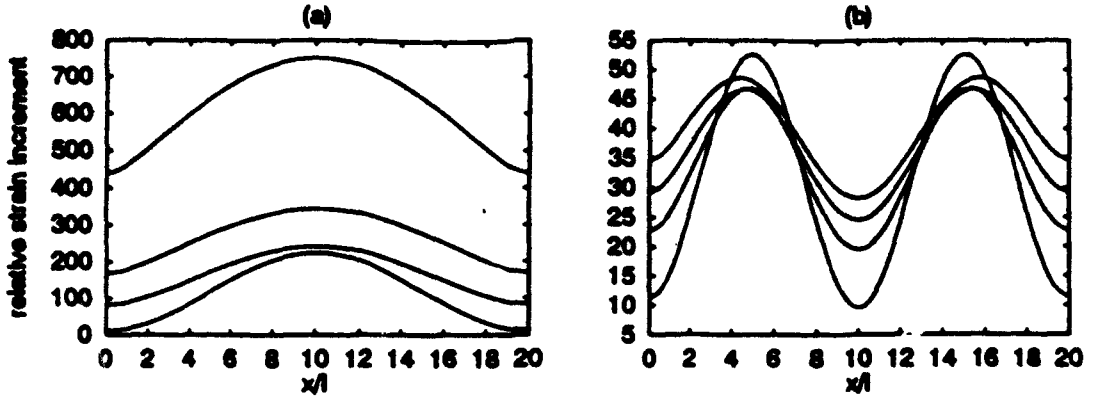

Figure 6

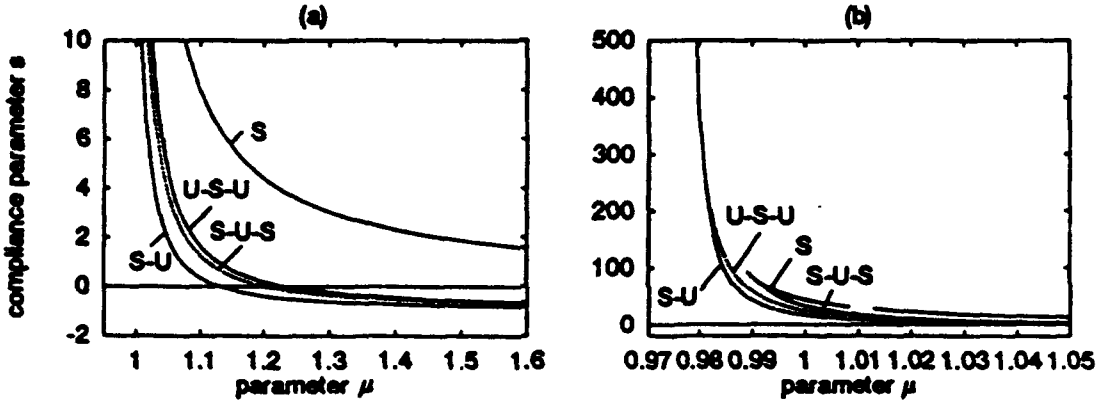

Figure 7

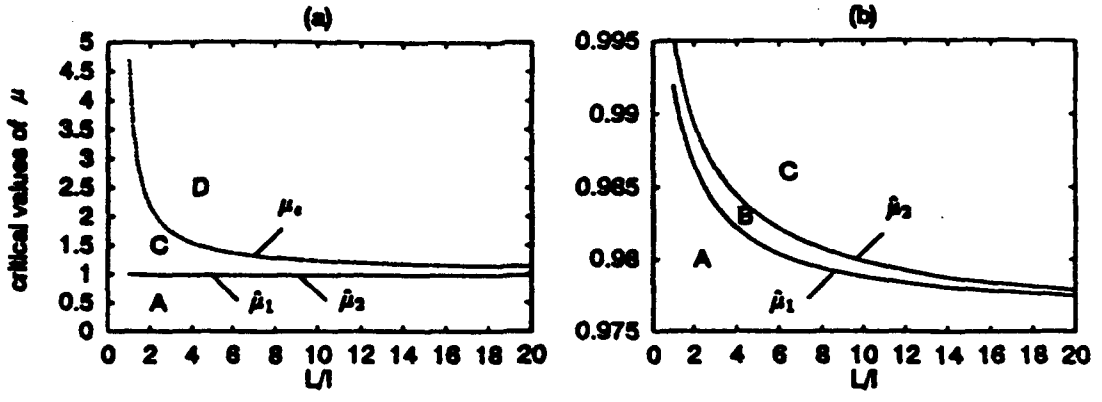

Figure 8

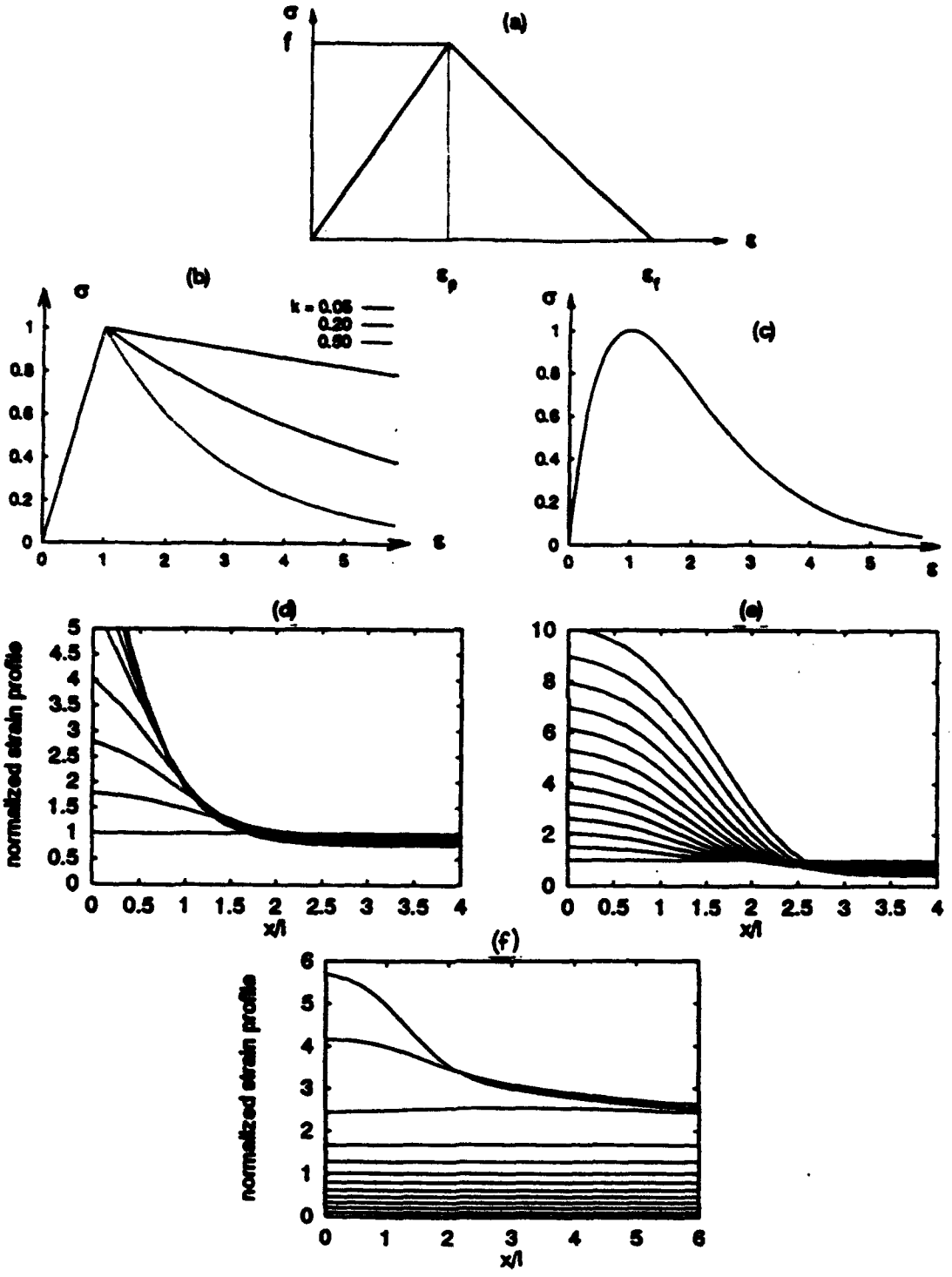

Figure 9

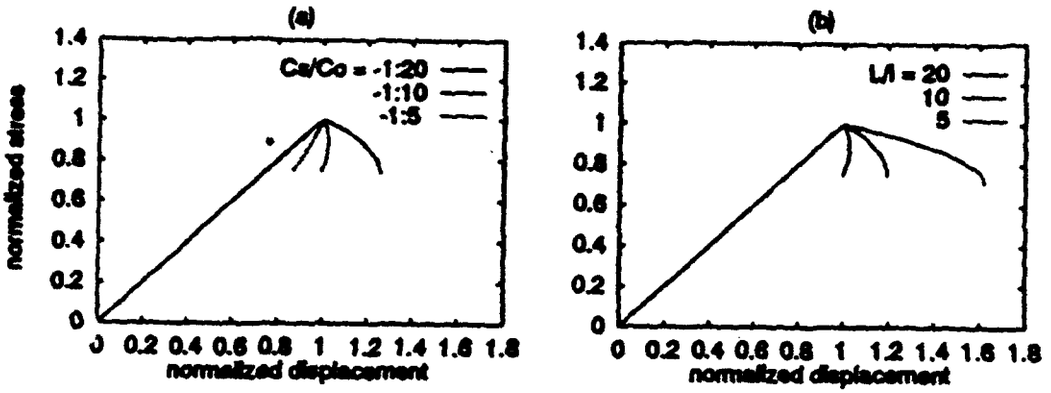

Figure 10

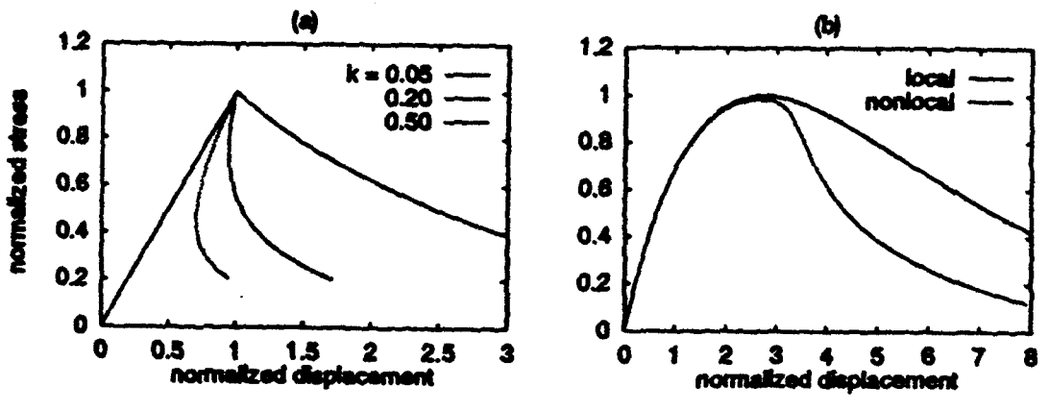

Figure 11

Size Effect and Fracture Characteristics of Fiber Composite Laminates

Zdeněk P. Bažant[1], Zhengzhi Li[2] and Isaac M. Daniel[3]

ABSTRACT. — Measurements of the size effect on the nominal strength of notched geometrically similar specimens of fiber composite laminates are reported. Teste were made on graphite-epoxy laminates made of 0.127 mm thick plies, unidirectionally reinforced by carbon fibers and bonded together by high pressure hot curing. The specimens were rectangular strips of widths 0.25, 0.5, 1 and 2 in. and lengths 1, 2, 4 and 8 in. One set of specimens had double-edge notches and cross-ply $[0/90_2]_s$ arrangement, and another set of specimens had a single-sided edge notch and a quasi-isotropic $[0/\pm 45/90]_s$ arrangement. It is found that there is a significant size effect. It approximately agrees with the size effect law proposed by Bažant, according to which the curve of the logarithm of nominal strength versus the logarithm of size represents a smooth transition from a horizontal asymptote corresponding to the strength criterion (plastic limit analysis) to an inclined asymptote of slope -0.5 corresponding to linear elastic fracture mechanics. Optimum fits of the test results by the size effect law are obtained, and the size effect law parameters are then used to identify the material fracture characteristics, particularly the fracture energy and the effective length of the fracture process zone. Finally, the R-curves are also identified on the basis of the maximum load data. The results show that design situations with notches or large initial traction-free cracks require the size effect on the nominal strength of fiber composite laminates to be taken into account.

1 Introduction

Fiber composites such as graphite-epoxy laminates made by bonding a number of plies reinforced by unidirectional parallel fibers have become an important material in aerospace and other industries. However the laws governing their failure are far from completely understood. The material failure criteria used in practice are expressed in terms of the maximum stress (strength criterion), maximum strain or maximum deviatoric strain energy (Jones, 1975). However, in mechanics it is now generally well understood that such

[1]Walter P. Murphy Professor of Civil Engineering and Materials Science, Northwestern University, Evanston, IL 60208

[2]Graduate Research Assistant

[3]Professor of Civil and Mechanical Engineering, Northwestern University

criteria could be adequate only if the material failure were plastic. If the failure process involves fracturing, the material failure criteria expressed in terms of stresses and strains must be supplemented by an energy criterion, involving the energy release rate. In other words, fracture mechanics must be applied.

The necessity of using fracture mechanics is documented by the fact that the load-displacement diagram in the failure of fiber composite laminates does not exhibit a plastic yield plateau but a gradual decline of the load with increasing deflection after the peak load. Such a post-peak decline can be caused only by one of two phenomena: the geometrically nonlinear effects of buckling and the fracture effects. Since the post-peak decline is observed even in the absence of the former, the latter must be taking place.

If the material failure criterion involves energy, there are some important consequences. The most important one is the size effect, that is, effect of the characteristic dimension D of the structure on the nominal strength σ_N, provided that geometrically similar structures of different sizes are compared.

The size effect caused by fracture has recently come to the forefront of attention in the studies of concrete, rocks, ceramics and other so-called quasibrittle materials, which are characterized by the existence of a sizable fracture process zone at the tip of a macroscopic crack. It has been found (Bažant, 1984, 1993; Bažant and Kazemi, 1990) that in such materials the size effect is transitional between plasticity (for which there is no size effect) and linear elastic fracture mechanics (for which the size effect is as strong as possible). Thus the plot of $\log \sigma_N$ versus $\log D$ is a smooth curve approaching at very small sizes a horizontal asymptote corresponding to plasticity and at very large sizes an inclined asymptote of slope -0.5 corresponding to linear elastic fracture mechanics. Such a size effect must generally occur whenever the load-deflection diagram does not have a yield plateau after the maximum load is reached, provided that the geometrically nonlinear effects of buckling are absent. Therefore, a size effect of this type should be expected also for fiber composite laminates. The purpose of this paper is to verify this proposition, describe the size effect quantitatively and exploit measurements of the size effect for determining the material fracture characteristics.

Fracture of fiber composite laminates has already been studied and some important results have been obtained: see for example Cruse (1973). He attempted to predict the fracture energy of a multi-ply laminate, G_f, as the sum of the fracture energies G of all the individual angle-plies, that is, $G_f h = \sum_i G_{f_i} h_i$ where h = thickness of the laminate, h_i = thicknesses of the individual plies. An equivalent summation of the squares of the stress

intensity factors has also been proposed by Mandell et al. (1975). Based on linear elastic fracture mechanics, Whitney and Nuismer (1974) proposed two fracture criteria for fiber composite laminates, formulated in terms of stress and utilizing the energy release rate calculated by anisotropic elasticity. They called these criteria the equivalent point stress and the average stress criteria. To take into account the effect of a finite fracture process zone, they replaced the actual crack length by an extended equivalent crack length, which is an approach also used for other materials such as concrete (Nallathambi and Karihaloo, 1986). They found that a constant crack length extension allowed good fits of all their data for different crack lengths (however, for other materials such a simplification was found to be inadequate). They also translated their test results into an R-curve (resistance curve), describing the dependence of the apparent stress intensity factor on the crack length. Mandell et al. (1975) observed the damage zone at the crack tip in fiber composite laminates and found that the microcracks (also called the subcracks) in this damage zone (fracture process zone) extend parallel to the fibers in each ply or cause delamination between the plies. They found that the intensity of this microcracking is linearly proportional to the square of the stress intensity factor, which means proportional to the fracture energy, for a given composite lay-up configuration and ply stacking arrangement. Mandell et al. correctly pointed out that the microcracking zone plays the same role as plastic flow in metals, relaxing the high local stress concentrations and absorbing the energy release due to fracture propagation. They also observed some cracks to extend through the whole laminate thickness just before failure.

Daniel (1978, 1982, 1985) investigated cracks in typical aerospace graphite-epoxy laminates and found the size of the damage zone at the tip of the notch or at a small hole to be about 3 to 5 mm. These observations revealed the existence of a characteristic length in this composite material. Daniel then applied the concept of equivalent crack length and obtained a good fit of his experimental results with a modified crack length, with the apparent stress intensity factor being almost constant, for the range of his data. However, based on analogy with extensive studies of concrete fracture (ACI Committee 446, 1992), a good description of a very broad range of test data requires not only replacing the actual crack length with some equivalent extended crack length but also considering the critical energy release rate to depend on this equivalent crack length, that is introduce an R-curve.

From the studies of Daniel (1982) and others it became clear that failure of a fiber composite laminate involves a combination of several microscopic failure mechanisms,

including microcracking (subcracks), delamination, matrix splitting, fiber pullout and fiber breakage. Thus a detailed theoretical macroscopic fracture model would have to be based on fracture mechanics.

2 Fracture Tests of Composite Laminates

The composite consisted of sheets of epoxy unidirectionally reinforced with graphite (IM7) fibers. The laminate was produced from commercially available sheets (the individual plies) by the procedure described by Daniel et al. (1993). The temperature and pressure history used in curing of the laminate is described in Fig. 1. The cross section of one unidirectionally reinforced sheet (ply) is shown in Fig. 2. (where the white circle is the cross-section of fiber which is about 0.004 mm in diameter). Each unidirectionally reinforced ply has the following properties: Young's modulus E_1 in fiber direction = 24,500 ksi (168.9 GPa), Young's modulus E_2 in transverse direction = 1,360 ksi (9.38 GPa), tensile strength in fiber direction F_{1t} = 321 ksi (2.21 GPa), transverse tensile strength F_t = 9.4 ksi (0.0648 GPa), Poisson ratio ν_{12}= 0.30, elastic shear modulus G_{12} = 1,400 ksi (9.65 GPa), thickness of a single ply h_1= 0.005 in. (0.127 mm), and fiber-volume ratio F_f= 0.65.

Two sets of specimens were prepared, with different lay-ups: $[0/90_2]_s$ (cross-ply) and $[0/\pm 45/90]_s$ (quasi-isotropic). Each set involved geometrically similar rectangular specimens of four different sizes: 0.25 in. × 1 in., 0.5 in. × 2 in., 1 in. × 4 in., and 2 in. × 8 in., and thus the size ratio was 1:2:4:8. All the specimens were prepared with glass-fiber tabs of 1.5 in at each end (Fig. 3). The total thickness of the cross-ply laminates was 0.03 in. (0.762 mm), and that of quasi-isotropic laminates was 0.04 in. (1.02 mm). For the first set of specimens, representing cross-ply laminates, two geometrically similar edge notches, with lengths a and $2a/D = 1/8$, were cut (Fig. 3). In the second set of specimens, made of quasi-isotropic laminates, edge notches of $a/D = 1/5$ were cut from only one side (Fig. 3).

The notched laminate specimens were tested under direct tension. The tests were carried out in the Instron 8500 testing machine (Fig. 2c). The tests were controlled to a constant displacement rate, by the machine stroke for the double edge notched specimens, and by the crack opening displacement for the single edge notched specimens. The displacement rate in the tests was set to different values to make the strain rate = 0.2%/min. and to reach the peak load within about 10 min. for all sizes. Fig. 4 shows some typical load displacement curves for specimens of various sizes. For the large

specimen size, they are almost straight up to the failure, which indicates high brittleness. For the small specimen sizes, there is a significant nonlinear segment before the peak, which indicates hardening inelastic behavior and lower brittleness (or higher ductility). This behavior agrees with the fact that the size effect law represents a transition from ductile response for small sizes to brittle response for large sizes.

The machine stiffness and controls were not sufficient to control the test in the post-peak regime of descending load, even when the crack opening displacement was controled (a stable post-peak test might possibly be obtained for notched bending specimens, Wisnom, 1992; but such tests are harder to carry out for thin laminates). The failures of the specimens were catastrophic (dynamic), and occurred shortly after the peak load. Growth of damage consisting of subcracks in layers and delamination between layers before failure was observed in the tests (in agreement with the observations of Mandell et al., 1975). The typical appearance of the specimens after failure is shown in Fig. 5, where the microcracking damage can be detected. For the quasi-isotropic specimens, some fractures run at 45° inclination to the notch and there are 45° subcracks.

The test results for the double-edge and single-edge notched specimens are summarized in Table 1, in which the nominal strength is defined as the average stress in an unnotched cross section, $\sigma_N = P_{\max}/hD$; D = characteristic dimension (0.5—2.0 in.), and h = laminate thickness (0.03 in. for the cross-ply laminate and 0.04 in. for the quasi-isotropic laminate, respectively).

It may be noted that the double-edge notched specimen has one undesirable feature: the response path exhibits a bifurcation after which only one of the two curves can propagate (Bažant and Tabbara, 1990), and the response thus becomes nonsymmetric. This property however does not invalidate the foregoing procedure because the bifurcation happens only after the peak load. Nevertheless, the post-peak data from such tests are difficult to interpret. It was for this reason that the second series of tests used single-edge notched specimens. In that kind of specimen there is no bifurcation of the response path and the response is nonsymmetric from the beginning.

3 Observed Size Effect

The effect of structure size D on the nominal strength σ_N in quasibrittle materials generally follows the approximate size effect law (Bažant, 1984, 1993):

$$\sigma_N = Bf_u(1+\beta)^{-1/2}, \qquad \beta = D/D_0 \tag{1}$$

in which β = relative size, f_u = reference strength of the material, introduced for the convenience of dimensionality, and B, D_0 = constants. B characterizes the solution according to plastic limit analysis based on the strength concept. The curves in Fig. 6–7 show the plots of (1) in double logarithmic scales. These size effect plots represent a transition from the strength criterion (plastic limit analysis), representing a horizontal left-side asymptote, to an asymptote of slope -0.5, representing linear elastic fracture mechanics (LEFM). Intersection of the two asymptotes corresponds to $D = D_0$, called the transitional size.

The size effect law (1) has been verified by numerous tests, especially for concrete, but also for rocks, toughened ceramics and ice. The formula (1) has been derived, under certain reasonable simplifying assumptions, by dimensional analysis and similitude arguments, and for some simple specimen shapes also by energy release analysis. It has also been shown that (1) represents the limiting case of a more general statistical Weibull-type theory for the size effect, in which the material failure probability is considered to depend on the average strain of a certain characteristic volume of the material rather than the stress at the same point (Bažant and Xi, 1991c). It has been shown that the predictions of finite element codes with a nonlinear fracture model (such as the cohesive crack model) or with a nonlocal damage material model agree well with (1). Furthermore, fracture simulations by random particle models also agree with this law.

In regard to the statistical approach to the size effect, the recent study by Jackson et al. (1992) of the size effect in tensile and flexural tests of graphite-epoxy composites deserves mention. Geometrically similar specimens of sizes 1:2:3:4 were used and the results were analyzed on the basis of Weibull's statistical theory of random material strength. Good agreement with the test data was obtained. However, it should be pointed out that Weibull statistical theory can be applied only to failures that occur at crack initiation. The reason is that, in the classical form of this theory, the failure probability is considered to depend on the local stress, calculated from elasticity, and the stress redistributions and stress concentrations caused by prior fracture growth are disregarded. These phenomena make Weibull-type theories inapplicable to failures that occur after a large stable crack growth, which is in the present case simulated by the geometrically similar notches (see Bažant, Xi and Reid, 1991b). In that case, the aforementioned nonlocal generalization of the Weibull approach is required, and in the limit this leads to (1).

Comparisons of the present tests results to the size effect law for the cross-ply and quasi-isotropic laminates are shown in Figs. 6–7. The circular points represent the results

for the nominal strength in the individual tests. The top of each figure shows a linear regression plot of Y versus X, based on the relations

$$Y = A + CX, \quad Y = (1/\sigma_N)^2, \quad X = D, \quad Bf_u = 1/\sqrt{A}, \quad D_0 = A/C$$

By means of this linear regression, the parameters of the size effect can be easily identified from the slope C and the vertical intercept A. The resulting size effect plots of $\log \sigma_N$ versus $\log D$ are plotted in Figs. 6–7. The parameters for these plots are $D_0 = 1.223$ in. (31 mm), $Bf_u = 127.1$ ksi (0.876 GPa) for the cross-ply laminates, and $D_0 = 4.16$ in. (105.6 mm) and $Bf_u = 84{,}3$ ksi (0.581 GPa) for the quasi-isotropic laminates.

To sum up, the test results in Figs. 6–7 show that: (1) the failure of fiber composite laminates containing traction-free cracks (or notches) exhibits a significant size effect, and that (2) the size effect represents a gradual transition with increasing size from the strength criterion to linear elastic fracture mechanics, as described by the size effect (1). The scatter of the test results is of course significant, but is normal for this kind of heterogeneous material. The foregoing conclusions are verified on the average, as the mean statistical trend. These conclusions ought to be taken into account in all design situations and safety evaluations where a large traction-free crack can grow in a stable manner prior to the failure. Especially, these conclusions are important for extrapolation from small-scale laboratory tests to real size aerospace or other structures. The strength theory, which has no size effect, is for these applications inadequate.

4 Identification of Material Fracture Characteristics from Measured Size Effect

The size effect law (1) for quasibrittle fracture can also be expressed in terms of the nondimensionalized energy release rate $g(\alpha)$;

$$\sigma_N = c_n \left(\frac{E' G_f}{g'(\alpha_0) c_f + g(\alpha_0) D} \right)^{1/2} \tag{2}$$

Here c_f is a constant representing the effective length of the fracture process zone defined for extrapolation to infinite size, α_0 is teh initial value of α when $a = a_0$, and c_n = coefficient introduced for convenience, in order to make σ_N coincide with the actual stress at the desired point of the specimen; $g(\alpha) = G(\alpha)(EDh/P)^2/b$ (where $G(\alpha)$ = energy release rate per unit width of crack front edge, P = external load, E = Young's modulus, h = thickness, D = specimen width, $\alpha = a/b$, $b = D$ for single-edge-notch specimen, and

$b = D/2$ for double-edge-notch specimen), see Bažant et al. (1991).. By matching (2) and (1), one obtains (Bažant and Kazemi, 1990, 1991; Bažant et al., 1991):

$$G_f = \frac{(Bf_u)^2}{c_n^2 E} D_0 g(\alpha_0), \qquad c_f = \frac{g(\alpha_0)}{g'(\alpha_0)} D_0 \tag{3}$$

The fracture energy is here defined as the energy required for fracture propagation in a specimen of theoretically infinite size (Bažant and Pfeiffer 1987). According to this definition, the fracture energy is independent of both the shape and size of the specimen because in a specimen of infinite size the fracture process zone occupies an infinitely small portion of the specimen volume and can be considered as a point, which means that linear elastic fracture mechanics applies.

To determine the material fracture characteristic on the basis of (3), the expressions for the stress intensity factor K_I available for isotropic specimens (e.g. Tada, 1985) have been used. The assumption of isotropy is quite good for the quasi-isotropic laminates, but may involve a larger error for the cross-ply laminates (this should be checked in subsequent study). According to LEFM,

$$K_I = \sigma\sqrt{\pi b\alpha} F(\alpha), \qquad \alpha = a/b \tag{4}$$

where $\sigma = \sigma_N$ = average stress in the laminate strip and F is a function of variable α.

The cross-ply laminate is not isotropic but orthotropic. The energy release rate and the stress intensity factor for orthotropic specimens of the present geometry have recently been solved by Bao et al. (1991). Their solution uses elastic parameters:

$$\rho = \frac{\sqrt{E_x E_y}}{2G_{xy}} - \sqrt{\nu_{xy}\nu_{yx}}, \qquad \lambda = \frac{E_y}{E_x} \tag{5}$$

where $E_x, E_y, G_{xy}, \nu_{xy}, \nu_{yx}$ are the elastic constants of the orthotropic material, which can be calculated from the lamina properties (Jones, 1975). The stress intensity factor can be written as:

$$K_I = \sigma\sqrt{\pi b\alpha}\, Y(\rho) F(\alpha), \tag{6}$$

$$\text{where } Y(\rho) = [1 + 0.1(\rho - 1) - 0.016(\rho - 1)^2 + 0.002(\rho - 1)^3] \left(\frac{1+\rho}{2}\right)^{-1/4}$$

$F(\alpha)$ is the same function of the relative crack length $\alpha = a/b$ as for isotropic materials. $Y(\rho)$ is a material constant. The energy release rate for orthotropic material is:

$$G(\alpha) = \sqrt{\frac{1+\rho}{2E_x E_y \sqrt{\lambda}}} K_I^2 \tag{7}$$

Bringing (7) into (7), one can write $G(\alpha)$ in the same form as for the isotropic materials:

$$G(\alpha) = \frac{K_I^2}{E^*} = \frac{\sigma^2 b\pi\alpha}{E^*}F^2(\alpha) = \left(\frac{P}{hD}\right)^2 \frac{b}{E^*}g(\alpha) \tag{8}$$

$$\text{where } E^* = \frac{1}{[Y(\rho)]^2}\sqrt{\frac{2E_xE_y\sqrt{\lambda}}{1+\rho}}$$

and $g(\alpha)$ is the nondimensionalized energy release rate defined before. By virtue of (9), we can treat the orthotropic material fracture characteristics in the same way as the isotropic ones if we replace E by the equivalent Young's modulus E^* ($E^* = 6983$ ksi =48.15 GPa for the cross-ply specimen tested).

For the double-edge-notched specimen (Tada, 1985):

$$F(\alpha) = \left(1 + 0.122\cos^4\frac{\pi\alpha}{2}\right)\sqrt{\frac{2}{\pi\alpha}\tan\frac{\pi\alpha}{2}} \tag{9}$$

and for the single-edge notched specimen:

$$F(\alpha) = 1.122 - 0.231\alpha + 10.55\alpha^2 - 21.71\alpha^3 + 30.38\alpha^4 \tag{10}$$

Noting that $K_I^2 = GE$ where G = energy release rate and E = Young's elastic modulus, we have $g(\alpha) = \pi\alpha[F(\alpha)]^2$. So we have, for the double-edge-notched specimen

$$g(\alpha) = 2\left(1 + 0.122\cos^4\frac{\pi\alpha}{2}\right)^2 \alpha\tan\frac{\pi\alpha}{2} \tag{11}$$

$$g'(\alpha) = \pi\left[\left(1+\tan^2\frac{\pi\alpha}{2}\right)\left(1+0.122\cos^4\frac{\pi\alpha}{2}\right)^2 - 0.244\sin^2\pi\alpha\left(1+0.122\cos^4\frac{\pi\alpha}{2}\right)\right]$$

where, for $\alpha = 0.125$, $g(0.125) = 0.492716$, and $g'(0.125) = 3.91995$. For the single-edge notched specimens:

$$g(\alpha) = \pi\alpha[1.122 - 0.231\alpha + 10.55\alpha^2 - 21.71\alpha^3 + 30.38\alpha^4]^2 \tag{12}$$

$$g'(\alpha) = \pi[1.259 - 1.037\alpha + 71.18\alpha^2 - 214.4\alpha^3 + 947.5\alpha^4]$$

where, for $\alpha = 0.2$, we have $g(0.2) = 1.184, g'(0.2) = 11.624$. Thus, the for double-edge notched cross-ply laminates we obtain from (3) the effective fracture characteristics:

$$G_f = 1.39 \text{ ksi} \times \text{in.} = 0.243 \text{ MJ/m}^2, \qquad c_f = 0.154 \text{ in.} = 3.91 \text{ mm} \tag{13}$$

Because of orthotropic, these values apply only for fracture in the x-direction of orthotropy. For the singe-edge notched quasiisotropic laminates we obtain:

$$G_f = 3.67 \text{ ksi} \times \text{in.} = 0.642 \text{ MJ/m}^2, \qquad c_f = 0.424 \text{ in.} = 10.76 \text{ mm} \tag{14}$$

It is noteworthy that the effective length of the process zone, c_f, found from these size effect measurements is quite close to that experimentally derived by Daniel (1985) (the present values are a little larger, which is not surprising considering that Daniel's procedure did not consider extrapolation to infinite size).

Based on the size effect law, the R-curve can be determined as the envelope of the fracture equilibrium curves for geometrically similar specimens of different sizes. This leads to the equations

$$R(c) = G_f \frac{g'(\alpha)}{g'(\alpha_0)} \frac{c}{c_f}, \quad \frac{c}{c_f} = \frac{g'(\alpha_0)}{g(\alpha_0)} \left(\frac{g(\alpha)}{g'(\alpha)} - \alpha + \alpha_0 \right) \tag{15}$$

in which $R(c)$ represents the R-curve. These two equations define the R-curve parametrically; for any chosen value of relative crack length α, one first evaluates the crack extension from the notch, c, and then the R-value. The R-curve calculated from the present test results is shown in Fig. 8 for both the cross-ply laminate and the quasi-isotropic laminate.

5 Conclusions

1. The present tests show that the nominal strength of fiber composite laminate specimens that are geometrically similar and have geometrically similar notches or initial traction-free cracks exhibits a significant size effect.

2. The size effect agrees with the size effect law proposed by Bažant, according to which the curve of the logarithm of nominal strength versus the logarithm of characteristic dimension (size) exhibits a smooth transition from a horizontal asymptote corresponding to the strength criterion (plastic limit analysis) to an inclined asymptote of slope -0.5, corresponding to linear elastic fracture mechanics.

3. Measurements of the size effect on the nominal strength can be exploited for determining the fracture characteristics of fiber composite laminates, including their fracture energy and the effective length of the fracture process zone. From these characteristics, the R-curve can be also calculated. The size effect method of measuring the fracture characteristics is easier to implement than other methods because only peak load measurements are necessary (the post-peak behavior, crack tip displacement measurement and optical measurement of crack tip location are not needed, and even a soft testing machine without servo-control can be used).

4. The orthotropic properties of fiber composite laminates can and must be taken into consideration while analyzing the fracture characteristics. Replacing Young's modulus by Bao-Suo-Fan's equivalent Young's modulus, the formulas of the size effect method previously derived for isotropic materials can be generalized for the orthotropic materials. This makes it possible to determine size and shape independent values of the fracture energy, effective fracture process zone length, and R-curve for cross-ply laminates.

ACKNOWLEDGEMENT. — Partial financial support under AFOSR Grant 91-0140 to Northwestern University is gratefully acknowledged. Thanks are due also to H.-M. Hsiao, Graduate Research Assistant, for his expert help in the preparation of the tests.

References

ACI Committee 446 (1992). "State-of-art-report on fracture mechanics of concrete: concepts, model and determination ofmaterial properties." in *Fracture Mechanics of Concrete Structure*, ed. by Z. P. Bažant, Elsevier Applied Science, London, New York, 4-144.

Bao, G., Ho, S., Suo, Z., and Fan, B. (1992). "The role of material orthotropy in fracture specimens for composites." *Int. J. Solid Structures*, 29(9), 1105-1116.

Bažant, Z.P. (1984). "Size effect in blunt fracture: Concrete, rock, metal." *J. of Engrg. Mech.*, ASCE, 110, 518–535.

Bažant, Z.P., Pfeiffer, P.A. (1986). "Determination of fracture energy from size effect and brittleness number." *ACI Materials J.*, 84, 463-480.

Bažant, Z.P., and Kazemi, M.T. (1990a). "Determination of fracture energy, process zone length and brittleness number from size effect, with application to rock and concrete." *Int. J. of Fracture*, 44, 111–131.

Bažant, Z.P., and Kazemi, M.T. (1990b). "Size effect in fracture of ceramics and its use to determine the fracture energy and effective process zone length." *J. of American Ceramic Soiety*, 73(7), 1841-1853.

Bažant, Z.P., Gettu, R., and Kazemi, M.T. (1991a). "Identification of nonlinear fracture properties from size effect tests and structural analysis based on geometry-dependent R-curves." *Int. J. of Rock Mechanics, Mining Science & Geomechanical Abstracts*,

28(1), 43–51.

Bažant, Z.P., Xi, Y. and Reid, S.C. (1991b). "Statistical size effect in quasi-brittle structures: I. Is Weibull theory applicable?." *J. of Engrg. Mech.*, ASCE, 117(11), 2609–2622.

Bažant, Z.P., and Xi, Y. (1991c). "Statistical size effect in quasi-brittle structures: II. Nonlocal theory." *J. of Engrg. Mech.*, ASCE, 117(11), 2623–2640.

Bažant, Z.P. (1993). "Scaling laws in mechanics of failure." *J. of Engrg. Mech.*, ASCE, 119(9), 1828–1844.

Cruse, T.A. (1973). "Tensile strength of notched composites." *J. of Composite Materials*, 7, 218–228.

Daniel, I.M. (1978). "Strain and failure analysis of graphite/epoxy plate with cracks." *Experimental Mechanics*, 18, July, 246–252.

Daniel, I.M. (1982). "Failure mechanisms and fracture of composite laminates with stress concentrations." VIIth International Conference on Experimental Stress Analysis, Haifa, Israel, Aug. 23–27, 1–20.

Daniel, I.M. (1985). "Mixed-mode failure of composite laminates with cracks." *Experimental Mechanics*, 25, Dec., 413–420.

Daniel, I.M., Hsaio, H.-M., Wooh, S.C., and Vittoser, J. (1993). "Processing and compressive behavior of thick composites." *Mechanics of Thick Composites*, AMD, 162, ASME, edited by Y.D.S. Rajapakse, June, 107–126.

Jackson, K.E., Kellas, S., and Morton, J. (1992). "Scale effects in the response and failure of fiber reinforced composite laminates loaded in tension and in flexure." *J. of Composite Materials*, 26(18), 2674–2705.

Jones, R.M. (1975). *Mechanics of Composite Materials*, Hemisphere Publishing Corporation, New York, 71–83.

Mandell, J.F., Wang, S.-S., and McGarry, F.J. (1975). "The extension of crack tip damage zone in fiber reinforced plastic laminates." *J. of Composite Materials*, 9, July, 266-287.

Nallathambi, P., and Karihaloo, B. L. (1986). "Determination of specimen- size independent fracture toughness of plain concrete." *Mag. of Concrete Res.* 38(135), 67-76.

Pijaudier-Cabot, G., and Bažant, Z.P. (1991). "Cracks interacting with particles or fibers

in composite materials." *J. of Engrg. Mech.*, ASCE, 117(7) July, 1611-1630.

Tada, H., Paris, P.C., and Irwin, G.R. (1985). *The Stress Analysis of Cracks Handbook*, Second Edition, Paris Productions Inc., Missouri.

Whitney, J.M., and Nuismer, R.J. (1974). "Stress fracture criteria for laminated composites containing stress concentrations." *J. of Composite Materials*, 8, July, 253–264.

Winsom, M.R. (1992). "The relationship between tensile and flexural strength of unidirectional composite." *J. of Composite Materials*, 26(8), 1173–1180.

Table 1: Results of Tensile Tests of Notched Composite Laminates of Different Sizes and Different Notches (1 lb. = 4.4482 N, 1 ksi = 1000 psi = 6.8947 MPa).

length × width (in^2)	double-edge notch		single-edge notch	
	Max. load (lb)	σ_N (ksi)	Max. load (lb)	σ_N (ksi)
1 × 0.25	862	114.9	748	74.8
1 × 0.25	880	117.3	819	81.9
1 × 0.25			807	80.7
2 × 0.5	1720	114.7	1575	78.8
2 × 0.5	1714	114.3	1513	75.7
2 × 0.5	1696	113.1	1553	77.7
4 × 1.0	2675	89.2	3368	84.2
4 × 1.0	2782	92.7	2939	73.5
4 × 1.0	2512	83.7	2979	74.5
8 × 2.0	4934	82.2	5207	65.1
8 × 2.0	5042	84.0	6140	76.8
8 × 2.0	4425	73.8	5315	66.4

Figure 1: History of temperature and pressure used in curing of the specimens.

Figure 2: (a) Enlarged typical cross section of a single-ply with multidirectional carbon fibers; (b) Geometrically similar test specimens of four different sizes of ratio 1:2:4:8, before the cutting of notches; (c) Test arrangement in the Instron 8500 Testing Machine.

Figure 3: Geometry of test specimens; left: double-edge notches, right: single-edge notches.

Figure 4: Typical measured load-deflection diagrams of quasiisotropic and crossply specimens of various sizes and different notches, showing an increase of nonlinearity with a decrease of size.

Figure 5: Failure patterns as seen on quasi-isotropic test specimens after the test.

Figure 6: Size effect measured for cross-ply specimens with double-edge notches.

Figure 7: Size effect measured on quasi-isotropic specimens with single-edge notches.

Figure 8: Normalized R-curves for cross-ply and quasi-isotropic composites, deduced from size effect measurements.

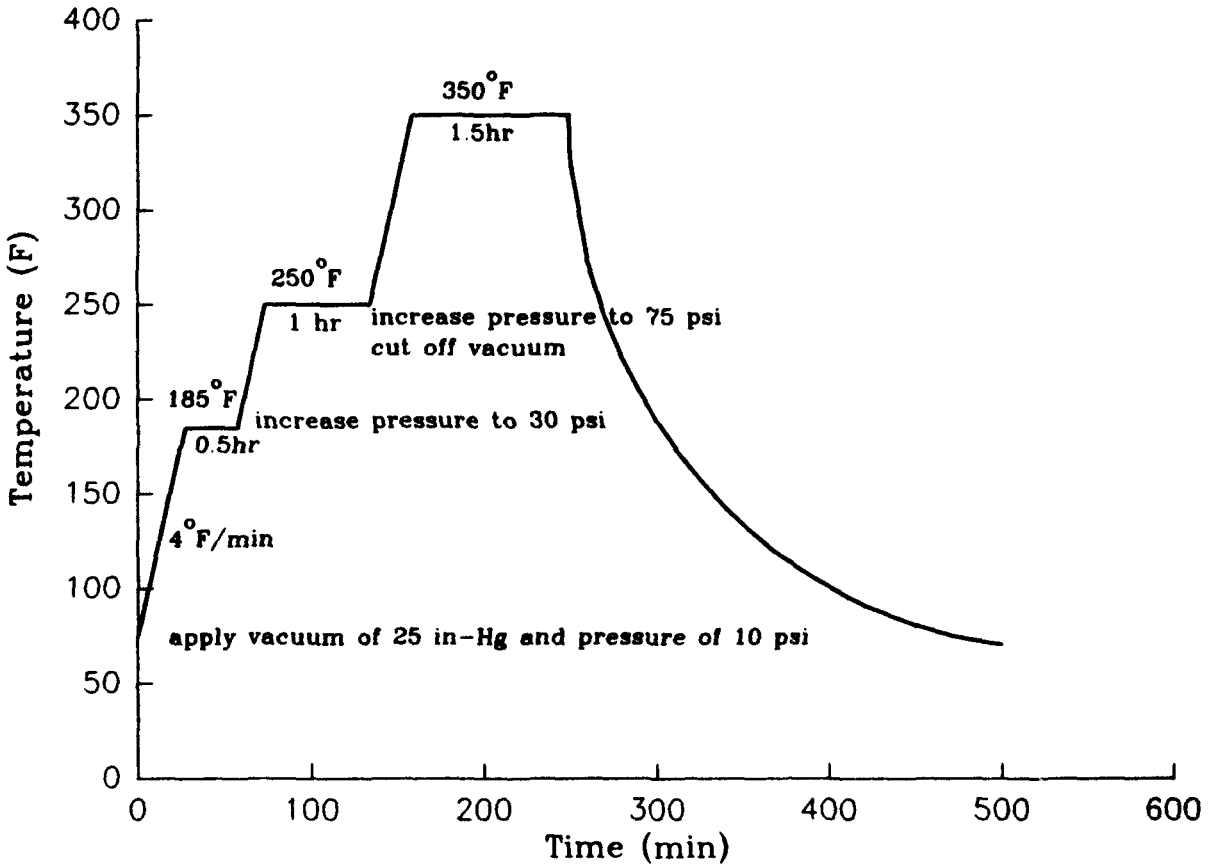
400
350
300
250
200
150
100
50
0
Temperature (F)
350°F
1.5hr
250°F
1 hr
increase pressure to 75 psi
cut off vacuum
185°F
increase pressure to 30 psi
0.5hr
4°F/min
apply vacuum of 25 in-Hg and pressure of 10 psi
0
100
200
300
400
500
600
Time (min)

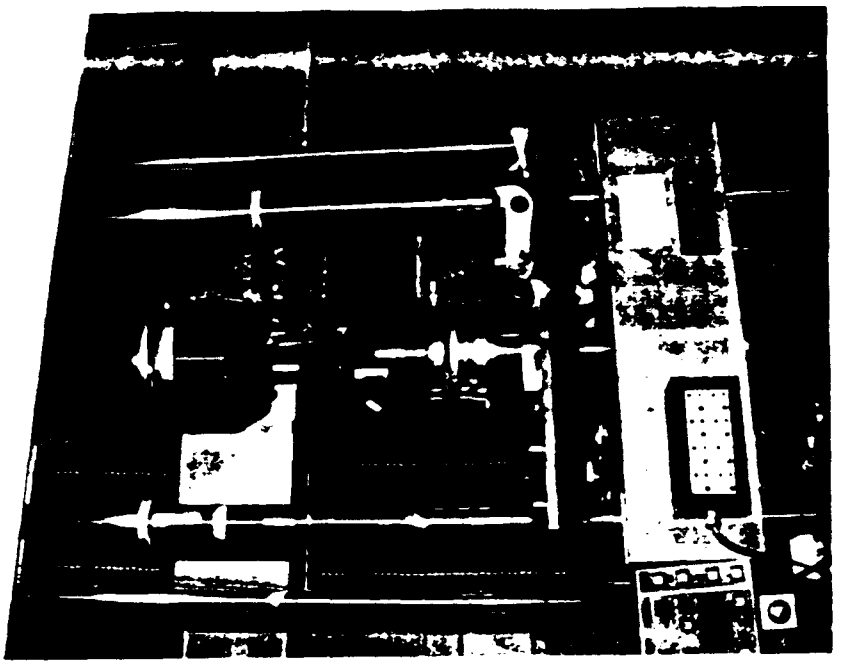

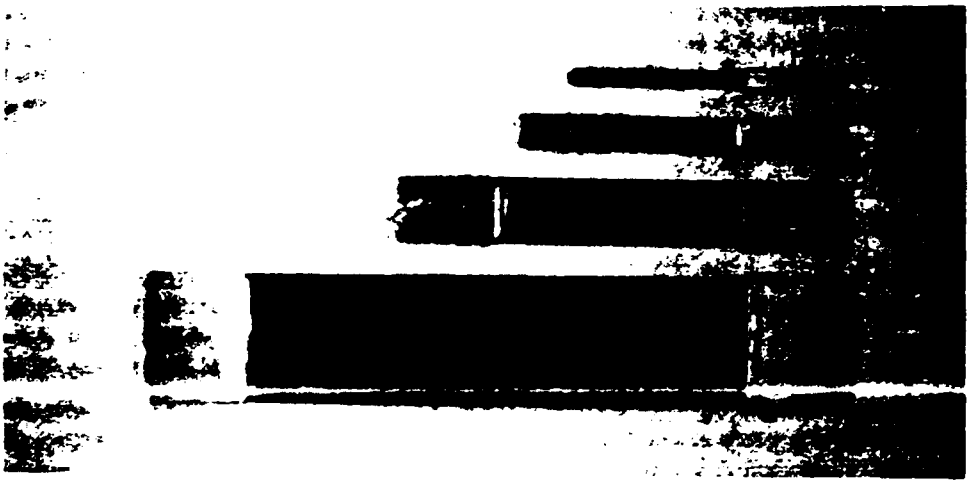

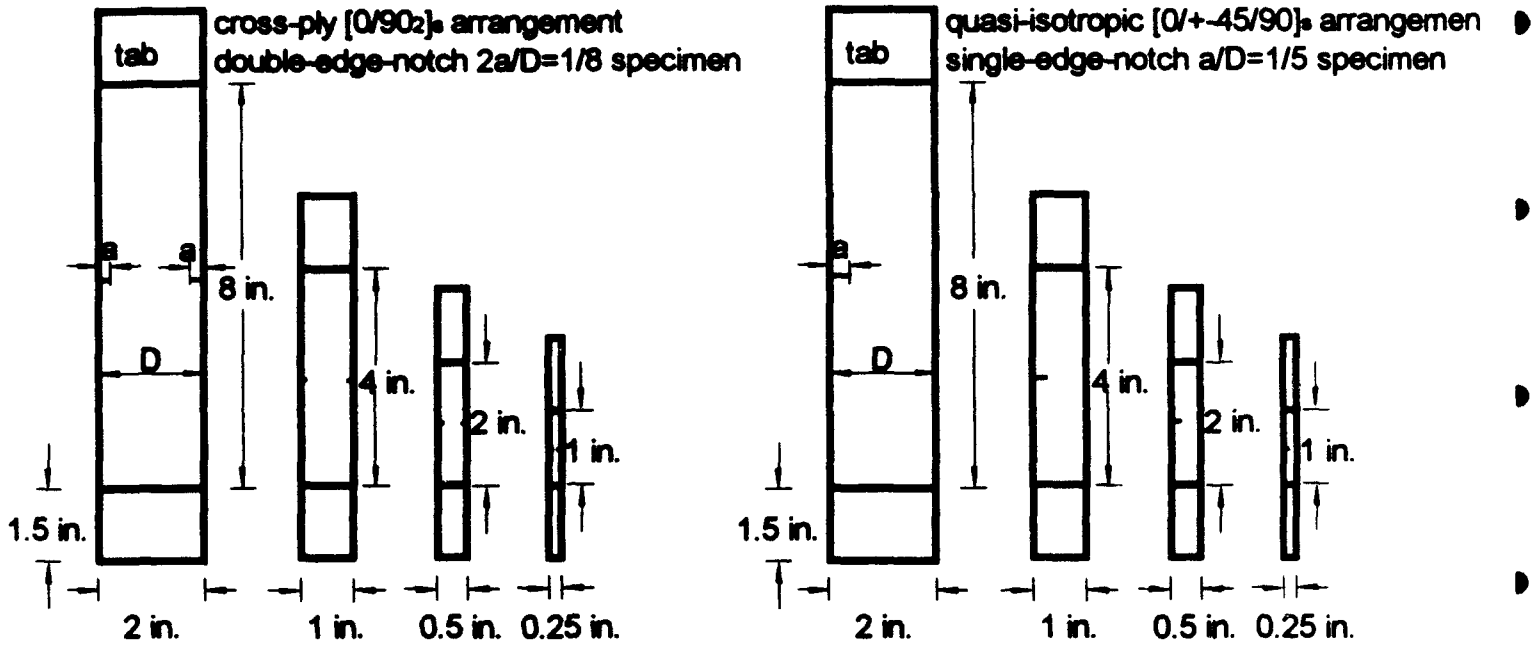
tab
cross-ply [0/90₂]ₛ arrangement
double-edge-notch 2a/D=1/8 specimen
a
a
8 in.
D
4 in.
2 in.
1 in.
1.5 in.
2 in.
1 in.
0.5 in.
0.25 in.
tab
quasi-isotropic [0/+-45/90]ₛ arrangemen
single-edge-notch a/D=1/5 specimen
a
8 in.
D
4 in.
2 in.
1 in.
1.5 in.
2 in.
1 in.
0.5 in.
0.25 in.

Fig. 3.

(a)

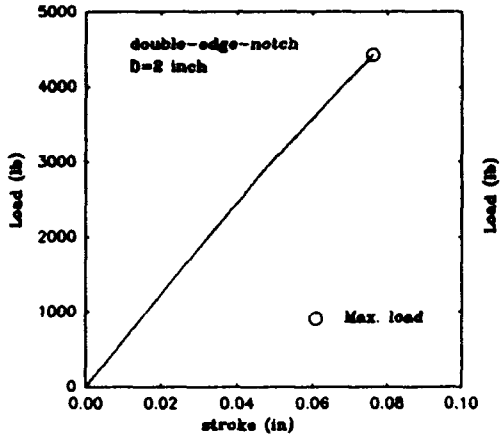
double-edge-notch
D=2 inch
Max. load
Load (lb)
stroke (in)

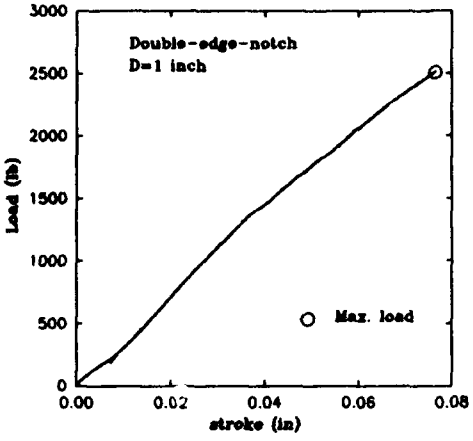
Double-edge-notch
D=1 inch
Max. load
Load (lb)
stroke (in)

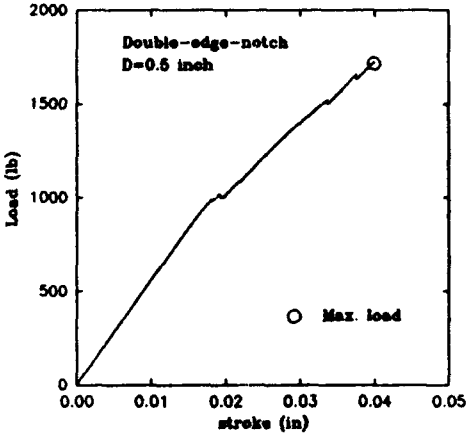
Double-edge-notch
D=0.5 inch
Max. load
Load (lb)
stroke (in)

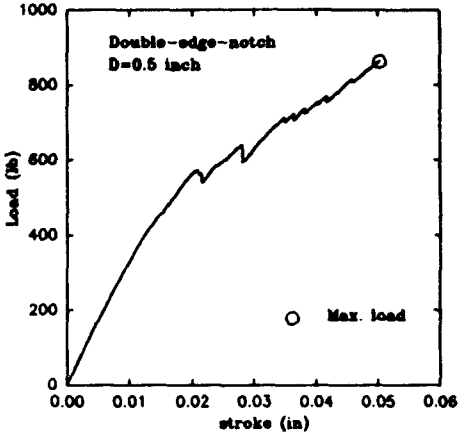
Double-edge-notch
D=0.5 inch
Max. load
Load (lb)
stroke (in)

(b)

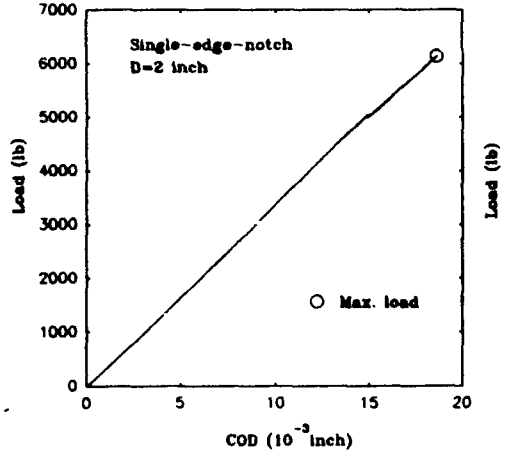
Single-edge-notch
D=2 inch
Max. load
Load (lb)
COD (10^-3 inch)

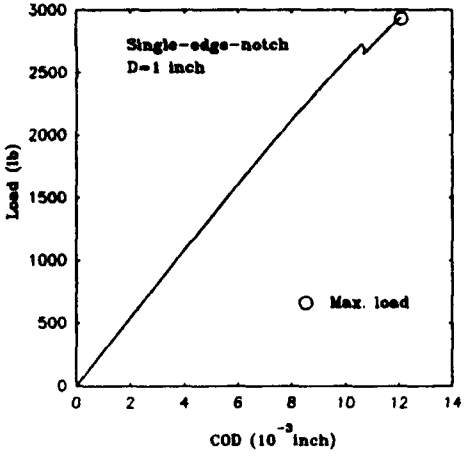
Single-edge-notch
D=1 inch
Max. load
Load (lb)
COD (10^-3 inch)

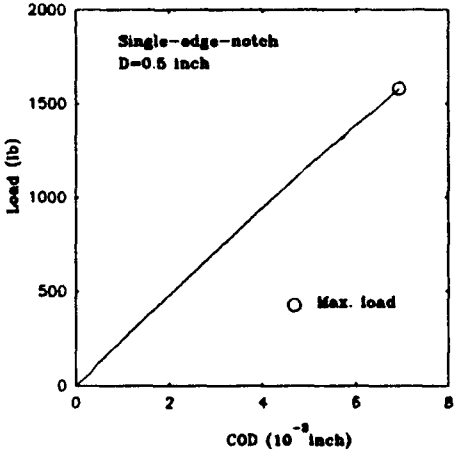
Single-edge-notch
D=0.5 inch
Max. load
Load (lb)
COD (10^-3 inch)

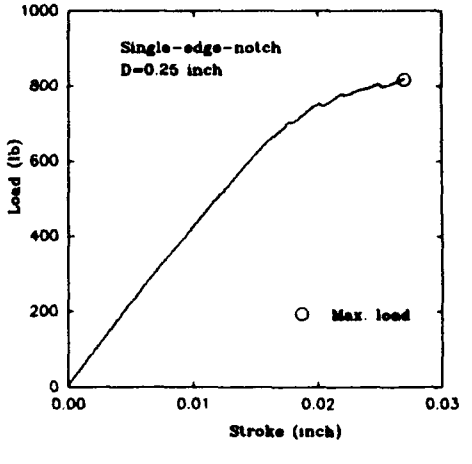
Single-edge-notch
D=0.25 inch
Max. load
Load (lb)
Stroke (inch)

(a)

(b)

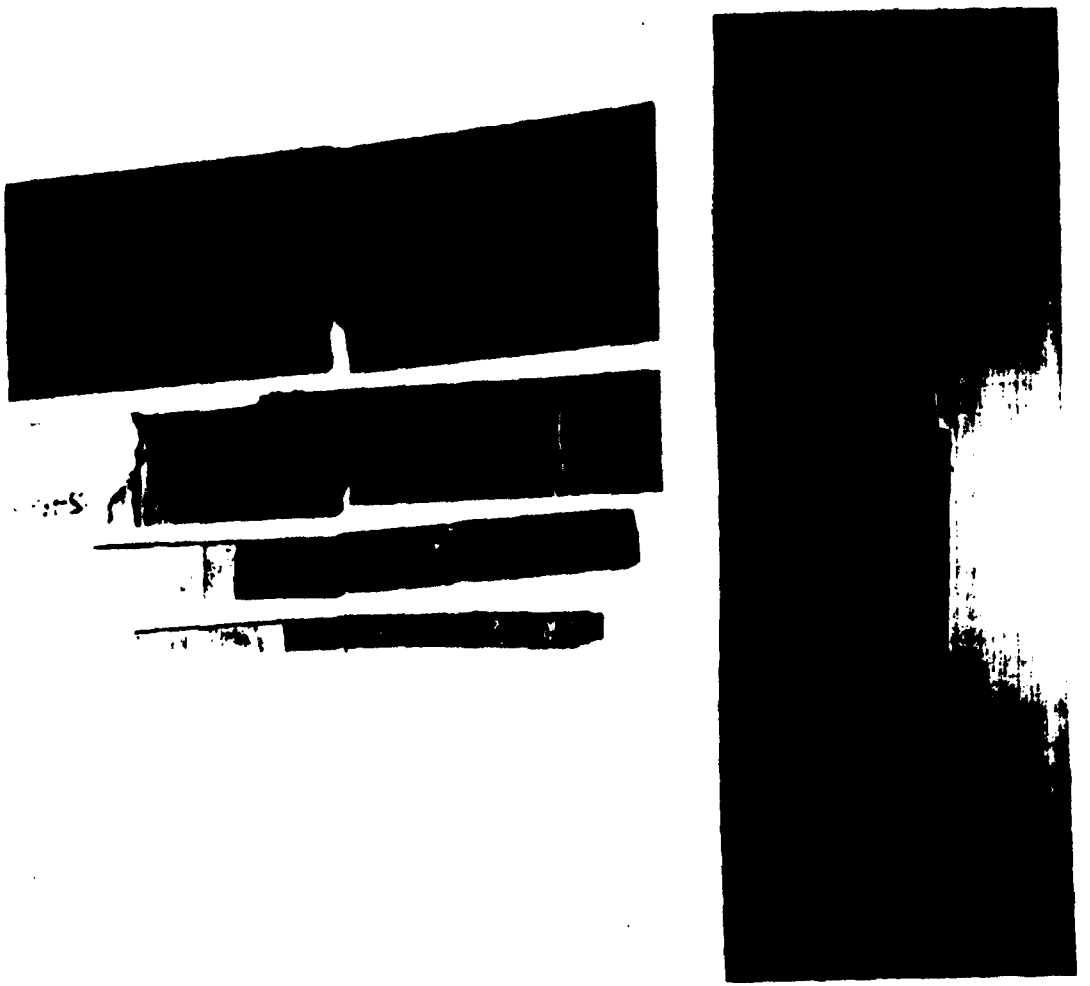

Fig. 5

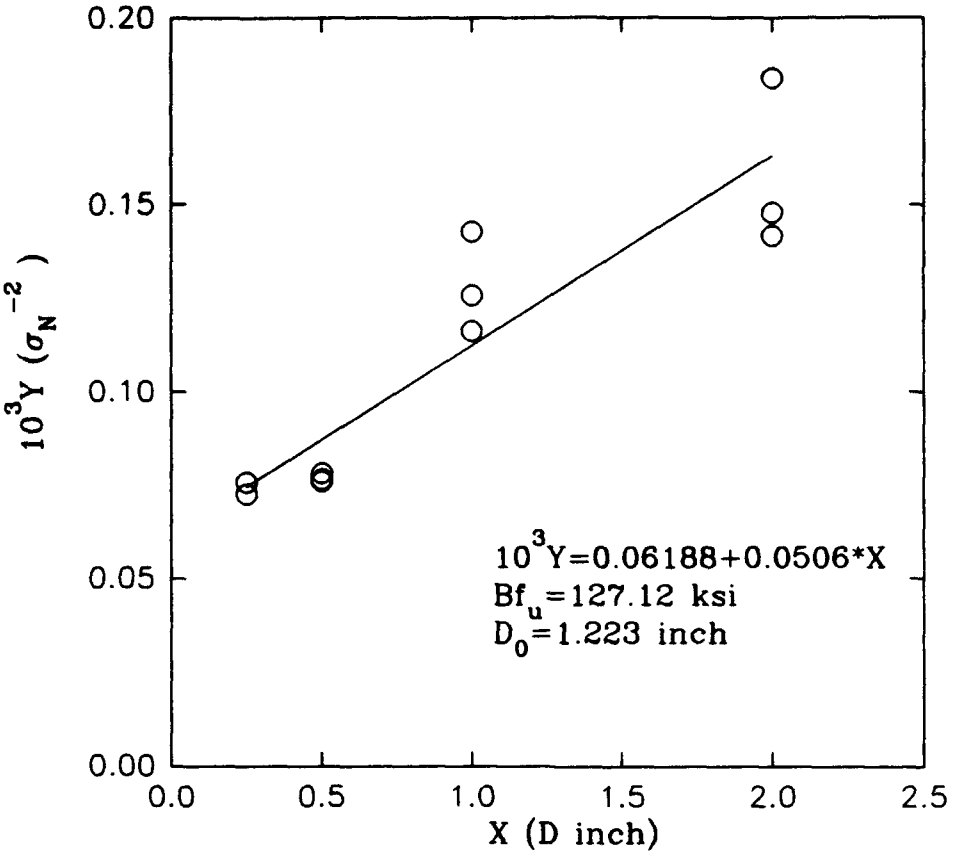
0.20
0.15
0.10
0.05
0.00
0.0
0.5
1.0
1.5
2.0
2.5
$10^3Y (\sigma_N^{-2})$
X (D inch)
$10^3Y=0.06188+0.0506*X$
$Bf_u=127.12$ ksi
$D_0=1.223$ inch

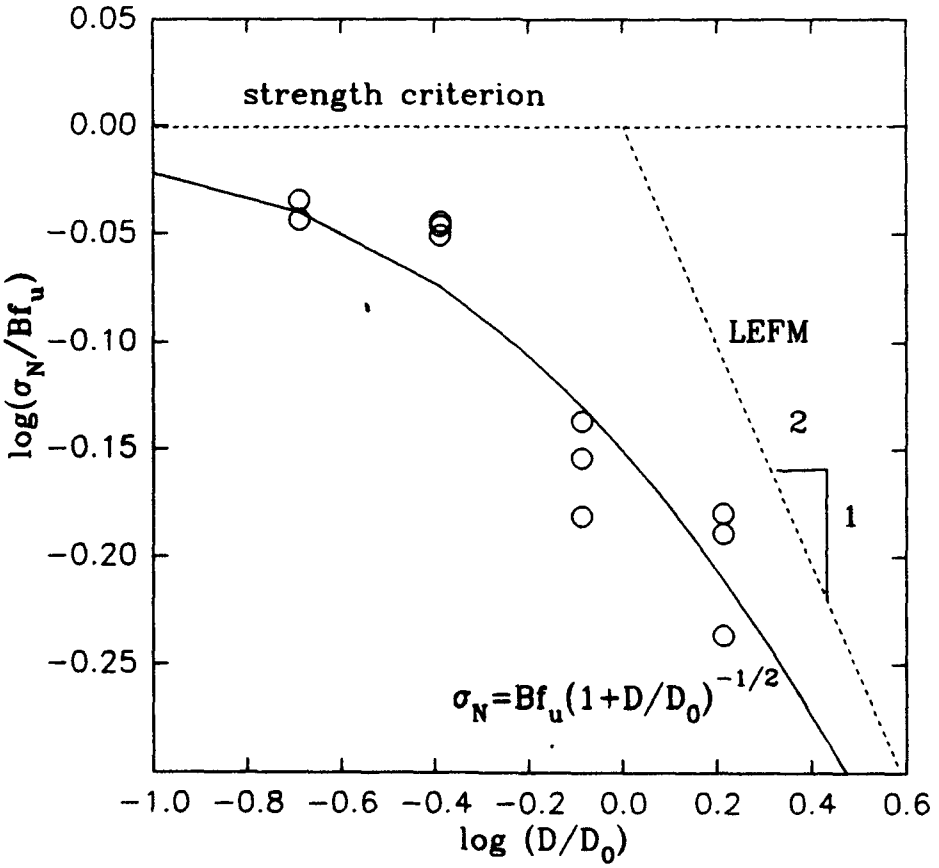
0.05
0.00
−0.05
−0.10
−0.15
−0.20
−0.25
−1.0
−0.8
−0.6
−0.4
−0.2
0.0
0.2
0.4
0.6
strength criterion
LEFM
2
1
$\log(\sigma_N/Bf_u)$
log (D/D_0)
$\sigma_N=Bf_u(1+D/D_0)^{-1/2}$

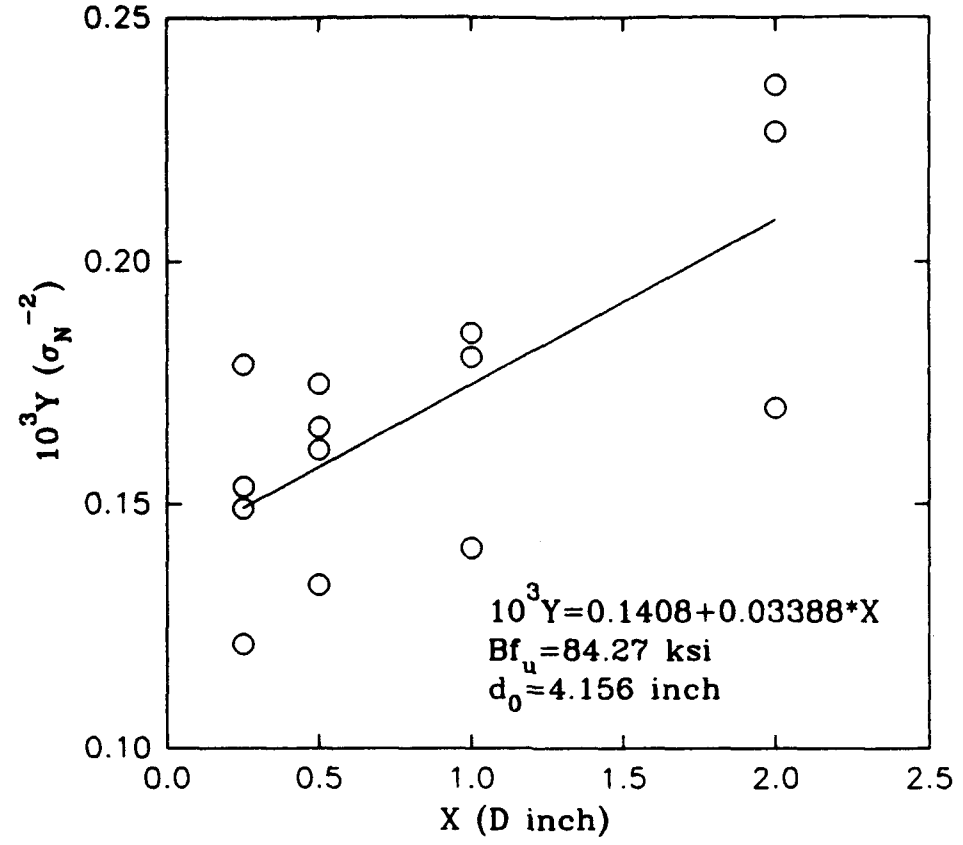
0.25
0.20
0.15
0.10
0.0
0.5
1.0
1.5
2.0
2.5
$10^3Y\ (\sigma_N^{-2})$
X (D inch)
$10^3Y=0.1408+0.03388*X$
$Bf_u=84.27$ ksi
$d_0=4.156$ inch

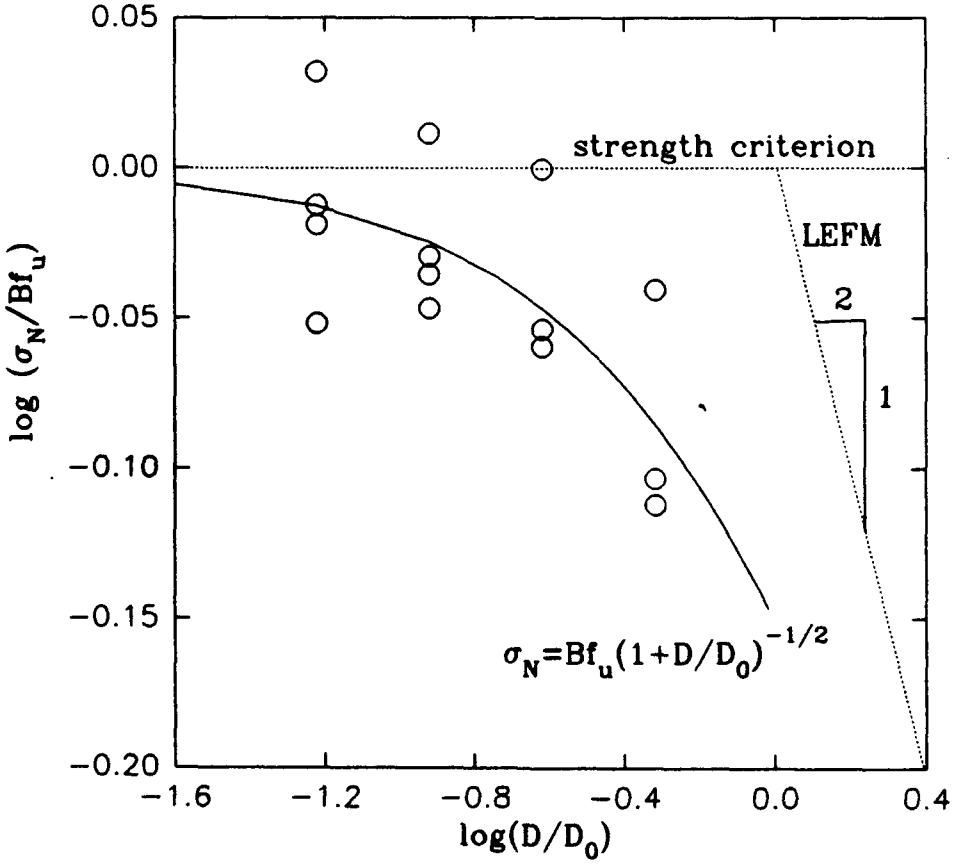
0.05
0.00
−0.05
−0.10
−0.15
−0.20
−1.6
−1.2
−0.8
−0.4
0.0
0.4
$\log\ (\sigma_N/Bf_u)$
$\log(D/D_0)$
strength criterion
LEFM
2
1
$\sigma_N=Bf_u(1+D/D_0)^{-1/2}$

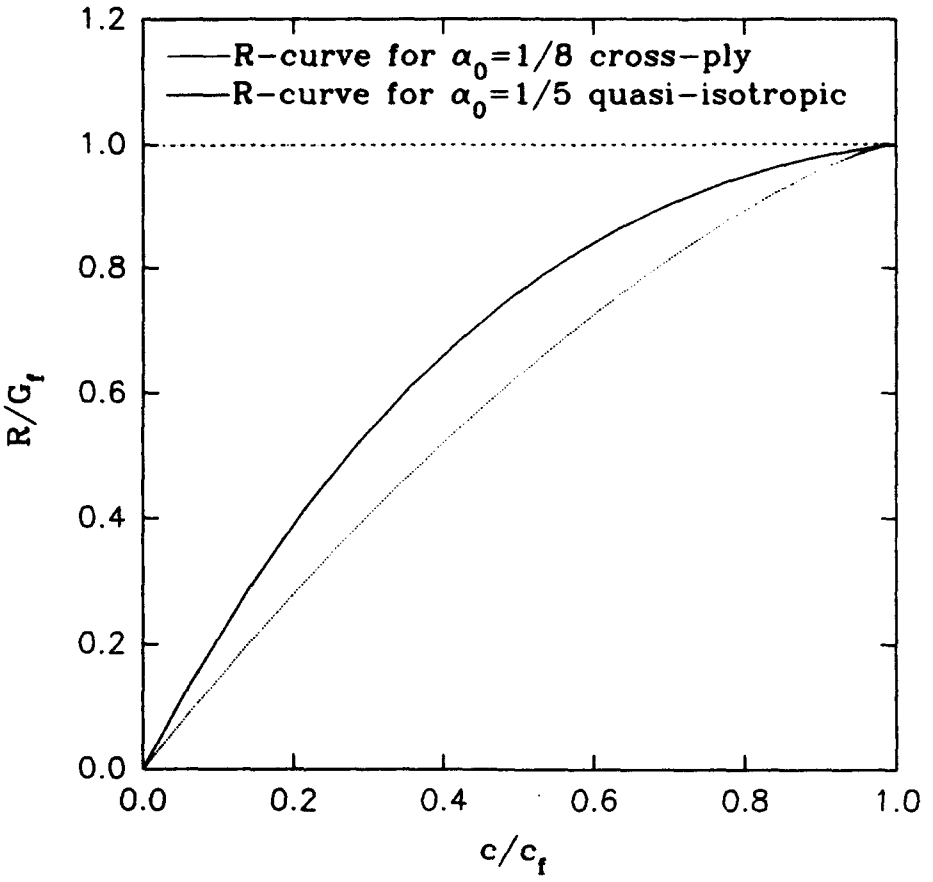
R-curve for α_0=1/8 cross-ply
R-curve for α_0=1/5 quasi-isotropic
1.2
1.0
0.8
0.6
0.4
0.2
0.0
R/G_f
0.0
0.2
0.4
0.6
0.8
1.0
c/c_f

Fig.

Size Effect in Fiber or Bar Pullout with Interface Fracture and Softening Slip

BY ZDENĚK P. BAŽANT AND RODRIGUE DESMORAT

Materials Science Report 93-12/457s
McCormick School of Engineering and Applied Science
Northwestern University
Evanston, Illinois 60208

December 1993

Size Effect in Fiber or Bar Pullout with Interface Fracture and Softening Slip

by ZDENĚK P. BAŽANT,[1] Fellow ASCE, and RODRIGUE DESMORAT [2]

ABSTRACT.— The paper analyzes the size effect, which is an inevitable consequence of post-peak softening in the relation of interface shear stress and slip displacement between a fiber or reinforcing bar and the surrounding matrix. To make a closed-form analytical solution feasible, the problem is simplified as one-dimensional. Solutions of pull-pull and push-pull failures are obtained for a linear softening stress-slip law with residual strength, and for an exponential law without residual strength. It is shown that the post-peak softening leads to localization of slip and interface shear fracture. The interface fracture process zone has a finite length. It propagates along the interface during the loading process, causing the distribution of the interface shear stress to become strongly nonuniform. The larger the bar or fiber size, the stronger the nonuniformity. The size effect in geometrically similar pullout tests of different sizes is found to represent a smooth transition between two simple asymptotic cases: (1) The case of no size effect, which occurs for very small sizes and is characteristic of plastic failure, and (2) the case of a size effect of the same type as in linear elastic fracture mechanics, in which the difference of the pullout stress in the fiber and the residual pullout stress corresponding to the residual interface shear stress is proportional to the inverse square root of the fiber or bar diameter. An analytical expression for the transitional size effect is obtained. This expression is found to approximately agree with the generalized form of the size effect law proposed earlier by Bažant. The shape of the size effect curve is shown to be related to the shape of the softening stress-slip law for the interface. Finally, it is shown how measurements of the size effect can be used for identifying the interface properties, and a numerical example is given.

[1]Walter P. Murphy Professor of Civil Engineering, Northwestern University, Evanston, Illinois 60208.
[2]Visiting Research Assistant, Northwestern University; on leave from Laboratoire de Mécanique et Technologie, E.N.S. de Cachan, Cachan, France

1 Introduction

The shear stress in the interface between fibers and matrix in composites or between steel bars and concrete is related to the slip displacement in the inteface. This relation is known to exhibit a post-peak softening. When softening occurs, analysis of the failure load according to plasticity becomes invalid. One must take into account localization of softening damage along the interface and consider fracture mechanics aspects of the problem. By analogy with studies of strain-softening damage, one must also expect a size effect on the nominal strength of geometrically similar structures of different sizes, which represents the most important practical consequence of the localization of softening damage. The objective of this paper is to analyze this size effect.

The problem of pullout of fibers or bars from the surrounding matrix has received considerable attention in recent years and many important results have been achieved; see e.g. Lawrence (1972), Freund (1992), Fuller et al. (1990), Gao et al. (1988), Leung and Li (1990 a,b), Li et al. (1991), Shah and Ouyang (1991), Stang et al. (1990), Steif and Hoysan (1986), Wang et al. (1988), Beaumond and Alezka (1978); Bowling and Groves (1979); and Gray (1984 a,b). An excellent review of the pullout test analysis has recently been presented by Shah and Ouyang (1991). Further light on the interface slip has been shed by studies of slip at interfaces of other types, including relative slip of rough crack surfaces (e.g. Bažant and Gambarova, 1980; Divakar et al., 1987; Feenstra et al., 1991).

Most interface models consider the shear stress at the interface to be a function of the slip displacement (e.g. Bažant and Gambarova, 1980; or Divakar et al., 1987). To make analytical solutions feasible, many previous authors have simplified the complex three-dimensional behavior at interface as one-dimensional (e.g. Gao et al., 1988; or Freund, 1992). In the one-dimensional solution, the influence of the normal pressure across the interface can be taken into account as long as this pressure is known. But if this pressure is unknown, a more general solution which takes into account the interface dilatancy, i.e. the normal relative displacement across the crack, is required. In the simplified one-dimensional analysis, the interface dilatancy can be approximately taken into account by adjusting the values of the parameters in the functional relationship $\tau(v)$ linking the interface shear stress τ to the relative slip displacement v; see e.g. Lawrence

et al. (1972), Bowling and Groves (1979), Hutchinson, and Jensen (1990). Stang et al. (1990) considered the stress–slip relation to consist of an elastic part followed by a sudden stress drop and a residual constant friction (Fig. 1a). However, it is no doubt more realistic to consider a gradual softening as shown in Fig. 1(b, c) (for a sufficiently large fiber size, the sudden stress drop with an increased strength limit but the same area under the curve giving the fracture energy must nevertheless give approximately equivalent results). As for the rising initial linear stress-displacement relation shown in Fig. 2a, it cannot be an interface property but must refer to the deformation in the layers of the matrix adjacent to the interface. For this reason, we will omit the rising linear part. As for the post–peak softening, we will consider it to be linear (Fig. 1c), in order to make a simple analytical solution feasible, although the real behavior is no doubt a smooth curve.

The size effect in the problem of fiber or bar pullout has apparently not yet been studied theoretically. However, its existence has already been demonstrated experimentally for the case of bar pullout from concrete (Bažant and Sener, 1988). In this paper, we will focus on the analysis of the size effect, considering a situation with a two–way debonding similar to that of Leung and Li (1990). We will deduce closed-form analytical formulas for the size effect, consider the asymptotic cases, and finally show how knowledge of the size effect can be exploited for determining the interfacial material properties solely from measurements of the maximum pullout forces.

Because we will simplify the problem as one-dimensional, we will be unable to make a distinction between fibers in composites and reinforcing bars in concrete, except in terms of the effective values of material parameters (such as the bond strength or the residual bond stress). Fibers and bars differ in fracture patterns, dilatancy and pressure sensitivity. But these phenomena can be specifically described only in a three-dimensional analysis.

2 Idealization of the Problem and Assumptions

For the sake of simplicity, our analysis will be one-dimensional. A cylindrical fiber or bar of diameter d is assumed to be embedded in an outer cylinder of diameter D representing the matrix of a composite material (Fig. 2). The cross sections of the fiber or bar and

of the outer cylinder are assumed to remain planar, but relative slip at the interface is possible. The stresses within the fiber as well as the matrix are uniform in each cross section. The interfacial debonding is characterized by the diagram of interface (bond) shear stress τ versus relative stress displacement v shown in Fig. 1c, where τ_s = initial bond strength (initial cohesion), τ_d = residual bond stress at sliding interface, and v_0 = critical slip determining the slope of the $\tau(v)$ diagram, which is assumed to be linear. The fiber and matrix are elastic, characterized by Young's elastic moduli E_f and E_m. Although in reality τ_s and τ_d are pressure dependent, in a one-dimensional model they must be assumed to be constant. The interface shear stress at the softening portion is

$$\tau = \tau_s\left(1 - \frac{v}{v_0}\right) \tag{1}$$

The cross-hatched area in Fig. 1c represents the bond fracture energy, which is expressed as:

$$G_f = \frac{1}{2}\tau_s v_0 \left(1 - \frac{\tau_d}{\tau_s}\right)^2 \tag{2}$$

Let z be the longitudinal coordinate. The fiber has a free end at $z = -l$. We will study two types of test: (1) Pull-pull, in which the cylinder representing the matrix has a free end at $z = 0$ and is supported at the opposite end (Fig. 2a), and (2) pull-push, in which the matrix cylinder is supported at $z = 0$ (Fig. 2b). First we consider the pull-pull test and leave consideration of the pull-push test to the end.

Equilibrium of a small element of the fiber, of length δz, requires that $\delta\sigma(\pi d^2/4) = \tau(\pi d)\delta z$ which yields

$$\frac{d\sigma}{dz} = \frac{4\tau}{d} \tag{3}$$

where σ = normal stress in the fiber. Equilibrium in the cross sections of fiber and matrix requires that $\sigma A_f + \sigma_m A_m = \sigma_a A_f$, which yields

$$\sigma_m = \frac{E_m}{E_f}\phi(\sigma_a - \sigma) \tag{4}$$

where σ_a = applied pull-out stress ($\sigma_a = P/A_f$ where P is the pull-out load), σ_m = normal stress in the matrix cylinder, $\phi = A_f E_f / A_m E_m$, $A_f = \pi d^2$, and $A_m = \pi(D^2 - d^2)$.

Noting that the difference between the strains in the fiber and the matrix is dv/dz, we have $dv/dz = \sigma/E_f - \sigma_m/E_m$, which yields

$$\frac{dv}{dz} = \frac{1+\phi}{E_f}\sigma - \frac{\phi}{E_f}\sigma_a \tag{5}$$

The displacement at the end of embedment (Fig. 2), $z = 0$, is:

$$\delta = v(-L) + \int_{-L}^{0} \frac{\sigma}{E_f}\, dz = \frac{v(0) + \phi v(-L)}{1+\phi} + \frac{\phi \sigma_a L}{(1+\phi)E_f} \tag{6}$$

For the case of softening slip, the differential equation for the fiber stresses ensues by differentiating (5) and substituting (3) and (1):

$$\frac{d^2\sigma}{dz^2} + \omega^2 \sigma = \frac{\phi}{1+\phi} \quad \omega^2 \sigma_a \tag{7}$$

in which

$$\omega^2 = \frac{4(1+\phi)\tau_s}{E_f v_0 d} \tag{8}$$

At the cross sections with no interface slip (no shear crack), the strains in the fiber and the matrix cylinder are equal, i.e. $\sigma/E_f = \sigma_m/E_m$; this yields

$$\sigma = \frac{\phi}{1+\phi}\sigma_a \tag{9}$$

3 Analysis of Pull–Pull Test

In the pull–pull case, two interface cracks grow from both ends of the fiber until they join. At that moment the maximum applied stress $\sigma_a = \sigma_N$, representing the nominal strength, is reached. If the load is controlled, failure occurs at that moment. The post–peak softening is observable only when the fiber displacement at the end is controlled, except when the response diagram exhibits a snapback. The snapback, as we will see, occurs for sufficiently large sizes.

Because of the discontinuities at the beginning of slip and at the attainment of residual bond shear strength, several stages must be distinguished in the solution. The number of states to consider is reduced in the case that $\phi = 1$ (Fig. 3). Therefore we restrict attention to this case, although the general conclusions and implications for the size effect are the same for any ϕ. For $\phi = 1$, we have $\omega^2 = 8\tau_s/E_f v_0 d$. The stages we must distinguish are as follows:

1. The initial stage, in which there are two separate cracks emanating from the ends of the fiber and the shear stress is everywhere larger than the residual strength τ_d;

2. The final stage, in which the two cracks have joined into one and the residual strength τ_d has been reached at both ends;

3. The intermediate stage, in which one must distinguish two cases:

   (a) The two cracks join before τ reaches τ_d at the ends, or

   (b) the shear stress τ_d is reached before the cracks join.

Initial Stage

In the middle portion of the fiber there is no slip and the shear stress $\tau = 0$. The maximum τ occurs at the fracture tips $z = -l_i$, at which $\tau = \tau_s$; $i = 1, 2$ refer to the right and left parts. From (7), for parts I and II,

$$\tau_i = \tau_s \cos\omega(z + l_i) \tag{10}$$

From (1), the interface slip is

$$v = v_0 \left[1 - \cos\omega(z + l_i)\right] \tag{11}$$

The slip increases from the crack tip to the end of the crack. The distances l_i of the tips from the right end of the fiber ($z = 0$) are $l_1 = a$ and $l_2 = L - a$, where a = length of each crack,

$$a = \frac{1}{\omega} \arcsin\left(\frac{\omega d}{8\tau_s}\ \sigma_a\right) \tag{12}$$

Between the cracks, the stress in the fiber is $\sigma = \sigma_a/2$. From the crack tips to the crack ends, the stress in the fiber increases as

$$\sigma_i = \frac{\sigma_a}{2}\left(1 + \frac{\sin\omega(z + l_i)}{\sin\omega a}\right) \tag{13}$$

The displacement of the end increases with σ_a, and the diagram of $\sigma_a(\delta)$ is given, in the first stage, by

$$\delta_1 = \frac{L\sigma_a}{2E_f} + v_0\left[1 - \sqrt{1 - \left(\frac{\omega\sigma_a d}{8\tau_s}\right)^2}\right] \tag{14}$$

The diagram of σ_a vs. δ has a negative curvature. The transition to the intermediate stage occurs when σ_a reaches a critical value that is the smaller of the following two values:

$$\sigma_a^* = \frac{8\tau_s}{\omega d}\sin\frac{\omega L}{2}, \quad \sigma_a^{**} = \frac{8\tau_s}{\omega d}\sqrt{1-\frac{\tau_d^2}{\tau_s^2}} \tag{15}$$

The critical value is σ_a^* if ωL is small enough and σ_a^{**} if ωL is large enough.

Intermediate stage

Case (1) of the intermediate stage, already defined (Fig. 3b), occurs if $\omega L < 2\arccos(\tau_d/\tau_s)$. Otherwise case (2) occurs.

In case (1), the cracks have already joined and the interface shear stress is everywhere smaller than τ_s, but slightly larger than τ_d. According to (1),

$$\tau = \sigma_a \frac{\omega d\cos\omega(z+\frac{L}{2})}{8\sin\omega\frac{L}{2}} \tag{16}$$

The stress in the fiber (Fig. 2) increases from the left end ($z=-L$) to the right end ($z=0$) and is

$$\sigma = \frac{\sigma_a}{2}\left(1+\frac{\sin\omega(z+\frac{L}{2})}{\sin\omega\frac{L}{2}}\right) \tag{17}$$

The displacement δ of the end of the fiber is, for the first case of the intermediate stage,

$$\delta_{21} = v_0 + \frac{L\sigma_a}{2E_f}\left[1-\frac{2}{\omega L}\cot\frac{\omega L}{2}\right] \tag{18}$$

The stress in the fiber varies from σ_a^* to

$$\sigma_a^I = \frac{8\tau_d}{\omega d}\tan\frac{\omega L}{2} \tag{19}$$

for which the residual interface shear stress τ_d is reached at the end. Because $\omega L < 2\arccos(\tau_d/\tau_s)$, σ_a^I is always smaller than σ_a^*, and so the failure occurs at $\sigma_a = \sigma_N = \sigma_a^*$. The equilibrium path of the structure exhibits snapback if L is sufficiently large or τ_d is sufficiently small. Precisely, the condition of snapback is

$$2x_0 < \omega L < 2\arccos\frac{\tau_d}{\tau_s} \tag{20}$$

in which x_0 is the root of $x_0\tan x_0 = 1$, i.e. $x_0 = 0.8603$.

In case (2) of the intermediate stage, i.e. for $\omega L > 2\arccos(\tau_d/\tau_s)$, there are two cracks (Fig. 3b). The interface fracture process zone exhibits linear softening and its length is c_f. The fracture process zone of length c_d is at constant residual interface shear stress $\tau = \tau_d$;

$$c_f = \frac{1}{\omega}\arccos\frac{\tau_d}{\tau_s}, \qquad c_d = \frac{d}{8\tau_d}(\sigma_a - \sigma_a^{**}) \tag{21}$$

and $a = l_1 = L - l_2 = c_f + c_d$. With G_f defined by (2) and ω by (8), the fracture process zone length is $c_f = \kappa_1\sqrt{l_0 d}$ in which $\kappa_1 = (\pi/4)\sqrt{E_f/E_m}$ and $l_0 = E_m G_f/\tau_s^2$ when $\tau_d = 0$. In the general case, κ_1 depends on both the fiber proportion in the matrix and the elastic moduli;

$$\kappa_1 = \frac{\pi}{2}\sqrt{\frac{E_f}{2(1+\phi)E_m}} \tag{22}$$

The expression for the normal stress in the portion of the fiber that has a linearly varying interface shear stress is the same as for the initial stage. For the portion of the fiber that has a constant interface shear stress, the normal stress is linear in z if $\tau_d = 0$, and otherwise it is constant. The end displacement δ increases with σ_a, and the diagram of σ_a vs. δ has a positive curvature;

$$\delta_{22} = \frac{L\sigma_a}{2E_f} + v_0\left(1 - \frac{\tau_d}{\tau_s}\right) + \frac{d}{16\tau_d E_f}\left(\sigma_a^2 - \sigma_a^{**2}\right) \tag{23}$$

Failure occurs when $\sigma_a = \sigma_N = \sigma_a^{II}$, which is always larger than σ_a^{**};

$$\sigma_a^{II} = \sigma_a^{**} + \frac{4\tau_d}{\omega d}\left(\omega L - 2\arccos\frac{\tau_d}{\tau_s}\right) \tag{24}$$

Final stage

The softening zone is now localized in the middle of the specimen (Fig. 3c). Its length ΔL gradually decreases to 0. The length of the fracture zone, in which $\tau = \tau_d$, is $c_d = (L - \Delta L)/2$. For a given applied stress σ_a, ΔL is the solution of

$$\sigma_a = \frac{4\tau_d}{d}\left(L - \Delta L + \frac{2}{\omega}\tan\frac{\omega\Delta L}{2}\right) \tag{25}$$

Displacement δ at the end of the fiber is

$$\delta_3 = \frac{L\sigma_a}{2E_f} + v_0\left(1 - \frac{\tau_d}{\tau_s}\right) + c_d\left(\frac{\sigma_a}{E_f} - \frac{4c_d\tau_d}{dE_f}\right) \tag{26}$$

Note that $d\sigma_a/d(\Delta L)$ is always positive, and $d(\Delta L) = -2dc_d$ is always negative. Therefore, $d\sigma_a$ is negative, and the equilibrium path decreases with the applied stress. Therefore, failure occurs in this case before the final stage is reached.

The condition of snapback is

$$\frac{\omega(L+2c_d)}{2}\tan\frac{\omega\Delta L}{2} - 1 > 0 \tag{27}$$

At L/d = constant, $\omega L \propto \sqrt{d}$ when $0 \leq \omega\Delta L/2 \leq \arccos(\tau_d/\tau_s)$, and so snapback must occur for sufficiently large sizes.

4 Size Effect

The scaling law is the most important attribute of any physical theory. In the classical theories of elasticity or plasticity, the problem of scaling law has not received much attention because the law is very simple—the nominal strength is independent of structure size. In the mechanics of damage and nonlinear fracture mechanics, the problem of scaling or size effect has received major attention in recent years, principally because there is a strong effect of size on the nominal strength and the scaling law is more complex, representing a transition from elasticity (or plasticity) to linear elastic fracture mechanics, in which the nominal strength is inversely proportional to the square root of the structure size (Bažant, 1984; Bažant and Cedolin, 1991).

The size effect can be defined only for structures with similar geometries and similar cracks. Therefore, we consider the ratios D/d and L/d to be constant and choose the fiber diameter d to play the role of characteristic dimension of the structure. We note that, in this case, ωd and ωL are both proportional to $\sqrt{d}$. The applied pullout stress σ_a at maximum load may be employed as the nominal strength σ_N. The value of σ_N can be calculated from (15) if $\omega L < 2\arccos\tau_d/\tau_s$, and otherwise from (24).

For numerical examples, we consider the material properties τ_s = 31MPa, τ_d = 3MPa, v_0 = 0.021 mm and E_f = 200 GPa, and run the calculations for sizes d = 1, 2.9, 6.4 and 12.7 mm at constant ratio $L/d = 4$. The results are plotted in Fig. 4. It is apparent that the maximum pullout stress decreases with increasing size. Furthermore, the type of the load–displacement diagram changes; for the smallest size we have a

gradual post-peak softening, for the next size we have a nearly vertical stress drop, and for the largest two sizes we have snapback instability right after the peak. This behavior is typical of the size effect in all structures exhibiting damage localization or nonlinear fracture. The size effect is caused by increasing localization of the softening regions along the fiber length as d increases. The softening region at maximum load, which represents the fracture process zone and is characterized by stress values between τ_s and τ_d (Fig. 1), extends in small specimens over a large portion of the fiber length and in large specimens over a small portion of the fiber length. This behavior is similar to all other failures due to damage growth or nonlinear fracture.

The size effect obtained for our example is shown in Fig. 5 by the diagram of $\log(\sigma_N - \sigma_0)$ vs. $\log d$, where σ_0 is the residual fiber strength corresponding to the residual interface bond stress τ_d.

Let us now examine the asymptotic behavior. In the limit of small sizes, $d \to 0$, we obtain

$$\sigma_N = \sigma_a^* = 4\tau_s \frac{L}{d} = \text{constant} \tag{28}$$

In the limit of the large sizes, $d \to \infty$, we obtain

$$\sigma_N = \sigma_a^{II} = \sigma_0 + \frac{\sqrt{8\tau_s E_f v_0}}{\sqrt{d}} \left(\sqrt{1 - \frac{\tau_d^2}{\tau_s^2}} - \frac{\tau_d}{\tau_s} \arccos \frac{\tau_d}{\tau_s} \right) \tag{29}$$

in which σ_0 is the residual pullout stress of the fiber when the interface is completely debonded and softened to τ_d,

$$\sigma_0 = 4\tau_d \frac{L}{d} \tag{30}$$

According to (29), the basic form of the size effect for the large sizes is

$$\sigma_N - \sigma_0 \quad \propto \quad \frac{1}{\sqrt{d}} \tag{31}$$

Except for the presence of σ_0, this represents the size effect characteristic of linear elastic fracture mechanics. In the plot of Fig. 5, it corresponds to the inclined straight-line asymptote of slope $-1/2$.

The size effect obtained by the present analysis and shown in Fig. 5 agrees with the general size effect of damage mechanics or nonlinear fracture. Under the hypothesis that the energy dissipated at failure is a smooth function of both the specimen (or structure)

size and the fracture process zone size, with the latter being a material property, it was shown (Bažant, 1985) by dimensional analysis an similitude arguments that, in general,

$$\sigma_N = Bf_t' \left[\xi(1 + \xi^{-1} + A_1\xi^{-2} + A_2\xi^{-3} + \ldots)\right]^{-1/2m} \qquad \xi = (d/d_0)^m \tag{32}$$

Here f_t' is the tensile strength of the material, introduced strictly for convenience, and m, $B, d_0, A_1, A_2, \ldots$ are positive empirical coefficients. Eq. (32) represents an asymptotic series expansion with respect to an infinitely large specimen. It was further shown (Bažant, 1987) that for size ranges up to about 1:20, the asymptotic series can be truncated after the linear term and that, for most applications to concrete and rock, one can take $m = 1$. Thus (32) reduces to the size effect law (Bažant, 1984):

$$\sigma_N = \frac{Bf_t'}{\sqrt{1+\beta}} \qquad \beta = \frac{d}{d_0} \tag{33}$$

For materials with a residual strength, represented here by τ_d, σ_N must be replaced in the foregoing equations with $\sigma_N - \sigma_0$ where σ_0 is the residual nominal strength. Thus, truncation of (32) after the linear term yields the law:

$$\sigma_N - \sigma_0 = Bf_t'(1 + \beta^m)^{-1/2m} \tag{34}$$

and the simple size effect law ($m = 1$) in (33) is generalized as

$$\sigma_N - \sigma_0 = \frac{Bf_t'}{\sqrt{1+\beta}} \tag{35}$$

It is obvious that, for $d \gg d_0$, (33)-(35) reduce to $\sigma_N - \sigma_0 \propto d^{-1/2}$, which is the form of size effect exhibited by every formula of linear elastic fracture mechanics. For $d \ll d_0$, (33) or (35) reduces to σ_N = constant (no size effect), which is characteristic of elasticity or plasticity. For the intermediate values of size d, (33) or (35) describes a gradual transition between these two asymptotic cases.

Matching the asymptotes to those calculated for fiber pullout, the simple size effect law in (33) gives in Fig. 5 the plot shown by the solid curve ($Bf_t' = 500$ MPa, $d_0 = 4.2$ mm).

The presently calculated size effect law may be rewritten for $\sigma_0 = \tau_d = 0$ as follows:

$$\sigma_N = \frac{Bf_t'}{\sqrt{\beta}} \sin\sqrt{\beta} \qquad \text{if} \qquad \beta \leq \frac{\pi^2}{4} \tag{36}$$

$$\sigma_N = \frac{B f_t'}{\sqrt{\beta}} \qquad \text{if} \qquad \beta > \frac{\pi^2}{4} \tag{37}$$

These results are exact for the pull-push problem for any ϕ, as we will see in the next section.

Equation (35) is not identical to (36)–(37), but it can be made nearly identical for a certain value of m. This value can be estimated by requiring (34) and (36) to coincide for $d = d_0$ or $\beta = 1$. This yields :

$$m = -\frac{\ln 2}{2 \ln (\sin 1)} = 2.009 \approx 2 \tag{38}$$

For $m = 2$, the agreement of (36)-(37) with (35) becomes virtually perfect.

For tensile fracture, the value of exponent m is known to be related to the shape of the strain–softening diagram (Bažant, 1985). Striving for the simplest analytical solution possible, we have assumed this diagram to be linear (Fig. 1c). For tensile fracture, it was shown that a softening diagram with a progressively decreasing slope and a long tail yields a more gradual transition in the size effect plot. It may be expected that if Fig. 1c were replaced by such a softening diagram, the calculated size effect could be made to match the dashed curve in Fig. 5, corresponding to the simple size effect law in (35). It remains to be seen whether the actual behavior of interfaces corresponds to the simple case $m = 1$ (as it approximately does for tensile fracture of concrete), or an $m-$value very different from 1 needs to be used. To illuminate this question, the simple nonlinear softening law $\tau = \tau_s \exp(-bv)$ (Fig. 1d) will be considered next.

5 Size Effect Law for a Nonlinear Softening Interface Behavior

The pullout equations (3) and (5), complemented by the general nonlinear law $\tau = \tau(v)$ lead to the general nonlinear differential equation for $v(z)$:

$$\frac{d^2v}{dz^2} = k\tau(v), \qquad \text{with} \qquad k = \frac{4(1+\phi)}{E_f d} \tag{39}$$

which is valid for both the pull-pull and pull-push tests. The axial stress in the fiber is given by $\sigma(z) = E_f(1+\phi)^{-1}v'(z) + \phi(1+\phi)^{-1}\sigma_a$ for the pull-pull test and by $\sigma(z) =$

$E_f(1+\phi)^{-1}v'(z)$ for the pull-push test. The boundary conditions are $v' = 0$ at the tip of interface crack ($v = 0$), $\sigma = \sigma_a$ at $z = 0$, and $\sigma = 0$ at $z = -L$. For simplicity, as before, the pull-pull case will be studied for $\phi = 1$, and the pull-push case for any ϕ.

The general solution of (39) is:

$$\int \frac{dv}{\sqrt{\int \tau(v)dv}} = (\sqrt{2k})z \tag{40}$$

To make integration easy, we will consider :

$$\tau(v) = \tau_s \exp(-bv) \tag{41}$$

The residual shear stress τ_d is here taken equal to zero, and b is related to the fracture energy G_f by $b = \tau_s/G_f$. From (40):

$$v = \frac{2}{b} \ln \left[\cosh \left(\sqrt{2kG_f} \frac{b(z+l_i)}{2} \right) \right] \tag{42}$$

The axial stress for the pull-pull case ($\phi = 1$) is:

$$\sigma = \frac{E_f\sqrt{2kG_f}}{2} \tanh \left[\sqrt{2kG_f} \frac{b(z+l_i)}{2} \right] + \frac{\sigma_a}{2} \tag{43}$$

and for the pull-push case:

$$\sigma = \frac{E_f\sqrt{2kG_f}}{1+\phi} \tanh \left[\sqrt{2kG_f} \frac{b(z+l)}{2} \right] \tag{44}$$

The stress at failure is reached when the interface is debonded along all of its length.

The size effect law for pullout with exponential softening and no residual stress may now be written as ($\beta = d/d_0$) :

$$\sigma_N = \frac{Bf_t'}{\sqrt{\beta}} \tanh \sqrt{\beta} \tag{45}$$

where $Bf_t = 4\tau_s L/d$, $d_0 = 16E_fG_f/(Bf_t')^2$ for the pull-pull test with $\phi = 1$, and $d_0 = 8E_fG_f(1+\phi)^{-1}/(Bf_t')^2$ for the pull-push test.

Again, to match (34) closely to (45), we require them to coincide for $\beta = 1 (d = d_0)$. This condition yields

$$m = -\frac{\ln 2}{2 \ln(\tanh 1)} \simeq 1.25 \tag{46}$$

As might have been expected, m is now found to be much closer to 1 than for the linear softening. This confirms the dependence of m on the shape of the interface stress-slip law. The corresponding size effect curves are plotted in Fig. 5b. We see the theoretical curve agrees almost perfectly with the size effect law with additional parameter (34) and is quite close to the simple size effect law (35).

The foregoing analysis with a softening exponential stress-slip law does not take in account the residual strength σ_0 of the interface. For its effect one must refer to our solution for linear softening.

The general conclusion of our nonlinear analysis is that the influence of the shape of the shear stress-slip curve on the size effect is appreciable only for the transitional sizes. For a softening stress-slip law of declining slope, the size effect is closer to the simple formula (33) than for a stress-slip linear law. The asymptotes of the size effect curve in a log-log plot remain the same; the interface strength τ_s governs the failure for very small sizes, and the interface fracture energy G_f the failure for very large sizes.

According to (40), closed-form analytical solutions could be obtained also for stress-slip laws other than (1) or (41).

6 Identification of Interface Properties from Size Effect Measured in Push-Pull Tests

In the mechanics of tensile fracture, the measured size effect can be exploited to determine the material fracture characteristics (Bažant, 1987; Bažant and Pfeiffer, 1987; Bažant and Kazemi, 1990). The same must be possible for fiber pullout.

Indeed, after calculating the asymptotes of the size effect plot, the size effect parameters for linear softening can be identified by matching these asymptote with equations (28) and (29). This yields

$$Bf_t' = 4(\tau_s - \tau_d)\frac{L}{d} \tag{47}$$

$$d_0 = \frac{8\tau_s E_f v_0}{(Bf_t')^2}\left(\sqrt{1-\frac{\tau_d^2}{\tau_s^2}} - \frac{\tau_d}{\tau_s}\arccos\frac{\tau_d}{\tau_s}\right)^2 \tag{48}$$

When the size effect law is to be matched to experimental data on σ_N, parameters of the (33) can be easily identified by linear regression $Y = AX + C$ where $X = d, Y = 1/(\sigma_N - \sigma_0)^2, Bf_t' = 1/\sqrt{C}$, and $d_0 = C/A$. A similar linear regression is possible for (34).

As an example, we will use the test data of Bažant and Sener (1988) (the circled points in Fig. 5). These data are for pullout of reinforcing bars from concrete cubes. We use these data only to illustrate the procedure while being fully aware that the failure mode observed in these tests did not fit the assumptions of the present analysis. The failure started by radial splitting cracks emanating from the bar. These cracks, which were caused mainly by lugs on the reinforcing bars, cannot be described by a one-dimensional model. Had smooth rather than deformed bars been used, the failure would have been due only to interface slip, and then the present example would represent the reality rather than just a mere illustration of the procedure.

Deformed reinforcing bars of yield strength 414 MPa and diameters 2.9, 6.4 and 12.7 mm were used. In each cube, there was one bar parallel to one edge of the cube and sticking out at the center of one face. The embedment length of the bar was $L = 4d$. The size effect law parameters, identified previously (Bažant and Sener, 1988) were $Bf_t' = 500$ MPa, $d_0 = 2.1$ mm and $\sigma_0 = 0$.

For the purpose of analyzing these data, the solution for the pull–push test has also been derived:

$$\text{for } \omega L \leq \arccos\frac{\tau_d}{\tau_s}: \quad \sigma_N = \frac{4\tau_s}{\omega d}\sin\omega L \tag{49}$$

$$\text{for } \omega L > \arccos\frac{\tau_d}{\tau_s}: \quad \sigma_N = \sigma_0 + \frac{4\tau_s}{\omega d}\left(\sqrt{1-\frac{\tau_d^2}{\tau_s^2}} - \frac{\tau_d}{\tau_s}\arccos\frac{\tau_d}{\tau_s}\right) \tag{50}$$

in which ω is given by (8) and $\sigma_0 = 4\tau_d L/d$, $\phi = A_f E_f / A_m E_m$. Knowing the exponent m, which is here taken as $m = 1$ (same as Bažant and Sener, 1988), we can use the aforementioned linear regression plot $Y = AX + C$ to determine the size effect law parameters Bf_t' and d_0. Matching of the asymptotes, we get the following expressions for the interface properties:

$$\tau_s = \frac{d}{4L}Bf_t' + \tau_d \tag{51}$$

$$v_0 = \frac{1+\phi}{4}\,\frac{(Bf_t')^2}{\tau_s E_f}\,d_0\left(\sqrt{1-\frac{\tau_d^2}{\tau_s^2}}\;-\;\frac{\tau_d}{\tau_s}\arccos\frac{\tau_d}{\tau_s}\right)^{-2} \tag{52}$$

Then, using the size effect law parameters obtained by Bažant and Sener (1988), we get from (51) and (52) the following interface properties

$$\tau_s = 31\ \text{MPa}, \quad v_0 = 2.1\ 10^{-2}\ \text{mm}, \quad G_f = 325\ \text{J/m}^2 \tag{53}$$

The value of τ_d has been neglected in these calculations. The optimum fit by the size effect law given by (33) is shown by the dashed curve in Fig. 6a, and the fit based on (49) and (50) with the values in (53) is given by the solid curve. Assuming progressively increasing values $\tau_d = 0, 1, 2, 3$ MPa, one obtains from (49) and (50) the solid curves shown in Fig. 6b, c, d. Unfortunately, the scatter of the data is insufficient to decide which of these curves is more correct. To avoid such ambiguity and obtain better estimates of interface properties, tests of a broader size range (1:10) would be necessary. The required breadth of range is generally proportional to the coefficient variation of the statistical scatter.

It is planned to carry out size effect tests of pullout in which the failure occurs by slip alone (without radial cracks). Then it will be possible to give an example that is more than just an illustration of the procedure.

Conclusions

1. The one-dimensional simplification of the fiber (or bar) pullout problems allows a simple analytical solution yielding closed form expressions for the stress–displacement diagram as well as the size effect.

2. The solution shows that, for geometrically similar situations: (1) the maximum pullout stress decreases with increasing size (characterized for example by the fiber diameter), (2) the post–peak slope of the load–deflection diagram becomes steeper as the size increases, and (3) for a sufficiently large size, snapback failure is obtained.

3. An inevitable consequence of softening in the relation of interfacial shear stress versus slip displacement is localization of the fracture process zone along the interface,

with a gradual approach to interface shear fracture. Due to localization, the distribution of the interface shear stress along the fiber or bar becomes strongly nonuniform, and the nonuniformity gets stronger as the size increases. The localization is the cause of size effect.

4. The solution confirms that the size effect is transitional between the case of elasticity or plasticity, for which there is no size effect, and the case of linear elastic fracture mechanics, for which the difference of the interface strength and the residual stress is inversely proportional to the square root of the size. This transitional size effect can be described by the approximate size effect law proposed by Bažant (1984) or its subsequent generalization with parameter m controlling the shape of the size effect curve.

5. The transitional size effect is shown to depend of the shape of the interface stress-slip law. A declining slope of the stress-slip law leads to a more gradual and more extended transition in the size effect plot.

6. Measurements of the size effect in fiber pullout can be exploited for determining the interface properties.

ACKNOWLEDGMENTS. — Financial support under AFOSR Grant 91-0140 to Northwestern University (monitored by Dr. Jim Chang) is gratefully acknowledged. The general size effect studies were partially supported by Center for Advanced Cement-Based Materials at Northwestern University. The second author (Rodrigue Desmorat) acknowledges the friendly hospitality of the Civil Engineering Department while he was a Visiting Research Assistant at Northwestern University.

References

Bažant, Z.P., and P. G. Gambarova (1980). "Rough cracks in reinforced concrete." *J. Structural Division*, ASCE, Vol. 106, No. ST4, April 1980 pp. 819-842.

Bažant, Z.P. (1984). "Size effect in blunt fracture: concrete, rock, metal." *J. Eng. Mech.*, ASCE, 110 [4] 518-535.

Bažant, Z.P. (1985). "Fracture mechanics and strain-softening of concrete." *Seminar on finite element analysis of reinforced concrete structures*, Tokyo, May 1985, Vol. 1 47-69, (sponsored by Japan Society for the Promotion of Science and U.S. National Science Foundation)

Bažant, Z.P. (1987). "Fracture energy of heterogeneous materials and similitude." *SEM-RILEM International Conference on Fracture of Concrete and Rock*, Houston, Texas, June 1987, ed. S. P. Shah, S. E. Swartz, pp. 390–402.

Bažant, Z.P., and Pfeiffer, P.A. (1987). "Determination of fracture energy from size effect and brittleness number." *ACI Materials Journal*, 84, 463–480.

Bažant, Z.P., and S. Sener (1988). "Size effect in pullout tests" *ACI Materials Journal* 85, 347–351.

Bažant, Z.P., and Kazemi, M.T. (1990). "Determination of fracture energy, process zone length and brittleness number from size effect, with application to rock and concrete." *Int. J. of Fracture*, 44, 111-131.

Bažant, Z.P., and Cedolin, L. (1991). *Stability of Structures: Elastic, Inelastic, Fracture and Damage Theories* (textbook and reference volume), Oxford University Press, New York, 1991.

Bažant, Z. P. (1985). "Comment on Hillerborg's size effect law and fictitious crack model." *Dei Poli Anniversary Volume*, Politecnico di Milano, Italy, ed. by L. Cedolin et al., 335–338.

Bažant, Z.P. (1992). "Scaling laws in mechanics of failure, Report 92-9/457s, Dept. of Civil Engrg., Northwestern University, Evanston, IL.

Beaumond, P.W.R., and Aleszka, J.C. (1978). "Cracking and toughening of concrete and polymer–concrete dispersed with short steel wires." *J. Material Science*, 13, 1749–60.

Bowling, J., and Groves, G.W. (1979). "The debonding and pull–out of ductile wires from a brittle matrix." *J. Material Science*, 14, 431–42.

Divakar, M.P., Fafitis, A., and Shah, S.P. (1987). "Constitutive model for shear transfer in cracked concrete." *J. Structural Division*, ASCE, Vol. 113, No 5, May 1987 pp. 1046-1062.

Feenstra, P.H., de Borst, R., and Rots, J.G. (1991). "Numerical study on crack dila-

tancy." *J. Eng. Mech.* , ASCE, 117 [4] 733-769.

Freund, L.B. (1992). "The axial force needed to slide a circular fiber along a hole in an elastic material and implications for fiber pull-out." *Eur. J. Mech., A/Solids*, 11, No 1, 1-19.

Fuller, Jr., E.R., Butler, E.P., and Carter, W.C. (1991). "Determination of fiber-matrix interfacial properties of importance to ceramic composite toughening." *Proceedings of NATO Advanced Research Workshop on Toughening Mechanisms in Quasi-Brittle Materials*, ed. S. P. Shah, Kluwer Academic Publishers, Dordrecht, Netherlands, 385–404.

Gao, B. Y.-C., Mai, Y.-W., and Cotterell, B. (1988). "Fracture of fiber-reinforced materials." *ZAMP*, Vol. 39., 550–572.

Gray, R.J. (1984a). "Analysis of the effect of embedded fiber length on fiber debonding and pullout from an elastic matrix. Part 1: Review of theories." *J. of Material Science*, 19, 861–70.

Gray, R.J. (1984b). "Analysis of the effect of embedded fiber length on fiber debonding and pullout from an elastic matrix. Part 2: Review of theories." *J. of Material Science*, 19, 1680–91.

Hutchinson, J.W., and Jensen, H.M. (1990). "Models of fiber debonding and pullout in brittle composites with friction." *Mech. Mater.*, 9, 139–63.

Lawrence, P.J. (1972). "Some theoretical considerations of fiber pull-out from an elastic matrix." *J. Mat. Sci.*, 7, 1-6.

Leung, C. K. Y., and Li, V.-C. (1990a). "A new theory for the debonding of discontinuous fibers in an elastic matrix." *Mat. Res. Soc. Proc.*, Vol. 170., pp. 45–53.

Leung, C. K. Y., and Li, V.-C. (1990b). "Applications of a two-way debonding theory to short fibre composites." *Composites*, Vol. 21, No 4., pp. 305–317.

Li, Z., Mobasher, B., and Shah, S.P. (1991) "Characterization of interfacial properties in fiber-reinforced cementitious composites." *J. Am. Ceram. Soc.*, 74 [9] 2156-64.

Shah, S.P., and Ouyang, C. (1991). "Mechanical behavior of fiber-reinforced cement-based composites." *J. Am. Ceram. Soc.*, 74 [11] 2727-38, 2947-53.

Stang, H., Li, Z., and Shah, S.P. (1990). "Pullout problem: stress versus fracture mechanical approach." *J. Eng. Mech.*, ASCE, 116 [10], 2136-50.

Steif, P.S., and Hoysan, S.F. (1986). "On load transfer between imperfectly bonded constituents." *Mechanics of Materials*, 5, 375-382.

Wang, Y., Li, V.-C., and Backer, S. (1988) "Modeling of fibre pull-out from a cement matrix." *Int. J. Cem. Comp. Lightweight Concrete*, Vol. 10, No 3., 143–149.

Figure Captions

Fig. 1 Various assumptions about the interface properties characterized in terms of interface shear stress and relative displacement.

Fig. 2 Geometry of the fiber or bar pullout tests.

Fig. 3 Fracture process zones and zones of residual stress along the fiber for various stages of loading.

Fig. 4 Diagrams of pullout stress versus displacement for tests of similar geometry and different sizes.

Fig. 5(a) Size effect law proposed by Bažant (1984), and (b) comparison of calculated size effect to the general forms of size effect law for quasibrittle fracture.

Fig. 6 Test data for bar pullout, used as an illustrative example, and comparisons with the present solution (solid curves) and with the simple form of the size effect law (dashed curve).

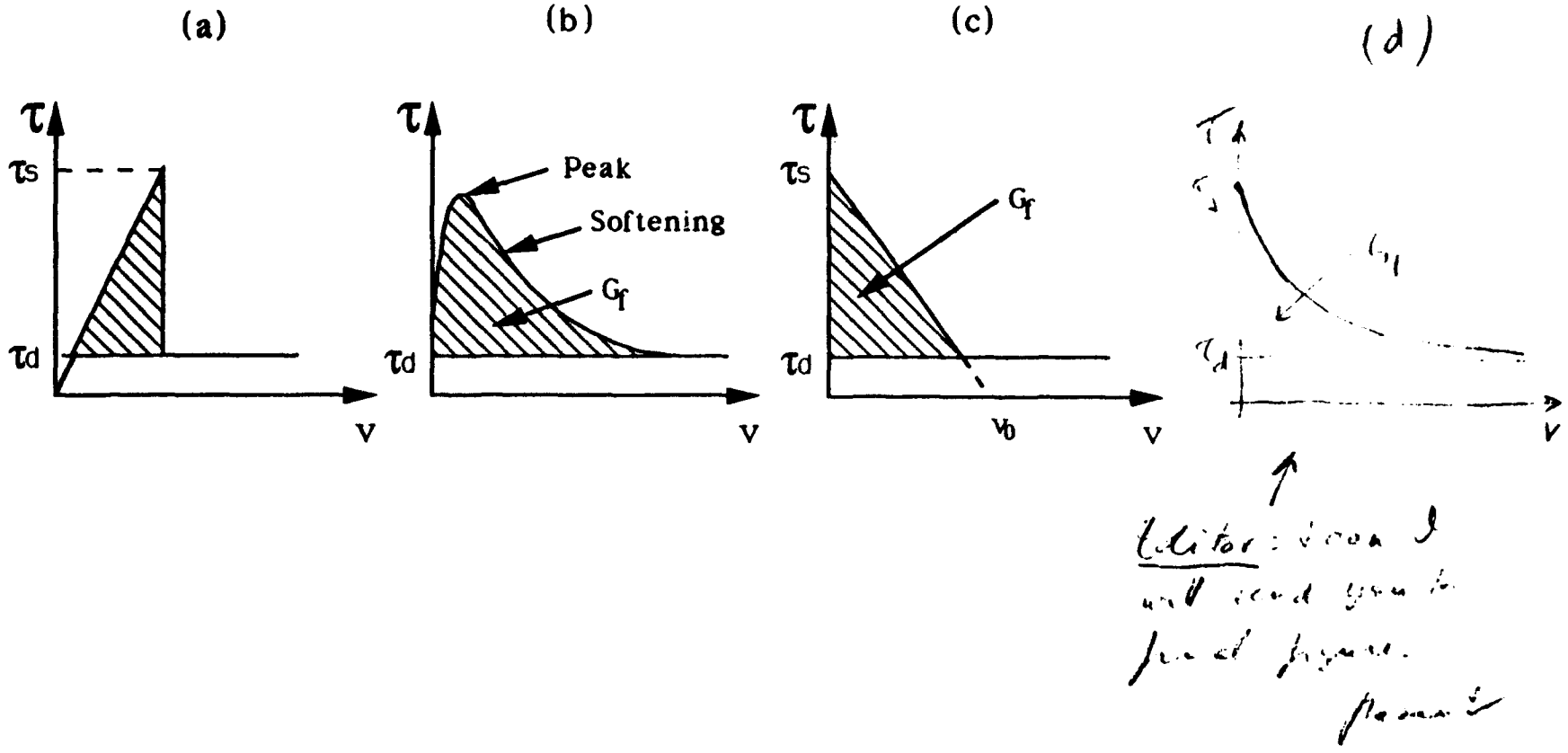

Editor: Soon I will send you the final figure. Please

Figure 1

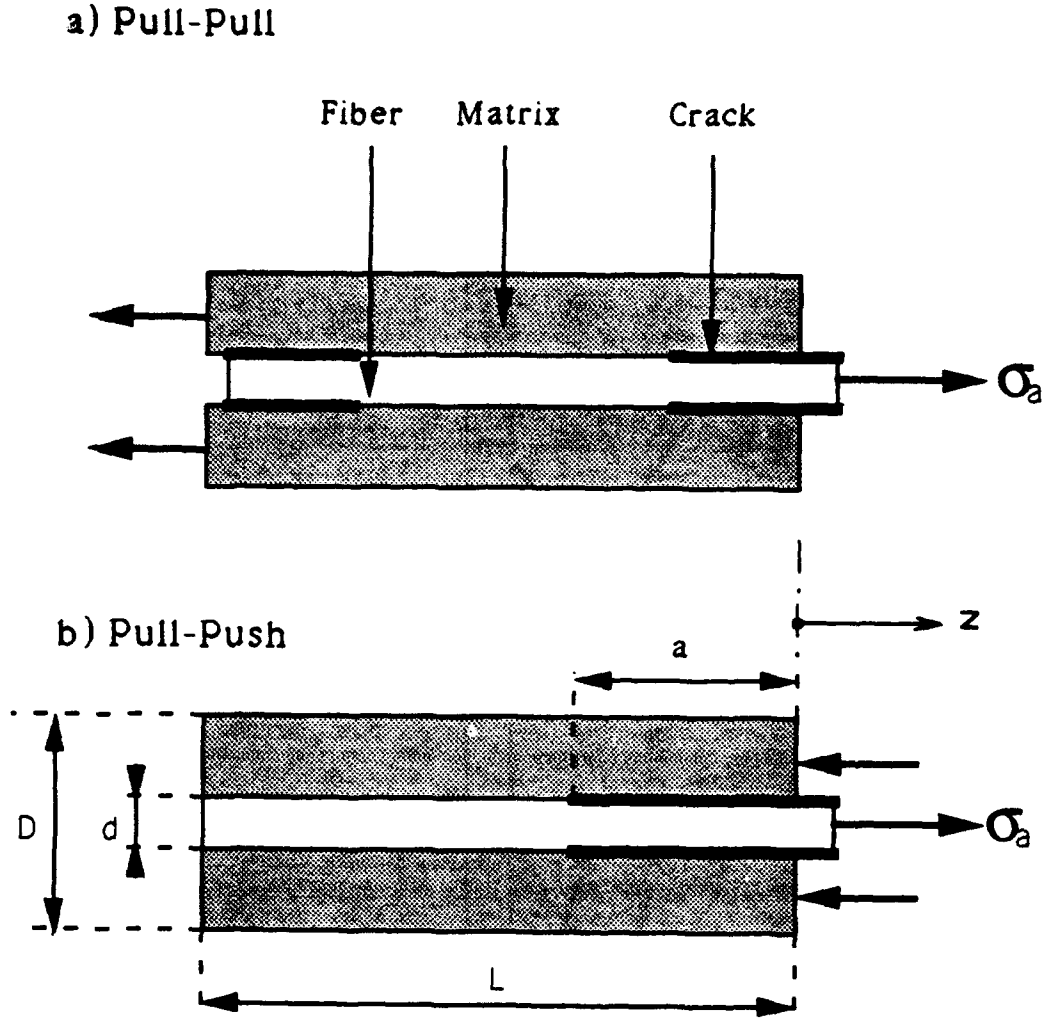
a) Pull-Pull
Fiber
Matrix
Crack
σ_a
b) Pull-Push
z
a
D
d
σ_a
L

Figure 2

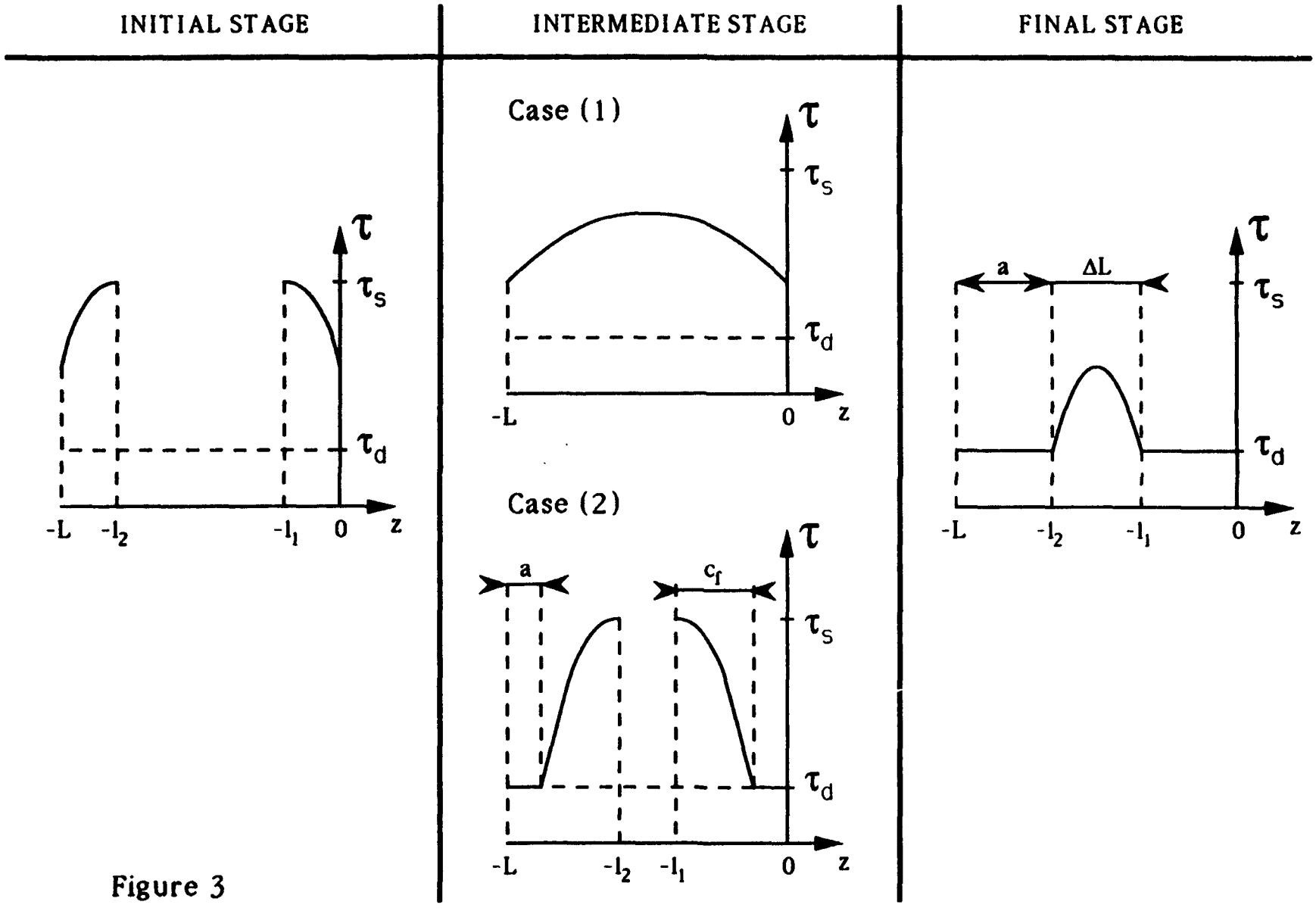
INITIAL STAGE
INTERMEDIATE STAGE
FINAL STAGE
Case (1)
Case (2)
τ
τs
τd
-L
-l2
-l1
0
z
a
ΔL
cf

Figure 3

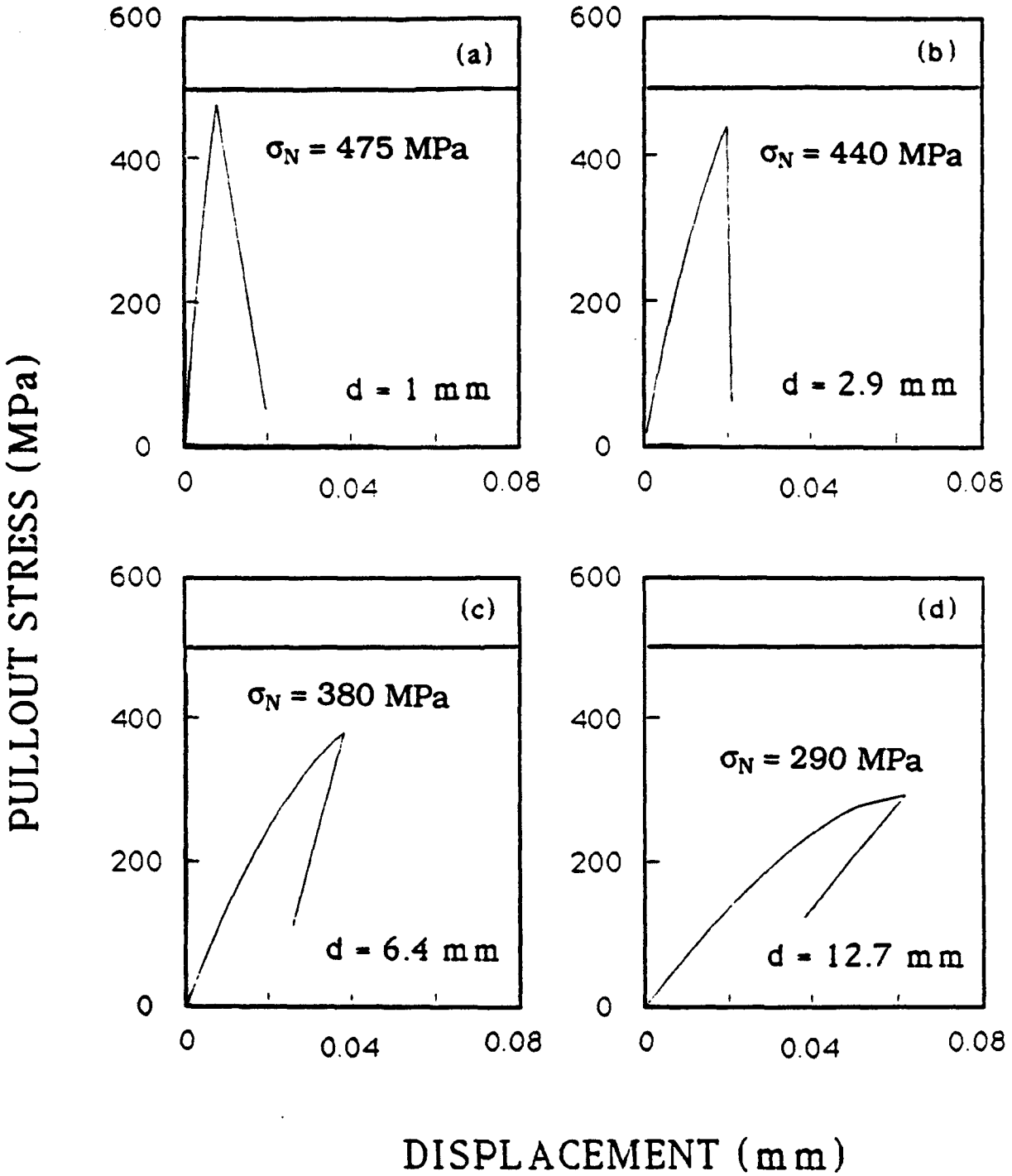
PULLOUT STRESS (MPa)
600
400
200
0
(a)
σ_N = 475 MPa
d = 1 mm
(b)
σ_N = 440 MPa
d = 2.9 mm
(c)
σ_N = 380 MPa
d = 6.4 mm
(d)
σ_N = 290 MPa
d = 12.7 mm
0
0.04
0.08
DISPLACEMENT (mm)

Figure 4

(a)

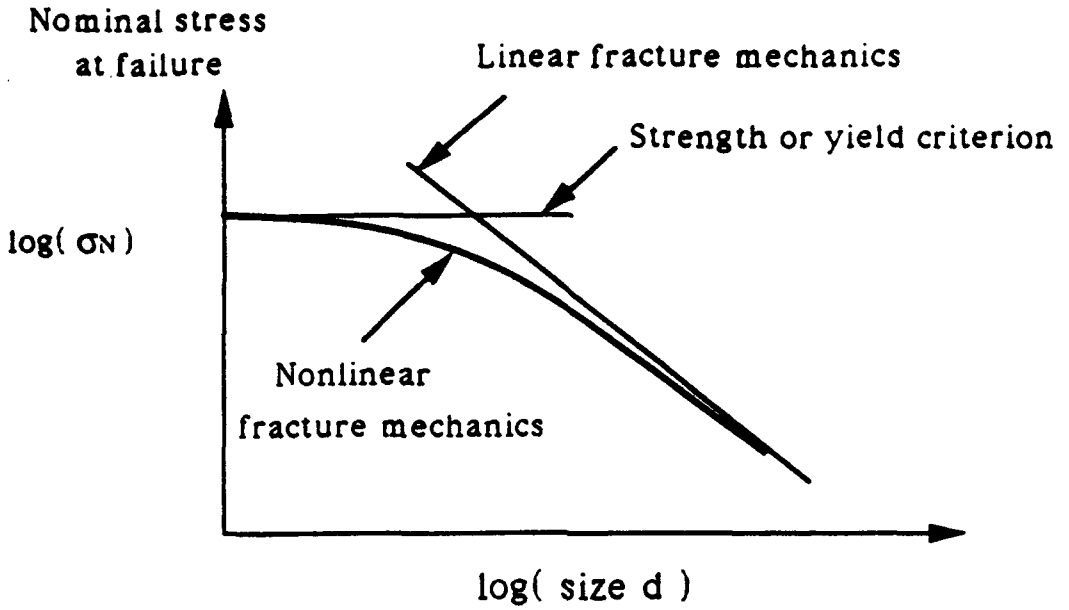
Nominal stress at failure
Linear fracture mechanics
Strength or yield criterion
log(σN)
Nonlinear fracture mechanics
log(size d)

(b)

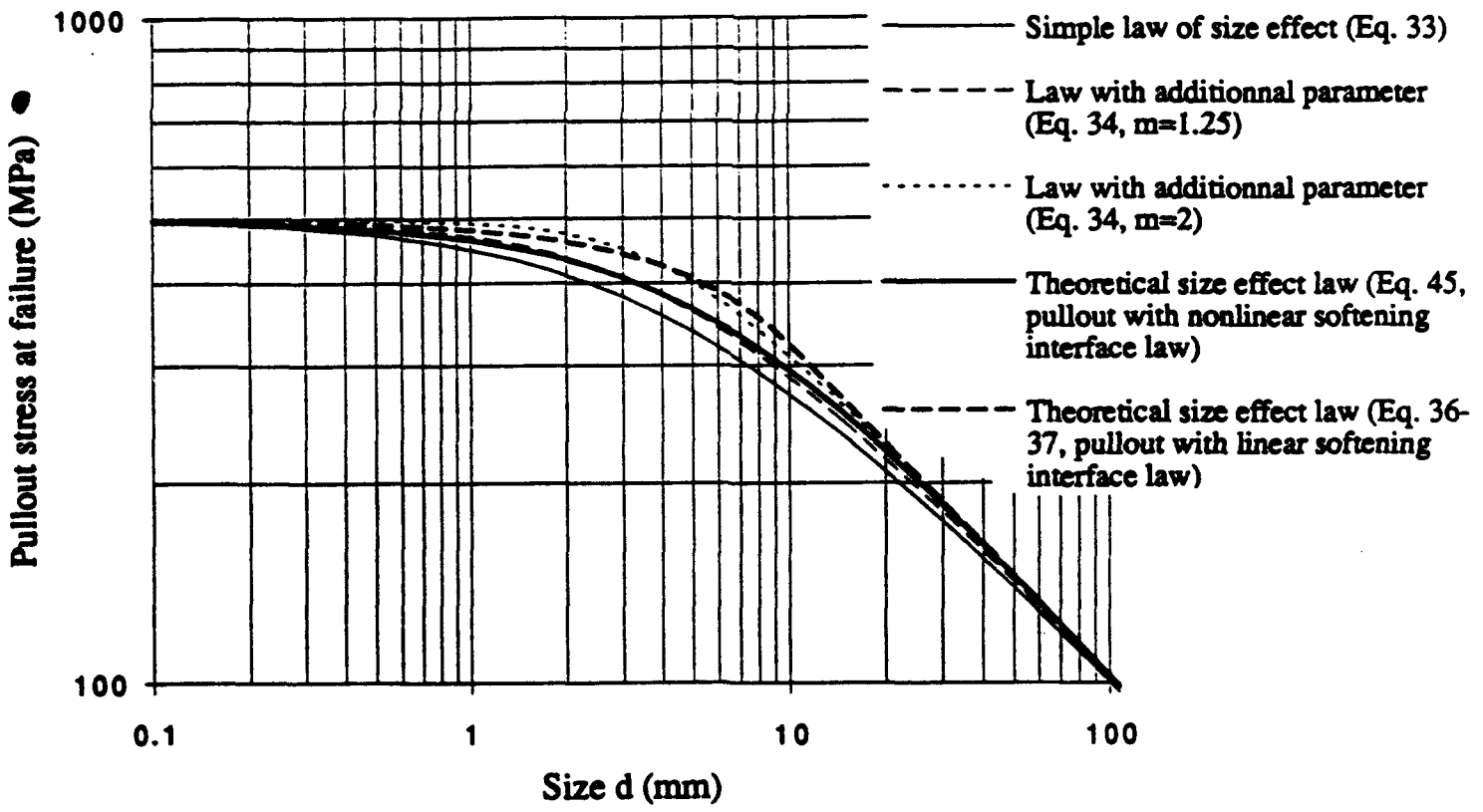
1000
100
0.1
1
10
100
Pullout stress at failure (MPa)
Size d (mm)
Simple law of size effect (Eq. 33)
Law with additionnal parameter (Eq. 34, m=1.25)
Law with additionnal parameter (Eq. 34, m=2)
Theoretical size effect law (Eq. 45, pullout with nonlinear softening interface law)
Theoretical size effect law (Eq. 36-37, pullout with linear softening interface law)

Fig. 5

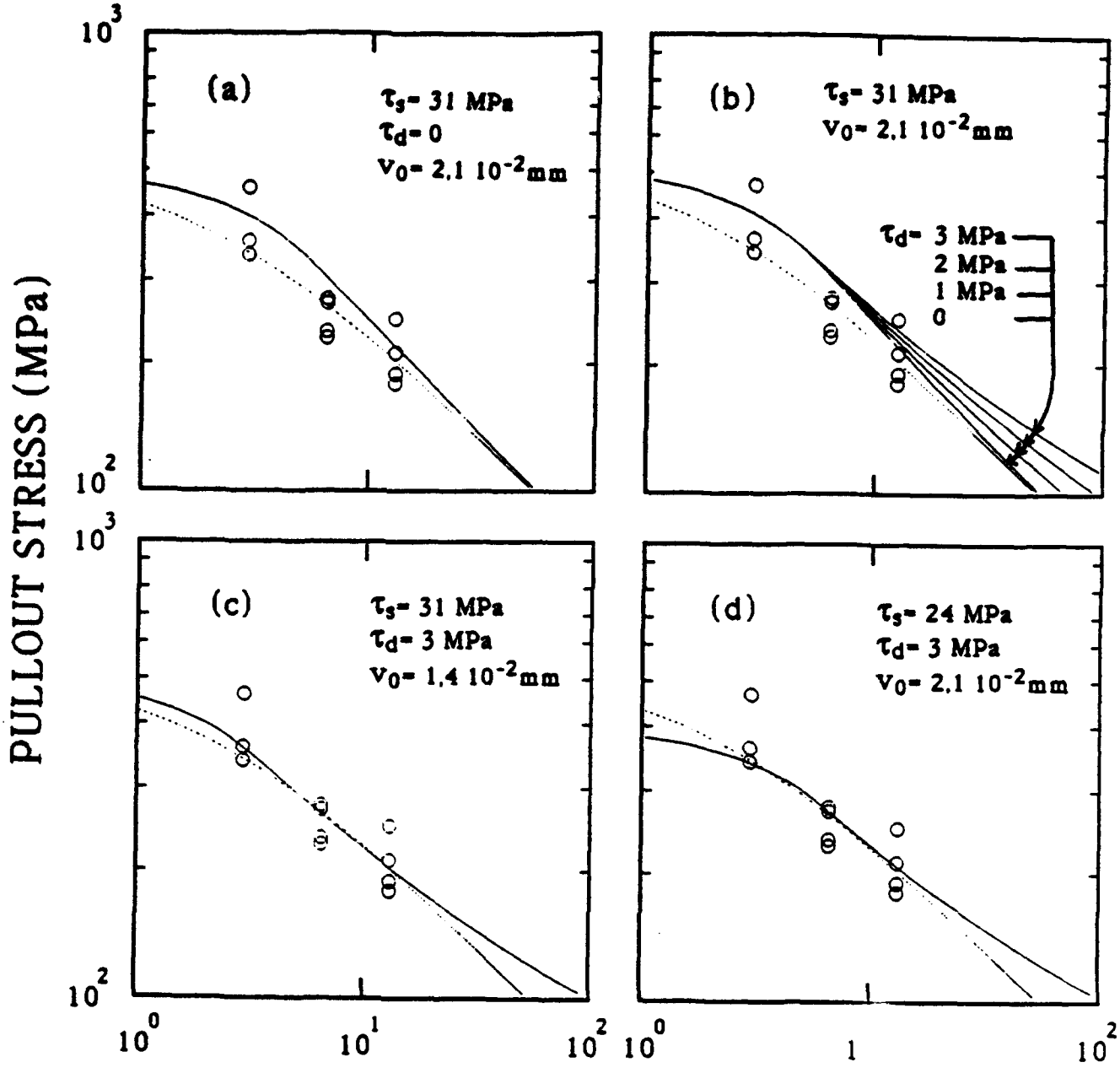
(a)
τ_s= 31 MPa
τ_d= 0
v_0= 2.1 10^{-2}mm
(b)
τ_s= 31 MPa
v_0= 2.1 10^{-2}mm
τ_d= 3 MPa
2 MPa
1 MPa
0
(c)
τ_s= 31 MPa
τ_d= 3 MPa
v_0= 1.4 10^{-2}mm
(d)
τ_s= 24 MPa
τ_d= 3 MPa
v_0= 2.1 10^{-2}mm
PULLOUT STRESS (MPa)
10^3
10^2
10^0
10^1
10^2
1
DIAMETER OF BAR OR FIBER (mm)

Figure 6

Identification of Stress-Slip Law for Fiber or Bar Pullout from Size Effect Tests

ZDENEK P. BAZANT, ZHENGZHI LI AND MICHAEL THOMA

Structuring Engineering Report 94-2/457s
Department of Civil Engineering
Northwestern University
Evanston, Illinois 60208

February 1994

Identification of Stress-Slip Law for Fiber or Bar Pullout from Size Effect Tests

by Zdeněk P. Bažant,[1] Fellow ASCE, Zhengzhi Li[2] and Michael Thoma[3]

ABSTRACT. — Test results on the size effect in pullout strength of reinforcing bars embedded in concrete are presented. Attention is focused on failures due soley to interface slip, with no cracking in the surrounding concrete. This type of failure is achieved by using smooth round bars and a sufficiently large ratio of bar diameter to embedment length. Elimination of cracking in the surrounding concrete makes it possible to study the characteristics of the interfacial shear fracture between steel and concrete. The results of tests of geometrically similar specimens show that interfacial shear fracture causes a size effect on the nominal strength in pullout. The size effect is found to be transitional between plastic failure (the current approach of concrete design codes, for which there is no size effect) and linear elastic fracture mechanics (for which the size effect is the maximum possible). This transitional size effect can be approximately described by the size effect law proposed by Bažant for quasibrittle failures in general. By fitting a theoretical formula obtained in the previous study to the size effect data, the basic material characteristics of the stress-slip law for interface fracture are determined. These include the interfacial fracture energy, the shear bond strength (debonding shear stress), the residual frictional shear stress, and the length of the shear fracture process zone. The same method could be used for identifying the interfacial fracture characteristics of other materials, e.g., fibers in composites.

1 Introduction

The problem of pullout of reinforcing bars from concrete or fibers from the matrix of a composite material has been studied intensely and many significant results have already been achieved. Two concepts have been used as the criterion of pullout failure: (1) The interface shear strength criterion (Lawrence, 1972; Takaru and Arridge, 1973; Yue and Cheung, 1992a, 1992b; and Hsueh, 1991a, 1991b, 1990a, 1990b); and (2) the fracture

[1]Walter P. Murphy Professor of Civil Engineering and Materials Science, Northwestern University, Evanston, IL 60208 U.S.A.

[2]Graduate Research Assistant, Northwestern University

[3]Visiting Research Assistant, Northwestern University; on leave from Lehrstuhl für Mechanik, Technische Münich, Germany

mechanics criterion of critical energy release rate (Guerney and Hunt, 1967; Outwater and Murphy, 1969; and Stang and Shah, 1986), which was in some works combined with the consideration of friction between the debonded fiber and the matrix (Gao et al., 1988; and Hutchinson and Jensen, 1990).

More realistic is a generalized fracture mechanics appraoch which combines both concepts. It is based on a relation of the interfacial shear stress τ_s (bond stress) to the interfacial slip, in short, the stress-slip law. This law involves the strength limit as well as the fracture energy. It may involve a rising linear part simulating the elastic shear deformation of a thin layer of matrix adjacent to the interface.

The stress-slip law is characterized by post-peak softening, which is sometimes considered as a sudden stress drop but is more realistically modeled as a progressive softening. Because of the softening, the interfacial slip represents shear fracture. Normally the stress-slip law possesses residual shear strength, τ_f, which can be regarded as friction (the dynamic friction). From the fracture mechanics viewpoint, the area under the stress-slip curve and above the friction limit represents the shear fracture energy of the interface, G_f, which is a basic interface property. The values of the shear strength, fracture energy and frictional stress can in general depend on the confining pressure from the surrounding matrix (the normal stress across the interface).

While the stress-slip law for the interface is a basic material characteristic, it is difficult to measure it directly. It must be deduced indirectly from some other types of observations. In a preceeding study (Bažant and Desmorat, 1994), it was shown that the stress-slip law can be identified from measurements of the size effect on the pullout strength when geometrically similar specimens of different sizes are tested. A simplified method of identification was proposed and illustrated by a numerical example, but practical application has not been given for lack of test data. The objective of the present paper is to report tests of size effect in pullout and identify from them the stress-slip law for the steel-concrete interface.

The identification problem requires a sufficiently simple solution, which is preferably in a closed form and is such that it can be inverted. Such a simple solution has been obtained in a preceeding study (Bažant and Desmorat, 1994), in which the pullout problem was simplified as one-dimensional, with the matrix represented as an elastic bar or tube surrounding the pulled bar or fiber. Although the one-dimensional simplification is no doubt too crude for some purposes, it is no worse than the assumption of elastic Winkler foundation as a replacement of an elastic half space. Of course, the equivalent elastic

stiffness of the surrounding bar that models the matrix must be properly determined, either by a more sophisticated analysis or by tests.

It is now well understood that softening material properties always engender size effect. Normally the size effect in pullout failures arises from two sources: (1) The fracturing of the matrix surrounding the fiber or bar, and (2) the softening in the stress-slip law, as already described. Obviously, to determine the stress-slip law, one must conceive a special type of pullout test in which there is no fracturing in the matrix, only the slip in the interface. This is the basic idea of the present experiments. As will be seen, pullout failure of reinforcing bars due to exclusively to interface slip can be obtained if a smooth round bar (without any lugs) is used and the embedment length of the bar or fiber is sufficiently short.

It may be noted that the pullout failures of reinforcing bars in concrete or fibers in composites exhibit some different characteristics. However, these differences are due mainly to the fracturing of the matrix surrounding the bar or fiber (for example the fracture induced by lugs on the reinforcing bars in concrete). These differences are probably small if the failure is due to the interfacial slip alone, which is the case here. Anyway, because the pullout problem is simplified as one-dimensional, it is impossible to make a distinction between fibers and bars (except in terms of the effective values of the material interface parameters).

2 Test of Pullout Due to Interfacial Slip Alone

The specimens tested, shown in Fig. 1, were concrete cubes of sides $L = 1.5, 3, 6$ and 12 in. (38.1, 76.2, 154.4 and 304.8 mm), in which steel bars of diameters $D = 0.125, 0.25, 0.5$ and 1 in. were embedded. In this manner, perfect geometric similarity of the specimens of different sizes was preserved. The bars were smooth, in order to achieve that the pullout failure be caused solely by interfacial slip, with no fracturing in the surrounding concrete. This mode of failure was borne out by the tests. It may be noted that the round smooth rods were slightly rusty at the time of casting, however, this condition is not undesirable since some rusting is normally present in practice. Based on the expected average bond strength (Naaman, 1991), the bar size was chosen so that yielding of the steel could not occur before the pullout failure of the interface, and this was also borne out by the tests. The part of the steel bars that was sticking out of the concrete cube was 10 in. long for each size.

The cubes were made of concrete of standard cylindrical strength $f'_c = 7,290$ psi

(50.26 MPa) for normally cured specimens and f'_c = 5,220 psi (36.0 MPa) for the concrete cured in an accelerated manner (tested on cylinders of diameter 3 in. or 76.2 mm, at the time of the tests). The Young's elastic modulus of concrete was 4.31 $\times 10^6$ psi (29.7 GPa), determined as the mean initial stress-strain slope from a set of the standard cylindrical compression tests for the same batch of concrete. The Young's modulus of the steel bars was 30.5 $\times 10^6$ psi (210.0 GPa). For both sets, the companion cylinders for the test of strength had the same curing history. In the concrete mix, the ratio water:cement:sand:gravel was 0.6:1:2:2, by weight. The aggregate consisted of granite, quartz etc. gravel and quartz sand of maximum grain sizes 3/8 in. (9.6 mm) and 0.132 in. (3.35 mm) respectively. Both were washed and air dried for 40 or 48 hours prior to mixing. Portland cement of ASTM type I, without any admixtures, was used. Two sets of specimens of all sizes, each from one batch of concrete, were cast in wooden moulds (Fig. 1a). The steel bars were vertical during casting. The specimens were unmoulded one day after casting. The first set of specimens was then stored in a fog room at nearly 100% relative humidity and 20° C temperature for 28 days, and then tested. The second set of specimens was cured in water for seven days at 50° C, so as to achieve accelerated curing. In the second set of specimens cured in water, the largest cube of 12 in. side was omitted because of the limited size of the heated chamber. Despite the lower strength of the specimens cured in accelerated manner, the bond strength was about the same as for the specimens cured in the standard manner.

The specimens were tested immediately after the curing. So the specimen bulk was still wet during the test, and thus no microcracking due to drying could have occurred in the specimens. All the specimens were tested in a 20 kip (89.0 kN) closed-loop controlled MTS testing machine. All the tests were displacement controlled. The displacement rate was kept constant during each test and was chosen so that the maximum load for the specimens of each size would occur in about 10 min. (for the 6 in. cubes the displacement rate was 0.003 in./min. or 0.076 mm/min.; for the 12 in. cubes it was slightly higher, and for the 1.5 in. cubes it was slightly smaller). The strain of the steel bar outside the cube was recorded by a MTS extensometer. The displacement was measured on the steel bar as close to the face of the cube as possible, that is, right above the steel plate providing the reaction (Fig. 1b).

3 Test Results and Size Effect Observed

All the specimens of both series failed by pure interfacial slip, in contrast to the previous pullout tests of Bažant and Sener (1988). No visible cracking occurred in the concrete cubes, this means that the objective of avoiding the fracturing of concrete around the bars has been achieved and the observed post-peak softening and size effect must be attributed strictly to the interface fracture. Some typical load-deflection diagrams observed are shown in Fig 3 (the initial increase of the slope is due to the gradual seating of the reaction plate). As seen in Fig. 3, the larger the specimen, the steeper the post-peak descent. This property is characteristic of all structures undergoing damage localization.

The test results for standard and accelerated curing are shown in Table 1. It was intended to test four specimens for each size in each set, however, a few tests did not work out.

Dividing the maximum load by the embedded steel surface area, one obtains the average shear bond strength, which is taken as σ_N. Its value for the present tests ranged from 189 to 429 psi (1.30 to 2.96 MPa), for both sets of specimens. It may be noted that this value is considerably smaller than that predicted by the formulas of Orangun et al. (1977) or ACI (1983). However, these formulas are not intended for smooth bars, but for deformed bars whose failure causes severe cracking of concrete.

Because the load-deflection diagram exhibits post-peak softening, and the softening is not caused by geometrically nonlinear effects of buckling, one must expect a size effect which is approximately described by the size effect law (Bažant, 1984, 1991):

$$\sigma_N - \sigma_0 = B f_t'(1+\beta)^{-1/2} \tag{1}$$

in which $\beta = D/D_0$ = relative size, D = characteristic size taken as the bar_diameter, σ_0 = residual frictional strength, f_t' = direct tensile strength of concrete (introduced solely for convenience); and B, D_0 = two constants to be determined by regression of test data. The direct tensile strength was estimated from the ACI formula $f_t' = 6\sqrt{f_c'}$ (where both f_c' and f_t' are in psi). The residual frictional strength is determined from the final plateau of the load-displacement diagram, as the final load value divided by the interface area. From the present tests, $\sigma_0 = 3,310$ psi (22.8 MPa).

As shown before, (Bažant, 1990) (1) can be converted to a linear regression plot $Y = AX + C$in which

$$Y = f_c'^{n}(\sigma_N - \sigma_0)^{-2}, \quad X = D \tag{2}$$

The measured data are shown as the circled points in the plot of Y versus X in Fig. 5a for the set of specimens cured in the standard manner and in Fig. 5b for the set of specimens cured in an accelerated manner. The regression lines $Y = AX + C$ are also shown in these plots. The constants of the size effect law (1) can then be obtained as $B = C^{-1/2}$ and $D_0 = C/A$, in which A is the slope of the regression line and C is the vertical intercept. In this manner, it has been found that $B = 2.18$ and $D_0 = 0.297$ in. (7.54 mm) for the case of standard curing, and $B = 3.05$ and $D_0 = 0.198$ in. (5.03 mm) for the case of accelerated curing. The size effect plots corresponding to these parameters are shown as the curves in Fig. 4a,b. The curve of the size effect represents a gradual transition from a horizontal asymptote representing the strength criterion to an asymptote of slope -0.5, representing the size effect of linear elastic fracture mechanics.

The scatter of the test data in Fig. 4 and 5 is quite large. However, large scatter has generally been typical of bond strength measurements in the past. Despite the large scatter, it is clear that the size effect is present and that the mean slope of the size effect plot in Fig. 4 is intermediate between the strength criterion and the linear elastic fracture mechanics, as expected. It cannot be claimed that the test results validate the use of the size effect law, however, they are not in disagreement with this law.

4 Identification of Interface Characteristics from Size Effect

In a previous study, Bažant and Desmorat (1994), assumed that the stress-slip law, that is, the relationship of the shear stress τ at the interface to the relative slip v at the interface, has the form shown in Fig. 6. The softening is considered to be linear, starting from the shear bond strength τ_d, and there is a terminal shear stress τ_f, representing friction. The area under the softening diagram above the frictional plateau (cross-hatched in Fig. 6) represents the interfacial fracture energy G_f per unit area of the interface. Its value determines the softening slope in Fig. 1a.

In the previous analysis the interaction of the reinforcing bar (or fiber) with the surrounding matrix was simplified as a one-dimensional problem. This means that the concrete surrounding the steel bar is treated as a bar in which the cross sections remain plain. Under this simplification, it was possible to obtain for the size effect an analytical solution that was sufficiently simple for the purposes of identification of interface material characteristics τ_d, τ_f and G_f. It was possible to solve these characteristics explicitly in terms of the parameters of the size effect law (1).

Two cases had to be distinguished in the previous solution: (1) The interface slip

cracks join before τ_f is reached (Fig. 7, left), and the (2) τ_f is reached before the cracks join (Fig. 7, right). The following equations have been obtained for these two cases:

$$\sigma_{dm}^{I} = \frac{8\tau_d}{\omega D}\sin\frac{\omega L}{2} \quad \text{for} \quad \omega L \leq 2\arccos\frac{\tau_f}{\tau_d} \tag{3}$$

$$\sigma_{dm}^{II} = \frac{8\tau_d}{\omega D}\sqrt{1-\frac{\tau_f^2}{\tau_d^2}} + \frac{4\tau_f}{\omega D}\left(\omega L - 2\arccos\frac{\tau_f}{\tau_d}\right) \quad \text{for} \quad \omega L > 2\arccos\frac{\tau_f}{\tau_d} \tag{4}$$

The superscripts I and II label the first and second cases; σ_{dm} is the maximum axial stress in the bar; $\omega^2 = 4(1+\phi)\tau_d/E_f v_0 D$ with $\phi = A_f E_f/A_m E_m$ where $A_f = \pi D^2/4, A_m = \pi(d^2 - D^2)/4$; v_0 is the critical slip shown in Fig. 6; D = reinforcing bar diameter; and d = outer diameter of the effective cross section area of the concrete (matrix) surrounding the steel bar.

When geometrically similar specimens are considered, L/D and d/D are constants. From Eqs. (3) and (4) one can plot the size effect curve of $\log\sigma_{dm}$ versus $\log D$. This curve has the same asymptotes as the size effect law (1) plotted in (4). By matching these asymptotes to the horizontal and inclined asymptotes of the size effect law (1), it has been shown that

$$\tau_d = \frac{D}{4L}Bf_c' + \tau_f \tag{5}$$

$$v_0 = \frac{1+\phi}{2}\frac{(Bf_c')^2}{\tau_d E_f}D_0\left(\sqrt{1-\frac{\tau_f^2}{\tau_d^2}} - \frac{\tau_f}{\tau_d}\arccos\frac{\tau_f}{\tau_d}\right)^{-2} \tag{6}$$

These equations make it possible to determine the values of the interface fracture characteristics. However, before these equations are evaluated, one must determine the residual frictional shear stress, which is simply given by

$$\tau_f = \frac{D}{4L}\sigma_0 \tag{7}$$

The interfacial fracture energy can then be calculated as

$$G_i = \frac{v_0}{2}\tau_d\left(1-\frac{\tau_f}{\tau_d}\right)^2 \tag{8}$$

Eqs. (6)–(8) have been applied to the size effect parameters obtained from the present test results. The resulting values of the interface fracture characteristics for the specimens cured in standard manner and in accelerated manner are listed in Table 2. The values of the debonding stress τ_d (interface shear strength) and the residual frictional shear stress

τ_f are similar for both methods of curing, however, the interfacial fracture energies are quite different and the post-peak softening is steeper for the accelerated curing tests.

The present test data, however, are too limited and their scatter is too high for determining the precise shape of the stress-slip law for the steel-concrete interface. The softening curve of the stress-slip law may of course be a smooth curve and may be more complicated than that in Fig. 6. The characteristics of the stress-slip law in Fig. 6 that have been identified from the test data should be regarded as merely approximate.

5 Conclusions

1. Slip and shear fracture at the steel-concrete interface engender a size effect on the nominal strength of structure, even if no fracture takes place in concrete. This implies that the interfacial stress-slip curve must exhibit post-peak softening.

2. The size effect caused by interface slip is transitional between plastic limit analysis and linear elastic fracture mechanics and is in agreement with the general size effect law proposed by Bažant (1984) on the basis of energy release analysis or dimensional analysis with similitude arguments.

3. The interface fracture characteristics, including the interface fracture energy, interface shear bond strength and a residual frictional strength, can be identified from the results of tests of the size effect in bar pullout from geometrically similar specimens of different sizes.

4. To be able to identify the interfacial shear fracture characteristics from the size effect tests, it is necessary to design the tests in such a manner that the failure is due exclusively to interfacial slip, with no cracking in the surrounding concrete. In the case of reinforced concrete, this can be achieved by using smooth round bars (with no lugs) of a sufficiently large rate of bar diameter to embedment length for interface slip analysis.

ACKNOWLEDGEMENT. — Partial financial support under AFOSR grant 91-0140 to Northwestern University is gratefully acknowledged. Further support for the conduct of experiments was also obtained from the Center of Advanced Cement-Based Materials at Northwestern University.

References

ACI Committee 318 (1983). "Building Code Requirements for Reinforced Concrete." Am. Concrete Institute, Detroit, MI.

Bažant, Z.P. and Desmorat, R. (1994). "Size effect in fiber or bar pullout with interface fracture and softening slip." *J. of Engineering Mechanics*, ASCE, in press.

Bažant, Z.P., and Cedolin, L. (1991). *Stability of Structures: Elastic, Inelastic, Fracture and Damage Theories*, Oxford University Press, New York.

Bažant, Z.P. (1990). "Size effect method for determining fracture energy and process zone of concrete" (RILEM Recommendation). *Materials and Structures* (RILEM, Paris) 23, 461–465 (submitted by RILEM Committee TC 89-FMT).

Bažant, Z. P., and Sener, S. (1988). "Size effect in pullout tests." *ACI Materials Journal* 85, 347–351.

Bažant, Z.P. (1984). "Size effect in blunt fracture: concrete, rock, metal." *J. of Engineering Mechanics*, ASCE, 110(4), 518-535.

Gao, Y.-C., Mai, Y.-W., and Cotterell, B. (1988). "Fracture of fiber-reinforced materials." *J. of Applied Mathematics and Physics*, 39, 550–572.

Guerney, C., and Hunt, J. (1967). "Quasi-static crack propagation." *Proceedings of the Royal Society of London*, series A, vol. 299, 508–524.

Hsueh, C.-H. (1991a). "Interfacial debonding and fiber pullout stresses of fiber reinforced composites, IV: Sliding due to residual stresses." *Materials Science and Engrg.*, A145, 143–150.

Hsueh, C.-H. (1991b). "Interfacial debonding and fiber pullout stresses of fiber reinforced composites, III: With residual radial and axial stresses." *Materials Science and Engrg.*, A145, 135–142.

Hsueh, C.-H. (1990a). "Interfacial debonding and fiber pullout stresses of fiber reinforced composites, II: Nonconstant interfacial bond strength." *Materials Science and Engrg.*, A125(5), 67–73.

Hsueh, C.-H. (1990b). "Interfacial debonding and fiber pullout stresses of fiber reinforced

composites." *Materials Science and Engrg.*, A123, 1–11.

Hutchinson, J.W., and Jensen, H.M. (1990). "Models of fiber debonding and pullout in brittle composites with friction." *Mechanics of Materials*, 9, 139–163.

Lawrence, P.J. (1972). "Some theoretical considerations of fiber pull-out from an elastic matrix." *J. of Materials Science*, 7, 1–7.

Naaman, A.E., and Najm, H.S. (1991). "Bond-slip mechanism of steel fibers in concrete." *ACI Materials Journal*, 88(2), 135–144.

Orangun, C.O., Jirsa, J.O., and Breen, J.E. (1977). "A reevaluation of test data on development length and splices." *ACI Journal*, March, 114–122.

Outwater, J.P., Murphy, M.C. (1969). "On the fracture energy of unidirectional laminate." *Proceedings, 24th Annual Thechnical Conference of Reinforced Plastics/Composite Division*, The Society of the Plastics Industry, Inc., New York, paper No. 11c.

Stang, H., and Shah, S.P. (1986). "Failure of fiber-reinforced composites by pullout fracture." *J. of Materials Science*, 953–957.

Takaku, A., and Arridge, R.G.C. (1973). "The effect of interfacial radial and shear stress on fiber pullout in composite materials." *J. of Physics*, D, applied physics, 6, 2038–2047.

Yue, C.Y., and Cheung, W.L. (1992a). "Interfacial properties of fibrous composites: Model for the debonding and pullout process." *J. of Materials Science*, 27, 3173–3180.

Yue, C.Y., and Cheung, W.L. (1992b). "Interfacial properties of fibrous composites. Determination of interfacial shear strength, interfacial coefficient of friction and the shrinkage of the fiber." *J. of Materials Science*, 27, 3181–3191.

Table 1: Test Results for Standard and Accelerated Curing Specimens

Standard Curing				Accelerated Curing			
Diam. D (in)	Cube Side (in)	Max. Load (lb)	σ_{dm} (psi)	Diam. D (in)	Cube Side (in)	Max. Load (lb)	σ_{dm} (psi)
1.5	1/8	253	16297	1.5	1/8	230	18742
1.5	1/8	171	18229	1.5	1/8	175	14260
1.5	1/8	224	13957	1.5	1/8	201	16379
1.5	1/8	200	20616	3	1/4	613	12488
3	1/4	561	11429	3	1/4	588	11979
6	1/2	3605	18360	3	1/4	859	17499
6	1/2	3500	17825	3	1/4	763	15544
6	1/2	2700	13751	6	1/2	1781	9070
12	1	10300	13114	6	1/2	3750	19098
12	1	8009	10117	6	1/2	2249	11454
12	1	7754	9872	6	1/2	3247	16537

Table 2: Fracture Characteristics Identified from Tests

	28-day standard curing	accelerated curing
τ_f	68.9 psi (0.47 MPa)	87.1 psi (0.59 MPa)
τ_d	400.3 psi (2.76 MPa)	429.3 psi (2.96 MPa)
v_0	2.9×10^{-3} in. (75.4×10^{-3} mm)	1.4×10^{-3} in. (35.6×10^{-3} mm)
G_i	72 J/m^2	34 J/m^2

Figure 1: (a) Geometry of pullout tests specimens, (b) loading frame and test arrangement.

Figure 2: Set of test specimens of various sizes (before testing) and of the test setup for the 6 in. specimen.

Figure 3: Typical load deflection diagrams for specimens of various sizes (for standard curing and for accelerated curing).

Figure 4: Size effect plots of the test results in double logarithmic scales and their optimum fit by the size effect law; (a) for standard curing, (b) for accelerated curing.

Figure 5: Linear regressions of the test data according to the size effect law; (a) for standard curing, and (b) for accelerated curing.

Figure 6: Stress-slip law for the steel-concrete interface.

Figure 7: Two types of interface shear stress distribution at maximum load.

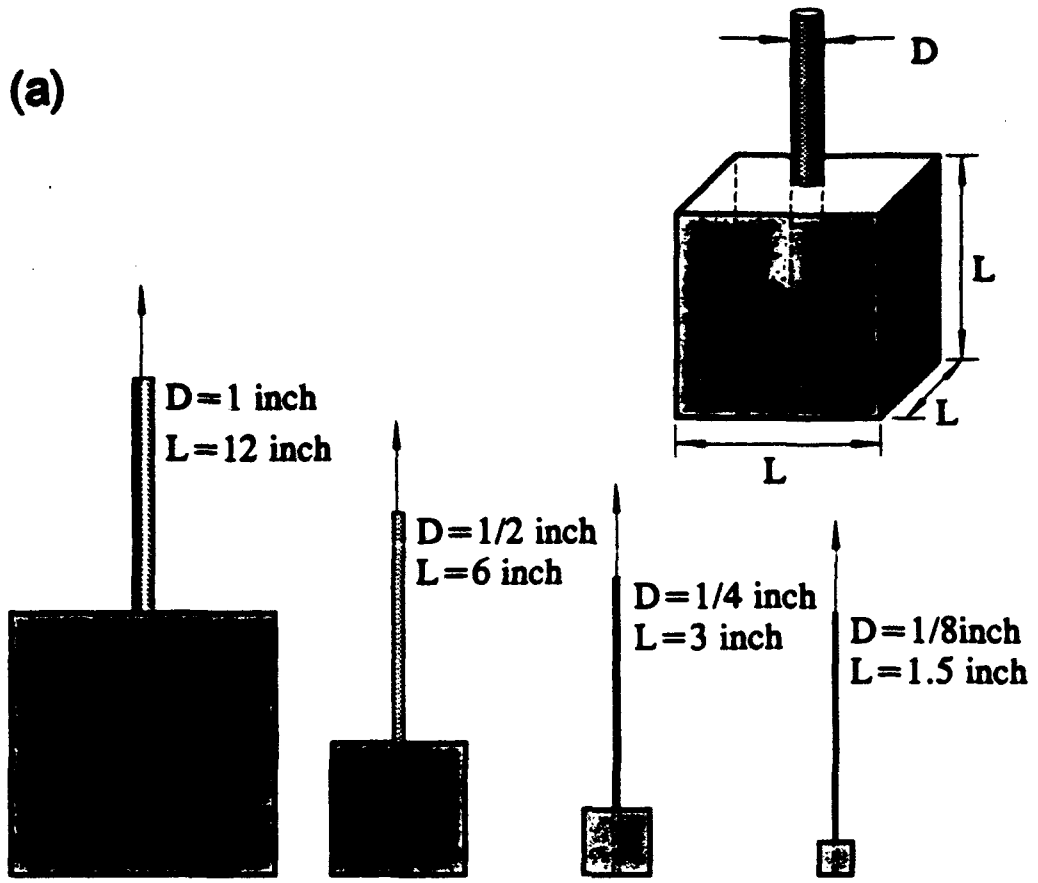
(a)
D
L
L
L
D=1 inch
L=12 inch
D=1/2 inch
L=6 inch
D=1/4 inch
L=3 inch
D=1/8inch
L=1.5 inch

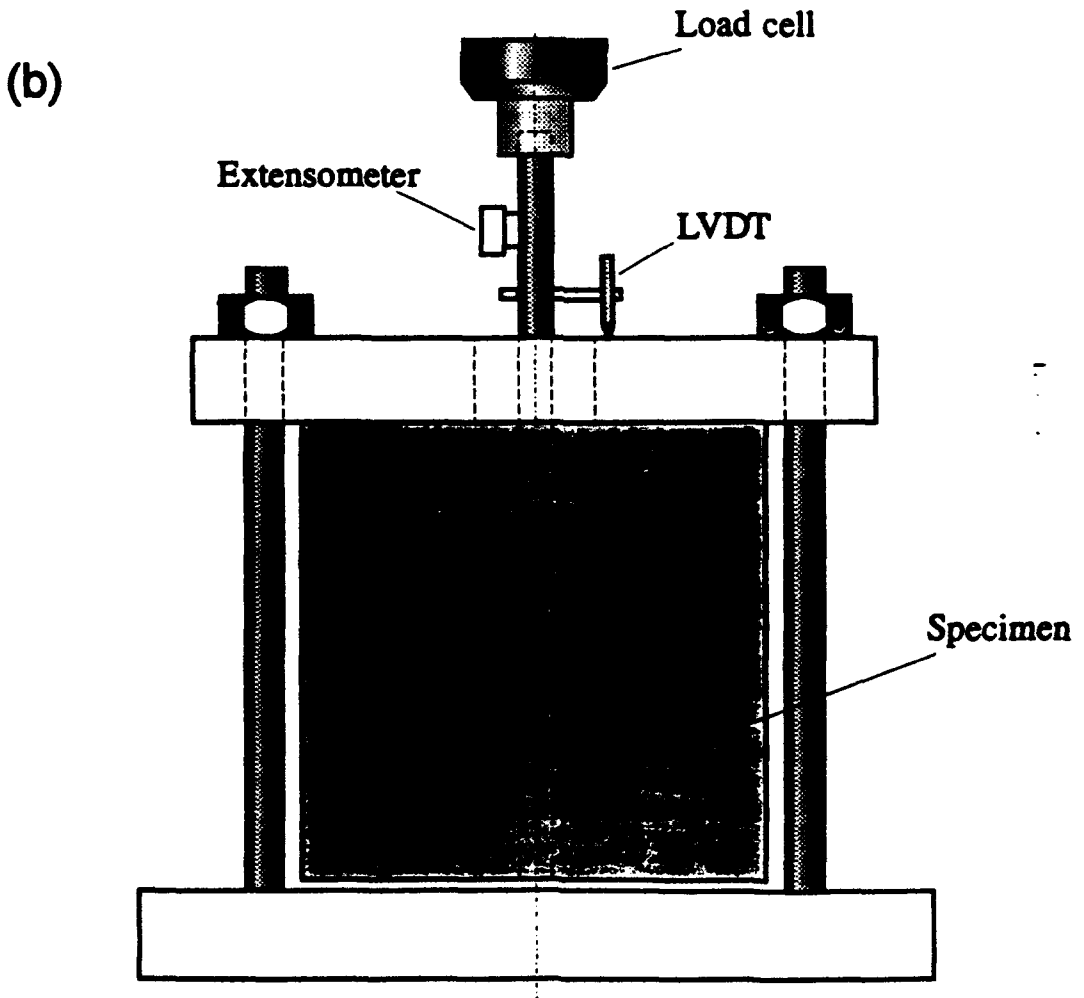
(b)
Load cell
Extensometer
LVDT
Specimen

Fig. 1

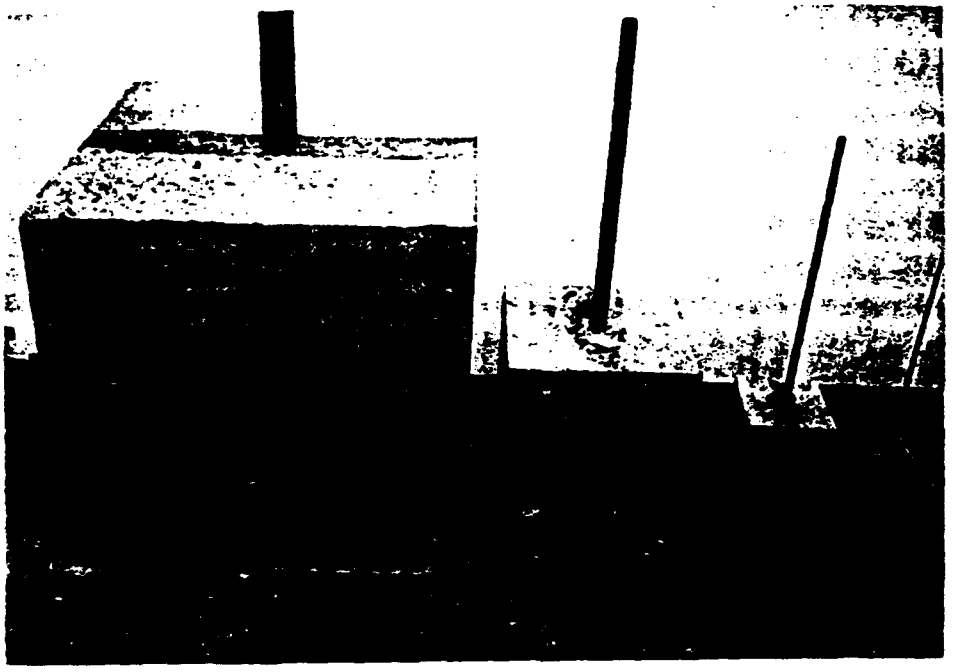

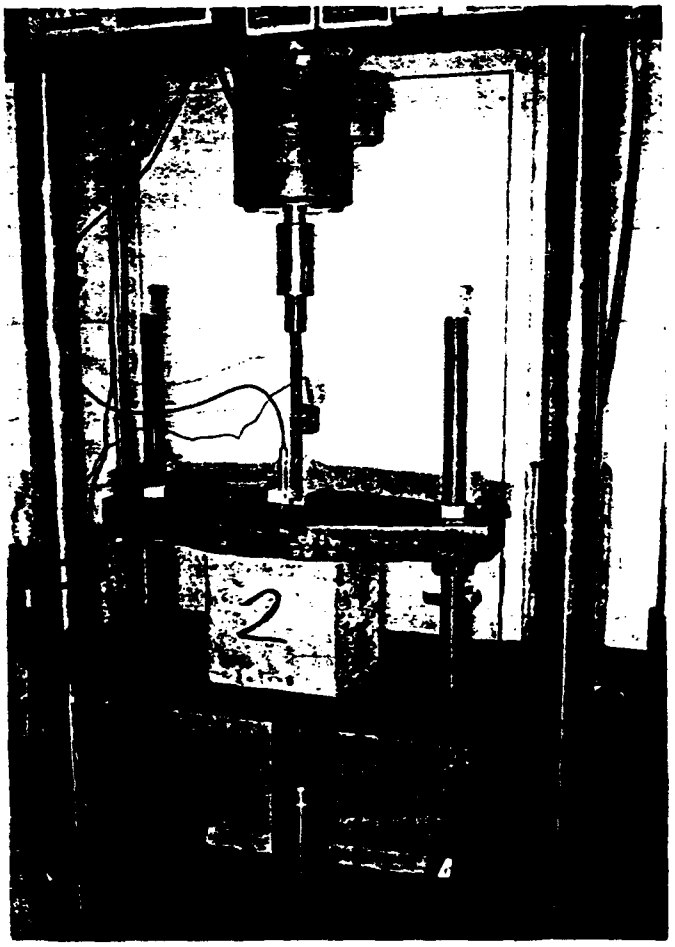

Fig. 2

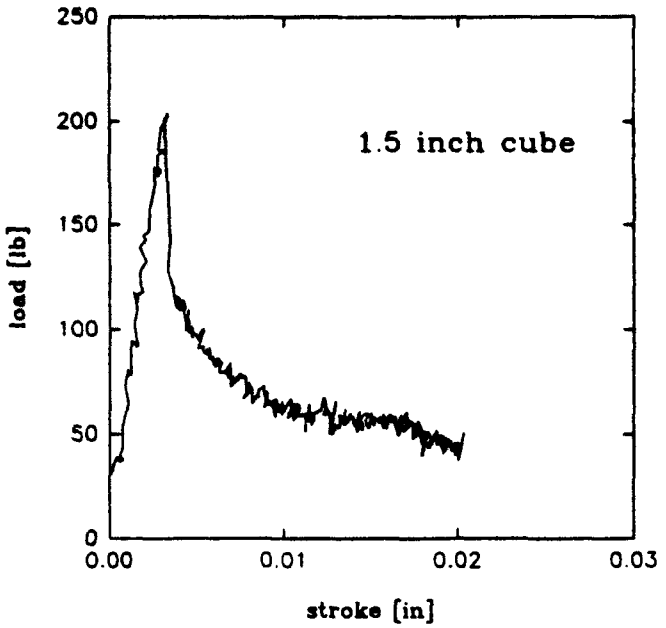
1.5 inch cube
load [lb]
stroke [in]
250
200
150
100
50
0
0.00
0.01
0.02
0.03

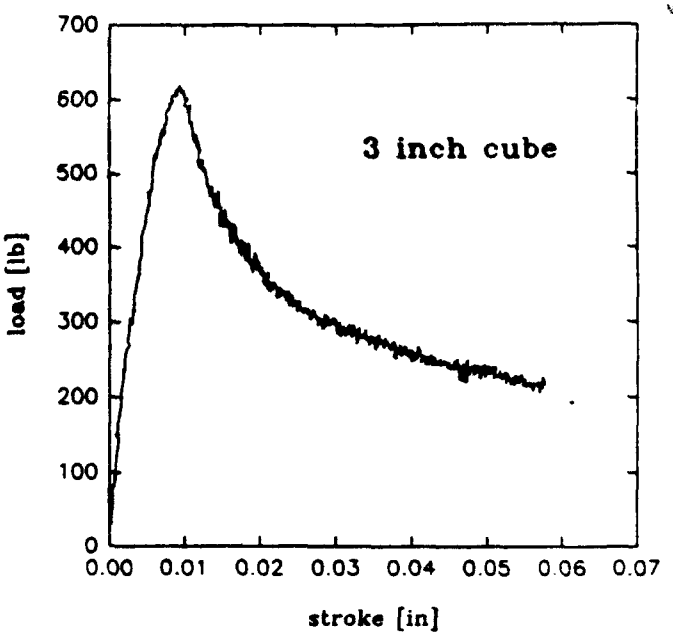
3 inch cube
load [lb]
stroke [in]
700
600
500
400
300
200
100
0
0.00
0.01
0.02
0.03
0.04
0.05
0.06
0.07

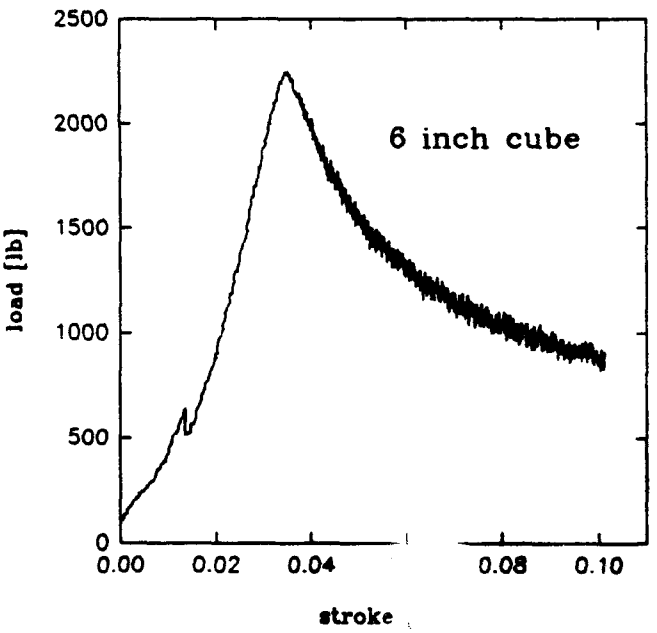
6 inch cube
load [lb]
stroke
2500
2000
1500
1000
500
0
0.00
0.02
0.04
0.08
0.10

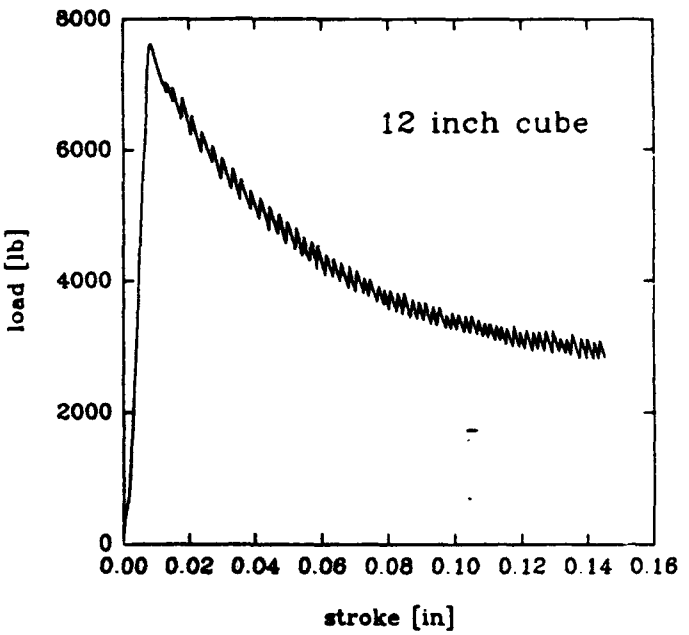
12 inch cube
load [lb]
stroke [in]
8000
6000
4000
2000
0
0.00
0.02
0.04
0.06
0.08
0.10
0.12
0.14
0.16

Fig. 3

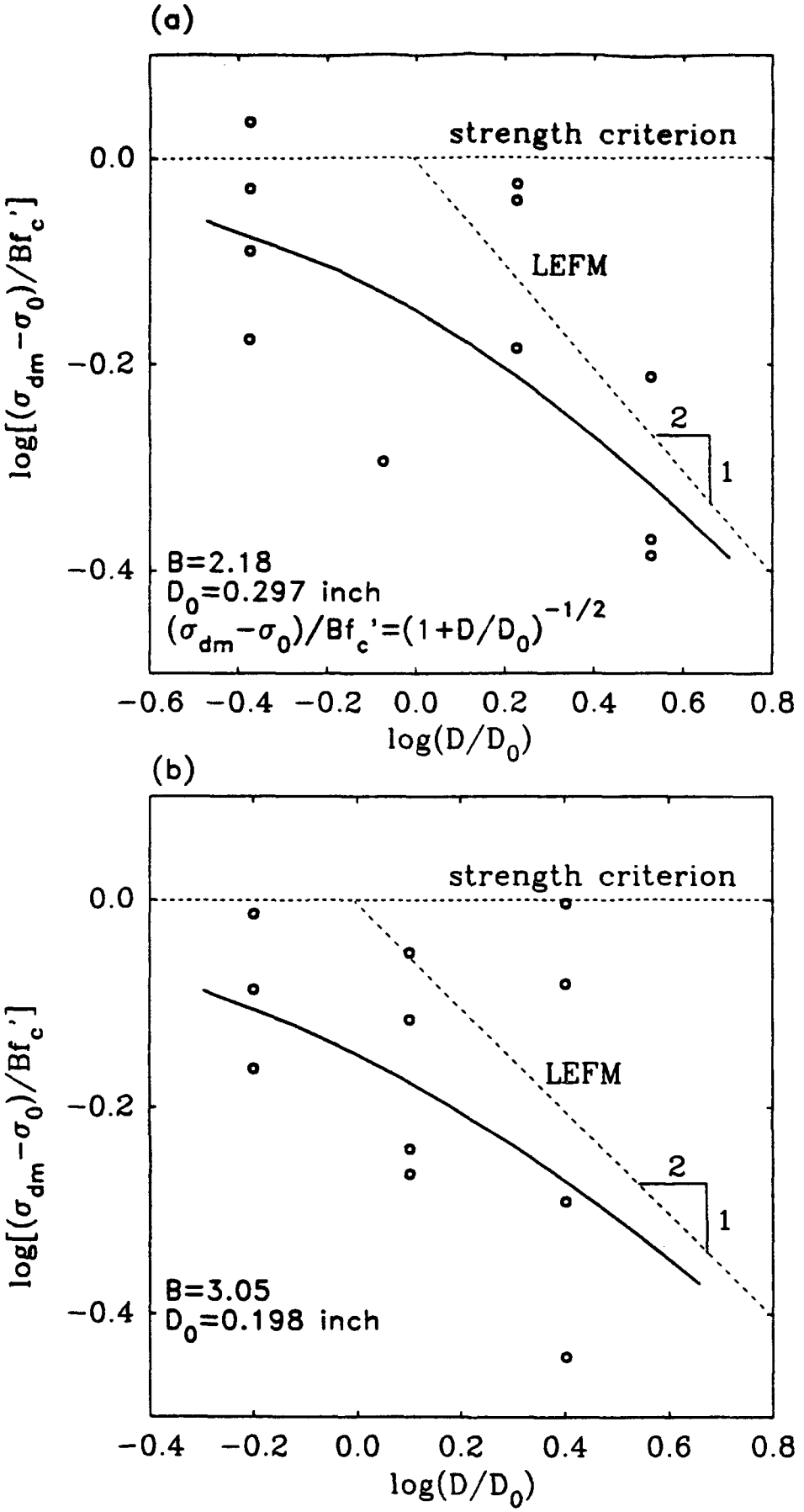
(a)
strength criterion
LEFM
2
1
B=2.18
D_0=0.297 inch
$(\sigma_{dm}-\sigma_0)/Bf_c' = (1+D/D_0)^{-1/2}$
$\log[(\sigma_{dm}-\sigma_0)/Bf_c']$
$\log(D/D_0)$
0.0
−0.2
−0.4
−0.6 −0.4 −0.2 0.0 0.2 0.4 0.6 0.8
(b)
strength criterion
LEFM
2
1
B=3.05
D_0=0.198 inch
$\log[(\sigma_{dm}-\sigma_0)/Bf_c']$
$\log(D/D_0)$
0.0
−0.2
−0.4
−0.4 −0.2 0.0 0.2 0.4 0.6 0.8

Fig 4

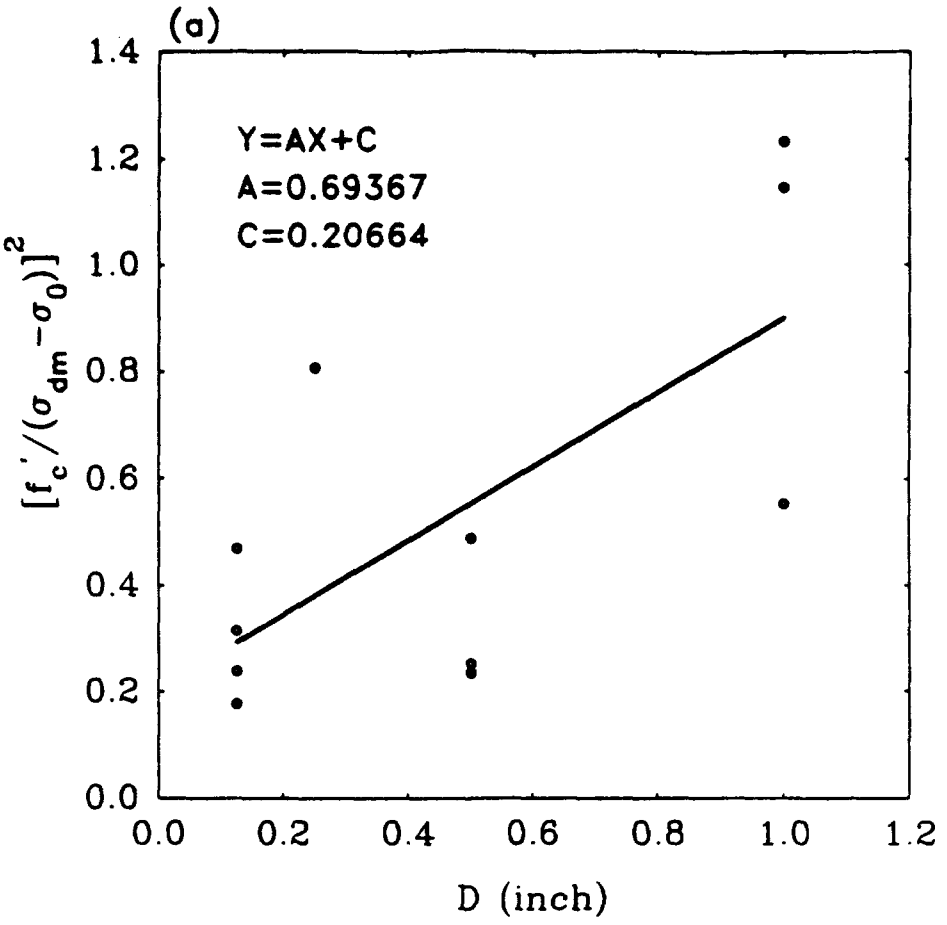
(a)
Y=AX+C
A=0.69367
C=0.20664
$[f_c'/(\sigma_{dm}-\sigma_0)]^2$
D (inch)
0.0
0.2
0.4
0.6
0.8
1.0
1.2
1.4

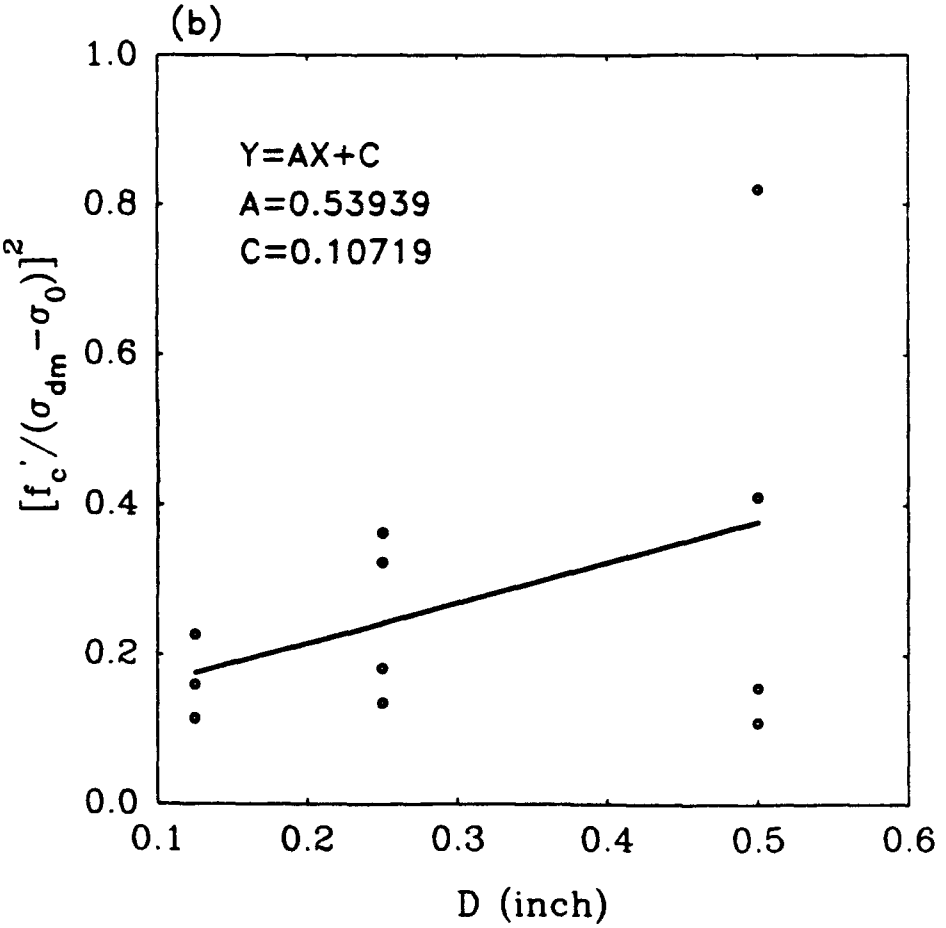
(b)
Y=AX+C
A=0.53939
C=0.10719
$[f_c'/(\sigma_{dm}-\sigma_0)]^2$
D (inch)
0.0
0.2
0.4
0.6
0.8
1.0
0.1
0.2
0.3
0.4
0.5
0.6

Fig. 5

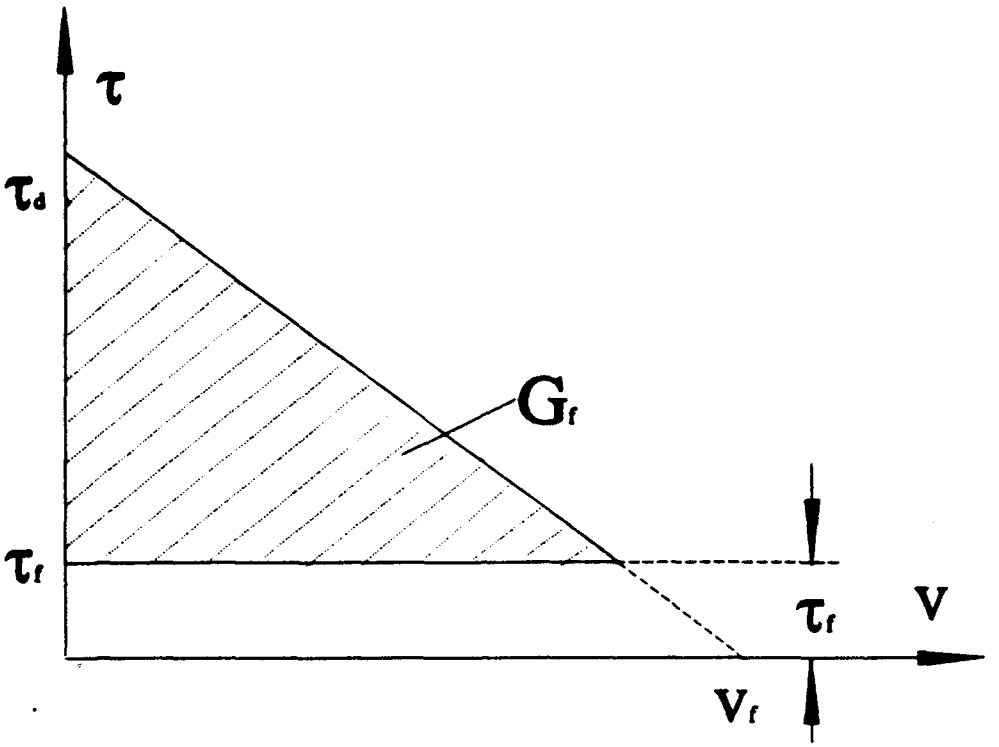

Fig. 6

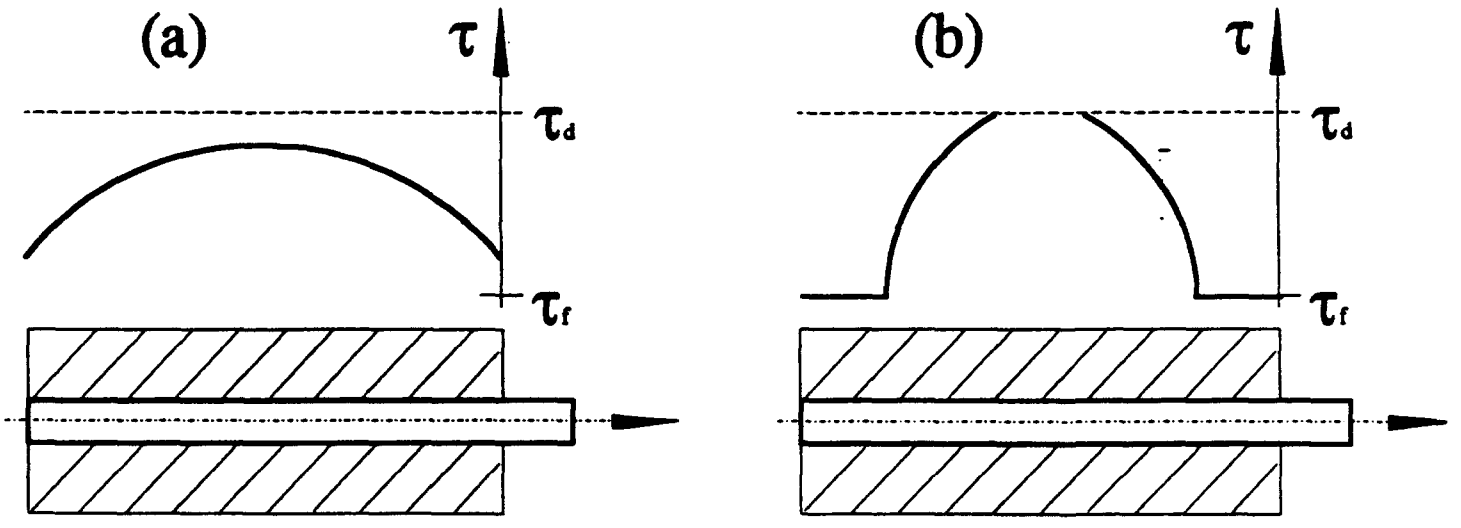

Fig. 7

INTERNATIONAL JOURNAL FOR NUMERICAL AND ANALYTICAL METHODS IN GEOMECHANICS, VOL. 17, 1–14 (1993)

FRACTURE ENERGY RELEASE AND SIZE EFFECT IN BOREHOLE BREAKOUT

ZDENĚK P. BAŽANT*

Department of Civil Engineering, Northwestern University, 2145 Sheridan Rd. Evanston, Illinois 60201, U.S.A.

FENG-BAO LIN†

Department of Civil Engineering, New York Polytechnic, New York, NY, U.S.A.

AND

HORST LIPPMANN‡

Lehrstuhl A für Mechanik, Technische Universität München, Germany

SUMMARY

The paper presents a simple approximate analytical solution of the remote stresses that cause the collapse of a borehole or other circular cylindrical cavity in an infinite elastic space. Regions of parallel equidistant splitting cracks are assumed to form on the sides of the cavity. Their boundary is assumed to be an ellipse of a growing horizontal axis, the other axis remaining equal to the borehole diameter. The slabs of rock between the splitting cracks are assumed to buckle as slender columns, and their post-critical stress is considered as the residual stress in the cracked rock. The buckling of these slab columns is assumed to be resisted not only by their elastic bending stiffness but also shear stresses produced on rough crack faces by relative shear displacements. The energy release from the infinite medium caused by the growth of the elliptical cracking region is evaluated according to Eschelby's theorem. This release is set equal to the energy dissipated by the formation of all the splitting cracks, which is calculated under the assumption of constant fracture energy. This yields the collapse stress as a function of the elastic moduli, fracture energy, ratio of the remote principal stresses, crack shear resistance characteristic and borehole diameter. The collapse stress as a function of crack spacing is found to have a minimum, and the correct crack spacing is determined from this minimum. For small enough diameters, the crack spacing increases as the (4/5)-power of the borehole diameter, while for large enough diameters a constant spacing is approached. In contrast to plastic solutions, the breakout stress exhibits a size effect, such that for small enough diameters the breakout stress decreases as the $(-2/5)$-power of the borehole diameter, while for large enough diameters a constant limiting value is approached. Finally, some numerical estimates are given and the validity of various simplifying assumptions made is discussed.

1. INTRODUCTION

The sudden catastrophic collapse of boreholes in rock, called the breakout, as well as the collapse (such as rock burst) of various other types of cavities due to high compressive stresses in the rock mass, has been studied extensively and various important results have been obtained.[1–22] However, most studies have been based on the theory of plasticity, which does not give a sufficiently realistic description of the inelastic behaviour of rock, except at very high confining

* Walter P. Murphy Professor.
† Assistant Professor.
‡ Professor and Director.

0363–9061/93/010001–14$12.00

Received 3 October 1991
Revised 9 April 1992

pressures. Such pressures, however, never exist near the sides of cavities. Cavities usually appear to fail due to fracture of rock, and the failure process is described by fracture mechanics better than plasticity. A fully realistic description would no doubt require a combination of both theories, but the analysis would then become rather complicated.

The most important practical consequence of fracture mechanics is that it predicts size effect, that is, the remote compressive stress that causes a borehole to fail must decrease as the borehole size increases. On the other hand, according to plasticity (or any other failure theory expressed in terms of stress and strain), there is no size effect. But the existence of the size effect has been detected experimentally (e.g. References 19, 23, 24).

Fracture mechanics has so far been well developed only for tensile fractures, and to some extent shear fractures; their microscopic mechanism, however, still usually consists of tensile cracks. Compressive fractures are not very well understood at present, although it is clear that their mechanism involves, in one way or another, some form of tensile cracking depending on the structure geometry. The purpose of this study is to formulate appropriate simplifying assumptions and use fracture mechanics concepts to obtain an analytical solution of borehole collapse that reveals the size effect and is sufficiently simple to be clearly understood—one benefit that numerical solutions cannot provide. The plasticity aspects of failure will have to be neglected to make an analytical solution feasible. The reality may be expected to be somewhere between the solutions of plasticity and fracture mechanics, but probably in most situations much closer to the latter.

2. ENERGY RELEASE DUE TO GROWTH OF ELLIPTICAL CAVITY

Consider a circular cylindrical borehole of radius R and horizontal axis z in an infinite elastic space that is in a state of plane strain (Figure 1a) and is subjected at infinities to uniform compressive stresses $\sigma_{x\infty}$ and $\sigma_{y\infty}$ in the directions of Cartesian co-ordinates x and y. We will assume that failure tends to enlarge the circular cavity into an ellipse of horizontal axis $a \geq R$, with the vertical axis remaining equal to R.

Based on Eshelby's solution of the stress field and using the superposition method, explained in detail for example by Mura,[25] one can calculate the loss of the potential energy (per unit thickness in the z-direction) of an infinite, initially uniformly stressed elastic space caused by cutting out an elliptical hole

$$\Delta\Pi_1 = -\frac{\pi}{2E'}[(a + 2R)R\sigma_{x\infty}^2 + (2a + R)a\sigma_{y\infty}^2 - 2aR\sigma_{x\infty}\sigma_{y\infty}] \tag{1}$$

where $E' = E/(1 - \nu^2)$, E = Young's elastic modulus of the rock, ν = Poisson's ratio, and $\nu' = \nu/(1 - \nu)$. $\Delta\Pi_1$ represents the sum of the work of the stresses on the strain changes outside the ellipse, which are non-uniformly distributed and decay with the distance from the ellipse, and the work of the stresses on the strain changes inside the removed elliptical cutout, which are, according to the famous Eshelby's theorem, uniformly distributed within the ellipse.

Equation (1) gives the potential energy change when the stresses within the elliptical region are reduced to zero. Later we will need also the potential energy change $\Delta\Pi'$ when the initial vertical stress $\sigma_{y\infty}$ is reduced to a certain finite critical stress σ_{cr} rather than to zero. In that case the calculations according to Eshelby's theorem yield

$$\Delta\Pi_1' = -\frac{\pi}{2E'}[(a + 2R)R\sigma_{x\infty}^2 + (2a + R)a\sigma_{y\infty}^2 - 2aR\sigma_{x\infty}\sigma_{y\infty} - 2a^2\sigma_{cr}^2] \tag{2}$$

Equation (1) may be checked by considering the limiting case $R \to 0$, for which the elliptical hole

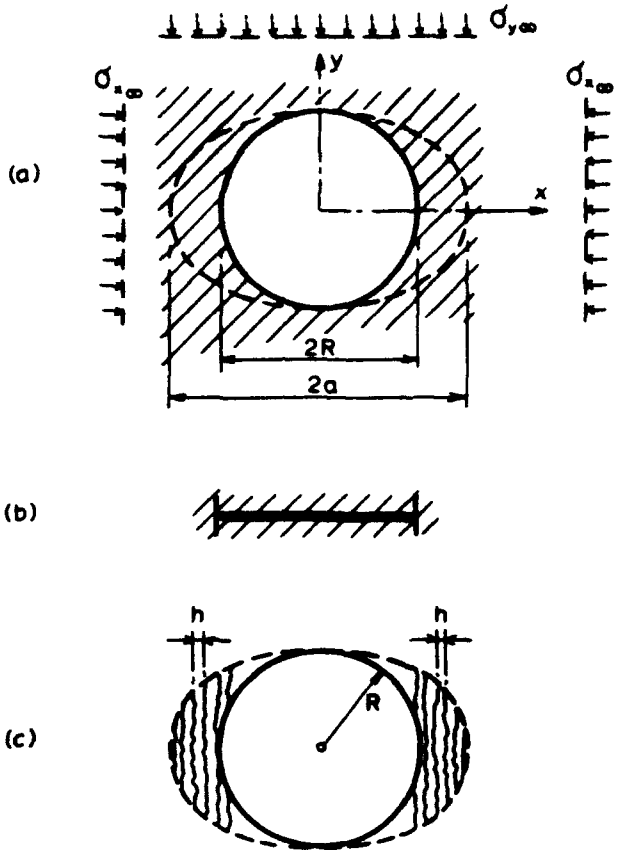

Figure 1. (a) Growth of an elliptical cracking region from a circular borehole, and (b) limit case of a crack

becomes a horizontal crack (Figure 1b). In that case Equation (1) reduces to:

$$\Delta\Pi = -\frac{\pi}{E'}\sigma_{y\infty}^2 a^2 \tag{3}$$

This coincides with the expression for the energy loss of an infinite space due to creating a crack of length $2a$. Indeed, as is well-known (e.g. References 26 and 27), the energy release rate per crack tip is K_I^2/E' where $K_I = \sigma_{y\infty}\sqrt{(\pi a)} =$ stress intensity factor, and by integrating one has, for both crack tips combined, $\Delta\Pi = 2\int(K_I^2/E')da$, which is the same result as equation (3).

Proof of equation (2). Consider an infinite elastic body subjected at infinity to a uniform applied stresses σ_∞, let a uniform eigenstrain ε^* be applied to an ellipsoidal domain Ω contained in this infinite body. The values of the eigenstrain ε^* are such that the stress is zero every where in the ellipsoid after ε^* is applied. This means that (if the infinite body is free from any external force) the stress in the ellipsoid induced by ε^* will be $-\sigma_\infty$. Because the stress is zero everywhere in the ellipsoid, the ellipsoid can be cut out from the infinite body without affecting its stresses and deformation. Thus, the change of potential energy of the infinite body caused by the applied eigenstrain is the same as the loss of potential energy caused by cutting out the ellipsoid from the

infinite body. This potential energy loss can be calculated as follows (e.g. Reference 25):

$$\Delta\Pi = -\frac{1}{2}\int_\Omega \sigma^T\varepsilon^* \, dV - \int_\Omega \sigma_0^T\varepsilon^* \, dv = -\frac{V}{2}\sigma^T\varepsilon^* - V\sigma_0^T\varepsilon^* \tag{4}$$

where V is the volume of the ellipsoid; σ_0 and σ are the stress vectors in the ellipsoid when the infinite body is subjected to external forces alone or eigenstrain ε^* alone, respectively.

If plane-strain cases are considered, the ellipsoid becomes an elliptic cylinder and the relationship between eigenstrain ε^* and the stress induced in the elliptic cylinder is:[25]

$$\frac{\mu}{1-\nu}\left[-2+\frac{R^2+2aR}{(a+R)^2}+\frac{R}{a+R}\right]\varepsilon_x^* + \frac{\mu}{1-\nu}\left[\frac{R^2}{(a+R)^2}-\frac{R}{a+R}\right]\varepsilon_y^* - \frac{2\mu\nu}{1-\nu}\frac{a}{a+R}\varepsilon_z^* = \sigma_x \tag{5}$$

$$\frac{\mu}{1-\nu}\left[-2+\frac{a^2+2aR}{(a+R)^2}+\frac{a}{a+R}\right]\varepsilon_y^* + \frac{\mu}{1-\nu}\left[\frac{a^2}{(a+R)^2}-\frac{a}{a+R}\right]\varepsilon_x^* - \frac{2\mu\nu}{1-\nu}\frac{R}{a+R}\varepsilon_z^* = \sigma_y \tag{6}$$

$$\frac{-2\mu\nu}{1-\nu}\frac{a}{a+R}\varepsilon_x^* - \frac{2\mu\nu}{1-\nu}\frac{R}{a+R}\varepsilon_y^* - \frac{2\mu}{1-\nu}\varepsilon_z^* = \sigma_z \tag{7}$$

where μ and ν are the Lamé constants; a and R are the axes of the ellipse in the x- and y-directions. If the applied stress components at infinity are $\sigma_{x\infty}$ and $\sigma_{y\infty}$, the stress component in the z-direction is $\nu(\sigma_{x\infty}+\sigma_{y\infty})$. Substituting $-\sigma_{x\infty}$, $-\sigma_{y\infty}$ and $-\nu(\sigma_{x\infty}+\sigma_{y\infty})$ for σ_x, σ_y and σ_z in the above three equations and solving them, we obtain the eigenstrain components

$$\varepsilon_x^* = \frac{(\nu-1)(a+2R)}{2\mu a}(-\sigma_{x\infty}) + \frac{1-\nu}{2\mu}(-\sigma_{y\infty}) \tag{8}$$

$$\varepsilon_y^* = \frac{1-\nu}{2\mu}(-\sigma_{x\infty}) + \frac{(\nu-1)(2a+R)}{2\mu R}(-\sigma_{y\infty}) \tag{9}$$

with $\varepsilon_z^* = 0$. The energy loss $\Delta\Pi$ per unit thickness in the z-direction can now be calculated from substituting the above expressions into Equation (A1).

$$\Delta\Pi = -\frac{V}{2}(-\sigma_\infty^T)\varepsilon^* - V\sigma_\infty^T\varepsilon^* = -\frac{V}{2}\sigma_\infty^T\varepsilon^* = -\frac{\pi aR}{2}(\sigma_{x\infty}\varepsilon_x^* + \sigma_{y\infty}\varepsilon_y^*)$$

$$= -\frac{\pi}{2E'}[(a+2R)\sigma_{x\infty}^2 + (2a+R)a\sigma_{y\infty}^2 - 2aR\sigma_{x\infty}\sigma_{y\infty}] \tag{10}$$

where $E = 2(1+\nu)\mu$ and $E' = E/(1-\nu^2)$.

Now consider the loss of potential energy when a uniformly stressed infinite body is cut by an elliptic cylinder whose surface tractions along the surface of the elliptic hole corresponding to the uniform stress state $\sigma_y = \sigma_{\infty}$, with other components being zero. The loss of potential energy for this case is expressed similarly to equation (4), except that one term must be added as follows:

$$\Delta\Pi = -\frac{V}{2}\sigma^T\varepsilon^* - V\sigma_0^T\varepsilon^* - \frac{V}{2}(\sigma+\sigma_0^T)e \tag{11}$$

Here the last term represents the elastic strain energy stored in the elliptic cylinder when both the external forces at infinity are applied and the eigenstrain ε^* occurs; e is the elastic strain vector in the elliptic cylinder. Substitution of the expressions for e, σ_0, ε^* and e into equation (11) finally yields

$$\Delta\Pi = -\frac{V}{2}[-\sigma_{xx}\varepsilon_x^* + (-\sigma_{yx} + \sigma_{cr})\varepsilon_y^*] - V[\sigma_{xx}\varepsilon_x^* + \sigma_{yx}\varepsilon_y^*] - \frac{V}{2}\sigma_{cr}\frac{\sigma_{cr}}{E'} \tag{12}$$

Substitution of equations (8) and (9) then proves equation (2). QED

Equation (1) gives the potential energy change from the case of no cavity to the case of an elliptical cavity. By setting in equation (1) $a = R$, we get the potential energy change from the case of no cavity to the case of circular cavity of radius R (Figure 1a):

$$\Delta\Pi_0 = -\frac{\pi R^2}{2E'}(3\sigma_{xx}^2 + 3\sigma_{yx}^2 - 2\sigma_{xx}\sigma_{y\infty}) \tag{13}$$

Subtracting equation (13) from equation (2), we obtain the potential energy change when the stress in the regions between the original circle and the circumscribed ellipse is reduced from σ_{yx} to σ_{cr}

$$\Delta\Pi = \Delta\Pi_1' - \Delta\Pi_0 = -\frac{\pi}{2E'}[(aR - R^2)\sigma_{xx}^2 + (2a^2 + Ra - 3R^2)\sigma_{y\infty}^2 + 2R(R - a)\sigma_{xx}\sigma_{yx} - 2a^2\sigma_{cr}^2] \tag{14}$$

3. RESIDUAL STRAIN ENERGY AFTER COMPRESSION FRACTURING

If $\sigma_{cr} = 0$, the foregoing expression includes the release of all the strain energy originally stored in the zone between the ellipse and the original circle (Figure 1c). However, it is a particular feature of compression fracturing that this zone cannot be assumed unloaded to zero stress. Compression fracture in quasibrittle microinhomogeneous materials such as most rocks initiates as a system of parallel, roughly equidistant, splitting cracks having the direction of the minimum principal stress (in our case $\sigma_{y\infty}$). These vertical splitting cracks (which initially cause exfoliation at borehole surface and later extensive slabbing[23,24,28]) may eventually get organized to form inclined bands, equivalent to shear bands (Bažant and Ožbolt[29]), which in our case may be imagined to form along the contour of the ellipse. This aspect, however, does not seem to be essential for calculating the residual strain energy.

Now what is the mechanism that dictates the residual vertical stress σ_{cr}? If the spacing of the vertical cracks is relatively small, the stress that can be carried by the thin slabs of the material between the adjacent vertical splitting cracks must obviously be limited by elastic buckling[30] (this is a discrete version of the idea proposed, for an elastic continuum weakened by smeared parallel cracks, in Reference 31; see also Section 11.7 in Reference 32). So we will consider that these slabs (Figure 1), of thickness h, buckle in the manner of fixed-end columns of a certain length $2L$, equal to the crack length.

It is now useful to recall the initial post-critical behaviour of a perfect elastic column (e.g. Section 1.9 in the textbook of Bažant and Cedolin[32]). The diagram of the axial load P of such a column versus the axial load-point displacement u becomes nearly horizontal upon reaching the critical load, i.e. the Euler bifurcation load (the post-critical slope is still positive, equal to $P_{cr}/2L$, but this is negligible compared to the pre-critical slope); see Figure 2. According to this idea, the

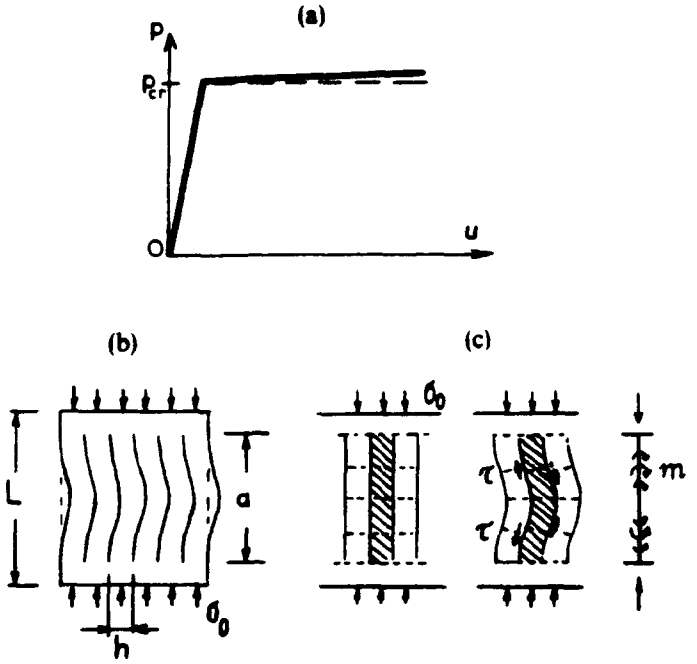

Figure 2. (a) Diagram of axial load vs. axial load-point displacement for column buckling, (b) simultaneous buckling of rock slabs between parallel cracks, and (c) crack shear stresses

vertical compressive stress in the parallel slab-columns of thickness h will not be zero but

$$\sigma_{cr} = -\frac{\pi^2}{L^2}\frac{E'I}{h} = -\frac{\pi^2}{L^2}\frac{E'h^2}{12} \tag{15}$$

where $I = h^3/12$ = centroidal moment of inertia of the cross-section of the slab (per unit thickness in the z-direction), h = spacing of the equidistant splitting cracks, and L = average (effective) half-length of the vertical cracks at the moment of failure.

We will now assume the deformation fields at the moment of failure of small and large boreholes (i.e. the modes of failure) to be geometrically similar, proportional to the borehole radius R. This means we assume that

$$L = kR \tag{16}$$

where k = empirical positive constant < 1. (This assumption is supported by the following argument: if L were not proportional to R, then we would have $L = kR^n$, where n = constant $\neq 1$; but then, for increasing R, the ratio L/R would tend either to infinity or to zero, that is, the mechanism of collapse would change, which seems irrational.)

In contrast to tensile cracks, the compression splitting cracks have one particular property—their opening displacement is, according to the present model of simultaneously buckling parallel slab-columns (Figure 2b), zero. At the same time, the cracks in rock are rough and transmit shear stresses τ when the opposite faces are subjected to shear. Now, to accomodate the buckling deflections of the adjacent slabs, relative shear displacements Δ between the contacting crack faces must inevitably arise (Figure 2c); $\Delta = w'(y)h$, where $w(y)$ = deflection curve of each

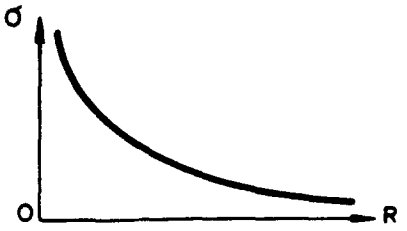

Figure 3. Calculated dependence of remote effective stress causing borehole collapse on the borehole radius

slab-column. The shear stress transmitted across the crack due to surface roughness (Figure 3) may be approximately assumed to be proportional to Δ; thus, $\tau = G\gamma_{ef}$, where $\gamma_{ef} = \Delta/\lambda = w'h/\lambda$; G = elastic shear modulus of rock and λ = empirical length = material property representing the thickness of an intact rock layer whose elastic shear relative displacement due to unit shear stress is the same at that between the crack faces. The shear stresses acting from both sheared cracks exert on the slab-column a distributed moment $m = rh$ (Figure 2c). The moment differential equation of equilibrium of the slab-column is $M' + Pw' + m' = -V$, where M = bending moment, V = shear force and $P = -\sigma_y h$ = axial compression force. Therefore, the differential equation for the deflection curve is $E'Iw'''' + (P - Gh^2/\lambda)w'' = 0$, where $I = h^2/12$. The lowest critical stress for fixed-end boundary conditions is then easily found to be

$$\sigma_{cr} = -\frac{\pi^2 E' h^2}{12L^2} - \frac{h}{\lambda}G \tag{17}$$

The work of shear stress τ is not included in the strain energy since crack shear is inelastic, irreversible (this work might be included in the dissipated energy expression, but it is negligible at the start of buckling.

The residual strain energy (per unit thickness in the z-direction) contained between the ellipse and the initial circle is given by the bending energy of all the slab-columns, which may now be approximately expressed as

$$\Pi_{cr} = (\pi aR - \pi R^2)\frac{\sigma_{cr}^2}{2E'} = \frac{\pi R(a-R)}{2E'}\left(\frac{\pi^2 E' h^2}{12k^2R^2} + \frac{h}{\lambda}G\right)^2 \tag{18}$$

4. ENERGY DISSIPATED BY FRACTURING AND ENERGY BALANCE

The energy dissipated by fracturing of the rock is the sum of the energies dissipated by all the vertical splitting cracks, i.e.

$$\Delta W_f = (\pi aR - \pi R^2)\frac{G_f}{h} \tag{19}$$

(per unit thickness in the z-direction), in which G_f/h is the energy dissipated per unit volume of the rock and G_f is the fracture energy of the rock ($G_f = K_{Ic}^2/E'$, where K_{Ic} = fracture toughness of the rock).

The net energy loss due to passing from a circular borehole in intact rock to an elliptical damage zone with vertical splitting cracks now is, instead of equation (14),

$$\Delta\Pi = \Delta\Pi_1' - \Delta\Pi_0 + \Pi_{cr} \tag{20}$$

The energy balance (principle of conservation of energy) requires that $-\Delta\Pi = \Delta W_f$. Assuming the parallel cracks to form progressively, one after another, we need to differentiate equation (14) with respect to a. Thus, we get the incremental energy balance condition:

$$-\frac{\partial(\Delta\Pi)}{\partial a} = \frac{\partial(W_f)}{\partial a} \tag{21}$$

which yields

$$\frac{\pi}{2E'}[R\sigma_{x\infty}^2 + (4a + R)\sigma_{y\infty}^2 - 2R\sigma_{xx}\sigma_{yx} - 4a\sigma_{cr}^2] = \frac{\pi R}{2E'}\left(\frac{\pi^2 E' h^2}{12k^2R^2} + \frac{h}{\lambda}G\right)^2 + \frac{\pi R G_f}{h} \tag{22}$$

We are interested in the start of borehole breakout, which occurs when $a = R$. Substituting this value of a into the last equation, we obtain

$$\sigma_{x\infty}^2 + 5\sigma_{y\infty}^2 - 2\sigma_{xx}\sigma_{yx} - 4\sigma_{cr}^2 = \left(\frac{\pi^2 E' h^2}{12k^2R^2} + \frac{h}{\lambda}G\right)^2 + \frac{2E'G_f}{h} \tag{23}$$

Now, introducing the following definition of the effective applied stress:

$$\sigma_{ef} = \sigma_{yx}\left(1 - \frac{2\sigma_{xx}}{5\sigma_{yx}} + \frac{\sigma_{x\infty}^2}{5\sigma_{y\infty}^2}\right)^{1/2} \tag{24}$$

and denoting

$$F(R, h) = \left(\frac{\pi^2 E' h^2}{12k^2R^2} + \frac{h}{\lambda}G\right)^2 + \frac{2E'G_f}{5h} \tag{25}$$

Equation (13) may now be written simply in the form

$$\sigma_{ef}^2 = F(R, h) \tag{26}$$

where F is a function of R and h.

The question now is how to estimate the spacing h of the vertical splitting cracks. In this regard, it is interesting to note that $F(R, h)$ as a function of h possesses a minimum. From this, a new, simple concept comes to mind.[30] The spacing h that will occur is that which minimizes the applied effective stress σ_{ef}. In other words, the splitting cracks will occur at the lowest compressive stress they can (this concept could be proven on the basis of the Gibbs' statement of the second law of thermodynamics in the manner shown in Chapter 10 of the textbook of Bažant and Cedolin).[32] The necessary condition of minimum is that

$$\frac{\partial F(R, h)}{\partial h} = 0 \tag{27}$$

After substituting equation (25) for $F(R, h)$ and differentiating, we obtain

$$\frac{5\pi^4 E'^2}{72k^4R^4}h^5 + \frac{11\pi^2 E'G}{12k^2R^2\lambda}h^4 + \frac{5G^2}{\lambda^2}h^3 - E'G_f = 0 \tag{28}$$

This is an algebraic equation of fifth degree for h. Although a numerical solution would be easy, a closed-form solution of h is not possible. However, it will suffice to examine the asymptotic cases.

For sufficiently small R, the terms with h^4 and h^3 become negligible compared to the term with h^5, and the solution then is

$$h = C_s R^{4/5} \qquad C_s = \left(\frac{72k^4 G_f}{5\pi^4 E'}\right)^{1/5} \quad \text{(small } R\text{)} \tag{29}$$

From this result[30] we see that the spacing of the splitting cracks should increase with the borehole diameter. This property has been observed by Cook[33] and co-workers.

On the other hand, for sufficiently large R, the first two terms of equation (28) may be neglected, and the solution is

$$h = \left(\frac{E' G_f \lambda^2}{5G^2}\right)^{1/3} = \text{constant} \quad (\text{large } R) \tag{30}$$

If we substitute equation (29) into equation (26) and take the asymptotic approximation of equation (26) for small R, we obtain

$$\sigma_{ef} = C_1 R^{-2/5}, \qquad C_1 = \left(\frac{\pi^2 5^{1/2}}{48k^2} E'^3 G_f^2\right)^{1/5} \quad (\text{small } R) \tag{31}$$

while, if we substitute equation (30) into equation (26) and take the asymptotic approximation of equation (26) for large R, we obtain

$$\sigma_{ef} = 3\left(\frac{GE' G_f}{5\lambda}\right)^{1/3} = C_0 = \text{constant strength} \quad (\text{large } R) \tag{32}$$

For the intermediate values of R we cannot get a closed-form expression. However, the following combination of equations (31) and (32) has the right asymptotic properties for both small and large R and is probably a good approximation that should suffice for practical purposes:

$$\sigma_{ef} \approx C_1 R^{-2/5} + C_0 \tag{33}$$

5. DISCUSSION OF SIZE EFFECT AND NUMERICAL ESTIMATES

Equation (19) indicates that there is a size effect, which is understood as the dependence of the nominal stress at failure (nominal strength, in our case coincident with σ_{ef}) on the size—in our case the borehole radius R, provided that geometrically similar situations are compared. A basic property of plasticity, as well as all other theories with failure criteria expressed in terms of stress and strain tensors, is that there is no size effect (see e.g. Reference 32, Chapters 12 and 13; and References 34–36). Linear elastic fracture mechanics (LEFM) exhibits in general the strongest possible (deterministic) size effect—the nominal strength decreases as size$^{-1/2}$.

Since the foregoing analysis used LEFM, it is, thus, interesting to realize why the size exponent in equation (31) is $-2/5$ rather than $-1/2$. The reason is that, instead of localizing into a single dominant crack, fracture has been assumed to be distributed over a large zone with an area proportional to the diameter of the borehole. If we assumed a single splitting crack with a length proportional to the borehole diameter, the exponent in equation (31) would have come out as $-1/2$. On the other hand, the exponent would have come out as 0 (i.e. we would have no size effect even for small R) if we assumed the crack spacing h to be the same for every borehole diameter, with the cracking zone area proportional to the diameter (in this case the energy dissipation due to fracture per unit volume would be constant, independent of the borehole diameter, same as in plasticity). It is because of the theory of elastic buckling (and because L increases with R) that we found the crack spacing to increase with the borehole diameter less than proportionally. It is for this reason that the size effect exponent in equation (31) has come out to be intermediate between $-1/2$ and 0, that is, intermediate between the exponents for single-crack LEFM and for plasticity.

The fact that the compressive stress that causes borehole breakout exhibits a size effect has been observed experimentally[6,23] and has been also predicted by finite element models of non-local type, for example models with couple stresses.[9,37]

The foregoing analysis tacitly implied the assumption that the failure mode of the borehole is symmetric. Based on the experience with certain other fracture problems (Reference 32, Section 12.5 and Reference 38), one may expect that the loading path might exhibit a bifurcation, after which the failure process proceeds along a non-symmetric secondary path, corresponding to a borehole collapsing non-symmetrically, only on one side of the cavity. Unfortunaltely, the non-symmetric collapse mode does not seem amenable to a simple analytical solution. The present symmetric solution should represent an upper bound on the actual critical stress for collapse. It may also be pointed out that the symmetric and non-symmetric response paths probably give the same type of size effect and dependence on other basic parameters. Thus, it may well be possible to use the present solution at least qualitatively, even if the actual collapse is non-symmetric.

Another important simplification has been our use of LEFM. The fracture of rock, of course, shows significant departures from LEFM (e.g. References 35 and 39). This may be approximately described by assuming the energy release rate required for fracture growth to be variable (rather than being equal to constant G_f) and to increase with the crack length a according to a given function $R(a)$ called the R-curve (resistence curve). If an increasing R-curve were introduced into the present type of analysis, the resulting size effect would become weaker. However, measurements of the R-curve for the present type of situation are lacking. It is debatable whether any increase of $R(a)$ is appropriate at all when many parallel closely spaced cracks propagate simultaneously, or when the cracks are much longer than the size of the inhomogeneities in rock.

Related to possible R-curve behaviour, the splitting cracks in rock may be discontinuous, capable of transmitting some reduced transverse tensile stresses as well as shear stresses. Capability of shear stress transmission must further arise from the fact that these cracks are no doubt rather tortuous, permitting interlock of the asperities opposing relative slip of the crack surfaces which must take place during buckling. These properties, which have been neglected, would increase the value of σ_{cr}.

A further simplification has been the geometry of the cracking region. Experimental observations of borehole breakout show that the cracking regions on the sides of the borehole tend to have a roughly triangular shape and generally a smaller height than the length of the vertical cross-sections of the ellipse (Figure 4). But for such geometry a simple analytical solution would probably be impossible. Moreover, implicit to our assumption of an elliptical cracking region has been the hypothesis that the cracking regions for boreholes of different diameters are geometrically similar and their size is proportional to the borehole diameter. If the ratio of the average length of the splitting cracks to the borehole diameter decreased with increasing borehole

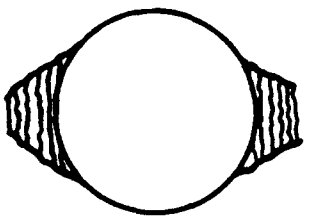

Figure 4. More realistic shape of cracking regions on the sides of a borehole

diameter (i.e. the cracking localized), then the size effect would be stronger than we have calculated.

Let us now consider rock properties typical of limestone; $G_f = 31$ J/m^2, $E' = 30$ GPa and $G = 11{\cdot}25$ GPa. To estimate λ, we exploit the similarity of rock to concrete, for which extensive crack shear tests have been conducted. Taking the results of Paulay and Loeber's[40] tests plotted in Figure 2 of Bažant and Gambarova,[41] we have, for crack opening displacement $\delta_n = 0{\cdot}125$ mm, $\tau/\Delta \approx 40$ N/mm^3, which yields for λ the value of 0·25 m. No results seem to be available for $\delta_n = 0$, however, we may use Paulay and Loeber's tests for $\delta_n = 0{\cdot}25$ and 0·50 mm to approximately extrapolate to 0; this leads to the crude estimate $\lambda = 0{\cdot}1$ m, which we will use. Nevertheless, there is enormous uncertainty about the value of λ, especially for the small initial displacements that matter for initial buckling.

From equation (32), for very large R we have $\sigma_{ef} = 82{\cdot}7$ MPa (12,000 psi). This means that a sufficiently large borehole would break out at the depth of about 3000 m below the earth surface. This is certainly a reasonable estimate, as an order of magnitude. However, the corresponding value obtained for the spacing of the splitting cracks, which is obtained from equation (30) as 0·25 mm, does not seem reasonable, since at such a small spacing LEFM ceases to be valid and the aforementioned G_f-value, obtained on laboratory samples, is probably inapplicable. But the aforementioned differential equation for buckling degenerates to the form $w'''' = 0$, i.e. the slab-columns do not bend at all, which signifies that the idea of buckling makes no sense in the limit case $R \to \infty$. Probably, the constant C_0 in equation (32) should be interpreted merely as an empirical large-scale compression strength limit, rather than a theoretical value derived by slab buckling analysis.

Next consider a borehole of radius $R = 0{\cdot}2$ m and assume that $k = 0{\cdot}25$. Equation (31) then yields $\sigma_{ef} = 21{\cdot}7$ MPa (3140 psi), which is the stress at the depth of about 740 m. From this result we observe that, if the crack shear resistance were neglected, the predicted breakout stress would be, compared to experience, much too low, by an order of magnitude. This shows that some other mechanism, which we proposed to be the crack shear resistance, must serve to elevate the breakout stress by an order of magnitude. Together with the foregoing value associated with crack shear, equation (33) yields the estimate $\sigma_{ef} = 104{\cdot}4$ MPa (15,140 psi), which corresponds to depth 3740 m. The thickness and length of the slab-columns are obtained as $h = 2{\cdot}6$ mm and $L = 50$ mm. For such a close spacing, the cracks are more likely to be discontinuous rows of microcracks than continuous cracks, and the crack tortuosity due to heterogeneous microstructure is likely to cause significant local weakening of the slab-columns. In that case, the formula for buckling of a perfect column of a uniform cross-section might be too far from reality and imperfections might have to be introduced into the buckling analysis. Nevertheless, the aspect ratio of the slab columns, $L/h = 19{\cdot}2$, is certainly just right within the range where the carrying capacity is indeed governed by the theory of buckling of slender columns.

In the preceding numerical estimation, the size-independent part due to crack shear resistance, C_0, dwarfs the size-dependent part due to bending stiffness, $C_1 h^{-2/5}$. One must be aware, though, of the strong speculative nature of the foregoing estimates. Particularly, the value we used for λ is highly uncertain, and so is the value of k. Consequently, the values of C_0 and C_1 could be quite different, and the magnitude of the size-dependent term could be relatively much more significant than in the foregoing calculation. Experimental studies are needed.

The preceding analysis of crack shear ignored the volume expansion which is always caused by the slip of rough cracks. This expansion is partially prevented by the surrounding rock, which causes hydrostatic compressive stress to develop in the cracking zone. When the volume expansion is not opposed, as in prismatic test specimens with lubricated ends (Appendix I), the crack shear stiffness may be very low, and when it is completely prevented, very high. In addition

to this, the energy of hydrostatic compression needs to be subtracted from the energy that is released from the surrounding rock, which means that less energy is available to create the splitting cracks. This may well be another reason why the collapse stress estimate from the slab-column buckling analysis seems much too low.

6. SUMMARY AND CONCLUSIONS

The basic simplifying hypotheses of the present solution may be summarized as follows:

1. The compression failure of rock on the side of the borehole is caused by densely distributed parallel splitting cracks in the direction of the minimum principal stress, rather than by plastic yielding.
2. The zones of parallel splitting cracks for boreholes of various diameters are geometrically similar and the length of these cracks is proportional to the borehole diameter.
3. For estimating the energy release, the inner boundary of the infinite elastic solid may be considered to expand during failure from a circle to an ellipse.
4. After uniformly spaced splitting cracks parallel to the minimum principal stress develop, the region between the ellipse and the original circle retains a certain residual stress governed by post-critical buckling behaviour of the rock slabs between the cracks.
5. The residual stress value is governed by buckling of rock slabs between the splitting cracks.
6. The buckling stress can be approximately calculated from the average length of the splitting cracks, which is assumed to be proportional to the borehole diameter.
7. Buckling of the slab-columns is resisted not only by their elastic bending stiffness but also by shear stresses produced at the rough crack faces by crack shear.
8. The energy (per unit area) required for crack growth in rock is constant, i.e. independent of the crack length and spacing.

The following basic observations and conclusions can be made:

1. Considering the boundary of the cracking region in borehole breakout to be symmetric and elliptical, and assuming the energy that drives the parallel compression splitting cracks to be released due to buckling of the slabs of rock between the cracks, one can obtain a simple analytical solution for the collapse stress.
2. The dependence of the collapse stress on the spacing of the splitting cracks exhibits a minimum, and the actual crack spacing may be considered to correspond to this minimum.
3. Borehole breakout exhibits a size effect such that, for sufficiently small diameters, the effective breakout stress decreases as the $(-2/5)$ power of the borehole diameter. For sufficiently large diameters, the size dependence disappears.
4. For sufficiently small diameters, the spacing of splitting cracks increases as the (4/5)-power of the borehole diameter, while for sufficiently large diameters a constant spacing is approached.
5. The energy release calculation for a growing ellipse according to Eschelby's theorem also predicts the effect of stress triaxiality, i.e. of the ratio of the remote principal stresses [equation (24)] (which is different from the result obtained by plastic analysis).

ACKNOWLEDGEMENTS

The paper has been written during the first author's sojourn at Lehrstuhl A für Mechanik (director Prof. Horst Lippmann), Technische Universität München, supported by A. von Hum-

boldt Award of Senior U.S. Scientist. The calculations based on Eshelby's theorem were carried out during F. -B. Lin's Visiting Scholar appointment at Northwestern University in 1990. Partial funding for some background general studies of size effect has been received under AFOSR grant 91-0140 to Northwestern University.

REFERENCES

1. H. Lippmann, 'Mechanics of 'bumps' in coal mines: a discussion of violent deformation in the sides of roadways in coal seams', *Appl. Mech. Rev. ASME*, **40**(8), 1033–1043 (1987).
2. H. Lippmann, 'Mechanik des Bohrens in vorgespanntem spröden oder granularen Material, speziell in Kohleflözen', *Ingenieur-Archiv* **48**, 347–361 (1979a).
3. H. Lippmann, 'The mechanics of translatory rock bursting', in J. C. Thompson (ed.), *Advances in Analysis of Geotechnical Instabilities*, University of Waterloo, Waterloo, ON, 1979b, pp. 25–63.
4. G. Bräuner, W. G. Burgert and H. Lippmann, Zur Theorie des Gebirgsschlages. *Glückauf—Forschungshefte*, 37, 169–175 (1976).
5. G. Tokar, 'Gebirgsschlaggefahr und Testbohren', *Doctor-Ingenieur Dissertation*, Technische Universität München, 1987.
6. B. Haimson and C. Herrick, 'Borehole breakouts and *in situ* stress', Proc. *Drilling Symp. at ETCE, ASME*, Houston, TX, Vol. 22, 1989, pp. 17–22.
7. I. Vardoulakis, 'Rock bursting as a surface instability phenomenon', *Int. J. Rock Mech. Min. Sci.*, **21**, 137–144 (1984).
8. I. Vardoulakis and P. Papanastasiou, 'Bifurcation analysis of deep boreholes. I. Surface instabilities', *Int. J. Numer. Anal. Methods Geomech.*, **12**, 379–399 (1988).
9. P. Papanastasiou and I. Vardoulakis, 'Bifurcation analysis of deep boreholes: II. Scale effect', *Int. J. Numer. Anal. Methods Geomech.*, **13**, 183–198 (1989).
10. H. Lippmann, 'Die Mechanik des Gebirgsschlages bei elastischem Nebestein', *Glückauf—Forschungshefte*, **43**, (4) (1982).
11. Z. Mróz, 'Current problems and new directions in mechanics of geomaterials', in Z. P. Bažant (ed.), *Mechanics of Geomaterials*, Wiley, Chichester and New York, (Chapter 24), 1985, pp. 539–566.
12. P. J. Périé, R. E. Goodman and T. J. Doe, 'Simulation of Borehole Breakouts in a Model Material', *Int. J. Rock Mech. Min. Sci.*, **25** (2), 97–98.
13. I. M. Petukhov and A. M. Linkov, 'Theoretical principles and fundamentals of rock burst prediction and control', *Proc. 5th Congress Int. Soc. Rock. Mech.*, held in Melbourne, A. A. Balkema, Rotterdam, Vol. 2, 1983, pp. D113–D120.
14. G. Tokar, 'Experimental analysis of the elasto-plastic zone surrounding a borehole in a specimen of rock-like material under multiaxial pressure', *Eng. Fracture Mech.*, **35**, 879–887 (1990).
15. A. Guénot, 'Contraintes et rupture autour des forages pétroliers, *Proc. 6th Int. Congr., Soc. Rock Mech.*, Montreal, Vol. 1, 1987, pp. 109–118.
16. I. Vardoulakis, J. Sulem and A. Guenot, 'Borehole instabilities as bifurcation phenomena', *Int. J. Rock. Mech. Min. Sci.*, **25** (3), 158–170 (1988).
17. C. A. Veeken, J. V. Walters, C. J. Kenter and D. R. Davis, 'Use of plasticity models for predicting borehole stability', in *Rock at Great Depth*, Maury and Fourmaintraux, (ed.), Balkema, Netherlands, Vol. 2, 1989, pp. 835–844.
18. D. J. Gates, 'Strain-softening around cavities in rock-like materials', *Mech. Mater.* (Elsevier) 309–331 (1990).
19. N. G. W. Cook, E. Hoek, J. P. G. Pretorius, W. D. Ortlepp and M. D. G. Salamon, 'Rock mechanics applied to the study of rockbursts', *J. South African Inst. Min. Met.*, **66**, 436–528 (1966).
20. A. Zubelewicz and Z. Mróz, 'Numerical simulation of rock burst processes treated as problems of dynamic instability', *Rock Mech. Rock Eng.*, **16**, 253–274.
21. G. Bräuner, *Gebirgsdruck und Gebirgsschläge, Glückauf*, Essen, 1981.
22. S. L. Crouch and C. Fairhust, 'Mechanics of coal mine bumps', *Trans., Soc. Min. Engrs AIME*, **256**, 317–323 (1974).
23. B. Haimson and C. Herrick, 'Borehole breakouts—a new tool for estimating *in situ* stress?', *Proc. Int. Symp. on Rock Stress and Rock Measurements*, Stockholm, 1986.
24. R. Ewy and N. Cook, 'Fracture processes around highly stressed boreholes', *Proc. Drilling Symp. at ETCE*, ASME, Houston, TX, Vol. 22, 1989, pp. 63–70.
25. T. Mura *Micromechanics of Defects in Solids*, Martinus Nijhoff, The Hague.
26. D. Broek, *Elementary Engineering Fracture Mechanics*, 4th edn, Martinus Nijhoff, Dordrecht, Boston, 1986.
27. J. F. Knott, *Fundamentals of Fracture Mechanics*, Butterworth, London, 1973.
28. P. Périé and R. Goodman, 'Evidence of new patterns in a thick-walled cylinder experiment', *Proc. Drilling Symp. at ETCE*, ASME, Houston, TX, Vol. 22, 1989, pp. 32–27.
29. E. Papamichos, J. F. Labuz and I. Vardoulakis, 'Surface instabilities in brittle rock', *Int. Conf. on Micromechanics of Failure of Quasibrittle Materials*, S. P. Shah and M. Wang (ed.), Albuquerque, NM.
30. Z. P. Bažant, 'Fracture analysis of compression failure and borehole collapse', Note privately communicated to F.-B. Lin (1990).
31. Z. P. Bažant, 'L'instabilité d'un milieu continu et la résistence en compression', *Bull. RILEM* (Paris) **35**, 99–112 (1967).
32. Z. P. Bažant and L. Cedolin, *Stability of Structures: Elastic, Inelastic, Damage and Fracture Theories*, Oxford University Press, New York, 1991.

33. N. G. W. Cook, Private communication to Z. P. Bažant, University of California, Berkeley, 1990.
34. Z. P. Bažant, 'Size effect in blunt fracture: concrete, rock, metal', *J. Eng. Mech. ASCE*, **110**, 518–535 (1984).
35. Z. P. Bažant, R. Gettu and M. T. Kazemi, 'Identification of nonlinear fracture properties from size effect tests and structural analysis based on geometry-dependent R-curves', *Int. J. Rock. Mech. Min. Sci.*, **28** (1), 43–51 (1991).
36. Z. P. Bažant and M. T. Kazemi, 'Determination of fracture energy, process zone length and brittleness number from size effect, with application to rock and concrete', *Int. J. Fracture*, **44**, 111–131 (1990).
37. P. C. Papanastasiou, Numerical analysis of localization phenomena with application in deep boreholes, *Ph.D. Dissertation*, University of Minnesota, Minneapolis, 1990.
38. Z. P. Bažant and M. R. Tabbara, 'Bifurcation and stability of structures with interacting propagating cracks', *Int. J. Fracture*, **53**, 273–279 (1992).
39. Z. P. Bažant and B.-H. Oh, 'Microplane model for progressive fracture of concrete and rock', *J. Eng. Mech. ASCE*, **111**, 559–582 (1985).
40. T. Paulay and P. J. Loeber, Shear transfer by aggregate interlock, Special Publication SP42, Am. Concrete Institute, Detroit, pp. 1–15 (1974).
41. Z. P. Bažant and P. Gambarova 'Rough cracks in reinforced concrete', *J. Struct. Div. ASCE*, **106** (ST4), 819–842 (1980).
42. Z. P. Bažant, M. R. Tabbara, M. T. Kazemi and G. Pijaudier-Cabot, 'Random particle model for fracture of aggregate or fiber composites', *ASCE J. Eng. Mech.*, **116**, 1686–1705 (1990).

APPENDIX I: COMPRESSION STRENGTH OF A PRISMATIC SPECIMEN

The present use of buckling analysis has been inspired by a similar previous analysis of a prismatic specimen of length L and width b;[30] see Figure 2(b). We assume that compression failure is caused by the formation of a band of vertical splitting cracks of length a and spacing h and is accompanied by buckling of the slabs between the cracks which behave as fixed-end columns. The initial longitudinal stress σ_0 in each slab is reduced by buckling to $\sigma_{cr} = -(E'h^2/3)\pi^2/a^2$. The total energy loss due to buckling is $-\Delta\Pi = Lb(\sigma^2 - \sigma_{cr}^2)/2E'$. The number of cracks is b/h and the energy dissipated by fracture is $\Delta W_f = aG_f b/h$. Energy balance requires that $-\Delta\Pi = \Delta W_f$. From this, the stress required for the formation of the band of splitting cracks is

$$\sigma_0^2 = \frac{2E'G_f}{h}\frac{a}{L} + \frac{\pi^4 E'^2}{9a^4}h^4 \tag{34}$$

We see that this expression has a minimum as a function of the crack spacing h. From the necessary condition of a minimum, $\partial(\sigma_0^2)/\partial h = 0$, we find that

$$h = \frac{a}{L}\left(\frac{9G_f}{\pi^4 E'}\right)^{1/5} L^{4/5} \tag{35}$$

Substituting this into equation (21), we conclude that the specimen fails at the stress

$$\sigma_0 = C_1 L^{-2/5}, \quad \text{with} \quad C_1 = (\sqrt{27}\pi^2 E'^3 G_f^2)^{1/5} \tag{36}$$

This size effect is the same as found for a borehole. Note also that σ_0 is independent of band width a, which means there is no tendency for the band width to localize.

[7]

JCI International Workshop on

Size Effect in Concrete Structures

Oct. 31 - Nov. 2, 1993

Sendai, Japan

PREPRINTS

Size Effect in Tensile and Compressive Quasibrittle Failures

ZDENĚK P. BAŽANT
Walter P. Murphy Professor of Civil Eng., Northwestern University, Evanston, Illinois 60208, USA.

Abstract
The lecture consists of two parts. The first part presents a rigorous mathematical analysis of scaling in various basic types of failure. First it is shown that the scaling law is a power law if, and only if, a characteristic dimension is absent. For all the theories in which the failure condition is expressed in terms of stress or strain only, including elasticity with a strength limit, plasticity, and continuum damage mechanics, the nominal strength of the structure is shown to be independent of its size. For linear elastic fracture mechanics, in which the failure criterion is expressed in terms of energy per unit area, the scaling law for the nominal strength is shown to be $(size)^{-1/2}$, provided that the cracks in structures of different sizes are geometrically similar. When the failure condition involves both the stress (or strain) and the energy per unit area, which is typical of quasi-brittle materials, the scaling law represents a gradual transition between asymptotes corresponding to the strength theory and LEFM. The size effect described by Weibull statistical theory of random material strength is also considered and the reasons for its inapplicability to quasi-brittle materials are explained. The second part of the lecture focuses attention on compression failures, particularly the failures of reinforced concrete columns, in which the size effect has recently been observed experimentally. This size effect is explained by energy release due to lateral propagation of a band of axial splitting cracks, taking into account buckling of compressed slabs of the material between adjacent axial splitting cracks and their postcritical deflections.
Keywords: Fracture Mechanics, Size Effect, Scaling Laws, Quasibrittle Materials, Concrete Structures, Compression Failure, Columns, Damage Mechanics, Plasticity.

Introduction

The problem of scaling is the most fundamental aspect of every physical theory. If the question of scaling is not understood, the problem itself is not understood, there is no theory. Questions of scaling have historically been the driving force of advances in physics. When the classical Newtonian mechanics failed at very large scales, the theory of relativity had to be invented, and when it failed at very small scales, the theory of quantum mechanics had to be invented. The questions of scaling played a dominant role in the

evolution of fluid mechanics; recall for example the Reynolds number and other numbers characterizing fluid flows at different scales.

In structural mechanics the questions of scaling have for a long time been neglected. From the practical viewpoint, this is perhaps not too serious for mechanical and aerospace engineers, who can test all their structures and components a full size, and for whom the main question is extrapolation in time rather than in size. For civil engineers, however, the question of scaling is paramount. Many civil engineering structures cannot be tested at full size, and the engineer must inevitably extrapolate from reduced scale laboratory tests to much larger structure sizes.

The reason that the questions of scaling have been neglected is that the classical theories of failure, in which the failure is determined by stress or strain at a critical point of the structure or is characterized by a constitutive law in terms of stresses and strains, exhibit no size effect. However, beginning with Griffith, it has been recognized that rational analysis of failure must take into account the energy release caused by failure and its balance with the energy needed to produce fracture or damage zones. Any theory in which the failure depends on the energy release inevitably leads to a size effect.

In quasibrittle materials such as concrete, the size effect is more complicated than it is for linear elastic fracture mechanics. The size effect for tensile failures (which includes also shear failures) has been studied for various kinds of concrete structures. An approximate size effect law which agrees with experiments as well as certain theoretical deductions has been developed. There is no doubt that the size effect needs to be introduced into the provisions of the design codes for concrete structures which deal with diagonal shear failure of beams, punching shear failure of slabs, torsional failures, pullout of bars and anchors, failure of splices, etc. However, although the principles appear to be clear, further work is needed to develop detailed formulas for various situations and calibrate them experimentally.

Recently, it has further been recognized that the size effect also occurs in compression failures of quasibrittle materials. Compressive fracture is a formidably complex problem which has been already intensely studied. However, despite many useful results, the global mechanics of compressive failure has not been sufficiently illuminated and the size effect has not been determined.

The purpose of the present lecture is two-fold. First, the general scaling laws of the mechanics of failure will be reviewed, considering the elementary scaling for theories such as elasticity, plasticity and linear elastic fracture mechanics, and then the more complicated scaling for quasibrittle materials. Second, the global mechanics of compression fracture in quasibrittle columns will be analyzed in an approximate manner, which is however believed the capture the principal phenomena. The fracture analysis of compressive quasibrittle failures, and the corresponding size effect which will be presented, should eventually be introduced into the design code provisions for reinforced concrete columns and possibly also prestressed structures in which compressive failure is promoted by prestress. The analysis outlined in the first part of this lecture will appear in detail in a forthcoming journal article (Bažant, 1993).

1 Basic Scaling Laws

1.1 Power Scaling for Structures Lacking Characteristic Length

The size effect is defined by comparing geometrically similar structures of different sizes. We denote as Y the response quantity whose size dependence is to be determined—for example, the nominal strength, the maximum deflection or the maximum strain. In this paper, our interest is in comparing the nominal strength (or nominal stress at failure), $Y = \sigma_N$, which is defined as

$$\sigma_N = c_N \frac{P_u}{bD} \text{ (for } 2D\text{)} \qquad \text{or} \qquad \sigma_N = c_N \frac{P_u}{D^2} \text{ (for } 3D\text{)} \tag{1}$$

in which P_u = maximum (ultimate) load, b = structure thickness in the case of two-dimensional similarity, D = characteristic dimension (or characteristic size), which can be chosen arbitrarily (for instance, as the depth of beam, the span, the half span, the notch depth, etc.), and c_N = coefficient introduced for convenience if one desires σ_N to correspond to some commonly used stress formulae.

Let us first consider those theories in which there is no characteristic length. This means that the scaling ratio $\bar{Y}/Y$ of the corresponding responses $\bar{Y}$ and Y depends only on the size ratio $\lambda = \bar{D}/D$ of two different sizes $\bar{D}$ and D but is independent of the choice of the reference size D. Plasticity, elasticity with a strength limit, continuum damage mechanics (without nonlocal concepts), and also linear elastic fracture mechanics (LEFM) belong to this class of theories, and so do many other theories in physics. As is well known, the scaling law for all these theories is a power law. We will now show it by adapting an argument used in fluid mechanics (Barenblatt, 1979, 1987). Let the scaling law be $f(\lambda)$, that is

$$\frac{\bar{Y}}{Y} = f(\lambda) \tag{2}$$

where f is an unknown function that we want to find. Considering another structure size $\tilde{D} = \mu D$ with the corresponding response $\tilde{Y}$, we have

$$\frac{\tilde{Y}}{Y} = f(\mu) \tag{3}$$

Now, because there exists no characteristic size, the size $\bar{D}$ can alternatively be chosen as the reference size. In that case Eq.(2) implies that

$$\frac{\tilde{Y}}{\bar{Y}} = f\left(\frac{\mu}{\lambda}\right) \tag{4}$$

Substituting now the ratio of Eqs. (2) and (3) into Eq. (4), we obtain

$$f\left(\frac{\mu}{\lambda}\right) = \frac{f(\mu)}{f(\lambda)} \tag{5}$$

This is a functional equation from which the function $f(\lambda)$ can be solved. To this end, we differentiate Eq. (5) with respect to μ and then set $\mu = \lambda$;

$$\frac{f'(1)}{\lambda} = \frac{f'(\lambda)}{f(\lambda)} \tag{6}$$

in which f' is the derivative of function f. The last equation is a differential equation for the unknown function f, which can be easily solved by separation of variables. With the notation $f'(1) = m$ = constant, the integral is $\ln f(\lambda) = m \ln \lambda + C$, and determining the integration constant C from the condition $C = \ln f(1) = 0$ for $\lambda = 1$, we have $f(1) = 1$. So we finally conclude that function f must be a power function,

$$f(\lambda) = \lambda^m \tag{7}$$

The power scaling law we obtained must hold for every physical system in which there is no characteristic dimension. This includes plasticity or elasticity with a strength limit. Further this includes LEFM. This is so despite the fact that the tensile strength f_t', Young's elastic modulus E and fracture energy G_f can be combined to give a length quantity, $l_0 = EG_f/f_t'^2$ (which has often been called the characteristic length, but is better called the characteristic process zone size because the former term means something else in the previously established terminology of nonlocal continuum theory). The reason that the presence of l_0 in LEFM does not destroy the validity of the power law scaling (as will also be shown by another approach later) is that, in LEFM, the fracture process zone is treated as a point, and that there is no change in failure mechanism associated with l_0 (this is in contrast to nonlinear fracture mechanics, e.g., the crack band model or the cohesive crack model).

Proving the converse, i.e., that there is no characteristic size if the scaling law is a power law, is obvious and trivial.

Note that the Weibull-type statistical strength theory in which the spatial density of the material failure probability is given by a power law with a zero threshold leads to a power-type size effect. This implies that there is no characteristic length. It follows that this theory is unrealistic for structures where a characteristic length is obviously provided by the material inhomogeneities or the size of the fracture process zone (this conclusion was reached in a different manner in Bažant and Xi, 1991).

1.2 Boundary Value Problem of Continuum Mechanics

Geometrically similar structures of different sizes are related by the affine transformation (affinity), which is the transformation of change of scale:

$$\bar{x}_i = \lambda x_i \tag{8}$$

where x_i are the Cartesian coordinates for the reference structure of characteristic dimension (size) D, and $\bar{x}_i$ are the coordinates for a geometrically similar scaled structure (Fig. 1) and $\lambda = \bar{D}/D$ where $\bar{D}$ is the characteristic dimension of the scaled structure. The primes are used to label the quantities referring to the scaled structure. For the sake of brevity, we will denote $\partial/\partial x_i = \partial_i$, $\partial/\partial \bar{x}_i = \bar{\partial}_i$. From the chain rule of differentiation, $\partial_i = \lambda \bar{\partial}_i$, $\bar{\partial}_i = \lambda^{-1} \partial_i$.

For the reference structure of size D and the similar scaled structure of size $\bar{D}$, the field equations and the boundary conditions are

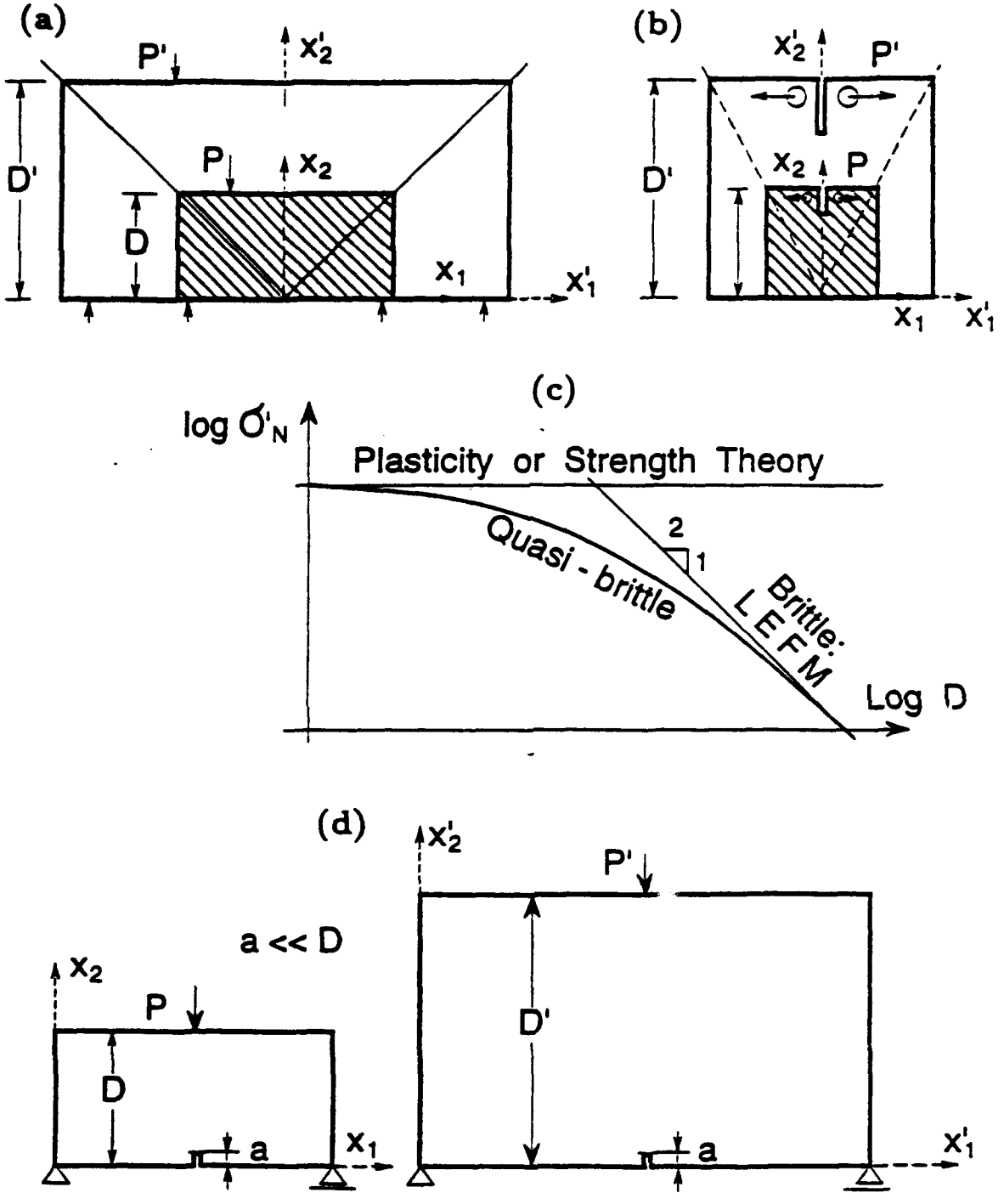

Figure 1: (a–b) Geometrical scaling of structures and affinity, (c) size effect plot, and (d) geometrically similar structures with very small cracks whose size is a material property.

For D:			For $\bar{D}$:			
$\partial_j \sigma_{ij}$	+	$f_i = 0$	$\bar{\partial}_j \bar{\sigma}_{ij}$	+	$\bar{f}_i = 0$	(9)
ε_{ij}	=	$(\partial_j u_i + \partial_i u_j)/2$	$\bar{\varepsilon}_{ij}$	=	$(\bar{\partial}_j \bar{u}_i + \bar{\partial}_i \bar{u}_j)/2$	(10)
$\sigma_{ij} n_j$	=	p_i on Γ_1	$\bar{\sigma}_{ij} \bar{n}_j$	=	$\bar{p}_i$ on $\bar{\Gamma}_1$	(11)
u_i	=	U_i on Γ_2	$\bar{u}_i$	=	$\bar{U}_i$ on $\bar{\Gamma}_2$	(12)

in which σ_{ij} and ε_{ij} are the stresses and strains in Cartesian coordinate x_i (the strains are assumed to be small), u_i = displacements of material points, Γ_1 and Γ_2 are the portions of the boundary with prescribed surface tractions p_i and with prescribed displacements U_i; f_i = prescribed volume forces; and $n_j = \bar{n}_j$ = direction cosines of unit outward normals on the stress boundary.

From equation (7) we already know that the scaling law must be a power function. Let us now assume that the displacements are related by the scaling law

$$\bar{u}_i = \lambda^{m+1} u_i \tag{13}$$

where m is an unknown exponent. Substituting this into the differential equations and boundary conditions (9)-(12), we find $\bar{\varepsilon}_{ij} = \lambda^m (\partial_j u_i + \partial_i u_j)/2$. Then according to (10) and assuming further that the stresses and strains obey the same scaling law, the following transformation rules ensue:

$$\begin{aligned} \bar{\varepsilon}_{ij} &= \varepsilon_{ij}\lambda^m, \quad \bar{\sigma}_{ij} = \sigma_{ij}\lambda^m, \quad \bar{\sigma}_N = \sigma_N \lambda^m \\ \bar{p}_i &= p_i \lambda^m, \quad \bar{f}_i = f_i \lambda^{m-1}, \quad \bar{u}_i = u_i \lambda^{m+1} \end{aligned} \tag{14}$$

These rules indicate how a solution for one size can be transformed to a solution for another size. However, the value of m is indeterminate. To determine it, we cannot ignore the constitutive law and the failure condition. Next we consider in this regard two important special cases.

1.2.1 Elastic-plastic constitutive law

The constitutive relation and the condition of no failure (either the yield condition or the condition of allowable stress) have the general form:

$$\sigma_{ij} = \mathcal{F}_{ij}(\varepsilon_{km}), \qquad \phi(\sigma_{ij}, \varepsilon_{ij}) < \sigma_0 \tag{15}$$

in which $\mathcal{F}_{ij}$ are tensor-valued functions or functionals of a tensorial argument (satisfying proper tensorial invariance restrictions), ϕ is a nonlinear scalar function of tensorial arguments, and σ_0 is the material yield limit or allowable stress limit. After transformation of scale, (15) takes the form $\bar{\sigma}_{ij} = \mathcal{F}_{ij}(\bar{\varepsilon}_{km})$, $\phi(\bar{\sigma}_{ij}, \bar{\varepsilon}_{ij}) < \sigma_0$. Since at least function ϕ (and possibly also function $\mathcal{F}$) is nonlinear (and nonhomogenous), this is possible only if $\bar{\sigma}_{ij} = \sigma_{ij}$ and $\bar{\varepsilon}_{km} = \varepsilon_{km}$, which means that $m = 0$. The transformation rules from Eqs. (13) and (15) then become

$$\begin{aligned} \bar{u}_i &= \lambda u_i, \quad \bar{\varepsilon}_{ij} = \varepsilon_{ij}, \quad \bar{\sigma}_{ij} = \sigma_{ij} \\ \bar{p}_i &= p_i, \quad \bar{f}_i = f_i/\lambda, \quad \bar{u}_i = u_i \lambda \end{aligned} \tag{16}$$

Also $\bar{\sigma}_N = \sigma_N$ (17)

that is, the nominal stress at failure does not depend on the structure size. We say in this case that there is no size effect. This is characteristic for all failure analyses according to elasticity with allowable stress limit, plasticity and classical continuum damage mechanics (as well as viscoelasticity and viscoplasticity, because time has no effect on this analysis).

1.2.2 Linear elastic fracture mechanics

a) J-integral

In this case, the constitutive relation and the condition of no failure can be written as

$$\sigma_{ij} = D_{ijkm}\varepsilon_{km}, \quad J < G_f \tag{18}$$

in which D_{ijkm} is the fourth-order tensor of elastic constants, G_f is the fracture energy (considered as a material property), and J is the J-integral;

$$J = \oint \left(\frac{1}{2}\sigma_{ij}\varepsilon_{ij}\mathrm{d}y - \sigma_{ij}n_j\partial_1 u_i \mathrm{d}s\right) \tag{19}$$

(e.g., Kanninen and Popelar, 1985; Knott, 1973). Using the transformation rules in (13)–(15), we find that the J-integral transforms as

$$\begin{aligned} \bar{J} &= \oint \left[\frac{1}{2}(\lambda^m\sigma_{ij})(\lambda^m\varepsilon_{ij})\lambda \mathrm{d}y - \lambda^m\sigma_{ij}n_j\lambda^{-1}\partial_1(\lambda^{m+1}u_i)\lambda \mathrm{d}s\right] \\ &= \lambda^{2m+1}\oint\left(\frac{1}{2}\sigma_{ij}\varepsilon_{ij}dy - \sigma_{ij}n_j\partial_1 u_i ds\right) = \lambda^{2m+1}J \end{aligned} \tag{20}$$

Since both $\bar{J}$ and J must satisfy the same inequality, that is, $\bar{J} < G_f$ and $J < G_f$ in all cases, it is obviously necessary and sufficient that $2m + 1 = 0$, that is,

$$m = -1/2 \tag{21}$$

Thus, according to (14) and (15), the transformation laws for linear elastic fracture mechanics are

$$\begin{aligned} \bar{u}_i &= u_i\sqrt{\lambda}, \quad \bar{\varepsilon}_{ij} = \varepsilon_{ij}/\sqrt{\lambda}, \quad \bar{\sigma}_{ij} = \sigma_{ij}/\sqrt{\lambda} \\ \bar{p}_i &= p_i/\sqrt{\lambda}, \quad \bar{f}_i = f_i\lambda^{-3/2}, \quad \bar{U}_i = U_i\sqrt{\lambda} \end{aligned} \tag{22}$$

$$\bar{\sigma}_N = \frac{\sigma_N}{\sqrt{\lambda}} \tag{23}$$

where $\lambda = D/\bar{D}$. So the nominal stress at failure depends on the structure size $D, \sigma_N \sim 1/\sqrt{D}$ or

$$\log\sigma_N = \text{constant} - \frac{1}{2}\log D. \tag{24}$$

In the plot of $\log\sigma_N$ versus $\log D$, the linear elastic fracture mechanics failures are represented by a straight line of slope $-\frac{1}{2}$, while all stress- or strain-based failure criteria correspond to a horizontal line (Fig. 2).

The foregoing argument can be generalized to nonlinear elastic behavior, to which the J-integral is also applicable.

b) Work of stresses during separation

For the case of LEFM, the same result can alternatively be obtained in a more elementary manner. The energy release rate can be calculated by imagining a small crack advance of length h to happen in the following manner: 1) A slit of length h is cut ahead of the crack but is held closed. 2) The normal stresses σ_y acting across the slit are then gradually reduced in proportion to $(1-\tau)$ where τ is a parameter growing from 0 to 1. 3) At the same time, because the body is linear elastic, opening displacements of the crack faces grow in proportion to τ until they reach the final opening displacements of a crack with the tip advanced by h. The work of σ_y on u_y at both crack faces gives the energy release per length h which must be consumed by the fracture process. Because $\int_0^1(1-\tau)\mathrm{d}\tau = 1/2$ and the stresses σ_y work on both crack faces, the work per unit crack advance, i.e., the energy release rate, is

$$\mathcal{G} = \lim_{h\to 0}\frac{1}{h}\int_0^h \sigma_y u_y \mathrm{d}x \tag{25}$$

(e.g., Eq. 4.5.2 in Knott, 1973, or Eq. 12.1.7 in Bažant and Cedolin, 1991) where x is the coordinate in the crack direction. Using the foregoing transformation rules, we find that for the scaled structure the energy release rate is

$$\begin{aligned}\bar{\mathcal{G}} &= \lim_{h\to 0}\frac{1}{h}\int_0^h (\lambda^m\sigma_y)(\lambda^{m+1}u_y)\mathrm{d}x \\ &= \lambda^{2m+1}\lim_{h\to 0}\frac{1}{h}\int_0^h \sigma_y u_y \mathrm{d}x = \lambda^{2m+1}\mathcal{G}\end{aligned} \tag{26}$$

which must be the same as the energy release rate given by the preceding equation. Consequently, $\lambda^{2m+1} = 1$ or $m = -1/2$.

1.3 Alternative derivation: dimensional analysis

In an alternative way which is shorter but more abstract, and thus to a novice less convincing, the size effect can be determined by dimensional analysis. When the structure is elastic-plastic, its failure is governed by the yield stress τ_0, whose metric dimension is N/m^2. The failure also depends on the nominal stress σ_N, whose metric dimension is also N/m^2. Further, it depends on the characteristic structure size dimension D and other dimensions such as span L, notch length a and various other geometric characteristics all of which have the metric dimension of m.

The number of nondimensional variables governing the problem can be determined from Buckingham's Π theorem of dimensional analysis (Buckingham 1914, 1915; see also Bridgman, 1922; Porter, 1933; Giles, 1962; Streeter and Wylie, 1975; Barenblatt, 1979, 1987; Iyanaga and Kawada, 1980). This theorem states that the number of nondimensional variables governing any physical problem is equal to the total number of variables (in these cases five or more) minus the number of parameters with independent dimensions (in these cases two). Thus, it turns out that the failure condition must have the form

$$\Phi\left(\frac{\sigma_N}{\tau_0}, \frac{L}{D}, \frac{a}{D}, \ldots\right) = 0 \tag{27}$$

where Φ is a function. Since τ_0 is a constant, and for geometrically similar structures also $L/D, a/D, \ldots$ are constants, it follows that the nominal stress at failure, σ_N, must be proportional to τ_0, and therefore a constant when the structure size D is varied.

In linear elastic fracture mechanics, the failure is determined by the value of the critical stress intensity factor K_{I_f}, the metric dimension of which is $Nm^{-3/2}$. The other quantities determining failure are the same as before, including σ_N, D, L, a, etc. Again, the number of nondimensional variables on which the failure can depend follows from Buckingham's Π theorem and it turns out that the failure condition must now have the form

$$\Phi\left(\frac{\sigma_N\sqrt{D}}{K_{I_f}}, \frac{L}{D}, \frac{a}{D}, \ldots\right) = 0 \tag{28}$$

Since K_{I_f} is a material constant, and since the ratios $L/D, a/D, \ldots$ are all constant for geometrically similar structures, it follows that $\sigma_N\sqrt{D}$ must also be constant. Hence, $\sigma_N \sim D^{-1/2}$, which agrees with what we have already shown (e.g. Bažant, 1983, 1984; Carpinteri 1984, 1986).

1.4 Scaling Laws for Structures with Characteristic Dimension

1.4.1 Transitional Scaling for Nonlinear Fracture Mechanics or Quasibrittle Behavior

In nonlinear fracture mechanics, the criterion of crack propagation is characterized by both an energy quantity (the fracture energy G_f) and a stress quantity (strength f'_t or yield stress f_y). At first one might think that the size effect would be a power law with a constant exponent intermediate between 0 and $-1/2$. However, this is not true. Because the ratio G_f/f'_t has the dimension of length (in the metric system, it is N/m divided by N/m^2), a characteristic length is present in the problem, and so the assumptions underlying equation (7) are invalid. Hence, the scaling law cannot be a power law.

Previous studies (Bažant, 1983, 1984; Bažant, 1987; Bažant and Pfeiffer, 1987; Bažant and Kazemi, 1990; etc.) have shown that the scaling law represents a gradual transition from the strength theory to LEFM. This transition has the shape of the curve plotted in Fig. 1c, which was experimentally obtained for notched three-point-bend specimens already by Walsh (1979). This curve approaches asymptotically the horizontal line for the strength theory when the size is becoming very small, and the inclined straight line for LEFM when the size is becoming very large. A general exact expression for this curve cannot be obtained. However, under certain simplifying assumptions, on can derive the following approximate size effect law (Bažant, 1983, 1984): $\sigma_N = C_0(1+\beta)^{-1/2}$ with $\beta = D/D_0$ where β = relative size and C_0, D_0 = positive constants (see the curve in Fig. 1c).

The simple size effect law proposed by Bažant(1983, 1984), whose applicability range is surprisingly broad, albeit not unlimited, has been extensively experimentally verified and applied for quasi-brittle materials such as concrete, rocks, ice, tough ceramics and composites, in which the fracture process zone has a non-negligible size and consists of distributed microcracking. This law has been shown to describe well the typical brittle failures of concrete structures, particularly the diagonal shear failure of beams, torsional

failure of beams, punching shear failure of slabs, pullout of bars and anchors, failure of bar splices, certain types of compressions failures, failure of short and slender columns, and beam and ring failures of pipes. It has also been shown that this law can be used for unambiguous definition of material fracture characteristics, especially the fracture energy (or fracture toughness) and the effective length of the fracture process zone, and for their determination from the peak loads measured on similar specimens of different sizes (e.g.Bažant and Kazemi, 1990).

1.5 Weibull Theory for Structures with Critical Crack Size Independent of Structure Size

There is a fundamental difference between the classical applications of fracture mechanics to metallic structures and the modern applications to quasi-brittle structures such as concrete structures:

- In the former, the maximum load occurs (or failure must be assumed to occur) while the crack size is still negligible compared to the structural dimensions (Fig. 1d) and is determined by material characteristics such as the spacing of major defects, the grain size, or the ratio of fracture energy to yield stress.
- In the latter, there is large stable crack growth (with distributed damage) before the maximum load is reached, and the maximum load occurs when the crack extends over a significant portion of the cross section (in concrete structures it is typically 50% to 90%).

Consider now geometrically similar metallic structures of different sizes, made of the same material. The cracks at maximum load are, in each of them, roughly of the same size, and they are so small that the disturbance of the stress field caused by the crack is negligible and the energy release caused by the crack is much smaller than the strain energy stored in the structure. In that case, the energy release rate $\mathcal{G}$ can be approximately determined from the stress σ (maximum principal stress) that is calculated for the crack location as if no crack existed. Then, considering for example a crack of length $2a$ in two dimensions, the stress intensity factor (obtained from the energy release as $K_I = \sqrt{E\mathcal{G}}$) is approximately calculated from the formula $K_I = \sigma\sqrt{\pi a}$ which is exact for a crack in a homogeneously stressed infinite solid. The condition of no failure is written as $K_I < K_c$ where K_c is the given fracture toughness of the material. Obviously, this condition of no failure is equivalent to

$$\sigma < f_u, \qquad \text{with} \quad f_u = K_c(\pi a)^{-1/2} \tag{29}$$

This is the same as the strength criterion, with f_u regarded as the strength of the material.

In some other situations, the crack size at maximum load is not negligible but is independent of the structure size. Then again the fracture mechanics failure criterion is equivalent to the strength criterion, which means that the scaling law is such that there is no size effect on the nominal strength.

In the situations just discussed, in which the critical crack size is independent of the structure size, there can be size effect on the nominal strength, but it is not deterministic.

Rather, it is caused by randomness of material strength, as described by Weibull-type statistical theories (Weibull, 1939; Freudenthal, 1968; Bolotin, 1969; Elishakoff, 1983).

The Weibull law for the spatial density of material failure probability in general involves a stress threshold below which the failure probability is zero. In practical applications this threshold is almost always taken as zero because the test data can be matched by this law also almost equally well with very different threshold values. It is interesting to note that, for a zero threshold, the size effect predicted by the Weibull theory is a power law (e.g., Bažant Xi and Reid, 1991). It follows that, according to (7), the Weibull theory for a zero threshold implies that no characteristic structure dimension exists. But this implies Weibull theory cannot apply to structures in which the fracture process zone size has a certain nonnegligible characteristic dimension. Indeed, the statistical size effect is significant only when the structure fails while the crack is still very small, such that the stress redistribution caused by the crack is globally insignificant and the energy release caused by the crack is negligible compared to the total energy in the structure.

Randomness of the material strength is of course an inevitable property of materials and its influence is never exactly zero. In quasi-brittle structures, however, the Weibull-type statistical size effect is overshadowed by the size effect due to energy release and gets completely suppressed as the size approaches infinity. Proposing a nonlocal adaptation of Weibull theory in which the material failure probability depends on the strain average over a certain characteristic neighborhood of the point rather than on the local stress, Bažant and Xi (1991) derived the following approximate formula:

$$\sigma_N = C_0 (\beta^{2n/m} + \beta)^{-1/2}, \qquad \beta = D/D_0 \tag{30}$$

in which C_0, D_0, m and n are positive constants; n is the number of dimensions (1, 2 or 3) and m is the Weibull modulus of the material. Normally the exponent $2n/m$ is much less than 1. According to this formula, the classical Weibull-type statistical size effect $\sigma_N \propto D^{2n/m}$ is approached asymptotically for sufficiently small structures ($\beta \to 0$). But the available test results show this asymptotic behavior to apply, in theory, only to structure sizes that are less than the smallest practical size. In other words, the material strength is random but causes no significant size effect, for any size range. For large structures ($\beta \to \infty$), the last equation indicates that $\sigma_N \propto D^{-1/2}$, that is, the statistical size effect asymptotically disappears. The reason, briefly, is that a significant contribution to the Weibull-type probability integral comes only from the fracture process zone which is large but for structures of different sizes has roughly the same size.

2 Theory of Size Effect in Quasibrittle Compressive Failure

Theoretically it is clear that a non-statistical size effect must also exist in quasibrittle compression failures. The reasons are as follows:

- Quasibrittle materials such as concrete, rock and most advanced composites are not elasto- plastic in compression because the stress gradually decreases after the peak and the load-deflection diagram exhibits post-peak gradual softening instead of terminating with a long plastic plateau.

- The failure is a fracture process, in which the energy release matters.

- The coarse microstructure of quasibrittle materials indicates that there must be a characteristic dimension. This excludes the scaling according to a power law, and in particular the case of zero exponent corresponding to the absence of size effect.

That quasibrittle compressive failures exhibit size effect has been confirmed experimentally. For example, Bažant and Kwon (1992, 1993) conducted tests of geometrically similar tied reinforced columns made from microconcrete with reduced size aggregate (maximum size 1/8 in.), and found a significant size effect. This size effect is contradicted by the existing design codes, which all predict no size effect as they are based on elasticity and plasticity. The columns in these tests were geometrically similar, and the reinforcement was of course scaled, too. The cross sections were squares of sides 0.5 in., 1 in., and 2 in., and the slendernesses were 19, 36 and 53.

Compression fracture is a formidable problem, more complex than tensile fracture. Many results have already been obtained (Bažant, 1967; Biot, 1965; Horii and Nemat-Nasser, 1985, 1986; Kendall, 1978; Sammis and Ashby, 1986; Shetty et al., 1986; Batto and Schulson, 1993; and others). However, most studies were actually solving the problem of initiation of compression fracture from various types of defects, such as wedging inclusion configurations or the spread of wing-tip cracks from an inclined microcrack, which govern the initial behavior long before the maximum load is approached. The maximum load is determined by a global mechanism, which has not been adequately illuminated, although it is clear that internal instability of the damaged material must play a dominant role (Biot, 1985; Bažant, 1987).

In the second part of this lecture, we will now concisely outline a new mathematical model characterized by (1) energy release analysis, and (2) instability with post-critical buckling of microslabs of the material between adjacent splitting cracks. The detailed analysis will be presented in Bažant and Xiang (1993).

2.1 Stocky Columns

Consider a column (a beam) shown in Fig. 2a, having length L, width D (characteristic dimension) and unit thickness $b = 1$. One end cross section is fixed. The other is subjected to axial displacement u and rotation θ and is loaded by axial compressive force P of eccentricity e. The initial normal stress in the cross sections before any fracturing is

$$\sigma_0(x) = -\frac{E}{L}\left[u + \theta\left(\frac{D}{2} - x\right)\right] \tag{31}$$

where E = Young's elastic modulus, and x = transverse coordinate measured from the compressed face (Fig. 2a). We now assume that, a certain moment of loading, axial cracks of spacing s and length h, forming a band as shown in Fig. 2a,b,c, suddenly appear and the slabs of the material between the axial cracks, behaving as beams of depth s, lose stability and buckle. This can happen in any one of the three mechanisms shown in Fig. 2a,b,c, and for all of them the mathematics turns out to be identical. If the length of the cracks in the two inclined bands in Fig. 2c is denoted as $h/2$. The critical stress for the microslab buckling shown in Fig. 2a,b,c is, in all cases,

$$\sigma_{cr} = -\frac{\pi^2 E s^2}{3h^2} \tag{32}$$

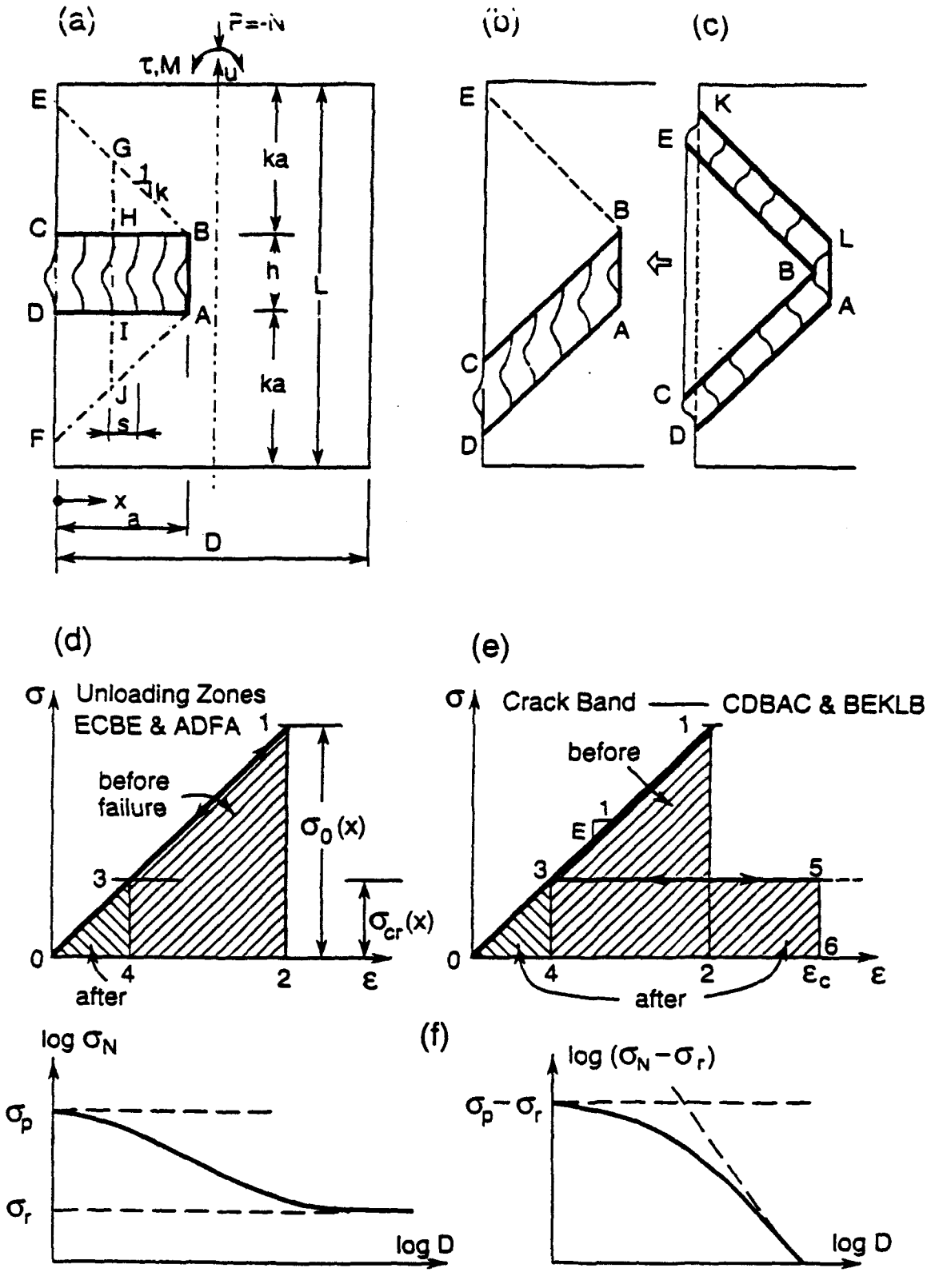

Figure 2: (a-c) Splitting cracks, buckling of microslabs and stress relief zone, (d-e) stress-strain diagrams with an without buckling and areas representing strain energy changes, (f) size effect deduced for compression failures

The key idea is now the calculation of the change in stored strain energy caused by buckling. On the side of the crack band, there is obviously a zone in which the initial stress σ_0 is reduced. For the sake of simplified analysis we assume that the stress in the shaded triangle areas of Fig. 2a,b,c is reduced all the way to σ_{cr} and outside these areas the initial stress does not change. The triangular areas are limited by the so-called "stress diffusion lines" of slope k, whose magnitude is close to 1 but can be reliably determined only by experiment or by accurate solution of the two-dimensional boundary value problem. For the analysis of size effect, however, the only important fact is that k is a constant if geometrically similar columns are considered. In these shaded triangular stress-relief zones, the strain energy density before and after fracture is indicated by triangles 0120 and 0340 in Fig. 2d, and so the loss of strain energy density on a vertical line of coordinate x is

$$\Delta\bar{\Pi}_r = \frac{\sigma_0^2(x)}{2E} - \frac{\sigma_{cr}^2(x)}{2E} \tag{33}$$

The situation is more complicated in the crack band. The microslabs buckle, and the energy associated with the postbuckling behavior must be taken into account, which is a key idea proposed in this lecture. The strain energy density before buckling of the microslabs is given by the area 0120 in Fig. 2e. The analysis of postbuckling behavior of columns (Bažant and Cedolin, 1991, Sec. 1.9 and 5.9) indicates that the stress in the axis of the microslab follows after the attainment of the critical load the straight line 35 which has a very small positive slope (precisely equal to $\sigma_{cr}/2$). This slope is far smaller than the slope E before buckling and can therefore be neglected. So the postbuckling behavior is approximately a horizontal plateau 35 in Fig. 2e, however, is not the same as plastic behavior because unloading proceeds along the path 530. Because the microslabs remain elastic during buckling, the stress-strain diagram 035 is fully reversible and the energy under this diagram is the stored elastic strain energy. The triangular area 0340 in Fig. 2e represents the axial strain energy density of the microslabs and the rectangular area 35643 represents the bending energy density. The change in strain energy density in the microslabs is the difference of areas 0120 and 03560 in Fig. 2e, that is,

$$\Delta\bar{\Pi}_c = \frac{\sigma_0^2(x)}{2E} - \left[\sigma_{cr}(x)\epsilon_c(x) - \frac{\sigma_{cr}^2(x)}{2E}\right] \tag{34}$$

where ϵ_c is the axial strain of the microslabs in the crack band after buckling (it is important that it is generally not equal to 04 or 02 in Fig. 2e).

Integration of (33) and (34) yields the total loss of potential energy at constant u and σ:

$$\begin{aligned}\Delta\bar{\Pi} &= \int_0^a \left(\frac{\sigma_0^2(x)}{2E} - \frac{\sigma_{cr}^2(x)}{2E}\right) 2k(a-x)dx \\ &+ \int_0^a \left\{\frac{\sigma_0^2(x)}{2E}\left[\sigma_{cr}(x)\epsilon_c(x) - \frac{\sigma_{cr}^2(x)}{2E}\right]\right\} h dx\end{aligned} \tag{35}$$

where a = horizontal length of the crack band (Fig. 2a,b,c). This energy must be equal to the energy consumed by the formation of the surfaces of all the axial splitting cracks. Thus, the energy balance criterion of fracture mechanics may be written as:

$$-\left[\frac{\partial\Delta\Pi}{\partial a}\right]_{\theta,u} = \frac{\partial}{\partial a}\left(G_f h\frac{a}{s}\right) = \frac{h}{s}G_f \tag{36}$$

where G_f is the fracture energy of the axial splitting cracks, assumed to be a material property.

The axial strain in the crack band can be determined from the compatibility condition. Because the end cross sections are assumed to be fixed during buckling (i.e., u, θ = constant), the stress in the blank areas of the column in Fig. 2a,b,c remains constant, and so the line segment GJ in Fig. 2a at any * does not change length. Expressing the change of length of this segment on the basis of σ_{cr}, ϵ_c and σ_0 and setting this change to zero, one obtains the following compatibility condition

$$\epsilon_c(x) = \frac{\sigma_0(x)}{Eh}[h + 2k(a-x)] - \frac{2k}{h}(a-x)\frac{\sigma_{cr}(x)}{E} \tag{37}$$

The length h of the axial cracks, representing the width of the crack band in Fig. 2a,b or double the crack band width in Fig. 2c, is an important parameter that must be determined. The critical stress according to (32) would decrease with increasing h, and so the largest energy release would be obtained for $h \to \infty$. Since the largest energy release is what must happen (because of thermodynamic considerations; Bažant and Cedolin, 1991, chapters 10 and 12) the prediction would be $\sigma_{cr} = 0$, which is however unreasonable. In a recent study of the role of axial splitting cracks in borehole breakout (Bažant, Lin, and Lippmann, 1993), the microslab buckling was assumed to be opposed by shear stresses on the microcracks taken as proportional to the slip on the microcracks. That assumption leads to a more complicated formula for σ_{cr} than before, and it is noteworthy that the minimum σ_{cr} is now obtained for a certain finite value of h. Furthermore, in reinforced concrete columns the crack length is no doubt strongly influenced by the elastic stiffness and spacing of the ties or the pitch of the spiral.

In this preliminary exposition, we prefer to keep only the essential ingredients of the analysis necessary to illustrate the idea, and so we will simply assume that h is a given constant (the problem will explored deeper in Bažant and Xiang, 1993).

We must now substitute Eqs. (31) - (34) and (36) into (36) and integrate. Although it is no problem to calculate the integral exactly, the resulting expression is lengthy and in view of the approximate nature of the entire analysis we prefer to evaluate the integral approximately, taking the value of the integrand at the centroid of the triangles, $x = a/3$ and multiplying it by length L. This yields

$$\begin{aligned}\Delta\Pi \;=\; & a\frac{4ka}{Eh}\left(\frac{\sigma_0^2}{2E} - \frac{\pi^4 E s^4}{18h^4}\right) \\ & + ah\left(\frac{\sigma_0^2}{2E} - \left\{-\frac{\pi^2 E s^2}{3h^2}\left[\frac{\sigma_0}{Eh}\left(h + \frac{4ka}{3}\right) + \frac{4ka}{3h}\frac{\pi^2 s^2}{3h^2}\right] - \frac{\pi^4 E s^4}{18h^4}\right\}\right)\end{aligned} \tag{38}$$

Substituting this into the energy criterion of crack band propagation, we get

$$\begin{aligned}\frac{8k}{3}\quad & \alpha D\left(\frac{\sigma_0^2 s}{2h} - \frac{\pi^4}{18}\frac{E^2 s^5}{h^5}\right) + s\left\{\frac{\sigma_0^2}{2} + \frac{\pi^2 E^2 s^2}{3h^2}\left[\frac{\sigma_0}{E}\left(1 + \frac{2k\alpha D}{3h}\right)\right.\right. \\ & \left.\left. + \frac{4\pi^2 k\alpha D s^2}{9h^2}\right] + \frac{\pi^4 E^2 s^4}{18h^4}\right\} + \alpha D E^2 \frac{\pi^2 s^3}{3h^3}\left(\frac{4k\sigma_0}{E} + \frac{4k\pi^2 s^2}{9h^2}\right) = EG_f\end{aligned} \tag{39}$$

It is also helpful to relate stress σ_0 at $x = a/3$ to the nominal stress σ_N defined as the maximum stress in the beam just before fracturing;

$$\sigma_N = -k_N\sigma_0 \qquad k_N = \left(1 + \frac{6e}{D}\right)\left[1 + \frac{6e}{D}\left(1 - \frac{2a}{3D}\right)\right]^{-1} \tag{40}$$

Now, k_N is a constant when geometrically similar columns with similar cracks are considered, and so is α. So Eq. (40) can be written as

$$C_1\sigma_0^2 D + C_2\sigma_0^2 + C_3\sigma_0 D + C_4\sigma_0 + C_5 D + C_6 = 0 \tag{41}$$

in which $\alpha = a/D$ and $C_1, \ldots C_6$ are constants if geometrically similar columns with geometrically similar crack bands are considered. From this equation we have

$$D = -\frac{C_2\sigma_0^2 + C_4\sigma_0 + C_6}{\alpha(C_1\sigma_0^2 + C_3\sigma_0 + C_5)} = \frac{C_0(\sigma_q - \sigma_N)(\sigma_p - \sigma_N)}{(\sigma_s - \sigma_N)(\sigma_N - \sigma_r)} \tag{42}$$

C_0 = constant; σ_s, σ_r are the larger and smaller roots of the quadratic polynomial in the denominator of (42), and σ_q, σ_p are the larger and smaller roots of the quadratic polynomial in the numerator of (42). For physical reasons, we expect the roots to be real and such that $\sigma_s > \sigma_p > \sigma_r$ and $\sigma_q > \sigma_p$.

Eq. (42) yields the size effect plot sketched in Fig. 2f. This plot represents a transition from the plastic limit σ_p approached for $D \to 0$ to the residual nominal stress σ_r approached for $D \to \infty$. So the conclusion from our analysis is that compression failure caused by lateral propagation of bands of axial splitting cracks and buckling of the microslabs between the cracks ought to exhibit a size effect.

It is interesting to note that the foregoing result is similar to the generalization of the size effect law proposed in Bažant (1987) for the compression failure in the Brazilian split-tensile test, which reads

$$\sigma_N = (\sigma_p - \sigma_r)\left(1 + \frac{D}{D_0}\right)^{-1/2} + \sigma_r \tag{43}$$

where D_0 = constant (transitional size). The plot of this equation has a same shape as Fig. 2f. Inverting this equation, one has

$$D = D_0 \frac{-\sigma_N^2 + 2\sigma_r\sigma_r + \sigma_p(2\sigma_r - \sigma_p)}{\sigma_N^2 - 2\sigma_r\sigma_N + \sigma_r^2} \tag{44}$$

It is interesting to note the analogy to (42), although both equations do not coincide.

2.2 Slenderness Effect

In the experiments of Bažant and Kwon (1993) it was observed that the size effect in columns becomes more pronounced with increasing slenderness. The foregoing solution of size effect, given by (42), corresponds to small slenderness L/D_0. The size effect that this equation describes may be denoted as $\sigma_N = f(D)$ where f is the function implicitly defined by (42).

If the column is slender, one must take into account the release of potential energy from the deflected column. An easy way to calculate it is to imagine the end cross sections of the column segment that undergo relative displacement u and relative rotation θ and are distance L apart (Fig. 2) to be right next to the stress relief zone and assume that $L \ll l$. To determine the energy release from the column, we assume that during the advance of crack length, da, the values of u and θ remain constant. This means that the applied load, P, the load-point displacement at the end of the column, u_a, and the

midspan deflection u all change. In this case, the change of stresses and deformations due to column buckling does not interfere with the triangular energy release zones we considered earlier (Fig. 2). We could of course calculate the energy release at fixed load-point displacement or at a fixed load, but in that case the strains and stresses in the unshaded area in Fig. 2 would not remain constant, but would change, which would invalidate our preceding calculation. This is a basic idea of the present approach.

Consider the column to be hinged and take the deflection curve approximately as $z \approx w \sin(\pi y/l)$ where w = midheight deflection, y= longitudinal coordinate. The change in the axial force and moment at midlength can be calculated from the change of the stress distribution due to the extension of the band of splitting cracks by da:

$$dP = [\sigma_{cr} - \sigma_0(a)]da, \quad dM = [\sigma_{cr} - \sigma_0(a)]\left(\frac{P}{2} - a\right)da \tag{45}$$

where σ_{cr} is the critical stress in the microslabs. Load P is assumed to have a constant eccentricity e at the ends of column, and so $M = P(e + w)$ or $w = (M/P) - e$. Differentiating, we have

$$dw = \frac{1}{P}[dM - (e + w)dP] \tag{46}$$

The axial shortening due to deflections w is $u_a = \int_0^\ell (z')^2 dy/2 = \pi^2 w^2/4\ell$, and so the work of the axial load during da is

$$dW = P du_0 = P\frac{\pi^2}{2\ell} w dw \tag{47}$$

The change of stored bending energy during da is $dU = d\int_0^\ell EI(z'')^2 dy/2 = d(\pi^4 EI w^2/4\ell^3)$, that is

$$dU = \pi^4 EI w dw/2\ell^3 \tag{48}$$

where I = moment of inertia of the cross section of column.

The change of potential energy due to axial elastic strains is $d\Pi_a = -d\Pi_a^* = -d(P^2\ell/2EA)$ where A = cross section area of column and Π_a^* is the complementary energy due to axial deformations. Now the change of potential energy during da due to column deformation is $d\Pi = dU - dW + d\Pi_a$, and the additional energy release due to column deformation, which needs to be added to that calculated before in Eq. (36), is given by

$$d\Pi = \mathcal{G}_2 da = -\frac{\pi^2}{2\ell}(P_{cr} - P)\, w dw - \frac{\ell}{EA} P dP \tag{49}$$

In this equation $P_{cr} = \pi^2 EI/l^2$ = first critical load of hinged column.

It may be now be noted that if the column is axially very stiff and $P = P_{cr}$, there is no energy release due to column deformation, which might have been expected. When $P_{cr} > P$, there is a positive energy release because dw and PdP are negative during crack band extension. The additional energy release must obviously promote fracture, and thus it must intensify the size effect. It remains to study the foregoing results numerically, which will be done in Bažant and Xiang (1993).

2.3 Alternative Simpler Approach to Slenderness

The influence of column slenderness on the size effect can also be approximately described by a simpler alternative calculation based on matching the midheight maximum stress from column buckling with the stress associated with crack band growth. The effect of slenderness is to cause lateral deflection, which is in the mid-span of the column approximately equal to μe where μ is the magnification factor $\mu = [1 - (P/P_{cr_1})]^{-1}$; P_{cr_1} is the first critical load of the column, whose value decreases with increasing slenderness D/L. Writing now the same definition of the nominal stress as for small slenderness and imposing the condition that the stress given by the size effect law be the maximum stress in the deflected slender column, we have:

$$\sigma_N = \frac{P}{D}\left(1 + \frac{6e}{D}\right), \qquad \frac{P}{D}\left[1 + \frac{6e}{D}\left(1 - \frac{P}{P_{cr_1}}\right)^{-1}\right] = f(D) \tag{50}$$

The size effect plot of σ_N versus D is the solution of these two equations, in which P is a parameter to be eliminated. Obviously, the size effect will be more pronounced for higher slenderness.

2.4 Borehole Break-out

A size effect has also been deduced for borehole breakout in rock under certain simplifying hypotheses. In an infinite elastic space that is initially under uniform triaxial stress with minimum principal stress σ_N, a cylindrical borehole of diameter D is drilled. This causes a zone of parallel splitting cracks to form at the sides of the borehole. For various borehole diameters D, these zones are considered to be similar and have elliptical shapes. The growth of the cracking zone causes a release of the stored energy which must be equal to the energy consumed by the growth of the cracks. Using this condition and assuming the splitting cracks to follow LEFM, Bažant, Lin and Lippmann (1991) showed that $\sigma_N \propto D^{-2/5}$. The reason that the exponent in not $-1/2$ is twofold: (1) There is not one but many cracks, and (2) the spacing s of the cracks is not proportional to D but to $D^{4/5}$, which results from the analysis of buckling of the intact rock slabs between the parallel cracks.

3 Conclusions

The scaling law for nominal stress at failure is a power law if and only if there is no characteristic dimension of the structure. This applies to elasticity, plasticity, continuum damage mechanics and linear elastic fracture mechanics. In quasibrittle or nonlinear fracture, the scaling law is a transition between asymptotes representing plasticity and linear elastic fracture mechanics, provided that the fractures at the maximum load are geometrically similar. When a structure fails at the crack initiation from a flaw whose size is a material property, independent of the structure size, there is no deterministic size effect, but a size effect is obtained as a consequence of the randomness of strength, as described by Weibull-type statistical theory. The size effect in compressive failure, which has been brought to light by recent experiments, can be theoretically explained by lateral propagation of a band of axial splitting cracks and buckling of microslabs of the material

between the adjacent cracks. Analysis of the fracture energy release in this mechanism must take into account the postcritical deflections of the microslabs. This theory leads to a transitional size effect law terminating with a finite residual stress. An increase of column slenderness intensifies the size effect.

ACKNOWLEDGMENT.—The study of scaling laws was supported under ONR Grant N00014-91-J-1109 to Northwestern University, and the study of the splitting microcrack mechanism compression failure was supported under AFOSR Grant 91-0140 to Northwestern University.

References

Ashby, M.F., and Hallam, S.D. (1986). The failure of brittle solids containing small cracks under compressive stress states. *Acta Metall.*, Vol. 34, No. 3, 497–510.

Barenblatt, G.I. (1979). *Similarity, self-similarity, and intermediate asymptotics.* Consultants Bureau, New York and London.

Barenblatt, G.I. (1987). *Dimensional analysis*, Gordon and Breach, New York.

Batto, R.A., and Schulson, E.M. (1993). On the ductile-to-brittle transition in ice under compression, *Acta metall. mater.*, 41(7), 2219–2225.

Bažant, Z.P. (1967). Stability of continuum and compression strength, (in French), *Bulletin RILEM*, Paris, No. 39, 99-112.

Bažant, Z.P. (1983). Fracture in concrete and reinforced concrete, Preprints, IUTAM Prager Symposium on *Mechanics of Geomaterials: Rocks, Concretes, Soils.* ed. by Z.P. Bažant, Northwestern University, Evanston, IL, 281–316 (Eq. 16).

Bažant, Z. P. (1984). Size effect in blunt fracture: concrete, rock, metal, *J. of Engng. Mechanics*, ASCE, 110, 518–535.

Bažant, Z. P. (1987). Fracture energy of heterogeneous material and similitude. Preprints, *SEM-RILEM Int. Conf. on Fracture of Concrete and Rock* (held in Houston, Texas, June 1987), ed. by S. P. Shah and S. E. Swartz, publ. by SEM (Soc. for Exper. Mech.) 390–402.

Bažant, Z.P. (1992a). Large-scale fracture of sea ice plates, *Proc., 11th IAHR International Ice Symposium* (held in Banff, Alberta, in June), ed. by T.M. Hrudey, Univ. of Alberta, Edmonton, Vol. 2, 991–1005.

Bažant, Z.P. (1992b). Large-scale thermal bending fracture of sea ice plates, *J. of Geophysical Research* 97 (No. C11), 17,739–17,751.

Bažant, Z.P. (1993). Scaling Law in Mechanics of Failure, *J. of Engineering Mechanics ASCE* 119, in press.

Bažant, Z. P., and Pfeiffer, P. A. (1987). Determination of fracture energy from size effect and brittleness number, *ACI Materials Jour.*, 84, 463–480.

Bažant, Z. P. and Kazemi, M. T. (1990). Size effect in fracture of ceramics and its use to determine fracture energy and effective process zone length, *J. of American Ceramic Society* 73(7), 1841–1853.

Bažant, Z.P., and Cedolin, L. (1991). *Stability of Structures: Elastic, Inelastic, Fracture and Damage Theories* (textbook and reference volume), Oxford University Press, New York, 1991 (984 + xxvi pp.).

Bažant, Z.P., Lin, F.-B., and Lippmann, H. (1991). Fracture energy release and size effect in borehole breakout, Structural Engineering Report 91-11/457f, Northwestern University; also *Int. J. of Num. and Anal. Methods in Geomechanics*—in press.

Bažant, Z.P. Xi, Y., and Reid, S.G. (1991). Statistical size effect in quasi-brittle structures: I. Is Weibull theory applicable? ASCE *J. of Engineering Mechanics* 117(11), 2609–2622.

Bažant, Z.P., and Xi, Y. (1991). Statistical size effect in quasi-brittle structures: II. Nonlocal theory. ASCE *J. of Engineering Mechanics* 117(11), 2623–2640.

Bažant, Z.P., and Xiang, Y. (1993). Stability analysis of size effect in compression fracture of quasibrittle short and slender R.C. columns, Report in preparation, Northwestern University.

Biot, M.A. (1965). *Mechanics of Incremental Deformations*, John Wiley & Sons, New York.

Bridgman. P.W. (1922). *Dimensional analysis*, Yale University Press, New Haven.

Bolotin, V.V. (1969). *Statistical methods in structural mechanics*. Holden Day, San Francisco (transl. from Russian).

Buckingham, E. (1914). On physically linear systems; illustrations of the use of dimensional equations, *Physical Review* Ser.2. Vol.IV, No.4, 345–376.

Buckingham, E. (1915). Model experiments and the form of empirical equations. *Trans. ASME* 37, 263–296 (also *Phys. Rev.* 4, 345–376).

Carpinteri, A. (1984). Scale effects in fracture of plain and reinforced concrete structures, in *Fracture Mechanics of Concrete: Structural Application and Numerical Calculation*, ed. by G.C. Sih and A. DiTommaso, Martinus Nijhoff Publ., The Hague, 95–140.

Carpinteri, A. (1986). *Mechanical damage and crack growth in concrete*, Martinus Nijhoff Publ., Dordrecht—Boston (chapter 8).

Elishakoff, I. (1983). *Probabilistic methods in the theory of structures*. John Wiley & Sons, New York.

Freudenthal, A.M. (1968). Statistical approach to brittle fracture. in *Fracture—An advanced treatise*. H. Liebowitz, ed., Vol.2, Academic Press, 591–619.

Giles, R.V. (1962). *Theory and problems of fluid mechanics and hydraulics*, McGraw Hill, New York (chapter 5). *Application of Fracture Mechanics to Cementitious Composites*, ed. S. Shah, Martinus Nijhoff Publ., Dordrecht, pp. 617–638.

Horii, H., and Nemat-Nasser, S. (1985). Compression-induced microcrack growth in brittle solids: Axial splitting and shear failure, *J. of Geophys. Res.*, Vol. 90, 3105–3125.

Horii, H., and Nemat-Nasser, S. (1986). Brittle failure in compression, splitting, faulting and brittle-ductile transition, Phil. Tran. Royal Soc. London, 319(1549), 337–374.

Iyanaga, S., and Kawada, Y., Editors (1980). *Encyclopedic dictionary of mathematics*, MIT Press, Cambridge, Sec. 120 (pp. 412–413).

Kanninen, M.F., and Popelar, Carl H.(1985). *Advanced fracture mechanics*, Oxford University Press, New York, 1985.

Kendall, K. (1978). Complexities of compression failure, Proc. Royal Soc. London., A., 361, 245–263.

Knott, J.F. (1973). *Fundamentals of fracture mechanics*, Butterworth, London.

Porter, A.W. (1933). *The method of dimensions*, Methuen.

Sammis, C.G., and Ashby, M.F. (1986). The failure of brittle porous solids under compressive stress state, *Acta Metall*, 34(3), 511–526.

Shetty, D.K., Rosenfield, A.R., and Duckworth, W.H. (1986). Mixed mode fracture of ceramics in diametral compression, *J. Am. Ceram. Soc.*, 69(6), 437–443.

Streeter, V.L., and Wylie, E.B. (1975). *Fluid mechanics* (6th ed.), McGraw Hill, New York (chapter 4).

Walsh, P.F. (1979). Fracture of plain concrete, *The Indian Concrete Journal* 46 (11), pp. 469, 470 and 476.

Weibull, W. (1939). A statistical theory of the strength of materials. *Royal Swedish Academy of Engng. Sci., Proc.*, 151, 1–45.

[87]

FRACTURE MECHANICS OF CONCRETE STRUCTURES

Edited by

ZDENĚK P. BAŽANT

Walter P. Murphy Professor of Civil Engineering, Northwestern University, Evanston, Illinois, USA

ELSEVIER APPLIED SCIENCE
LONDON and NEW YORK

SIZE EFFECT IN STRENGTH OF REINFORCED CONCRETE COLUMNS

ZDENĚK P. BAŽANT[1] AND YOUNG WENG KWON[2]

[1]Walter P. Murphy Professor of Civil Engineering, Northwestern University, Evanston, Illinois 60208

[2]Visiting Scholar, Northwestern University; Associate Professor on leave from Inchoen University, Seoul, Korea

ABSTRACT

The results of tests of geometrically similar tied reinforced concrete columns of different sizes, with size ratio 1:2:4 and slendernesses 16, 32 and 48, are reported. The model columns were made of reduced-size aggregate with maximum size 1/8 in. and reduced-size steel bars. It is found that, for all slendernesses, there exists a strong size effect in which the nominal stress at maximum load decreases as the size is increased. This contradicts the current design codes. The results are in good agreement with the previously proposed size effect law. The higher the slenderness, the stronger is the size effect.

INTRODUCTION

The diagram of axial load versus the load-point deflection (axial shortening) of reinforced concrete columns does not exhibit a horizontal plateau after the maximum load is reached, as would be expected for short columns if the assumptions of plastic limit analysis, serving as the basis of the current design codes, were valid. Rather, the columns, both short and long, exhibit post-peak softening. This can be caused only by fracture phenomena and implies that size effect ought to be at play.

Although important advances have been made in the past in understanding the behavior of reinforced concrete columns [1,2] (for further references see also [3,4]), the size effect in columns escaped attention so far. But no physical phenomenon is understood until the scaling law is understood, and this applies to concrete columns, too. The objective of this study is to briefly report the initial results of an experimental investigation of the size effect in columns. A detailed report will be given in a forthcoming article [5].

TEST SPECIMENS AND EXPERIMENTAL PROCEDURE

The test specimens (Fig. 1) were tied reinforced concrete columns of square cross sections with sides D = 0.5, 1 and 2 in. Three column slendernesses λ = 16, 32, and 48, were used ($\lambda = L/r = L/D$). The corresponding column lengths were L = 2.5, 5, and 7.5 in. for the smallest

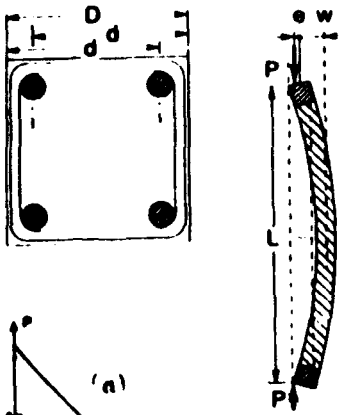

Fig.1 Column specimens tested.

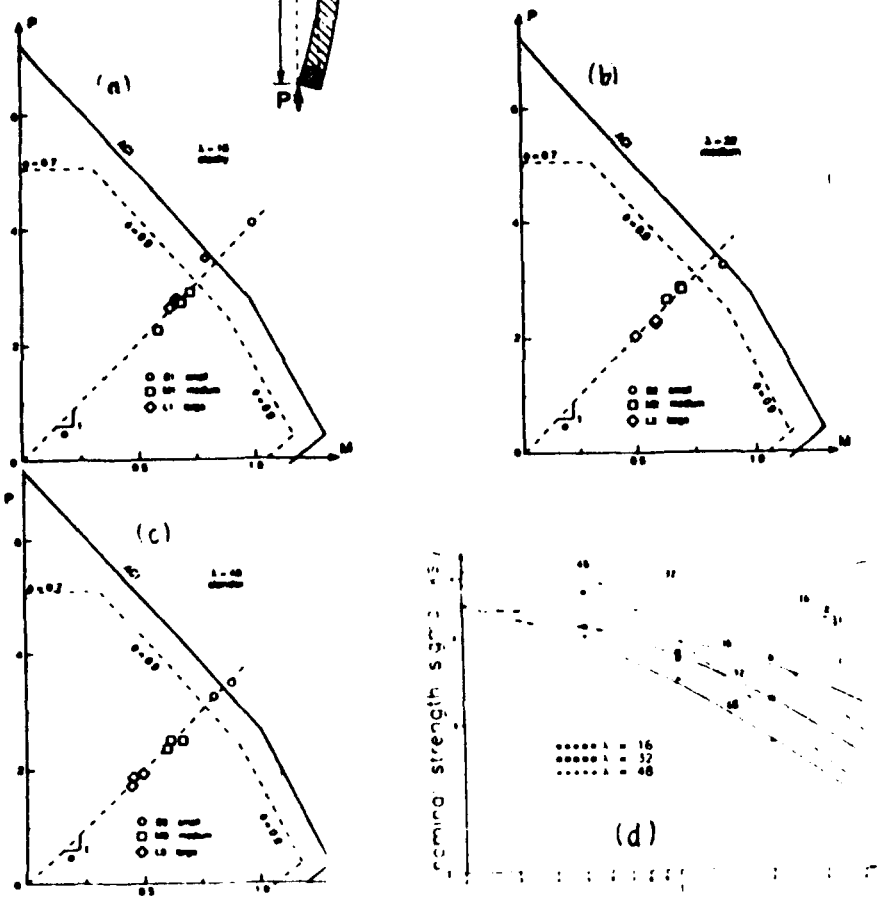

Fig. 2 Test results: (a-c) Interaction diagrams, (d) Size effect plots.

cross section, L = 5, 10, and 15 in. for the middle cross section, and L = 10, 20, and 30 in. for the largest cross section. The columns in each group of the same slenderness and different sizes were geometrically similar. The geometric similarity was enforced scrupulously—the reinforcing bars, their locations and cover, as well as the diameter and spacing of the ties, were all scaled in proportion to the characteristic column dimension D, taken as the cross section side. Because of the unavailability of deformed reinforcing bars of sufficiently small diameter, smooth steel bars were used. This nevertheless should have caused no problems with bond slip, because the column ends were provided with steel cover plates (Fig. 1c) at which the vertical bars were anchored by threaded nuts.

The columns were simply supported, and the load P was applied with end eccentricities e which were geometrically similar; $e = D/4$. Each column had four longitudinal bars (Fig. 1) of diameters d_b = 1/16, 1/8, and 1/4 in. for the smallest, middle and largest column sizes. The corresponding diameters of the steel ties were one half of the foregoing values. The center-to-center spacing of the ties was 0.3, 0.6 and 1.2 in. for the smallest, middle and largest cross sections, but near the ends the spacings were reduced to 0.2, 0.4 and 0.8 in., respectively, and very near the ends to 0.1, 0.2 and 0.4 in., respectively. The loads were applied onto the steel platens through steel balls and steel plates.

The average uniaxial compression strength of concrete, measured on 28-day-old companion cylinders of diameter 3 in. and length 6 in., was f'_c = 4,200 psi (28.96 MPa). The concrete (actually a micro-concrete or mortar) was made of Type I Portland cement with water-cement ratio 0.65 (for easy workability) and aggregate-cement ratio 2.5 (by weight). The aggregate used in the mix was an air-dried siliceous sand of maximum grain size 0.132 in., passing through sieve No. 6. All the specimens were cast from one and the same batch of concrete. The steel had Young's modulus E_s = 29,000,000 psi (200 GPa) and yield strength f_y = 80,000 psi (552 MPa). This value of yield strength was higher than that permitted for reinforced concrete structures, however this could not have had any significant effect since the calculated stresses reached in the steel bars before the peak load did not exceed 60,000 psi (414 MPa). The thickness of the concrete cover of longitudinal bars, measured from the bar center to the surface, was $d_c = 0.2D$.

The columns were cast in forms made of plywood with a smooth hard varnish-painted surface. The forms were stripped after one day, after which the columns, as well as the companion cylinders, were cured until 28 days of age in a water bath at 20°C temperature. At the age of 28 days, the columns were tested in a closed-loop (MTS) testing machine. The lateral deflection at the midheight of column was measured by an LVDT gauge (Fig. 1d). The stroke rate was kept constant in each test and was chosen so as to reach the peak load for any column size and slenderness within about 15 min.

RESULTS OF MEASUREMENTS AND THEIR ANALYSIS

The test results are summarized in Table 1 (1 kip = 1,000 lb.). In the specimen labels, S, M, and L mean the small, middle, and large cross sections; the subsequent numbers 1, 2, and 3 mean the low, middle, and high slenderness. Three identical specimens were tested for all cases, except S1 and S3. The corresponding mean nominal stresses at maximum load, defined as $\sigma_N = P/D^2$, are also given. Furthermore, Table 1 shows the values of the nominal bending moment Pz at midspan, in terms of the parameter $m_N = Pz/D^3 = \sigma_N(e + w)/D$; $z = e + w$ = deflection ordinate at midspan at maximum load, $e = D/4$ = eccentricity of the load, w = deflection at midspan. The mean values of m_N for each group of identical specimens are also given. The interaction diagram of maximum (ultimate) axial load P vs. the corresponding bending moment M, calculated according to the standard procedure [1,2], is shown by the solid line in Fig. 2. The dashed lines show the reduced interaction diagrams (in which ϕ are the ACI capacity reduction factors).

TABLE 1. Measured axial load P (of end eccentricity $e = D/4$) and midheight deflection w, with corresponding bending moment M, nominal stress $\sigma_N = P/D^2$ and nominal moment $m_N = M/D^3 = \sigma_N(e + w)/D$, for various column slendernesses λ and cross-section sizes D.

D	λ	Specimen	Prepeak State P	Prepeak State w	Peak Load State P	Peak Load State w	Postpeak State P	Postpeak State w	Peak Load State M	σ_N	Mean σ_N	m_N	Mean m_N
(in.)			(kip)	(in.)	(kip)	(in.)	(kip)	(in.)	(kip x in.)	(kip/in²)	(kip/in²)	(kip/in²)	(kip/in²)
	16	S1-1	0.205	0.005	1.03	0.025	0.288	0.118	0.13	4.12		1.04	
		S1-2	0.202	0.008	0.83	0.023	0.20	0.011	0.10	3.32	3.72	0.80	0.92
		S2-1	0.203	0.014	0.86	0.064	0.24	0.14	0.11	3.44		0.88	
0.5	32	S2-2	0.205	0.025	0.80	0.063	0.20	0.14	0.10	3.20	3.15	0.80	0.80
		S2-3	0.208	0.024	0.70	0.055	0.25	0.88	0.09	2.80		0.72	
		S3-1	0.208	0.019	0.875	0.085	0.20	0.140	0.11	3.52		0.88	
	48	S3-2	0.205	0.019	0.807	0.087	0.20	0.171	0.10	3.24	3.01	0.80	0.75
		M1-1	1.015	0.031	2.76	0.049	1.0	0.163	0.69	2.76		0.69	
	16	M1-2	1.02	0.049	2.93	0.023	1.0	0.179	0.73	2.93	2.65	0.73	0.71
		M1-3	1.02	0.011	2.32	0.038	1.0	0.185	0.58	2.32		0.58	
		M2-1	1.01	0.045	2.62	0.095	1.0	0.230	0.66	2.62		0.66	
1.0	32	M2-2	1.01	0.028	2.83	0.090	1.0	0.203	0.71	2.83	2.76	0.71	0.69
		M2-3	1.01	0.021	2.82	0.079	1.0	0.195	0.71	2.82		0.71	
		M3-1	1.01	0.0302	2.49	0.148	1.01	0.370	0.62	2.49		0.62	
	48	M3-2	1.02	0.038	2.37	0.165	1.0	0.377	0.59	2.37	2.44	0.59	0.61
		M3-3	1.0	0.050	2.47	0.188	1.03	0.252	0.62	2.47		0.62	
		L1-1	2.0	0.0068	10.85	0.0869	2.10	0.0346	5.43	2.71		0.68	
	16	L1-2	2.0	0.0048	10.67	0.0767	4.16	0.276	5.34	2.67	2.67	0.67	0.67
		L1-3	2.02	0.015	10.53	0.0625	2.0	0.371	5.27	2.63		0.66	
		L2-1	2.0	0.010	9.42	0.244	2.07	0.980	4.71	2.36		0.59	
2.0	32	L2-2	2.05	0.015	9.21	0.227	2.0	0.885	4.61	2.30	2.22	0.58	0.56
		L2-3	2.0	0.012	8.04	0.098	2.0	0.203	4.02	2.01		0.50	
		L3-1	2.0	0.016	7.38	0.360	2.0	0.982	3.69	1.85		0.46	
	48	L3-2	2.0	0.006	7.02	0.298	2.0	0.657	3.51	1.76	1.84	0.44	0.46
		L3-3	2.0	0.002	7.64	0.284	2.32	1.0	3.82	1.91		0.48	

The most interesting aspect of the results is that: (1) with increasing size, the data points generally move toward the origin of the interaction diagram, and (2) the size effect exists and is quite significant. These observations disagree with all the existing design codes. The maximum load points that lie inside the interaction diagram represent situations in which the code does not provide the required safety margin. For more slender columns, as expected, the response path moves more to the right and describes a wider loop.

Consider now the plots of the nominal strength $\sigma_N = P/D^2$ vs. log D. Fig. 1d gives such plots for all the slenderness, and each data point represents the average of a group of three like specimens. The plots clearly indicate a strong size effect. Based on previous theoretical arguments (cf. [3], chapters 12 and 13), the size effect should follow the approximate size effect law proposed by Bažant (1984) $\sigma_N = Bf_t'(1+\beta)^{-1/2}$ with $\beta = D/D_0$, in which Bf_t' and D_0 are two empirical constants (f_t' = tensile strength). The optimal fits by this size effect law are shown in Fig. 1d as the solid curves. Note that for a more slender column the size effect is stronger, with the response lying closer to the linear elastic fracture mechanics asymptote of slope -1/2. This is not surprising, since a more slender column of the same cross section stores more energy than a stockier column.

CONCLUSIONS

1. Tied reinforced concrete columns exhibit a strong size effect of fracture mechanics type.
2. The present test results are in agreement with the previously proposed size effect law.
3. The higher the slenderness, the stronger is the size effect.
4. The size effect ought to be introduced into the code provisions for columns. Until this is done, very large columns will have a significantly smaller safety margin than required.

ACKNOWLEDGMENT.—Partial financial support for the underlying theoretical studies of the size effect was received under AFOSR Grant No 91-0140 to Northwestern University. The second author wishes to express his gratitude for a fellowship from the Korean government supporting him during a one-year appointment as Visiting Scholar at Northwestern University. Thanks are due to Milan Jirásek, graduate research assistant, for his expert help in data evaluation after Y W Kwon returned to Korea

REFERENCES

1. McGregor, J.G., *Reinforced Concrete: Mechanics and Design*, Prentice Hall, Englewood Cliffs, NJ, 1988 (799 pp.)
2. Nilson, A.H., and Winter, G., *Design of Concrete Structures*, 10th ed., McGraw Hill, New York, 1986 (730 pp.)
3. Bažant, Z.P., and Cedolin, L., *Stability of Structures: Elastic, Inelastic, Fracture and Damage Theories* (textbook and reference volume). Oxford University Press, New York, 1991 (1010 pp.)
4. Bažant, Z.P., Cedolin, L., and Tabbara, M.R., New method of analysis for slender columns. *ACI Structural Journal* 1991, 88 (4), 391–401.
5. Bažant, Z.P., and Kwon, Y.W., Size effect in failure of short and slender reinforced concrete columns. Structural Engineering Report 91-9/456s, Northwestern University, Sept. 1991; submitted to *Journal of Structural Engineering ASCE*.

Cracks Interacting with Particles or Fibers in Composite Materials

By Gilles Pijaudier-Cabot,[1] Associate Member, ASCE, and Zdeněk P. Bažant,[2] Fellow, ASCE

Abstract: Micromechanics analysis of damage in heterogeneous media and composites cannot ignore the interactions among cracks as well as between cracks and inclusions or voids. Previous investigators can to this conclusion upon finding that states of distributed (diffuse) cracking (damage) cannot be mathematically represented merely as crack systems in a homogeneous medium, even though stable states with distributed damage have been experimentally observed in heterogeneous materials such as concrete. This paper presents a method for modeling interactions between a crack and many inclusions. Based on the Duhamel-Neuman analogy, the effect of the inclusions is equivalent to unbalanced forces acting on the contour of each inclusion in an infinite homogeneous solid. The problem is solved by superposition; it is decomposed into several standard problems of elasticity for which well-known solutions are available. The problem is finally reduced to a system of linear algebraic equations similar to those obtained by Kachanov for a system of interacting cracks without inclusions. The calculated estimates of the stress intensity factors differ from some known exact solutions by less than 10% provided the cracks or the inclusions are not very close to each other. Approximately, the problem can be treated as crack propagation in an equivalent homogeneous macroscopic continuum for which the apparent fracture toughness increases or decreases as a function of the crack length. Such variations are calculated for staggered inclusions. They are analogous to R-curves in nonlinear fracture mechanics. They depend on the volume fraction of the inclusions, their spatial distribution and the difference between the elastic properties of the inclusions and the matrix. Large variations (of the order of 100%) are found depending on the location of the crack and its propagation direction with respect to the inclusions.

Introduction

Most particulate or fiber-reinforced composites do not fail by propagation of a single microcrack. Typically, these materials are capable of sustaining significant loads while multiple microcracks propagate. In concrete loaded in uniaxial tension or compression, acoustic emission analyses (Legendre 1984; Maji et al. 1990) and X-ray microscopic observations (Darwin and Dewey 1989) show that distributed microcracks and damage localization exist in the material prior to failure. In these brittle heterogeneous composites, cracks are often initiated at the interface between the matrix and the aggregate pieces, and they propagate into the matrix eventually. Distributed cracking is also observed in fiber composites, the behavior of which in the planes normal to the fibers is similar to a two-dimensional particulate composite (Highsmith and Reifsnider 1982).

The key problem in developing a theory explaining such observations is how to take into account the effect of the heterogeneities. Pijaudier-Cabot

[1]Head, Civ. Engrg. Res. Group, Laboratoire de Mécanique et Technologie, ENS Cachan/CNRS/Université Paris VI, 61 Av. du Président Wilson, 94235 Cachan Cedex, France; formerly, Visiting Scholar, Northwestern Univ., Evanston, IL 60208.

[2]Walter P. Murphy Prof. of Civ. Engrg., Ctr. for Advanced Cement-Based Materials, Northwestern Univ., Evanston, IL.

Note. Discussion open until December 1, 1991. To extend the closing date one month, a written request must be filed with the ASCE Manager of Journals. The manuscript for this paper was submitted for review and possible publication on August 2, 1990. This paper is part of the ***Journal of Engineering Mechanics***, Vol. 117, No. 7, July, 1991. ©ASCE, ISSN 0733-9399/91/0007-1611/$1.00 + $.15 per page. Paper No. 26002.

and Dvorak (1990) recently proposed an approximation method for estimating the variation of the stress intensity factor and the inherent toughening effect at the tip of a crack that touches the interface between two elastic materials. In the case of concrete-like materials, which are the main motivation for this paper, most studies considered that the interactions among cracks or between aggregate pieces and cracks could reasonably be neglected, except in some special cases.

Zaitsev (1985) developed a rather comprehensive model in which the inclusion-crack interaction is neglected and each crack may interact only with its closest neighbor. However, the postpeak softening a response of concrete specimens could not be obtained with this method. More recently, Huang and Li (1989) and Hu et al. (1986) used similar ideas and proposed models in which the toughening (i.e., crack arrest) effect of the inclusions was incorporated. Although the mechanical interaction effects were still lacking, crack deflection mechanisms were represented statistically (Faber et al. 1983; Evans and Faber 1983). The effect of crack-inclusion interaction on dynamic crack propagation was studied by Sih and Chen (1980).

The effect of crack interaction has recently been considered in the studies of micromechanics of damage in concrete or ceramics (Horii et al. 1989; Ortiz 1988; Bažant et al. 1989; Kazemi and Pijaudier-Cabot 1989), and several approximation schemes for estimating crack-interaction effects have been proposed [see e.g., Kachanov (1987); Horii and Nemat-Nasser (1985)]. In particular, the importance of crack interaction at the onset of damage localization has been proven to be a fundamental aspect that justifies partial nonlocality of the constitutive relations at the macroscopic level, i.e., for the homogenized damaged medium (Pijaudier-Cabot and Berthaud 1990).

Some investigations have led to a striking conclusion: according to thermodynamics and stability analyses, most regular crack systems such as parallel equidistant cracks, periodic arrays of cracks and some colinear crack systems cannot be reached by a stable path under usual load or displacement control conditions (Bažant 1989; Bažant and Cedolin 1991; Bažant 1987b; Bažant and Tabbara 1989). Such models incorrectly predict that only a single crack ought to propagate. Thus, stable states of diffuse damage consisting of a system of tensile microcracks cannot exist according to these mathematical models in the first place, although they have been observed experimentally. Furthermore, the predicted shape of the softening postpeak load-displacement curve does not agree with experience and snap-back instability is predicted to occur earlier than seen in tests (Bažant 1987a). These discrepancies suggest that the mechanical effect of inhomogeneities cannot be ignored in modeling the evolution of damage and its progressive localization in concrete-like materials. This provided the motivation for the present study.

Solutions for some cases of the interaction between a crack and an inclusion in an elastic matrix exist [see e.g., Kunin and Gommerstadt (1985); Erodogan et al. (1974)]. They are based on a system of singular integral equations, which, however, appears to be intractable in the cases where several inclusions interact with the crack. Mura's equivalent inclusion method (Furuhashi et al. 1981) poses similar problems as it requires computation of integrals that may not converge absolutely when the inclusions are periodically distributed in an infinite medium.

In this paper [which is based on a conference paper by Pijaudier-Cabot et al. (1990)], we present an approximation scheme for solving the problem of

interaction between cracks and inclusions. The method can be viewed as an extension of Kachanov's superposition scheme (1987) for an interacting crack system without inclusions. Similar extensions could be made using the method of pseudotractions (Horii and Nemat-Nasser 1985).

The paper is organized as follows. First, the approximation method is developed, considering the simple case of one crack interacting with an inclusion, and verified by comparisons with solutions available in the literature. Second, an extension of this technique to the situation in which one crack interacts with several periodically distributed inclusions is carried out. Finally, the effect of the inclusions on crack propagation is interpreted in terms of an apparent fracture toughness of the homogenized composite. The ultimate objective is to develop a realistic model for the fracture process zone in composites.

The study is restricted to cases in which the bond between the matrix and the inclusion is perfect. Partial debonding and interfacial cracking will not be considered. This simplification is realistic especially for composites such as high-strength concrete or light-weight concrete.

Interaction between Crack and Inclusion

Consider an infinite two-dimensional solid subjected to remote uniform boundary tractions producing a uniform stress field $\boldsymbol{\sigma}_\infty$. The solid is made of a linear elastic material of stiffness matrix $\mathbf{D}_m$. It contains a crack of length $2c$ and an elastic circular inclusion (inhomogeneity) of radius R and stiffness matrix $\mathbf{D}_a$ [Fig. 1(*a*)]. The crack center is located at distance b from the center of the inclusion. The crack orientation is arbitrary. For such a solid, we seek an estimate of the stress intensity factors at the crack tips denoted as points A and B. For the sake of simplicity, we restrict attention to the case of circular inclusions, although the method we are going to develop is general and can, in principle, be extended to inclusions of arbitrary (smooth) shapes.

The stress and displacement fields for this problem can be solved by superposing the solutions of two simpler problems [Fig. 1(*a*)]:

- Subproblem I: The solution for the infinite solid without any crack containing the given inclusion and loaded by the remote tractions corresponding to $\boldsymbol{\sigma}_\infty$.
- Subproblem II: The solution for the infinite cracked solid loaded by distributed normal and tangential forces $\mathbf{p}(\mathbf{x})$ on the crack faces Γ_c, that cancel the stresses on the crack line obtained in I.

By superposition, the equilibrium condition for the crack surface may be written as

$$\boldsymbol{\sigma} \cdot \mathbf{n}(\mathbf{x}) + \mathbf{p}(\mathbf{x}) = 0 \quad \text{on} \quad \Gamma_c \qquad (1)$$

in which $\boldsymbol{\sigma}$ denotes the stress field solution of subproblem I calculated at the imaginary crack surface Γ_c and $\mathbf{n}(\mathbf{x})$ is the outward normal to Γ_c at a point with cartesian coordinates $\mathbf{x}$. Ideally, (1) should be satisfied exactly at every point of Γ_c and superposition would then yield an exact result. For the sake of simplicity, we assume that (1) is satisfied only approximately, in the average sense, that is

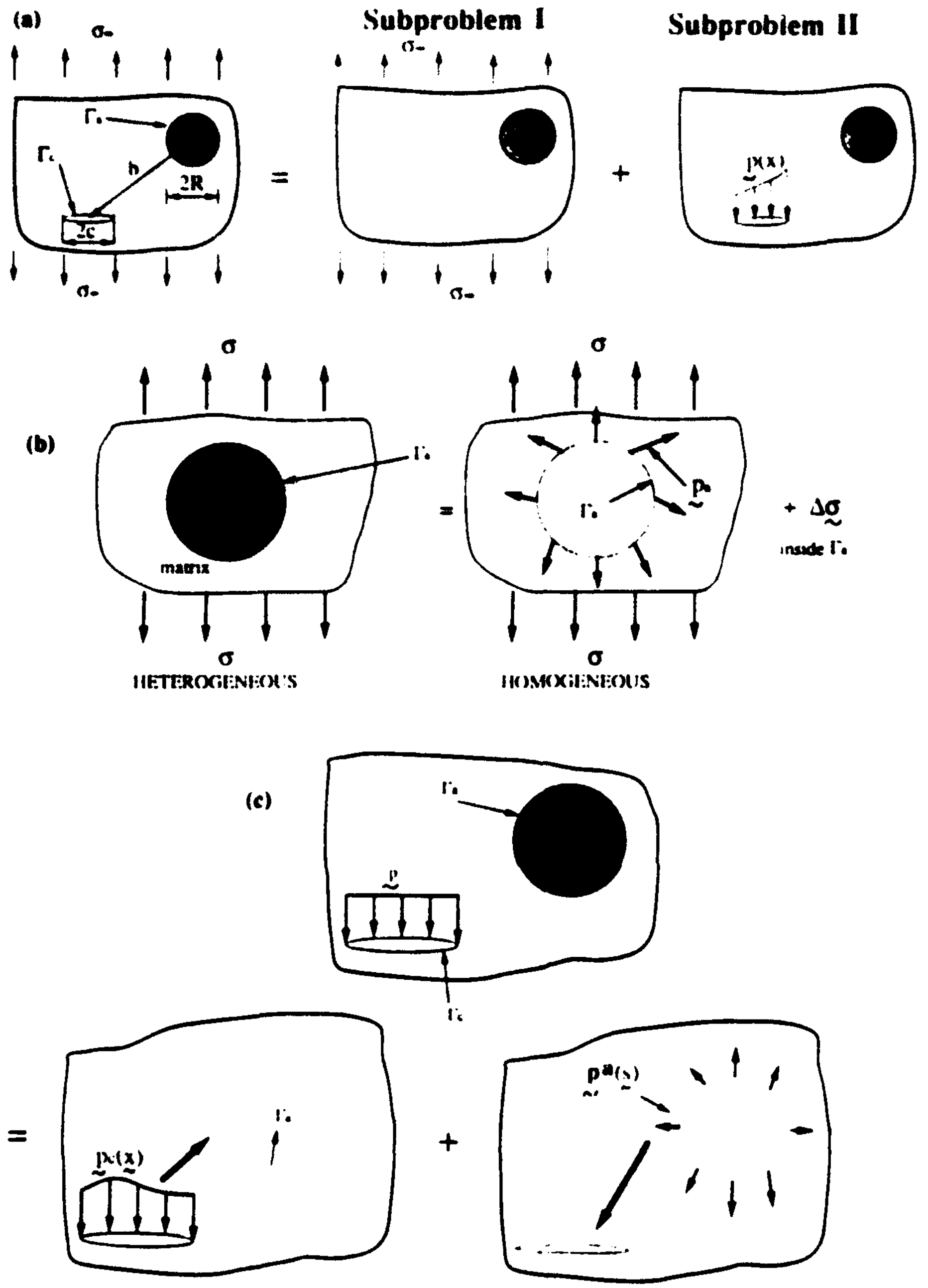

FIG. 1. Crack Interacting with Inclusion: (*a*) Superposition Scheme; (*b*) Duhamel-Neuman Analogy; (*c*) Superposition in Subproblem II

$$\langle \boldsymbol{\sigma} \cdot \mathbf{n}(\mathbf{x}) + \mathbf{p}(\mathbf{x}) \rangle = 0 \quad (2)$$

in which the brackets ⟨ ⟩ denote the averaging over Γ_c. This simplification is inspired by Kachanov's (1987) approximation scheme for interacting crack systems in homogeneous solids without inclusions, which has been showed to be satisfactory in most situations. In Kachanov's scheme as well as here, the averaging is justified by the St. Venant principle: the errors represent a self-equilibrated stress field that must be decaying very rapidly with the distance from the crack and is, therefore, negligible for a sufficient separation of the crack and inclusion. Moreover, even if the crack tip is close, its K_I

value depends on the energy release rate from the entire structure rather than just the stresses in the vicinity.

Subproblem I

For the sake of simplicity, attention is restricted to plane elasticity. The perturbation stress due to the presence of one inclusion is given by the well-known Eshelby's solution [see e.g., Mura (1987)]. Since we intend to deal with many inclusions as well as interacting cracks, it appears preferable to devise a simpler, iterative, solution. From the stress field $\boldsymbol{\sigma}$, which is a solution of subproblem I, we can calculate the unbalanced stress field $\Delta\boldsymbol{\sigma}$ inside the inclusion of contour Γ_a:

$$\Delta\boldsymbol{\sigma} = (\mathbf{D}_a - \mathbf{D}_m):\boldsymbol{\epsilon} \quad (3a)$$

with

$$\boldsymbol{\epsilon} = \mathbf{D}_m^{-1}:\boldsymbol{\sigma} \quad (3b)$$

while in the matrix outside Γ_a, the stresses $\Delta\boldsymbol{\sigma}$ vanish. The unbalanced stresses $\Delta\boldsymbol{\sigma}$ can be equilibrated by applying tractions $\Delta\boldsymbol{\sigma}\cdot\mathbf{n}_a$ on interface Γ_a. Since these tractions do not exist in reality, the opposite unbalanced interface tractions must act on the interface Γ_a in the composite

$$\mathbf{p}_a = -\Delta\boldsymbol{\sigma}\cdot\mathbf{n}_a \quad \text{on } \Gamma_a \quad (4)$$

in which $\mathbf{n}_a$ is the unit outward normal of the boundary curve Γ_a of the inclusion, and $\boldsymbol{\epsilon}$ and $\boldsymbol{\sigma}$ are the strain and stress tensor inside the inclusion. The stress field in subproblem I may be written as

$$\boldsymbol{\sigma} = \boldsymbol{\sigma}^* \quad \text{outside } \Gamma_a \quad (5a)$$

$$\boldsymbol{\sigma} = \boldsymbol{\sigma}^* + \Gamma\boldsymbol{\sigma} \quad \text{inside } \Gamma_a \quad (5b)$$

in which $\boldsymbol{\sigma}^*$ = an equilibrium stress field when stiffness $\mathbf{D}_a$ of the inclusion is changed to $\mathbf{D}_m$, i.e., when the properties of the infinite solid are uniform. Eqs. (3)–(5) can also be obtained from the Duhamel-Neuman analogy [see e.g., Lin (1968); Muhkelishvili (1953)], which is widely used in thermoviscoelasticity and creep and is illustrated in Fig. 1(*b*). This analogy transforms a problem of elasticity of a heterogeneous solid into an equivalent problem of a homogeneous solid that can be decomposed into a superposition of standard problems for which analytical solutions (e.g., complex potentials) exist. Obviously, the unbalanced stress field $\Delta\boldsymbol{\sigma}$ is the unknown in the equivalent problem. Its determination calls for an iterative procedure.

1. The starting solution is $\boldsymbol{\sigma}^* = \boldsymbol{\sigma}_\infty$ everywhere. It gives the first estimate of $\mathbf{p}_a$ according to (4). The curve Γ_a is subdivided into segments of length ds and the tractions $\mathbf{p}_a$ are replaced by concentrated forces $\mathbf{p}_a(\mathbf{s})\,ds$ acting at the center points of coordinate s of the segments. Then one may use the well-known two-dimensional solution for a concentrated force $\mathbf{p}$ applied at point s of an infinite homogeneous elastic space denoted as $\mathbf{f}[\mathbf{p}(\mathbf{s})]$; see e.g., Timoshenko and Goodier (1970) or Mukhelishvili (1953). The normal and shear components of the stress tensor $\mathbf{f}$ with respect to the rotated cartesian axes (x', y') at a point of cartesian coordinate (x, y) are

$$f'_{\cdot} = p[1 - \nu - 2(1 + \nu)\sin^2(\theta)]\cos(\theta)(4\pi r)^{-1} \quad \text{[Continued]}$$

$$f'_x = p[-3 - \nu - 2(1 + \nu)\sin^2(\theta)]\cos(\theta)(4\pi r)^{-1}$$

$$f'_y = -p[1 - \nu + 2(1 + \nu)\cos^2(\theta)]\sin(\theta)(4\pi r)^{-1} \quad \ldots\ldots (6)$$

in which r = distance between points (x, y) and s; axis x' coincides with the direction of p; and θ = the angular deviation of the line connecting points (x, y) and s from the direction of p. Superposition of these solutions yields the stress $\boldsymbol{\sigma}_a$ caused by tractions $\mathbf{p}_a(s)$ in an infinite homogeneous elastic space:

$$\boldsymbol{\sigma}_a = \int_{\Gamma_a} [\mathbf{p}_a(s)]ds \quad \ldots\ldots (7)$$

A new stress field $\boldsymbol{\sigma}^*$ inside Γ_a is obtained as:

$$\boldsymbol{\sigma}^* = \boldsymbol{\sigma}_a + \boldsymbol{\sigma}_\infty \quad \ldots\ldots (8)$$

2. The new unbalanced pressures $\mathbf{p}_a$ are then recalculated from (3)–(4). Eq. (7) yields the new field $\boldsymbol{\sigma}_a$.

3. Step 2 is iterated until the change $\mathbf{p}_a^{l+1} - \mathbf{p}_a^l$ of the unbalanced interface tractions from iteration becomes small enough. This is determined on the basis of the norm $\|\mathbf{p}_a(s)\| = \int_{\Gamma_a} |\mathbf{p}_a(s)|ds$ where $|\mathbf{p}_a(s)|$ is the length of vector $\mathbf{p}_a(s)$. The convergence criterion is that

$$\frac{\|\mathbf{p}_a(s)\|^{l+1}}{\|\mathbf{p}_a(s)\|^l} - 1 \leq e \quad \ldots\ldots (9)$$

in which e = a given small tolerance; $e = 0.01$ was used in computations and usually less than five iterations were needed. The convergence is very fast, and for small enough e this iterative procedure can approximate the exact solution (for uniform p) as closely as desired. It can be shown that the iterates of P_a form a geometric progression.

Subproblem II

Consider now that there is a crack in the matrix near the inhomogeneity and that the crack faces Γ_c are loaded by a uniform pressure distribution $\langle \mathbf{p}(\mathbf{x}) \rangle$. The boundary at infinity is stress free. Again, we can apply the Duhamel-Neuman analogy in order to compute the interaction stress field due to the presence of the inclusion, and subsequently the distribution of internal pressure on the crack faces. For this, we use the superposition scheme depicted in Fig. 1(*c*).

First, the body without the inclusion is loaded by an unknown average pressure $\langle \mathbf{p}_c(\mathbf{x}) \rangle$. This causes interface tractions $-\Delta\boldsymbol{\sigma}_c \cdot \mathbf{n}_a$ on the imagined contour of the inclusion as given by (4).

Next, we consider the uncracked heterogeneous body loaded by these unbalanced pressures on Γ_a. From subproblem I we can get the solution stress field and the pressure distribution on the imagined contour of the crack $\mathbf{p}_c^a(\mathbf{x})$:

$$\mathbf{p}_c^a(\mathbf{x}) = \left\{ \int_{\Gamma_a} \mathbf{f}[-\Delta\boldsymbol{\sigma}_c \cdot n_a(s)]ds \right\} \cdot \mathbf{n} \quad \ldots\ldots (10)$$

Superposition yields

$$\langle \mathbf{p} \rangle = \mathbf{p}_c(\mathbf{x}) + p_c^a(\mathbf{x}) \quad \text{on } \Gamma_c \quad \ldots\ldots (11)$$

Note that this superposition method, with the average pressure approximation on the crack surface, is similar to Kachanov's (1987) approximate solution for interacting cracks except that instead of two cracks we deal with one crack and one inclusion. In (11), the right-hand side terms are not constant. If we restrict the present analysis to configurations in which the interactions are small, the superposition equation may be approximated by:

$$\langle \mathbf{p} \rangle = \langle \mathbf{p}_c(\mathbf{x}) \rangle + \langle p_c^0(\mathbf{x}) \rangle \quad \text{on } \Gamma_c \qquad (12)$$

Under these two assumptions, the superposition equation [(11)] has a single vector unknown $\langle \mathbf{p}_c(\mathbf{x}) \rangle$:

$$\langle \mathbf{p} \rangle = (\mathbf{1} + \mathbf{\Lambda}_a) \cdot \langle \mathbf{p}_c(\mathbf{x}) \rangle \qquad (13)$$

with

$$\mathbf{\Lambda}_a \cdot \langle \mathbf{p}_c(\mathbf{x}) \rangle = \frac{1}{2c} \int_{\Gamma_c} \left\{ \int_{\Gamma_a} \mathbf{f}[-\Delta\boldsymbol{\sigma}_c \cdot \mathbf{n}_a(\mathbf{s})] ds \right\} \cdot \mathbf{n} dx \qquad (14)$$

in which $\mathbf{1}$ is the 2×2 identity matrix, and $\mathbf{\Lambda}_a$ is a full 2×2 matrix which couples the mode I crack opening and the mode II crack opening. It can be regarded as a transmission factor that represents the average influence of the inclusion on the crack. Note at this point that if $\boldsymbol{\sigma}_c$ is not computed from the constant pressure distribution $\langle \mathbf{p}_c(\mathbf{x}) \rangle$, the unknown in the problem would need to be solved iteratively (as in subproblem I) as $\mathbf{\Lambda}_a$ depends on $\mathbf{p}_c(\mathbf{x})$.

Substitution of (13) into (2) yields:

$$\langle \mathbf{p}_c(\mathbf{x}) \rangle = -(\mathbf{1} + \mathbf{\Lambda}_a)^{-1} \cdot \langle \boldsymbol{\sigma} \cdot \mathbf{n} \rangle \qquad (15)$$

The stress distribution on Γ_c is also computed using the right-hand side of (11) and, for example, the stress intensity factors for mode I crack opening are:

$$K_I(\pm c) = \frac{1}{\sqrt{\pi c}} \int_{-c}^{c} \sqrt{\frac{c \pm x}{c \mp x}}\, \mathbf{p}_c(\mathbf{x}) \mathbf{n} dx \qquad (16)$$

As an example, Fig. 2 shows the results for the mode I stress intensity factors for a crack in an epoxy matrix located near a metallic inclusion. The remote loading is uniaxial tension parallel to the crack faces and plane strain is assumed. For simplicity, we analyze cases where (1) The crack is radial to the inclusion [Fig. 2(*a*)]; and (2) the crack is tangential to the inclusion [Fig. 2(*b*)]. In both situations the average tangential pressure distribution is zero and (15) has a scalar unknown. The radius of the inclusion is such that $R/c = 2$ and the material properties are $E_a/E_m = 23$, $\nu_a = 0.3$, $\nu_m = 0.35$ where E_a, E_m and ν_a, ν_m are the Young's moduli and Poisson's ratios of the inclusion and matrix, respectively. In the figures, K_I is normalized with respect to the stress intensity factor K_{I_0} for a crack in an infinite homogeneous solid, which is $K_{I_0} = \sigma_\infty \sqrt{\pi c}$. The approximation is compared to the analytical solution of Erdogan et al. (1974). For a radial crack [Fig. 2(*a*)], the approximation turns out to be very accurate. The error is only a few percent except if the crack and the inclusion are very close. When the crack is tangential to an inclusion [Fig. 2(*b*)] the present averaged superposition equations become rather inaccurate if the crack is close to the inclusion ($a/c < 4$). The reason is that the stress fields in subproblems I and II have a large

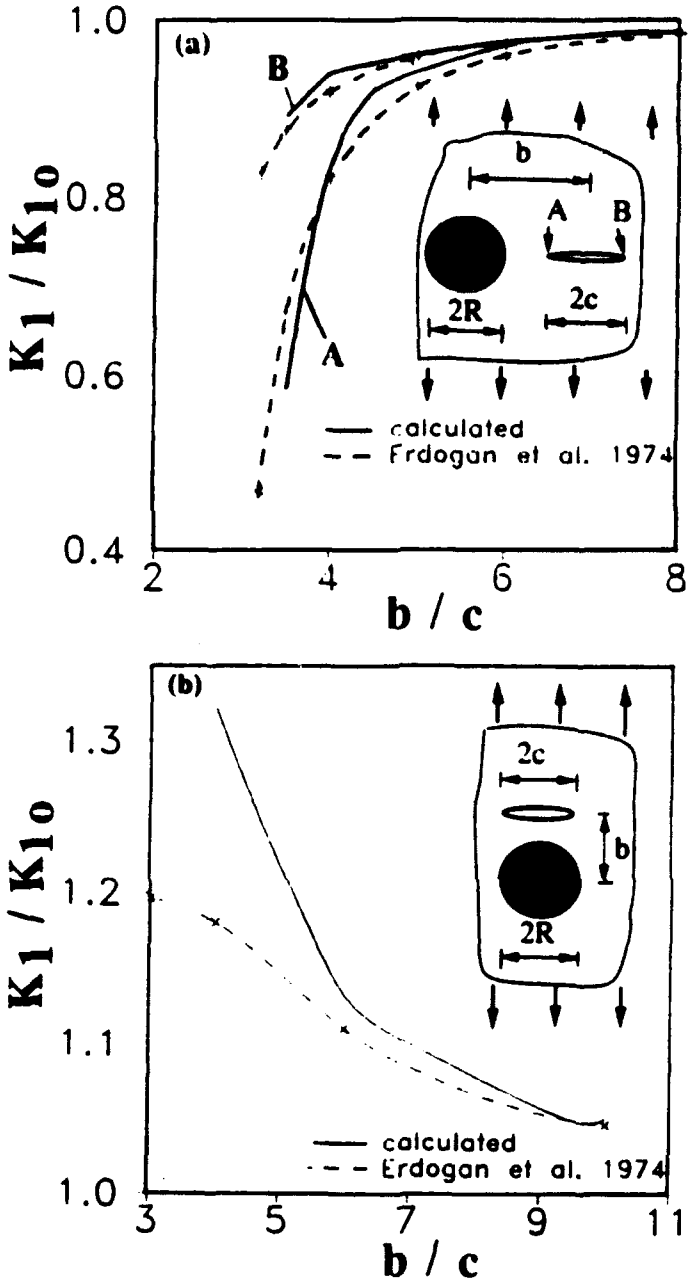

FIG. 2. Stress Intensity Factor for Crack in Epoxy near Inclusion: (*a*) Radial Crack; (*b*) Tangential Crack

variation over the imagined crack length.

Fig. 3 shows the results for a crack in an epoxy matrix located near a void. The same two configurations as in Fig. 2 are considered and the material stiffness of epoxy is equal to that in Fig. 2. Again, the quality of the approximation is quite acceptable unless crack and void become very close. Compared to the results in Fig. 2, the variation of stress intensity factors is the opposite. When the crack tip A approaches the void [Fig. 3(*a*)], the stress intensity factor K_I increases and tends to infinity, but when the tip approaches a stiffer inclusion, K_I decreases. The same remark holds when the

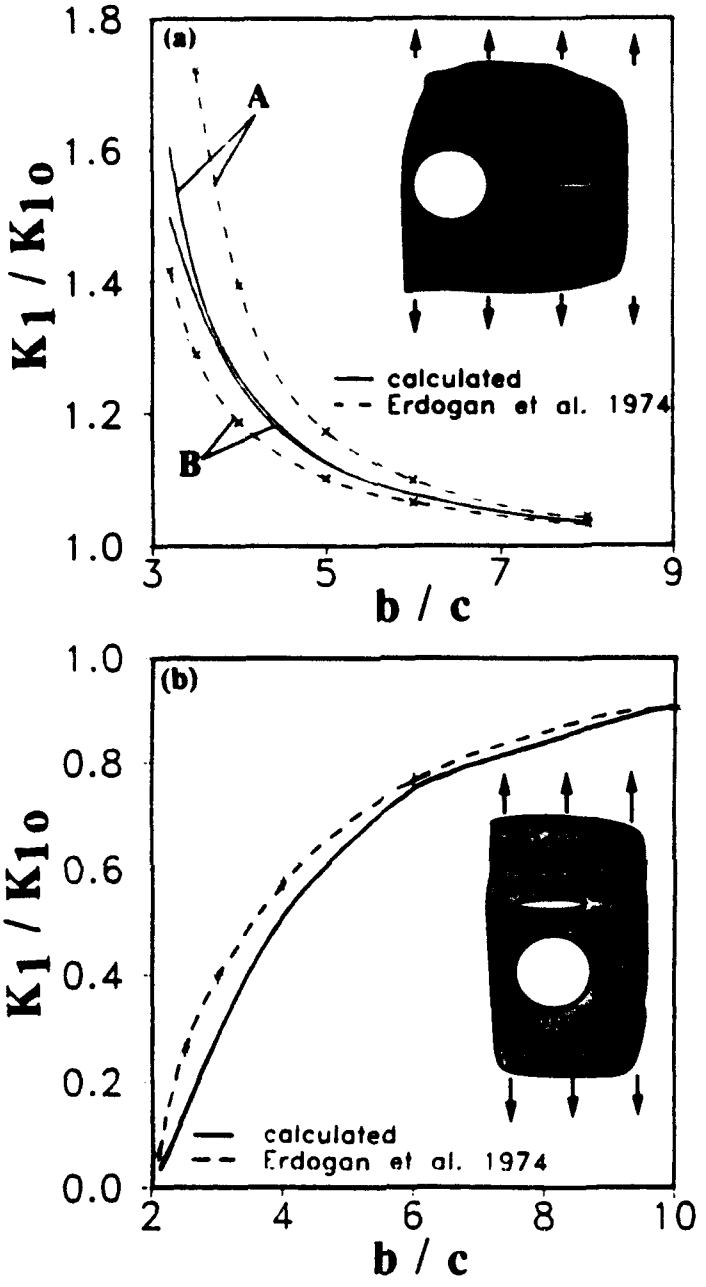

FIG. 3. Stress Intensity Factor for Crack in Epoxy near Void: (*a*) Radial Crack; (*b*) Tangential Crack

crack is tangential to the void or inclusion, although the stress intensity factors remain finite.

Interaction between Crack and Several Inclusions

We look now at an elastic solid that contains N elastic inclusions and one crack. The inclusions are arbitrarily distributed in the matrix. The inclusion contours are denoted as Γ_i $(i = 1, \ldots, N)$ and for the sake of simplicity all the inclusions are assumed to be made of the same material of stiffness $\mathbf{D}_a$.

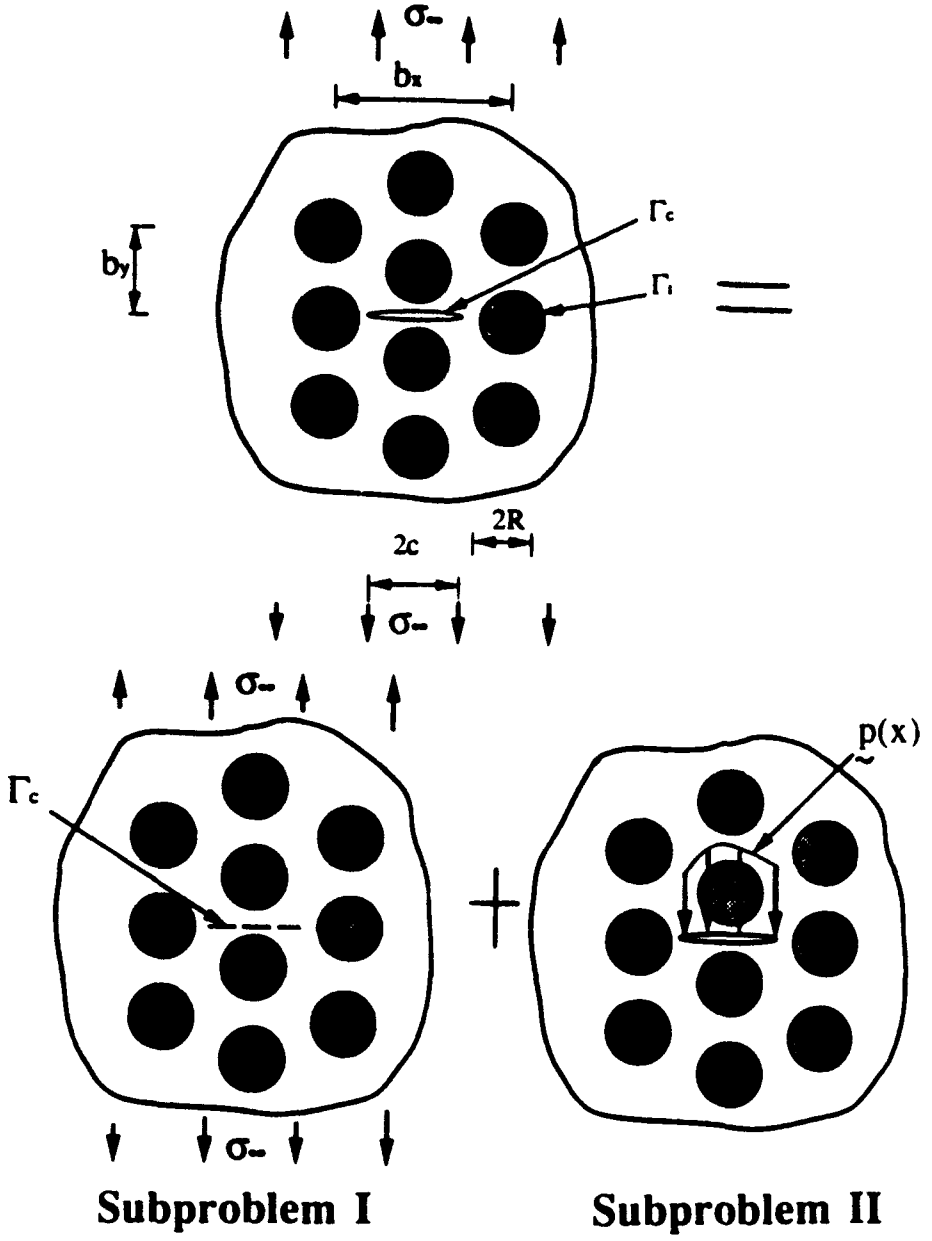

FIG. 4. Crack Interacting with Periodic Array of Inclusions: Superposition Scheme

The superposition method is now applied as follows (see Fig. 4).

First in subproblem I, we solve again for the stress field in the composite without the crack loaded by tractions corresponding to σ_∞. Then, in subproblem II, the composite is free from the remote boundary tractions and it is loaded by an unknown internal pressure $\mathbf{p}(\mathbf{x})$ on the crack contour Γ_c. The superposition equation [(2)] is again applied in the average sense.

Subproblem I

When the uncracked composite contains several inclusions, the interactions are an important factor in the evaluation of the local stress and strain fields. As we will see, the Duhamel-Neuman analogy is also easy to implement.

Since the problem remains elastic, the effect of each inclusion can be superposed as a first approximation neglecting the interactions. The following iterative procedure, similar to that described before, yields the effect of the interactions on the local stress field in the matrix.

1. The initial stress field is

$$\boldsymbol{\sigma}^* = \boldsymbol{\sigma}_\infty + \sum_{i=1}^{N} \boldsymbol{\sigma}_i \quad (17)$$

in which the $\boldsymbol{\sigma}_i$ = the stress due to the presence of inclusion i alone in the matrix (Eshelby's solution). The unbalanced pressures $\mathbf{p}_i$ on the contour Γ_i of each inclusion i are calculated from $\boldsymbol{\sigma}^*$ according to (4)–(5). The stress $\boldsymbol{\sigma}_i$ due to $\mathbf{p}_i$ is then calculated as if each inclusion i were alone in the infinite solid, i.e.

$$\boldsymbol{\sigma}_i = \int_{\Gamma_i} \mathbf{f}[\mathbf{p}_i(\mathbf{s})]ds \quad (18)$$

A new total stress field is computed from (17) using superposition.

2. From $\boldsymbol{\sigma}$ (5), the unbalanced pressures $\mathbf{p}_i$ on each contour Γ_i are recalculated using (4). Then again the stress $\boldsymbol{\sigma}_i$ due to $\mathbf{p}_i$ is calculated from (18) as if the inclusions were alone, and by superposing $\boldsymbol{\sigma}_i$, the new total stress field obtained from (17).

3. Step 2 is iterated until the unbalanced tractions $\mathbf{p}_i^l$ ($i = 1, \ldots N$) resulting from $\boldsymbol{\sigma}$ in iteration number l differ negligibly from those at iteration number $l - 1$. This is determined according to the convergence criterion in (9).

The foregoing algorithm converges quite rapidly. Normally, convergence is reached in less than five iterations provided the inclusions are not too stiff compared to the matrix ($E_a/E_m < 7$) (but for perfectly rigid inclusions the present iterative method does not work). When the inclusions are periodically distributed, the unbalanced pressures $\mathbf{p}_i$ should be identical on each contour Γ_i ($i = 1, \ldots, N$), and in that case the convergence criterion does not need to be applied for each inclusion.

Fig. 5 gives an example of the calculated stress distribution of stress in a two-dimensional composite with periodically spaced circular inclusions of radius R. The remote loading is a unit uniaxial tension in the y-direction. The inclusion centers are located on a square grid of spacing $b_x = b_y = 3R$. The material properties are $E_a/E_m < 3$ and $\nu_a = \nu_m = 0.2$. Plane stress is assumed and the central inclusion is assumed to interact only with its 48 closest neighbors. The stresses σ_{xx} and σ_{yy} are computed along the axis of symmetry of two adjacent inclusions, and obviously $\sigma_{xy} = 0$. Convergence was achieved in 3 iterations, with tolerance $e = 0.01$. The results are graphically undistinguishable from those obtained by the equivalent inclusion method (Furuhashi et al. 1981).

Subproblem II

The crack is loaded by a uniform internal pressure $\mathbf{p}(\mathbf{x})$ on its contour Γ_c. From superposition,

$$\mathbf{p}(\mathbf{x}) = \mathbf{p}_\infty(\mathbf{x}) + \sum_{k=1}^{N} \mathbf{p}_{\text{int}}^k(\mathbf{x}) \quad \text{on } \Gamma_c \quad (19)$$

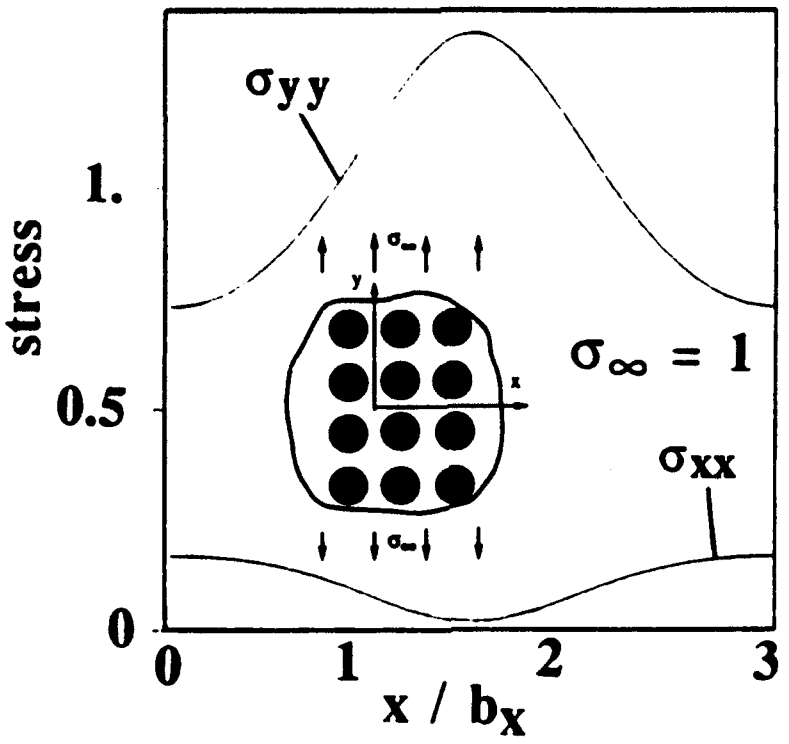

FIG. 5. Local Stress Field in Composite with Periodically Distributed Inclusions

In this equation, which is similar to (11), $\mathbf{p}_c$ = the distribution of the internal pressure applied on Γ_c, and $\mathbf{p}_{int}^k$ ($k = 1, \ldots, N$) = the interaction terms due to the presence of the inclusions. $\mathbf{p}_{int}^k$ is computed at the imagined location of the crack as if the composite were uncracked. Again, there are two types of contributing terms in $\mathbf{p}_{int}^k$.

The first type of contribution arises from the effect of the loading $\mathbf{p}_c$ on the inclusion k which is assumed to be alone in the matrix with the crack (same as in the previous section of the paper). This term denoted as $\mathbf{p}_k^k$ is computed according to (10):

$$\mathbf{p}_k^k = \left\{ \int_{\Gamma_k} \mathbf{f} | -\Delta\boldsymbol{\sigma}_c \cdot \mathbf{n}_k(\mathbf{s}) | ds \right\} \cdot \mathbf{n} \quad \ldots\ldots\ldots\ldots\ldots\ldots\ldots\ldots\ldots\ldots\ldots\ldots\ldots\ldots (20)$$

in which $\boldsymbol{\sigma}_c$ = the stress field due to the crack loaded by $\mathbf{p}_c(\mathbf{x})$, calculated for the infinite solid without inclusions; $\Delta\boldsymbol{\sigma}_c$ = the unbalanced stresses computed on the imagined contour Γ_k of the inclusion k; and $\mathbf{n}_k$ = the outward unit normal vector of Γ_k.

The second type of contribution is the interaction between the inclusion $j (j \neq k)$ and inclusion k, and its influence on the crack faces. Each inclusion in the composite is subjected to the stress $\boldsymbol{\sigma}_c$. The value of $\mathbf{p}_j^k$ can be computed in the same manner as in subproblem I but the stress fields $\boldsymbol{\sigma}_c$ is substituted to the remote field $\boldsymbol{\sigma}_r$. From (17) and (18) we obtain:

$$\mathbf{p}_j^k(\mathbf{x}) = \left\{ \int_{\Gamma_k} \mathbf{f} | -\Delta\boldsymbol{\sigma}_j \cdot \mathbf{n}_k(\mathbf{s}) | ds \right\} \cdot \mathbf{n} \quad \ldots\ldots\ldots\ldots\ldots\ldots\ldots\ldots\ldots\ldots\ldots\ldots\ldots\ldots (21)$$

in which $\Delta\boldsymbol{\sigma}_i$ = the stress field due to the unbalanced pressure $\mathbf{p}_i$ acting on contour Γ_i, of normal vector $\mathbf{n}_i$:

$$\boldsymbol{\sigma}_i = \int_{\Gamma_i} \mathbf{f}[-\Delta\boldsymbol{\sigma}_i \cdot \mathbf{n}_i(s)]ds \quad \ldots\ldots (22)$$

Superposition yields:

$$\mathbf{p}^k_{int}(\mathbf{x}) = \sum_{j=1}^{N} \mathbf{p}^k_j(\mathbf{x}) \quad \ldots\ldots (23)$$

and after substitution into (19),

$$\mathbf{p}(\mathbf{x}) = \mathbf{p}_c(\mathbf{x}) + \sum_{k=1}^{N} \sum_{j=1}^{N} \mathbf{p}^k_j(\mathbf{x}) \quad \ldots\ldots (24)$$

We assume again that (24) needs to be satisfied only in the average sense:

$$\langle \mathbf{p}(\mathbf{x}) \rangle = \left[\mathbf{1} + \sum_{k=1}^{N} \sum_{j=1}^{N} \Lambda^k_j \right] \cdot \langle \mathbf{p}_c(\mathbf{x}) \rangle \quad \ldots\ldots (25)$$

in which Λ^k_k = the transmission factor due to inclusion k considered to be alone with the crack; and Λ^k_j = the transmission factor due to interaction between inclusion k and inclusion j.

If $\boldsymbol{\sigma}_c$ is the stress field due to the crack alone subjected to the uniform internal pressure $\langle \mathbf{p}_c(\mathbf{x}) \rangle$, (25) is linear in $\langle \mathbf{p}_c(\mathbf{x}) \rangle$ and has a single vector unknown. According to this assumption, the transmission factors do not depend on the shape of the distribution of $\mathbf{p}_c(\mathbf{x})$. This simplifying assumption is acceptable if the distances between any two inclusions are not too small, as we will see next in comparisons with the results from the literature.

Fig. 6 shows an example of the calculated variation of the mode I stress intensity factor K_I at the tip of a crack located between two circular voids as a function of the crack length and of the spacing between the voids. The remote loading is uniaxial tension perpendicular to the crack. The center of the crack is equidistant from the centers of the adjacent voids. The results are compared with the known analytical solution given in Tada et al. (1985).

If the distance between the voids is large compared to their radius, the approximation is seen to be adequate (error less than 10%). However, when the crack length increases, the effect of the voids becomes localized in a small segment of the crack surface Γ_c and the agreement with the analytical solution is less than satisfactory. This discrepancy is mainly due to the two successive averagings of the distributions of internal pressures on the crack faces [averaging of $\mathbf{p}(\mathbf{x})$ first and of $\mathbf{p}_c(\mathbf{x})$ second]. Another limitation is that the approximation loses its accuracy when the voids get too close to each other.

The example in Fig. 7 shows the variation of K_I for a crack propagating in a composite containing a square array of identical circular inclusions ($b_c = b_v$). The center of the crack is at equal distances from two neighbor inclusions along the y-axis and the crack propagates in the x-direction due to tensile stress σ_{yy} (see Fig. 5). Plane stress is considered, with $\nu_i = \nu_m = 0.2$ and $E_i/E_m = 3$. The spacings between the inclusions are equal, $b_c = b_v$.

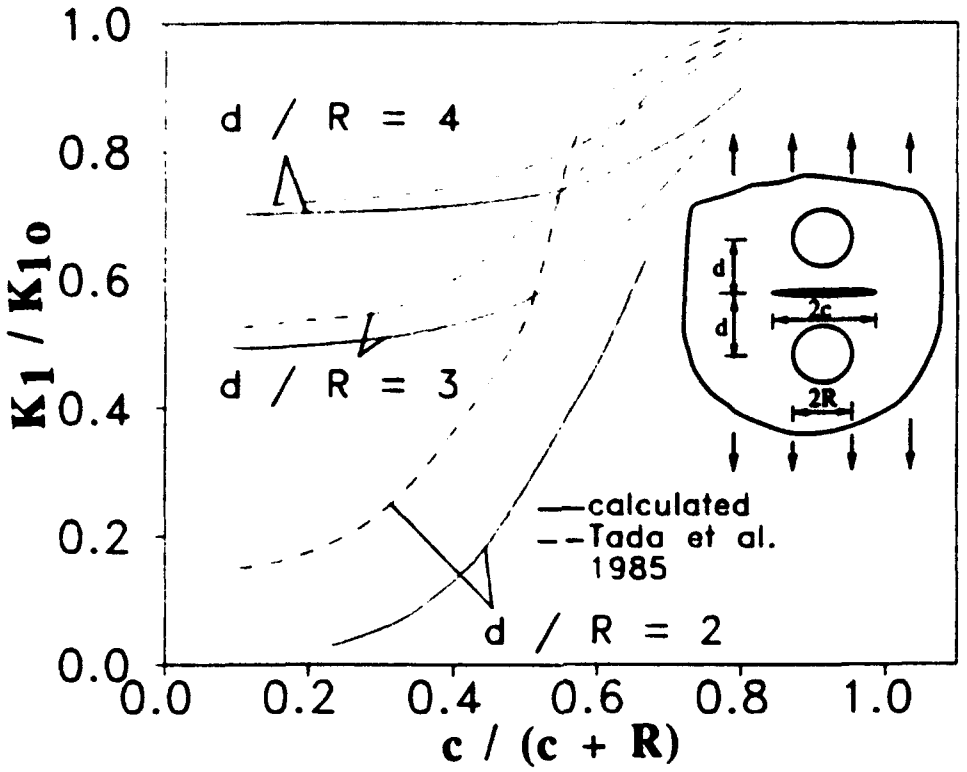

FIG. 6. Stress Intensity Factor for Crack Interacting with Two Circular Voids

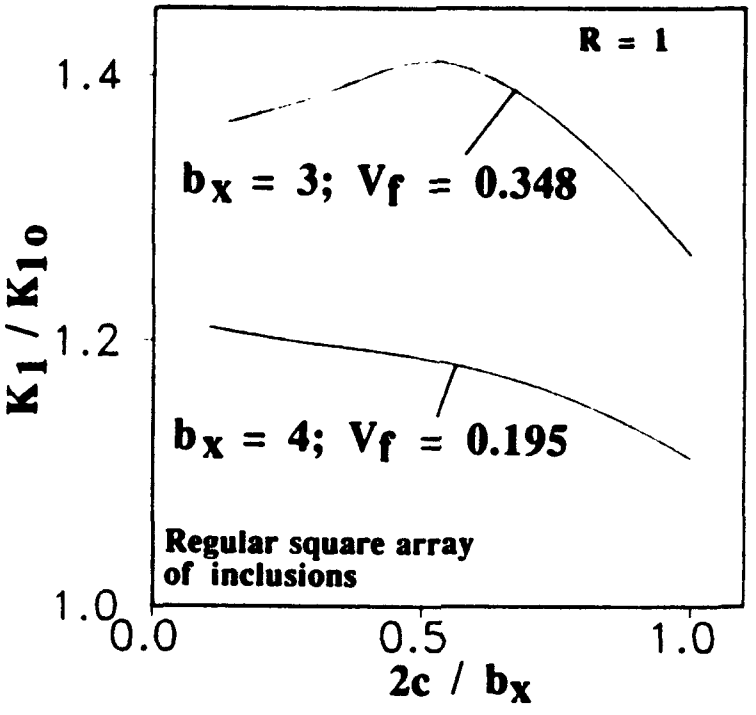

FIG. 7. Stress Intensity Factor at Tip of Crack Propagating in Composite with Square Array of Inclusions for Two Different Volume Fractions of Inclusions

Two volume fractions V_f of inclusions are chosen: $V_f = 0.195$: $b_1/R = 4$, and $V_f = 0.35$: $b_1/R = 3$. Denoting K_{I_0} = stress intensity factor if there were no inclusions, we see that the effect of the inclusions is to cause the ratio K_I/K_{I_0} to decrease with the crack length c, except when the spacing b_1 is too small. This means that the apparent stress intensity factor increases during crack propagation. So the composite behaves as if the crack followed an R-curve. Furthermore, the stress intensity factor increases with the volume fraction of inclusions. According to this result, cracks in a densely packed composite must occur earlier than in a loosely packed composite. Finally, we can see that even for a low-volume fraction of inclusions, the amplification of the stress intensity factor compared to K_{I_0} is quite important.

The present approximate method could no doubt be combined with Kachanov's method (1987) and thus be generalized for a system of cracks in a composite. However, programming the computation of the various transmission coefficients seems to be too tedious.

Apparent Fracture Toughness of Composite

As we have observed from Fig. 7, inclusions may cause the composite to behave as a homogeneous solid with a rising R-curve. The knowledge of such an apparent R-curve would permit a much simpler calculation of fracture in composites. In such an approach, the interaction between cracks is uncoupled from the interaction between the cracks and the inclusions. Similar assumptions have been made by Mori et al. (1988) and Gao and Rice (1988), who used a perturbation method to analyze fiber-reinforced composites in which the values of the elastic moduli of the matrix and the inclusions are sufficiently close. More precisely let K_{Ic} be the fracture toughness of the matrix. According to Griffith's criterion, crack propagation occurs when $K_I = K_{Ic}$. For a crack length c in a macrohomogeneous composite loaded with tensile stress σ_∞, we may write $K_I = K_{I_0} F(c)$ where $K_{I_0} = \sigma_\infty \sqrt{\pi c}$, and where $F(c)$ is a certain amplification function that is computed from the crack-inclusions interaction. The estimation of K_I yields the apparent fracture toughness K_c of the composite

$$K_c = \frac{K_{Ic}}{F(c)} \qquad (26)$$

In most studies [see e.g., Zaitsev (1985) and Zaitsev et al. (1986)], $F(c)$ was assumed to remain constant or to change only when the crack touches an inclusion (Huang and Li 1989). Fig. 8 presents the approximate variation of fracture toughness for a crack propagating symmetrically in a composite made of regular staggered circular inclusions embedded in an elastic matrix. The radii of the inclusions are equal and denoted as R ($R = 1$). The volume fraction of inhomogeneities is $V_f = 0.7$. Plane stress is assumed with $E_a/E_m = 3$ and $\nu_a = \nu_m = 0.2$. The remote boundary traction is uniaxial tension perpendicular to the crack faces (mode I crack opening).

Three configurations have been analyzed [Fig. 8(*a*)]. In configuration 1, the crack propagates toward the centers of two inclusions. In configuration 3, the center of the crack is at equal distances from two rows of inclusions. Configuration 2 is intermediate between configurations 1 and 3.

Fig. 8(*b*) shows the variation of the apparent fracture toughness with the

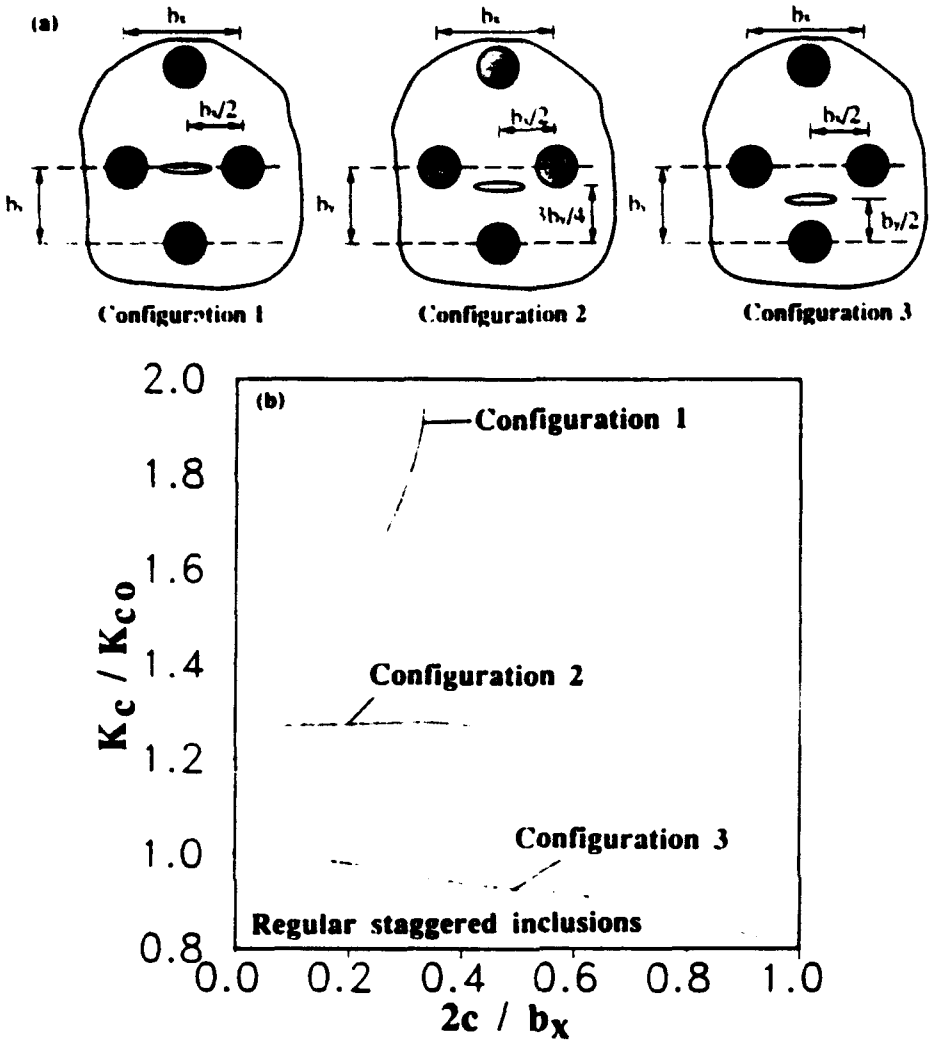

FIG. 8. Apparent Fracture Toughness of Composite with Staggered Inclusions: (*a*) Configurations Analyzed; (*b*) Fracture Toughness versus Crack Length

crack length according to (26). We see that these variations may be radically different depending on the configurations analyzed. Configurations 1 and 3 give the highest and lowest values of the apparent mode I fracture toughness, respectively. The more drastic variation is obtained when the crack propagates toward an inclusion; this corresponds to the maximum possible toughening.

These variations of apparent fracture toughness have a great influence on stability of interactive crack systems. As we see, the mechanical effect of the inclusions cannot be neglected in crack propagation studies as the fracture toughness of the equivalent medium may vary by as much as 100%. It should be stressed that these curves are valid only if the crack does not touch the inclusions. Otherwise, the singular stress field at the tips of the crack would need to be modified.

To exemplify the influence of the spatial distribution of the inclusions at a constant volume fraction, Fig. 9 shows the variation of apparent toughness for a regular ($b_x = b_y = 3R$) staggered distribution of inclusions and a non-

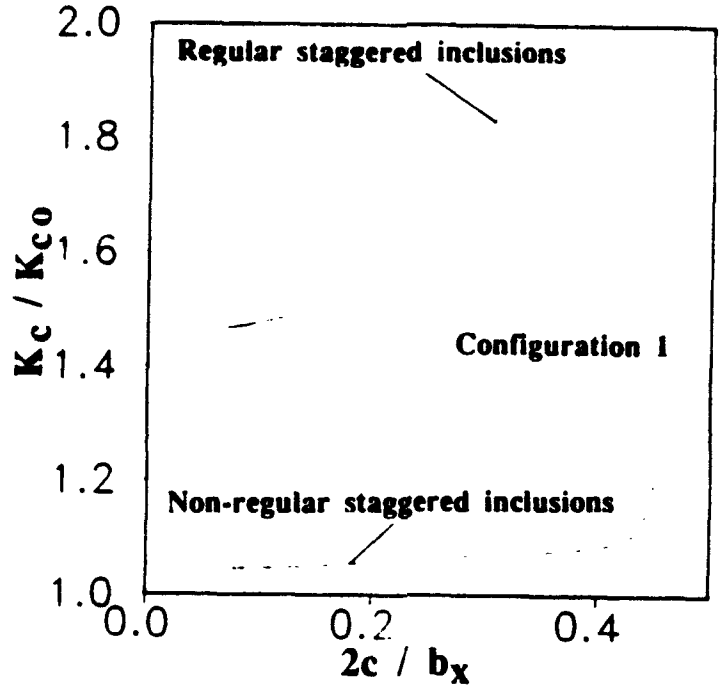

FIG. 9. Influence of Spatial Distribution of Inclusions on Apparent Toughness of Composite

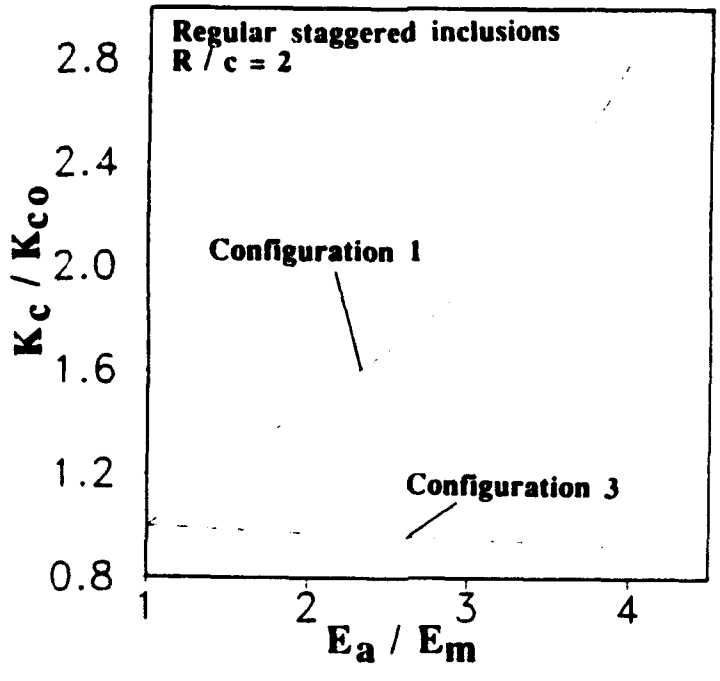

FIG. 10. Influence of Relative Elastic Young's Modulus of Inclusions on Apparent Toughness of Composite

regular staggered distribution of inclusions ($b_1 = 4R$, $b_2 = 2.25R$). The inclusion spacings are such that the volume fraction is the same, $V_f = 0.7$. Configuration 1 is chosen with the same material properties as in Fig. 8. Again, there is a large difference between the two cases. The nonregular staggered distribution (dashed curve) provides the lowest apparent fracture toughness. This suggests that inclusions that are radial to the crack have the largest influence since b_1 has been increased. The toughening effect, which is important for the regular distribution, is delayed as the tips of the crack are more distant from the inclusions.

The effect of the variation of the ratio E_a/E_m of the elastic moduli of the inclusion and the matrix is shown in Fig. 10. The apparent fracture toughness of the composite has been computed for the crack length $2c = R$, with $\nu_a = \nu_m = 0.2$. The composite contains a regular staggered distribution of inclusions with $V_f = 0.7$. The solid line corresponds to configuration 1 and the dashed line corresponds to configuration 3 [see Fig. 8(*a*)]. We obtain the upper and lower bounds of variation of toughness for a crack opened under mode I as a function of the ratio E_a/E_m. For configuration 1 this curve is certainly not linear. It should be pointed out that for large values of E_a/E_m, convergence could not be reached in subproblem 1 ($E_a/E_m > 7$). The range of variation of E_a/E_m showed in Fig. 10 corresponds to the usual values for concrete.

From the present analysis one might get the impression that the length of crack extension needed to reach the asymptotic value of an R-curve is about as long as the inclusion spacing. No doubt this can be true only for periodic inclusion arrays. For random arrays, this length could be much longer.

Conclusions

1. The interaction between a crack and several inclusions can be analyzed by superposing known solutions of standard problems of elasticity. The method uses first Duhamel-Neuman analogy in order to transform the problem into a problem of elasticity of a homogeneous body in which the inclusions are replaced by the matrix and the boundary conditions are modified. A superposition scheme is proposed, similar to Kachanov's method for interacting cracks. The solution of the problem of interaction of one crack with many inclusions is reduced to the solution of a linear algebraic equation with transmission factors characterizing the interactions of the crack with each inclusion and of any two inclusions. Comparisons with exact results from the literature show that in most cases the method is sufficiently accurate for practical purposes (with an error better than 10%) when the inclusions and the crack are not too close to each other.

2. The variation of the apparent fracture toughness of the equivalent homogeneous medium (representing the inverse of the calculated variation of the mode I stress intensity factor at the tip of a crack propagating in the composite) is analogous to the R-curve in nonlinear fracture mechanics. Calculations show that the apparent fracture toughness depends on the volume fraction of the inclusions, on their spatial distribution, and finally on the elastic properties of the constituents of the composite. The largest (mode I) toughness is obtained when the crack propagates toward an inclusion and the lowest toughness corresponds to a crack propagating between two inclusions. The difference between these two cases can be of the order of 100%.

3. Finally, the results show that, for a given composite and for a fixed crack

configuration, the mechanical effect of the interaction between the crack and the inclusions is not negligible. This effect is important for explaining stability of simultaneous propagation of many interacting cracks in a heterogeneous medium, as well as for determining the conditions under which stable states of diffuse damage can exist.

Acknowledgments

Financial support from AFOSR contract F49620-87-0030DEF with Northwestern University, and from the Center for Advanced Cement-Based Materials at Northwestern University, is gratefully acknowledged. The work of the second author was partially carried out at Lehrstuhl für Mechanik, Munich (Prof. H. Lippmann), and supported by the German Government under the Humboldt Award of Senior U.S. Scientist.

Appendix. References

Bažant, Z. P. (1987a). "Snapback instability at crack ligament tearing and its implication for fracture micromechanics." *Cem. Concr. Res.*, 17(6), 951–967.

Bažant, Z. P. (1987b). "Why continuum damage is nonlocal: Justification by quasi-periodic microcrack array." *Mech. Res. Commun.*, 14(5/6), 407–419.

Bažant, Z. P. (1989). "Stable states and paths of structures with plasticity or damage." *J. Engrg. Mech.*, ASCE, 114(12), 2013–2034.

Bažant, Z. P., and Cedolin, L. (1991). *Stability of structures: Elastic, inelastic, fracture and damage theories*. Oxford Univ. Press, New York, N.Y.

Bažant, Z. P., and Tabbara, M. R. (1989). "Stability, bifurcation and localization in structures with propagating interacting cracks." *Report No. 89-7/4*.

Bažant, Z. P., Tabbara, M. R., Kazemi, M. T., and Pijaudier-Cabot, G. (1990). "Random particle model for fracture of aggregate or fiber composites." *J. Engrg. Mech.*, ASCE, 116(11), 2484–2504.

Darwin, D., and Dewey, G. R. (1989). "Image analysis of microcracks." *Cracking and damage*, J. Mazars and Z. P. Bažant, eds., Elsevier App. Sciences Pub., 65–77.

Erdogan, F., Gupta, G. D., and Ratwani, M. (1974). "Interaction between a circular inclusion and an arbitrary oriented crack." *J. Appl. Mech.*, 41, 1007–1013.

Evans, A. G., and Faber, K. T. (1983). "On the crack growth resistance of microcracking brittle materials." *Fracture in ceramic materials*, A. G. Evans, ed., 109–136.

Faber, K. T., Evans, A. G., and Drory, B. D. (1983). "A statistical analysis of crack deflection as a toughening mechanism in ceramic materials." *Fracture mechanics of ceramics*, Vol. 6, C. Bradt et al., eds., 79–91.

Furuhashi, R., Kinoshita, N., and Mura, T. (1981). "Periodic distribution of inclusions." *Int. J. Engrg. Sci.*, 19, 231–236.

Gao, H., and Rice, J. R. (1988). *A first order perturbation analysis of crack trapping by arrays of obstacles*. Report Div. of Appl. Sci., Harvard Univ., Cambridge, Mass.

Highsmith, A. L., and Reifsnider, K. L. (1982). "Stiffness reduction mechanisms in composite laminates." *Damage in composite materials, ASTM-STP 115*, K. L. Reifsnider, ed., American Society for Testing and Materials (ASTM), Philadelphia, Pa.

Horii, H., and Nemat-Nasser S. (1985). "Elastic fields of interacting inhomogeneities." *Int. J. Solids and Struct.*, 21, 731–745.

Horii, H., Zihai, S., and Gong, S. X. (1989). "Models of fracture process zone in concrete, rock, and ceramics." *Cracking and damage*, J. Mazars and Z. P. Bažant, eds., Elsevier App. Sciences Pub., London, England, 104–115.

Hu, X. Z., Cotterell, B., and Mai, Y. W. (1986). *Computer simulation models of*

fracture in concrete. F. H. Wittmann, ed., Elsevier App. Sciences Pub., London, England, 91–100.
Huang, J., and Li, V. C. (1989). "A meso-mechanical model of the tensile behavior of concrete. Parts I and II." *Composites*, 20(4), 361–378.
Kachanov, M. (1987). "Elastic solids with many cracks-simple method of analysis." *Int. J. Solids and Struct.*, 23, 23–43.
Kunin, I., and Gommerstadt, B. (1985). "On elastic crack-inclusion interaction." *Int. J. Solids and Struct.*, 21(7), 757–766.
Legendre, D. (1984). "Prévision de la ruine des structures en béton par une approache combinee: Mécanique de l'endommagement-Mécanique de la rupture. Thèse de doctorat de 3ème cycle, Université Paris 6, France.
Lin, T. H. (1968). *Theory of inelastic structures*. John Wiley and Sons, Inc., New York, N.Y.
Maji, A. K., Ouyang, C., and Shah, S. P. (1990). "Fracture mechanics of quasi-brittle materials based on acoustic emission." *J. Mater. Res.*, 5(1), 206–217.
Mori, T., Saito, K., and Mura, T. (1988). "An inclusion model for crack arrest in a composite reinforced by sliding fibers." *Mech. Mater.*, 7, 49–58.
Mura, T. (1987). *Micromechanics of defects in solids*. 2nd Ed., Martinus Nijhoff Publishers, the Hague, the Netherlands.
Muskhelishvili, N. I. (1953). *Some basic problems of the mathematical theory of elasticity*. Noordhoff, the Netherlands.
Ortiz, M. (1988). "Microcrack coalescence and macroscopic crack growth initiation in brittle solids." *Int. J. Solids and Struct.*, 24, 231–250.
Pijaudier-Cabot, G., Bažant, Z. P., and Berthaud, Y. (1990). "Interacting crack systems in particulate or fiber reinforced composites." *Proc. Fifth Conf. on Numerical Methods in Fracture Mechanics*, D. R. J. Owen et al., eds., Pineridge Publishers, Swansea, United Kingdom, 403–414.
Pijaudier-Cabot, G., and Berthaud, Y. (1990). *Effets des interactions dans l'endommagement d'un milieu fragile—Formulation non-locale*. Comptes Rendus Acad. Sc., t. 310, Serie II, 1577–1582, (in French).
Pijaudier-Cabot, G., and Dvorak, G. J. (1990). "A variational approximation of stress intensity factors in cracked laminates." *European J. Mechanics, A/Solids*, in press.
Sih, G. C., and Chen, E. P. (1980). "Effect of material nonhomogeneity on crack propagation characteristics." *Engrg. Fract. Mech.*, 13, 431–438.
Tada, H., Paris, P. C., and Irwin, J. K. (1985). *The stress analysis of cracks handbook*. 2nd Ed., Paris Productions Inc., St. Louis, Mo.
Timoshenko, S. P., and Goodier, J. N. (1970). *Theory of elasticity*. 3rd Ed., McGraw Hill, New York, N.Y., 127.
Zaitsev, Y. V. (1985). "Inelastic properties of solids with random cracks." *Mechanics of geomaterials*, Z. P. Bažant, ed., John Wiley and Sons, Inc., New York, N.Y., 89–128.
Zaitsev, Y. V., Kazatsky, M. B., and Saralidze, T. O. (1986). "Simulation of plain concrete behaviour and its experimental examination." *Fracture toughness and fracture energy of concrete*, F. H. Wittman ed., Elsevier App. Sciences Pub., London, England, 201–205.

STATISTICAL SIZE EFFECT IN QUASI-BRITTLE STRUCTURES: I. IS WEIBULL THEORY APPLICABLE?

By Zdeněk P. Bažant,[1] Fellow, ASCE, Yunping Xi,[2] and Stuart G. Reid[3]

ABSTRACT: The classical applications of Weibull statistical theory of size effect in quasi-brittle structures such as reinforced concrete structures, rock masses, ice plates, or tough ceramic parts are being reexamined in light of recent results. After a brief review of the statistical weakest-link model, distinctions between structures that fail by initiation of macroscopic crack growth (metal structures) and structures that exhibit large macroscopic crack growth prior to failure (quasi-brittle structures) are pointed out. It is shown that the classical Weibull-type approach ignores the stress redistributions and energy release due to stable large fracture growth prior to failure, which causes a strong deterministic size effect. Further, it is shown that, according to this classical theory, every structure is equivalent to a uniaxially loaded bar of variable cross section, which means that the mechanics of the failure process is ignored. Discrepancies with certain recent test data on the size effect are also pointed out. Modification of the Weibull approach that can eliminate these shortcomings is left for a subsequent paper.

INTRODUCTION

Quasi-brittle structures are those in which: (1) Failure is caused by fracture rather than plastic yield; and (2) the fracture front is surrounded by a large fracture-process zone in which progressive distributed cracking or other damage takes place. Brittle structures, which can be analyzed according to linear elastic fracture mechanics (LEFM), are the limiting special case of quasi-brittle structures for which the size of the fracture-process zone at failure becomes negligible compared to the structure size. Quasi-brittle structures do not follow LEFM, and nonlinear fracture mechanics is required. Both structure types are characterized by post-peak softening and absence of yield plateau on the load-deflection diagram. For quasi-brittle structures, the peak of the diagram is rounded, while for brittle structures there is an almost sudden change from rising slope to descending slope of the load-displacement diagram. Quasi-brittle failures are typical of reinforced concrete structures (here the established term is *brittle* failure, but *quasi-brittle* would be a better term since purely brittle failures are not seen in reinforced concrete structures). They are also typical of certain kinds of rock, ice, modern tough ceramics, various composites, etc.

Traditionally, the size effect in failure of concrete structures has been explained in Weibull's (1939, 1951) statistical theory, which extended to multidimensional solids the weakest-link model for a chain proposed by Peirce (1926) and used the extreme value statistics originated by Tippett (1925), Fréchet (1927), and others; see also Freudenthal (1968), Mihashi and Zaitsev (1981), Zech and Wittmann (1977), Carpinteri (1989), Mihashi (1983), Mihashi and Izumi (1977); for recent works and reviews, see Kittl

[1]Walter P. Murphy Prof. of Civ. Engrg., Northwestern Univ., Evanston, IL 60208.
[2]Grad. Res. Asst., Northwestern Univ., Evanston, IL.
[3]Visiting Scholar, Northwestern Univ., Evanston, IL; on leave from the Dept. of Civ. Engrg., Univ. of Sydney, Sydney, N.S.W., Australia.

Note. Discussion open until April 1, 1992. Separate discussions should be submitted for the individual papers in this symposium. To extend the closing date one month, a written request must be filed with the ASCE Manager of Journals. The manuscript for this paper was submitted for review and possible publication on June 16, 1990. This paper is part of the *Journal of Engineering Mechanics*, Vol. 117, No. 11, November, 1991. ©ASCE, ISSN 0733-9399/91/0011-2609/$1.00 + $.15 per page. Paper No. 26346.

and Diaz (1988, 1989, 1990). In Weibull's theory, the failure is determined by the minimum value of the strength of the material, and the statistical size effect is due to the fact that the larger the structure, the smaller is the strength value likely to be encountered in the structure. This explanation is certainly valid for one-dimensional structures such as a long chain or a long fiber, but extension to multidimensional structures depends on certain simplifying hypotheses that do not have to be satisfied for all types of structures. These hypotheses appear to be applicable to structures consisting of ceramics, glasses, and fatigue-embrittled metals. But they do not apply to quasi-brittle structures, such as concrete structures, because of their ability to develop large fractures in a stable manner prior to failure. The central idea in Weibull-type statistical analysis of failure and size effect is that the survival probability of the structure is the joint probability of survival of all its elementary parts. Implementation of this idea, however, is clear and simple only for a long fiber or a long chain. It is difficult for two-dimensional and three-dimensional structures.

This paper will examine the limitations of the classical Weibull theory of size effect from the viewpoint of quasi-brittle structures, such as reinforced concrete structures. A companion paper will present a new formulation which overcomes the main limitations. The basic idea of the present formulation has been briefly outlined in a previous conference paper (Bažant 1987).

Review of Weibull Theory

We need to start by reviewing the principles of Weibull theory. First, we consider a one-dimensional structure consisting of many elements coupled in series, for example a chain [Fig. 1(*a*)]. All of the elements (links of the chain) have the same distribution of strength σ, characterized by the cumulative probability distribution $P_1(\sigma)$, which represents the probability of failure of one element, i.e.,the probability that the strength in the element is less than the applied stress σ. The survival probability of one element is $1 - P_1$. If the whole chain should survive, all of its elements must survive. This means that the probability of survival of the chain is the joint probability of the survival of all of the elements. According to the joint-probability theorem, the survival probability of a chain of N elements is, $1 - P_f = (1 - P_1)(1 - P_1) \ldots (1 - P_1)$, or

$$1 - P_f = (1 - P_1)^N \quad \ldots\ldots (1)$$

where P_f = failure probability of the chain. Now

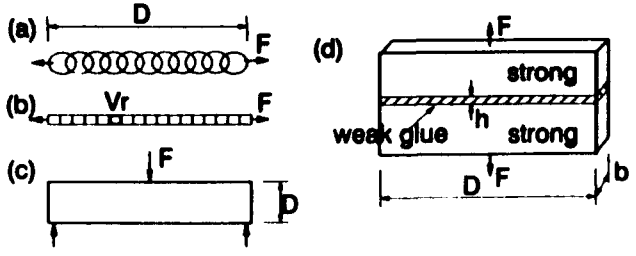

FIG. 1. Some Different Cases for Weibull Distribution

$$\ln(1 - P_f) = N \ln(1 - P_1) \quad \ldots\ldots (2)$$

and since P_1 is very small in practical application, $\ln(1 - P_1) \simeq -P_1$. Therefore

$$\ln(1 - P_f) = -NP_1 \quad \ldots\ldots (3)$$

This may be extended to a continuous, homogeneously stressed solid [e.g., a long fiber, Fig. 1(*b*)] by setting $N = V/V_r$; thus $\ln(1 - P_f) = -(V/V_r)P_1$ or

$$P_f(\sigma) = 1 - \exp\left[-\frac{V}{V_r} P_1(\sigma)\right] \quad \ldots\ldots (4)$$

Here V = volume of the body; and V_r = representative volume of the material. In the greatest generality, V_r represents the smallest volume for which the material can be treated as a continuum (and for which the concept of stress on the macroscopic scale makes sense). In this definition, V_r is defined as the smallest volume for which the main statistical characteristics of the microstructure do not change substantially if the volume is displaced within the material. The size of the representative volume is the characteristic length l of the material—a central concept in the nonlocal-continuum theory. The foregoing definition of V_r coincides with that used in nonlocal or statistical theories of microinhomogeneous materials. For practical purposes, though, V_r can be taken as any material volume for which the strength distribution has been experimentally determined.

To describe the statistical distribution of P_1. Weibull (1939) [also Weibull (1951)] introduced the following empirical form (Fig. 2)

$$P_1(\sigma) = \left(\frac{\sigma - \sigma_u}{\sigma_0}\right)^m; \text{ for } \sigma > \sigma_u$$

$$P_1(\sigma) = 0; \text{ for } \sigma \le \sigma_u \quad \ldots\ldots (5)$$

in which σ_0 and σ_u = empirical material parameters; m = shape parameter (Weibull modulus); σ_0 = scale parameter; and σ_u = datum parameter

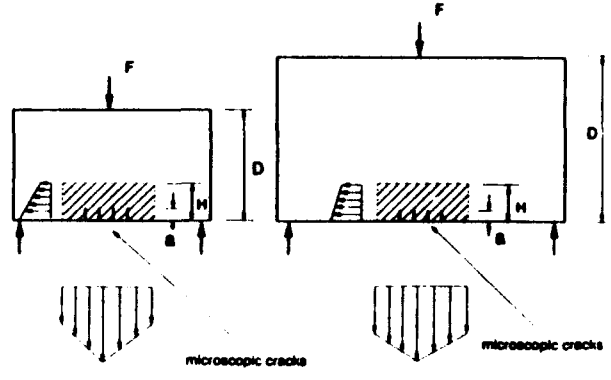

FIG. 2. Geometrically Similar Structures with Microscopic Cracks

(streng reshold). For calculations it is convenient to assume that $\sigma_u = 0$, and then the results of direct tensile tests of concrete indicate approximately $m = 12$ (Zech and Wittmann 1977). In reality, the threshold σ_u is of course nonzero, but it is hard to determine σ_u reliably due to scatter of test results. Unless the strength range of data is very broad, and random scatter is small, different σ_u-values (with different corresponding values of σ_u and m) allow almost equally good fits of the data on $P_1(\sigma)$.

To generalize (4) for a structure with nonuniform stress [(e.g., a beam, Fig. 1(c)], one may imagine the structure to consist of many parts of small volumes, $\Delta V_{(j)}$, each with uniform stress $\sigma_j (j = 1, \ldots, \bar{n})$. The probability of survival of the structure is the joint probability of survival of all its parts, and so

$$1 - P_f = \exp\left\{ -\frac{\Delta V_{(1)}}{V_r} P_1[\sigma_{(1)}] \right\} \exp\left\{ -\frac{\Delta V_{(2)}}{V_r} P_1[\sigma_{(2)}] \right\} \ldots$$

$$\exp\left\{ -\frac{\Delta V_{(\bar{n})}}{V_r} P_1[\sigma_{(\bar{n})}] \right\} = \exp\left\{ -\sum_{j=1}^{\bar{n}} \frac{\Delta V_{(j)}}{V_r} P_1[\sigma_{(j)}] \right\} \quad \ldots\ldots\ldots\ldots\ldots (6)$$

Now, if the volume of each part tends to zero and the number of the parts tends to infinity, one obtains a structure with continuously variable stress $\sigma(\mathbf{x})$. Eq. (6) thus becomes

$$1 - P_f = \exp\left[-\int_V \left\langle \frac{\sigma(\mathbf{x}) - \sigma_u}{\sigma_0} \right\rangle^m \frac{dV(\mathbf{x})}{V_r} \right] \quad \ldots\ldots\ldots\ldots\ldots\ldots (7)$$

where $\langle\ \rangle$ denotes the positive part of the argument, i.e., $\langle x \rangle = x$ if $x > 0$, and $\langle x \rangle = 0$ if $x \le 0$; and $\mathbf{x}$ = the coordinate vectors of material points.

Eq. (7) needs to be further generalized to triaxial-stress states. For this, in principle, the triaxial failure surface in the stress space needs to be used. However, for the sake of simplicity, one may assume that the cracks may form only in the planes normal to the principal stresses $\sigma_i(\mathbf{x})(i = 1, 2, 3)$ and that the formation of any crack depends only on the principal stresses normal to it, but not on the other principal stresses, as proposed by Freudenthal (1968). Considering the joint probability of survival of the material on all three principal stress planes, similarly to (6), one gets, for a structure with triaxial stresses, the following probability of survival (P_f = probability of failure)

$$1 - P_f = \exp\left[-\int_V \sum_{i=1}^{n} \left\langle \frac{\sigma_i(\mathbf{x}) - \sigma_u}{\sigma_0} \right\rangle^m \frac{dV(\mathbf{x})}{V_r} \right] \quad \ldots\ldots\ldots\ldots\ldots\ldots (8)$$

where n = number of dimensions (1, 2, or 3). In anisotropic materials, furthermore, subscript i needs to be also attached to m, σ_0 and σ_u.

It may be noted that more sophisticated multiaxial formulations have been proposed. For example, Petrovic (1987) considered that a crack can form on a plane of any orientation and the failure probability depends only on the normal stress on that plane. In that case the joint probability of survival for the planes of all orientations leads to an integral over all spatial directions at each point. However, this might be no more realistic than (8), since the fact that the cracking probability may depend also on the stresses that act on the planes of other orientations (as well as on the strain and the invariants of stress and strain) is still neglected.

Statistical Size Effect due to Random Strength

The size effect is defined by comparing geometrically similar structures of different characteristic dimensions (sizes) D. For this purpose, one introduces the nominal strength (nominal stress at maximum load),

$$\sigma_N = \frac{F}{bD} \quad \ldots\ldots\ldots\ldots\ldots\ldots\ldots\ldots\ldots\ldots\ldots\ldots\ldots\ldots\ldots\ldots (9)$$

where F = failure load (maximum load); and b = thickness of the structure, which may either be constant (two-dimensional similarity), or proportional to D (three-dimensional similarity). Now the basic property of all structures is that, according to elastic analysis with allowable stress limit as well as plastic analysis or any analysis based on some material failure criterion in terms stress or strain, σ_N is independent of structure D, i.e., there is no size effect. This is not true, however, when the material properties are random, as shown by Weibull. To demonstrate it, we may represent the stress distributions in the structure as

$$\sigma_i(\mathbf{x}) = \sigma_N S_i(\boldsymbol{\xi}), \qquad \boldsymbol{\xi} = \frac{1}{D}\mathbf{x} \quad \ldots\ldots\ldots\ldots\ldots\ldots\ldots\ldots\ldots\ldots (10)$$

in which S_i = functions of the relative coordinate vectors $\boldsymbol{\xi}$, calculated according to elasticity or plasticity or any other suitable theory. Substituting $dV = dx_1 \ldots dx_n = D^n d\xi_1 \ldots d\xi_n$, where $x_1, \ldots, x_n$ = Cartesian-coordinate components, and $\xi_1, \ldots, \xi_n$ = corresponding elastic-coordinate components of the vector $\boldsymbol{\xi} = (\xi_1, \ldots, \xi_n)$, we obtain

$$\ln(1 - P_f) = -\frac{D^n}{V_r} \int_\Omega \cdots \int \sum_{i=1}^{n} \left\langle \frac{\sigma_N S_i(\boldsymbol{\xi}) - \sigma_u}{\sigma_0} \right\rangle^m d\xi_1 \ldots d\xi_n \quad \ldots\ldots\ldots (11)$$

in which Ω = the domain of the structure in relative coordinates $\boldsymbol{\xi}$, which is the same for similar structures of all sizes.

The strength threshold is usually neglected in practical calculations, that is $\sigma_u = 0$, not only for the sake of simplicity but also because it is very difficult to identify the value of σ_u from test data reliably, as already pointed out. With this simplification, (11) may be rewritten as follows

$$\ln(1 - P_f) = -\frac{D^n}{V_r}\left(\frac{\sigma_N}{\sigma_0}\right)^m I_n, \qquad \text{with}$$

$$I_n = \int_\Omega \cdots \int \sum_{i=1}^{n} [S_i(\boldsymbol{\xi})]^m d\xi_1 \ldots d\xi_n \quad \ldots\ldots\ldots\ldots\ldots\ldots\ldots\ldots (12)$$

Here I_n, σ_0, and V_r = constants when the structure size D is varied. Thus, when the failure probability P_f is specified, the following dependence of the nominal strength of the structure on its size D or volume $V (V \propto D^n)$ results:

$$\sigma_N = k_0 D^{-n/m} \quad \ldots\ldots\ldots\ldots\ldots\ldots\ldots\ldots\ldots\ldots\ldots\ldots\ldots\ldots\ldots\ldots (13)$$

in which $k_0 = \sigma_0[-V_r \ln(1 - P_f)/I_n]^{1/m}$ = constant. When one substitutes $P_f = 0.5$, one gets the size dependence of the median strength, which is known for concrete to be almost the same as the mean strength, $\bar{\sigma}_N$ [for the calculation of $\bar{\sigma}_N$, see the companion paper (Bažant and Xi 1991)].

From direct tensile tests, the typical value of m for concrete is about 12. Then, for two-dimensional similarity ($n = 2$)

$$\sigma_N \propto D^{-1/6} \quad (14)$$

and for three-dimensional similarity ($n = 3$)

$$\sigma_N \propto D^{-1/4} \quad (15)$$

Eq. (13) is also valid for one-dimensional similarity. This case is obtained, e.g., for the body in Fig. 1(d), which consists of two strong blocks joined by a thin layer of weak glue (of Weibull distribution with modulus $m = 12$). The blocks cannot fail and failure is assumed to occur in the glue layer as soon as one elementary volume of the glue fails. In that case $n = 1$ and (13) yields

$$\sigma_N \propto D^{-1/12} \quad (16)$$

provided that block thickness b and glue layer thickness h are not varied.

Basic Criticisms of Classical Weibull-Type Approach

Stress Redistribution

The key to the calculation of failure probability of the structure is the function $S_i(\xi)$, characterizing the stress at point $x = D\xi$. In this regard, one must distinguish two types of structures: (1) Those failing at the initiation of the macroscopic crack growth (i.e., the structure just before failure contains only microscopic cracks or other flaws, as is typical of many ceramics and fatigue-embrittled metal structures); and (2) those failing only after a large stable macroscopic crack growth (which is the case of reinforced concrete structures).

For the first type of structure, the key point is that function $S_i(\xi)$ just before failure is known, since microscopic flaws have negligible influence on the overall stress distribution within the structure. In such structures there exists a region of size H (Fig. 2) such that

$$H << D \text{ and } H >> a \quad (17)$$

where D = structure dimension; and a = crack or flaw size. The condition $H << D$ means that the stress distribution within region H would be nearly uniform if the flaw did not exist. If the size of the flaw or initial crack is very small, $a << D$, it is a characteristic of the state of the material. It is related to the inhomogeneity size and is independent of the structure dimension D. Since $H << D$, the presence of the flaw of size a affects the stress distribution only locally, and the situation is nearly the same as that of a crack in an infinite space with a uniform-stress state at infinity equal to the stress in region H. Thus, the only effect of the flaw of size a is a reduction of the effective macroscopic strength of the material. This permits that the random variation of the sizes of the initial flaws can be related to the random variation of the material strength, as described by Weibull distribution.

For the second type of structure, for example, reinforced concrete structures, the behavior is completely different. Due to reinforcement as well as to the existence of strain softening in a large zone of microcracking and crack bridging near the front of a continuous fracture, reinforced concrete structures do not fail at crack initiation. Large cracks, typically cutting through 50% to 90% of the cross section, grow in a stable manner before the maximum load is reached (see the typical macroscopic crack patterns in Fig. 3). The design codes, in fact, require the failure load to be significantly higher than the crack-initiation load (for bending, at least 1.25 times higher, according to ACI Standard 318, but in practice this ratio is usually much larger). Consequently, a reinforced concrete structure normally undergoes pronounced inelastic deformation with large macroscopic stable crack growth prior to reaching the failure load (maximum load). This inevitably engenders stress redistributions, such that the stress distribution $\sigma(x)$ at incipient failure is very different from the elastic stress distribution, which has commonly been assumed in the previous studies of the statistical size effect. The existence of macroscopic crack growth is also documented by the load-deflection diagram, in which the start of macroscopic crack growth is manifested by a significant reduction of slope, as seen in Fig. 4(a). This contrasts with metal or some kinds of rock structures, for which the load-deflection diagram typically looks as shown in Fig. 4(b).

To sum up, Weibull theory cannot be applied to the failure of reinforced concrete structures unless the effect of stable macroscopic crack growth on the stress distribution function $S_i(\xi)$ is taken into account (Bažant 1988).

Equivalence to Uniaxially Stressed Bar

Another limitation of the existing Weibull-type formulations is revealed by realizing that, if the stress-distribution function $S_i(\xi)$ is known a priori, every structure is equivalent to a uniaxially stressed bar of variable cross-sectional area, A. To demonstrate it, consider the bar in Fig. 5, where x is the longitudinal coordinate. For the real structure, one can calculate the

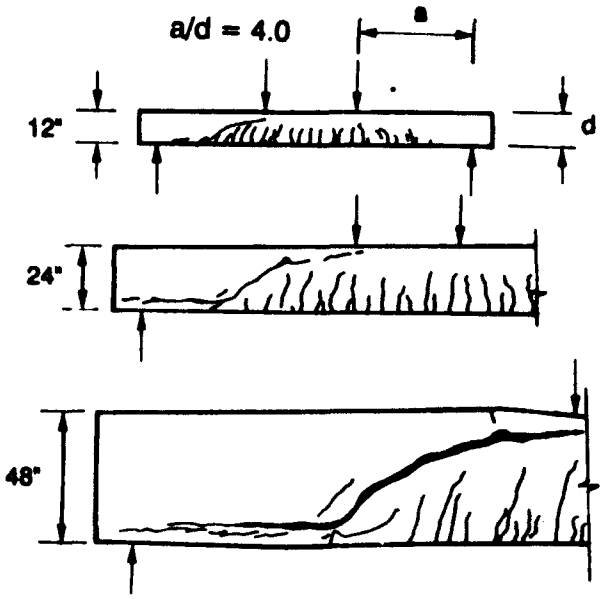

FIG. 3. Example of Geometrically Similar Reinforced Concrete Structures with Stable Macroscopic Fracture Growth before Failure [adapted from Kani (1967)]

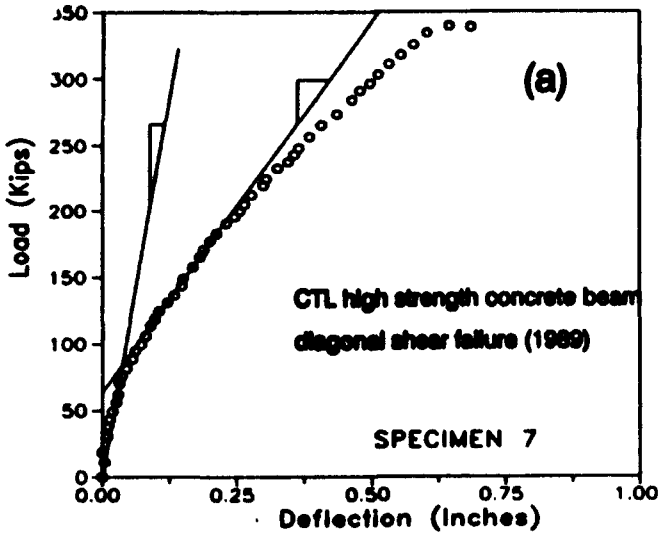

FIG. 4(a). Typical Load-Deflection Diagram of Reinforced Concrete Structures in which Slope Reduction Indicates Start of Actual Growth of Macroscopic Cracks

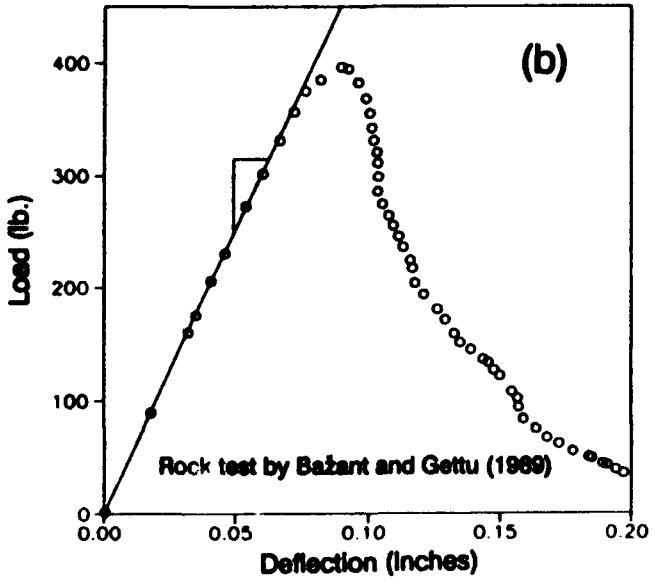

FIG. 4(b). Geometrically Similar Structures in which Fracture Length at Maximum Load is Small (Microscopic), and Typical Load-Deflection Diagram

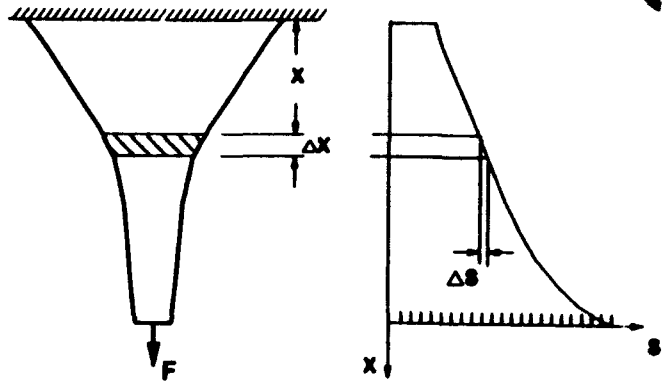

FIG. 5. Uniaxially Loaded Bar of Variable Cross Section

volume $V(S)$ of the part of the structure in which the equivalent uniaxial stress, $\bar{S}(\xi) = [\Sigma_{i=1}^{n} S_i^m(\xi)]^{1/m}$, exceeds the value S, representing the stress at some cross section of a uniaxial bar (Fig. 5)

$$V(S) = \int_V H[\sigma_N \bar{S}_i(\xi) - S]\, dV(\xi) \quad \ldots\ldots\ldots\ldots\ldots\ldots\ldots\ldots\ldots\ldots (18)$$

in which H = Heaviside step function. Now one may subdivide the stress range into small steps ΔS with S representing the value at the middle of each step. Then one can calculate function $V(S)$ from (18), and also get the derivative $V'(S) \simeq \Delta V(S)/\Delta S$. Beginning with $S = 0$, one must satisfy for each step ΔS (with the value S at the middle of the step) the condition of equal volume in the real structure, i.e., $V'(S)\Delta S = A\Delta x = \sigma_N \Delta x/S$. The cross-sectional area of the bar corresponding to each stress value S is then calculated as $A = \sigma_N/S$ (in which σ_N is imagined as the load applied on the uniaxial bar, Fig. 5), and the length of the bar element having this cross-sectional area is

$$\Delta x = V'(S)\Delta S \frac{S}{\sigma_N} \quad \ldots\ldots\ldots\ldots\ldots\ldots\ldots\ldots\ldots\ldots\ldots\ldots\ldots\ldots\ldots\ldots (19)$$

Putting all these segments Δx with areas $A = \sigma_N/S$ together, one obtains the profile of the equivalent bar. So, we see that, indeed, for every multidimensional structure for which the stress-distribution function at incipient failure is known a priori, an equivalent uniaxial bar of variable cross section can be found (Bažant 1988). This bar, according to the classical application of Weibull theory, behaves in the same way as the actual structure.

Obviously, in this approach, all information about the mechanics of failure is lost, and the structural geometry becomes irrelevant. Of course this cannot be true. So the Weibull-type approach cannot be regarded as realistic, unless the stress-distribution function realistically describes the stress field at imminent failure.

Differences between Two- and Three-Dimensional Geometric Similarities

Another questionable aspect of the classical Weibull-type approach is the effect of the number of dimensions, n, implied by (13). Consider, for ex-

ample, that the beam dimensions are increased in the ratio D_2/D_1 according to either two-dimensional similarity, in which case, the beam thickness b is kept constant, or according to three-dimensional similarity, in which case, the beam thickness is also increased in proportion to D. According to (13), the nominal strength σ_N should change in the ratio $(D_2/D_1)^{-2/m}$ or $(D_2/D_1)^{-3/m}$, respectively. Now, although systematic data on the effect of thickness is unavailable, it appears from experience that there is no significant difference between these two cases.

No significant difference is manifested by comparing the slopes of the plots of $\log(\sigma_N)$ versus $\log(D)$ for tests with two-dimensional similarity and three-dimensional similarity. The effect of the number of dimensions, n, can be checked by using Bažant and Kazemi's (1989) tests of diagonal shear failure of concrete beam (reinforced by longitudinal bars with hooks at the ends), which were similar to two dimensions (same thickness), and the pull-out tests of bars by Bažant and Sener (1988) or the torsional shear fracture tests by Bažant et al. (1990), which were similar in three dimensions; see the data points in Fig. 6. Taking the diagonal shear test as reference, the fact that the slope of the mean trend of the data is approximately $-1/2$ implies that $m = 4$ (let us pretend we do not know any uniaxial test data that indicate a much larger m). Then, for three-dimensional similarity, the slope of the line should be $-n/m = -3/4$ (Bažant 1988). But the pull-out tests made with the same concrete indicate the slope to be also $-1/2$, which does clearly disagree with the classical Weibull-type analysis [but agrees with the modified statistical theory presented in the companion paper (Bažant and Xi 1991)].

The classical Weibull-type theories are further put in question when one tries to compare the results of tests on bars of different sizes failing in uniaxial tension with the diagonal shear tests. The former tests indicate that, approximately, $m = 12$ (Zech and Wittmann 1977). But if $m = 12$, then the slope of the line in Fig. 6 on the left would have to be $-1/6$ rather than $-1/2$. This is a serious discrepancy indeed [it is remedied in the companion paper (Bažant and Xi 1991)].

Energy Release Due to Large Stable Crack Growth

From the mechanics viewpoint, the basic problem with the classical Weibull-type approaches to reinforced concrete structures is that they generally ignore the effect of macroscopic fracture growth on the energy-release rate of the structure. Experiments confirm that in concrete structures, the fracture length at maximum load is usually proportional to the structure dimension, while the width of the fracture process zone, h, is almost the same for any size and is a material property, as shown by the example of rectangular panel in Fig. 7 (Bažant 1984). The fracture length a_0 before failure of this panel may be imagined to release the stress from the sparsely shaded triangular areas in the figure. When, during failure, the fracture extends by Δa, the stress is further relieved from the densely cross-hatched narrow strips, the area of which gets larger as the structure size gets larger. This means that the release of the stored energy of the structure into the fracture extension Δa, which comes from the strip, is larger for a larger structure if the nominal stress is the same. However, fracture extension requires roughly the same energy per unit length of extension, regardless of the structure size. Therefore, the nominal stress at failure must get smaller if the structure gets larger, so that the strain energy density in the densely cross-hatched strip would be smaller in a larger structure, thus making it possible to obtain the same energy release per unit length of the fracture.

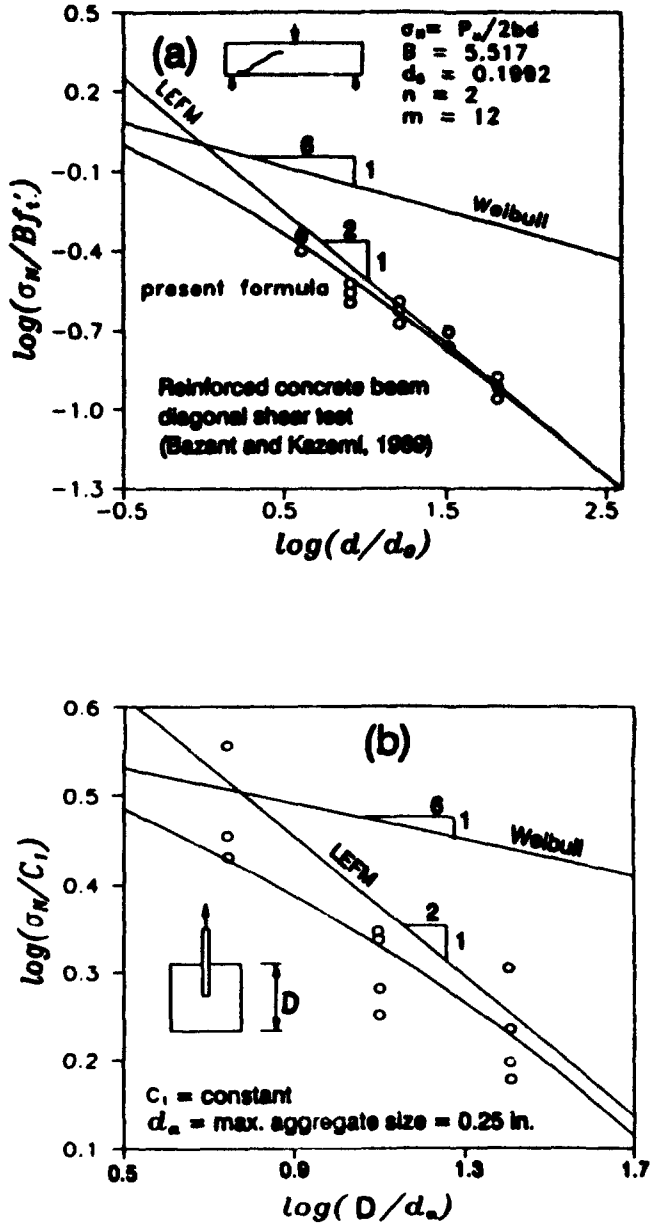

FIG. 6. Test Results of Bažant and Kazemi (1989) for Diagonal Shear Failure (a) and of Bažant and Sener (1988) for Pull-Out (b), and Comparisons with Size Effect Lines Obtained from Classical Weibull-Type Theory

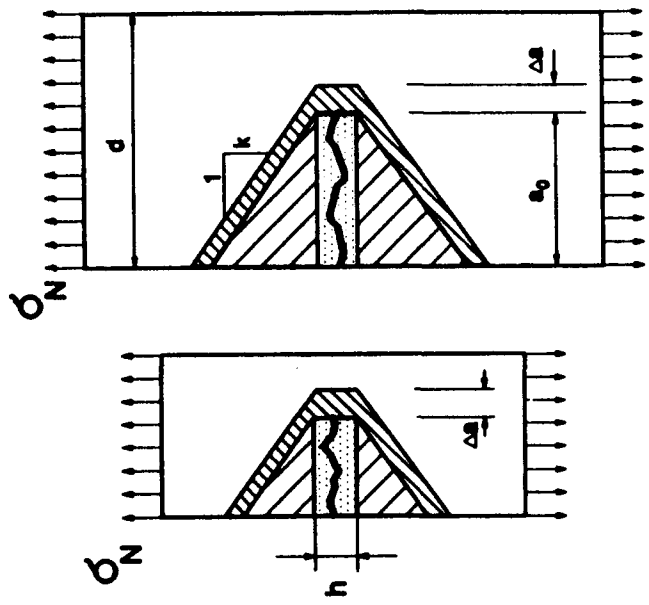

FIG. 7. Stress Relief Zone in Geometrically Similar Panels with Large Similar Fractures

The foregoing argument has been used to derive a deterministic size effect law that is different from that in (13) and agrees quite well with a broad range of test results (Bažant 1984; Bažant and Kazemi 1990). That law has also been supported by certain other, more general, arguments.

Spatial Correlation

Another questionable aspect of classical Weibull-type theories based on (2) is the neglect of spatial correlation. This might be justified for the links in a chain, but not for continuous bodies of concrete cast at one time. If the strength value realized in one small material element is on the low side of the average strength, the strength value realized in the adjacent material elements is more likely to be also on the low side than on the high side of average strength. The standard way to deal with spatial correlation would be to introduce a spatial autocorrelation function for material behavior, such as strength, but that approach would be rather complicated for the present purpose. There is, nevertheless, another simpler way to introduce spatial correlation—the nonlocal concept, advanced in the subsequent paper.

Conclusion

The classical applications of Weibull theory to failure of reinforced concrete structures suffer from several serious shortcomings.

1. The stress-distribution function used in the applications cannot be assumed as the elastic stress distribution, but must take into account the stress redistributions caused by large macroscopic stable crack growth prior to reaching maximum load. That growth causes a strong deterministic (or systematic) size effect, which prevails over the statistical size effect due to random strength.
2. According to classical applications of Weibull theory, every structure is equivalent to a uniaxial bar with a variable cross section, which means that all information on the failure mechanism and structure geometry is lost.
3. According to classical theories, the differences in the size effect between two-dimensional similarity and three-dimensional similarity are predicted to be too strong, contradicting experience.
4. Tests of geometrically similar concrete structures, e.g., diagonal shear tests, show a much stronger size than that predicted by classical Weibull-theory applications (provided that the Weibull modulus value is taken the same as that obtained from direct tension test).
5. The classical Weibull-type theories neglect spatial statistical correlation of random material properties.

Modifications of the Weibull theory required to eliminate the aforementioned shortcomings are relegated to the subsequent paper.

Acknowledgment

Partial financial support under National Science Foundation Grant BCS-88182302 to Northwestern University is gratefully acknowledged. Partial funding for the underlying studies of the size effect were also obtained from the Center for Advanced Cements Based Materials at Northwestern University.

Appendix I. References

Bažant, Z. P. (1984). "Size effect in blunt fracture: Concrete, rock, metal." *J. Engrg. Mech.*, ASCE, 110(4), 518–535.
Bažant, Z. P. (1987). "Fracture Energy of Heterogeneous Materials and Similitude," Preprints, SEM-RILEM, *Conference on Fracture of Concrete and Rock*, Houston, TX, S. P. Shah and S. E. Swartz, eds., *Soc. for Exper. Mech.*, 390–402.
Bažant, Z. P. (1988). "Fracture of concrete." *Lecture Notes for Course 720-D95*, Northwestern Univ., Evanston, Ill.
Bažant, Z. P., and Sener, S. (1988). "Size effect in pullout tests." *ACI Materials J.*, 85(5), 347–351.
Bažant, Z. P., and Kazemi, M. T. (1989). "Size effect on diagonal shear failure of beams without stirrups." *Report No. 89-8/498s*, S and T Ctr. on Advanced Cement-Based Materials, Northwestern Univ., Evanston, Ill.
Bažant, Z. P., and Kazemi, M. T. (1990). "Size effect in fracture of ceramics and its use to determine fracture energy and effective process zone length." *J. Am. Ceram. Soc.*, 73(7), 1841–1853.
Bažant, Z. P., Prat, P. C., and Tabbara, M. T. (1990). "Antiplane Shear Fracture Texts (Mode III)." *ACI Materials J.*, 87(1), 12–19.
Carpinteri, A. (1989). "Decrease of apparent tensile and bending strength with specimen size: Two different explanations based on fracture mechanics." *Int. J. Solids Struct.*, 25(4), 407–429.
Fréchet, M. (1927). *Ann. Soc. Polon. Mat.*, (Cracow) 6, 93.
Freudenthal, A. M. (1968). "Statistical approach to brittle fracture." *Fracture—An advanced treatise*, H. Liebowitz, ed., Vol. 2, Academic Press, 591–619.
Kani, G. N. J. (1967). "How safe are our large reinforced concrete beams?" *ACI J.*, March, 64, 128–141.

Kittl, P., and Díaz, G. (1988). "Weibull's fracture statistics, or probabilistic strength of materials: state of the art." *Res. Mechanica*, 24, 99–207.
Kittl, P., and Díaz, G. (1989). "Some engineering applications of the probabilistic strength of materials." *Appl. Mech. Rev.*, 42(11), 108–112.
Kittl, P., and Díaz, G. (1990). "Size effect on fracture strength in the probabilistic strength of materials." *Reliability Engrg. Syst. Saf.*, Vol. 28, 9–21.
Mihashi, H., and Izumi, M. (1977). "Stochastic theory for concrete fracture." *Cem. Concr. Res.*, 7, 411–422.
Mihashi, H., and Zaitsev, J. W. (1981). "Statistical nature of crack propagation." *Report to RILEM TC 50-FMC*, 1–21.
Mihashi, H. (1983). "A stochastic theory for fracture of concrete." *Fracture mechanics of concrete*, F. H. Wittmann, ed., Elsevier Science Publishers, B. V., Amsterdam, the Netherlands, 301–339.
Petrovic, J. J. (1987). "Weibull statistical fracture theory for the fracture of ceramics." *Metall. Trans. A*, 18a, Nov., 1829–1834.
Peirce, F. T. (1926). *J. Textile Inst.*, 17, 355.
Tippett, L. H. C. (1925). *Biometrika*, 17, 364.
Weibull, W. (1939). "A statistical theory of the strength of materials." *Royal Swedish Academy of Engrg. Sci. Proc.*, 151, 1–45.
Weibull, W. (1951). "A statistical distribution function of wide applicability." *J. Appl. Mech.*, 18, 293–297.
Zech, B., and Wittmann, F. H. (1977). "A complex study on the reliability assessment of the containment of a PWR, Part II. Probabilistic approach to describe the behavior of materials." *Trans. 4th Int. Conf. on Structural Mechanics in Reactor Technology*, T. A. Jaeger and B. A. Boley, eds., European Communities, Brussels, Belgium, Vol. H, J1/11, 1–14.

2820

(1-3

STATISTICAL SIZE EFFECT IN QUASI-BRITTLE STRUCTURES: II. NONLOCAL THEORY

By Zdeněk P. Bažant,[1] F. ASCE, and Yunping Xi[2]

ABSTRACT: The failure probability of structures must be calculated from the stress field that exists just *before failure*, *rather than the initial elastic field*. Accordingly, fracture-mechanics stress solutions are utilized to obtain the failure probabilities. This leads to an amalgamated theory that combines the size effect due to fracture energy release with the effect of random variability of strength having Weibull distribution. For the singular stress field of linear elastic fracture mechanics, the failure-probability integral diverges. Convergent solution, however, can be obtained with the nonlocal-continuum concept. This leads to nonlocal statistical theory of size effect. *According to this theory, the asymptotic* size-effect law for very small structure sizes agrees with the classical-power law based on Weibull theory. For very large structures, the asymptotic size-effect law coincides with that of linear elastic fracture mechanics of bodies with similar cracks, and the failure probability is dominated by the stress field in the fracture-process zone while the stresses in the rest of the structure are almost irrelevant. The size-effect predictions agree reasonably well with the existing test data. The failure probability can be approximately calculated by *applying the failure-probability integral* to spatially averaged stresses obtained, according to the nonlocal-continuum concept, from the singular stress field of linear elastic fracture mechanics. More realistic is the use of the stress field obtained by nonlinear finite element analysis according to the nonlocal-damage concept.

INTRODUCTION

In the preceding paper (Bažant et al. 1991), it was shown that the classical Weibull-type analysis of the size effect in brittle failure is invalid for quasi-brittle structures such as reinforced concrete structures, rock masses, ice sheets, or parts made of tough ceramics. This is due to the existence of a large macroscopic stable crack growth prior to reaching the maximum load.

The objective of this paper is to propose a modified statistical theory that takes into account the effect of large macroscopic fractures and distributed cracking at fracture front. This theory, which represents an amalgamation of Weibull theory and the size-effect theory based on energy release, will be shown to agree well with the existing experimental evidence. All the definitions and notations from the preceding paper are retained.

NONLOCAL CONCEPT AND HANDLING OF STRESS SINGULARITY

As argued in the preceding paper (Bažant et al. 1991), the stress-distribution function to be used in the integral for failure probability of the structure must be the stress distribution at incipient failure, rather than some stress distribution that exists long before failure. This distribution must reflect the localization of strains and stresses that occur prior to reaching

[1]Walter P. Murphy Prof. of Civ. Engrg., Northwestern Univ., Evanston, IL 60208.
[2]Grad. Res. Asst., Northwestern Univ., Evanston, IL.

Note. Discussion open until April 1, 1992. Separate discussions should be submitted for the individual papers in the symposium. To extend the closing date one month, a written request must be filed with the ASCE Manager of Journals. The manuscript for this paper was submitted for review and possible publication on June 16, 1990. This paper is part of the *Journal of Engineering Mechanics*, Vol. 117, No. 11, November, 1991. ©ASCE, ISSN 0733-9399/91/0011-2623/$1.00 + $.15 per page. Paper No. 26347.

the maximum load. In the extreme case, a complete localization of cracking, a sharp crack develops upon reaching the maximum load, as illustrated in Fig. 1. The stress distribution is then singular and has the form:

$$\sigma_i = \sigma_N \rho^{-1/2} \phi_i(\rho, \theta) \quad \ldots\ldots (1)$$

in which $\sigma_i (i = 1, \ldots, n)$ = the principal stresses; $\rho = r/D$; D = characteristic dimension of the structure; ρ, θ = polar coordinates centered at the tip of the crack; $\sigma_N = F/bD$, where b = structure thickness; F = applied load; σ_N = the nominal strength (nominal stress at maximum load); $\phi_i(\rho, \theta)$ = a nonsingular function that is bounded, continuous, and smooth (except at concentrated loads and at boundary corners).

Stress singularity is an abstraction that does not exist in reality. The stresses near the tip of a sharp crack are blunted due to inelastic phenomena such as microcracking or other damage, which are the consequence of heterogeneity of the material. One effective way to take this heterogeneity into account is the nonlocal-continuum concept (Kröner 1967; Eringen 1965, 1966, 1972), which is properly applied only to the variables associated with failure or damage (Bažant and Pijaudier-Cabot 1988; Bažant and Lin 1988a, 1988b; Bažant and Ožbolt 1990). Thus, recognizing that failure at a point of a heterogeneous material must depend not only on the continuum stress at that point but also on the stress resultant or average stress within a certain representative volume V_R of the material, we realize that the probability of failure should not depend on the local stresses $\sigma_i(\mathbf{x})$ but on the average stresses

$$\bar{\sigma}_i(\mathbf{x}) = \int_{V_R} \sigma_i(\mathbf{s}) W(\mathbf{x} - \mathbf{s})\, dV(\mathbf{s}) \quad \ldots\ldots (2)$$

in which $W(\mathbf{x} - \mathbf{s})$ = a given empirical weight function, which must satisfy the normalizing condition, $\int_{V_R} W(\mathbf{x} - \mathbf{s})\, dV = 1$. When the representative volume V_R protrudes across the body boundary or the crack boundary, the protruding part must be chopped off and the weights α must be scaled up,

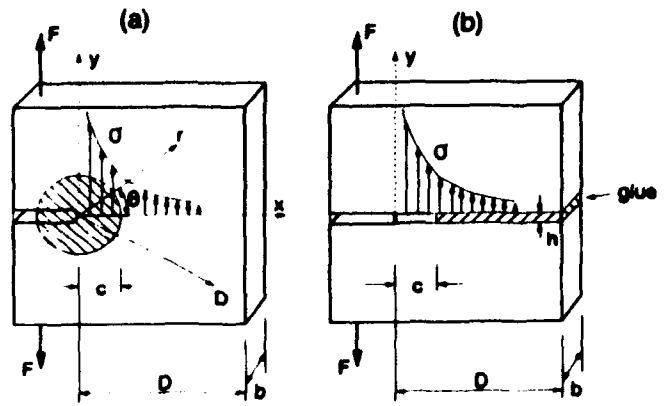

FIG. 1. Stress Distributions and Crack Process Zone in Specimens

so as to satisfy the normalizing condition. The weight function introduces the nonlocal material properties. For the special case that W = Dirac δ-function, one has $\bar{\sigma}_i(\mathbf{x}) = \sigma_i(\mathbf{s})$, which is the case of local continuum. For zero strength threshold ($\sigma_u = 0$), an equation from the companion paper (Bažant et al. 1991) may now be rewritten as

$$-\ln(1 - P_f) = \int_V \sum_{i=1}^{n} \left(\frac{\bar{\sigma}_i(\mathbf{x})}{\sigma_0} \right)^m \frac{dV}{V_r} \quad \ldots\ldots (3)$$

There is also another argument for the nonlocal concept—the fact that the random material properties in adjacent small material elements cannot be uncorrelated. The spatial integral in (4) does not introduce spatial correlation of failure probabilities for any two points for which the domains of integration in (4) overlap, i.e., stresses $\bar{\sigma}_i(\mathbf{x}^A)$ and $\bar{\sigma}_i(\mathbf{x}^B)$ such that their averaging integrals both involve the same stress $\sigma_i(\mathbf{x}^C)$.

Eqs. (2) and (3) are too difficult for an analytical solution. Therefore, one must take the nonlocal aspect into account in the simplest possible manner. As is known from the previous studies, the nonlocal averaging (2) is unnecessary in the regions of small damage, i.e., far from the fracture front (large ρ). However, within volume V_c of the fracture-process zone (shaded in Fig. 1), some form of nonlocal averaging is necessary. As an approximation, we may consider a constant average stress value $\bar{\sigma}_i$ through this entire zone, which is physically justified by the stress limit posed by inelastic deformation (and is similar to a yield limit). Eq. (3) may thus be simplified as follows

$$-\ln(1 - P_f) = \sum_{i=1}^{n} \left(\frac{\bar{\sigma}_i}{\sigma_0} \right)^m \frac{V_c}{V_r} + \int_{V_r} \sum_{i=1}^{n} \left(\frac{\sigma_i}{\sigma_0} \right)^m \frac{dV}{V_r} \quad \ldots\ldots (4)$$

in which $V_r = V - V_c$ = volume of the rest of the body outside the fracture-process zone.

One may now be tempted to consider the value of $\bar{\sigma}_i$ as a constant yield stress. However, regardless of the absence of a clearly defined yield limit in the material, this would be incorrect since the $\bar{\sigma}_i$-value must be considered a random variable and must be determined also on the basis of extreme value distribution such as Weibull's, in relation to the random nominal strength σ_N. Therefore, it is proposed to approximate $\bar{\sigma}_i$ as the value of the elastically calculated stress σ_i at a point that lies on the crack extension line ($\theta = 0$) at a certain fixed distance $r = c$ from the tip of the ideal sharp crack. Thus, for the region $V_c(\rho \le c/D)$, we introduce the approximation

$$\bar{\sigma}_i \approx k(\sigma_i)_{\substack{r=c \\ \theta=0}} = \phi_N \left(\frac{c}{D} \right)^{-1/2} k\phi_{ci}, \qquad \phi_{ci} = \phi_i\left(\frac{c}{D}, 0 \right) \quad \ldots\ldots (5)$$

in which D = characteristic dimension (size of the structure); k and c = empirical constants; and c may be interpreted as the effective radius of the fracture-process zone [see Bažant and Kazemi (1990)], which in turn is related to the characteristic length of the nonlocal-continuum model approximating the heterogeneous material (Bažant and Pijaudier-Cabot 1988, 1989). The value of $\bar{\sigma}_i$ is random because σ_N is random.

Approximate Nonlocal Analysis

In the integral (4), we have $dV = bD^2\rho\, d\theta\, d\rho$, where b = thickness of the body. This expression applies for the case of two-dimensional similarity.

To be more general and cover also the case of three-dimensional similarity, one may generalize the foregoing expression as follows:

$$dV = b_0 D^n \rho \, d\theta \, d\rho \quad \ldots\ldots (6)$$

in which b_0 = *nondimensional constant; and* n = *number of spatial dimensions.* For two-dimensional similarity ($n = 2$), we have $b = b_0$, and for three-dimensional similarity ($n = 3$), $b = b_0 D$. In the case of axisymmetric fracture situations, b_0 is a constant without any meaning of thickness. The effect of the number of dimensions on the first expression in (4) is a more difficult question. Strictly speaking, the volume of the fracture-process zone is $V_c = \pi c^2 b_0$ ($b_0 = b$) for two dimensions ($n = 2$) and $V_c = \pi c^2 b_0 D$ for three dimensions ($n = 3$), which in general may be written as $V_c = \pi c^2 b_0 D^{n-2}$. For three dimensions, however, this would mean that the cracks would propagate independently in various parts of the fracture-process zone throughout the thickness of the fracture specimen, which is impossible except if the fracture-process zone is very thick ($b >> c$). It seems more reasonable to assume that once the crack forms or propagates, it must do so simultaneously throughout the whole thickness b of the specimen, so that the probability of survival depends on the fracture-process zone area rather than the volume. Consequently, we will assume that, for the purpose of survival probability in (4),

$$V_c = \pi c^2 b_0 D^p \quad \ldots\ldots (7)$$

where $p = 0$. Later, however, we will also explore the case $p = n - 2$.

Substituting (5) and (7), we may rearrange (4) as follows

$$-\ln(1 - P_f) = \left[A_0 \left(\frac{D}{c}\right)^{(p+m/2)} + A_1 \left(\frac{D}{c}\right)^n H_D \, I\left(\frac{c}{D}\right) \right] \sigma_N^m \quad \ldots\ldots (8)$$

in which $A_0 = \pi b_0 c^{p+2} k^m \sigma_0^{\ m} \Sigma_i \varphi_i^m / V_r$, $A_1 = b_0 c^n \sigma_0^{\ m} / V_r$, which are size-independent constants; H_D = parameter to be defined later, and

$$I\left(\frac{c}{D}\right) = \int_\pi^\pi \int_{c/D}^{\hat\rho(\theta)} \sum_{i=1}^{n} [\rho^{-1/2} \phi_i(\rho,\theta)]^m \, \rho \, d\rho \, d\theta, \qquad \text{except if } c << D \quad \ldots (9)$$

Here function $\hat\rho(\theta)$ represents the relative radial distances to the boundary points and defines the geometry of the structure. For geometrically similar specimens, the value of $I(c/D)$ is constant.

Furthermore, it has been necessary to introduce in (8) parameter H_D which takes into account interaction of the fracture process zone with the specimen boundaries. For the extreme cases of very large and very small specimens relative to the fracture-process zone size c, one must obviously have

$$\text{For } \frac{c}{D} << \hat\rho(\theta): \qquad H_D = 1 \quad \ldots\ldots (10a)$$

$$\text{For } \frac{c}{D} \approx \hat\rho(\theta): \qquad H_D = 0 \quad \ldots\ldots (10b)$$

Eq. (10*a*) pertains to the case where the fracture-process zone size is negligible compared to the structure size (dimension) D. Eq. (10*b*) pertains to the case where the fracture-process zone extends roughly over the entire structure (or at least the entire ligament length). In that case the domain V_r of the integral in (4) is vanishing, and the vanishing of the integral is ensured by setting $H_D = 0$. For the intermediate body sizes, for which the fracture-process zone is neither small nor large, parameter H_D must be considered to be a smooth function of the relative size of the process zone, c/D, i.e., $H_D = H_D(c/D)$. We leave it as an empirical function, although it could conceivably be calculated after solving the boundary value problem in its nonlocal form [(2) and (3)].

From (9), one can easily demonstrate that the singular stress distribution of linear elastic fracture mechanics cannot be used in the integral for failure probability, i.e., in (8) of the preceding paper (no doubt this is the reason why the stress redistributions due to large cracks have so far been ignored in the literature on Weibull-type size effect). For c/D approaching zero, the integral in (9) converges if and only if $m \le 4$. But this is not a realistic situation. The typical value of Weibull modulus for concrete is $m \approx 12$ (with $\sigma_u = 0$). Therefore, it is inevitable to consider c finite, as proposed in this paper.

The preceding consideration shows that the stress distribution in (2), with σ_i proportional to σ_N, is unrealistic for the fracture-process zone when the body is very large, i.e., $D >> c$. For that case the stresses at the ideal crack tip become very large and would exceed the intrinsic strength f^* of the material with no flaws or microcracks. Therefore, the stress must be limited as $\sigma_i \le f^*$ and must be taken as $\sigma_i = f^*$ when (2) exceeds this value. From this consideration it follows that, for $c << D$, the integral in (4) should be proportional to f^{*m}, i.e., a constant. This may be achieved by setting

$$\text{For } c << D: \qquad I\left(\frac{c}{D}\right) \approx k_0 \left(\frac{f^*}{\sigma_N}\right)^m \quad \ldots\ldots (11)$$

in which k_0 = some constant.

If the failure probability P_f is fixed, (8) yields for the size effect the following relation

$$\sigma_N = \left\{ \frac{1}{-\ln(1 - P_f)} \left[A_0 \left(\frac{D}{c}\right)^{(p+m/2)} + H_D A_1 I(c/D) \left(\frac{D}{c}\right)^n \right] \right\}^{-1/m} \quad \ldots (12)$$

For $P_f = 0.5$, (12) yields the median strength, which is known from experiments on concrete to be close to the mean strength.

Let us now discuss the limiting cases, assuming that $p = 0$ and $m/2 > n$ ($n = 2$ or 3). For very small D/c, $(D/c)^{m/2} << (D/c)^n$, while for very large D/c, $(D/c^{m/2} >> (D/c)^n$. Also note that $I(c/D)$ tends to a finite value for very small sizes (11) because σ_i is bounded. So the first term in the bracket of (12) must dominate for very large sizes, while the second term must dominate for very small sizes. Thus we obtain the following asymptotic size effect laws (*with* $p = 0$):

$$\text{For small } D/c: \qquad \sigma_N \propto D^{-n/m} \quad \ldots\ldots (13)$$

$$\text{For large } D/c: \qquad \sigma_N \propto D^{-1/2} \quad \ldots\ldots (14)$$

In the foregoing asymptotic results, it is particularly noteworthy that for very large structures (14) the size effect is the same as that obtained by deterministic analysis on the basis of energy release, i.e., $\sigma_N \propto D^{-1/2}$. The

reason is that, for large structures, the stress peak in the fracture-process zone dwarfs the stresses in the rest of the structure, thus making the statistical variability of the strength in the rest of the structure irrelevant. Only the statistical variability of strength within the fracture-process zone matters. But the size of this zone is essentially fixed, independent of the body dimensions. Consequently, the statistical part of the size effect disappears and the only size effect left is deterministic—namely that due to the increase in the energy release rate as the structure size (along with the fracture length at imminent failure) is increased.

Eq. (14) for large D/c is based on the hypothesis that in the fracture-process zone a crack must form or propagate simultaneously within the entire specimen thickness b. For very thick specimens, however, it is conceivable that a crack might form or propagate only in a part of thickness and be stationary in the remaining part of thickness. In that case, as already explained, it might be more appropriate to use some value of p between 0 and $p = n - 2 = 1$ in (7) for three-dimensional similarity ($n = 3$). Eq. (14) would then be replaced by:

$$\text{For large } c/D\text{: } \sigma_N \propto D^{-(p/m+1/2)} \text{ (three-dimensional similarity only)} \quad \ldots (15)$$

Assuming $m = 12$, we would have $0 < p/m < 1/12$, which is relatively small correction. But it is noteworthy that a statistical size effect slightly stronger than $D^{-1/2}$ cannot be ruled out. Experimentally, though, it has not been observed in tests with three-dimensional similarity (torsion, pull-out, punching shear), and so we will not consider this possibility any further.

To calculate the mean strength $\bar{\sigma}_N = E(\sigma_N)$, in which E = expectation, one may use the following well-known relation

$$\bar{\sigma}_N = E(\sigma_N) = \int_0^1 \sigma_N \, dP_f = \int_0^\infty (1 - P_f) d\sigma_N \quad \ldots (16)$$

which follows from the fact that the cross-hatched area in Fig. 2 can be obtained by integrating either over the horizontal strips or over the vertical strips. Now, denoting the expression in the square brackets in (12) as Z, one obtains [from (12)] $1 - P_f = \exp(-Z\sigma_N^m)$. So (16) yields:

$$\bar{\sigma}_N = \int_0^\infty \exp(-Z\sigma_N^m)\, d\sigma_N = Z^{-1/m} \frac{1}{m} \int_0^\infty t^{1/m-1} e^{-t} dt$$

$$= Z^{-1/m} \Gamma\left(1 + \frac{1}{m}\right) \quad \ldots (17)$$

in which Γ = Gamma function. Substituting the bracketed expression in (12) for Z, one gets for the mean strength the following size effect law

$$\bar{\sigma}_N = \Gamma\left(1 + \frac{1}{m}\right)\left[A_0\left(\frac{D}{c}\right)^{m/2} + H_D A_1 I\left(\frac{c}{D}\right)\left(\frac{D}{c}\right)^n\right]^{-1/m} \quad \ldots (18)$$

As we see, except for a factor, this law is formally identical to the size-effect law in (11) for a fixed failure probability P_f. The limiting behavior for very small and very large sizes is, for the mean strength, again the same as that in (13) and (14). By a similar procedure, one can easily also calculate the variance of σ_N.

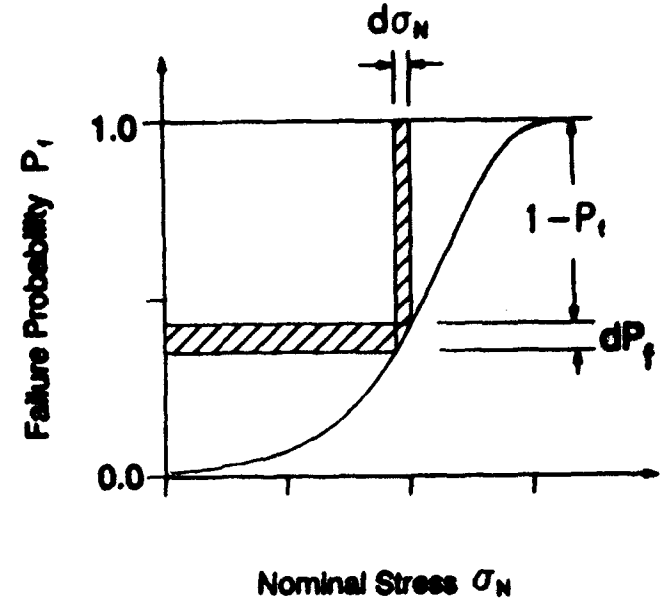

FIG. 2. Cumulative Distribution of Failure Probability of Structure

Special Case of One-Dimensional Similarity

In the preceding paper (Bažant et al. 1991) we saw that one-dimensional similitude, exemplified by failure of a glue layer between two blocks, gives a different law of size effect. Consider now a similar case but with a stress singularity produced by an existing crack or notch—the specimen in Fig. 1(*b*), consisting of two strong parts glued by a thin layer, the strength of which is much less than the strength of the adjacent parts. Let the thickness b be the same for specimens of various sizes D. Similar to (2), the normal stress in the glue layer is $\sigma = \sigma_N \rho^{-1/2} \varphi(\rho)$ where $\rho = x/D$ [Fig. 1(*b*)] and φ is a continuous smooth function. Similar to (5), the nonlocal stress in the fracture-process zone is approximated as $\bar{\sigma} = \kappa(\sigma)_{x=c} = \sigma_N (c/D)^{-1/2} k\varphi(c/D)$. Substituting this into (3) and integrating over the volume of the thin glue layer, we get

$$-\ln(1 - P_f) = \left[A_0\left(\frac{D}{c}\right)^{m/2} + A_1 H_D I\left(\frac{c}{D}\right)\frac{D}{c}\right]\sigma_N^m \quad \ldots (19)$$

in which $A_0 = bhc\sigma_0^{-m} k^m \phi^m(c/D)/V_0$, $A_1 = bhc\sigma_0^{-m}/V_0$ and

$$I\left(\frac{c}{D}\right) = \int_{c/D}^1 \rho^{-m/2} \phi^m(\rho)\, d\rho \quad \ldots (20)$$

and coefficient H_D, (10) is introduced for the same reasons as before. By the same arguments as those that lead from (12) to (13) and (14), we may conclude that the term with A_1 dominates for very large sizes and the term with A_2 dominates for very small sizes. Therefore,

For small D/c: $\sigma_N \propto D^{-n/m}$ ..... (21)

For large D/c: $\sigma_N \propto D^{-1/2}$ ..... (22)

This agrees with (13) and (14), since $n = 1$ in this case.

Empirical Interpolation between Asymptotic Size Effects

The asymptotic size-effect laws for very small and very large sizes in (13) and (14) are very simple. More importantly, they are also independent of the geometry of the structure. The complete size-effect law described by (12) is of little value because the intermediate variation of coefficients I and H_0 between the asymptotic cases is difficult to determine, and is sure to depend on the geometry of the structure. Therefore, (12) cannot be proposed for practical use.

From extensive experimentation (Bažant and Kazemi 1989; Bažant and Sener 1988; Bažant et al. 1990; Bažant and Cao 1987; Gettu et al. 1990) it appears that, as a good approximation relative to the scatter of the test result, the form of the size-effect law can be considered as shape-independent through the entire range of sizes up to about 1:20. This has been confirmed by the success of the approximate size-effect law

$$\sigma_N = \frac{Bf_t'}{\sqrt{1 + \beta}}, \qquad \beta = \frac{D}{D_0} \quad \text{..... (23)}$$

proposed in Bažant (1984), with Bf_t' and D_0 as empirical constants (f_t' is the direct tensile strength, introduced to make B nondimensional). In view of this observation, it is not inappropriate to obtain the complete statistical size-effect law for bodies with large fractures by a simple empirical interpolation formula that agrees with both asymptotic cases in (13) and (14) and at the same time reduces to (23) for $m \to \infty$ (the deterministic limit). The simple formula with these asymptotic properties is

$$\sigma_N = \frac{Bf_t'}{\sqrt{\beta^{2n/m} + \beta}} \quad \text{..... (24)}$$

Possibly one might consider a more general interpolation formula:

$$\sigma_N = \frac{Bf_t'}{(\beta^{2r/m} + \beta^r)^{1/2r}} \quad \text{..... (25)}$$

where r = an arbitrary empirical constant, analagous to that considered in Bažant (1987) and Bažant and Pfeiffer (1987) for deterministic size effect. But for the deterministic case, Bažant and Pfeiffer found $r = 1$.

Determination of Material Parameters

Same as for (23), it is possible to identify parameters D_0 and B by linear regression of σ_N-data for geometrically similar specimens of various sizes. To this end, we may algebraically rearrange (25) to the linear plot $Y = AX + C$ in which

$$X = D^{r(2n/m)}, \qquad Y = \left(\frac{f_t'}{\sigma_N}\right)^{2r} D^{2rn/m},$$

$$A = B^{-2r} D_0^{rn}, \qquad C = D_0^{2rn/m} B^{-2r} \quad \text{..... (26)}$$

(n = the given number of dimensions). Thus, if r and m are kno[illegible] and C, along with the coefficients of variation of A and of the deviations of the data points from the regression line, can be determined from the plot of Y versus X by linear regression, and B and D_0 follow from (26). As for the value of r, one needs to try various values and then determine that for which the coefficient of variation of the deviations from the regression line is minimum. The linear regression previously introduced for the deterministic size-effect law (23) is the special case of (26) for $m \to \infty$, $r = 1$.

Similar to the previous use of (23) (Bažant and Pfeiffer 1987; Bažant et al. 1989), the regression results for B can be used to determine the fracture energy, G_f, defined as the critical energy release rate in an infinitely large fracture specimen. According to LEFM, one has $G_f = F^2 g(\alpha)/E' b^2 D$ where $E' = E/(1 - \nu^2)$ for plane strain, $E' = E$ = Young's modulus for plane stress (ν = Poisson ratio); α = relative crack length; and $g(\alpha)$ = nondimensional energy release rate for the given specimen geometry, which can be easily determined by elastic analysis. Inserting $F = \sigma_N bD$, one gets $\sigma_N = [E' G_f / g(\alpha) d]^{1/2}$. From (24) or (25), the asymptotic behavior for large D is $\sigma_N = Bf_t'/\sqrt{\beta}$, while $\alpha \to \alpha_0$ (initial crack or notch length). Setting these two expressions equal, one gets

$$G_f = \frac{B^2 f_t'^2 d_0}{E'} g(\alpha_0) \quad \text{..... (27)}$$

which happens to coincide with the expression obtained previously from (23). This means that the statistical strength effects on G_f are nil, which is not surprising.

Similar to Bažant and Kazemi (1990), one could also deduce from (24) or (25) the effective length c_f of the fracture-process zone length, but this value is affected by the Weibull statistical parameters m and σ_0.

Question of Weibull Modulus m for Fracture-Process Zone

In our derivation, Weibull's distribution of material strength has been used in a somewhat different sense than in the classical problem of failure of a long fiber or chain. Is our value of Weibull modulus m the same as for direct tension tests of long fibers or bars? Probably not, and probably it is larger. The reason is that Weibull modulus m increases with increasing uniformity of the distribution of the flaws in the material (Freudenthal 1968), and the distribution of flaws that must be considered is that just before failure. The uniformity of flaws in the fracture-process zone should be much higher than in the initial state of the material. Therefore, the value of m may be larger than the value obtained from direct tension tests of bars of different lengths, which is about 12. However, due to the absence of test results that would suffice for determining m, we will consider in the numerical examples that follow the value $m = 12$ because it is conservative. The larger the m-value, the weaker is the size effect. In future research, however, an estimate of the m-value for the fracture-process zone should be obtained.

Comparison with Test Results

To be able to check the asymptotic trend defined by (13) and (14) and the empirical interpolation formula in (24), test data of a rather broad size range are needed. Although no known data are perfect in this regard, the

recent data in Fig. 5(*a*) are of a sufficiently broad range. They show the optimum fits by (23) (nonstatistical) and (24) (statistical) for the test results of Bažant and Kazemi (1989) on diagonal shear failure of longitudinally reinforced concrete beams without stirrups. The size range of these data, 1:16, was quite broad. We see that the statistical (24) fits these data somewhat better than the deterministic (23). The difference between these two size-effect laws is discernible only for small specimen sizes, and the small-size asymptotic slope $-n/m$ seems to be acceptable.

In evaluating these tests, there is a question with regard to the failure mode of the smallest specimen, which was of a different type: it is essentially a bending-type failure, while all the large beams exhibited typical diagonal shear failure [see Bažant and Kazemi (1989)]. In the present phenomenologic analysis of failure, this would hardly be a sufficient argument for excluding the smallest beam data. So it seems justified to keep the smallest beam data in Fig. 5(*a*). But if one speaks strictly of diagonal shear, these data must of course be excluded. For that case, the optimum fit by (23) and (24) is shown in Fig. 3(*b*), which is however not too different from Fig. 3(*a*).

To check how good the interpolation formula in (24) and (25) might be, one may for example use the exact solution for the stress distribution in an infinite space with a crack of length $2a$, subjected to remote uniaxial stress at infinity [Fig. 4(*a*)]. The solution (Westergaard 1939) is

$$\sigma_{1,2} = \frac{\sigma}{\sqrt{|R|}}\left(x\cos\frac{\theta + 2k\pi}{2} - y\sin\frac{\theta + 2k\pi}{2}\right) \pm \frac{y\sigma a^2}{(|R|)^{3/2}} \quad \ldots\ldots (28)$$

where

$$R^2 = (x^2 - a^2 - y^2)^2 + 4x^2y^2 \quad \ldots\ldots (29)$$

$$\theta = \bar{\theta} \text{ if } x^2 - a^2 - y^2 > 0$$

$$\theta = -(\pi - \bar{\theta}) \text{ if } x^2 - a^2 - y^2 < 0 \quad \ldots\ldots (30)$$

$$\bar{\theta} = \arctan\frac{-2xy}{x^2 - a^2 - y^2} \quad \ldots\ldots (31)$$

We now consider square specimens with centric cracks of length $2a$. To obtain the simple stress field in (28), we assume that the rectangular boundary is subjected to traction distributions that correspond to the stress field according to (28). (The stress at infinity, σ, no longer exists but represents merely the nominal stress σ_N, playing the role of a parameter of the loading by these boundary tractions.) The stress field in (28) [Fig. 5(*a*)] has been subjected to the spatial averaging according to (2), using the weight function $W(x) = [1 - (r/R)^2]^2$ for $r < R$; $W = 0$ for $r \geq R$, in which $R = \sqrt[3]{3/4}\, l = 0.9086\, l$, and l = characteristic length of nonlocal continuum [a material property whose measurement was reported by Bažant and Pijaudier-Cabot (1989)]. The averaging has been carried out by representing the solution from (28) by nodal values of a square mesh and approximating the integral in (2) by a discrete sum. This has been done for various sizes of the rectangular specimen, using of course the same value of l (and R) for each size. The results of nonlocal averaging is plotted in Fig. 5(*b*). The optimum fits by (23) and (24) are shown in Fig. 4(*b*). It is clear that (24) gives the

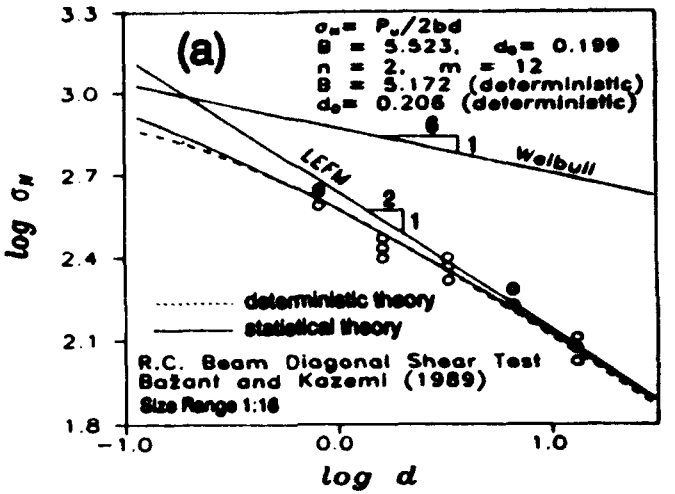

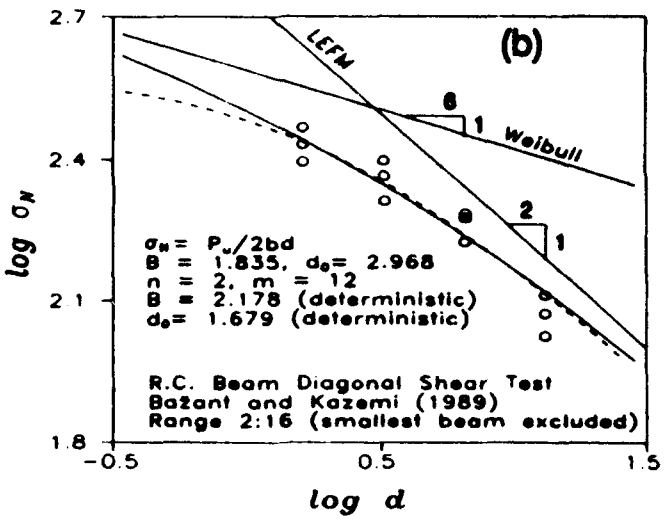

FIG. 3. Test Result on Diagonal Shear Failure of Reinforced Concrete Beam without Stirrups, and Optimum Fits by (23) and (24) (*a*) is for Five Beams; (*b*) is for Four Beams

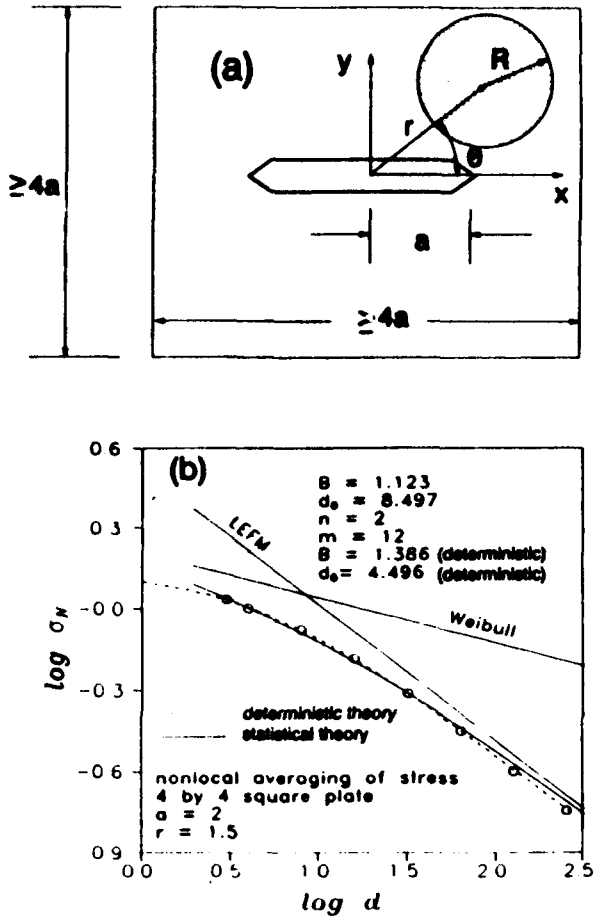

FIG. 4. Numerical Result by Nonlocal Averaging and Linear Finite Element Analysis on Square Specimen with Centric Cracks (a), and Optimum Fit by (23) and (24) (b). Singular Stress Field (c) and Stress Field After Nonlocal Averaging (d)

better fits of the test results and that the shape of these curves is quite satisfactory.

Failure Probability Based on Nonlocal Damage Analysis by Finite Elements

A more realistic, but also more complex, approach is that of nonlocal damage. In that case, the failure probability at a point of the body may be assumed to be governed by the spatially averaged (nonlocal) principal strains

$$\bar{\epsilon}_i(\mathbf{x}) = \int_V \epsilon_i(\mathbf{x}) W'(\mathbf{x},\mathbf{s}) dV(\mathbf{s}) \quad \ldots\ldots\ldots\ldots\ldots\ldots\ldots\ldots\ldots\ldots\ldots\ldots (32)$$

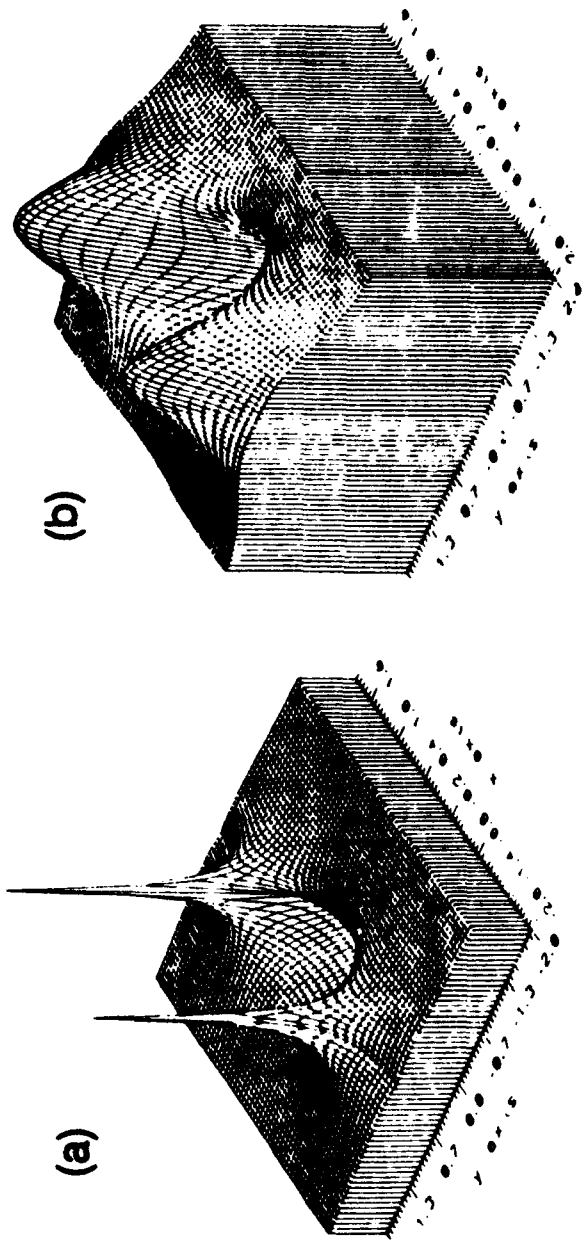

FIG. 5. Numerical Result by Nonlinear Nonlocal Damage Model on Rectangular Specimen, and Optimum Fit by (23) and (24)

where ε_i = principal strains (local); $W'(x,s)$ = given nonlocal weighting function based on the characteristic length of the material (Bažant and Pijaudier-Cabot 1988). The averaging can be carried out with uniform weight (W' = constant) over a circle, as shown in Fig. 3(*a*) (however, near the crack surface or boundary, the protruding part must be chopped off). But it seems more appropriate to consider W' as a smooth bell-shaped function, declining smoothly to zero with the distance from the point (see Bažant and Ozbolt 1990). The values of $\bar{\varepsilon}_i(x)$ may be obtained from a nonlinear nonlocal finite element program as shown (Bažant and Lin 1988a, 1988b). It is important to note that in this approach, the failure probability must be considered to be a function of strain rather than stress. The reason is that the nonlocal damage admits strain softening, i.e., a decrease of stress with increasing strain, so that the failure probability considered as a function of stress would decrease rather than increase during the post-peak strain-softening deformation. In elastic analysis of fracture, dependence on stress or strain is of course equivalent.

The nonlocal damage concept automatically yields a finite size of the fracture-process zone, a basic ingredient of the present theory. I of this study is, in this approach, replaced by:

$$1 - P_f = \exp\left[-\int_V \sum_{i=1}^{n} \left\langle \frac{k_n E \bar{\varepsilon}_i(x) - \sigma_u}{\sigma_0} \right\rangle^m \frac{dV(x)}{V_r} \right] \quad \text{..... (33)}$$

where E = the initial Young's elastic modulus; k_n = empirical constant, and $\bar{\varepsilon}_i(x)$ = principal strain field from finite element program for nonlocal damage. The results of these calculations are shown in Fig. 4, and one can see that the result is good.

Limitations of Proposed Theory

The survival probability of the structure is the joint probability of survival of all its elementary parts. The basic hypothesis of the classical Weibull-type theory is that the probability of survival of each part depends only on the stress in that part and is independent of the stresses as well as of the loading history in all the other structure parts. None of this, of course, can be expected to be exactly true. The survival probabilities of various elementary parts are not, in reality, independent. For example, the survival probability of one elementary part may depend also on the stress in the adjacent parts. This dependence is approximately described by the nonlocal concept [which leads to (3)], and by the approximate form of (5) and (8). Moreover, the failure is not a sudden, random event. Rather, it is a random process, and a fully realistic theory would have to consider the probabilistic nature of the steps in this process; for example, the question how the survival probability of one elementary part is influenced by the preceding failure of an adjacent elementary part. In particular, this requires following the incremental jumps of the fracture process in a probabilistic manner.

In the present theory, the failure probability is calculated from an instantaneous picture of the strain field at one critical moment of the loading process. Probability, however, does not enter the calculation of the process that leads to this critical moment. This is certainly a simplification. For a fully realistic method of probabilistic analysis, one would have to consider the probabilities in each loading step. When the major crack extends to a certain point, one would have to consider the probabilities of various propagation directions, and the probabilities of the lengths of the jump of the crack tip for a given load increment. Weibull-type probabilistic considerations have been made for the crack jump process [e.g., Bruckner and Munz (1984) and Chudnovsky and Kunin (1987)]. Numerical simulations have been made as well. But it seems hardly possible to obtain in this manner the general trends such as (13) and (14).

Conclusions

1. The Weibull-type integral that yields the failure probability must be based on the stress field at imminent failure, which reflects the stress redistributions due to large fracture. However, the singular stress field obtained according to linear elastic fracture mechanics cannot be used, since the probability integral diverges.
2. Divergence of the probability integral is avoided in general by the nonlocal concept, in which the failure probability at any point depends not only on the stress at that point but also on the stresses in a small neighborhood of the point.
3. Nonlocal statistical analysis of failure probability indicates that the classical Weibull-type size-effect law (applicable only to bodies without large fractures) is valid asymptotically for very small specimen sizes, while the size-effect law of linear elastic fracture mechanics is approached asymptotically for very large sizes. The failure probability for a very large size of a structure with a macroscopic crack proportional to the structure size is dominated by the stress field in the fracture-process zone and is nearly independent of the stress field in the rest of the structure.
4. The aforementioned asymptotic behavior as well as the presently proposed empirical interpolation formula (24) agrees reasonably well with the existing test data. But the agreement cannot be regarded as a proof.
5. Estimates of the failure probability can be obtained by using the probability integral spatially averaged stress values determined according to the nonlocal-continuum concept from the singular stress field calculated according to linear elastic fracture mechanics. Still more realistic is the use of the stress field obtained by nonlocal nonlinear finite element analysis.
6. Finally, the reasons that, for very large specimens, the present statistical theory yields a nonstatistical size effect, the same as linear elastic fracture mechanics (conclusion 3), may be summed up as follows: (1) The mechanics of localization causes the failure to depend in the limit of infinite size solely on the properties of the fracture-process zone; (2) the size and state of this zone, in an infinitely large specimen, becomes independent of the structure size (as well as shape).

Acknowledgment

Partial financial support under NSF Grant BCS-88182302 to Northwestern University is gratefully acknowledged. Partial support for the underlying studies of size effect were also obtained from the Center for Advanced Cements Based Materials at Northwestern University and from AFOSR grant 91-0140 to Northwestern University.

Appendix I. Structures That Can Fail by One of Many Large Cracks

Our analysis has been predicated upon the hypothesis that, at imminent failure, only one major crack has the potential of growing. Conceivably, it might happen that, at imminent failure, there are many large cracks, each of which is in a critical state and has the potential of growing, and that the crack that grows is decided by chance. For the sake of simplicity, we now restrict attention to very large structures, for which only the stresses in the fracture-process zone very near the tips of large fractures are decisive. In the presence of many large cracks ($k = 1,2,\ldots N_c$), (1) and (5) for the nonlocal averaged value of the principal stress σ_1 in the fracture-process zone of the kth crack may be approximately expressed as

$$\bar{\sigma}_{1k} = \sigma_N\left(\frac{c}{D}\right)^{1/2} k\phi_{1k}\left(\frac{c}{D}, 0\right) \quad \ldots\ldots (34)$$

in which ϕ_{1k} = nonsingular smooth functions describing the stress state near the tip of each crack. Substituting this into (3) and assuming, for the purpose of integration, that the stress value given by (28) governs for each entire fracture-process zone, we get

$$-\ln(1 - P_f) = \frac{V_c}{V_r}\sum_{k=1}^{N_c}\left[\frac{\sigma_N}{\sigma_0}\left(\frac{c}{D}\right)^{\frac{1}{2}} k\phi_{1k}\left(\frac{c}{D}, 0\right)\right]^m \quad \ldots\ldots (35)$$

Instead of the summation over all the crack tips, we can introduce the average function $\bar{\phi}_1$ of all the functions ϕ_{1k}. We also make the assumption that the number of large cracks that can potentially cause failure is proportional to the volume of the structure, i.e.,

$$N_c = N_0 D^n \quad \ldots\ldots (36)$$

in which $n = 2$ for two-dimensional similarity and $n = 3$ for three-dimensional similarity. Then (35) may be rewritten as

$$-\ln(1 - P_f) = \frac{V_c}{V_r} N_0 D^n\left[\frac{\sigma_N}{\sigma_0}\left(\frac{c}{D}\right)^{\frac{1}{2}} k\bar{\phi}_1\left(\frac{c}{D}, 0\right)\right]^m \quad \ldots\ldots (37)$$

Solving this for the nominal stress at failure, we get for very large structure sizes the following asymptotic size-effect law

$$\sigma_N = B_0 D^{(1/2 + n/m)} \quad \ldots\ldots (38)$$

in which B_0 = a constant,

$$B_0 = \frac{-\ln(1 - P_f)\sigma_0^m V_r c^{m/2}}{V_c N_0 k\bar{\phi}_1^m\left(\frac{c}{D}, 0\right)} \quad \ldots\ldots (39)$$

The size effect in (38) is stronger than that according to linear elastic fracture mechanics, which is the asymptotic case for the previous formulation. The reason for this difference is that now we assume that each of many large cracks can cause failure, with the number of large cracks being proportional to the structure volume. By contrast, our previous analysis implies that even if there are many large cracks, the mechanics of the problem dictates that only one of them grow during failure. In view of the latest re[illegible]ches on stable path of interactive system and associated thermodynamic stability criterion (i.e., Bažant 1988a, 1988b; Bažant and Cedolin 1991) it is generally found that even if there are two or more cracks in a critical state, only one of them can grow as a stable response path. This is a manifestation of the tendency to localization of failure—a general characteristic of the damage and fracture processes.

For the case of very small structures, the size effect again must asymptotically conform to the classical Weibull-type theory (13). The intermediate size effect must represent a continuous transition from (13) to (38). A simple formula for this transition, which is a special case of that proposed in Bažant (1987), is as follows

$$\sigma_N = Bf_t'\frac{\beta^{n/m}}{\sqrt{1 + \beta}}, \qquad \beta = \frac{D}{D_0} \quad \ldots\ldots (40)$$

At present, however, it is questionable whether any situations exist where this function might be appropriate. None of the existing test data show the final asymptotic slope of the curve of $\log(\sigma_N)$ versus $\log(D)$ to be any steeper than $-1/2$.

Appendix I. References

Bažant, Z. P. (1988a). "Stable states and stable paths of propagation of damage zones and interactive fractures." *France-U.S. Workshop on "Strain Localization and Size Effect Due to Cracks and Damage*, J. Mazars and Z. P. Bažant, eds., Elsevier, London, U.K., 183–207.

Bažant, Z. P. (1988b). "Stable states and paths of structures with plasticity or damage." *J. Engrg. Mech.*, ASCE, 114(12), 2013–2034.

Bažant, Z. P., Xi, Y., and Reid, S. G. (1991). "Statistical size effect in quasi-brittle structures: I. Is Weibull theory applicable?" *J. Engrg. Mech.*, 117(11), 2623–2640.

Bažant, Z. P., and Cao, Z. (1987). "Size effect in punching shear failure of slabs." *ACI Struct. J.*, 84(1), 44–53.

Bažant, Z. P., and Gettu, R., and Kazemi, M. T. (1989). "Identification of nonlinear fracture properties from size effect tests and structural analysis based on geometry-dependent R-curves." *Report No. 89-3/498p*, Ctr. for Advanced Cement-Based Materials, Northwestern Univ., Evanston, Ill; also *Int. J. Rock Mech. and Mining Sci.*, 28(1) (1991), 43–51.

Bažant, Z. P., and Lin, F. B. (1988a). "Nonlocal smeared cracking model for concrete fracture." *J. Struct. Engrg.*, ASCE, 114(11), 2493–2510.

Bažant, Z. P., and Lin, F. B. (1988b). "Nonlocal yield limit degradation." *Int. J. Numer. Methods in Engrg.*, 26, 1805–1823.

Bažant, Z. P., and Ožbolt, J. (1990). "Nonlocal microplane model for fracture, damage, and size effect in structures." *J. Engrg. Mech.*, ASCE, 116(11), 2485–2505.

Bažant, Z. P., Pfeiffer, P. A. (1987). "Determination of fracture energy from size effect and brittleness number." *ACI Mater. J.*, 84(6), 463–480.

Bažant, Z. P., and Pijaudier-Cabot, G. (1989). "Measurement of characteristic length of nonlocal continuum." *J. Engrg. Mech.*, ASCE, 115(4), 755–767.

Bažant, Z. P., and Pijaudier-Cabot, G. (1988). "Nonlocal continuum damage localization instability and convergence." *J. Appl. Mech. Trans. ASME*, 55, 287–293.

Bažant, Z. P., and Cedolin, L. (1991). "Stability of structures: Elastic, inelastic, fracture and damage theories." Oxford Univ. Press, N.Y.

Bruckner, A., and Munz, D. (1984). "Scatter of fracture toughness in the brittle-ductile transition region of a ferritic steel." *Advances in Probabilistic Fracture Mechanics*, C.(Raj) Sundararajan, ed., Vol 92, ASME, New York, N.Y., 105–111.

Chudnovsky, A., and Kunin, B. (1987). "A probubilistic model of brittle cack formation." *J. Appl. Phys.*, 62(10), 4124–4129.
Eringen, A. C. (1965). "Theory of micropoler continuum." *Proc 9th Midwestern Mechnics Conf.*, Univ. of Wisconsin, Madison, 23–40.
Eringen, A. C. (1966). "A unified theory of thermomechanical materials." *Int. J. Engrg. Sci.*, 4, 179–202.
Eringen, A. C. (1972). "Linear theory of nonlocal elasticity and dispersion of plane waves." *Int. J. Engrg. Sci.*, 10(5), 425–435.
Gettu, R., and Bažant, Z. P., and Karr, M. G. (1990). "Fracture properties and brittleness of high strength concrete." *ACI Mater. J.*, 87, 608–618.
Kröner, E. (1967). "Elasticity theory of materials with long-range cohesive forces." *Int. J. Solids Struct.*, 3(5), 731–742.
Westergaard, H. M. (1939). "Bearing pressures and cracks." *J. Appl. Mech. Trans. ASME*, 6, 49–53.

Engineering Fracture Mechanics Vol. 45, No. 3, pp. 393–398, 1993
Printed in Great Britain.

0013-7944/93 $6.00 + 0.00

FRACTURE OF ROCK: EFFECT OF LOADING RATE

ZDENĚK P. BAŽANT, SHANG-PING BAI and RAVINDRA GETTU
Center for Advanced Cement-Based Materials, Northwestern University, Evanston, IL 60208, U.S.A.

Abstract—Fracture parameters of limestone at loading rates ranging over four orders of magnitude in the static regime are determined using the size effect method. Three sizes of three-point bend notched specimens were tested under crack-mouth opening displacement control. The fracture toughness and nominal strength decrease slightly with a decrease in rate, but the fracture process zone length and the brittleness of failure are practically unaffected. The effect of material creep on the fracture of limestone is negligible in the time range studied here. However, the methodology developed for characterizing rate effects in static fracture can be easily applied to other brittle-heterogeneous materials. The decrease of fracture toughness as a function of the crack propagation velocity is described with a power law. A formula for the size- and rate-dependence of the nominal strength is also presented.

INTRODUCTION

BOND RUPTURE is a rate process governed by Maxwell distribution of molecular thermal energies and characterized by activation energy. Therefore, fracture in all materials is rate-sensitive. This has been experimentally demonstrated for rock in the dynamic range, but not in the static range. However, knowledge of this rate effect is very important for may practical applications in mining, geotechnical engineering and geology. The present paper reports new experimental results on the static fracture of limestone at loading rates ranging over four orders of magnitude. The corresponding times to failure range from about 2 sec to almost 1 day.

EXPERIMENTAL DETAILS

All specimens were cut from the same block of Indiana (Bedford) limestone. Three sizes of three-point bend (single-edge-notched) fracture specimens (Fig. 1) were tested. The depths, d, of the beams were 25, 51 and 102 mm (1, 2 and 4 in.), and the thickness, b, of each was 13 mm (0.5 in.). The specimens were cut such that the bending plane of the rock was normal to the load. Notches of 1.3 mm (0.05 in.) width were cut with a steel saw blade. Aluminum bearing plates of length equal to half the beam depth were epoxied at the ends to provide support. The fracture tests were conducted under constant crack-mouth opening displacement (CMOD) rates in a 89 kN (20 kip) closed-loop controlled machine with a load cell operating in the 890 N (200 lb) range. The CMOD was monitored with a transducer (LVDT of 0.127 mm range) mounted across the notch. Four series of tests were performed; each series consisted of six specimens, two in each size (see Table 1). The CMOD rates were chosen so that all specimens in a series reached their peak load in about the same time, t_p. The average t_p values were 2.3, 213, 21,420 and 82,500 sec for the different series. The typical load–CMOD curves for each size are shown in Fig. 2. From the initial slopes of these curves, the initial elastic modulus E_0 of the rock was calculated, for each test, using linear elastic fracture mechanics (LEFM) formulas [1]; see Table 1.

IDENTIFICATION OF FRACTURE PARAMETERS

The size effect method [2] is used to determine the material fracture parameters from the test data. The method has previously been verified for the fracture of limestone [3], as well as other rocks and concrete [4, 5]. Recently, it has also been used in a study of the effect of loading rate on the fracture of concrete [6]. The method is based on the size effect law [7], which is:

$$\sigma_N = \frac{Bf_u}{\sqrt{(1+\beta)}}, \quad \beta = \frac{d}{d_0}, \tag{1}$$

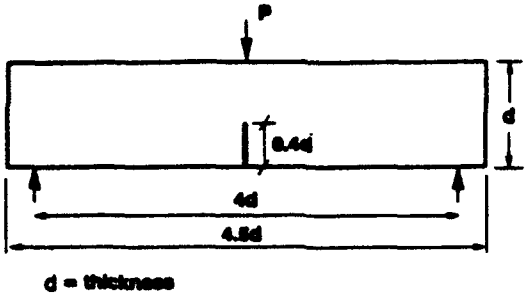

Fig. 1. Fracture specimen geometry.

where $\sigma_N = P_u/bd$ = maximum nominal stresses of geometrically similar fracture specimens, P_u = maximum load, d = characteristic dimension (chosen here as the beam depth), b = specimen thickness (constant, for two-dimensional similarity), Bf_u and d_0 = empirical parameters, and β = brittleness number. When β is very small (e.g. $\beta \ll 0.1$), σ_N is almost independent of size, as in plastic limit analysis. When β is large (e.g. $\beta \gg 10$), the size-dependence follows LEFM (i.e. $\sigma_N \propto 1/\sqrt{d}$). In the transition zone, nonlinear fracture mechanics needs to be applied.

For determining the parameters from σ_N data, eq. (1) can be transformed to $Y = AX + C$, where $X = d$ and $Y = 1/\sigma_N^2$. Then, $Bf_u = 1/\sqrt{C}$ and $d_0 = C/A$ [4]. By linear regression analysis of the data for the four series of tests, the parameters and coefficients of variation of errors, ω_{rms}, have been computed and are listed in Table 2. The data and the fits [eq. (1)] are shown in Fig. 3. It can be seen that the size effect law represents the trend reasonably well, at all the loading rates. It is clear that the data cannot be represented by either LEFM (a straight line with a slope of $-1/2$) or strength criteria (horizontal line $\sigma_N = Bf_u$).

Using the values of Bf_u and d_0, fracture parameters can be calculated as follows [4, 5, 7]:

$$K_{Ic} = Bf_u\sqrt{(d_0 g(\alpha_0))}, \quad c_f = \frac{d_0 g(\alpha_0)}{g'(\alpha_0)}, \quad G_f = \frac{K_{Ic}^2}{E'}, \tag{2}$$

Table 1. Test data

Series	Dimensions† (mm × mm × mm)	CMOD rate (10^{-6} mm/sec)	Peak load (N)	Time to peak (sec)	E_0† (GPa)
	457 × 102 × 13	15,900	445	2.1	40
		15,900	472	2.2	32
Fast	229 × 51 × 13	10,600	281	2.0	35
		10,600	291	2.4	24
	114 × 25 × 13	5770	178	2.4	35
		5770	165	2.2	35
	457 × 102 × 13	159	436	176	33
		141	414	194	30
Usual	229 × 51 × 13	106	269	237	30
		106	271	210	30
	114 × 25 × 13	57.7	153	248	29
		63.5	165	215	30
	457 × 102 × 13	1.42	394	23,175	30
		1.42	383	16,875	32
Slow	229 × 51 × 13	0.978	245	26,000	28
		0.978	240	20,475	25
	114 × 25 × 13	0.706	147	15,750	32
		0.508	153	26,250	34
	457 × 102 × 13	0.353	385	81,900	27
		0.318	387	79,000	34
Very slow	229 × 51 × 13	0.236	262	87,800	32
		0.236	265	82,350	27
	114 × 25 × 13	0.160	140	72,000	26
		0.160	136	92,000	25

†Length × depth × thickness.
‡Initial modulus from load–CMOD compliance.

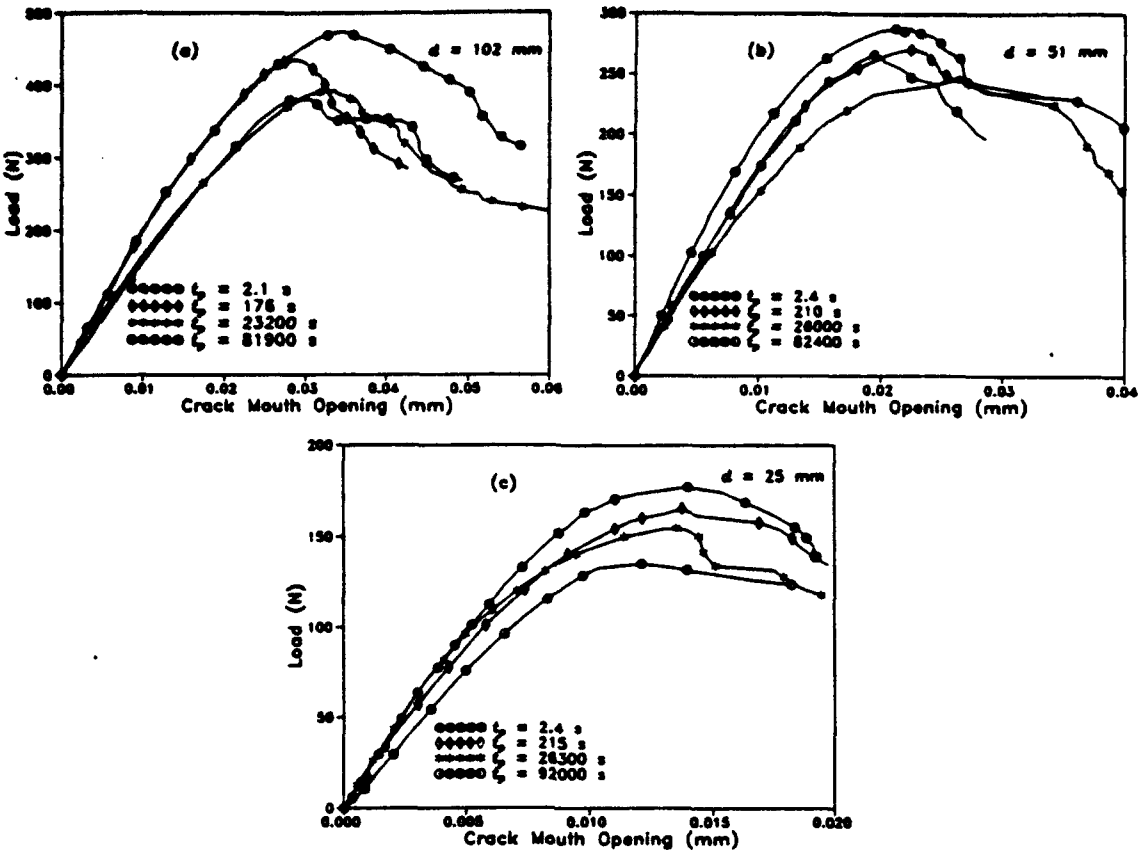

Fig. 2. Typical load–CMOD curves for each specimen size.

where K_{Ic} = fracture toughness, c_f = effective length of the fracture process zone, and G_f = fracture energy. Function $g(\alpha)$ is the non-dimensionalized energy release rate defined by the LEFM relation $G = P^2 g(\alpha)/E' b^2 d$, where G = energy release rate of the specimen, P = load, $\alpha = a/d$ = relative crack length, $g'(\alpha) = dg(\alpha)/d\alpha$, a = crack length, $\alpha_0 = a_0/d$, a_0 = notch length of traction-free crack length, $E' = E$ for plane stress, $E' = E/(1 - \nu^2)$ for plane strain, E = Young's modulus, and ν = Poisson's ratio. Function $g(\alpha)$ can be obtained from handbooks (e.g. [1]) or from LEFM analysis.

Fracture parameters are defined here for the limiting case of an infinitely large specimen at failure. Then, an infinite-size extrapolation of eq. (1) provides material parameters [eq. (2)] that are practically size- and shape-independent [5]. Using the values $g(\alpha_0) = 62.84$ and $g'(\alpha_0) = 347.7$ (from [1]), and assuming plane stress conditions, the fracture parameters for the four series can be computed; see Table 2, in which the average values of K_{Ic} and c_f as well as their coefficients of variation are listed. The E-value for each series is taken as the average initial modulus E_0, and is used in eq. (2) for computing G_f (see Table 2).

VARIATION OF FRACTURE PARAMETERS

The test results show that as the time to peak load, t_p, increases, the fracture toughness K_{Ic} decreases. Since the fracture energy G_f is proportional to K_{Ic}^2, its decrease with slower loading rates is even stronger. The same trends have also been observed in similar materials, such as hardened cement paste [8], concrete [6], and ceramics at high temperatures [9].

To describe the influence of loading rate, we follow several other investigators by adopting a power function of crack velocity v:

$$K_{Ic} = K_0 \left(\frac{v}{v_0}\right)^n, \tag{3}$$

Table 2. Fracture parameters

Series	Avg. t_p (sec)	Bf_u (MPa)	d_0 (mm)	ω_{max}	K_{Ic} Avg. (MPa$\sqrt{\text{mm}}$)	K_{Ic} ω	c_f Avg. (mm)	c_f ω	Avg. E_0 (GPa)	G_f (N/m)
Fast	2.3	0.693	36.2	0.07	33.1	0.13	6.5	0.19	33.5	32.7
Usual	213	0.645	36.3	0.07	30.8	0.12	6.6	0.19	30.3	31.3
Slow	21,400	0.614	31.9	0.04	27.5	0.08	5.8	0.12	30.2	25.0
Very slow	82,500	0.589	36.5	0.11	28.2	0.19	6.6	0.28	28.5	27.9

ω = coefficient of variation.

where K_0 is the fracture toughness corresponding to a reference velocity, v_0, chosen here as $v_0 = 0.01$ mm/sec. Since the effective (LEFM) crack tip is roughly at a distance c_f from the notch tip at the peak load, we use the approximation

$$v = c_f/t_p. \tag{4}$$

Then, by fitting the test results with eq. (3) (see Fig. 4), we obtain $n = 0.0173$ and $K_0 = 30.0\ \text{MPa}\sqrt{\text{mm}}$. Note that, alternatively, beam deflection or crack opening rates have been used instead of v in other studies.

In similar tests of concrete [6], it was found that, with an increase in time to failure, the group of data for the three sizes of specimens shifts to the right, i.e. toward the LEFM asymptote, when plotted as in Fig. 3. This implies that, for higher t_p, the process zone length c_f decreases and the brittleness of failure, characterized by β [eq. (1)], increases.

Rather interestingly, no such trend is observed from the present results of limestone. For all t_p, the data remain within the same part of the size effect curve. This is reflected by the fact that c_f is practically constant ($c_f \simeq 6$ mm; Table 2), implying that the brittleness of fracture in limestone is rate-independent within the time range studied here. This difference in the behavior (for the present load durations) from concrete may be explained by the lack of significant creep [10]. Concrete exhibits marked viscoelastic creep in the bulk of the test specimen, as well as high nonlinear creep in and near the fracture process zone.

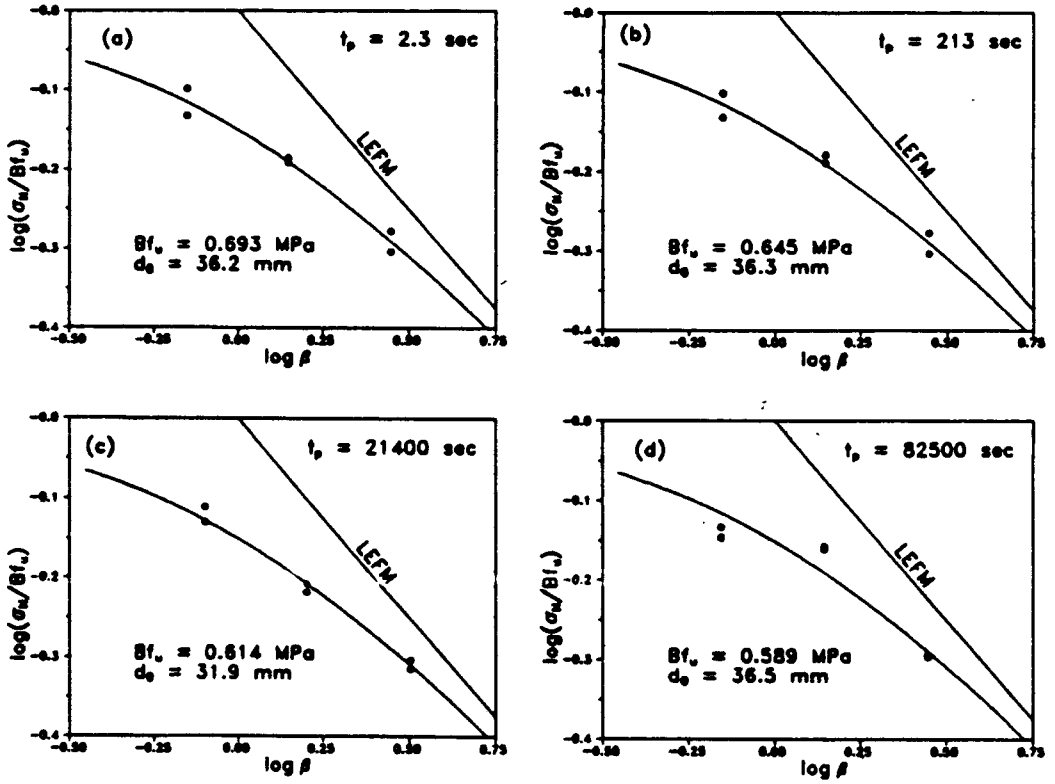

Fig. 3. Size effect curves at different times to peak load.

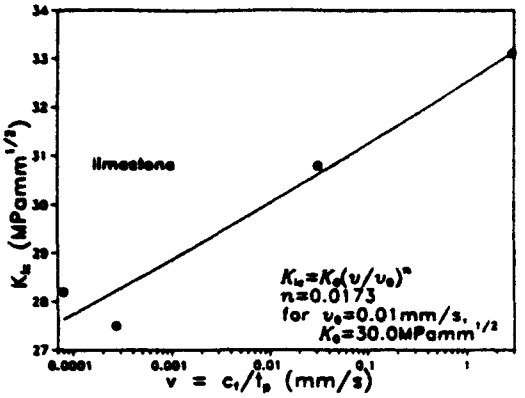

Fig. 4. Variation of fracture toughness with crack velocity.

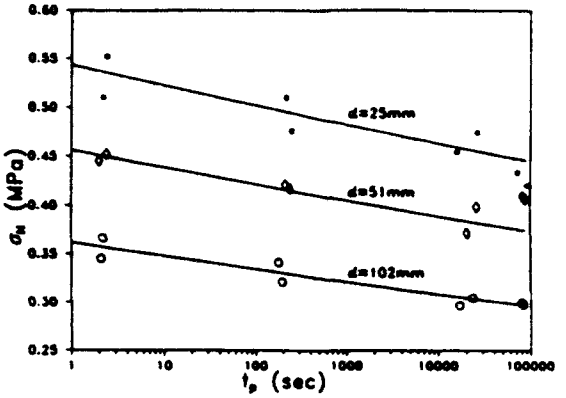

Fig. 5. Influence of specimen size and time to failure on nominal strength.

EFFECT OF RATE ON STRENGTH AND YOUNG'S MODULUS

Several investigators have demonstrated that the strength of rock generally increases with an increase in the loading rate (e.g. [11, 12]). This is also observed here from Table 1. When the loading rate slows by four orders of magnitude, the maximum nominal stress decreases by more than 16%. This phenomenon, which is similar to the change in K_{Ic}, has also been observed in other materials [13]. It may be attributed to the statistical nature of the failure of molecular bonds (particularly the activation energy theory and the Maxwell distribution of thermal energies).

The strength of a quasi-brittle heterogeneous material is generally difficult to measure objectively because of its dependence on specimen size and shape, and because failure does not occur simultaneously at all points but is progressive. However, strength (or failure stress) is correlated to the fracture toughness since failure occurs by unstable crack propagation; higher toughness implies higher resistance against failure.

Equations (1) and (2) can be combined to give the size effect on the nominal strength (maximum nominal stress) in terms of the material fracture parameters [5]:

$$\sigma_N = \frac{K_{Ic}}{\sqrt{(g'(\alpha_0)c_f + g(\alpha_0)d)}}. \tag{5}$$

Substituting for K_{Ic} from eq. (3), and c_f from eq. (4), one obtains a relation for the dependence of the nominal strength on the failure time:

$$\sigma_N = \frac{K_0}{\sqrt{(g'(\alpha_0)c_f + g(\alpha_0)d)}}\left(\frac{c_f}{v_0 t_p}\right)^n. \tag{6}$$

Since c_f is not systematically affected by the loading rate, the average value of 6.4 mm is considered. Equation (6) may then be plotted, along with the test data, for the different sizes tested (Fig. 5). The agreement is acceptable.

The test results also indicate that the average initial elastic modulus decreases slightly with an increase in the time to peak load (Table 2). Such an effect has been observed for several rocks in the dynamic range [14].

CONCLUSIONS

(1) For times to peak load ranging from 2 to 80,000 sec, the measured nominal strengths of fracture specimens of limestone agree with the size effect law.
(2) The fracture toughness and failure stress decrease with increasing failure time. However, the fracture process zone size and the brittleness of failure appear to be unaffected by the loading rate.
(3) Since there is insignificant creep outside the process zone of limestone in the time range studied, the effective process zone size does not change as the loading rate is varied.

Acknowledgements—This work was partially supported by AFOSR contract 91-0140 with Northwestern University, and the Center for Advanced Cement-Based Materials at Northwestern University (NSF Grant DMR-8808432). S. P. Bai is grateful for support from ISTIS, Taiyuen, P.R.C., during the course of this study.

REFERENCES

[1] H. Tada, P. C. Paris and G. R. Irwin, *The Stress Analysis of Cracks Handbook*, 2nd Edn. Paris Productions, St. Louis, MO (1985).
[2] RILEM TC89, Size-effect method for determining fracture energy and process zone size of concrete. *Mater. Structures* **23**, 461–465 (1990).
[3] Z. P. Bažant, R. Gettu and M. T. Kazemi, Identification of nonlinear fracture properties from size effect tests and structural analysis based on geometry-dependent *R*-curves. *Int. J. Rock Mech. Min. Sci.* **28**, 43–51 (1991); Corrigenda. **28**, 233 (1991).
[4] Z. P. Bažant and P. A. Pfeiffer, Determination of fracture energy from size effect and brittleness number. *ACI Mater. Jl* **84**, 463–480 (1987).
[5] Z. P. Bažant and M. T. Kazemi, Determination of fracture energy, process zone length and brittleness number from size effect, with application to rock and concrete. *Int. J. Fracture* **44**, 111–131 (1990).
[6] Z. P. Bažant and R. Gettu, Rate effects and load relaxation in static fracture of concrete. Rep. No. 90-3/498r, Center of Advanced Cement-Based Materials, Northwestern Univ., Evanston, IL (1990). Also *ACI Mater. Jl* **89**(5), 456–468 (1992).
[7] Z. P. Bažant, Size effect in blunt fracture: concrete, rock, metal. *J. Engng Mech.* **110**, 5128–5135 (1984).
[8] S. Mindess, Rate of loading effects on the fracture of cementitious materials, in *Application of Fracture Mechanics to Cementitious Composites* (Edited by S. P. Shah), pp. 617–638. Martinus Nijhoff, Dordrecht (1985).
[9] S. H. Knickerbocker, A. Zangvil and S. D. Brown, Displacement rate and temperature effects in fracture of a hot-pressed silicon nitride at 1100° to 1325°C. *J. Am. Ceram. Soc.* **67**, 365–368 (1984).
[10] D. Griggs, Creep of rocks. *J. Geology* **47**, 225–251 (1939).
[11] A. Kumar, The effect of stress rate and temperature on the strength of basalt and granite. *Geophysics* **33**, 501–510 (1968).
[12] S. S. Peng, A note on the fracture propagation and time-dependent behavior of rocks in uniaxial tension. *Int. J. Rock Mech. Min. Sci.* **12**, 125–127 (1975).
[13] C. C. Hsiao, Kinetic strength of solids, in *Advances in Fracture Research* (Edited by K. Salama, K. Ravi-Chandar, D. M. R. Taplin and P. Rama Rao), Volume 4, pp. 2913–2919. Pergamon Press, Oxford (1989).
[14] K. P. Chong, J. S. Harkins, M. D. Kuruppu and A. I. Leskinen, Strain rate dependent mechanical properties of Western Oil Shale, in *28th U.S. Symp. on Rock Mechanics* (Edited by I. W. Farmer, J. J. K. Daemen, C. S. Desai, C. E. Glass and S. P. Neuman), pp. 157–164. A. A. Balkema, Rotterdam (1987).

(*Received* 8 *April* 1992)

ACI MATERIALS JOURNAL TECHNICAL PAPER

Title no. 89-M49

Rate Effects and Load Relaxation in Static Fracture of Concrete

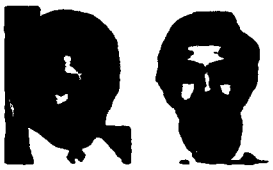

by Zdeněk P. Bažant and Ravindra Gettu

Reports an experimental study of the fracture of concrete at various crack mouth opening displacement (CMOD) rates with time to peak loads ranging from about 1 sec to 3 days (over five orders of magnitude). Tests were conducted on three-point bend specimens of three sizes in the ratio 1:2:4. Quasi-elastic fracture analysis, based on the effective modulus from creep theory, is used to evaluate the results according to the size effect method. The fracture toughness is found to decrease in agreement with the trend known for the dynamic range. The effective length of the fracture process zone is found to decrease with increasing rate, which implies increasing brittleness and a shift toward linear elastic fracture mechanics behavior for slow loading. Load relaxation at constant CMOD in the prepeak and post-peak stages of fracture tests was also investigated. The response tends to a straight line in the logarithm of elapsed time, and the post-peak relaxation is nearly twice as strong as the linear viscoelastic relaxation of unnotched specimens. The difference between these two relaxations must be caused by time-dependent processes in the fracture zone. The results reveal that in concrete there is a strong interaction between fracture and creep, which might cause the load-carrying capacity of structures with cracks to decrease significantly with load duration. However, extrapolations to loads beyond several days of duration would be speculative.

Keywords: beams (supports); concretes; cracking (fracturing); creep properties; loads (forces); relaxation (mechanics).

In all materials, even those that do not exhibit significant creep, fracture is rate-sensitive. That is, the effective fracture properties depend on the crack growth rate, which is determined by the loading rate. This is due to the fact that the rupture of interatomic or intermolecular bonds is a thermally activated process. The probability that the thermal vibration energy of an atom or molecule (depending on the load) would exceed the activation energy barrier of the bond increases with the number of oscillations. It is (according to the Maxwell distribution of thermal energies) equal to zero for an infinitely short time interval. In a material such as concrete, the rate sensitivity is expected to be particularly marked due to creep of the material in the fracture process zone, as well as in the entire structure. Studies by Shah and Chandra,[1] Wittmann and Zaitsev,[2] Liu et al.,[3] and others have suggested that fracture is affected by creep. Yet a detailed investigation of this effect has not been conducted. Substantial studies (Mindess and Shah[4]) have been carried out under very high (dynamic) rates of loading, in which the maximum load is reached under 1 s. Since the creep effect in this range is weak, a comprehensive understanding of rate effects can be obtained without accounting for creep. However, for slower rates, the contribution of creep becomes significant. Fracture, with rates that correspond to reaching maximum load within anywhere between an hour and several years, is of great interest for predicting the long-term cracking and failure of many types of concrete structures. For example, as is now widely accepted, the failure of dams should be analyzed according to fracture mechanics, but certain types of fracture in dams develop gradually over a period of many years. Without any test data, one cannot but speculate about the effective fracture properties to be used under such slow rates.

This paper presents the results of fracture tests of concrete at various loading rates in the static range, with the time to peak load ranging from 1 s to 2.5 days, and the results of complementary tests of load relaxation in fracture specimens. (A preliminary report was made earlier at two conferences.[5,6]) The size effect method, combined with the assumption of a quasi-elastic effective modulus representation of concrete creep, is used to determine the fracture energy, fracture toughness, effective length of the process zone, and effective crack-tip opening displacement at various loading rates.

REVIEW OF RATE PROCESSES IN CONCRETE FRACTURE

The significance of rate effects may be illustrated by comparing the results of two tests on identical three-

ACI Materials Journal, V. 89, No. 5, September-October 1992.
Received June 25, 1991, and reviewed under Institute publication policies.

Zdeněk P. Bažant, FACI, holds the W. P. Murphy professional chair at Northwestern University, Evanston, Ill., where he served as Director of Center for Concrete and Geomaterials (a predecessor to the current Center for Advanced Cement-Based Materials). Dr. Bažant, a registered structural engineer, has served as consultant to Argonne National Laboratory and other firms; is Editor (in chief) of the ASCE Journal of Engineering Mechanics; *President of the newly formed International Association for Fracture Mechanics of Concrete Structures (FraMCoS); Chairman of ACI Committee 446, Fracture Mechanics, RILEM creep committee, ASCE-EMD Programs Committee, and SMiRT's Division H; and is on the Board of Directors of the Society of Engineering Science. He has received numerous awards, the latest of which is the 1990 Gold Medal from the Building Research Institute of Spain, and an honorary doctorate from Czech Technical University at Prague.*

ACI member Ravindra Gettu is a Senior Researcher in Construction Engineering at the Technical University of Catalunya, Barcelona, Spain. He has a PhD from Northwestern University and a BEngng from the University of Madras, India. He is a member of ACI Committee 446, Fracture Mechanics. His current research interests include the behavior and modeling of structural materials, fracture mechanics, and high-strength concrete.

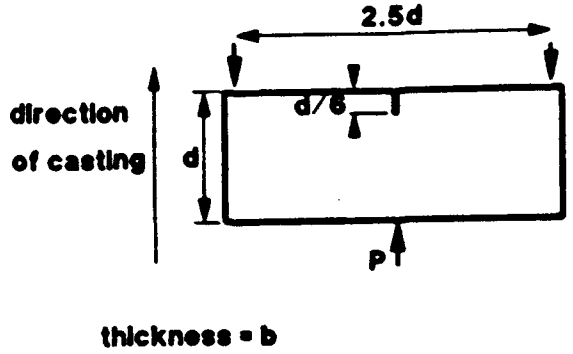

Fig. 1 — Three-point bend fracture specimen

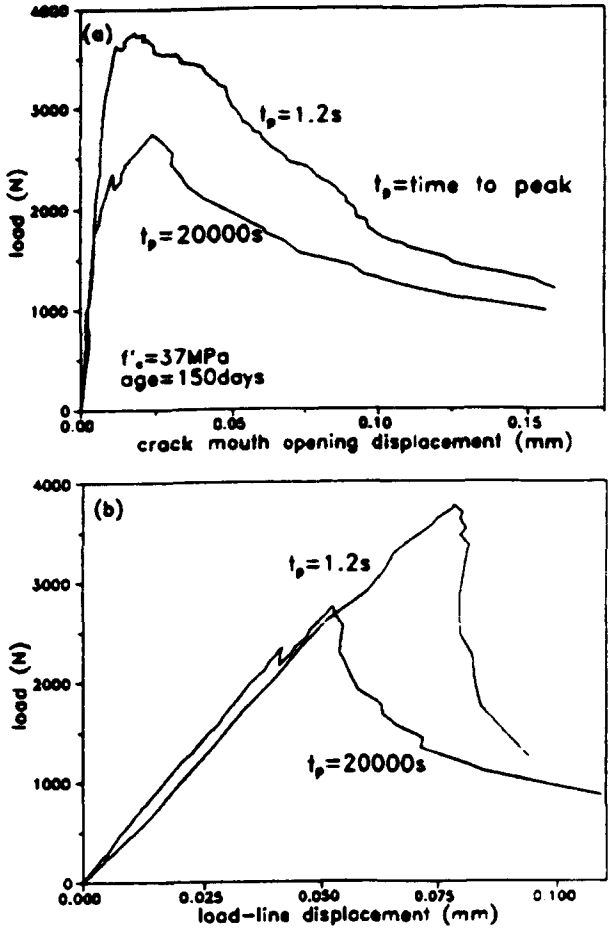

Fig. 2 — Rate effects on (a) load-CMOD response and (b) load-deflection response

point bend (3PB) fracture specimens (see Fig. 1: b = 38 mm, d = 76 mm, f'_c = 37 MPa, age = 150 days), at very different crack mouth opening displacement (CMOD) rates. The peak load of one specimen was reached in 1.2 s, and that of the other in about 20,000 s (5.6 hr). The load versus CMOD and load-versus-load-line displacement curves are shown in Fig. 2(a) and (b). The peak load of the faster test is more than 25 percent higher than that of the slower test. A similar increase in the failure stress or "strength" has been observed previously in the static range by several investigators.[7] A similar trend exists under dynamic or impact loading.[8,9]

Comparison of the post-peak response is also very interesting. While the load-CMOD plots [Fig. 2(a)] for both specimens are quite similar, the load-displacement plots [Fig. 2(b)] differ significantly. For the faster test, the load-displacement curve descends steeply, whereas in the slower test the drop is gradual and closer to ductile behavior. This difference can be attributed to creep in the bulk of the specimen, since the load-line displacement reflects the cumulative response of the entire specimen, whereas CMOD is affected primarily by the deformations of the crack and the fracture process zone. It is therefore important that the effect of creep outside the process zone be separated from the rate process producing fracture. It also appears that CMOD-controlled tests are more relevant for studying fracture properties than deflection-controlled tests.

It has been suggested that the cause for the increase in concrete strength under fast loading is the change in crack path with rate. At very high (dynamic) loading rates, it has been observed (e.g., from compressive impact tests of Hughes and Watson[10]) that cracks tend to be less tortuous, and often pass through the aggregates instead of following the aggregate-mortar interfaces. Since aggregates, in normal concrete, are stronger than both the mortar and the interfaces, a crack passing through the aggregates will encounter a higher resistance than one following the interfaces. To investigate whether this change in mechanism occurs in the static regime, the fractured surfaces of two 3PB specimens (see Fig. 1: b = 38 mm, d = 76 mm, age = 45 days) — one with time to peak load t_p = 0.5 s (and peak load = 4000 N), and the other with t_p = 30,000 s (and peak load = 2340 N) — were studied. It can be seen, from Fig. 3, that a few more aggregates were fractured in the faster case than in the slower, but no significant change in the fracture mechanism is apparent.

The straightening of the crack path could also have an opposite effect — strength decrease due to the higher stress intensity of planar cracks. Crack bridging and deflection by the aggregates increase the overall fracture resistance. To check for difference in tortuos-

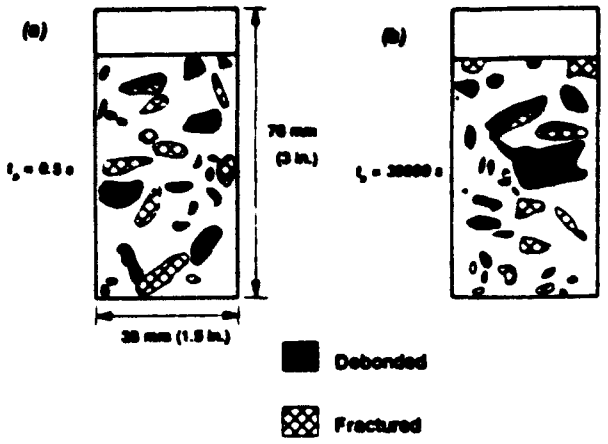

Fig. 3 — Crack surfaces for (a) t_p = 0.5 s and (b) t_p = 30,000 s

ity, the fractured areas of the specimens mentioned previously were approximately determined. After complete fracture, the cracked surfaces were covered with 2.4-mm (0.094-in.) wide tape, and the crack area was calculated from the length of the tape used. Although this method is not very accurate, it seems to suffice for the present purpose. The crack area for the faster fracture was 2900 mm² (4.5 in.²) and for the slower one, 3000 mm² (4.7 in.²). (The crack-plane areas were 2420 mm² (3.75 in.²) for both.) This difference is insignificant. Therefore, it seems that the same mechanisms dominate fracture in this range. (A similar observation was made from tests of certain ceramics by Suresh et al.[11]; they showed that fracture initiation in alumina was predominantly intergranular for both dynamic and static rates.)

Several micromechanical processes could give rise to rate effects, as, for example, the presence of moisture at the crack tip. As is well known, wet surfaces require less energy to form than dry surfaces, i.e., the fracture energy decreases in the presence of moisture. Water corrosion and disjoining pressure mechanisms that weaken the bonds at the fracture front may also be involved.[12] Such effects could explain the lowering of fracture energy and strength in rock[13] and concrete.[14] The detrimental effect of moisture is more significant at slower rates and tends to increase the crack velocity. It has even been suggested that the water in concrete is the primary source of rate effects.[9,15]

Creep dominates the response of cracked as well as uncracked concrete under slow and sustained loading. It may considerably decrease the strength and the effective modulus as loading rate becomes slower. The effects of creep on fracture, however, may be complicated.[12] One effect may be a decrease in fracture resistance, and another effect may be relaxation at the crack tip, which removes part of the stress concentration. However, the second effect would also reduce the extent of microcrack initiation ahead of a propagating crack.[16,17] Since the microcracked zone causes crack blunting or toughening, a smaller zone implies more brittle fracture.

Table 1 — Fracture test data

Series	Specimen depth, mm	CMOD rate, mm/s	Time to peak t_p, sec	Age at loading, days	Peak load, N
Fast	38	1.1×10^{-2}	0.9	28	2225
		8.4×10^{-3}	2.2	28	1800
f'_c = 36.6 MPa		1.1×10^{-2}	1.5	28	1890
ω = 1.3 percent	76	1.4×10^{-2}	1.3	28	3625
		1.4×10^{-2}	2.2	28	3960
		1.4×10^{-2}	1.3	28	3025
	152	2.1×10^{-2}	1.3	28	6180
		2.1×10^{-2}	1.1	28	5940
		2.1×10^{-2}	1.1	28	5425
Usual	38	1.8×10^{-3}	595	28	1825
		1.8×10^{-3}	595	28	1780
f'_c = 36.5 MPa		2.4×10^{-3}	570	28	1645
ω = 6.1 percent	76	5.3×10^{-3}	460	28	3070
		3.6×10^{-3}	520	28	2800
		4.3×10^{-3}	505	28	2760
	152	7.1×10^{-3}	495	28	5025
		7.1×10^{-3}	360	28	4225
		7.1×10^{-3}	420	28	4200
Slow	38	7.1×10^{-4}	10,350	40	2315
		7.1×10^{-4}	17,100	38	1935
f'_c = 37.2 MPa		7.1×10^{-4}	13,500	39	2180
ω = 5.5 percent	76	1.0×10^{-4}	10,625	46	3580
		9.4×10^{-5}	17,550	42	3515
		1.1×10^{-4}	11,900	30	3180
	152	1.4×10^{-4}	15,300	32	4270
		1.4×10^{-4}	14,850	38	4180
		1.7×10^{-4}	14,600	31	5295
Very slow	38	3.8×10^{-6}	266,500	120	2135
	76	7.4×10^{-6}	255,500	108	3180
f'_c = 36.9 MPa	152	1.3×10^{-5}	236,000	90	4580
ω = 4.4 percent					

f'_c = 28-day compressive strength of 76 × 152-mm cylinders.
ω = coefficient of variation of f'_c.
1 MPa = 145.04 psi; 1 N = 0.2248 lb.

Even at dynamic strain rates, it is not clear whether a slower rate causes more or less brittleness. Assuming the behavior to be analogous to that of a plastic material with coalescing voids, Reinhardt[18] proposed that when the crack velocity is comparable in magnitude to the wave speed near the crack tip, the fracture process zone becomes larger than usual. To a certain extent, this hypothesis is supported by tests. Impact tests show more distributed cracking and more fragmentation at higher strain rates.[9,19] These results further imply that faster fracture is more ductile, since it dissipates more energy in a larger zone.[20] On the other hand, since the nonlinearity of the prepeak load-deformation relationship decreases with an increase in loading rate, several investigators have argued that fracture becomes more brittle.[21] That argument applies only when the nonlinearity is primarily due to the fracture process, and the effects of time-dependent phenomena outside the fracture zone are negligible. It is also possible that different trends could exist due to a change in fracture mechanisms, for example, fracture through or around aggregates and inertia effects. Reversals suggesting such explanations have been documented for failure strain[12] and fracture parameters.[22] The present study is limited to static rates, and, therefore, will not attempt to answer these questions for fracture in the dynamic range.

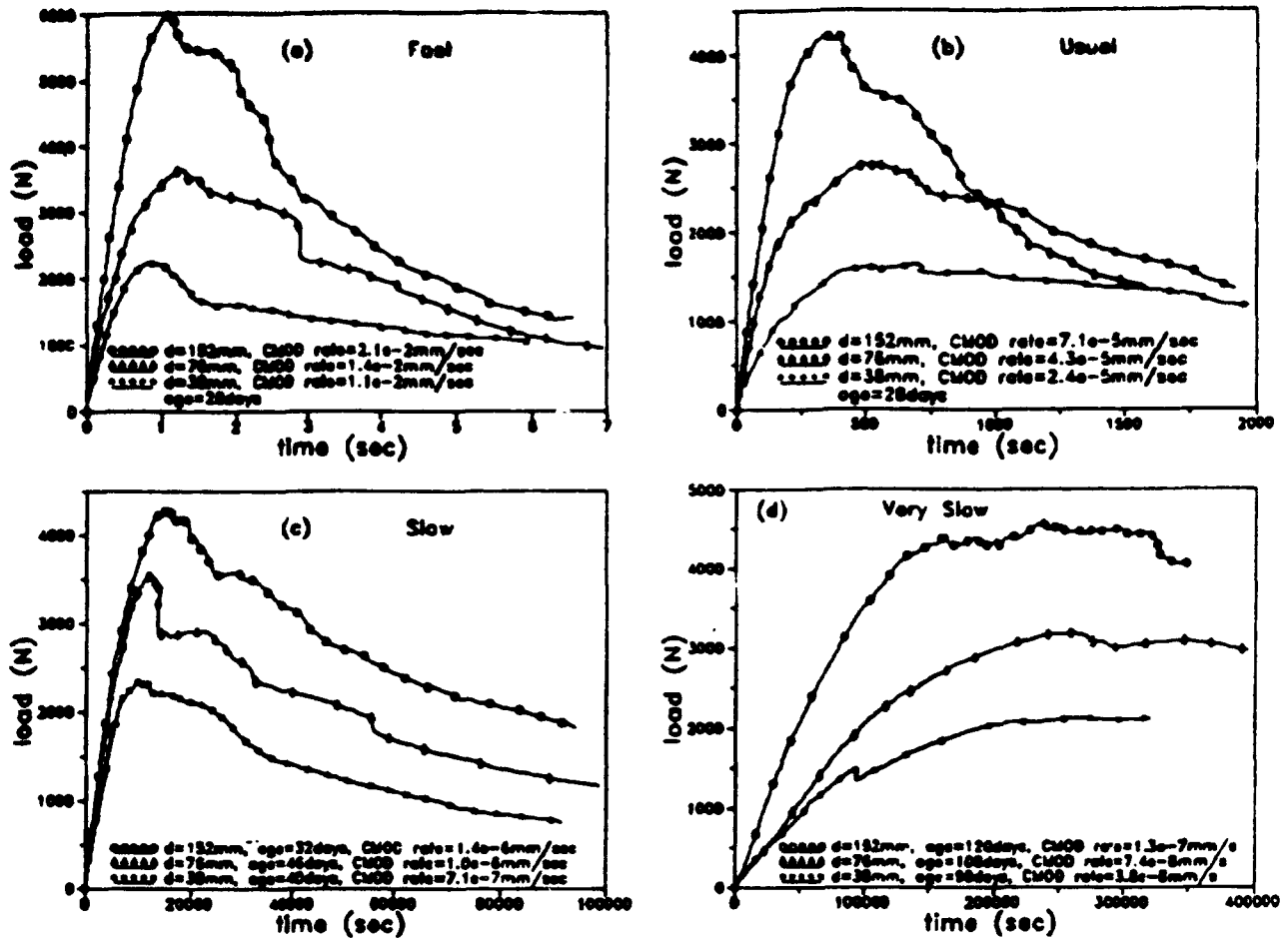

Fig. 4 — Typical load-CMOD curves (e − n means × 10^{-n})

TEST SPECIMENS

Three-point (single-edge notched) bending specimens (Fig. 1) were used with concrete of cement:sand:gravel:water ratio 1:2:2:0.6, Type I cement, crushed limestone gravel (maximum grain size = 13 mm), and standard No. 2 sand (maximum grain size = 5 mm). The beams were cast with the notch face at the bottom. The thickness of the specimens was 38 mm (1.5 in.), and the notch length was ¼ of the beam depth. The notches, cut with a diamond band saw, were 1.8 mm (0.07 in.) wide. All the specimens were cured under water until testing, and had their surfaces sealed with siliconized acrylic latex during testing to prevent loss of moisture. The fracture tests were conducted under CMOD control in a 89-kN (20-kip) load frame with a load cell operating in the 8.9-kN (2000-lb) range. Companion cylinders of 76-mm (3-in.) diameter and 152-mm (6-in.) length were used to determine the compressive strength f'_c 28 days after casting. The cylinders were capped with a sulfur compound, and tested in a 534-kN (120-kip) load frame under stroke control such that failure occurred in about 10 min.

SIZE EFFECT TESTS AT VARIOUS CMOD RATES

Four series of tests, each with specimens that were geometrically similar in two dimensions and of three sizes [d = 38, 76, and 152 mm (1.5, 3, and 6 in.)], were conducted. The measured peak loads and other details are listed in Table 1. The typical measured load-CMOD curves are presented in Fig. 4. The CMOD rates were chosen to give almost the same t_p for all the sizes in each series (Table 1). The range of CMOD rates, or t_p, exceeds five orders of magnitude (1:10^5).

In choosing the loading rates at different sizes, one must realize that the same displacement rate used for specimens of different sizes will result in different rates of deformation of the fracture process zone. Assuming linear viscoelastic behavior through the whole volume of the specimen, one could calculate the load-point displacement rates that give the same rate $\dot{K}_I$ of the stress intensity factor K_I for specimens of different sizes (this is achieved for $dP/dt = \sqrt{d} \times const.$). But due to nonlinear behavior and the presence of a large fracture process zone, this does not achieve the same rates of deformation of the fracture process zone, which is the condition for which the results for large and small specimens can be legitimately compared. To calculate the CMOD rates that meet this condition, one would need a priori a good mathematical model for the rate effect in fracture. But such a model is unavailable. Among various simple possibilities, the condition of equal rates of deformation of the fracture process zone

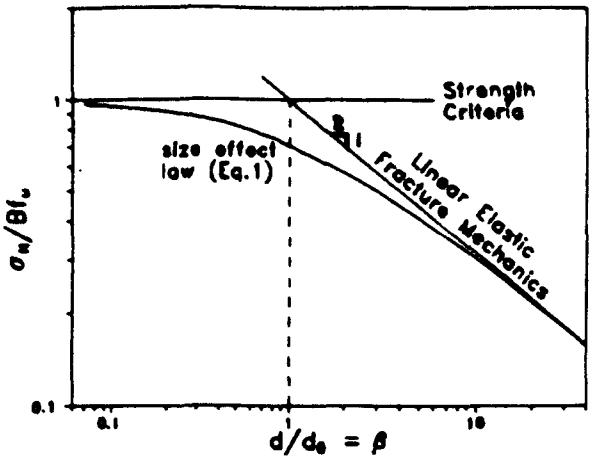

Fig. 5 — Size effect law

is probably best achieved by rates that give approximately the same time t_p to peak load. This conditon at the same time insures that the relative creep deformations outside the process zone at time t_p are about the same — another conditon desired for comparability of different sizes. The rates to achieve equal t_p were selected on the basis of prior experimentation, and the condition of equal t_p has of course been achieved only approximately. The corresponding CMOD rates for various specimen sizes were not equal, but they were of the same order of magnitude (Table 1). However, once the test results are translated into a mathematical model, the loading rate selection should in the future be done by calculations.

The purpose of using specimens of different sizes was to apply the size effect method for determining fracture parameters. The method is based on the size effect law,[23] which in its simplest form reads (Fig. 5)

$$\sigma_N = \frac{Bf_u}{\sqrt{1+\beta}}, \beta = \frac{d}{d_0} \qquad (1)$$

where $\sigma_N = P_u/bd$ = nominal strength (maximum nominal stress), P_u = peak (maximum) load, d = characteristic dimension of specimen (here, chosen as the specimen depth), b = thickness, β = brittleness number, Bf_u and d_0 are the parameters of the model, and f_u is some estimate of the material strength. When the size is very small, i.e., $\beta \ll 1$, σ_N is not significantly affected by size, and the behavior is then governed by strength limit (or allowable stress) criteria. This implies that energy is dissipated during failure in a relatively large region. When β is large, $\beta \gg 1$, the behavior follows linear elastic fracture mechanics (LEFM), and $\sigma_N \propto 1/\sqrt{d}$. In this case, energy is dissipated in a region of infinitesimal size at the crack tip. The transition zone (taken as $0.1 < \beta < 10$), in which the test results usually lie, is the nonlinear fracture regime.

Eq. (1) has been extensively verified for the fracture of concrete and extended to determine fracture parameters and material brittleness.[24,25] The method has also been used to determine the change in fracture properties with temperature[14] and strength.[26] However, all the tests have so far been conducted at conventional loading rates, i.e., with t_p between 5 and 10 min. Applicability of the method at various rates is to be experimentally validated. For Eq. (1) to apply, specimens of each size should attain the peak load in about the same time, for reasons already explained (differences up to 50 percent are probably not serious, but differences in orders of magnitude certainly would be). The reason is that, for all sizes, the fracture process zone should be deformed at about the same rate, and the relative creep deformations outside the process zone should be about the same.

To determine the size effect parameters in Eq. (1) from σ_N-data, this study used nonlinear regression analysis in which the sum of the squared errors in σ_N is minimized. The optimized values of Bf_u and d_0, obtained by means of the Marquardt-Levenberg algorithm (available in standard computer libraries), are listed in Table 2 for each series of tests. The curves in Fig. 6 are the optimum fits of the data points by Eq. (1). The coefficients of variation of the deviations of σ_N from the fits are also given. The results demonstrate that the size effect is significant at all the rates used, and that Eq. (1) fits the data reasonably well through the entire time range.

The applicability of Eq. (1) might be questioned, since its theoretical derivation assumes the behavior outside the process zone to be elastic. There are, nevertheless, two justifications: 1) according to the double power creep law,[27] the ratio of creep strain to the true instantaneous strain, at 28 days, is about 0.9 for t_p = 8 min (the usual static test), about 0.4 for t_p = 1 s, and about 1.9 for t_p = 2.5 days. If elastic analysis is acceptable for the ratio 0.9, it should also be acceptable in the range 0.4 through 1.9, provided, of course, the duration of the loading is the same for all the sizes; 2)

Table 2 — Material fracture parameters

Series	Average t_p, sec	Average age, days	Bf_u, MPa	d_0, MPa	ω	K_{Ic}, MPa$\sqrt{m}$	c_f, mm	E_{cr}, GPa	G_f, N/m	δ_{cr}, mm
Fast	1.4	28	1.60	102.5	0.10	39.5	17.2	36.0	43.4	0.0146
Usual	500	28	1.68	41.3	0.06	26.3	6.9	28.6	24.1	0.0077
Slow	13,650	38	2.94	13.3	0.09	26.1	2.2	24.1	28.4	0.0052
Very slow	253,000	106	3.47	8.5	0.01	24.6	1.4	22.4	26.9	0.0042

ω = coefficient of variation of the deviations of the fit from test data.

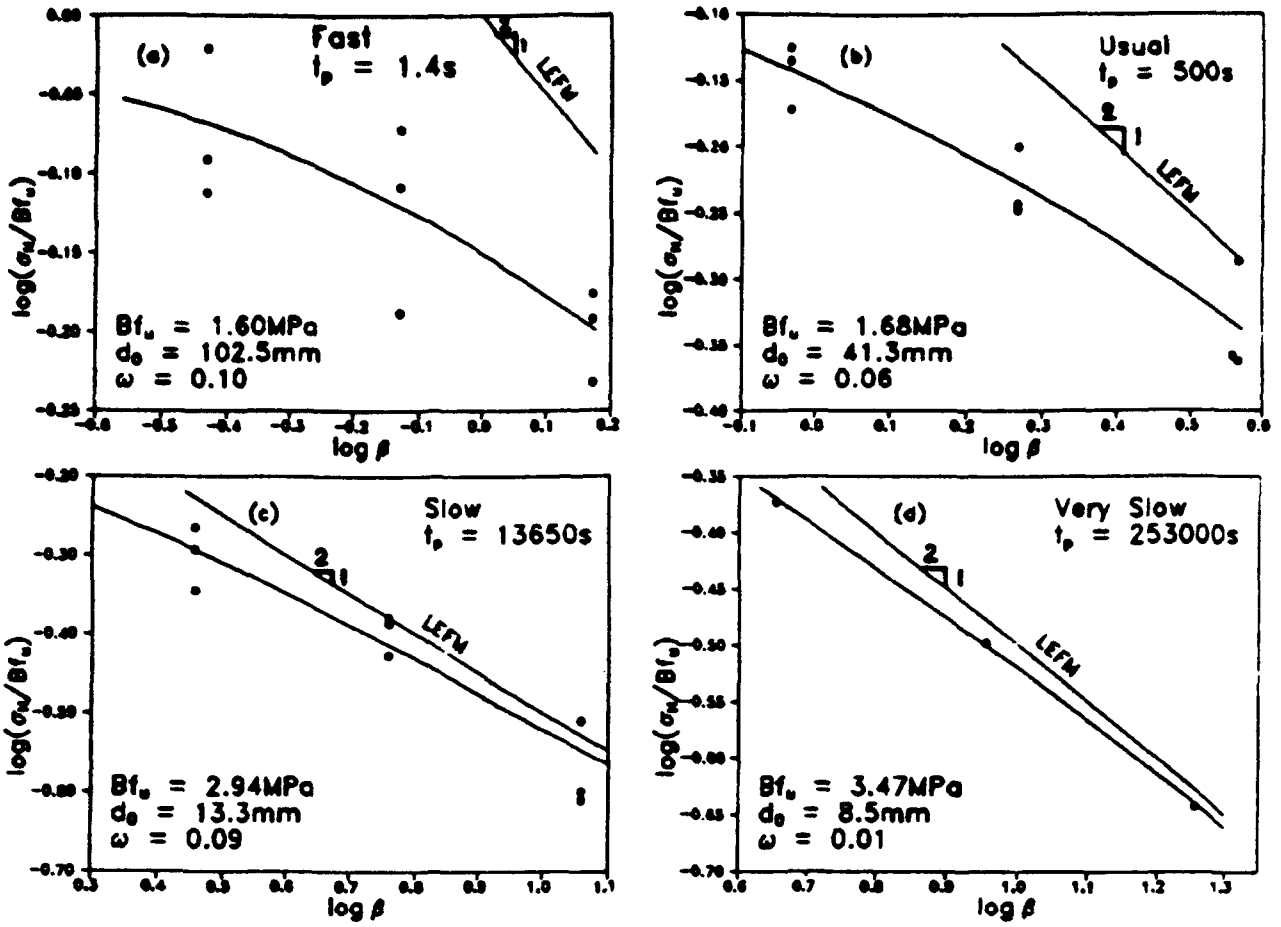

Fig. 6 — Optimum size effect curves for the test data

due to linearity of creep and the rapidly decaying nature of the creep curve of concrete (for stresses up to about half the strength), quasi-elastic analysis based on the effective modulus is a reasonable approximation to the viscoelastic solution.[27]

SHIFT IN BRITTLENESS

Since the test results for all the rates agree reasonably well with the size effect law, they can be combined into one plot, as in Fig. 7. Such a combined plot was used previously to show the increase in the brittleness of concrete with increasing strength.[26] This clarifies the effect of rate on the brittleness number. In each series there are three sets of data. In each set, the most brittle (largest β) are the largest specimens, and the least brittle are the smallest. Now, the interesting aspect is that there is a significant shift of the data sets toward the right (toward LEFM, i.e., ideal brittle failure) as t_p increases. This means that fracture becomes more brittle as the loading becomes slower; i.e., the intensity of the crack-tip shielding mechanism decreases as the loading rate becomes slower. The damage and energy dissipation are more distributed for higher rates. It should be emphasized, however, that even though the present quasi-elastic approximation approaches LEFM for very slow loading rates, consideration of creep in the analysis of structural response becomes more important.

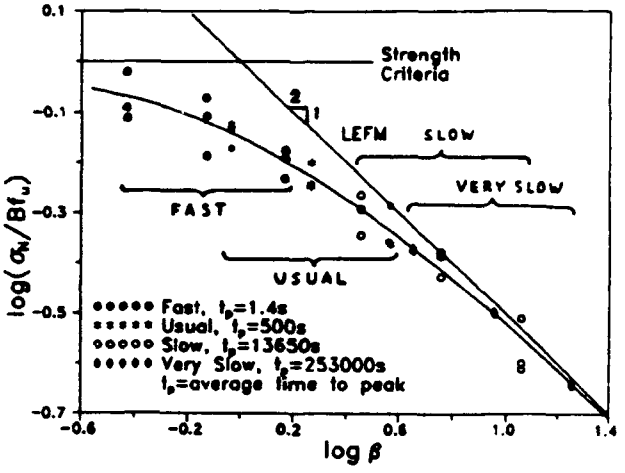

Fig. 7 — Change in mode of failure with loading rate

This result is similar to that of Bažant and Prat,[14] who applied the size effect method to tests of fracture specimens at different temperatures. From their data it can be seen that the brittleness of concrete increases with temperature. The effect of time on fracture is analogous to the effect of high temperature, since a higher temperature means higher creep. This similarity reinforces the present conclusion.

Another extrapolation of the effect of creep on brittleness could be made to the failure of early-strength concrete. Since creep mechanisms are more dominant at

Table 3 — Fracture parameters corrected for 28 days

Series	E_{eff}, GPa	K_{Ic}, MPa$\sqrt{mm}$	c_f, mm	G_f, N/m	δ_{cf}, mm
Fast	36.0	39.5	17.2	43.4	0.0146
Usual	28.6	26.3	6.9	24.1	0.0077
Slow	22.9	25.3	2.2	28.1	0.0052
Very slow	18.2	22.7	1.3	28.2	0.0047

younger ages, one could infer from this study that fracture is more brittle in concrete at earlier ages. The data of Wong and Miller[28] on fracture tests at different ages (t_p = 5 to 10 min) support this inference.

FRACTURE PARAMETERS OBTAINED BY THE SIZE EFFECT METHOD

The steepness of post-peak load-deflection curves, or the amount of distributed cracking in unnotched specimens, have previously been interpreted as indicators of material brittleness. Though valid in certain cases, such indicators are not size-independent and general measures. Rather, objective measures must be based on fracture mechanics. In the present study, the size of the fracture process zone is taken as the measure of brittleness; a material with a smaller process zone is more brittle. The structural brittleness, on the other hand, may be generally characterized by the brittleness number β = Eq. (1). Another important fracture parameter is the fracture toughness; higher fracture toughness implies higher resistance against failure. These quantities are also necessary for nonlinear fracture mechanics analysis of concrete structures.

Since specimen size and shape could have a strong effect on the measurements of fracture parameters, extrapolation to an infinitely large size has been proposed for obtaining unambiguous values.[29] It has also been shown that parameters obtained in this manner are practically independent of specimen geometry.[24] Based on the infinite size extrapolation of Eq. (1), simple expressions for fracture energy G_f, fracture toughness K_{Ic}, effective length of the fracture process zone c_f, and effective critical crack-tip opening displacement δ_{cf} have been derived[25,29,30] (see also RILEM recommendation[31])

$$G_f = \frac{1}{E'}(Bf_u')^2 d_0 g(\alpha_0) \quad (2)$$

$$K_{Ic} = Bf_u'\sqrt{d_0 g(\alpha_0)} \quad (3)$$

$$c_f = \frac{d_0 g(\alpha_0)}{g'(\alpha_0)} \quad (4)$$

$$\delta_{cf} = \frac{8K_{Ic}}{E'}\sqrt{\frac{c_f}{2\pi}} \quad (5)$$

where function $g(\alpha)$ is the nondimensionalized energy release rate defined by the LEFM relation $G = P^2 g(\alpha)/E' b^2 d$, G = the actual energy release rate, P = load, α = (crack length)/d = relative crack length, $\alpha_0 = a_0/d$, a_0 = notch or traction-free crack length, $E' = E$ for plane stress, $E' = E/(1 - \nu^2)$ for plane strain, E = Young's modulus, ν = Poisson's ratio, and $g'(\alpha) = dg(\alpha)/d\alpha$. The function $g(\alpha)$ can be obtained from handbooks[32] or from LEFM analysis.

Parameter c_f lumps together the effect of all the toughening mechanisms in concrete, including the deflection and bridging of the crack by aggregates, and microcracking ahead of the crack tip. Note also that the crack tip is defined here as the point where the traction-free crack ends.

For the present specimen geometry, finite element analysis provided the values $g(\alpha_0)$ = 5.927 and $g'(\alpha_0)$ = 35.24. The values of Bf_u' and d_0 obtained earlier (Table 2) can then be used in Eq. (3) and (4) to calculate K_{Ic} and c_f; see Table 2. (Note that the calculated values of K_{Ic} and c_f can have coefficients of variation up to 0.3 and 0.5, respectively.)

In view of the preceding comments, the validity of Eq. (2) through (5) may be extended to linear viscoelastic creep, which occurs in most of the specimens except in (and very near) the fracture process zone. This is done by replacing E with the effective modulus E_{eff} (inverse of the compliance function) corresponding to load duration t_p. To determine E_{eff} the BP model for the prediction of concrete creep[27,33] was used. Only the basic creep was considered, since the specimens were sealed to prevent moisture loss. In applying the BP model, the asymptotic modulus was modified such that the effective modulus for the loading time of 10 min would coincide with the ACI code formula $E = 4735\sqrt{f_c'}$, in MPa (or $E = 57{,}000\sqrt{f_c'}$, in psi). The E-values for the various test series are listed in Table 2. Using the effective moduli in Eq. (2) and (5), the values of G_f and δ_{cf} are computed and listed in Table 2.

Since two series of tests were conducted at ages other than the standard 28 days, the fracture parameters obtained from them should be corrected before comparisons are made. The following formulas were used for this purpose: $f_t' = 0.50\sqrt{f_c'}$ (ACI); $f_c'(t) = f_c'(28)\, t/(4 + 0.85t)$ (ACI); and $G_f \propto (2.72 + 3.103 f_t')\, f_t'^2 d_a/E_{eff}$ (Reference 34), where f_t' is the tensile strength; f_c', f_t', and E are in MPa; d_a is the maximum aggregate size in mm; G_f is in N/mm; t is the age in days; and E_{eff} is obtained from the BP model, as before. It was also assumed that the parameter Bf_u' varies linearly with f_t'. (Possible errors in these formulas cannot be important, since the corrections are small.) The adjusted 28-day values of all the parameters are listed in Table 3.

DISCUSSION OF TRENDS OBSERVED IN CONSTANT-RATE TESTS

From Table 3, it is clear that the fracture toughness K_{Ic} tends to decrease with increase in t_p. This agrees with the well-known reduction in concrete strength as the loading rate becomes slower. The trend agrees with those obtained by other methods for mortar and cement paste.[35]

A new result from the present tests is the significant decrease in the fracture process zone c_f as the loading rates decrease. This implies that the material brittle-

ness, and consequently the brittleness of structural failure, increases due to creep. The decrease in c_f is probably due to the relaxation of the high stresses in the material ahead of the crack tip, causing the stress drop to be more concentrated. The trend can be approximately described by the formula [see Fig. 8(a)]

$$c_f = c_0 \left(\frac{t_0}{t_p}\right)^n \tag{6}$$

where t_0 is the reference value of time to peak and c_0 is the corresponding value of c_f; $n = 0.22$; and for $t_0 = 600$ s (about the conventional testing time), $c_0 = 5.04$ mm.

Along with K_k and c_f, δ_{cf} is found to also decrease for slower loading. This trend agrees with that observed by Wittmann et al.,[22] who, however, concluded that for very slow loading, the trend reverses. The trend may also be different in the dynamic range.[21]

The variation of the fracture toughness of mortar and cement paste with loading rate has been described by means of a power function[35] $K_k = K_0 v^m$, where K_0 and m are parameters determined experimentally, and v is the rate of change of deflection, crack length, or stress. Similarly, the present test results have been fitted [Fig. 8(b)] by the equation

$$K_k = K_0 \left(\frac{v}{v_0}\right)^m \tag{7}$$

where $v \cong \delta_{cf}/t_p$, v_0 is the chosen reference deformation rate, and $K_0 = K_k$ for $v = v_0$. From the present data, $m = 0.041$, and for $v_0 = 5 \times 10^{-5}$ mm/s, $K_0 = 30.4$ MPa$\sqrt{\text{mm}}$.

For loading rates faster than the usual static test, the fracture energy G_f has previously been found to increase significantly with an increase in rate.[8,36] However, at low rates, this trend is not obvious from the present results. This may be because G_f is strongly affected by the decrease in the effective modulus due to creep. Wittmann et al.[22] proposed that fracture energy increases under very slow loading due to the influence of creep. The present variation tends to agree with their conclusion, but the scatter of the present results for G_f is too high to draw a firm conclusion. If linear elastic fracture mechanics were applicable, then one could use the relation $G_f = K_k^2/E$ to determine that the scatter is due to E, but the relation of G_f and K_k is more complicated.

RELAXATION TESTS OF UNNOTCHED BEAMS

To determine the creep or relaxation behavior of the concrete used, four unnotched beams, with $b = 38$ mm (1.5 in.), $d = 76$ mm (3 in.), and span = 191 mm (7.5 in.), were tested under three-point loading. A transducer (LVDT of 0.127-mm range) fixed on the beams measured the deformation over a gage length of 25.4 mm (1 in.) centered along the tension face. A computer-based data acquisition system monitored the load and deformation. Test details are listed in Table 4. Using the beam theory, the maximum bending stress and strain were calculated as a function of time. The initial load P_1 was applied at a rate of maximum strain equal to 3.6×10^{-4}/s, which corresponds to the time to peak $t_p \cong 1$ s. After time t_1, at which the desired P_1 was reached, the deformation was held constant, and the specimen was allowed to relax the load. The tests were conducted with different P_1-values. The measured relaxation curves of maximum bending stress σ versus elapsed time $(t - t_1)$ are shown in Fig. 9(a). It so happened after that some time the tests could not be controlled, since the transducer started to slip; only the data for the duration of proper control are shown.

The relaxation is strongest in Specimen U4, which had the highest P_1-value. It appears that U4 is in the

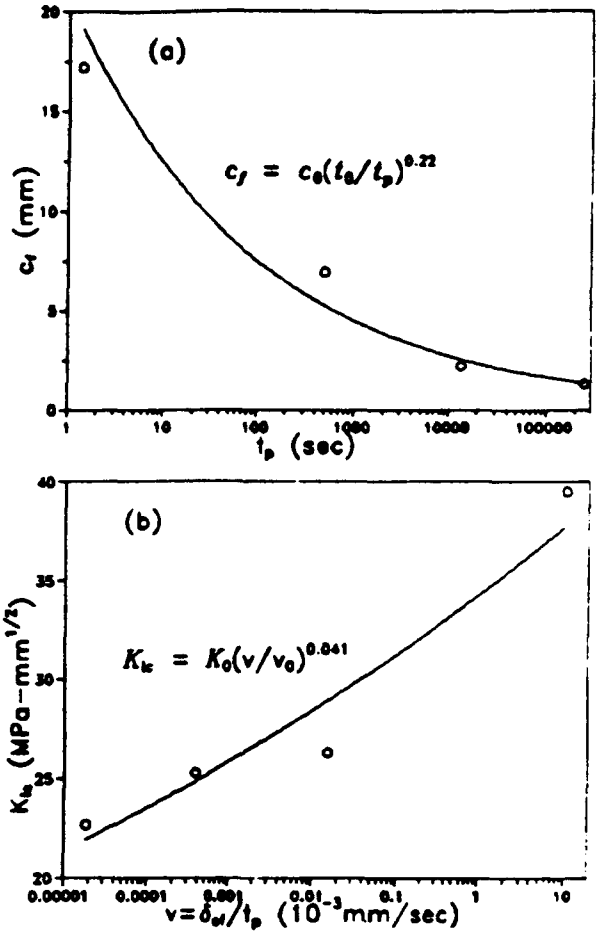

Fig. 8 — Effect of time to peak load on (a) fracture process zone size and (b) fracture toughness

Table 4 — Details of relaxation tests of unnotched beams

Specimen	Age, days	P_1, N
U1	34	990
U2	39	3420
U3	31	3760
U4	30	4580

P_1 = load at which relaxation started.
Approximate peak load = 5600 N at 35 days.
Strain rate during loading = 3.6×10^{-4}/sec.
f_t' = 28.1 MPa (4076 psi); coefficient of variation = 0.023.

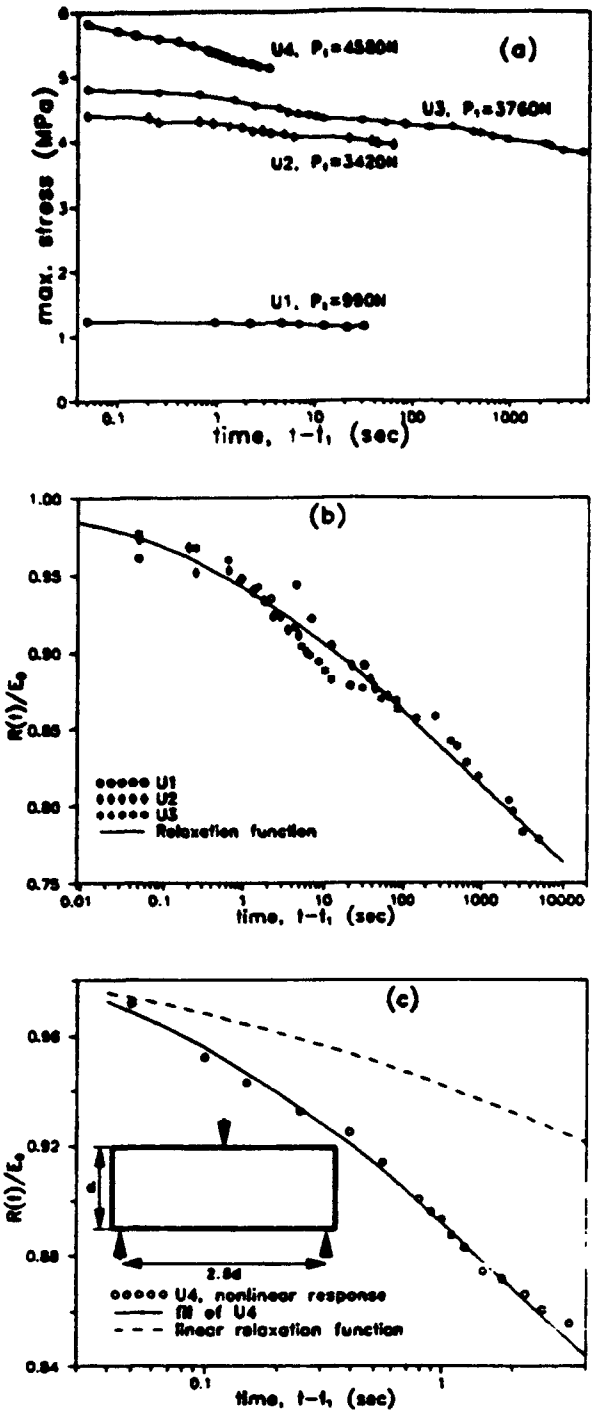

Fig. 9 — Relaxation tests of unnotched beams: (a) experimental data, (b) relaxation in linear range, and (c) relaxation in nonlinear range

nonlinear creep range where relative creep is stress-dependent. This is the case if an initial maximum bending stress greater than about 60 percent of the strength is imposed. At lower stresses, the relative creep or relaxation is generally linear, i.e., independent of stress.[27]

CREEP PROPERTIES OF CONCRETE

To interpret the relaxation tests of fracture specimens (discussed later), one must first know the relaxation properties of the concrete outside the process zone, characterized by the relaxation function $R(t,t_1)$, where t = current time and t_1 = age at the start of relaxation. The appropriate expression for $R(t,t_1)$ may be deduced from the compliance function $J(t,t_1)$ for creep. The log-double power law[37] for the creep of concrete gives a good approximation: $R(t,t_1) \cong 1/J(t,t_1)$. Here, $J(t,t_1) = E_0^{-1}(1 + \xi)$ and $\xi = a\ ln[1 + b(t - t_1)^n]$, where E_0, a, b, and n = empirical constants. For relatively short-term relaxation (hours rather than years), ξ is small. Then $1/(1 + \xi) \cong 1 - \xi$. This leads to the approximation

$$\frac{\sigma}{\epsilon_0} = R(t, t_1) = E_0\{1 - a\ ln[1 + b(t - t_1)^n]\} \quad (8)$$

where σ = current bending stress, ϵ_0 = strain during relaxation, and E_0 = instantaneous modulus, i.e., modulus for extremely fast load application. This modulus is typically 1.5 to 2 times larger than the conventional elastic modulus E that corresponds to the initial slope of the stress-strain diagram in a typical static test (the reason is that loads of several minutes duration suffice to produce considerable creep).[38]

The relaxation tests that were in the linear range (U1, U2, U3) were fitted with Eq. (8) using nonlinear optimization with the Marquardt-Levenberg algorithm. The parameters obtained were n = 0.36, a = 0.063, and b = 1.52, with t and t_1 in sec. Fig. 9(b) shows the fit and the data sets. The coefficient of variation was ω = 0.053. The average E_0 was 54,000 MPa (7.83 × 10⁶ psi), with coefficient of variation 0.1.

For the nonlinear (high-stress) range of relaxation, the values for Specimen U4 [see Fig. 9(c)] were E_0 = 56,000 MPa (8.12 × 10⁶ psi), n = 0.69, a = 0.056, and b = 5.91, with ω = 0.019.

RELAXATION TESTS OF FRACTURE SPECIMENS

To gain further insight into the rate effect, time-dependent tests of a different type are desirable. Creep tests are not feasible in the post-peak stage, since the load cannot be held constant. But load relaxation tests are possible, as the deformation (e.g., CMOD in fracture tests) can be held constant. In this study, two series of relaxation tests were conducted on 3PB fracture specimens (Fig. 1) with d = 76 mm (3 in.). In the first series, the beams were loaded at several CMOD rates into the post-peak stage and relaxation was initiated at about 80 percent of the peak load. In the second series (described later), the same CMOD rate was used for all specimens but relaxation was initiated at different loads.

The beams NA1, NA2, NA3, and NA4 (first series) were loaded at constant CMOD rates [see Fig. 10(a) and Table 5, where P_{max} = peak load), until a load P_1 ($\cong 0.8\ P_{max}$) was reached at time t_1. Subsequently, the CMOD was held constant, and the relaxation of load with elapsed time $t - t_1$ was then recorded. The measured curves of load versus elapsed time are shown in Fig. 10(b). It is obvious that not only the maximum

Table 5 — Details of fracture relaxation tests

Specimen	f'_c, MPa	Age, days	CMOD rate,* mm/sec	P_{max}, N	P_i, N
NA1†	33.7	136	8.5×10^{-1}	3690	3370
NA2†		138	8.5×10^{-1}	3670	3050
NA3†		140	8.5×10^{-4}	3290	2530
NA4†		136	8.5×10^{-7}	2710	2250
NB1†	35.2	38	8.5×10^{-3}	3600	3460
NB2†		37		3870	3680
NB3†		50		3810	2130
NB4‡		36		3880	1620
NB5§		51		3430	3430
NB6§		43		—	2390

*Loading rate before relaxation.
†Relaxation initiated in post-peak stage.
‡Relaxation initiated near peak load.
§Relaxation initiated in prepeak stage.
1 MPa = 145.04 psi.

load but also the relaxation is strongly influenced by the loading rate. Initially, the rate of relaxation is higher for specimens that are loaded faster, but the final slopes are almost the same regardless of the rate of initial loading. This was expected for two reasons: 1) according to the hereditary aspect of linear viscoelasticity, the initial stress relaxation is higher for a specimen loaded faster, as indicated by the superposition integral over the past stress history;[27] and 2) when a specimen is loaded at a higher rate, there is more damage (larger fracture process zone), and higher stresses near the crack tip. After some time, the delayed linear viscoelastic effect of the early loading history becomes negligible, and the stresses in the process zone relax to about the same values. Therefore, the relaxation rate eventually becomes the same for all specimens.

For the load relaxation after time t_1, the expression for linear stress relaxation [Eq. (8)] may be used as

$$P(t)/P_1 = 1 - A \ln[1 + B(t - t_1)^N] \qquad (9)$$

but the values of the empirical parameters A, B, and N are expected to differ from a, b, and n. For short times $t - t_1$, this equation can be approximated by $P(t)/P_1 = 1 - AB(t-t_1)^N$, and for long times $t - t_1$, by $P(t)/P_1 = (1 - A \ln B) - AN \ln(t-t_1)$. Thus, the product AN represents the final slope of the plot $P(t)/P_1$ versus $\ln(t-t_1)$, and Parameter B engenders a horizontal shift representing acceleration or retardation.

The data of Specimens NA1, NA2, NA3, and NA4 were fitted with Eq. (9) by optimizing $P(t)/P_1$ [see Fig. 10(c)]. In the fitting, the final slope (Parameters A and N) was taken to be the same for all four specimens, while B varied. The trends are modeled reasonably well. The parameters and the coefficient of variation ω of the fit are listed in Table 6.

The effects of load and loading stage on relaxation were investigated in the second test series. Six specimens were tested: four in the post-peak stage, one near the peak, and one in the prepeak stage [see Table 5 and Fig. 11(a) and (b)]. (Note that Specimen NB5, loaded until the estimated peak was reached, could lie in either the prepeak or post-peak stage.) The CMOD rate before relaxation was 8.5×10^{-3} mm/s for all these specimens. The load relaxation plots are shown in Fig.

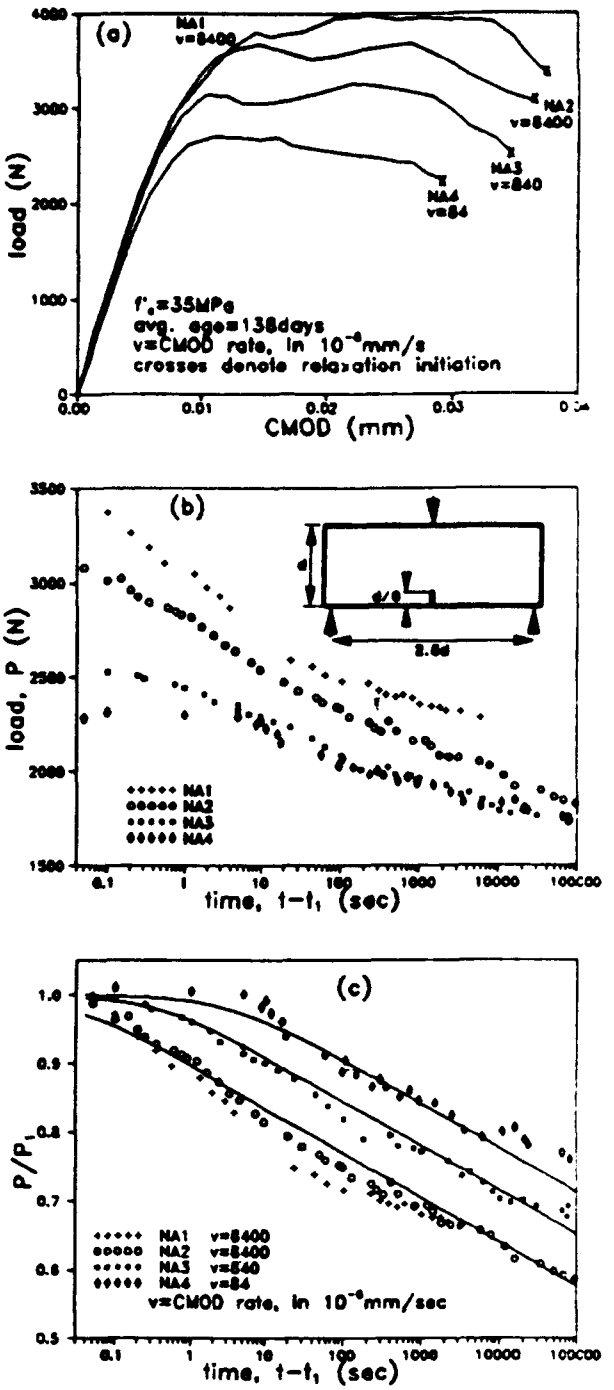

Fig. 10 — Relaxation tests of fracture specimens in post-peak state for various CMOD rates: (a) load-CMOD curves before relaxation, (b) load relaxation, and (c) fits of data with model

Table 6 — Parameters of relaxation function

Specimen	A	B	N	ω
NA1, NA2	0.032	23.8	0.875	0.020
NA3	0.032	2.25	0.875	
NA4	0.032	0.335	0.875	
NB1, NB2, NB3, NB4	0.036	23.8	0.864	0.032
NB5	0.034	23.8	0.770	0.018
NB6	0.034	9.42	0.683	0.008

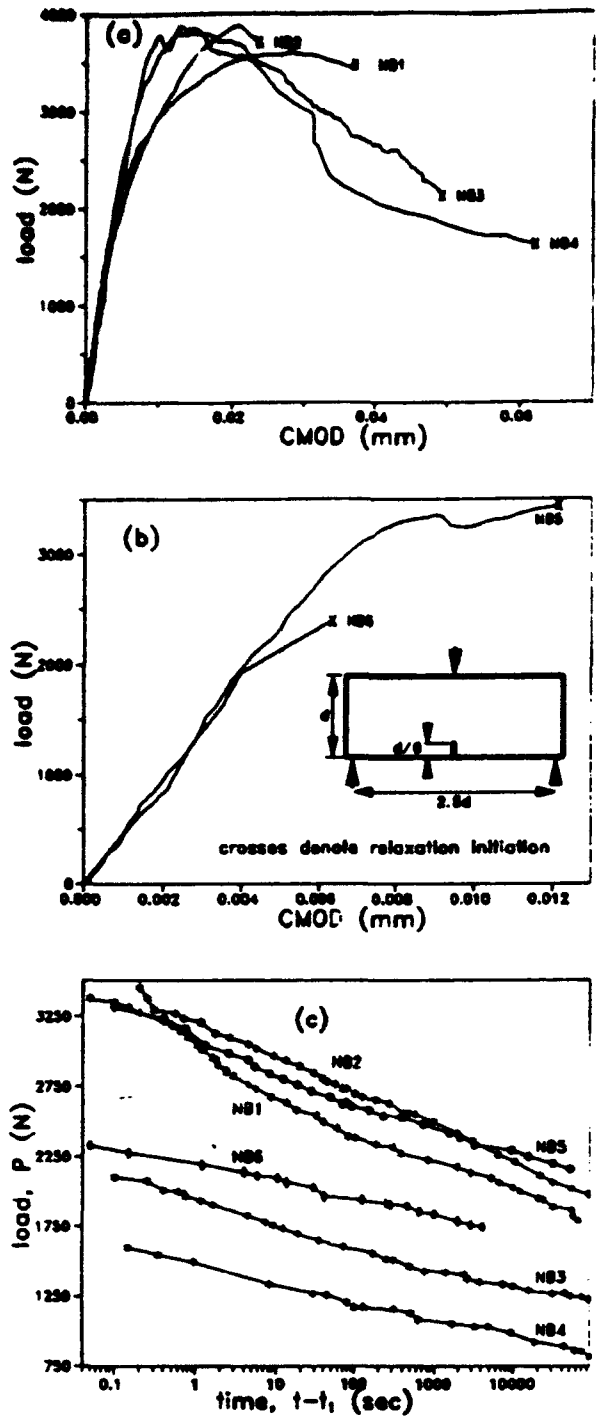

Fig. 11 — Relaxation tests of fracture specimens same CMOD rates but different load ratios: (a) load-CMOD curves before relaxation of specimens loaded beyond the peak, (b) load-CMOD curves before relaxation of specimens at and before peak, (c) load relaxation

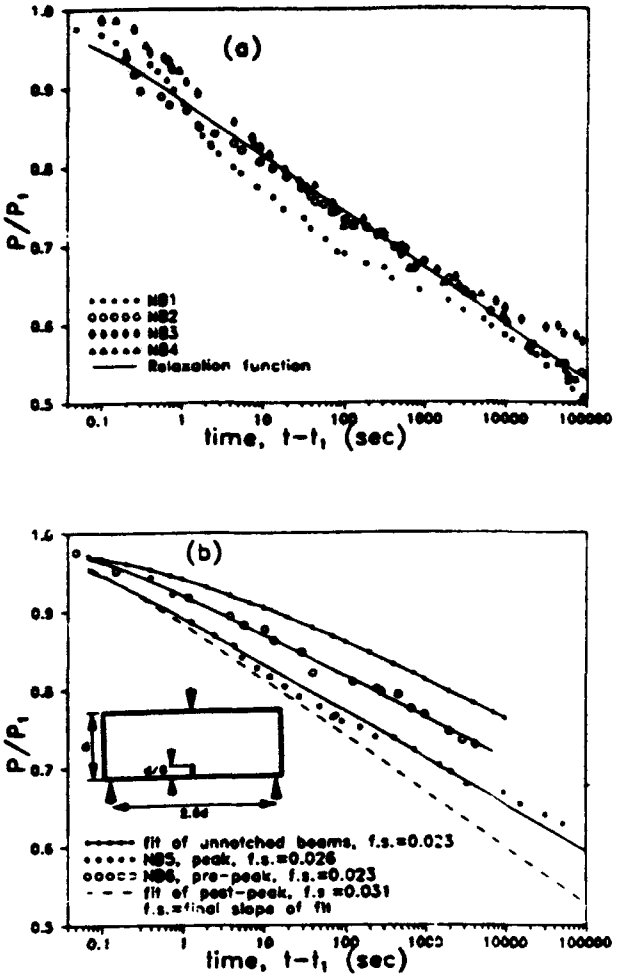

Fig. 12 — Fits of specimen relaxation with model: (a) response in post-peak stage, and (b) response at different levels of loading compared with unnotched beams

11(c). One interesting result is that the relaxation in the post-peak state appears unaffected by the load P_1 at which the relaxation begins. In other words, irrespective of where relaxation is initiated after the peak, $P(t)/P_1$ is the same.

The data of Specimens NB1, NB2, NB3, and NB4 (post-peak state) were fitted by Eq. (9) with $B = 23.8$, which was the value obtained for the same CMOD rate when Specimens NA1 and NA2 of the first series were fitted [see Tables 5 and 6, and Fig. 12(a)]. The values obtained for N and A are about the same. The data for relaxation near the peak (NB5) and in the prepeak stage (NB6) were also fitted with Eq. (9). For NB5, due to lack of sufficient data, the value $B = 23.8$ (from post-peak fits) was used. The fits are shown in Fig. 12(b), and the parameters in Table 6. For comparison, the fits of the post-peak data [from Fig. 12(a)] and linear relaxation [unnotched beams from Fig. 9(b)] are also shown.

It is important to note that the relative relaxation in the post-peak regime is significantly greater than linear relative relaxation. The difference between these two relaxations must be entirely attributed to time-dependent behavior of the fracture process zone.

The responses at the peak and in the prepeak stage lie between the post-peak and linear responses. The basic finding is that, in the time range of these tests, relaxation coincides with the linear behavior at low initial loads before the peak, later increases as the initial load increases towards the peak and, most importantly, remains constant through the post-peak range. Also,

there seems to be an acceleration in relaxation with increase of initial load before the peak. This is similar to the acceleration due to increase in the loading rate [see Fig. 10(c)], and can be explained similarly. To understand these results, it can be hypothesized that the process zone size increases monotonically with the load in the prepeak range, but propagates without much change in size during the post-peak stage (until it gets too close to the end of the ligament); see References 5, 6, 30, and also 39. The delayed linear viscoelastic effect in the post-peak range does not change if the initial loading rate remains the same. Thus, a dependence of the load relaxation on the damage or process zone size can explain the observed trends.

It appears that when a large crack is present in a concrete specimen or structure, the effects of creep are much more significant than without such a crack. Vice versa, creep decreases the load-carrying capacity of the cracked structure considerably. Thus, the interaction of creep and fracture is very important for calculating the response, and eventually for determining the serviceability of structures. This is crucial because long-term creep deformations in concrete structures are considerably larger than the instantaneous deformations.

CONCLUSIONS

1. The size effect law proposed by Bažant agrees with concrete fracture test results over a wide range of loading rates, with times to peak ranging from 1 s to 250,000 s.

2. The test results also show that a decrease of loading rate in this range causes a shift to the right in the size effect plot, i.e., toward higher brittleness and linear elastic fracture mechanics behavior.

3. The fracture toughness, effective length of the fracture process zone, and effective critical crack-tip opening decrease with an increase in the time to peak load. These material fracture parameters were obtained through the size effect method by quasi-elastic analysis based on the effective modulus for creep. An explanation for the decrease in process zone size might be the relaxation of high stresses in the fracture process zone.

4. For the fracture specimen type and time range studied, there is strong load relaxation at constant CMOD in the post-peak regime. The post-peak relaxation is about 1.7 times stronger than that of unnotched specimens. This significant difference may be attributed to 1) additional creep in the fracture process zone, and 2) time-dependent crack growth.

5. The load-relaxation curves tend to a straight line in the logarithm of the elapsed time.

6. There is a strong interaction between fracture and creep in concrete, which is very important for both failure and serviceability analyses of structures. Analysis of long-term fracture propagation in concrete must take this interaction into account.

ACKNOWLEDGMENTS

This work was partially supported by the NSF Center for Advanced Cement-Based Materials (Grant DMR-8808432), and by AFOSR Contract 49620-87-C-0030DEF with Northwestern University. The help of undergraduate research assistants D. Klein and D. Coe in specimen preparation and analysis of data is gratefully acknowledged.

REFERENCES

1. Shah, S. P., and Chandra, S., "Fracture of Concrete Subjected to Cyclic and Sustained Loading," ACI JOURNAL, *Proceedings*, V. 67, No. 10, Oct. 1970, pp. 816-825.

2. Wittmann, F. H., and Zaitsev, Ju., "Behavior of Hardened Cement Paste and Concrete under High Sustained Load," *Mechanical Behavior of Materials*, Proceedings of 1971 International Conference, V. 4, Society of Materials Science, Japan, 1972, pp. 84-95.

3. Liu, Z.-G.; Swartz, S. E.; Hu, K. K.; and Kan, Y.-C., "Time-Dependent Response and Fracture of Plain Concrete Beams," *Fracture of Concrete and Rock: Recent Developments* (International Conference, Cardiff, UK), S. P. Shah, S. E. Swartz, and B. Barr, eds., Elsevier Applied Science, London, 1989, pp. 577-586.

4. Mindess, S., and Shah, S. P., eds., *Cement-Based Composites: Strain Rate Effects on Fracture*, Materials Research Society Symposium Proceedings, V. 64, 1986, 270 pp.

5. Bažant, Z. P., and Gettu, R., "Determination of Nonlinear Fracture Characteristics and Time Dependence from Size Effect," *Fracture of Concrete and Rock: Recent Developments* (International Conference, Cardiff, UK), S. P. Shah, S. E. Swartz, and B. Barr, eds., Elsevier Applied Science, London, 1989, pp. 549-565.

6. Bažant, Z. P., and Gettu, R., "Size Effect in Concrete and Influence of Loading Rate," *Serviceability and Durability of Construction Materials* (Proceedings, First Materials Engineering Conference, Denver), B. A. Suprenant, ed., ASCE, New York, 1990, pp. 1113-1123.

7. Rüsch, H., "Researches toward a General Flexural Theory for Structural Concrete," ACI JOURNAL, *Proceedings* V. 57, July 1960, pp. 1-28.

8. Reinhardt, H. W., "Strain Rate Effects on the Tensile Strength of Concrete as Predicted by Thermodynamic and Fracture Mechanics Models," *Cement-Based Composites: Strain Rate Effects on Fracture*, Materials Research Society Symposium Proceedings, V. 64, S. Mindess and S. P. Shah, eds., 1986, pp. 1-14.

9. Harsh, S.; Shen, Z.; and Darwin, D., "Strain-Rate Sensitive Behavior of Cement Paste and Mortar in Compression," *ACI Materials Journal*, V. 87, No. 5, Sept.-Oct. 1990, pp. 508-516.

10. Hughes, B. P., and Watson, A. J., "Compressive Strength and Ultimate Strain of Concrete under Impact Loading," *Magazine of Concrete Research*, V. 30, No. 105, Dec. 1978, pp. 189-199.

11. Suresh, S.; Nakamura, T.; Yeshurun, Y.; Yang, K.-H.; and Duffy, J., "Tensile Fracture Toughness of Ceramic Materials: Effects of Dynamic Loading and Elevated Temperatures," *Journal of the American Ceramic Society*, V. 73, No. 8, 1990, pp. 2457-2466.

12. Wittmann, F. H., "Influence of Time on Crack Formation and Failure of Concrete," *Application of Fracture Mechanics to Cementitious Composites*, S. P. Shah, ed., Martinus Nijhoff Publishers, Dordrecht, The Netherlands, 1985, pp. 593-616.

13. Lajtai, E. Z.; Schmidtke, R. H.; and Bielus, L. P., "Effect of Water on the Time-dependent Deformation and Fracture of a Granite," *International Journal of Rock Mechanics and Mineral Science*, V. 24, No. 4, 1987, pp. 247-255.

14. Bažant, Z. P., and Prat, P. C., "Effect of Temperature and Humidity on Fracture Energy of Concrete," *ACI Materials Journal*, V. 87, No. 4, July-Aug. 1988, pp. 262-271.

15. Rossi, P., and Boulay, C., "Influence of Free Water in Concrete on the Cracking Process," *Magazine of Concrete Research*, V. 42, No. 152, 1990, pp. 143-146.

16. Darwin, D., and Attiogbe, E. K., "Effects of Loading Rate on Cracking of Cement Paste in Compression," *Cement-Based Composites: Strain Rate Effects on Fracture*, Materials Research Society Symposium Proceedings, V. 64, S. Mindess and S. P. Shah, eds., 1986, pp. 167-180.

17. Chong, K. P., and Boresi, A. P., "Strain Rate Dependent Mechanical Properties of New Albany Reference Shale," *International Journal of Rock Mechanics and Mineral Science*, V. 27, No. 3, 1990,

pp. 199-205.

18. Reinhardt, H. W., "Tensile Fracture of Concrete at High Rates of Loading," *Application of Fracture Mechanics to Cementitious Composites*, S. P. Shah, ed., Martinus Nijhoff Publishers, Dordrecht, The Netherlands, 1985, pp. 559-592.

19. Ross, C. A., and Kuennen, S. T., "Fracture of Concrete at High Strain-Rates," *Fracture of Concrete and Rock: Recent Developments*, S. P. Shah, S. E. Swartz, and B. Barr, eds., Elsevier Applied Science, London, 1989, pp. 152-161.

20. Zielinski, A. J., "Fracture of Concrete and Mortar under Uniaxial Impact Tensile Loading," PhD thesis, Delft University, The Netherlands, 1982.

21. John, R.; Shah, S. P.; and Jenq, Y.-S., "Fracture Mechanics Model to Predict the Rate Sensitivity of Mode I Fracture of Concrete," *Cement and Concrete Research*, V. 17, 1987, pp. 249-262.

22. Wittmann, F. H.; Roelfstra, P. E.; Mihashi, H.; Huang, Y.-Y.; Zhang, X.-H.; and Nomura, N., "Influence of Age of Loading, Water-Cement Ratio and Rate of Loading on Fracture Energy of Concrete," *Materials and Structures, Research and Testing* (RILEM, Paris), V. 20, 1987, pp. 103-110.

23. Bažant, Z. P., "Size Effect in Blunt Fracture: Concrete, Rock, Metal," *Journal of Engineering Mechanics*, ASCE, V. 110, No. 4, 1984, pp. 518-535.

24. Bažant, Z. P., and Pfeiffer, P. A., "Determination of Fracture Energy from Size Effect and Brittleness Number," *ACI Materials Journal*, V. 84, No. 6, Nov.-Dec., 1987, pp. 463-480.

25. Bažant, Z. P., and Kazemi, M. T., "Determination of Fracture Energy, Process Zone Length and Brittleness Number from Size Effect, with Application to Rock and Concrete," *International Journal of Fracture Mechanics*, V. 44, 1990, pp. 111-131.

26. Gettu, R.; Bažant, Z. P.; and Karr, M. E., "Fracture Properties and Brittleness of High-Strength Concrete," *ACI Materials Journal*, V. 87, No. 6, Nov.-Dec. 1990, pp. 608-618.

27. RILEM TC69, Chapter 2, *Mathematical Modeling of Creep and Shrinkage of Concrete*, Z. P. Bažant, ed., John Wiley, Chichester and New York, 1988, pp. 99-216.

28. Wong, W., and Miller, R. A., "Mixed Mode Fracture at Early Ages," *Micromechanics of Failure of Quasi-Brittle Materials* (Proceedings of International Conference, Albuquerque), S. P. Shah, S. E. Swartz, and M. L. Wang, eds., Elsevier Applied Science, London, 1990, pp. 166-175.

29. Bažant, Z. P., "Fracture Energy of Heterogeneous Materials and Similitude," *Fracture of Concrete and Rock* (SEM-RILEM International Conference), S. P. Shah and S. E. Swartz, eds., Springer-Verlag, New York, 1989, pp. 229-241.

30. Bažant, Z. P.; Gettu R.; and Kazemi, M. T., "Identification of Nonlinear Fracture Properties from Size Effect Tests and Structural Analysis Based on Geometry-Dependent R-Curves," *International Journal of Rock Mechanics and Mineral Science*, V. 28, No. 1, 1991, pp. 43-51; Corrigenda, V. 28, No. 2/3, 1991, p. 233.

31. RILEM TC89 Draft Recommendation, "Size-Effect Method for Determining Fracture Energy and Process Zone Size," *Materials and Structures, Research and Testing* (RILEM, Paris), V. 23, 1990, pp. 461-465.

32. Tada, H.; Paris, P. C.; and Irwin, G. R., *Stress Analysis of Cracks Handbook*, 2nd ed., Paris Products, St. Louis, 1985.

33. Bažant, Z. P., and Panula, L., "Practical Prediction of Time-Dependent Deformations of Concrete, Part I: Shrinkage and Part II: Basic Creep," *Materials and Structures, Research and Testing* (RILEM, Paris), V. 11, No. 65, 1978, pp. 307-328.

34. Bažant, Z. P., and Oh, B. H., "Crack Band Theory for Fracture of Concrete," *Materials and Structures, Research and Testing* (RILEM, Paris), V. 16, No. 93, 1983, pp. 155-177.

35. Mindess, S., "Rate of Loading Effects on the Fracture of Cementitious Materials," *Application of Fracture Mechanics to Cementitious Composites*, S. P. Shah, ed., Martinus Nijhoff Publishers, Dordrecht, The Netherlands, 1985, pp. 617-638.

36. Oh, B.-H., and Chung, C.-H., "Fracture Energy of Concrete under Static and Dynamic Loading," Preprints of the *Proceedings*, International Workshop on Fracture Toughness and Fracture Energy — Test Methods for Concrete and Rock, Sendai, Japan, 1988, pp. 360-372.

37. Bažant, Z. P., and Chern, J.-C., "Double-Power Logarithmic Law for Concrete Creep," *Cement and Concrete Research*, V. 14, 1984, pp. 793-806.

38. Bažant, Z. P., ed., *Mathematical Modeling of Creep and Shrinkage of Concrete*, J. Wiley, Chichester and New York, 1988, 459 pp.

39. Liu, Z.-G.; Swartz, S. E.; and Hu, K. K. "Two-Dimensional Finite Element Modeling of Crack Growth in Concrete Using Three-Dimensional Damage Data," *Micromechanics of Failure of Quasi-Brittle Materials* (Proceedings of International Conference, Albuquerque), S. P. Shah, S. E. Swartz, and M. L. Wang, eds., Elsevier Applied Science, London, 1990, pp. 176-187.

ACI Materials Journal - in press

SOFTENING REVERSAL AND OTHER EFFECTS OF A CHANGE IN LOADING RATE ON FRACTURE OF CONCRETE

by ZDENĚK P. BAŽANT, W.-H. GU and K.T. FABER

Structural Engineering Report
No. 93-7/B667s

Department of Civil Engineering
Northwestern University
Evanston, Illinois 60201 USA

November 1992

Revised July 1993

SOFTENING REVERSAL AND OTHER EFFECTS OF A CHANGE IN LOADING RATE ON FRACTURE OF CONCRETE

Zdeněk P. Bažant, Wei-Hwa Gu, and K.T. Faber [1]

Abstract

The time-dependence of concrete fracture, and particularly the effect of loading rate, has so far been studied mainly in the dynamic range. The present study extends a preceding investigation of the rate effect in the static range which covered times to peak from 1 s to 300,000 s. Geometrically similar three-point-bend specimens of three different sizes are subjected to either a sudden 1000–fold increase of the loading rate or a 10–fold sudden decrease of the loading rate. It is found that the post-peak softening can be reversed to hardening, followed by a second load peak which can be either higher or lower than the previous load peak. The rise to the second peak depends on the previous post-peak load drop from the first peak load. A sudden decrease in the loading rate causes initially a steeper softening slope. The source of these time-dependent effects appears to be not only the thermally activated nature of the process of bond ruptures in the fracture process zone but also the effect of creep, both a nonlinear creep in the fracture process zone and a linear creep in the bulk of the specimen. The results of this study and a previous study suggest that there is a significant difference in fracture behavior for short-time and long-time loads. The phenomena observed are of interest, for example, for the analysis of concrete dams with cracks that evolve over many years. Mathematical modeling of the present test results is left for a subsequent study.

Introduction

Understanding of fracture mechanics of concrete is necessary for improving the design of concrete structures against various type of brittle failure, and particularly for taking into account the size effect and ductility limitations. Although the classical fracture mechanics is a rate-independent (time-independent) theory, the fracture properties of all materials depend upon the loading rate. One source of the rate sensitivity is the process of rupture of interatomic or intermolecular bonds at the tips of microcracks, which represents a thermally activated process governed by a certain activation energy. The rate sensitivity is explained by the fact that the probability that the thermal vibration energy of an atom or molecule would exceed the activation energy barrier of the bond increases with the superimposed potential due to applied stress or load.

A second source of rate sensitivity is creep (or stress relaxation) in the fracture process zone, as well as in the bulk of the specimen. The creep effect is negligible at very fast, dynamic loading rates, but inertia (or wave propagation) effects complicate dynamic fracture. The creep effect becomes important only at sufficiently slow loading rates, complicating the fracture theory, while the inertia effects vanish. Whereas Wittmann and Zaitsev (1972), Shah and Chandra (1970), Liu et al. (1989) and others have already suggested that concrete fracture is affected by creep, a detailed investigation of this effect has not been conducted. On the other hand, the rate effect in concrete fracture has been extensively investigated in the dynamic range of loading, in which the maximum load is reached in less than one second; see Mindess and Shah (1986). In a material such as concrete, which exhibits

[1]McCormick School of Engineering and Applied Science, Northwestern University, Evanston, IL 60208 USA

pronounced creep under long-time loading, the rate effect in the static range and the contribution of creep to it may be expected to be particularly strong.

For this reason, a preceding study by Bažant and Gettu (1992) investigated the rate effect in the static range experimentally, using crack mouth opening displacement (CMOD) rates with times to peak load ranging from 1 s to 300,000 s (3.5 days). The size effect method, coupled with the effective modulus approximation of creep, has been used to determine the rate dependence of fracture properties. The fracture toughness was found to decrease with a decreasing rate, as a continuation of the trend previously known for the dynamic range. As a new, surprising result, the effective length of the fracture process zone was found to decrease with decreasing rate, which implies that for slow loading the brittleness number increases and the response shifts closer to linear elastic fracture mechanics (LEFM). Load relaxation at constant CMOD in the post-peak regime was also investigated and found to be very pronounced. The time curves of relaxing load where found to be approximately straight lines in the logarithm of the elapsed time, and the load drop to be several times larger than for a linearly viscoelastic relaxation of unnotched specimens for the same relaxation duration. The difference between these two relaxations has been attributed to time-dependent processes, principally creep, in the fracture process zone.

From Bažant and Gettu's (1992) study it became clear that there is a strong interaction between fracture and creep, which must be taken into account in predicting the long-term load-carrying capacity of structures with cracks. This is particularly important for analyzing the failure of concrete dams, in which large fractures often develop gradually over a period of many years.

As far as materials other than concrete are concerned, the effects of loading rate in the static range were recently investigated by Bažant, Bai and Gettu (1991) on limestone. The effect of the loading rate was found to be significant, but less pronounced than for concrete, and no shift of brittleness with a decreasing loading rate has been observed. This is no doubt explained by the fact that limestone does not exhibit any significant creep, so that most of the rate effect must be due to the thermally activated process of bond ruptures.

The preceding study of Bažant and Gettu (1992) was limited to constant loading rates. The purpose of the present study, on which preliminary reports were made in several conference papers by Bažant and Gettu (1989, 1990, 1992), is to present the experimental results on the effect of a sudden change of loading rate. Knowledge of this effect is essential for formulating a time-dependent mathematical model for the fracture process zone, which will be the subject of a subsequent study. By adopting the R-curve (resistance curve) model for nonlinear fracture, the effect of the constant loading rate has already been successfully described in three brief conference papers (Bažant and Gettu, 1989; Bažant, 1990; and Bažant and Jirásek, 1992), and it may be expected that an extension of this approach would work also in the case of sudden changes of the loading rate.

Material, Test Specimens and Test Procedure

The material studied was plain concrete, with a mix ratio of cement : sand : gravel : water = 1 : 2 : 2 : 0.6, by weight. ASTM Type I Portland cement was used. The aggregate consisted of crushed limestone gravel of maximum grain size 13 mm (0.5 in.) and siliceous sand passing standard sieve No. 2, corresponding to maximum grain size 5 mm. The average standard 28-day cylinder strength of the concrete was $f'_c = 37$ MPa (5370 psi).

The specimens were three-point-bent notched beams shown in Fig. 1. Specimens of three sizes, characterized by beam depths $d = 38, 76$, and 152 mm (1.5, 3 and 6 in.), were tested (labeled as S–small, M–middle, L–large). The specimens of different sizes were geometrically similar in two-dimensions and the beam thickness $b = 38$ mm (1.5 in.) was constant for specimens of all the sizes. The beam length was $8d/3$, the span was $2.5d$, and the notch length was $d/6$. The specimens were

cast with the notch face at the bottom. The notches were cut with a diamond band saw, and were 1.8 mm (0.07 in.) wide.

The specimens were cured in water for 65 days, at which time they were tested (within a few hours after retrieval from the water bath). During the tests, the specimens had their surfaces sealed with siliconized acrylic latex to prevent moisture loss. The specimens and their material were the same as in the preceding study by Bažant and Gettu (1992).

The specimens were tested at controlled CMOD rates. To bring the effects of the loading rate to light, the loading rate must change by several orders of magnitude, and the change of loading rate must be sudden, almost instantaneous. This can be achieved only in a computer controlled closed-loop testing machine. The testing frame must also be sufficiently stiff and the pumps sufficiently powerful to make such a sudden change of loading rate possible. These conditions were met by using an MTS closed–loop testing machine (MTS model 318.10, 20 kip load frame using test star digital controls—MTS Corp. Minneapolis, MN).

Fig. 2(a,b) shows, as an example, the record of the CMOD time history produced by the loading equipment. It is seen from Fig. 2(a) that, compared to the previous history, the loading rate changes practically instantaneously since the time curve becomes immediately an almost vertical line. In Fig. 2(b) the time scale is greatly expanded to show the detail of the CMOD history at the time of the rate change. Here one can discern some imperfections (such as load oscillations just before the steep rise), however, these imperfections are insignificant compared to the duration of the test.

Effect of Sudden Increase or Decrease of Loading Rate

For a sufficiently large increase of the loading rate, the results shown in Fig. 3 reveal that the post-peak softening can be reversed to hardening which is followed by a second peak, after which a new post-peak softening branch begins. The second peak can be higher or lower than the first peak at the previous slow rate of loading, depending on the ratio of rate increase and on the magnitude of the load decrease prior to the increase of rate. A typical response is seen in Fig. 3(c), in which the initial loading rate was 10^{-5} mm/s, (CMOD rate) and, relatively soon after the peak load P_u, the loading rate was suddenly increased a 1000-times to 10^{-2} mm/s, at the moment when the load had dropped to 97% of P_u. The second peak P_u' occurs at 3725 N (837 lbf.). For loading histories of this type, the second peak P_u' generally occurs at the load of about 110% – 135% of the first peak P_u.

The test results obtained on various individual specimens are given in Table 1. The response diagrams of load vs. CMOD are shown in Fig. 3(a–f) for specimens of three sizes (small, medium, large) and for different values of the load drop from the previous peak at which the rate was chosen to be suddenly increased.

Some load-CMOD diagrams exhibit small pseudo-peaks (S5, L2, L4 in Fig. 3(b), (e) (f)) before the first peak is reached. In some specimens one can see a relatively flat region (M2 and L2) (Fig. 3(c) and (e)) occurring after the first peak . These two phenomena are probably not systematic and are caused by random effects, specimen microstructural heterogeneity and similar influences.

In another test series, the faster rate started after a much greater load drop, namely from P_u to $0.65\%P_u$. The second peak still ocurred, however it was lower, only about 0.75% P_u; see Table 2 and Fig. 4(a–c).

No second peak was found when the faster rate started after a much greater load drop, from P_u to 0.26% P_u (Fig. 5).

In a second group of tests, the specimens were loaded at the fast rate and, in the post-peak regime, the loading rate was suddenly decreased 10-times, from 10^{-4} mm/s to 10^{-5} mm/s. The results are shown in Fig. 6(a–c) and also given in Table 3. The sudden decrease in loading rate was always accompanied by an almost instantaneous drop in load followed by a conventional post–peak softening reponse.

Discussion of Results and Conclusions

Testing several identical specimens at the same loading history reveals that there can be substantial scatter. This is exemplified by specimens MA1 and MA2 (Fig. 6(b) and (c)). In future extensions of this program, it would therefore be desirable to test a larger number of specimens and conduct their statistical evaluation. Nevertheless, despite the limited scope of the presently reported tests, the results show overall a coherent picture. Similar effects are seen for different but similar loading histories and certain trends are clearly discernible. From these overall trends, the following conclusions may be drawn.

1. An increase of the loading rate in the post-peak regime causes a stiffening of the response, and if the rate increase is sufficiently large (several orders of magnitude), the post-peak softening is reversed to hardening and is followed by second peak.

2. The second peak may be larger or lower than the first peak under the previous constant rate of loading. The greater the post-peak load drop prior to the rate increase, the smaller is the rise to the second peak.

3. After a decrease of the loading rate, the descending post-peak slope first becomes steeper but later the previous slope is resumed again.

4. The effects of the loading rate change are similar for specimens of various sizes (the data for specimens of various sizes will be needed for developing a mathematical model).

It is also interesting to compare the present results to the results of relaxation tests from Bažant and Gettu (1992). The relaxation tests correspond to a decrease of the loading rate to zero. The present results show that the response to a decrease of the loading rate gradually approaches the relaxation tests.

On the basis of this study as well as the previous study by Bažant and Gettu (1992), one may infer that by a certain sudden change of the loading rate it is possible to produce any of the loading slopes shown by arrows in Fig. 7.

Acknowledgement.– Partial financial support for Z.P. Bažant has been obtained under AFOSR Grant 91-0140 to Northwestern University. Support for W.-H. Gu and K.T. Faber has been received from the NSF Center for Advanced Cement-Based Materials at Northwestern University.

References

Shah, S.P., and Chandra, S. (1970). "Fracture of concrete subjected to cyclic and sustained loading." *ACI J.*, Vol. 67, 816–825.

Wittmann, F.H., and Zaitsev, Y. (1972). "Behavior of hardened cement paste and concrete under high sustained load." Mechanical behavior of materials, Proc. of 1971 Int. Conf., *Soc. of Mat. Sci.*, Japan, Vol. 4, 84–95.

Liu, Z.-G., Swartz, S.E., Hu, K.K., and Kan, Y.-C. (1989). "Time-dependent response and fracture of plain concrete beams." Fracture of concrete and rock: Recent developments (Int. Conf., Cardiff, U.K.), eds. S.P. Shah, S.E. Swartz, and B.I.G. Barr, Elsevier Applied Science, London, 577–586.

Mindess, S., and Shah, S.P., eds. (1986). " Cement-Based Composites: Strain-Rate Effects on Fracture", Mat. Res. Soc. Symp. Proc., Vol. 64, 270 pp.

Bažant, Z.P., and Gettu, R. (1989). "Determination of nonlinear fracture characteristics and time-dependence from size effect." Fracture of Concrete and Rock: Recent Developments (Int. Conf., Cardiff, U.K.), eds. S.P. Shah, S.E. Swartz, and B.I.G. Barr, Elsevier Applied Science, London, 549–565.

Bažant, Z.P., and Gettu, R. (1990). "Size effect in concrete and influence of loading rate." Serviceability and Durability of Construction Materials (Proc., First Materials Engrg. Conf., Denver), ed. B.A. Supernant, ASCE, New York, 1113–23.

Bažant, Z.P. and Gettu, R. (1992). "Rate effects and load relaxation in static fracture of concrete," *ACI Materials Journal* 89(5), 456–468.

Reinhardt, H.W. (1986). "Strain rate effects on the tensile strength of concrete as predicted by thermodynamic and fracture mechanics models." Cement-Based Composites: Strain-Rate Effects on Fracture, *Mat. Res. Soc. Symp. Proc.*, eds. S. Mindess and S.P. Shah, vol. 64, 1–14.

Harsh, S., Shen, Z., and Darwin, D. (1990). "Strain-rate sensitive behavior of cement paste and mortar in compression." *ACI Mater. J.* 87(5), 508–516.

Wittmann, F.H. (1985). "Influence of time on crack formation and failure of concrete." Application of Fracture Mechanics to Cementitious Composites, ed. S.P. Shah, Martinus Nijhoff Publ., Dordrecht, The Netherlands, 593–616.

Reinhardt, H.W. (1985). "Tensile fracture of concrete at high rates of loading." Application of Fracture Mechanics to Cementitious Composites, ed. S.P. Shah, Martinus Nijhoff Publ., Dordrecht, The Netherlands, 559–593.

Ross, C.A., and Kuennen, S.T. (1989). "Fracture of concrete at high strain rates." Fracture of Concrete and Rock: Recent Developments, eds. S.P. Shah, S.E. Swartz, and B.I.G. Barr, Elsevier Applied Science, London, U.K., 152–161.

Bažant, Z.P., and Jirásek, M. (1992). "R-curve modeling of rate effect in static fracture and its interference with size effect." *Fracture Mechanics of Concrete Structures* (Proc. Int. Conf. on Fracture Mechanics of Concrete Structures, Breckenridge, Colorado, June), ed. by Z.P. Bažant , Elsevier Applied Science, London, 918–923.

Bažant, Z.P. (1990). "Rate effect, size effect and nonlocal concepts for fracture of concrete and other quasi-brittle materials." Preprints, NATO Advanced Research Workshop on "Toughening Mechanisms in Quasi-Brittle Materials," Northwestern University, S.P. Shah, ed., 143–166.

Bažant, Z.P., Bai, S.-P. and Gettu, R. (1991). "Effect of loading rate on static fracture of limestone." Report 90-5/498e, ACBM Center, Northwestern University, May 1990; also *Engineering Fracture Mechanics*, in press.

Figure Captions

Fig. 1 Geometry of the three-point-bend fracture specimens tested.

Fig. 2 Typical recorded time histories of CMOD and load achieved by the controls of the test equipment used. Part (b) is an expanded version of (a).

Fig. 3(a–f) Measured responses for a 1000–fold rate increase after a load drop to 90–95%P_u (S–small, M–medium, L–large specimen).

Fig. 4 (a–c) Measured responses for a 1000–fold rate increase after a load drop to 65%P_u (S–small, M–medium, L–large specimen).

Fig. 5 Measured responses for a 1000–fold rate increase after a load drop to 26%P_u.

Fig. 6 (a–c) Measured responses for a 10–fold rate decrease. (S–small, M–medium)

Fig. 7 Load deflection slopes accessible by changing the loading rate in the post-peak softening regime.

Table. 1
S(d=38 mm), M(d=76mm), L(d=152 mm)

Spec.	Age (day)	1st Rate (mm/sec)	1st Peak Pu	Rate Change	2nd Rate (mm/sec)	2nd Peak Pu'
S1	66	0.7×10^{-5}	1575 N 20 μm 2940 sec	(91% Pu) 1428 N 23 μm 3350 sec	0.7×10^{-2}	(110% Pu) 1726 N 27 μm 3355 sec
S3	66	0.9×10^{-5}	1468 N 21 μm 2730 sec	(95% Pu) 1388 N 26 μm 3070 sec	0.9×10^{-2}	(112% Pu) 1646 N 37 μm 3076 sec
S5	66	0.95×10^{-5}	1486 N 15 μm 1700 sec	(93% Pu) 1379 N 20 μm 2145 sec	0.95×10^{-2}	(107% Pu) 1588 N 24 μm 2150 sec
M2	64	1.0×10^{-5}	2758N 8 μm 800 sec	(97% Pu) 2669 N 10 μm 1000 sec	1.0×10^{-2}	(135% Pu) 3725 N 20 μm 1001 sec
M3	64	1.0×10^{-5}	3292 N 15.6 μm 1560 sec	(91% Pu) 3003 N 16.2 μm 1680 sec	1.0×10^{-2}	(116% Pu) 3803 N 27.0 μm 1687 sec
L1	67	1.4×10^{-5}	4279N 35.6 μm 2516 sec	(91% Pu) 3874 N 53.0 μm 3785 sec	1.4×10^{-2}	(103% Pu) 4408 N 64.2 μm 3789.9 sec
L2	67	1.8×10^{-5}	4248 N 30.4 μm 1690 sec	(90% Pu) 3817 N 44.2 μm 2450.4 sec	1.8×10^{-2}	(102% Pu) 4319 N 49.4 μm 2453.9 sec
L4	67	1.8×10^{-5}	4163 N 35.9 μm 2020.4 sec	(89% Pu) 3701 N 39.8 μm 2235.4 sec	1.8×10^{-2}	(107% Pu) 4469 N 60.6μm . 2242.3 sec

Table 2.

S(d=38 mm), M(d=76mm), L(d=152 mm)

Spec.	Age (day)	1st Rate (mm/sec)	1st Peak Pu	Rate Change	2nd Rate (mm/sec)	2nd Peak Pu'
S2	66	1.0×10^{-5}	1600 N 12 μm 1150 sec	(63% Pu) 1001 N 45 μm 4520 sec	1.0×10^{-2}	(71% Pu) 1134 N 51 μm 4527 sec
M5*	55	1.0×10^{-5}	4404 N 15 μm 1500 sec	(66% Pu) 2891 N 30.5 μm 3115 sec	1.0×10^{-2}	(75% Pu) 3314 N 37 μm 3119 sec
L3	67	1.8×10^{-5}	3345 N 25.9 μm 1420 sec	(64% Pu) 2148 N 91.7 μm 5115 sec	1.8×10^{-2}	(77% Pu) 2562 N 134 μm
S4	66	2.0×10^{-5}	1824 N 16 μm 1105.4 sec	(26% Pu) 467 N 144 μm 7060.3 sec	5.0×10^{-2}	NO 2nd Peak

Table 3.

S(d=1.5 in), M(d=3 in)

Spec.	Age (day)	1st Rate (mm/sec)	1st Peak Pu	Rate Change	2nd Rate (mm/sec)
SA1	68	1.0×10^{-5}	2103 N 27 μm 2778 sec	(82% Pu) 1717 N 43 μm 4444 sec	1.0×10^{-6}
SA2	68	5.0×10^{-4}	2259 N 26 μm 53 sec	(81% Pu) 1828 N 53 μm 108 sec	5.0×10^{-6}
SA3	68	1.0×10^{-4}	2028 N 19 μm 182 sec	(70% Pu) 1419 N 35 μm 344 sec	1.0×10^{-5}
MA1	68	1.0×10^{-4}	2268 N 33 μm 321 sec	(74% Pu) 1668 N 82 μm 789 sec	1.0×10^{-5}
MA2	68	1.0×10^{-4}	2820 N 14 μm 132 sec	(64% Pu) 1806 N 52 μm 537 sec	1.0×10^{-5}

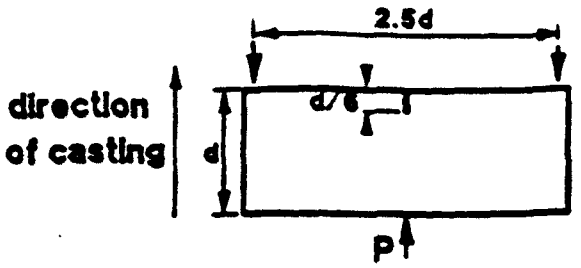

FIG. 1

thickness = b

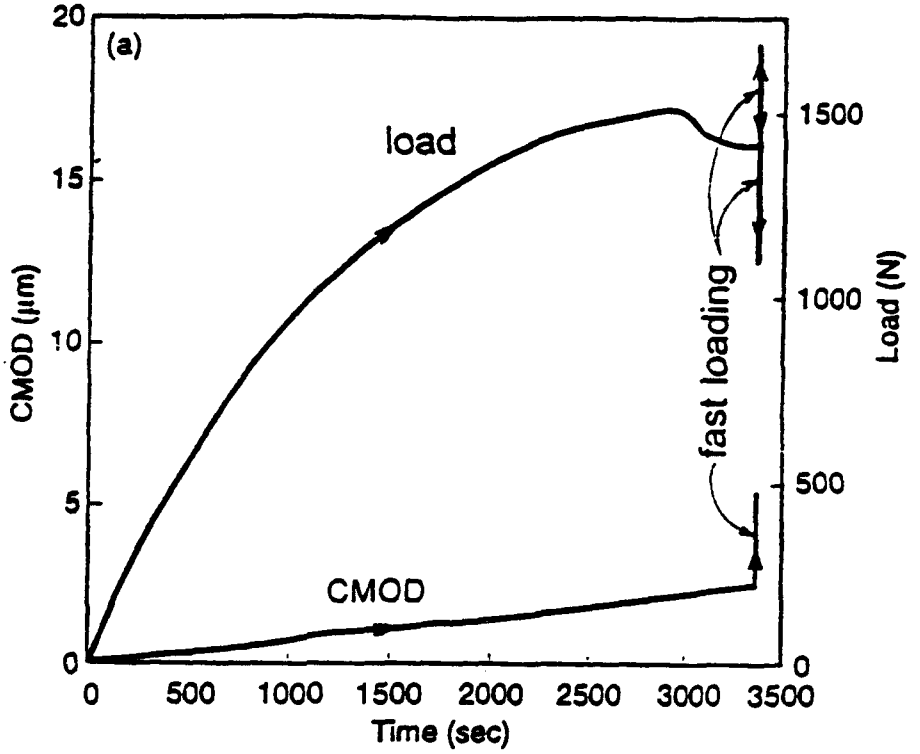

FIG. 2

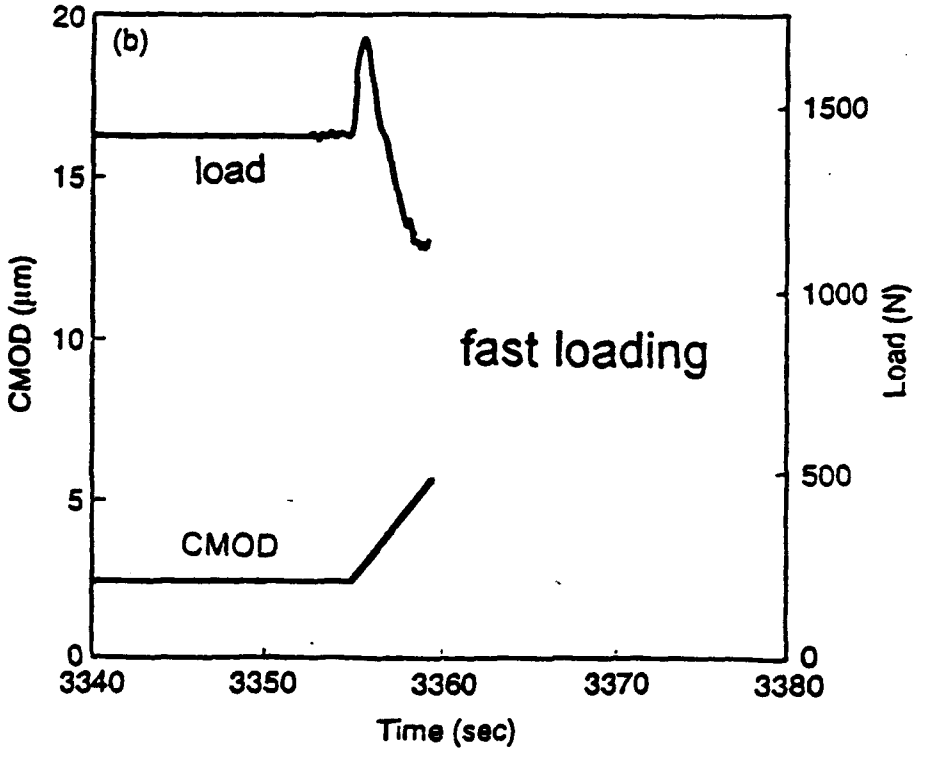

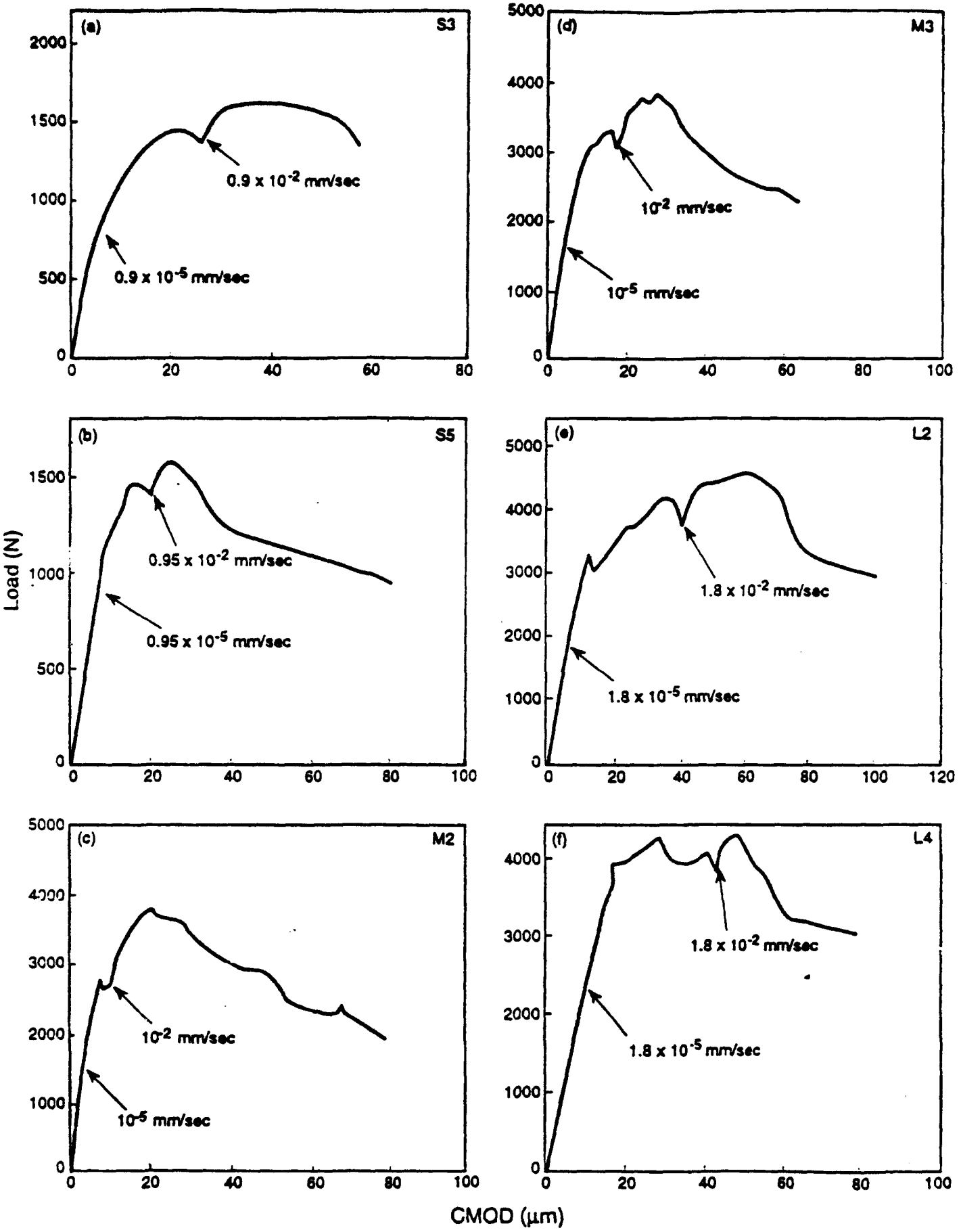
(a)
S3
0.9 x 10^-2 mm/sec
0.9 x 10^-5 mm/sec
(d)
M3
10^-2 mm/sec
10^-5 mm/sec
(b)
S5
0.95 x 10^-2 mm/sec
0.95 x 10^-5 mm/sec
(e)
L2
1.8 x 10^-2 mm/sec
1.8 x 10^-5 mm/sec
(c)
M2
10^-2 mm/sec
10^-5 mm/sec
(f)
L4
1.8 x 10^-2 mm/sec
1.8 x 10^-5 mm/sec
Load (N)
CMOD (μm)

FIG. 3

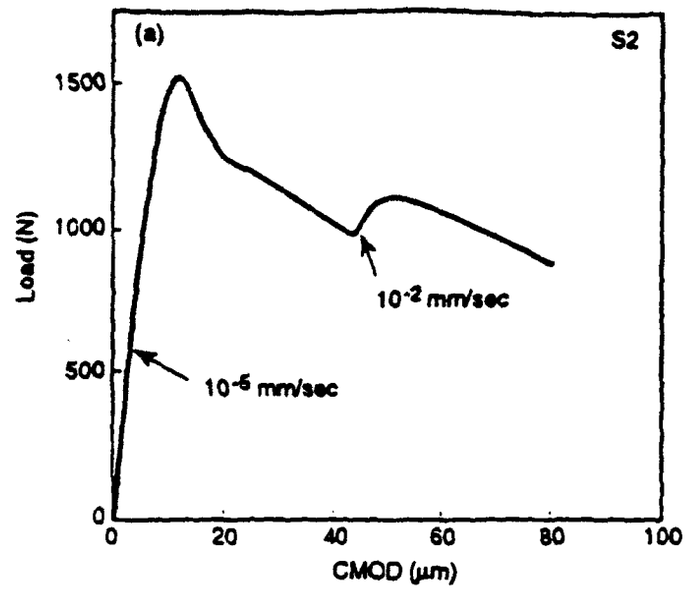
(a)
S2
1500
1000
500
0
Load (N)
10^{-2} mm/sec
10^{-5} mm/sec
0
20
40
60
80
100
CMOD (μm)

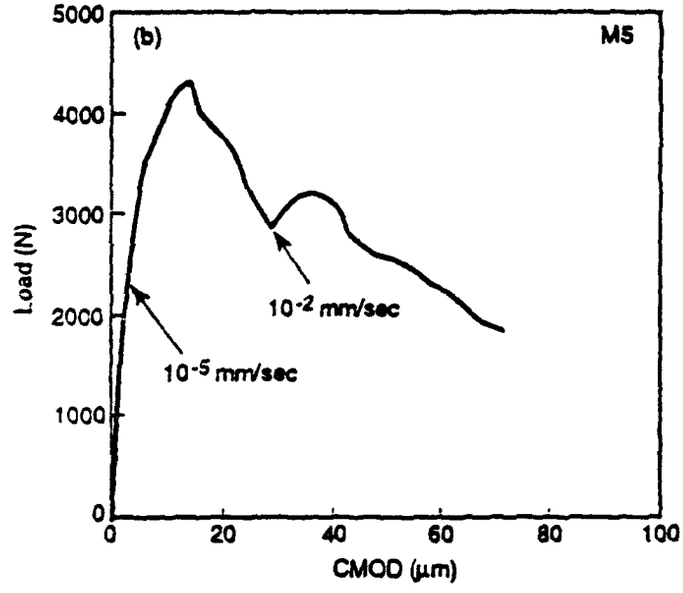
(b)
M5
5000
4000
3000
2000
1000
0
Load (N)
10^{-2} mm/sec
10^{-5} mm/sec
0
20
40
60
80
100
CMOD (μm)

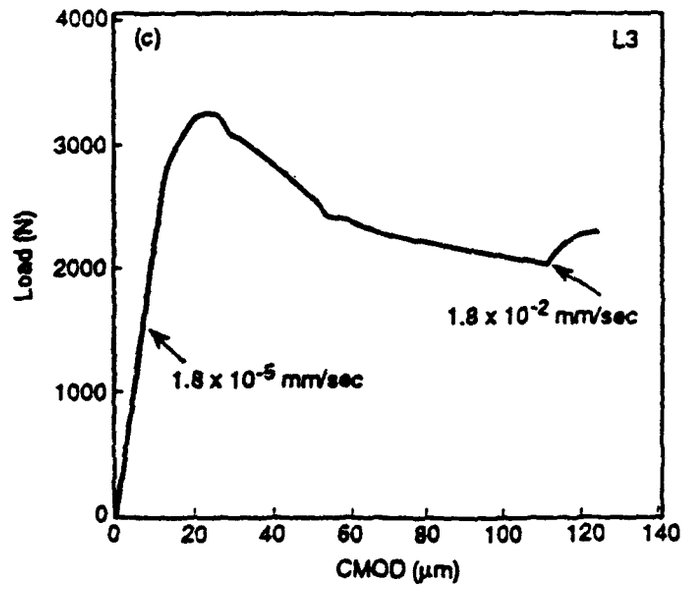
(c)
L3
4000
3000
2000
1000
0
Load (N)
1.8×10^{-2} mm/sec
1.8×10^{-5} mm/sec
0
20
40
60
80
100
120
140
CMOD (μm)

FIG.4

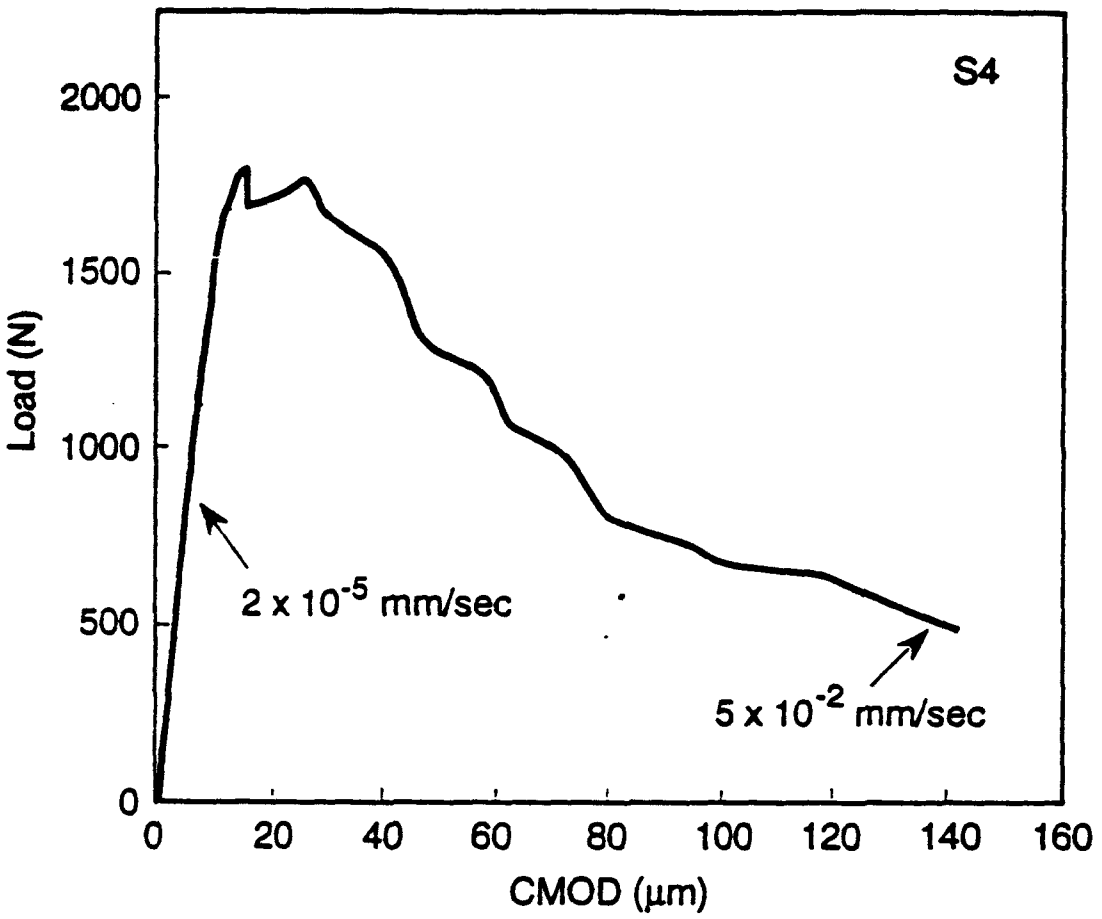
S4
2000
1500
1000
500
0
Load (N)
2 x 10-5 mm/sec
5 x 10-2 mm/sec
0
20
40
60
80
100
120
140
160
CMOD (μm)

FIG. 5

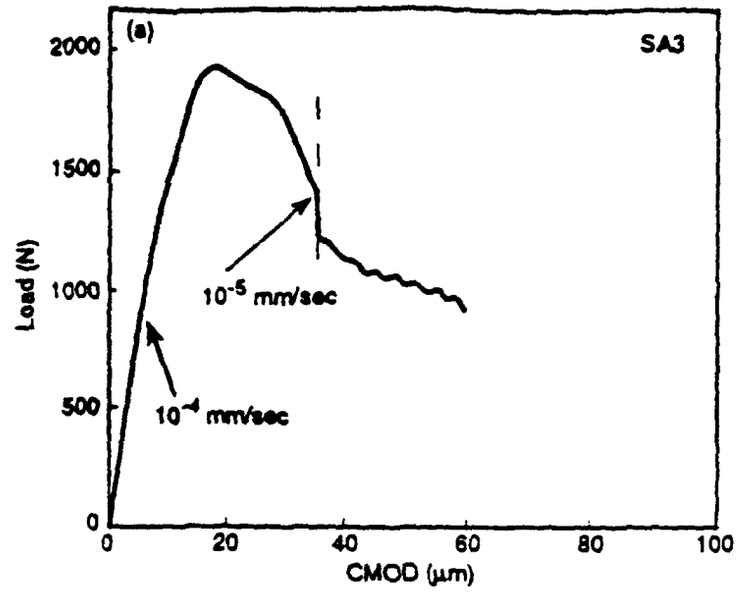
(a)
SA3
2000
1500
1000
500
0
Load (N)
10^{-5} mm/sec
10^{-4} mm/sec
0
20
40
60
80
100
CMOD (μm)

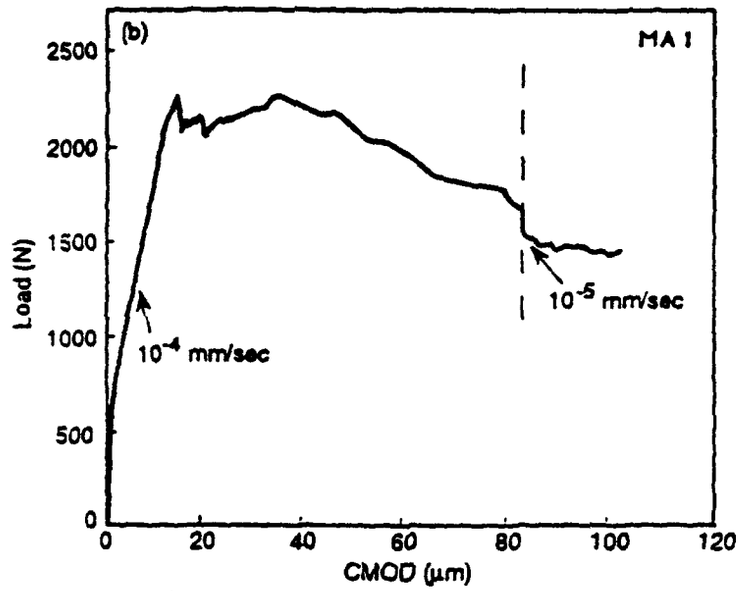
(b)
MA 1
2500
2000
1500
1000
500
0
Load (N)
10^{-5} mm/sec
10^{-4} mm/sec
0
20
40
60
80
100
120
CMOD (μm)

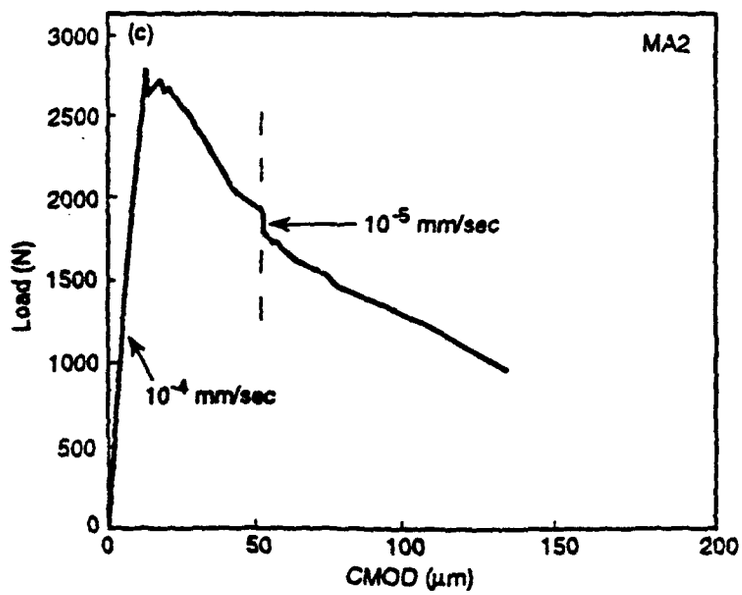
(c)
MA2
3000
2500
2000
1500
1000
500
0
Load (N)
10^{-5} mm/sec
10^{-4} mm/sec
0
50
100
150
200
CMOD (μm)

FIG. 6

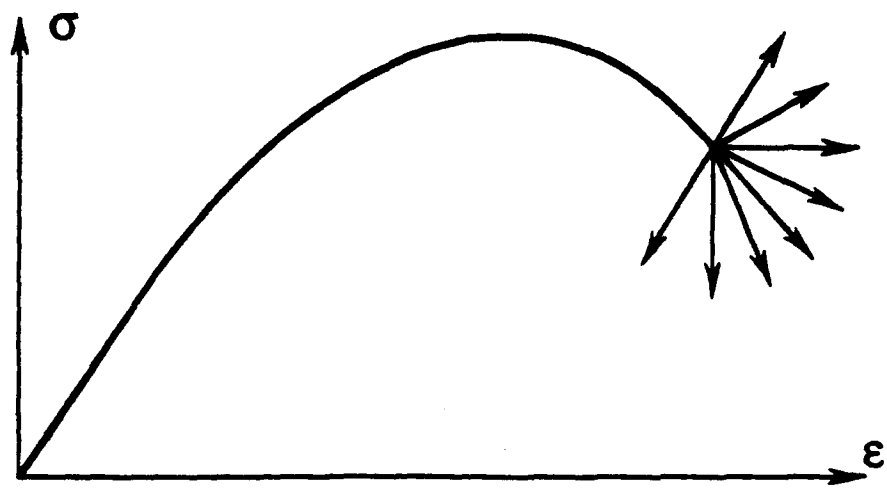

FIG. 7

International Journal of Fracture **62**: 355–373, 1993.

R-curve modeling of rate and size effects in quasibrittle fracture

ZDENĚK P. BAŽANT[1] and MILAN JIRÁSEK
Northwestern University, Evanston, Illinois 60208, USA

Received 1 November 1992; accepted 26 April 1993

Abstract. The equivalent linear elastic fracture model based on an *R*-curve (a curve characterizing the variation of the critical energy release rate with the crack propagation length) is generalized to describe both the rate effect and size effect observed in concrete, rock or other quasibrittle materials. It is assumed that the crack propagation velocity depends on the ratio of the stress intensity factor to its critical value based on the *R*-curve and that this dependence has the form of a power function with an exponent much larger than 1. The shape of the *R*-curve is determined as the envelope of the fracture equilibrium curves corresponding to the maximum load values for geometrically similar specimens of different sizes. The creep in the bulk of a concrete specimen must be taken into account, which is done by replacing the elastic constants in the linear elastic fracture mechanics (LEFM) formulas with a linear viscoelastic operator in time (for rocks, which do not creep, this is omitted). The experimental observation that the brittleness of concrete increases as the loading rate decreases (i.e. the response shifts in the size effect plot closer to LEFM) can be approximately described by assuming that stress relaxation causes the effective process zone length in the *R*-curve expression to decrease with a decreasing loading rate. Another power function is used to describe this. Good fits of test data for which the times to peak range from 1 sec to 250000 sec are demonstrated. Furthermore, the theory also describes the recently conducted relaxation tests, as well as the recently observed response to a sudden change of loading rate (both increase and decrease), and particularly the fact that a sufficient rate increase in the post-peak range can produce a load-displacement response of positive slope leading to a second peak.

1. Introduction

The rate of loading as well as the load duration is known to exert a strong influence on the fracture behavior of concrete. Much has been learned in the previous studies of Shah and Chandra [1]; Wittmann and Zaitsev [2]; Hughes and Watson [3]; Mindess [4]; Reinhardt [5]; Wittmann [6]; Darwin and Attiogbe [7]; Reinhardt [8]; Liu et al. [9]; Ross and Kuennen [10] and Harsh et al. [11]; in particular, it has been well established that the strength as well as the fracture energy or fracture toughness increases with increasing rate of loading, roughly as a power function of the loading rate. The previous studies, however, focused mainly on the size effect under dynamic loading, at which the loading rates are very high. At such high rates, the rate effect is mainly due to the thermally activated process of bond ruptures, arising from the effect of stress on the Maxwell-Boltzmann distribution of thermal energies of atoms and molecules.

In this study, we focus on the rate effect at static loading rates at which the creep properties of a material such as concrete begin to play also a significant role, aside from the thermal activation of bond ruptures. The rate effect at such low rates, which is no doubt closely related to the effect of load duration, needs to be known for the design of civil engineering structures carrying high permanent loads or subjected to long time thermal or shrinkage stresses. For such conditions (which are, for example, important for the fracture of dams), the rate effect in concrete

[1]Walter P. Murphy Professor of Civil Engineering.

fracture has been essentially unexplored until the recent experimental studies of Bažant and Gettu [12–15].

The difficulty for materials such as concrete (which also includes rocks and tough ceramics) is that a nonlinear fracture model taking into account the existence of a large fracture process zone is required. Such materials, nowadays widely called quasibrittle, exhibit a transitional size effect in terms of their nominal strength; for small sizes, the behavior is close to plasticity, for which there is no size effect, while for very large sizes the behavior approaches linear elastic fracture mechanics (LEFM), for which the size effect is the strongest possible. As recently discovered (Bažant and Gettu [12–15]), the size effect plot, i.e. the plot of the nominal strength versus the characteristic structure size, is significantly influenced by the loading rate or loading duration. Generally, the loading rate or duration significantly influence the brittleness. Mathematical modeling of this phenomenon is the principal aim of this study.

In previous work, the effect of loading rate on the size effect has been approximately described by quasielastic analysis, in which the behavior at each loading rate for all the specimen sizes is described according to LEFM with an elastic modulus that in effect represents the well-known effective modulus for creep. Such analysis brought to light the changes of brittleness; it, however, cannot be used as a general model if, e.g., the loading rate would vary with time.

In this study, we will attempt a more general and fundamental model, which can be readily generalized to arbitrary loading histories. The model will represent an adaptation of quasilinear elastic fracture analysis by means of the so-called *R*-curves. The general principles of this approach, without any experimental verification, have already been suggested in Bažant [16, 17]. In the present study we refine and extend this mathematical model and compare it to test data.

The most general and fundamental approach for capturing both the size and rate effects in the fracture of concrete and other quasibrittle materials is of course a constitutive model for the evolution of damage in the fracture process zone, with an appropriate localization limiter. Such a model, which will be required for general finite element codes, should be the objective of future investigations.

2. Basic equations

The *R*-curve (resistance curve) approach represents an attempt to describe the nonlinearity of the law of crack propagation in quasibrittle materials using an approximately equivalent linear model in which the fracture energy is considered to depend on the length of an equivalent linear elastic crack. This equivalent crack is defined as a crack in a linear elastic material having the same compliance as the actual specimen with a large nonlinear fracture process zone (Fig. 1).

Let us denote the initial crack length by a_0 and the current crack length by a. It is often more convenient to work with nondimensional quantities $\alpha_0 = a_0/d$ and $\alpha = a/d$, where d is the total length of the ligament (Fig. 1). According to LEFM, an applied load P causes a load-point displacement

$$u = \frac{P}{E'b}\bar{C}(\alpha), \tag{1}$$

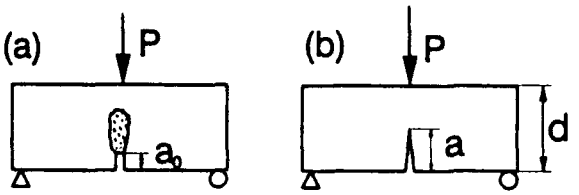

Fig. 1. 3PB specimen with (a) a nonlinear process zone, (b) an equivalent elastic crack.

a crack-mouth opening displacement (CMOD)

$$\Delta = \frac{P}{E'b}\delta(\alpha), \tag{2}$$

and a stress singularity described by the stress intensity factor

$$K = \frac{P}{b\sqrt{d}}k(\alpha), \tag{3}$$

where $E' = E$ for plane stress, $E' = E/(1 - \nu^2)$ for plane strain (E and ν are Young's modulus and Poisson's ratio, respectively), b is thickness of the specimen and $\bar{C}(\alpha)$, $\delta(\alpha)$, $k(\alpha)$ are nondimensional functions depending on geometry. It can be shown (e.g. Bažant and Cedolin [16]) that $\bar{C}(\alpha)$ and $k(\alpha)$ are related by

$$\bar{C}(\alpha) = \bar{C}(0) + 2\int_0^{\alpha} k^2(\tilde{\alpha})\,d\tilde{\alpha}, \tag{4}$$

where $\bar{C}(0)$ is the compliance of the same specimen without any crack. For a three-point-bend (3PB) specimen with span-to-depth ratio $l:d = 2.5:1$ we have (Bažant and Kazemi [19]

$$\bar{C}(0) = \frac{l^3}{4d^3} + \frac{3l(1+\nu)}{5d} = 5.406 + 1.5\nu, \tag{5}$$

$$k(\alpha) = 3.75\sqrt{\pi\alpha}(1-\alpha)^{3/2}(1 - 2.5\alpha + 4.49\alpha^2 - 3.98\alpha^3 + 1.33\alpha^4), \tag{6}$$

$$\delta(\alpha) = 14.1\alpha[0.76 - 2.28\alpha + 3.87\alpha^2 - 2.04\alpha^3 + 0.66(1-\alpha)^{-2}]. \tag{7}$$

The graphs of nondimensional functions $k(\alpha)$ and $\delta(\alpha)$ are shown in Fig. 2a,b.

The Griffith criterion for crack propagation in perfectly brittle materials states that the crack can propagate if the energy needed to create a new free surface is balanced by the elastic energy release from the structure. This condition is equivalent to $K = K_c$, where K is the actual stress intensity factor and K_c its critical value, called fracture toughness.

The usual rate-independent version of the R-curve model for crack propagation in quasi-brittle materials is based on the assumption that the energy needed to propagate the crack is not constant, but increases due to growth of the nonlinear fracture process zone with increasing crack length. According to this assumption, K_c is replaced by the function,

$$K_R(c) = \sqrt{E'R(c)}, \tag{8}$$

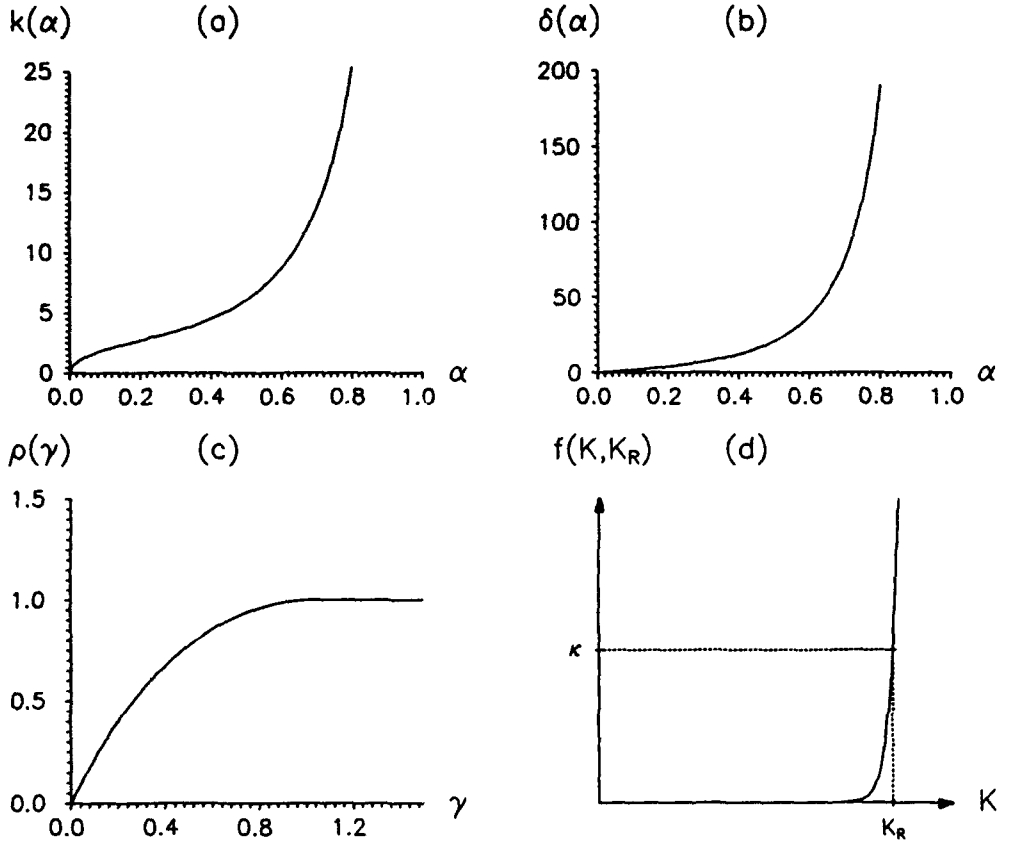

Fig. 2. Graphs of (a) $k(\alpha)$, (b) $\delta(\alpha)$, (c) $\rho(\gamma)$, (d) $f(K, K_R)$.

which depends on the crack propagation distance $c = a - a_0$. The resistance function $R(c)$, whose graph is called the R-curve, can be determined solely from maximum loads of similar specimens of different sizes, using the size effect method described in Bažant, Gettu and Kazemi [20]. Aside from geometry, $R(c)$ depends on two material constants G_f and c_f representing the fracture energy and the fracture process zone length at the peak load for an infinitely large specimen. Based on the size effect law (see [18], Sec. 12.3 and 13.9), it has been shown (Bažant and Kazemi [19, 20]) that the shape of the R-curve is determined by the equations

$$\frac{R}{G_f} = \frac{c}{c_f} \frac{g'(\alpha)}{g'(\alpha_0)}, \tag{9}$$

and

$$\frac{c}{c_f} = \left[\frac{g(\alpha)}{g'(\alpha)} - \alpha + \alpha_0 \right] \frac{g'(\alpha_0)}{g(\alpha_0)}, \tag{10}$$

where $g(\alpha) = k^2(\alpha)$ = nondimensional function depending only on geometry. Choosing a sequence of α-values, one calculates for each of them the value of c/c_f and the corresponding R/G_f.

Obviously, the relation between R/G_f and c/c_f depends only on the shape (geometry) of the structure. It is therefore convenient to separate the effects of geometry from the material properties and write

$$R(c) = G_f \rho(\gamma), \quad \gamma = \frac{c}{c_f}, \tag{11}$$

where ρ is the normalized resistance function depending on geometry only. Its graph (the normalized R-curve) for a three-point bend (3PB) specimen with span-to-depth ratio 2.5:1 is shown in Fig. 2c.

Combining (8) and (11), we get

$$K_R(c) = \sqrt{E'G_f}\sqrt{\rho(\gamma)} = K_f\sqrt{\rho(\gamma)}, \tag{12}$$

where K_f is the fracture toughness for an infinitely large specimen.

To capture the effects of the loading rate, we assume that the crack propagation rate $\dot{a} = \mathrm{d}a/\mathrm{d}t$ depends on the current values of K and K_R:

$$\dot{a} = f(K, K_R). \tag{13}$$

Since $K = \sqrt{E'G(a)}$, $K_R = \sqrt{E'R(c)}$, this is equivalent to assuming that $\dot{a}$ is a function of $G(a)$ and $R(c)$ where $G(a)$ is the energy release rate. It is clear that $\dot{a}$ should increase with increasing K and with decreasing K_R. But what should be the actual form of the crack growth rate function $f(K, K_R)$? Experimental evidence indicates that changing the loading rate by several orders of magnitude causes the peak loads to change only by a factor less than 2 [14, 15, 26]. Therefore, the crack growth rate function should allow for a very large variation of $\dot{a}$ with only moderate changes of its arguments. This can be achieved by setting

$$f(K, K_R) = \kappa\left(\frac{K}{K_R}\right)^n, \tag{14}$$

where κ and n are constants. It is expected that $n \gg 1$, so that $\dot{a}$ varies with K as indicated in Fig. 2d.

Equations (1) and (2) have been based on the assumption of linear elasticity. Under loading rates spanning over several orders of magnitude, creep effects can play an important role. Creep in the bulk of the specimen can be taken into account by replacing $1/E'$ by an appropriate compliance operator, which yields

$$u(t) = \frac{1}{b}\int_{t_0}^{t} J(t, t')\,\mathrm{d}[P(t')\bar{C}(t')], \tag{15}$$

$$\Delta(t) = \frac{1}{b}\int_{t_0}^{t} J(t, t')\,\mathrm{d}[P(t')\delta(t')]. \tag{16}$$

$J(t, t')$ is the compliance function, which must be determined in advance by measuring or estimating the creep properties of the material. The geometric compliances $\bar{C}$, δ are time dependent because they vary with the relative crack length α, which increases as the crack propagates.

Experiments performed under load control become unstable after the peak load has been reached. To study the descending part of the load-displacement curve, displacement control must be adopted. The available experiments [14, 15, 21] have been performed under a constant CMOD rate. In such a case, the time history of CMOD is described by a linear function

$$\Delta(t) = r(t - t_0), \tag{17}$$

where t_0 is the time at the beginning of the experiment and constant r is the prescribed CMOD rate. The unknown functions $P(t)$ and $\alpha(t)$ describing the variation of the applied load and evolution of the crack length can be determined by solving the crack propagation equation (13) along with (16). Using relations (3), (12), (17) and $a = \alpha d$, we can rewrite the basic equations as

$$\dot{\alpha}(t) = \frac{1}{d} f\left(\frac{P(t)}{b\sqrt{d}} k[\alpha(t)],\ K_f \sqrt{\rho\left[(\alpha(t) - \alpha_0)\frac{d}{c_f}\right]}\right), \tag{18}$$

$$b\Delta(t) = \int_{t_0}^{t} J(t, t')\, \mathrm{d}[P(t')\delta(t')], \tag{19}$$

where the function f is defined by (14). The CMOD history $\Delta(t)$ is specified as input, to simulate the present tests. Alternatively, the load point deflection history $u(t)$ can be specified as input. As still another alternative, the load history $P(t)$ may be specified as input and then, first, (18) is solved for $\alpha(t)$ and, second, $\Delta(t)$ is evaluated from (19). The initial conditions are

$$\alpha(t_0) = \alpha_0, \quad P(t_0) = 0, \quad \Delta(t_0) = 0. \tag{20}$$

3. Numerical solution

To solve the problem numerically, we divide time into equal intervals $\langle t_i, t_{i+1}\rangle$, $i = 0, 1, 2, \ldots, N$, with $t_i = t_0 + i\Delta t$. Suppose that we have already computed approximate values $\alpha_i = \alpha(t_i)$, $P_i = P(t_i)$ for $i = 0, 1, 2, \ldots, j$ and we want to proceed to α_{j+1}, P_{j+1}. Equations (18), (19) can be discretized in $\langle t_j, t_{j+1}\rangle$ as follows:

$$\frac{\alpha_{j+1} - \alpha_j}{\Delta t} = \frac{1}{d} f\left[\frac{P_{j+1} + P_j}{2b\sqrt{d}} k\left(\frac{\alpha_{j+1} + \alpha_j}{2}\right), K_f \sqrt{\rho\left[\left(\frac{\alpha_{j+1} + \alpha_j}{2} - \alpha_0\right)\frac{d}{c_f}\right]}\right], \tag{21}$$

$$b\Delta_{j+1} = \sum_{i=0}^{j} J\left(t_{j+1}, \frac{t_{i+1} + t_i}{2}\right)[P_{i+1}\delta(\alpha_{i+1}) - P_i\delta(\alpha_i)], \tag{22}$$

where $\Delta_{j+1} = \Delta(t_{j+1}) = r(j+1)\Delta t$ for tests with a constant CMOD rate. For convenience let us denote

$$J_{j,i} = J\left(t_{j+1}, \frac{t_{i+1} + t_i}{2}\right), \tag{23}$$

$$\delta_i = \delta(\alpha_i), \tag{24}$$

$$S_{j-1} = \sum_{i=0}^{j-1} J_{j,i}(P_{i+1}\delta_{i+1} - P_i\delta_i). \tag{25}$$

Equations (21), (22) are two nonlinear equations for unknowns P_{j+1}, α_{j+1}. Noting that (22) is linear with respect to P_{j+1}, we can express P_{j+1} as

$$P_{j+1} = \left[\frac{b\Delta_{j+1} - S_{j-1}}{J_{j,j}} + P_i\delta_j\right]\frac{1}{\delta(\alpha_{j+1})}, \tag{26}$$

and substitute this expression into (21). We end up with a nonlinear equation with only one unknown α_{j+1}. As the right-hand side of (21) is highly nonlinear, a robust numerical procedure must be chosen to assure convergence. After some experimentation, an algorithm based on a secant rather than tangent formula has been adopted.

Special treatment is necessary in the first few time steps when the process zone is very small and K_R is therefore close to zero. In fact, at time t_0 we have $K_R = 0$, $K = 0$ and the ratio K/K_R is not defined. Even though we do not need to evaluate this ratio at t_0 but only at $t_0 + (\Delta t/2)$, α is at the beginning of crack propagation very close to α_0 and numerical problems arise due to strong sensitivity of the high power $(K/K_R)^n$ to even very small changes of α.

To overcome these difficulties, we need to make use of an approximate analytical solution, which can be derived under the simplifying assumptions that $\alpha - \alpha_0 \ll 1$ and that P is a linear function of time

$$P(t) = \bar{P}(t - t_0), \tag{27}$$

where $\bar{P}$ is a constant to be determined later. For small values of $\alpha - \alpha_0$, $k(\alpha)$ can be replaced by $k_0 = k(\alpha_0)$ and $\rho[(\alpha - \alpha_0)d/c_f]$ by $\bar{\rho}(\alpha - \alpha_0)d/c_f$, where $\bar{\rho} = \rho'(0)$. Equation (14) can now be transformed to

$$\dot{\alpha} = \frac{\kappa}{d}\left(\frac{K}{K_R}\right)^n = C_0\left(\frac{t - t_0}{\sqrt{\alpha - \alpha_0}}\right)^n, \tag{28}$$

where

$$C_0 = \frac{\kappa}{d}\left(\frac{\bar{P}k_0\sqrt{c_f}}{bdK_f\sqrt{\bar{\rho}}}\right)^n. \tag{29}$$

Solving the approximate crack propagation equation (28) by separation of variables, we get

$$\alpha = \alpha_0 + C_1(t - t_0)^{(2n+2)/(n+2)}, \tag{30}$$

where

$$C_1 = \left(C_0 \frac{n+2}{2n+2}\right)^{2/(n+2)} \tag{31}$$

It is interesting to note that if n is large, $\alpha - \alpha_0$ is approximately proportional to $(t - t_0)^2$.

Except for $\bar{P}$, all the quantities in expressions (29) and (31) defining C_1 are known. $\bar{P}$ can be determined from the load-CMOD relation (16). If $\alpha - \alpha_0 \ll 1$, we can treat $\delta(\alpha(t))$ as approximately equal to $\delta_0 = \delta(\alpha_0)$. Using $P = \bar{P}(t - t_0)$ and $\Delta = r(t - t_0)$, (16) can be simplified to $br(t - t_0) = \bar{P}\delta_0 \int_{t_0}^{t} J(t, t')\,dt'$, from which

$$\bar{P} = \frac{br(t - t_0)}{\delta_0 \int_{t_0}^{t} J(t, t')\,dt'}. \tag{32}$$

The fact that the right-hand side of (32) depends on time contradicts the assumption $\bar{P} = \text{const.}$, but we can think of each time instant $t = t_i$ separately, approximating the history of $P(t)$ in the interval $\langle t_0, t_i \rangle$ by a linear function whose slope depends on the time instant under consideration. The analytical solution (30) is used only in the first few steps. We exploit it to initialize the crack propagation and get a reasonable estimate for the initial crack propagation rate. In fact we need only an order-of-magnitude estimate as the initial approximation for the previously described numerical procedure. The rates of crack propagation at the very beginning have nearly no influence on the later stages of the process and they are needed only as the approximations to start with. Therefore, the present simplifications are justified.

It has been observed experimentally [20] that after the peak load $R(c)$ ceases increasing but remains constant. The explanation is that after the peak load the process zone length ceases growing and travels across the ligament approximately as a rigid body.

4. Comparison of theory to constant CMOD rate tests

Performance of the proposed model has been compared with the experimental results reported [14], [15], [21] and [26].

Bažant and Gettu investigated simultaneous rate and size effect for three-point-bend concrete specimens. Each experiment was performed under a constant CMOD rate. They tested specimens of three different sizes (d = 38 mm, 76 mm, 152 mm) and applied the CMOD rates ranging from 4×10^{-11} m/s to 10^{-5} m/s, with the corresponding times to peak ranging from 3 days to 1 second. Table 1 shows the peak loads recorded for each test. Most of the specimen were tested at 28 days after casting, but some of them were much older (up to 120 days). To get comparable data, the measured peak loads have been adjusted to the same age (28 days) using a

Table 1. Experimental results by Bažant and Gettu [14]

Depth [mm]	CMOD rate [m/s]	Age [days]	Peak load [N]
38	$1.1\,10^{-5}$	28	2217
38	$1.1\,10^{-5}$	28	1883
38	$8.4\,10^{-6}$	28	1794
38	$2.4\,10^{-8}$	28	1639
38	$1.8\,10^{-8}$	28	1774
38	$1.8\,10^{-8}$	28	1818
38	$7.1\,10^{-10}$	40	2256
38	$7.1\,10^{-10}$	38	1891
38	$7.1\,10^{-10}$	39	2128
38	$3.8\,10^{-11}$	120	2007
76	$1.4\,10^{-5}$	28	3612
76	$1.4\,10^{-5}$	28	3946
76	$1.4\,10^{-5}$	28	3014
76	$5.3\,10^{-8}$	28	3059
76	$4.3\,10^{-8}$	28	2750
76	$3.6\,10^{-8}$	28	2790
76	$1.1\,10^{-9}$	30	3153
76	$1.0\,10^{-9}$	46	3465
76	$9.4\,10^{-10}$	42	3417
76	$7.4\,10^{-11}$	108	2995
152	$2.1\,10^{-5}$	28	6158
152	$2.1\,10^{-5}$	28	5919
152	$2.1\,10^{-5}$	28	5406
152	$7.1\,10^{-8}$	28	5007
152	$7.1\,10^{-8}$	28	4210
152	$7.1\,10^{-8}$	28	4185
152	$1.7\,10^{-9}$	31	5239
152	$1.4\,10^{-9}$	32	4216
152	$1.4\,10^{-9}$	38	4085
152	$1.3\,10^{-10}$	90	4332

simple approximate empirical formula

$$P_{\text{peak},28} = P_{\text{peak},t_0}\sqrt{0.86 + \frac{4}{t_0}}, \tag{33}$$

where t_0 is the age at testing in days, P_{peak,t_0} is the measured peak load and $P_{\text{peak},28}$ is the corrected peak load. The creep compliance function $J(t, t')$ has been approximated by the well-known double-power law (see [18], Sec. 9.4):

$$J(t, t') = \frac{1}{E_0}\left[1 + \phi_1(t'^{-m} + \alpha)(t - t')^n\right]. \tag{34}$$

In agreement with the data from [14], the parameters of this law were set as follows: $E_0 = 48.4\,\text{GPa}$, $\phi_1 = 3.93$, $m = 0.306$, $n = 0.133$, $\alpha = 0.00325$.

It is clear from Table 1 and Fig. 3a that the experimentally determined values of the peak load suffer from considerable scatter, which can be explained by the fact that the specimens

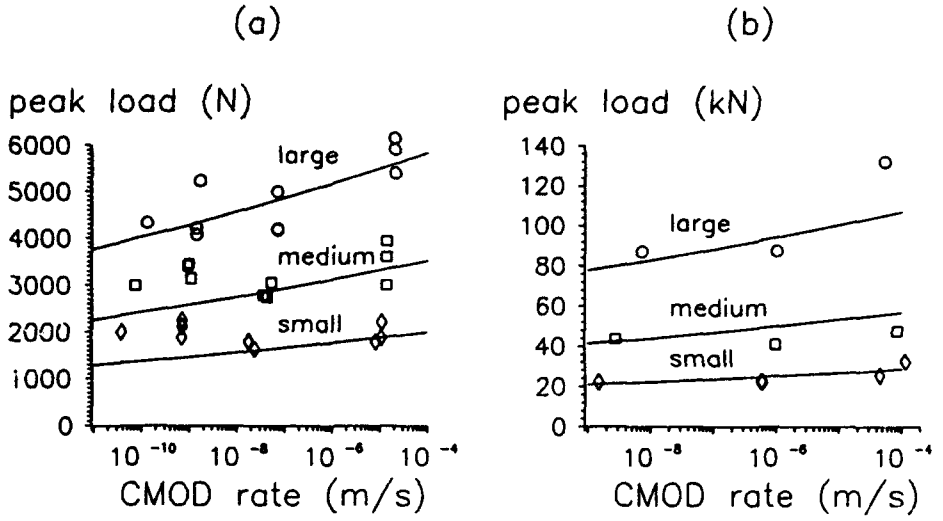

Fig. 3. Comparison with experiments for concrete: (a) three point bending, (b) wedge splitting.

were cast from several batches of concrete. Nevertheless, some general trends can still be observed:

- The peak loads increase with increasing rate of loading.
- The rate dependence of peak loads is stronger for large specimens than for small ones.
- The nominal strength decreases with increasing size, approximately following the size effect law proposed by Bažant [24].
- The size effect on peak loads is stronger for slow loading rates than for fast ones.

It may be somewhat surprising that the size effect and the rate effect in concrete appear to be mutually dependent. In terms of size effect, a decreasing rate of loading causes a shift towards more brittle behaviour. The same phenomenon can be described in terms of rate effect as an increase of rate sensitivity with increasing size.

In contrast to concrete, no interaction of size and rate effect could be observed for limestone [15]. This could probably be explained by absence of creep in limestone, both within the bulk of the specimen and within the fracture process zone. This means that the rate effect in limestone is due solely to the thermally activated process of bond ruptures, producing the crack surfaces.

In an attempt to fit the aforementioned experimental data by the proposed rate-dependent *R*-curve model, it has been discovered that the originally proposed version does not exhibit any shift of brittleness. It was therefore not difficult to get a reasonable agreement between theory and experiments for limestone (Fig. 4), while for concrete (Fig. 3a) it was impossible to get a good agreement for all the rates and all the sizes at the same time.

It is nevertheless encouraging that the model can capture both the size effect and the rate effect, although not their mutual interaction. Let us briefly describe the role of free parameters, whose values can be adjusted to get the best fit of experimental data:

- Parameters κ and K_f are mutually dependent, so that only one of them can be regarded as a free parameter. By increasing K_f or decreasing κ, the peak loads are increased for all the rates and sizes in the same ratio.

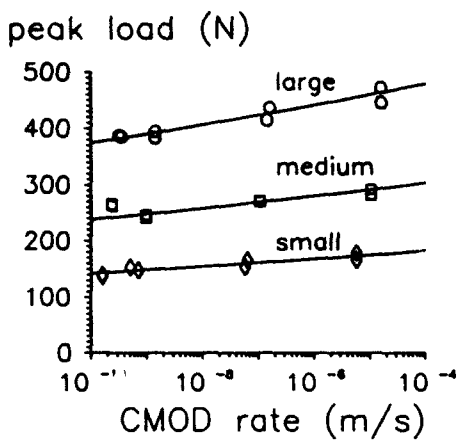

Fig. 4. Comparison with experiments for limestone.

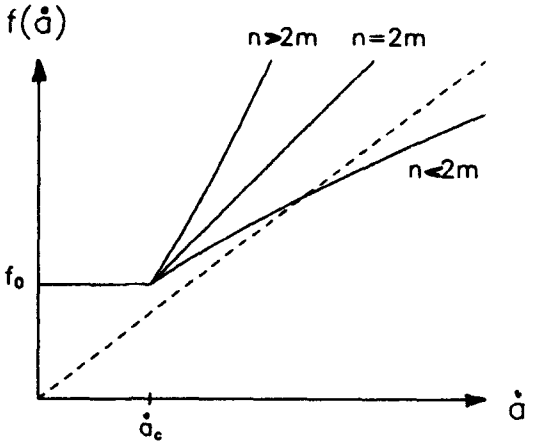

Fig. 5. Graph of f for different ratios $n/2m$.

- Parameter n affects mainly the rate sensitivity (for all the sizes in the same manner). By increasing n, one can decrease the slope of the rate effect curve, which is indicated by experiments to be roughly linear when the CMOD rate is plotted in a logarithmic scale.
- Parameter c_f affects brittleness, and does so for all the rates in roughly the same manner. Increasing c_f causes a shift toward the left on the size effect curve, i.e. to a more ductile behaviour.

To decrease the rate sensitivity of the model to realistic values, a very large exponent n is needed. For example to fit the data on 3PB experiments on concrete [14], n had to be set equal to 38 (Fig. 3a), and for similar experiments on limestone [15] even to 55 (Fig. 4)!

The rate dependent R-curve model has also been used to model wedge-splitting tests on concrete reported in [21]. Due to considerable scatter in these large-scale tests, it is impossible to make any quantitative conclusions. However, similar trends as in 3PB tests can be observed (Fig. 3b). The value of the exponent n came out to be 35, which is about the same as for the aforementioned 3PB experiments.

5. A generalization: rate-dependent process zone length

The original version of the rate-dependent R-curve model presented in the foregoing suffers by a serious drawback: It is not capable of modeling the rate-dependent shift of brittleness observed experimentally by Bažant and Gettu [14]. In an attempt to increase flexibility of our model, we may replace the constant value of c_f (process zone length at peak load for an infinitely large specimen) by a rate-dependent function $c_f(\dot{a})$. The rate-dependence of c_f is not illogical. Stress relaxation in the fracture process zone may be expected to cause the stress profile along the crack extension line to develop a steeper drop to zero, spanning a shorter length, which means that the effective fracture process zone length should be smaller at slower crack propagation.

As explained in Section 3, c_f is the basic parameter affecting brittleness. Because brittleness is seen to decrease with increasing rate, c_f should be an increasing function of $\dot{a}$. However, c_f should vary only by a factor of 10 while the rate of loading (and therefore also the rate of crack

propagation) varies over five orders of magnitude. It is therefore reasonable to use a power function with a low exponent

$$c_f = c_{f0}\left(\frac{\dot{a}}{\dot{a}_0}\right)^{1/m}, \tag{35}$$

where $m \gg 1$. For the sake of dimensionality we have introduced here, in addition to m, two more parameters $c_{f0}, \dot{a}_0$, but only one of them is independent. The other one can be preset to any (positive) fixed value without any loss of generality.

With c_f dependent on $\dot{a}$, the crack propagation equation (13) now becomes an implicit law for the crack propagation rate $\dot{a}$. If the model is to be physically reasonable, there must exist a unique nonnegative solution $\dot{a}$ for any possible situation. This condition imposes a serious restriction on the value of m. A simple analysis of this restriction can be performed if we approximate $\rho(c/c_f)$ by a piecewise linear function

$$\rho\left(\frac{c}{c_f}\right) = \frac{c}{c_f} \quad \text{if } \frac{c}{c_f} < 1, \qquad \rho\left(\frac{c}{c_f}\right) = 1 \quad \text{if } \frac{c}{c_f} \geqslant 1. \tag{36}$$

The function f defined by (14) can now be written as

$$f(K, K_R) = \kappa\left(\frac{Pk}{b\sqrt{d}K_f}\right)^n \left[\rho\left(\frac{c}{c_f(\dot{a})}\right)\right]^{-n/2} = f_0\left[\rho\left(\frac{c}{c_f(\dot{a})}\right)\right]^{-n/2}. \tag{37}$$

Suppose that the current values of P, k, c are given and we want to solve (14) for unknown $\dot{a}$. Denote by $\dot{a}_c$ the value of $\dot{a}$ for which $c_f(\dot{a}) = c$. If $0 < \dot{a} < \dot{a}_c$, then $c_f(\dot{a}) < c$, $\rho(c/c_f(\dot{a})) = 1$ and $f(K, K_R) = f_0$. If $\dot{a} > \dot{a}_c$, then $c_f(\dot{a}) > c$, $\rho(c/c_f(\dot{a})) = c/c_f(\dot{a})$ and

$$f(K, K_R) = f_0\left[\frac{c}{c_{f0}(\dot{a}/\dot{a}_0)^{1/m}}\right]^{-n/2} = f_0\left(\frac{\dot{a}}{\dot{a}_c}\right)^{n/2m}. \tag{38}$$

The right hand side of (38) is graphically presented in Fig. 5 for three different cases. It is clear that if $n/2m < 1$, equation $\dot{a} = f(K, K_R)$ has a unique positive solution for any values of f_0 and $\dot{a}_c$. However, if $n/2m > 1$, the equation has no solution or two solutions depending on whether $f_0 > \dot{a}_c$ or $f_0 < \dot{a}_c$. Thus, to ensure a proper formulation of the crack propagation equation, the parameter m in (35) must be larger than $n/2$, n being the exponent in (14). This condition has been derived under the simplifying assumption (36), but numerical calculations reveal that the method indeed does not converge if $m < n/2$ and sometimes even if m is only slightly above $n/2$.

It has been mentioned in Section 4 that, in order to ensure realistic rate sensitivity, n must assume very large values, typically between 30 and 40. On the other hand, m should not be too large if we want to get a substantial shift of brittleness. Unfortunately, $m > n/2$ must hold, otherwise the problem of crack propagation is not well-posed. The best fit of experimental results that could be constructed with rate-dependent c_f is still underestimating the measured peak

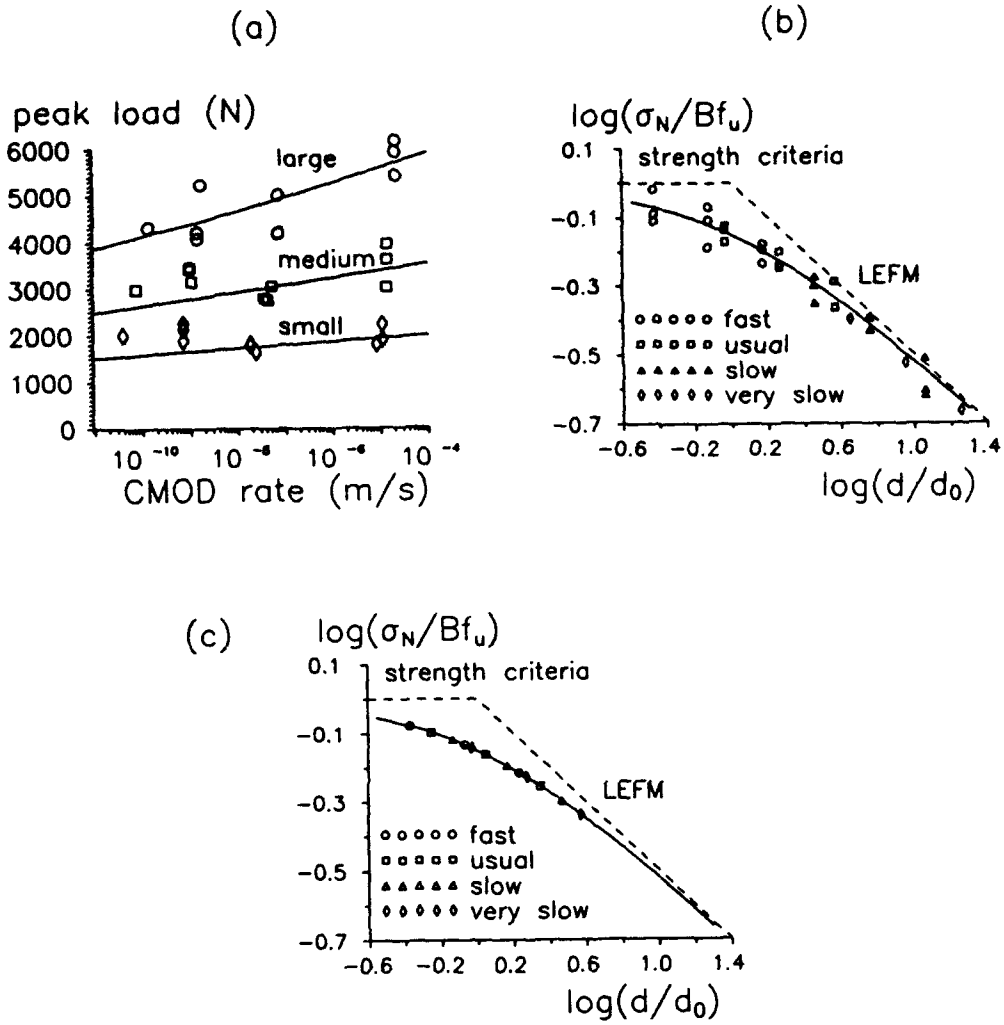

Fig. 6. Generalized model with variable c_f: (a) rate effect, (b) experimental size effect, (c) numerical size effect.

loads for small specimens under slow loading rates (Fig. 6a). In terms of the size effect, this means that the parameter d_0 in the size effect law [24]

$$\sigma_N = \frac{Bf_t}{\sqrt{1 + \dfrac{d}{d_0}}} \tag{39}$$

does not change with rate as much as it should, according to the tests of concrete (see Fig. 6b, c).

The theoretical curves in Fig. 6a correspond to the following set of parameters: $\kappa = 8 \times 10^{-6}$ m/s, $K_f = 9 \times 10^5$ Nm$^{-3/2}$, $n = 29$, $c_{f0} = 0.014$ m, $\dot{a}_0 = 0.01$ m/s, $m = 17$. Let us emphasize again that only four of these six parameters are independent.

6. Comparison to tests with a sudden rate change

Another set of experiments on rate effect in concrete fracture was performed by Bažant, Gu and Faber [25], who studied the effect of a sudden change of loading rate. In their tests on 3PB notched specimens, the initial CMOD rate was held constant in the prepeak range and in a part of the post-peak range. After the load decreased from its peak value P_1 to some lower value P_c, the CMOD rate was suddenly increased or decreased by several orders of magnitude and the test continued with the new value of a constant CMOD rate. This resulted into a sudden change of slope in the load-CMOD diagram. For a sufficiently large increase of the loading rate, the load started increasing again and a second peak P_2 could be observed (Fig. 7a). On the other hand, a decrease of the loading rate was followed by a fast drop of the load-CMOD curve (Fig. 7b). The rate-dependent R-curve model exhibits qualitatively the same behavior (Fig. 7c). The tests suggest that, after a rate change, the curve for the new rate asymptotically approaches the curve for a constant rate test with a rate equal to the new rate. The theory agrees with this behavior also (Fig. 7c).

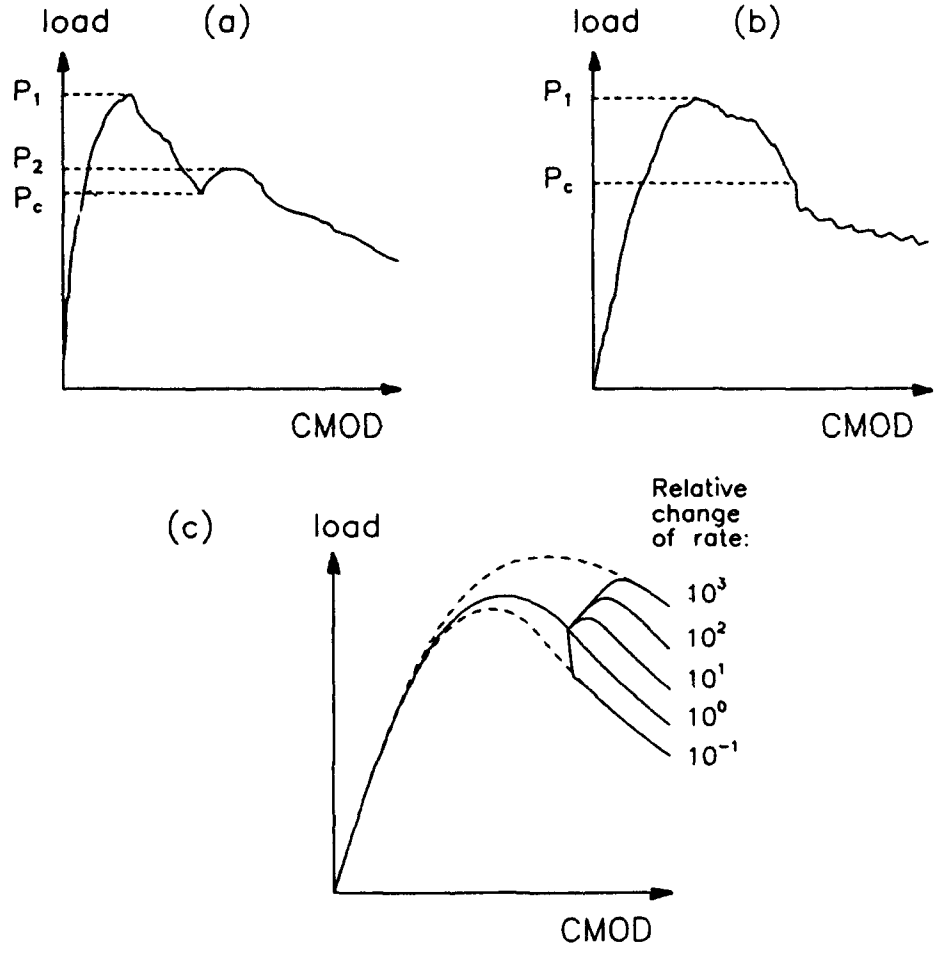

Fig. 7. Load-CMOD curves: (a) experimental curve (rate increased), (b) experimental curve (rate decreased), (c) theoretical curves.

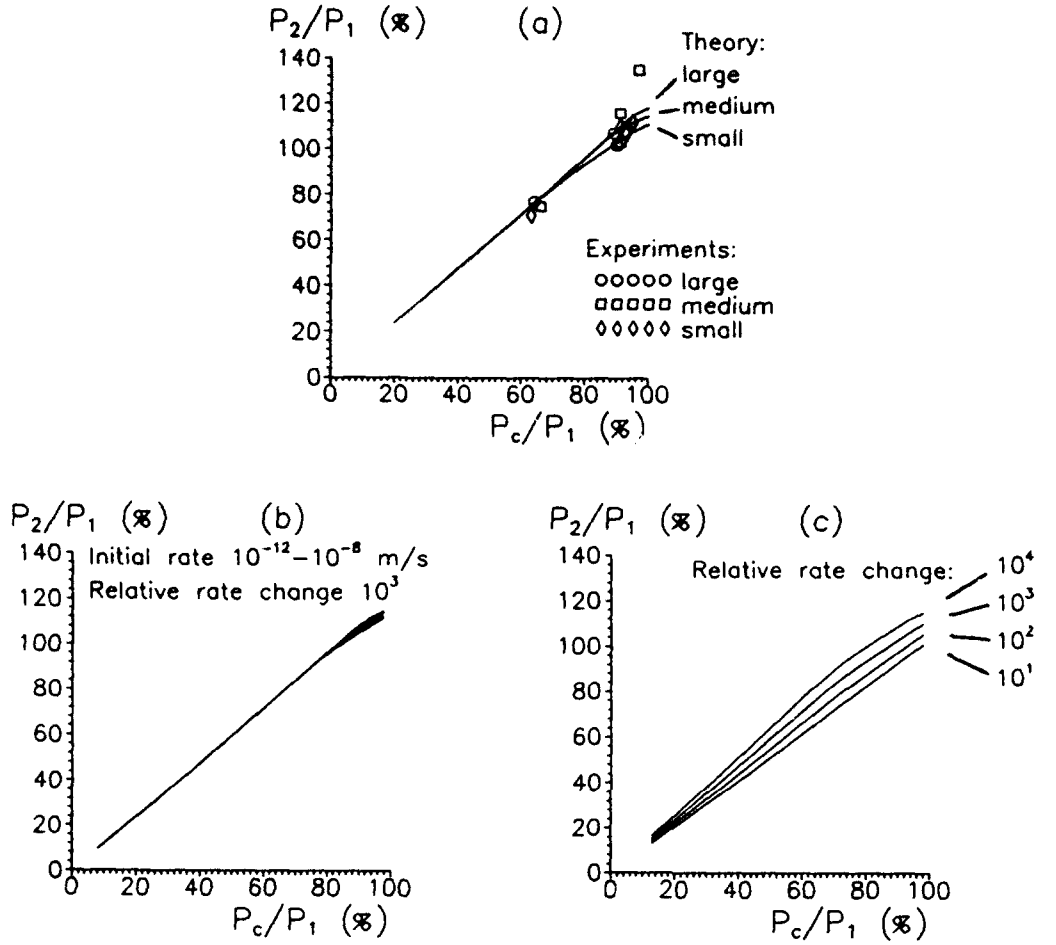

Fig. 8. Second peak versus load at rate change: (a) effect of size, (b) effect of initial rate, (c) effect of relative rate change.

Quantitative agreement between theory and experiments can be verified by plotting the ratio P_2/P_1 versus P_c/P_1 for all available results. The points marked by different symbols in Fig. 8a correspond to tests on specimens with three sizes (d = 38 mm, 76 mm, 152 mm) in which the rate increased by three orders of magnitude (on the average from 10^{-8} m/s to 10^{-5} m/s). The results seem to be independent of size.

The relationship between the two nondimensional ratios P_c/P_1 and P_2/P_1 can be calculated using the rate-dependent R-curve model described in previous sections. Instead of trying to adjust the parameters so as to fit the experimental data, their values were taken from the best fit of tests by Bažant and Gettu [14] constructed in Section 5. It is gratifying that these parameter values lead to a satisfactory agreement with measurements by Bažant, Gu and Faber [25].

The theoretical curves are only slightly dependent on size (Fig. 8a) and almost independent of the initial rate (for the same relative rate change—Fig. 8b). But, as expected, they are sensitive to the relative rate change (Fig. 8c).

7. Comparison to relaxation tests

The paper by Bažant and Gettu [14] reported still another type of experiment on the rate effect in concrete fracture – relaxation tests. The CMOD rate was initially held constant and after some time (usually in the post-peak range) suddenly decreased to zero. This type of test can be

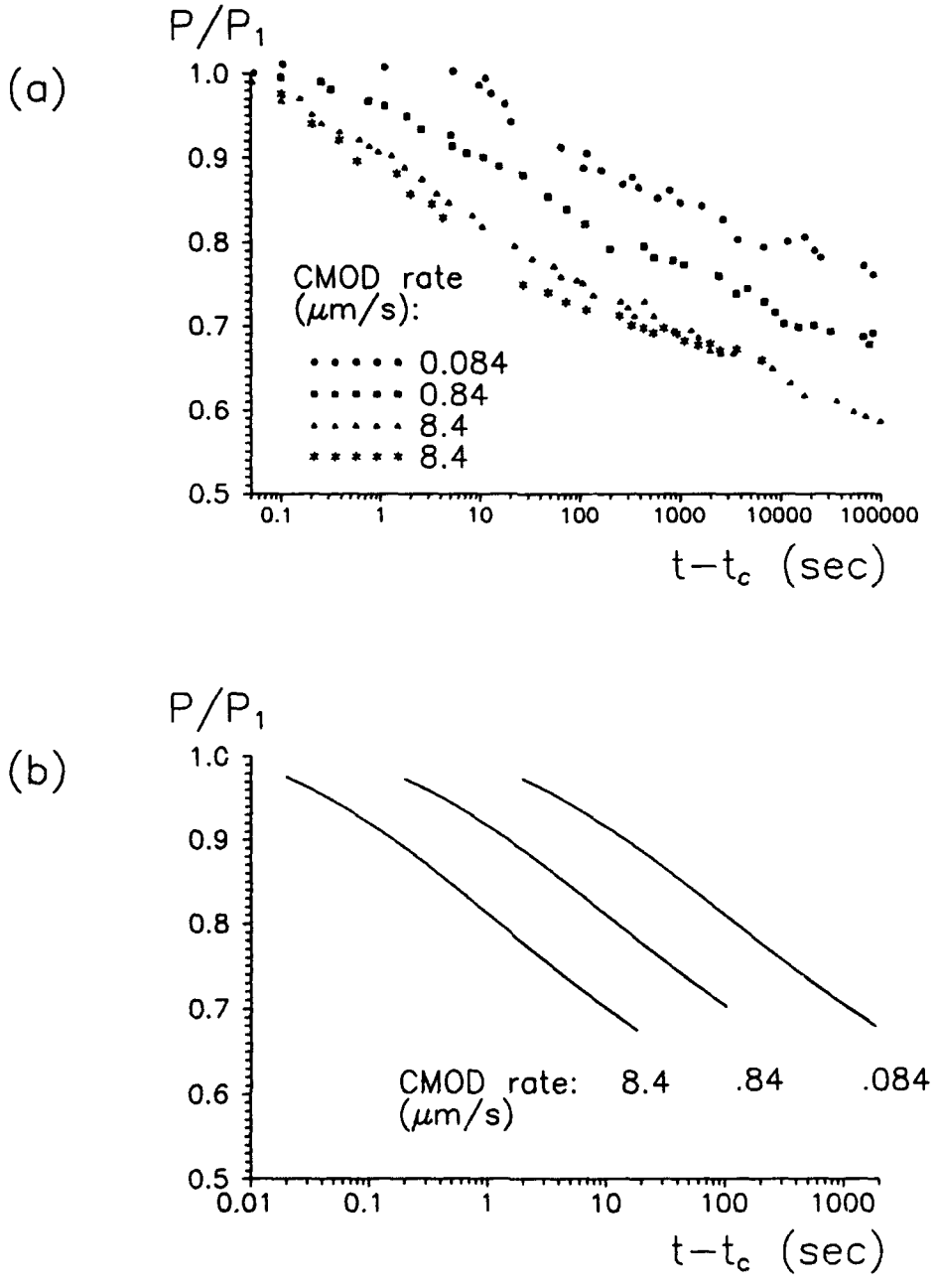

Fig. 9. Relaxation curves for different initial rates: (a) experimental, (b) theoretical.

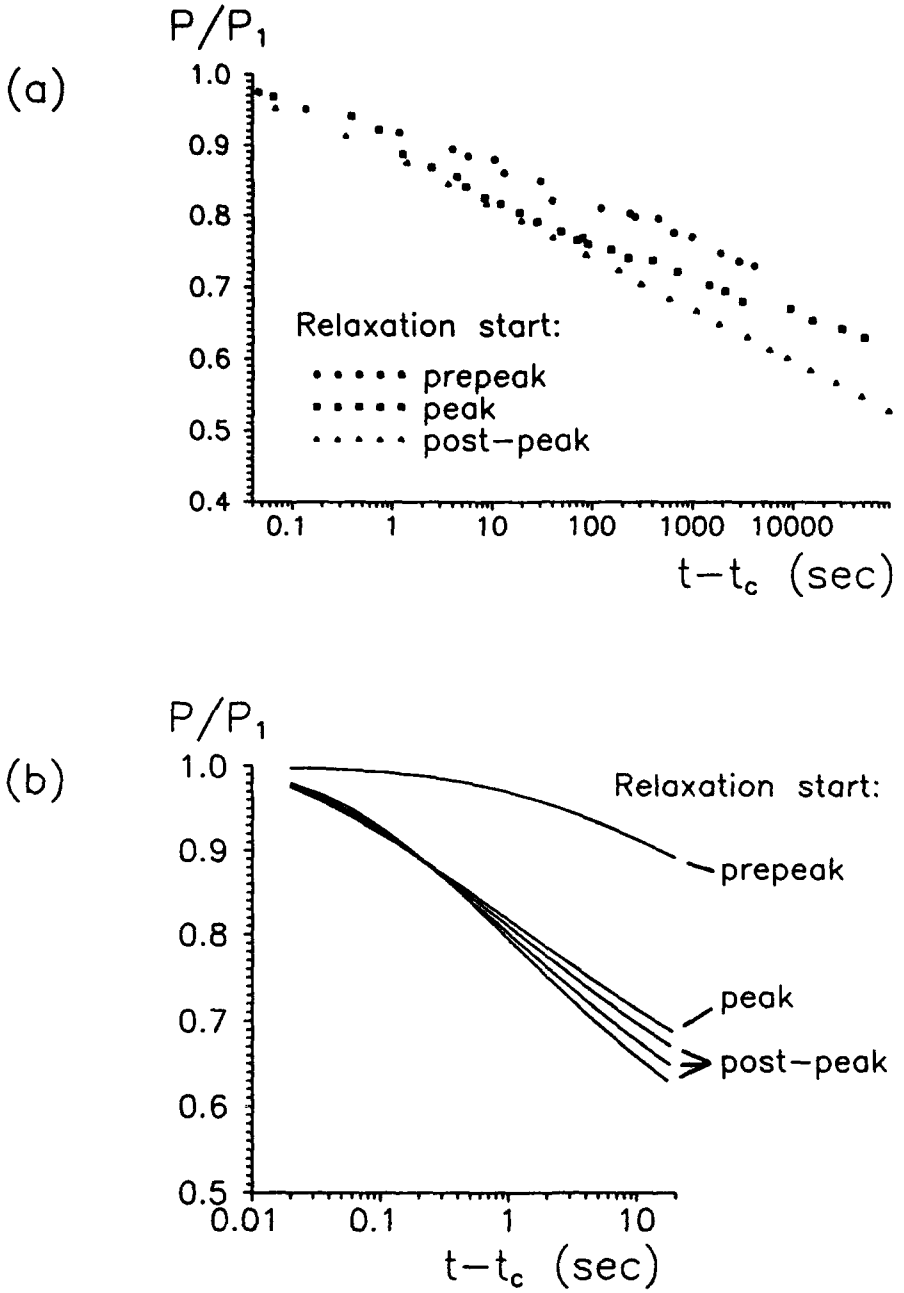

Fig. 10. Relaxation curves for different loads at relaxation start: (a) experimental, (b) theoretical.

regarded as a limit case of the experiments with a sudden change of rate. All tests were performed on medium size 3PB specimens ($d = 76$ mm).

In the first series of experiments, the initial rates were different and relaxation started in the post-peak range at about 85 percent of the peak load. Denoting the time at which relaxation started by t_c and the corresponding load by P_c, one can plot the relaxation curves $P(t)/P_c$ versus $t - t_c$. The experimental and theoretical relaxation curves are shown in Fig. 9. A qualitative

agreement can be observed – the curves corresponding to different initial rates have the same final slope in a logarithmic plot and are shifted with respect to each other. However, the slope of the theoretical curves is much steeper than of the experimental ones.

The second series of experiments was conducted with the same initial rate ($r = 8.5 \times 10^{-6}$ m/s) but relaxation started at different stages – in the prepeak range, at peak, and at different load levels in the post-peak range. Figure 10c reveals again only a qualitative agreement – the relaxation curves starting in the post-peak range lie below the curve starting approximately at peak, which in turn lies below the curve starting in the pre-peak range. The theoretical curves are again steeper than the experimental ones.

8. Conclusions

1. The equivalent linear elastic fracture model based on an R-curve (a curve characterizing the variation of critical energy release rate with crack propagation length) can be generalized to the rate effect if the crack propagation velocity is assumed to depend either on the ratio of the stress intensity factor to its critical value based on the R-curve, or on the difference between these two variables. This dependence may be assumed in the form of an increasing power function with a large exponent.
2. The creep in the bulk of a concrete specimen must also be taken into account, which can be done by replacing the elastic constants in the LEFM formulas with a linear viscoelastic operator in time. For rocks, which do not creep, this is not necessary.
3. The experimental observation that the brittleness of concrete increases with a decreasing loading rate (i.e. the response shifts in the size effect plot closer to linear elastic fracture mechanics) can be at least approximately modeled by assuming the effective fracture process zone length in the R-curve expression to decrease with a decreasing rate. This dependence may again be described by a power function.
4. Good agreement with the previous test results for concrete and limestone, recently measured at very different loading rates, with times to peak ranging from 1 second to 250000 seconds, is achieved.
5. The model can also predict the following phenomena recently observed in the laboratory:
   (a) When the loading rate is suddenly increased, the slope of the load-displacement diagram suddenly increases. For a sufficient rate increase, the slope becomes positive even in the post-peak range, and later in the test a second peak, lower or higher than the first peak, is observed.
   (b) When the rate suddenly decreases, the slope suddenly decreases and the response approaches the load-displacement curve for the lower rate.
   (c) When the displacement is arrested, relaxation causes a drop of load, approximately following a logarithmic time curve.

Acknowledgment

Financial support under NSF Grant No. MSS-9114476 to Northwestern University is gratefully acknowledged. Partial support for the experiments has been obtained from the Center for Advanced Cement-Based Materials at Northwestern University.

References

1. S.P. Shah and S. Chandra, *American Concrete Institute, Journal* 67 (1970) 816–825.
2. F.H. Wittmann and Y. Zaitsev, in *Mechanical Behavior of Materials, Proceedings, 1971 International Conference Society of Material Science*, Japan (1972) 84–95.
3. B.P. Hughes and A.J. Watson, *Magazine of Concrete Research* 30 (1978) 189–199.
4. S. Mindess, in *Application of Fracture Mechanics to Cementitious Composites*, S.P. Shah (ed.), Martinus Nijhoff Publishers, Dordrecht (1985) 617–638.
5. H.W. Reinhardt, in *Application of Fracture Mechanics to Cementitious Composites*, S.P. Shah (ed.), Martinus Nijhoff Publishers, Dordrecht (1985) 559–592.
6. F.H. Wittmann, in *Application of Fracture Mechanics to Cementitious Composites*, S.P. Shah (ed.), Martinus Nijhoff Publishers, Dordrecht (1985) 559–592.
7. D. Darwin and E.K. Attiogbe, in *Cement Based Composites: Strain Rate Effects on Fracture*, Mindess and Shah (eds.) (1986) 167–180.
8. H.W. Reinhardt, *Cement Based Composites: Strain Rate Effects on Fracture*, S. Mindess and S.P. Shah (eds.) (1986) 1–14.
9. Z.-G. Liu, S.E. Swartz, K.K. Hu and Y.-C. Kan, *Fracture of Concrete and Rock: Recent Developments*, S.P. Shah, S.E. Swartz and B. Barr (eds.) Elsevier Applied Science, London (1989) 577–586.
10. C.A. Ross and S.T. Kuennen, *Fracture of Concrete and Rock: Recent Developments*, S.P. Shah et al. (eds.), Elsevier, London (1989) 152–161.
11. S. Harsh, Z. Shen and D. Darwin, *American Concrete Institute Materials Journal* 87(5) (1990) 508–516.
12. Z.P. Bažant and R. Gettu, *Fracture of Concrete and Rock: Recent Developments*, S.P. Shah et al. (eds.), Elsevier, London (1989) 549–565.
13. Z.P. Bažant and R. Gettu, *Serviceability and Durability of Construction Materials*, B.A. Suprenant (ed.) (1990) 1113–1123.
14. Z.P. Bažant and R. Gettu, *American Concrete Institute Materials Journal* 89(5) (1992) 456–468.
15. Z.P. Bažant, S.-P. Bai and R. Gettu, *Engineering Fracture Mechanics*, in press.
16. Z.P. Bažant, in *Toughening Mechanisms in Quasi-brittle Materials*, S.P. Shah (ed.), Kluwer Academic Publishers, Dordrecht, (1990) 131–153.
17. Z.P. Bažant, in *Fracture Processes in Concrete, Rock and Ceramics*, J.G.M. van Mier (ed.), Noordwijk, Netherlands (1991).
18. Z.P. Bažant and L. Cedolin, *Stability of Structures: Elastic, Inelastic, Fracture and Damage Theories*, Oxford University Press, New York (1991).
19. Z.P. Bažant and M.T. Kazemi, *International Journal of Fracture* 51 (1991) 121–138.
20. Z.P. Bažant, R. Gettu and M.T. Kazemi, *International Journal of Rock Mechanics, Mining Science & Geomechanical Abstracts* 28(1) (1991) 43–51.
21. Z.P. Bažant and M.T. Kazemi, *International Journal of Fracture* 44 (1990) 111–131.
22. Z.P. Bažant and M.T. Kazemi, *Journal of the American Ceramic Society* 73(7) (1990) 1841–1853.
23. Z.P. Bažant, S. He, M.E. Plesha, R. Gettu and R.E. Rowlands, in *Proceedings International Conference on Dam Fracture*, University of Colorado, V. Saouma et al. (ed.), (1991) 413–425.
24. Z.P. Bažant, *Journal of Engineering Mechanics, ASCE* 110(4) (1984) 518–535.
25. Z.P. Bažant, W.H. Gu and K. Faber, "Effect of change of loading rate on post-peak softening of concrete." Internal report, Northwestern University (1992); also *ACI Materials Journal*, in press.
26. S. He, M.E. Plesha, R.E. Rowlands and Z.P. Bažant, *Dam Engineering* 3 (1992) 139–159.

ACI MATERIALS JOURNAL TECHNICAL PAPER

Title no. 90-M50

Fatigue Fracture of High-Strength Concrete and Size Effect

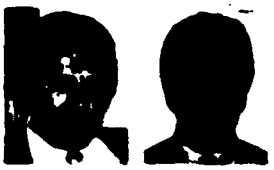

by Zdeněk P. Bažant and William F. Schell

Results of an experimental study of fatigue fracture of geometrically similar high-strength concrete specimens of very different sizes are reported and analyzed. Three-point bend notched beams 1.5, 4.24, and 12 in. deep were subjected to cyclic loading with a lower load limit of 0.07P_u and an upper limit between 0.73 and 0.84P_u, where P_u = maximum load in monotonic loading. The number of cycles to failure ranged from 200 to 41,000. It is found that the Paris law for the crack length increment per cycle as a function of the stress intensity factor, which was previously verified for normal concrete, is also applicable to high-strength concrete. However, for specimens of different sizes, an adjustment for the size effect needs to be introduced, of a similar type as previously introduced for normal concrete. This size adjustment represents a gradual transition from crack growth governed by stress amplitude to crack growth governed by stress intensity factor amplitude. The structure size for which this transition occurs is found to be about an order of magnitude smaller for high-strength concrete than for normal concrete, which means that the fracture process zone under cyclic loading is much smaller and the behavior is much closer to linear elastic fracture mechanics (LEFM). A linear regression plot estimating the size-adjusted parameters is derived. An LEFM-type calculation of the deflections under cyclic loading on the basis of the size-adjusted Paris law yields correct values for the terminal phase but grossly underpredicts the initial deflections. Overall, the results underscore the importance of considering fatigue fracture growth in the case of high-strength concrete structures subjected to large, repeated loads, and taking into account the very high brittleness under fatigue loading.

Keywords: deflection; fatigue (materials); fracture properties; high-strength concretes.

Due to its more homogeneous microstructure, high-strength concrete is more brittle than normal strength concrete. This is most apparent from size effect tests, which showed that the response of typical fracture specimens made of high-strength concrete is very close to linear elastic fracture mechanics.[1]

The fracture properties of high-strength concrete have been studied for monotonic loading;[2,3] however, no information appears to exist for fatigue loading. Such loading is very important for bridges, offshore structures, and structures subjected to heavy wind loads or machinery. Cyclic loading causes cracks to grow, which results in a growth of deflections and, after a certain number of cycles, may cause failure. Fatigue fracture has previously been experimentally studied for normal strength concrete.[4-6] It has been found that the well-known Paris law giving the crack length increment per cycle as a function of the amplitude of the stress intensity factor is invalid for concrete, although it has been widely used for metals. However, after an adjustment for the size effect,[5] fatigue fracture of normal ete can be described very well. The purpose of this w to determine the laws that describe the fatigue fracture gh-strength concrete. Such laws are needed for predicting the growth of cracks in concrete structures under large repeated loads due to traffic, nd, thermal cycles, etc.

EXPERIMENTAL INVESTIGATION

The test specimens were made of a high-strength concrete that is typical for the Chicago area. The concrete mix was designed for compressive strength exceeding 12,000 psi. The ratios of the mix components to cement, by weight, were as follows: portland cement: 1.00, water: 0.316, fly ash: 0.132, silica fume: 0.0507, $^3/_8$-in. maximum-diameter crushed aggregate: 2.18, siliceous sand: 1.51, retarder: 0.00190, and superplasticizer: 0.00951.

Three fracture specimens of varying size were cast from the same batch of concrete. The specimens were three-point bend fracture specimens shown in Fig. 1. Specimens of different sizes were geometrically similar in two dimensions, having the same thickness b equal to 38.1 mm (1.5 in.) (as explained in previous works, it is preferable to keep the thickness constant, because this minimizes the differences in hydration heat and drying effects, as well as in the so-called wall effect and effect of curvature of the fracture front throughout the thickness). The beam depths were D = 38.1, 107.8, and 304.8 mm (1.50, 4.24, and 12.00 in.), and the ratio of the sizes was $1:\sqrt{8}:8$. The span L was $2.5D$, where D is the beam depth. The notch, cut by a band saw, had the length $a_o = D/6$. Also, six companion cylinders with diameter 101.6 mm (4 in.) and length 203.2 mm (8 in.) were cast from the same batch. All the specimens were compacted, removed from the mold after 48 hr, and stored in a moist-curing room at 26 C for 56 days.

ACI Materials Journal, V. 90, No. 5, September-October 1993.

Rec d Apr. 27, 1992, and reviewed under Institute publication policies. Pertinent discussion will be published in the July-August 1994 *ACI Materials Journal* if received by Apr. 1, 1994.

Zdeněk P. Bažant, FACI, holds the W.P. Murphy professorial chair at Northwestern University, where he also served as Center Director and Structural Engineering Group Coordinator. He is a registered structural engineer in Illinois, consultant to Argonne National Laboratory, Editor of the ASCE Journal of Engineering Mechanics, Regional Editor of the International Journal of Fracture, President of the Society of Engineering Science, founding President of the International Association of Fracture Mechanics for Concrete Structures (IA-FraMCoS), and chairman of RILEM creep committee and of SMiRT Division H. He chaired ACI Committee 446, Fracture Mechanics. His latest honors: 1990 Gold Medal from the Building Research Institute of Spain, 1990 Humboldt Award, 1991 Honorary Doctorate from T.U. Prague, 1991 Best Engineering Book of the Year Award (for Stability of Structures, with L. Cedolin), 1992 Meritorious Publication Award from SEAOI, and 1993 Medal for Advances in Mechanics (Prague).

William F. Schell is currently a structural engineer with Hopper and Associates, Redondo Beach, Calif. He received his BS in civil engineering from the University of California, Berkeley, and MS in structural engineering from Northwestern University. His research interests include fatigue and fracture applications to structural design.

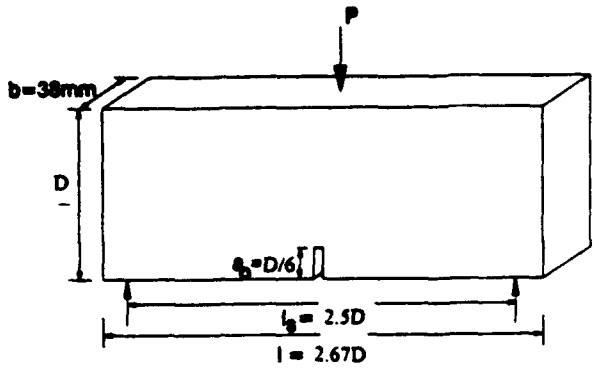

Fig. 1—Specimen geometry

The fatigue tests were conducted in a closed-loop, digitally controlled machine (MTS) with a 89,600 N (10 t) load capacity. The crack-mouth opening displacement (CMOD) was measured by an MTS extensometer. Data acquisition for both load and CMOD was performed by the computer controlling the test. The control variable was the load *P*.

The overall experimental setup for the largest specimen is shown in Fig. 2. To fit the largest beam in the testing frame, a stiff steel beam is used as the base. A photo of the frame with the medium specimen and configuration of the instruments is shown in Fig. 3.

The median age of the specimens at the time of test was 70 days, chosen higher than the usual 28 days to minimize the strength gain due to aging during the testing. All the tests were done within a span of 2 weeks. Companion cylinders tested just before and after the fatigue testing revealed a strength gain of only 3 percent, which was neglected in evaluating the tests.

Fatigue testing was preceded by compliance calibration of the fracture specimens. The compliance calibration method, verified for concrete in Reference 7, was used to determine the crack length during the loading cycles, because determination of the effective crack length by optical measurements is virtually impossible due to diffused cracking at the fracture front, as well as the curvilinear shape of the crack front through the specimen thickness, revealed by dye penetration tests. The compliance calibration method was shown to work

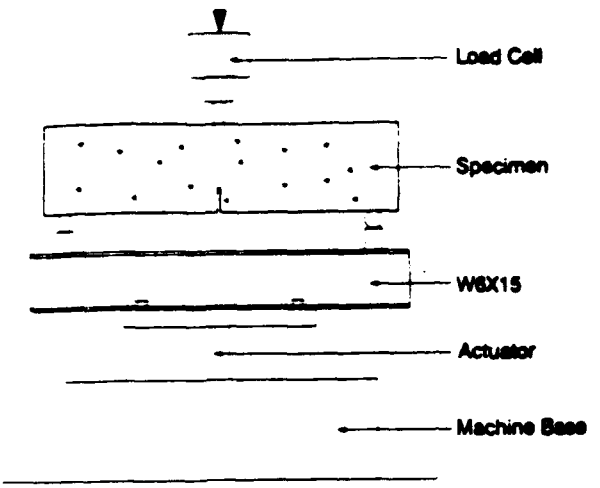

Fig. 2—Test setup for large specimen

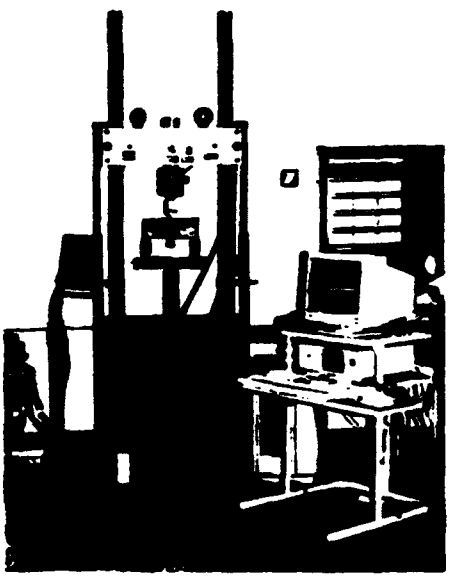

Fig. 3—Overall test arrangement and instrumentation of medium specimen

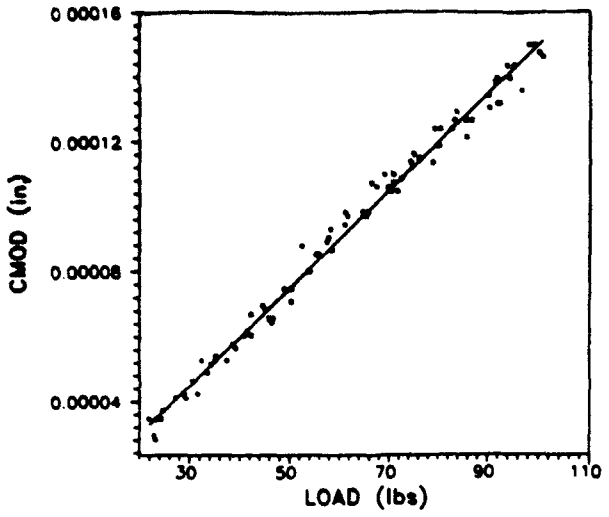

Fig. 4—Load-CMOD curve for compliance calibration method

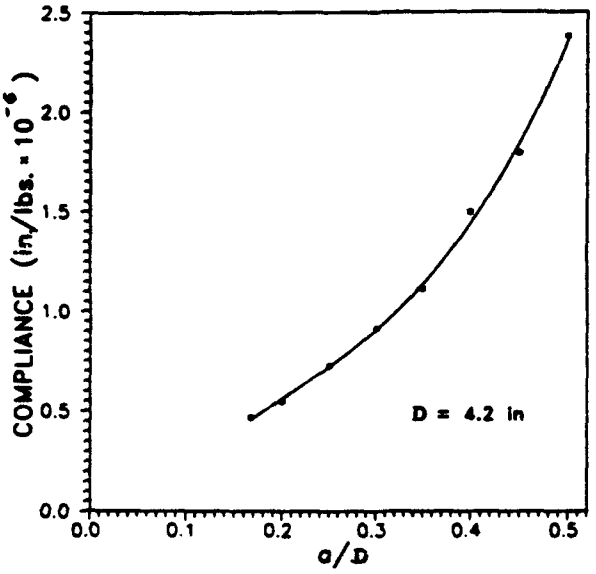

Fig. 5—Compliance calibration curve

for $a/D < 0.5$, which is sufficient for the present tests. The compliance calibration was done on the actual fatigue specimens, one calibration test for each size. The initial notch length, $a_o = D/6$, was the same as for the actual fracture specimens. Subsequently, making cuts with a band saw, the notch length was incremented. Each increment was assumed to remove the previously formed fracture process zone, which was rather small due to the small loads applied (the load was less than 20 percent of the maximum load). From such measurements, a plot of the load values versus crack-mouth opening displacement (CMOD) was obtained (Fig. 4) and a regression line was passed. The slope of the regression line is the compliance for the given crack length (actually it is not a compliance coefficient in the sense of an off-diagonal term of the compliance matrix, since the load P is not associated by work with CMOD). Repeating the tests shown in Fig. 4 for a range of crack lengths, the compliance calibration curve (shown in Fig. 5 for depth $D = 107.8$ mm = 4.24 in.) was obtained, one for each specimen size D. The elastic modulus values in the theoretical expression for the compliance curve are adjusted to obtain the best fit, as shown by the solid curve in Fig. 5. This curve is then used to estimate the corresponding crack length from the measured compliance during the fatigue test.

Table 1 — Peak loads and fatigue results

Size	P_u, N	P_{max}, percent*	N†	n	log C
Small	2940	73	33,409	8.64	−69.63
	2887	82	530	6.05	−49.44
		84	212	8.44	−65.22
Medium	5707	77	7450	9.99	−76.40
	6120	84	854	8.57	−67.30
Large	11,738	77	40,867	10.01	−79.77
	11,271	84	1348	9.61	−75.74

*P_{max} in percentage of ultimate load.
†N = number of cycles to failure

Prior to fatigue tests, monotonic load-controlled tests were carried out to determine the maximum loads of the specimens. These tests were used to determine the material fracture parameters according to the size effect method[8] and decide the load values to be used in the fatigue experiments. The measured peak loads P_u in monotonic tests are given in Table 1. A typical load-CMOD curve for $D = 76.2$ mm (3 in.) is shown in Fig. 6 for the high-strength concrete used in the current experiments.

The Young's modulus of high-strength concrete was estimated from the approximate empirical formulas: $E = 3320 f_c' + 6900 = 38{,}300$ MPa (5550 ksi) and the tensile strength $f_t = f_r = 0.94\sqrt{f_c'} = 8.9$ MPa (1290 psi), in which f_c' must be given in MPa. The compressive strength f_c' was determined by testing the companion cylinders according to ASTM standards; its average value at the beginning of the fatigue tests was 90.3 MPa (13,100 psi). The fracture parameters, obtained by the size effect method from the ultimate loads of specimens of various sizes measured under monotonic loading, were: fracture toughness $K_{If} = 44.7$ N mm$^{-3/2}$; fracture energy $G_f = 52.1$ N/m; transitional size in the size effect law $D_0 = 31.8$ mm; and effective length of the fracture process zone in an infinitely large specimen $c_f = 7.6$ mm $= 0.8\, d_a$, where d_a is the maximum aggregate size = ⅜ in. (note that the value of c_f is relatively small, which is the reason for the high degree of brittleness of high-strength concrete).

The fatigue tests were conducted at two different values of the upper load limit P_{max}, equal to $0.75P_u$ and $0.85P_u$. The minimum load limit was approximately $0.07P_u$ in all the tests (it was necessary to maintain a nonzero load to avoid separation between the specimen and the loading fixture). Maximum and minimum load limits were constant during the fatigue tests. The frequency chosen was 10 Hz. This is much higher than the frequency of 0.04 Hz used by Bažant and Xu,[5] but it appears that the frequency has a secondary influence compared to the influence of the number of cycles (although this might not be true for cycle periods stretching over months and years). Despite the high frequency, no measurement or stability problems were encountered during the test. The com-

puter data acquisition system recorded the load, CMOD, stroke, and cycle number for every peak and valley of the load history.

ANALYSIS OF RESULTS

The results of the fatigue tests are given in Table 1. The tests also include different load levels ranging from 73 to 84 percent of P_u (ultimate load in monotonic loading). It is seen from Table 1 that even such relatively small differences in the upper load limit lead to enormous differences in number of cycles to failure (ranging from 200 to 41,000). The loading system was not capable, at the fast rate of loading, to produce exactly the desired load limit in the cycle P_{max} set at the controls. This is why the recorded P_{max} values are slightly different. The evaluation was, of course, based on the actual measured P_{max}.

A typical plot of the relative crack length $\alpha = a/D$ versus the number of cycles N for the middle-size specimen is presented in Fig. 7(a). Considerable random differences among the results were encountered for the largest specimens; Fig. 7(b) shows that in one specimen the crack virtually did not grow until close to failure, while in another specimen the crack grew almost uniformly throughout the duration of the test (but the failure occurred after approximately the same number of cycles). Probably these differences are due to errors of control and measurement. Nevertheless, the mean trend described by these scattered results matches the other tests and agrees with the present theory. However, since only five specimens were tested for the two different upper load limits, more extensive testing is desirable in the future.

For many materials, the crack length increment per cycle approximately follows the empirical Paris law,[9,10] which is normally written as $\Delta\alpha/\Delta N = C_0 (\Delta K_I)^n$ (C_0 replaces Paris' notation C to avoid any confusion with compliance). This law can be rewritten in the nondimensional form as[5]

$$\frac{\Delta a}{\Delta N} = \kappa\left(\frac{\Delta K_I}{K_{Ic}}\right)^n \qquad (1)$$

in which $\kappa = C_0 K_{Ic}^n$; ΔK_I is the amplitude of the stress intensity factor for the current crack length a; κ or C_o and n = empirical constants; and K_{Ic} fracture toughness for monotonic loading = a critical value of K_I for monotonic loading, which is introduced for the convenience of dimensionality. The stress intensity factor is calculated from the applied load P, using the well-known formula of linear elastic fracture mechanics

$$K_I = \frac{Pf(\alpha)}{b\sqrt{D}} \qquad (2)$$

in which $\alpha = a/D$ = relative crack length; for the present three-point bend specimen, $f(\alpha) = 6.647\alpha^{1/2}(1 - 2.5\alpha + 4.49\alpha^2 - 3.98\alpha^3 + 1.33\alpha^4)/(1-\alpha)^{3/2}$ (which was obtained by curve-fitting of finite element results).[1] For other specimen geometries, function $f(\alpha)$ can be found in fracture textbooks and handbooks.[11,12] Using $f(\alpha)$, one has 5 $C_f = D_0 g(\alpha_0)/g'(\alpha_0)$ where $g(\alpha) = f^2(\alpha)$.

The validity of the Paris law [Eq. (1)] has been extensively verified for metals, and recently it has also been shown applicable to normal concrete.[5] However, it has been found that, in contrast to the previous experience with metals, the value of K_{Ic} cannot be kept the same for very different specimen sizes. It appeared that a good agreement with the test results for different sizes can be obtained if the value of K_{Ic} is considered to be a function of the specimen size and the law governing K_{Ic} is taken to be the same as that ensuing from the size effect law for ultimate loads in monotonic tests, as proposed in References 13 through 15. This previously derived law has the following form

$$K_{Ic} = K_{If}\sqrt{\frac{\beta}{1+\beta}} \qquad (3)$$

in which $\beta = D/D_o$ = relative specimen size (also called the brittleness number since it determines the proximity to linear elastic fracture mechanics) and K_{If} = a constant which represents the asymptotic value of fracture toughness for an infinitely large specimen coinciding with the asymptotic value of the R-curve. D_o is an empirical constant that may be interpreted as the size in the middle of the transition between the

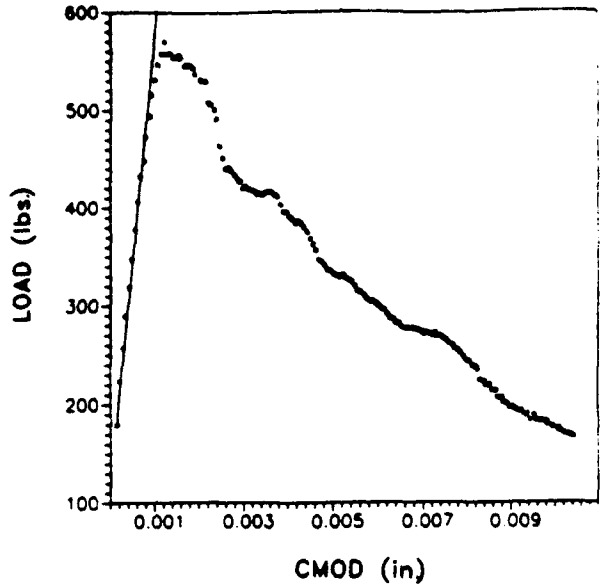

Fig. 6—Typical load-CMOD curve for high-strength concrete specimens used, D = 76.2 mm

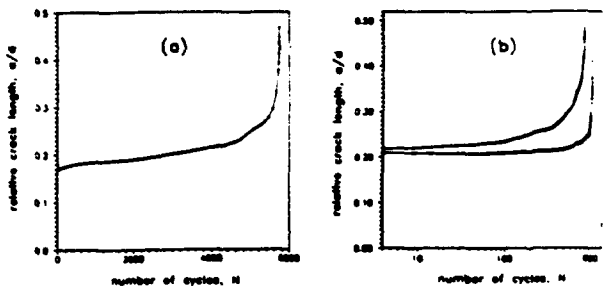

Fig. 7—Typical plots of relative crack length versus number of cycles N recorded for (a) one medium and (b) two large specimens

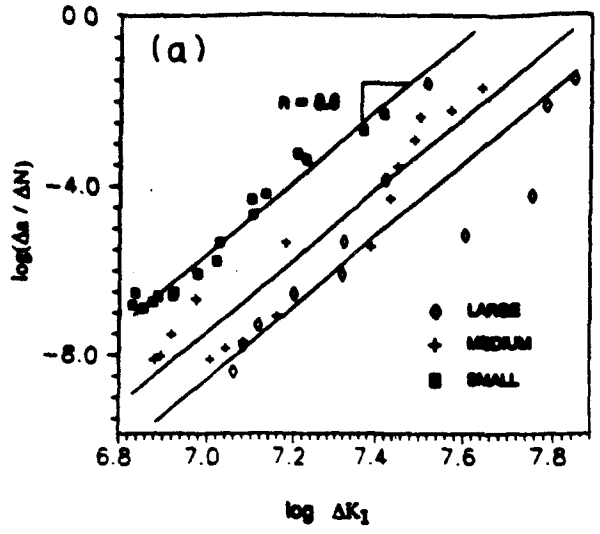

Fig. 8(a)—Linear regression according to original Paris Law (data points refer to individual specimens)

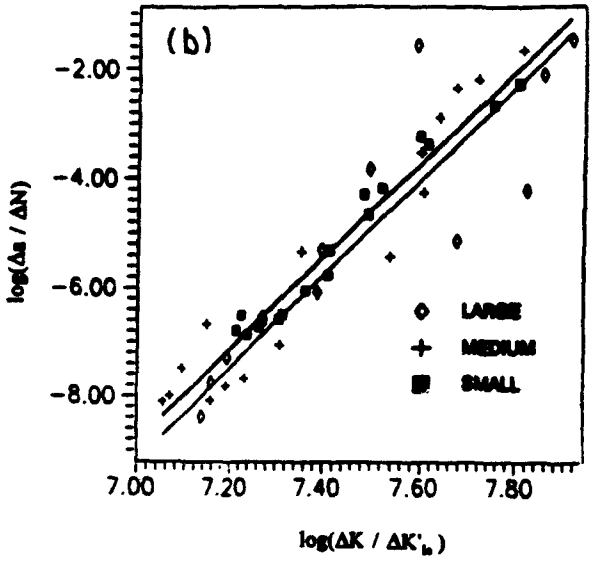

Fig. 8(b)—Linear regression according to size-adjusted Paris law (data include two specimens per size)

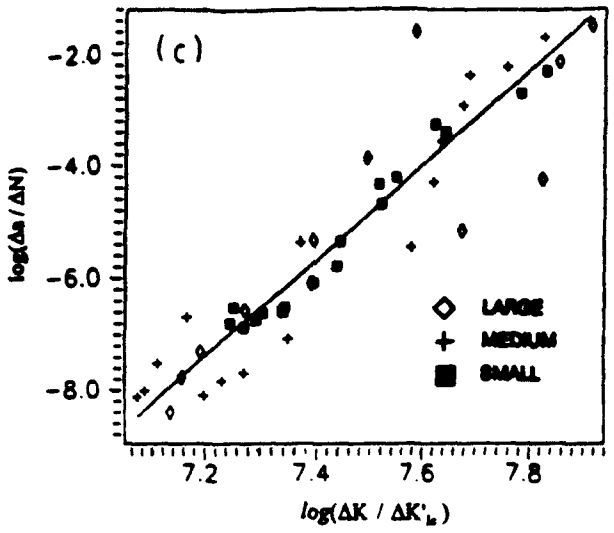

Fig. 8(c)—Linear regression with optimal fit (data include two specimens per size)

strength theory and linear elastic fracture mechanics. For $D \ll D_o$ ($\beta \ll 1$), Eq. (1) is equivalent to crack growth being proportional to the nth power of the nominal stress amplitude [Eq. (10), Reference 5], while for $D \gg D_o$ ($\beta \gg 1$), the crack growth per cycle according to Eq. (1) depends only on the amplitude of the stress intensity factor, as in the classical Paris law (which is asymptotically approached for sufficiently large sizes).

The size-adjusted Paris law [Eq. (3)] has been verified for normal concrete but not, however, for high-strength concrete. Eq. (1) can be reduced to a linear regression plot by plotting log ($\Delta a/\Delta N$) versus log(ΔK), as a means of size adjustment, versus log($\Delta K/K_{Ic}$). The slope of the regression lines in all the figures is the same (taken as the average value of the regression slopes for individual sizes); the slope is $n = 8.6$, which is a slightly smaller value than that obtained from normal concrete, which was $n = 10.6$. Fig. 8(a) shows the plot of the present test results for all specimen sizes when the value of K_{Ic} is replaced by $K'_{If} = 1.0$, as in the original (unadjusted) Paris law [Eq. (1)]; the regression lines represent the optimal fits obtained separately for each specimen size. The fact that these regression lines do not coincide and are not even close indicates that the original Paris law is not valid.

When the size adjustment according to Eq. (1) is introduced and the value of D_o equal to the monotonic value (31.8 mm) obtained from the size effect method is used, one obtains the plot shown in Fig. 8(b) in which $K'_{Ic} = K'_{If}[\beta/(1+\beta)]^{1/2}$ = relative values of K_{Ic} from Eq. (3) (note that two of the three straight lines nearly coincide). The fact that the regression lines for different sizes are now very close to each other confirms that the size-adjusted Paris law [Eq. (1)] is valid. Furthermore, Fig. 8(c) shows the plot when all the results are fitted by the same regression line, for which $D_o = 1.5d_o$ where d_o is the value for monotonic loading.[15] For normal strength concrete, the value of $D_o = 10d_o$ was found.[5] Since D_o is proportional to the length of the fracture process zone from the size effect method, it can be concluded that the fracture process zone is much smaller in high-strength concrete than in normal concrete during fatigue loading.

Note that Eq. (1) and (3) yield

$$\Delta K_I = K'_{If}\left(\frac{1}{\kappa}\frac{\Delta a}{\Delta N}\right)^{\frac{1}{n}}\sqrt{\frac{\beta}{1+\beta}} \qquad (4)$$

This equation can further be algebraically rearranged to the linear regression plot

$$Y = A_I + B_I X \qquad (5)$$

in which

$$Y = \left(\frac{\Delta a}{\Delta N}\right)^{\frac{2}{n}}\Delta K_I^{-2}, X = \frac{1}{D} \qquad (6)$$

$$A_1 = \kappa^{\frac{2}{n}} K_{ij}^{-2}, B_1 = \kappa^{\frac{2}{n}} K_{ij}^{-2} D_0 \quad (7)$$

Passing a regression line of measured Y-points versus X, one obtains the values of slope B_1 and Y-intercept A_1 from which one can evaluate

$$\kappa = A_1^{\frac{n}{2}} K_{ij}^n, D_0 = \frac{B_1}{A_1} \quad (8)$$

The result is $D_o = 1.42d_o$, which is close to the value $1.5d_o$ found from nonlinear optimization. This linear regression is an alternative to the direct nonlinear optimization in the plot of the Paris law in Fig. 8(c), which is nonlinear. However, with a nonlinear optimization subroutine such as the Marquardt-Levenberg algorithm, direct determination of D_o and κ is also quite easy.

DEFLECTION CURVE

Comparison of the calculated and measured deflection curve is the easiest and most unambiguous check of the fracture formulation for monotonic loading. For the special case of rate-independent elastic behavior and monotonic loading, the curve of load P versus load-point deflection u of a fractured specimen is given by the following well-known relations[16]

$$u = \frac{P}{E}\bar{C}(a), \alpha = \frac{a}{D} \quad (9)$$

$$\bar{C}(a) = \bar{C}_o + \frac{2}{b}\varphi(\alpha) \quad (10)$$

$$\varphi(\alpha) = \int_0^\alpha [f(\alpha')]^2 d\alpha' \quad (11)$$

$$P = b\sqrt{D}\frac{K_k}{f(\alpha)} \quad (12)$$

in which $\bar{C}(a)$ is the unit load-point compliance (i.e., compliance for unit value of elastic modulus E) and $\bar{C}_o$ is the initial unit compliance at $a = a_o$. To determine the monotonic load-deflection curve, one chooses a series of values of the crack length a, and calculates u from Eq. (10) and (11) and P from Eq. (12). Thus, Eq. (10) through (12) define the load-deflection curve parametrically.

For fatigue loading, the load-deflection curve may be calculated similarly to Eq. (10) through (12). From Eq. (1), we express ΔN as a function of $\Delta\alpha$ and substitute the expression $\Delta K_I = \Delta P f(\alpha)/\sqrt{D}$. Integration then yields

$$N(\alpha) = \frac{1}{\kappa}\left(\frac{K_k b\sqrt{d}}{\Delta P}\right)^n \int_0^\alpha [f(\alpha')]^{-n} d\alpha' \quad (13)$$

Eq. (10) can be rewritten in the form

$$\Delta u = \frac{PD}{E}\left[\frac{d\bar{C}(a)}{da}\right]\Delta\alpha \quad (14)$$

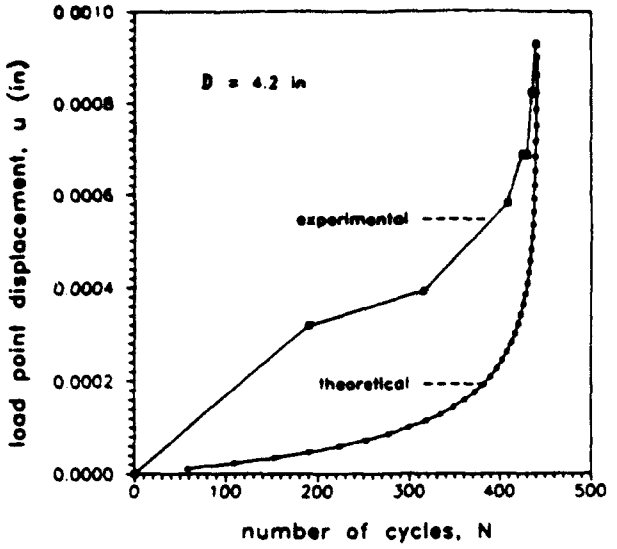

Fig. 9—Measured and calculated load-point displacements for medium-size specimen

Thus Eq. (13) and (14) define the load-deflection curve for cyclic loading. Choosing a sequence of values of α, one can calculate from Eq. (13) the number of cycles to reach this value and the corresponding displacement value from Eq. (14).

The load-point deflection curve calculated in this manner is shown in Fig. 9. For comparison, the experimental curve is also plotted. At the end there is a good agreement, but at the beginning of the test there is a large discrepancy. To eliminate this discrepancy is probably beyond the capability of the present theory, which represents a generalization of LEFM to fatigue. Probably it will be necessary to make generalizations akin to the R-curve for monotonic loading that take into account in a simplified manner the growth of the apparent fracture toughness associated with the growth of the process zone size.[17]

CONCLUSIONS

1. As previously shown for normal concrete, the Paris law is also applicable to high-strength concrete, but only if the specimen sizes do not vary significantly.

2. For a broad range of specimen or structure sizes, the Paris law needs to be adjusted in the same manner as previously proposed for normal concrete. The classical, unadjusted Paris law is approached asymptotically for large specimen sizes.

3. The transitional size D_o of the size adjustment of the Paris law has a value rather close to that for monotonic fracture, while previous investigations of normal concrete indicated this value to be an order of magnitude higher. This means that the behavior of typical laboratory fracture specimens of high-strength concrete under cyclic loading is quite close to linear elastic fracture mechanics, while that of normal concrete was previously found roughly in the middle of the transition between the strength theory and linear elastic fracture mechanics. This further implies that the fracture process zone under cyclic loading is in high-strength concrete about

an order of magnitude smaller than in normal concrete, and that the classical Paris law, unadjusted for size, is asymptotically approached for smaller specimen sizes than those for normal concrete.

4. The determination of the parameters governing the size adjustment of the Paris law can be reduced to a linear regression plot. From this plot, the necessary size adjustment for fatigue can be determined without direct fitting of the Paris law by nonlinear optimization.

5. The size-adjusted Paris law shows good agreement with test data for the entire range of the number of cycles to failure, which was from 200 to 41,000 at various levels of the upper load limit.

6. The size adjustment of the Paris law approximately agrees with the terminal deflection measurements when the deflections are calculated according to linear elastic fracture mechanics. However, the early deflection history is grossly underpredicted in this manner.

ACKNOWLEDGMENTS

Partial financial support from AFOSR under Grant 91-0140 to Northwestern University and from NSF Science and Technology Center for Advanced Cement Based Materials at Northwestern University is gratefully acknowledged. Thanks for valuable cooperation are also due to Dr. Jaime Moreno of the Material Service Corporation, Chicago, who provided the high-strength concrete used in this investigation. Finally the authors would like to thank Milan Jirásek for valuable comments on the analysis of the test results, and Daniel Jansen and John Chirayil for their invaluable assistance with the laboratory experiments.

REFERENCES

1. Getu, Ravindra; Bažant, Zdeněk P.; and Karr, Martha E., "Fracture Properties and Brittleness of High-Strength Concrete," *ACI Materials Journal*, V. 87, No. 6, Nov.-Dec. 1990, pp. 608-618.

2. Carrasquillo, Ramon L.; Nilson, Arthur H.; and Slate, Floyd O., "Properties of High-Strength Concrete Subjected to Short Term Loads," ACI JOURNAL, *Proceedings* V. 78, No. 3, May-June 1981, pp. 171-178.

3. Shah, Surendra P., "Fracture Toughness of High-Strength Concrete," *ACI Materials Journal*, V. 87, No. 3, May-June 1990, pp. 260-265.

4. Baluch, M. H.; Qureshy, A. B.; and Azad, A. K., "Fatigue Crack Propagation in Plain Concrete," *SEM/RILEM International Conference on Fracture of Concrete and Rock*, Houston, June 1987.

5. Bažant, Z. P., and Xu, Kangming, "Size Effect in Fatigue Fracture of Concrete," *ACI Materials Journal*, V. 88, No. 4, July-Aug. 1991, pp. 390-399.

6. Perdikaris, P. C., and Calomino, A. M., "Kinetics of Crack Growth in Plain Concrete," *SEM/RILEM International Conference on Fracture of Concrete and Rock*, Houston, June 1987.

7. Swartz, S. E., and Go, C. G., "Validity of Compliance Calibration to Cracked Concrete Beams in Bending," *Journal of Experimental Mechanics*, V. 24, No. 2, June 1984, pp. 129-134.

8. RILEM Recommendations, "Size Effect Method for Determining Fracture Energy and Process Zone Size of Concrete," *Materials and Structures, Research and Testing* (RILEM, Paris), V. 23, 1990, pp. 461-465.

9. Paris, P. C., and Erdogan, F., "Critical Analysis of Propagation Laws," *Transactions of ASME Journal of Basic Engineering*, V. 85, 1963, pp. 528-534.

10. Paris, P. C.; Gomez, M. P.; and Anderson, W. E., "Rational Analytic Theory of Fatigue," *Trend in Engineering*, V. 13, No. 1, Jan. 1961.

11. Broek, David, *Elementary Engineering Fracture Mechanics*, Martinus Nijhoff Publishers, 1986.

12. Tada, H.; Paris, P. C.; and Irwin, G. R., *Stress Analysis of Cracks Handbook*, Del Research Corporation, 1973.

13. Bažant, Z. P., "Size Effect in Blunt Fracture: Concrete, Rock, Metal," *Journal of Engineering Mechanics*, ASCE, V. 110, No. 4, Apr. 1984, pp. 518-535.

14. Bažant, Z. P., and Kazemi, M. T., "Determination of Fracture Energy, Process Zone Length and Brittleness from Size Effect, with Application to Rock and Concrete," *International Journal of Fracture*, V. 44, pp. 111-131.

15. Bažant Zdeněk P., and Pfeiffer, Phillip A., "Determination of Fracture Energy from Size Effect and Brittlenss Number," *ACI Materials Journal*, V. 84, No. 6, Nov.-Dec. 1987, pp. 463-480.

16. Bažant, Zdeněk P., and Cedolin, Luigi, *Stability of Structures*, Oxford University Press, 1991, pp. 760-798.

17. Bažant, Z. P., "Size Effects on Fracture and Localization: Aperçu of Recent Advances and Their Extension to Simultaneous Fatigue and Rate-Sensitivity," *Fracture Processes in Concrete, Rock and Ceramics*, E & F N Spon, Noordwijk, The Netherlands, June 1991, pp. 417-429.

18. Hordijk, D. A., "Local Approach to Fatigue of Concrete," PhD thesis, Delft University of Technology, 1991.

19. Kim, Kunsoo, and Mulbeen, Abdul, "Relationship between Differential Stress Intensity Factor and Crack Growth Rate in Cyclic Tension in Westerly Granite," *Fracture Mechanics Methods for Ceramics, Rocks, and Concrete, ASTM STP 745*, S. W. Freimen and E. R. Fuller Jr., eds., American Society for Testing and Materials, 1981, pp. 157-168.

20. Parker, A. P., *Mechanics of Fracture and Fatigue*, E & F N Spon Ltd., 1981.

21. Swartz, Stuart E.; Hu, Kuo-Kuang; and Jones, Gary L., "Compliance Monitoring of Crack Growth in Concrete," *Journal of Engineering Mechanics*, EM4, Aug. 1978, p. 789.

Geometric Damage Tensor Based on Microplane Model

By Ignacio Carol,[1] Associate Member, ASCE, Zdeněk P. Bažant,[2] Fellow, ASCE, and Pere C. Prat,[3] Associate Member, ASCE

Abstract: An appealing approach to formulate constitutive models for characterizing distributed damage due to microcracks and voids is continuum damage mechanics with the concepts of effective stress and strain equivalence. In that approach, in which damage is imagined to characterize the reduction of the net stress-transmitting cross-section area of the material, the constitutive model is separated into two independent parts, one for damage and the other for elastic and inelastic behavior (rheology) other than damage, which, if combined appropriately, give the overall constitutive behavior. However, the existing multidimensional formulations for damage are quite complex, and practical implementations capable of fitting experimental data are hard to obtain. The microplane models, by contrast, provide conceptual simplicity and close fits of multiaxial test data for concrete, soils, etc., although, as formulated in the past, various kinds of physical phenomena were mixed in the definition of the microplane stress-strain curves. In this work the microplane theory is reformulated in a manner that separates damage from rheology and makes the formulation fit the basic framework of continuum damage mechanics. Aside from a kinematic constraint between macrostrains and microstrains, the model satisfies a static constraint such that the effective microstresses are the resolved components of the effectiveness macrostresses.

Introduction

Inelastic phenomena are of two kinds: (1) Those that reduce material stiffness and cause strain-softening; and (2) those that do not. The former represent damage caused by nucleation, growth, and coalescence of microcracks and voids, and the latter consist of plastic slip, friction, creep, etc. Modeling each of these phenomena is difficult enough, but the complexity becomes formidable when both kinds of phenomena are combined, which occurs in many materials. In this paper we seek to separate these two phenomena to achieve simplification and clarity. We assume the microcracks and voids to remain homogeneously distributed so that the material can be microscopically treated as a continuum.

The real stress and strain fields at the microlevel are highly scattered and nonsmooth. Therefore, the continuum strains and stresses must be taken as the "average" values of these fields over a certain representative volume. However, applicability of damage in terms of such stresses and strains must be restricted to situations in which no localization phenomena take place, i.e., no macrocracking or shear-banding occurs. If the damage and strains

[1]Assoc. Prof. of Civ. Engrg., ETSECCPB-Tech. Univ. of Catalonia, 08034 Barcelona, Spain; formerly Visiting Scholar, Ctr. for Advanced Cement-Based Mat., Northwestern Univ., Evanston, IL 60208.

[2]Walter P. Murphy Prof. of Civ. Engrg., Ctr. for Advanced Cement-Based Mat., Northwestern Univ., Evanston, IL 60208.

[3]Assoc. Prof. of Civ. Engrg., ETSECCPB-Tech. Univ. of Catalonia, 08034 Barcelona, Spain; formerly Visiting Scholar, Ctr. for Advanced Cement-Based Mat., Northwestern Univ., Evanston, IL.

Note. Discussion open until March 1, 1992. To extend the closing date one month, a written request must be filed with the ASCE Manager of Journals. The manuscript for this paper was submitted for review and possible publication on September 22, 1990. This paper is part of the *Journal of Engineering Mechanics*, Vol. 117, No. 10, October, 1991. ©ASCE, ISSN 0733-9399/91/0010-2429/$1.00 + $.15 per page. Paper No. 26299.

can localize, unrealistic results can be obtained with this approach unless additional techniques such as crack band model, nonlocal models, or localization analysis are implemented in the context of the "smeared" approach to damage (Bažant and Cedolin 1979; Crisfield 1982; Pijaudier-Cabot and Bažant 1987; de Borst 1987; Ortiz 1987; Ortiz and Quigley 1989; Carol and Prat 1990). Alternatively, formulations can also be obtained by "discrete" crack models based on fracture mechanics with softening cohesive (crack-bridging) zone (Hillerborg et al. 1976; Hillerborg 1984).

The classical approach to distributed damage is the continuum damage mechanics. As originated by Kachanov (1958) for one-dimensional problems, the basic concept of continuum damage mechanics looks simple: a reduction of the net stress-carrying cross-section area fraction caused by the growth of microcracks and voids in the material microstructure. This is a purely geometric characteristic, reflecting the fact that the "effective" (or "true") stresses in the undamaged part of the cross section are higher than the stresses in the macroscopic continuum (the apparent stresses). A law can be postulated to predict the decrements of the current cross-sectional area in terms of stress, strain, and damage, and simple but useful results can be obtained for complex phenomena such as creep rupture of metals (Kachanov 1958; Rabotnov 1969a,b; Leckie 1978; Lemaitre 1984) and, more recently, the delayed failure of concrete under sustained uniaxial compression (Carol 1989).

The multiaxial generalization of continuum damage mechanics, however, poses a formidable challenge that, to a large extent remains unsolved. The net stress-carrying area fractions for the different directions in space cannot be easily integrated to give a vectorial or tensorial damage measure that would define the "effective" or "true" stress tensor from the macroscopic stress tensor and the apparent or reduced macroscopic stiffness tensor. A review of the existing multiaxial generalizations presented in the section headed "Existing Models for Distributed Damage" shows a number of possibilities, some of them rather complicated and not always very satisfactory in terms of data-fitting capabilities, especially when the classical macroscopic tensorial approach is pursued. This is the case when the constitutive model is formulated phenomenologically without recourse to any geometric concepts related to microstructure and the inelastic phenomena are formulated as functions of stress and strain invariants. Nevertheless, as will be shown in the section headed "Effective Stress and Damage Tensor Uncoupled from Rheology" some basic general structure for continuum damage models based on the concepts of true, or effective, stress and macro-micro strain compatibility can also be established in three dimensions. This basic structure provides a suitable framework for separating the constitutive model in two parts, one for damage and the other for rheology, each of which can be formulated independently and then combined. This provides a convenient flexibility for combining damage with various complex types of inelastic material behavior.

Compared to multiaxial continuum damage model theories, much closer fits of test data for concrete and considerable theoretical simplification (albeit at the expense of computer time requirements) is achieved by the microplane models. In general terms, already suggested for plasticity in a famous classical paper by G. I. Taylor (1938), this approach characterizes the material properties independently on planes of various orientation, which were initially called the slip planes (Batdorf and Budiansky 1949) but renamed microplanes when the concept was extended to materials incapable

of plastic slip (Bažant 1984). The basic material behavior is defined on the microplanes as a set of relations between the stresses and strains acting on that plane. These relations include all the rheologic phenomena involved in material behavior (elasticity, damage, plasticity) at the same time, in an inseparable manner. The microplane behavior is constrained to the macroscopic continuum behavior by a suitable macro-micro constraint having the form of a variational equation based for example on the principle of virtual work. In some studies (Bažant 1984; Bažant and Oh 1983, 1985; Bažant and Gambarova 1984; Bažant and Prat 1988; Carol et al. 1990) the microplane concept, originally developed for metal plasticity, was extended to materials exhibiting damage with strain softening. The resulting model, briefly described in the section headed "Kinematically Constrained Microplane Model," was shown to be capable of a very good description of the existing test data on tensile strain-softening of concrete due to microcracking as well as the nonlinear triaxial behavior of concrete, including strain-softening in compression and shear under different confining lateral stresses.

This paper [which was briefly summarized in a conference paper by Bažant and Carol (1990)] reconciles both types of constitutive models (continuum damage and microplane), and presents a new interpretation of the microplane formulation as a continuum damage model. This leads to the formulation of a fourth-order nonsymmetric geometric damage tensor. The term "geometric" reflects the fact that this tensor is independent of any particular rheologic model, and depends only on the reduction of the net stress-carrying area fraction in various directions in the material, which are geometric characteristics (the term "geometric," of course, does not imply that all the geometric characteristics, such as spatial crack and void configuration and statistical distributions, are taken into account). The proposed geometric damage tensor achieves a three-dimensional generalization of Kachanov's (1958) one-dimensional net stress-carrying area fraction. It is computed by integrating the geometric damage at each particular microplane over all the spatial directions. As a continuum damage model, it gives the relationship between the macroscopic and effective stress tensors and between the initial and current stiffness matrices, and can be combined with any rheologic model (elasticity, plasticity, viscoelasticity). As a microplane formulation, it also has the additional advantage of an a priori knowledge that very good data fitting can be obtained in practical applications. The derivation of the new damage tensor is presented in two different ways: In the section headed "Derivation of Geometric Damage Tensor from Concrete Model" it is derived from a version of the microplane model with particular microplane laws used previously for concrete (Carol et al. 1990), and in the section headed "Rheology-Independent Derivation of Geometric Damage Tensor" it is derived without recourse to any particular stress-strain laws.

Existing Models for Distributed Damage

Consider first the example of a simple one-dimensional continuum damage formulation. In this case damage such as microcracks or voids may be regarded as geometric, representing a reduction in some ratio α of the net stress-carrying area in the microstructure of the material [Fig. 1(*a*)]. For uniaxial stress (macrostress) σ, we may thus write

$$\sigma = \alpha\tau \qquad (1)$$

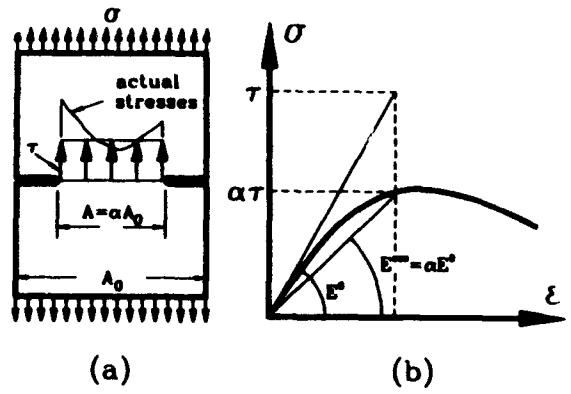

FIG. 1. Effective Stress and Damage in One Dimension: (a) Interpretation of τ and α (b) Stress-strain Diagram

in which τ is called the effective (or true) stress; and α varies from 1 to 0 when damage increases (alternatively, damage can also be represented by $\omega = 1 - \alpha$ varying from 0 to 1); τ represents the average stress in the stress-carrying portion of the cross-sectional area in the microstructure. Assuming a linear elastic relation, i.e., $\tau = E^0\varepsilon$, where E_0 is the elastic modulus of the undamaged material and ε the strain, one has

$$\sigma = \alpha E^0 \varepsilon \quad \ldots\ldots (2)$$

This equation may also be written as

$$\sigma = E^{sec}\varepsilon \quad \ldots\ldots (3a)$$

$$E^{sec} = \alpha E^0 \quad \ldots\ldots (3b)$$

where E^{sec} = secant modulus [Fig. 1(*b*)]. Now, a damage evolution law can be assumed for α. If it is defined in terms of ε and introduced in (2) or (3), an explicit one-dimensional stress-strain relation for damage ensues. As seen in this simple example, the formulation of a continuum damage model includes three steps.

1. Characterization of damage by means of a variable (α or ω) or set of variables.
2. Dependence of the effective stress or secant modulus on the damage variable ($\tau = \sigma/\alpha$ or $E^{sec} = \alpha E^0$)
3. Evolution laws for the damage variable; e.g. $\dot{\alpha} = F(\sigma, \dot{\epsilon}, \alpha \cdots$ (F = function or functional).

In triaxial generalization, some early models included damage-related concepts (e.g. stiffness degradation) that did not explicitly introduce a damage variable as such, but instead derived the evolution laws from a "fracturing surface" with attributes similar to the classical yield surface in plasticity, defining this surface in terms of stress and strain invariants with hardening-softening rules, internal variables, etc. (Dougill 1976; Bažant and Kim 1979). That was a phenomenologic approach to the problem whose

most sophisticated forms became impractical because of the high complexity and the presence of too many parameters and empirical functions, giving little insight into the physical processes actually occurring at the microstructural level.

Most of the existing theories dealing with three-dimensional stiffness degradation incorporate some kind of damage variable in their definition and can be satisfactorily described in terms of the foregoing three-step scheme. The simplest possible characterization of three-dimensional damage is a scalar variable, which can be thought of as the damage caused by a field of spherical microvoids with the same stress-carrying area reduction in all spatial directions (Leckie 1978; Lemaitre and Chaboche 1978; Mazars 1985; Resende 1987; Frantziskonis and Desai 1987). To capture the anisotropic nature of damage caused by microcracks with predominant orientation, damage tensors of various orders have been proposed: vectors (Davidson and Stevens 1973; Krajcinovic and Fonseka 1981; Suaris and Shah 1984; Costin 1985; Costin and Stone 1987); second-order tensors (Vakulenko and Kachanov 1971; Dragon and Mróz 1979; Kachanov 1980; Murakami and Ohno 1980; Betten 1983; Oda 1983; Murakami 1987; Suaris 1987); fourth-order tensors (Chaboche 1979, 1981; Ortiz 1985; Simó et al. 1987; Yazdani and Schreyer 1988), or even eighth-order tensors (Chaboche 1978).

The influence of the damage variable on the secant stiffness or effective stresses, along with the definition of the laws for damage evolution (steps 2 and 3), depend much on what kind of damage variable is adopted. Using a scalar damage variable, these assumptions can be made analogous to the one-dimensional case, but then no induced anisotropy can be accounted for. Some authors use the secant stiffness itself (or a related quantity such as the increment of compliance over the initial or elastic one) as a fourth-order damage tensor (Ortiz 1985; Simó et al. 1987; Yazdani and Schreyer 1988). With this approach, the dependence in step 2 is defined implicitly, but the stiffness tensor does not have a direct physical meaning as a damage variable, and the corresponding evolution laws (step 3) have to be established again, mainly on a phenomenologic basis.

In a certain sense the intermediate option of a second-order tensor as a damage variable seems appealing in the face of other possibilities. Consider for instance the "fabric tensor" proposed by Oda (1983) for the analysis of cracked rock masses, which was an improvement over other previous similar proposals. This tensor is defined as an integral over all the possible crack orientations and sizes of an expression including the crack density function. It is a symmetric dimensionless tensor, and some of its invariants can be interpreted in terms of the overall geometric effect caused by the field of microcracks. The concept of a second-order damage tensor also seems to be supported by theoretical considerations relative to frame invariance (Leckie and Onat 1980), as well as by experimental microstructural measurements of the corresponding "damage ellipsoid" in quite different materials (e.g. measurements of cancellous bone structure and granular soil fabric; Cowin 1985). Unfortunately, the attractive concept of a second-order fabric tensor contrasts with the absence of equally clear and direct relations for the degradation of the macroscopic secant stiffness tensor and for the effective stresses in the cracked medium. Cowin (1985) deduces the most general dependence of the secant stiffness on the second-order fabric tensor permitted by the condition of frame invariance, which turns out to be a complex polynomial expression, with the somewhat disappointing peculiarity that at least a quadratic (and likely even higher) dependence on the first invariant

of the fabric tensor must be involved in the relation if orthotropic symmetry is to be preserved in the cracked material. Some other authors, on the other hand, handle the problem of reduction of the net stress-carrying area due to microcracks through simulation of a finite deformation field with the equivalent effects of area reduction in various directions in space, or through certain geometric and tensorial considerations. However, either they do not use a second-order tensor as a damage variable [Krajcinovic and Fonseka (1981), who used a vector], or they get an awkward nonsymmetric effective stress tensor, which must further be symmetrized in some arbitrary way in order to obtain a practical formulation (Murakami and Ohno 1980; Betten 1983).

A different approach is suggested by studies of a homogeneous medium containing periodic arrays of inclusions or penny-shaped cracks. In such studies, the overall elastic modulus is obtained by calculating the approximate stress fields in the solid, by the so-called self-consistent method or other related techniques (Budiansky and O'Connell 1976; Nemat-Nasser et al. 1982; Horii and Nemat-Nasser 1983; Attiogbe and Darwin 1986; Kachanov 1987; Aboudi 1987). This approach can be useful when the overall modulus of a continuum (e.g. rock, a composite material) containing an a priori known field of cracks or inclusions needs to be computed. However, in most of those theories the field of microcracks and the configuration of inclusions must be known in some detail; in constitutive modeling a damage variable characterizes these effects in a smeared way. Also, the relationships obtained for step 2 are usually very complicated (and sometimes they even do not have an explicit form but are a set of nonlinear equations to be solved numerically for each practical case); they should be explicitly tractable expressions to be introduced as one component of the constitutive model. As a result [although some authors did use this approach to derive or support the choice of relations included in step 2; (Chaboche 1979; Oda 1983)], this approach in general seems to be only of limited usefulness for the development of complete macroscopic constitutive relationships.

Effective Stress and Damage Tensor Uncoupled from Rheology

To define the effective stress in three dimensions the following tensorial expression similar to (1) for one dimension has been introduced (Rabotnov 1969a,b; Chaboche 1979; Lemaitre and Chaboche 1985; Simó et al. 1987):

$$\sigma_{ij} = \alpha_{ijkm}\tau_{km} \quad \ldots\ldots (4)$$

where the repetition of lower-case indices implies summation over 1, 2, 3; σ_{ij} and τ_{km} = Cartesian components of the macroscopic and effective (or true) stress tensors σ and τ; and α_{ijkm} = components of a fourth-order dimensionless tensor α characterizing damage (which can also be expressed as $\alpha = I - \omega$, where I = fourth-order identity tensor; and ω = alternative damage tensor).

Symmetry is assumed for the macroscopic stresses σ as well as for the effective stress tensor τ. Thus, the components α_{ijkm} must preserve the interchangeability of index i with j and k and m, and can be grouped into a 6×6 matrix in the context of the six-component vectorial representation of symmetric stress tensors. However, no interchangeability of indices i, j with k, m is assumed, which means that no symmetry is required for the 6×6 matrix. This nonsymmetry is needed so as not to exclude the possibility of representing phenomena such as internal friction.

To establish more precisely the meaning and nature of the damage tensor α and effective stresses τ, the hypothesis of strain equivalence is also assumed (Chaboche 1979; Lemaitre and Chaboche 1985; Simó et al. 1987). According to this hypothesis, the effective stresses τ are defined as the stresses that would exist in the undamaged material subjected to the same strains ε as those that produce the macroscopic stress σ in the damaged material. With this definition the components of the 6×6 damage tensor α can be geometrically interpreted as a net (effective) stress-carrying area fraction in every coordinate direction, with each stress component considered to act independently on a plane of that direction.

In the relationship between τ and ε, any rheologic model can be used; e.g., using linear elasticity ($\tau_{km} = D^{el}_{kmpq}\varepsilon_{pq}$) as the rheologic model, one immediately obtains the expression for the secant or reduced elastic stiffness

$$\sigma_{ij} = D^{sec}_{ijpq}\varepsilon_{pq} \quad \ldots\ldots (5a)$$

$$D^{sec}_{ijkm} = \alpha_{ijrs}D^{el}_{rspq} \quad \ldots\ldots (5b)$$

These equations are the three-dimensional counterpart of (3).

In general, a nonlinear rheologic model may be used instead of linear elasticity to compute the effective stresses τ from prescribed strain ε (which can in general be done according to a step-by-step algorithm). Because the value of α can be computed independently according to the damage laws, the macroscopic stress σ can then be obtained using (4). Thus, the overall constitutive model can be decomposed in two independent parts, one for damage and another for rheology. Different models can be used for each part and then combined. Establishing the laws for the evolution of α, one can get an entire new class of models from the combination of the α evolution law with any rheologic model for τ. This opens new interesting possibilities and presents the challenge of developing a satisfactory law for the evolution of the damage tensor α, probably the weakest point at present and the main goal of this paper.

It should be pointed out that the idea of combining damage and rheology is not new, of course. For example Leckie (1978) and Lemaitre and Chaboche (1978) combined viscoplasticity and damage, and Bažant and Chern (1985) combined concrete creep with damage due to smeared cracking. The new idea is to combine damage and rheology by means of the microplane model, which has the benefit of yielding the form of the damage tensor.

Kinematically Constrained Microplane Model

As already mentioned, the new damage tensor proposed here was derived by reformulating the latest version of the microplane model for concrete in an explicit form (Carol et al. 1990). Therefore, only the basic hypotheses and main features need to be given here.

The model is based on the concept of a microplane. A microplane is an arbitrary plane on which the constitutive properties are defined. Instead of defining them by means of a relation between tensors σ_{ij} and ε_{ij}, these properties are defined by means of a relation between the stress and strain components on a microplane, which is conceptually much simpler because there are fewer stress and strain components and the problems of tensorial invariance do not arise on the microplane level. The macroscopic stress-

strain rc nship is then obtained by integrating under some suitable micro-macro constraint over the microplanes of all spatial orientations n. This integration guarantees the condition of tensorial invariance to be satisfied automatically. There are two simple alternatives for the macro-micro constraint relating the behavior of all the microplanes to the macroscopic behavior: the static and kinematic constraints, both suggested by Taylor (1938). In the static constraint, the microplane stresses represent the projections of the macroscopic stress tensor on the plane considered; the kinematic constraint does the same for strains. Note that both types of constraints cannot apply at the same time if general stress-strain laws are considered at the microplane level.

Although the static constraint was used exclusively in the works dealing with metal plasticity (Batdorf and Budiansky 1949; Lin 1968), the kinematic constraint was recognized to be necessary to ensure that the microplane system be stable in strain-softening behavior (Bažant 1984; Bažant and Oh 1983, 1985). If the kinematic constraint is assumed, the normal and shear strains ε_N and ε_T, on the microplane with unit normal n, [Figs. 2(*a* and *b*)] can be obtained as projections of the strain tensor ε_{ij}. Previous studies (Bažant and Prat 1988) revealed that in order to obtain any desired Poisson ratio $\nu(-1 \le \nu \le 0.5)$ as well as capture the effect of the hydrostatic pressure on the incremental stiffness, the normal microplane strain ε_N needs to be further split into its volumetric and deviatoric components ε_V and ε_D. This split, however, has no direct physical meaning; rather, the physical meaning is that the microplane stress depends not only on ε_N but also on the lateral normal stress ε_L along the directions lying within the microplane (the mean value of ε_L can be easily expressed in terms of ε_V and ε_D). The resulting expressions for the microplane strains are

$$\varepsilon_V = \frac{\varepsilon_{kk}}{3} = \frac{\delta_{km}}{3}\varepsilon_{km} \quad \text{..... (6a)}$$

$$\varepsilon_D = \left(n_k n_m - \frac{\delta_{km}}{3}\right)\varepsilon_{km} \quad \text{..... (6b)}$$

$$\varepsilon_{T_i} = \frac{1}{2}(\delta_{ik}n_m + \delta_{im}n_k - 2n_i n_k n_m)\varepsilon_{km} \quad \text{..... (6c)}$$

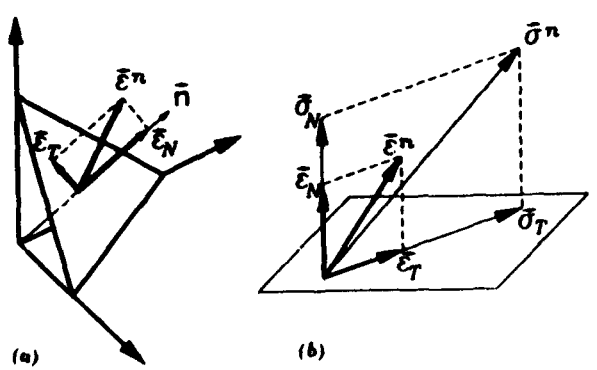

FIG. 2. Stress and Strain Components on Microplane

where δ_{ij} = Kronecker delta; and n_i = direction cosines of the vector n normal to the microplane. Note that ε_D and ε_T can also be obtained as the normal and shear components of the projection of the deviatoric strain tensor $e_{ij} = \varepsilon_{ij} - \varepsilon_V\delta_{ij}$ on the microplane, but that the deviatoric part of the strain projection, which is $\varepsilon_{T_i} = \varepsilon_{ij}n_j - \varepsilon_N n_i$, differs from (6). Eq. (6) for ε_{T_i} is obtained as the symmetric part of this tensor (the asymmetric part has no effect on stresses).

In view of the kinematic constraint imposed, the microplane stresses in general do not and cannot represent the resolved components of the (macroscopic) stress tensor. Equilibrium must nevertheless be imposed in an approximate overall sense. For this purpose, application of the principle of virtual work was proposed by Bažant (1984). This principle yields the following condition of static equivalence of the stress (macrostress) tensor σ_{ij} with the normal ($\sigma_N = \sigma_V + \sigma_D$) and shear stresses ($\sigma_{T_i}$), on the microplanes:

$$\frac{4\pi}{3}\sigma_{ij}\delta\varepsilon_{ij} = 2\int_\Omega (\sigma_N\delta\varepsilon_N + \sigma_{T_i}\delta\varepsilon_{T_i})f(n)\,d\Omega \quad \text{..... (7)}$$

The left-hand side represents the virtual work of the macrostresses in an elementary unit sphere; and the right-hand side represents the virtual work of the microplane stresses on the microplane strains on all the elementary facets on this sphere, representing the microplanes. The integration needs to be carried out only over the area of a unit hemisphere, Ω, because the stresses and strains at its diametrically opposite points are equal. Function $f(n)$ may be used to introduce initial material anisotropy. For isotropic materials, $f(n) \equiv 1$.

Substituting microplane strain variations according to (1) and (2), and setting $\sigma_N = \sigma_V + \sigma_D$, where σ_N, σ_V, and σ_D are the normal, volumetric, and deviatoric stress components on the microplanes, we obtain

$$\left\{\int_\Omega\left[(\sigma_V + \sigma_D)n_i n_j + \frac{\sigma_{T_i}}{2}(n_i\delta_{rj} + n_j\delta_{ri} - 2n_i n_j n_r)\right]f(n)\,d\Omega - \frac{2\pi}{3}\sigma_{ij}\right\}\delta\varepsilon_{ij} = 0 \quad \text{..... (8)}$$

This is a variational equation that must be true for any variation $\delta\varepsilon_{ij}$. This occurs if and only if the expression within braces, { }, vanishes. Noting also that $\int_\Omega n_i n_j\,d\Omega = 2\pi\delta_{ij}$, one obtains the expression

$$\sigma_{ij} = \sigma_V\delta_{ij} + \int_\Omega \sigma_D n_i n_j\,d\Omega + \int_\Omega \frac{\sigma_{T_i}}{2}(n_i\delta_{rj} + n_j\delta_{ri} - 2n_i n_j n_r)\,d\Omega \quad \text{..... (9)}$$

Notice that, in fact, not all the components of $\delta\varepsilon_{ij}$ in (8) can have independent variations, since ε is a symmetric tensor. In principle, this would complicate somewhat the elimination of this term from both sides of the equation (Carol et al. 1990). However, thanks to the symmetry (between i and j) in the expressions used [(6)], the resulting expression between brackets, [ ], in (8) is also symmetric with respect to the interchange of indices i and j, which makes this simplification possible (the same remark also applies to other similar simplifications of tensorial variables from other expressions with similar structure later in the paper).

The formulation needs to be supplemented by particular microplane stress-strain laws for σ_V, σ_D, and σ_{T_i} as functions of ε_V, ε_D, and ε_{T_i}. As shown by

Bažant and Prat (1988), these can be assumed to be algebraic explicit relations (rather than differential equations) separate for each component, i.e. (for loading)

$$\sigma_V = F_V(\varepsilon_V) \quad (10a)$$

$$\sigma_D = F_D(\varepsilon_D) \quad (10b)$$

$$\sigma_{T_i} = \frac{F_T(\gamma)}{\gamma}\,\varepsilon_{T_i} \quad (10c)$$

where $\gamma = \sqrt{\varepsilon_{T_i}\varepsilon_{T_i}}$ (the response, however, is in general path-dependent because various combinations of loading and unloading on various microplanes arise, even for macroscopically monotonic loading). A further simplifying hypothesis, that the shear stress σ_{T_i} is parallel to the shear strain ε_{T_i}, is also made. In that case it suffices to specify the constitutive relation for the magnitude $\sigma_T = \sqrt{\sigma_{T_i}\sigma_{T_i}}$ rather than all the components σ_{T_i}. In previous works (Bažant and Prat 1988; Carol et al. 1990) the simplified relations in (10) did not prevent achieving good fits of a wide range of test data for concrete.

The computation of a prescribed-strain macroscopic load step can be performed explicitly: the microplane strain increments are computed from the macroscopic strain increment using (6). Then the new microplane stresses are obtained using the microplane laws, (10) (for each microplane one must know whether unloading started and, if so, which unloading path it is following). And, finally, the microplane stresses are integrated according to (9) to obtain the new macroscopic stresses.

Derivation of Geometric Damage Tensor from Concrete Model

The microplane constitutive laws from (10) can be rewritten in the form of elastic-damage laws with secant moduli E_V^{sec}, E_D^{sec}, and E_T^{sec}

$$\sigma_V = E_V^{sec}\varepsilon_V \quad (11a)$$

$$\sigma_D = E_D^{sec}\varepsilon_D \quad (11b)$$

$$\sigma_{T_i} = E_T^{sec}\varepsilon_{T_i} \quad (11c)$$

where $E_V^{sec} = f_V(\varepsilon_V)$, etc. ($f_V$ = function). Introducing (11) and the expressions of microplane strains from (6) in the right-hand side of (9), replacing the macroscopic stress in the left term by its elastic-damage expression with secant stiffness tensor from (5) for σ_{ij}, and eliminating ε_{ij} from both sides of the resulting equation one obtains the macroscopic secant stiffness tensor expressed as an integral of the secant stiffness at microplane level over the unit hemisphere

$$D_{klmpq}^{sec} = \frac{E_V^{sec}}{3}\delta_{km}\delta_{pq} + \frac{3}{2\pi}\int_\Omega E_D^{sec} n_k n_m \left(n_p n_q - \frac{\delta_{pq}}{3}\right) d\Omega$$

$$+ \frac{3}{2\pi}\int_\Omega \frac{E_T^{sec}}{4}\left(n_k n_p \delta_{mq} + n_k n_q \delta_{mp} + n_m n_p \delta_{kq}\right.$$

$$\left. + n_m n_q \delta_{kp} - 4 n_k n_m n_p n_q\right) d\Omega \quad (12)$$

Now the following substitutions may be introduced: (1) The secant stiffness

at macroscopic level is replaced by the product of the initial elastic stiffness and the damage tensor [(5) for D_{ijpq}^{sec}]; (2) similar replacements are made for the microplane secant moduli:

$$E_V^{sec} = \alpha_V E_V^0 \quad (13a)$$

$$E_D^{sec} = \alpha_D E_D^0 \quad (13b)$$

$$E_T^{sec} = \alpha_T E_T^0 \quad (13c)$$

where α_V, α_D, and α_T = microplane damage variables reflecting the net stress-carrying area fraction at microplane level; and E_V^0, E_D^0, and E_T^0 = initial elastic moduli; (3) the initial moduli E_V^0, E_D^0, and E_T^0 are replaced by their expressions in terms of the macroscopic elastic parameters E and ν and the additional parameter η_0 (Bažant and Prat 1988)

$$E_V^0 = \frac{E}{1 - 2\nu} \quad (14a)$$

$$E_D^0 = \eta_0 E_V^0 \quad (14b)$$

$$E_T^0 = \frac{1}{3}\left[\frac{5(1 - 2\nu)}{1 + \nu} - 2\eta_0\right] E_V^0 \quad (14c)$$

and (4) the elastic stiffness matrix is replaced by its expression:

$$D_{klmpq}^{el} = \frac{\nu E}{(1 + \nu)(1 - 2\nu)}\delta_{kl}\delta_{pq} + \frac{E}{(1 + \nu)}\delta_{kp}\delta_{mq} \quad (15)$$

Once all these expressions are introduced into (12) and simplified, an expression for α_{ijkl} is obtained in terms of α_V, α_D, and α_T. Now an interesting idea comes to mind: parameters E, ν, and η_0 can vanish from the expression for α_{ijkm} when the following assumption is made:

$$\eta_0 = \frac{1 - 2\nu}{1 + \nu} \quad (16)$$

As we will see later, this hypothesis appears to be acceptable for practical purposes, and one gets

$$\alpha_{ijpq} = \frac{\alpha_V}{3}\delta_{ij}\delta_{pq} + \frac{3}{2\pi}\int_\Omega \alpha_D n_i n_j \left(n_p n_q - \frac{\delta_{pq}}{3}\right) d\Omega$$

$$+ \frac{3}{2\pi}\int_\Omega \frac{\alpha_T}{4}\left(n_i n_p \delta_{jq} + n_i n_q \delta_{jp} + n_j n_p \delta_{iq}\right.$$

$$\left. + n_j n_q \delta_{ip} - 4 n_i n_j n_p n_q\right) d\Omega \quad (17)$$

The fact that this tensor is purely geometric, i.e., does not involve E and ν, is the main contribution of this paper. We thus gain a new form of the microplane model in which the basic material behavior is not defined as a set of laws for microplane stresses [(10)] but as a set of laws for the evolution of the microplane damage variables α_V, α_D, and α_T. Then, the macroscopic damage tensor α_{ijkm} is obtained by integration of the microplane damage variables over the hemisphere using (17).

Rheolog. .dependent Derivation of Geometric Damage Tensor

The foregoing derivation of the damage tensor started from a particular version of the microplane model. At least, the following assumptions were implicitly present in the derivation: (1) The microplane laws are of the form $\sigma = \alpha E^n \varepsilon$ [(11) and (13)]; (2) the macroscopic stress-strain relationship is of the same type [(5)], involving linear elasticity in its definition [(15)]; (3) the initial moduli at microplane level are related to the elastic parameters E, ν, [by (14) and (16)]; and (4) the shear stresses and strains on a microplane are parallel [(10)]. No references to these hypotheses remain in the final expression in (17), which depends on geometric dimensionless quantities only. Thus, from a practical point of view it is obvious that (17) can be used as a damage model in combination with any rheologic model in the general context described in the section headed "Effective Stress and Damage Tensor Uncoupled from Rheology." However, from a theoretical viewpoint the question remains whether the damage tensor derived under these restrictive assumptions could also have been derived using any alternative companion rheologic model or the derivation is exclusive for this case.

Let us start a rheology-free derivation of α_{ijkm} from the assumed basic micro-macro kinematic and equilibrium relations in (6) and (9), which are both rheology independent. On the microplane level we may define the effective (true) stresses, τ_V, τ_D, and τ_T, such that

$$\sigma_V = \alpha_V \tau_V \quad \ldots\ldots (18a)$$

$$\sigma_D = \alpha_D \tau_D \quad \ldots\ldots (18b)$$

$$\sigma_T = \alpha_T \tau_T \quad \ldots\ldots (18c)$$

This may be also regarded as a rheology-free definition of damage at microplane level, alternative to (13).

Having assumed the kinematic micro-macro constraint and introduced general microplane stress-strain laws, the microplane stresses cannot (except by chance) represent the resolved components of any stress (macrostress) tensor. The microplane effective stresses in general need not represent the resolved components of any effective stress tensor, i.e., no such tensor needs to exist. However, for a certain special form of the damage ratio tensor, this could occur. Such a property would bring about considerable simplification. To explore it let us introduce the hypothesis that the microplane effective stress components are in fact such resolved components of an effective stress tensor at the macroscopic level, τ_{ij}. This means that, in analogy to (6) for strains, we can write

$$\tau_V = \frac{\tau_{kk}}{3} = \frac{\delta_{km}}{3}\tau_{km} \quad \ldots\ldots (19a)$$

$$\tau_D = \left(n_k n_m - \frac{\delta_{km}}{3}\right)\tau_{km} \quad \ldots\ldots (19b)$$

$$\tau_T = \frac{1}{2}(\delta_{ik}n_m + \delta_{im}n_k - 2n_i n_k n_m)\tau_{km} \quad \ldots\ldots (19c)$$

Let us now substitute (18) and (19) into the right-hand side of (9), and (4) into the left-hand side. After some rearrangements we can factor out τ_{pq}

$$\left\{\frac{\alpha_V}{3}\delta_{ij}\delta_{pq} + \frac{3}{2\pi}\int_\Omega \alpha_D n_i n_j\left(n_p n_q - \frac{\delta_{pq}}{3}\right)d\Omega + \frac{3}{2\pi}\int_\Omega \frac{\alpha_T}{2}(n_i n_p \delta_{jq} + n_i n_q \delta_{jp} + n_j n_p \delta_{iq} + n_j n_q \delta_{ip} - 4n_i n_j n_p n_q)\,d\Omega - \alpha_{ijpq}\right\}\tau_{pq} = 0 \quad \ldots\ldots (20)$$

This equation should hold for any tensor τ_{pq}. This is possible if and only if the expression within braces, { }, vanishes. From this condition we obtain the expression for α_{ijpq} already given in (17). Furthermore, if (19) were violated, it would not be possible to factor out τ_{pq} in (20), and (17) would not result. Therefore, the static constraint in (19) is not only sufficient but also necessary to achieve uncoupling of damage from rheology, the latter being defined by the dependence of τ_V, τ_D, and τ_T on the microplane strains. It must be emphasized that this second derivation was not made with recourse to any particular rheologic model, but only on the basis of geometric, kinematic, and equilibrium considerations. This demonstrates from a theoretical viewpoint the general validity of the proposed geometric damage tensor.

Note also that the model represented by the new damage tensor [(17)] coupled with a particular rheologic model is equivalent to a microplane formulation in which there is not only a kinematic constraint for strains but also a static constraint for a certain kind of stresses, namely, the effective stresses. This is a more appealing formulation than that in which there is only a kinematic constraint. The kinematic constraint is reminiscent of parallel coupling of elements in a rheologic model; the static constraint is reminiscent of series coupling. From the modeling of composite materials it is known that the parallel coupling models give the stiffest possible response; whereas the series coupling models give the softest possible response (an example for elastic composites are the Voigt and Reuss bounds). The real behavior can usually be best described by some combination of both types of coupling. It thus appears satisfactory that the foregoing formulation combines both kinematic and static constraints.

Numerical Implementation and Demonstration for Concrete

Previous studies (Bažant and Prat 1988; Carol et al. 1990) showed that a good and remarkably broad description of the existing test data on the constitutive properties of concrete, encompassing multidirectional tensile strain-softening due to cracking as well as nonlinear triaxial response in the hardening and strain-softening ranges, could be achieved by the microplane model. In those studies all the micromechanics phenomena involved in the microplane laws for σ_V, σ_D, and σ_T were mixed. By contrast, in the new model a clear separation has been established between damage effects, represented through the new damage tensor, and rheology, represented by a companion model that can be simple since it does not represent damage (or strain-softening). In this new scheme a separation of tasks can be established between both parts of the model, each characterizing different aspects of the material behavior observed in tests.

In the first stage of development presented here, attention is focused on the new microplane damage tensor, and the companion rheologic model is chosen as the simplest possible, i.e. linear elasticity. Choosing a more sophisticated rheologic model, e.g., elastoplasic, would no doubt broaden the possibilities of representing complex material behavior.

The evolution laws for microplane damage variables were established on the basis of the laws used for σ_V, σ_D, and σ_T by Carol et al. (1990); they were of the form $\sigma(\varepsilon) = \alpha(\varepsilon)E^0\varepsilon$. Eliminating from these expressions the factor $E^0\varepsilon$, we obtain the equation $\alpha = \exp[-(\varepsilon/a)^p]$, which gives for α a smooth variation from 1 to 0 when the strain increases monotonically; see Fig. 3 for the effect of different values of p.

Fig. 4 depicts the general laws for α_V, α_D, and α_T. In the case of α_V, as seen in this figure, the basic behavior just described is used only for tension (positive ε_V), with parameters a_1 and p_1 and state parameter ε_V^{min}, which depends on the history. No damage is assumed to occur in hydrostatic compression, where we always have $\alpha_V = 1$. This is because the volumetric behavior observed in compression tests shows no stress peak and exhibits unloading-reloading branches with almost the initial slope [see Bažant and Prat (1988)], which seems to be modeled by the companion rheologic model of plasticity type better than by the damage tensor itself. If unloading-reloading occurs in tension, the curve given by (2) acts as an envelope, and the maximum strain reached so far is the state parameter depending on history. A jump is assumed for α_V if ε_V becomes positive after some damage occurred in tension or vice versa. This kind of jump (and the same kind of jump occuring for α_D) can represent in some way the effect of a strain-controlled microcrack opening and closing at microplane level.

In the case of α_D, two independent sets of material parameters and state parameters depending on history are used for tension and compression: a_1, p_1 (both the same as used for α_V), ε_D^{min} for tension; and a_2, p_2, ε_D^{max} for compression. A jump can also occur for α_D when crossing from tensile to compressive parts of the diagram. Finally, a_3, p_3, and γ^{max} are used for the tangential (shear) law, which only shows the positive side since γ is the magnitude of the tangential (shear) strain vector. In contrast to Bažant and Prat (1988) and Carol et al. (1990), no dependence of the tangential behavior on any volumetric variable is assumed. This is an aspect of behavior directly caused by internal friction rather than by damage itself, and therefore might be better handled by the companion rheologic model.

The model was implemented in a computer code in the manner described by Carol et al. (1990), with 28 spatial orientations of microplanes (Bažant and Oh 1985) for which history is recorded and damage evaluated. The

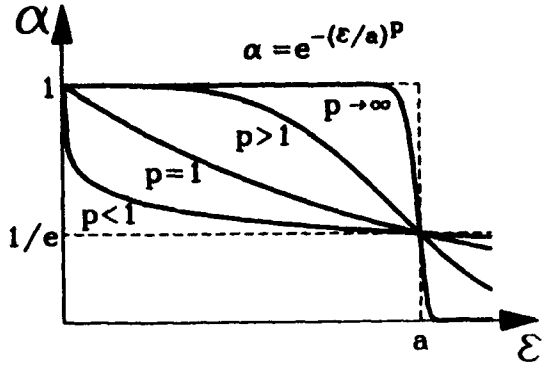

FIG. 3. Basic Exponential Curve for Damage Evolution

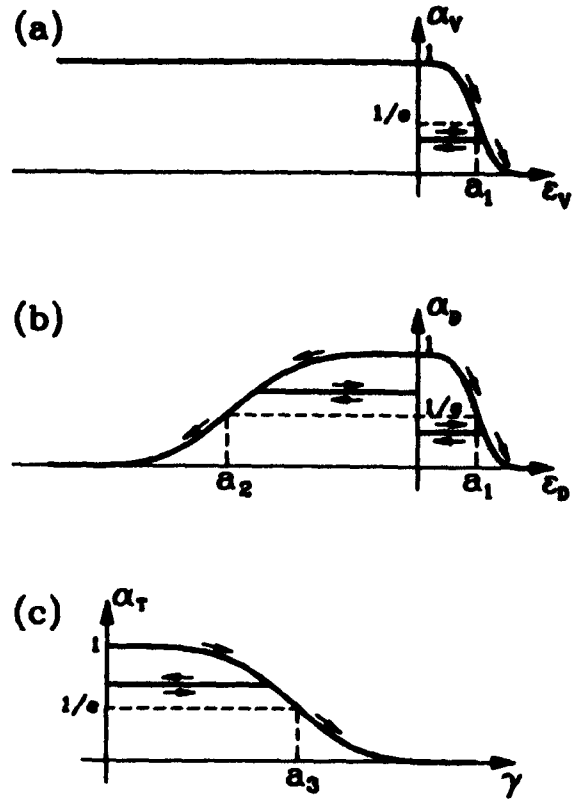

FIG. 4. Microplane Damage Laws: (a) Volumetric Damage α_V; (b) Normal Deviatoric Damage α_D; (c) Tangential (shear) Damage α_T

stresses are computed explicitly from specified strain increments of finite size, and subroutines co-opted from a "single-point" or "full-finite element (FE)" computer program are also used. In fact, no major differences with regard to the previous version of microplane model exist from this viewpoint except that the laws are established in terms of microplane damage variables instead of microplane stresses and that, after the damage tensor has been obtained, additional steps are needed to obtain the new values of τ_u and to evaluate the corresponding tensorial product in (4) that gives the new σ_u.

There are six material parameters of the model for the microplane damage tensor: a_1, p_1, a_2, p_2, a_3, and p_3. However, the values $p_1 = 0.5$; $p_2 = 1.5$; and $p_3 = 1.5$ can be assigned for most of practical cases, thus reducing the number of material parameters to be determined from test results to only three. The number of history-dependent state variables for 28 microplane directions is 85 (one for the volumetric curve, same for all microplanes; two for the deviatoric curve; and one for the shear curve on each microplane). Furthermore, the material parameters of the rheologic model (E and ν in this case) and possibly its internal variables (none in this case) may also be counted.

As a. ample, a uniaxial test reported by van Mier in 1984, in which both longitudinal stress and transverse strains were measured, is reproduced with the model. The parameters used to fit these data are: E = 2,406 MPa; ν = 0.18; a_1 = 0.0004; a_2 = 0.006; and a_3 = 0.0018. The remaining parameters have their general values already given. The results are represented in Fig. 5 by solid lines. The dots are the experimental data and the dashed lines are the results obtained with the previous version of microplane model for the same example. It can be observed that both curves are very similar in each diagram, which should not be surprising since both models are almost equivalent in this example, in which no volumetric dependence

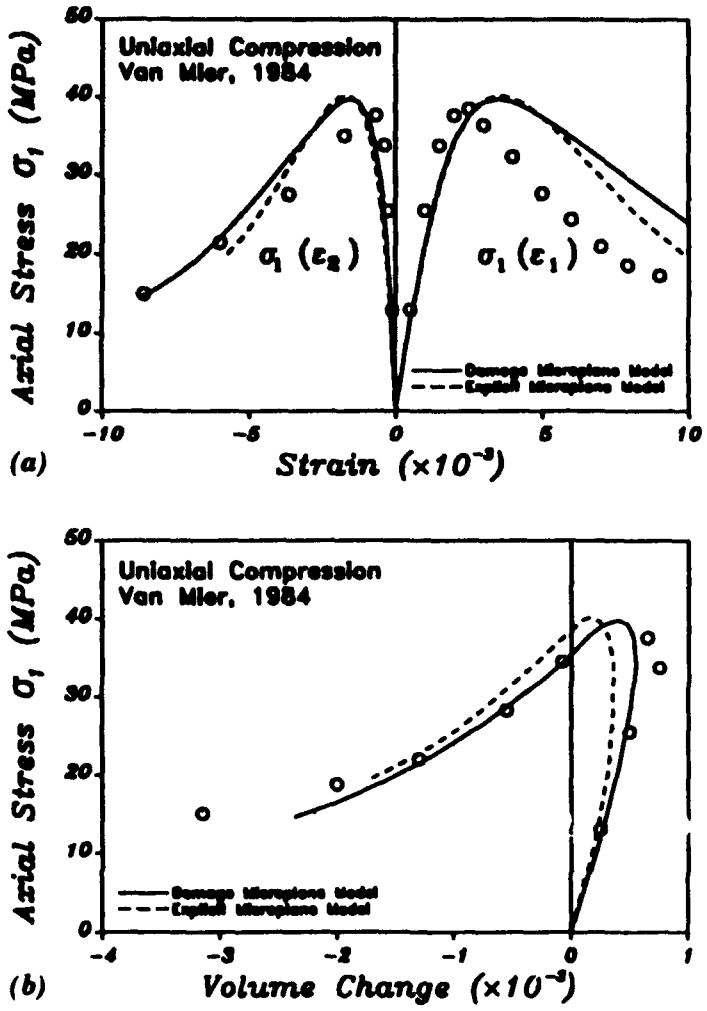

FIG. 5. Comparison with Uniaxial Test by van Mier (1984)

was assumed for σ_T in the computations with the previous micr[illegible]c model (Carol et al. 1990). The only difference arises from the parameter η_0, which existed in the old model but now has disappeared from the formulation. In the section headed "Derivation of Geometric Damage Tensor from Concrete Model" it was shown that the full equivalence between both models occurs for $\eta_0 = (1 - 2\nu)/(1 + \nu)$ in the old model. For $\nu = 0.18$ this means about $\eta_0 = 0.54$; the value taken in the previous computations for this example was 0.85. Due to that difference, the models are not completely equivalent, and the parameters a_1, a_2, and a_3 cannot have the same values. It is clearly shown in the example, however, that the restriction over the value of η_0 does not prevent the model from yielding a very good fit of experimental data. This is not surprising, since Bažant and Prat (1988) found the effect of η_0 in the closeness of fit to be minor and that the optimized η_0-values were mostly quite close to those from (16). Finally we must emphasize that Fig. 5 does not represent an experimental verification of the present model. Rather, this verification rests on the fact that: (1) The Predictions of the present and previous models are quite close; while (2) the experimental verification of the previous model was extensive.

Conclusions and Broader Implications

For the general microplane model characterized by a kinematic micro-macro constraint it is possible to formulate a fourth-order damage tensor in a form that is uncoupled from the rheologic constitutive properties of the material. In this formulation the damage is solely of geometric origin, being due to the reductions of the net stress-carrying cross-sectional area fractions for various orientations in the microstructure. The damage tensor characterizes the values of these area fractions for all spatial directions, and permits them to have any values. The damage tensor formulated in this manner fits well the framework of continuum damage mechanics.

Despite the assumed kinematic constraint between macrostrains and microstrains, it is possible to satisfy at the same time and additional static constraint such that the effective microstresses on the microplanes are the resolved components of the effective macrostresses.

The fact that the constitutive model is composed of two independent parts (one for damage, another for rheology) allows better insight, facilitates the fitting of test data, and increases versatility.

A recent microplane model for tensile and compressive strain softening and general nonlinear triaxial behavior of concrete, which has been amply verified by test data, can be easily adapted to the geometric damage form without any appreciable detriment to the closeness of test data fits.

The possibility of uncoupling geometric damage from constitutive (rheologic) properties is attractive for development of more general constitutive models combining damage with creep and rate effects, with complex unloading and reloading paths, and with cyclic loading. It might be possible to model such behavior adequately using some existing plastic, viscoelastic, viscoplastic, or nonlinear cyclic material model without damage, and then incorporating into it the geometric damage tensor deduced here (17)]. By separating damage, the constitutive (rheologic) model, which relates here the effective (microscopic, true) stress tensor (instead of the macroscopic stress tensor) to the strain tensor, can probably be much simpler than it would have to be if the damage were mixed with nondamage constitutive properties. By virtue of the geometric damage concept constitutive modeling

can be restricted to the material between the microcracks and voids in the microstructure, leaving the overall effect of the growth of the microcracks and voids as the only behavior to be described by the geometric damage tensor.

Acknowledgments

Partial financial support was obtained under NSF grants BCS-8818230 and AFOSR grant 91-0140 to Northwestern University in the early and later phases of research. Partial support for related studies of micromechanics of damage were received from the NSF Center for Science and Technology of Advanced Cement-Based Materials (ACBM), at Northwestern University. The first author is grateful for financial support under a NATO fellowship, and the third author is grateful for a fellowship from the Ministry of Education of Spain. Partial support from the Spanish CICYT under research projects PA85-0321 and PB87-0861 is also gratefully acknowledged.

Appendix I. References

Aboudi, J. (1987). "Constitutive relations for cracked metal matrix composites." *Mech. Mater. 6*, 303–315.

Attiogbe, E. K., and Darwin, D. (1987). "Self consistent model for transversely isotropic cracked solid." *J. Engrg. Mech.*, ASCE, 113(7), 984–999.

Batdorf, S. B., and Budiansky, B. (1949). "A mathematical theory of plasticity based on the concept of slip." *Tech. Note 1871*, National Advisory Committee for Aeronautics (NACA), Washington, D.C.

Bažant, Z. P. (1984). "Microplane model for strain—controlled inelastic behavior." *Mechanics of engineering materials*, C. S. Desai et al., eds., John Wiley, Chichester, NY, 45–59.

Bažant, Z. P., and Carol, I. (1990). "Geometric damage tensor, uncoupled from constitutive properties, and current status of strain-softening models." *Developments in theoretical and applied mechanics: Proc., 15th Southeastern Conf. on Theoretical and Appl. Mech., Vol. 15*, S. V. Hanagut et al., eds., Georgia Institute of Technology, Atlanta, Ga., 927–933.

Bažant, Z. P., and Cedolin, L. (1979). "Blunt crack band propagation in finite element analysis." *J. Engrg. Mech.*, ASCE, 105(2), 297–315.

Bažant, Z. P., and Chern, J. C. (1985). "Strain-softening with creep and exponential algorithm." *J. Engrg. Mech.*, ASCE, 111(3), 559–582.

Bažant, Z. P., and Gambarova, P. G. (1984). "Crack shear in concrete: Crack band microplane model." *J. Struct. Engrg.*, ASCE, 110(9), 2015–2035.

Bažant, Z. P., and Kim, S. S. (1979). "Plastic-fracturing theory for concrete." *J. Engrg. Mech.*, ASCE, 105(3), 403–428.

Bažant, Z. P., and Oh, B. H. (1983). "Crack band theory for fracture of concrete." *Mat. Struct.*, 16, 155–177.

Bažant, Z. P., and Oh, B. H. (1985). "Microplane model for progressive fracture of concrete and rock." *J. Engrg. Mech.*, ASCE, 111(4), 559–582.

Bažant, Z. P., and Prat, P. C. (1988). "Microplane model for brittle-plastic material. I: Theory." *J. Engrg. Mech.*, ASCE, 114(10), 1672–1702.

Bažant, Z. P., and Prat, P. C. (1988). "Microplane model for brittle-plastic material. II: Verification." *J. Engrg. Mech.*, ASCE, 114(10), 1672–1702.

Betten, J. (1983). "Damage tensors in continuum mechanics." *J. Mécanique Théorique et Appliquée*, 2(1), 13–32.

de Borst, R. (1987). "Computation of post-bifurcation and post-failure behavior of strain-softening solids." *Computers and Struct.*, 25(2), 211–224.

Budiansky, B., and O'Connell, R. J. (1976). "Elastic moduli of a cracked solid." *Int. J. of Solids and Struct.*, 12, 81–97.

Carol, I. (1989). "Explicit models for non linear time-dependent behavior of concrete in compression based on damage concepts and the aging Maxwell chain." *3rd Joint ASCE/ASME Mech. Conf.*, ASCE, New York, N.Y.

Carol, I., Bažant, Z. P., and Prat, P. C. (1990). "New explicit microplane model for concrete: Theoretical aspects and unified implementation for constitutive verification and finite element analysis." *Report GT015/1990, ETSECCPB-UPC*, Campus Nord, Edif. D2. Gran Capità, s/n. E-08034 Barcelona, Spain.

Carol, I., and Prat, P. C. (1990). "A statically constrained microplane formulation for the smeared analysis of concrete cracking." *Proc., 2nd. Int. Conf. on Computer-Aided Analysis and Design of Concrete Strut.*, Zell Am See, Austria, Vol. 2, 919–930.

Chaboche, J. L. (1978). "Description thermodynamique et phénoménologique de la viscoplasticité cyclique avec endommagement" (in French), thesis, presented to the University of Paris IV, at Paris, France, in partial fulfillment of the requirements for the degree of Doctor of Philosophy.

Chaboche, J. L. (1979). "The concept of effective stress applied to elasticity and viscoplasticity in the presence of anisotropic damage." *ONERA Report 1979/77*.

Chaboche, J. L. (1981). "Continuum damage mechanics: A tool to describe phenomena before crack initiation." *Nuclear Engrg. and Design* 64, 233–247.

Costin, L. S. (1985). "Damage mechanics in the post-failure regime." *Mech. of Mat.*, 4, 149–160.

Costin, L. S., and Stone, C. M. (1987). "Implementation of a finite element damage model for rock. *Constitutive laws for engineering materials: Theory and Applications*, C. S. Desai et al., eds., Elsevier, New York, N.Y.

Cowin, S. C. (1985). "The relationship between the elasticity tensor and the fabric tensor." *Mech. of Mat.*, 4, 137–147.

Crisfield, M. A. (1982). "Local instabilities in the non linear analysis of reinforced concrete beams and slabs." *Proc., Inst. of Civ. Engrg.*, 73, 135–145.

Davidson, L., and Stevens, A. L. (1973). "Thermomechanical constitution of spalling elastic bodies." *J. Appl. Phys.*, 44, 667–674.

Dougill, J. W. (1976). "On stable progressively fracturing solids." *J. of Appl. Mathematics and Physics (ZAMP)*, Basel, Switzerland, 27, 423–436.

Dragon, A., and Mróz, Z. (1979). "A continuum model for plastic-brittle behavior of rock and concrete." *Int. J. Engrg. Sci.*, 17, 121–137.

Franziskonis, G., and Desai, C. S. (1987). "Constitutive model with strain softening." *Int. J. of Solids and Struct.*, 23, 733–750.

Hillerborg, A. (1984). "Numerical methods to simulate softening and fracture of concrete." *Fracture mechanics applied to concrete structures*, G. C. Sih, ed., Martinus Nijhoff, The Netherlands.

Hillerborg, A., Modéer, M., and Pettersson, P. E. (1976). "Analysis of crack formation and crack growth in concrete by means of fracture mechanics and finite elements." *Cement and Concrete Res.*, 6(6), 773–782.

Horii, H., and Nemat-Nasser, S. (1983). "Overall moduli of solids with microcracks: Load-induced anisotropy." *J. of Mech. and Physics of Solids*, 31(2), 155–171.

Kachanov, L. M. (1958). "Time rupture process under creep conditions" (in Russian). *Izv Akad Nauk SSR, Otd Tekh Nauk 8*, 26–31.

Kachanov, M. (1980). "Continuum model of medium with cracks." *J. Engrg. Mech.*, ASCE 106(5), 1039–1051.

Kachanov, M. (1987). "Elastic solids with many cracks: A simple method of analysis." *Int. J. of Solids and struct.*, 23(1), 23–43.

Krajcinovic, D., and Fonseka, G. U. (1981). "The continuous damage theory of brittle materials." *J. of Appl. Mech.*, 48, 809–824.

Leckie, F. A. (1978). "The constitutive equations of continuum creep damage mechanics." *Phil. Trans. of the Royal Society*, London, England, 288, 27–47.

Leckie, F. A., and Onat, E. T. (1980). "Tensorial nature of damage measuring internan varibles." *Proc., IUTAM Symp.*, Senlis, France.

Lemaitre, J. (1984). "How to use damage mechanics." *Nuclear Engrg. and Design*, 80, 233–245.

Lemaitre, J., and Chaboche, J. L. (1978). "Aspect phénomenologique de la rupture par endommagement" (in French), *J. de Mécanique Appliquée*, 2(3), 317–365.

Lemaitre, J., and Chaboche, J. L. (19[illegible] *écanique des materiaux solides* (in French), Dunod, Paris.
Lin, T. M. (1968). *Theory of inelastic structures*. John Wiley and Sons Inc., New York, N.Y.
Mazars, J. (1985). "A model for a unilateral elastic damageable material and its application to concrete." *Proc., RILEM Int. Congress on Fracture Mech. of Concrete*, Lausanne, Switzerland.
van Mier, J. G. M. (1984). "Strain-softening of concrete under multiaxial loading conditions," thesis presented to the University of Eindhoven, at The Netherlands, in partial fulfillment of the requirements for the degree of Doctor of Philosophy.
Murakami, S. (1987). "Anisotropic damage theory and its application to creep crack growth analysis." *Constitutive laws for engineering materials: Theory and applications*, C. S. Desai et al., eds., Elsevier, New York, N.Y., 187–194.
Murakami, S., and Ohno, N. (1980). "A continuum theory of creep and creep damage." *Creep in Structures*. A. R. S. Ponter et al., eds., Springer Verlag, Berlin, Germany, 422–444.
Nemat-Nasser, S., Iwakuma, T., and Hejazi, M. (1982). "On composites with periodic structure." *Mech. of Mat.*, 1, 239–267.
Oda, M. (1983). "A method for evaluating the effect of crack geometry on the mechanical behavior of cracked rock masses." *Mech. of Mat.*, 2, 163–171.
Ortiz, M. (1985). "A constitutive theory for the inelastic behavior of concrete." *Mech. of Mat.*, 4, 67–93.
Ortiz, M. (1987). "An analytical study of the localized failure modes of concrete." *Mech. of Mat.*, 6, 159–174.
Ortiz, M., and Quigley, J. J. (1989). "Element design and adaptative meshing in strain localization problems." *Computational Plasticity*, D. R. J. Owen et al., eds., Pineridge Press, Swansea, Wales.
Pijaudier-Cabot, G., and Bažant, Z. P. (1987). "Non-local damage theory." *J. Engrg. Mech.*, ASCE, 113(10), 1512–1533.
Rabotnov, Y. N. (1969a). *Creep problems of structural members*. North-Holland, Amsterdam, The Netherlands.
Rabotnov, Y. N. (1969b). "Creep rupture." *Appl. Mech. Conf.*, Heteny et al., eds., Stanford University, Stanford, Calif., 342–349.
Resende, L. (1987). "A damage mechanics constitutive theory for the inelastic behavior of concrete." *Computer Methods in Appl. Mech. and Engrg.*, 60, 57–93.
Simó, J. C., Ju, J. W., Taylor, R. L., and Pister, K. S. (1987). "On strain-based continuum damage models: Formulation and computational aspects." *Constitutive laws for engineering materials: Theory and applications*, C. S. Desai et al., eds., Elsevier, New York, N.Y., 233–245.
Suaris, W. (1987). "A damage theory for concrete incorporating crack growth characteristics." *Constitutive laws for engineering materials: theory and applications*, C. S. Desai et al., eds., Elsevier, New York, N.Y.
Suaris, W., and Shah, S. P. (1984). "Rate-sensitive damage theory for brittle solids." *J. Engrg. Mech.*, ASCE, 110(6), 985–997.
Taylor, G. I. (1938). "Plastic strain in metals." *J. Inst. Metals*, 62, 307–324.
Vakulenko, A. A., and Kachanov, M. L. (1971). "Continuum theory of cracked media" (in Russian). *Mekh Tverdogo Tela*. U.S.S.R., 6, 159–166.
Yazdani, S., and Schreyer, H. L. (1988). "An anisotropic damage model with dilatation for concrete." *Mech. of Mat.*, 7, 231–244.

Compression Failure of Quasibrittle Material: Nonlocal Microplane Model

By Zdeněk P. Bažant,[1] Fellow, ASCE, and Jože Ožbolt[2]

Abstract: The previously presented constitutive model of microplane type for nonlinear triaxial behavior and fracture of concrete is used in nonlocal finite element analysis of compression failure in plane strain rectangular specimens. For specimens with sliding rigid platens there is a bifurcation of the loading path at the beginning of postpeak softening; a symmetric (primary) path exists but the actual (stable) path is the nonsymmetric (secondary) path, involving an inclined shear-expansion band that consists of axial splitting cracks and is characterized by transverse expansion. The secondary path is indicated by the first eigenvalue of the tangent stiffness matrix but can be more easily obtained if a slight nonsymmetry is introduced into the finite element model. In specimens with bonded rigid platens there is no bifurcation; they fail symmetrically, by two inclined shear-expansion bands that consist of axial splitting cracks. The transverse expansion produces transverse tension in the adjacent material, which serves as the driving force of propagation of the axial splitting cracks. Numerical calculations indicate no significant size effect on the nominal stress at maximum load.

Introduction

Under uniaxial compression, quasibrittle materials exhibiting progressive distributed damage, such as concrete, rocks, ceramics, and ice, fail by slip on inclined shear bands or by axial splitting, or by a combination of both. From experience, the axial splitting cracks appear to be an important part of the compression failure mechanism in quasibrittle materials. However, although various aspects of the microscopic fracture mechanism under compression have been illustrated in previous works [e.g., Griffith (1924); Kendall (1978); Miyamoto et al. (1977); Sammis and Ashby (1986); Shetty et al. (1968); Ingraffea (1977); Glucklich (1963); Bažant (1967)], no realistic comprehensive model for macroscopic compression failure process has been presented. The reason is that a sufficiently realistic constitutive model applicable to cracking damage under general triaxial stress states, including compressive stress states, has been unavailable, and a method to overcome the spurious mesh sensitivity and localization problems due to triaxial strain softening did not exist. Recently, both of these problems were overcome with the nonlocal version (Bažant and Ožbolt 1990) of the microplane model (Bažant and Prat 1988). The purpose of this paper is to apply this model to study the compression failure.

Compression failure of uniaxial concrete test specimens was recently analyzed by a nonlocal finite element code in Droz and Bažant (1988) [see also Bažant (1989a)]. The analysis indicated a shear-band mode of failure, but the axial splitting often seen in experiments could not be obtained. However, the constitutive model used, namely Drucker-Prager plasticity with a nonlocal degrading yield limit, was not sufficiently realistic for con-

[1]Walter P. Murphy Prof. of Civ. Engrg., Northwestern Univ., Evanston, IL 60208.
[2]Res. Engr., Institut für Werkstoffe im Bauwesen, Universität Stuttgart, Germany; formerly, Visiting Scholar, Northwestern Univ.

Note. Discussion open until August 1, 1992. To extend the closing date one month, a written request must be filed with the ASCE Manager of Journals. The manuscript for this paper was submitted for review and possible publication on February 27, 1991. This paper is part of the *Journal of Engineering Mechanics*, Vol. 118, No. 3, March, 1992. ©ASCE, ISSN 0733-9399/92/0003-0540/$1.00 + $.15 per page. Paper No. 1469.

crete. A nonlocal finite element approach based on a more realistic constitutive model for concrete was formulated in a preceding paper by Bažant and Ožbolt (1990). The present paper will apply this model to the study of compression failure. All the definitions and notations from the preceding paper are retained and the basic mathematical formulation is not repeated.

Axial Splitting Fracture

Axial splitting due to compression is a difficult problem in fracture mechanics, which has a long history. The difficulty arises principally due to the fact that, in uniaxially compressed specimens whose macroscopic strain field is uniform, calculation yields no release of stored elastic energy into a propagating axial fracture, that is, the driving force of fracture propagation is lacking. The reason is that, if a planar crack parallel to the compression direction is introduced into a uniaxial compressive stress field, there is no change in stress since the stresses on the crack planes are zero to begin with. Therefore, some mechanism that breaks the macroscopic uniformity of the strain field must exist.

One hypothesis, which was explored in some detail, was that transverse tensions are created due to three-dimensional buckling [e.g., Bažant (1967)]. From second-order three-dimensional buckling analysis with finite strains (reviewed in Bažant and Cedolin (1991), section 11.7), however, it transpired that three-dimensional buckling could have a significant effect only if the axial normal compressive stress reached approximately the same order of magnitude as the tangential transverse modulus (stiffness) or the tangential shear modulus of the material. This is possible only for highly anisotropic materials such as fiber composites or laminates, for which the three-dimensional buckling hypothesis had some success in explaining certain experimentally observed features of the response (Bažant 1967). In concrete, however, the initial anisotropy is negligible, and even the stress-induced anisotropy appears to be insufficient to permit explaining axial splitting fractures in terms of three-dimensional buckling—at least not as the initial triggering mechanism (although after the axial splitting failure of a concrete specimen is initiated, three-dimensional buckling might still play a role in the failure process).

In this study, another idea is advanced. The uniformity-breaking mechanism may be provided by the formation and propagation of a damage (cracking) band exhibiting strong volume dilatancy caused by growth of axial splitting microcracks that are parallel to the direction of compression. In such a band, one can expect an inelastic volume dilatancy to be produced due to high deviatoric stresses. The volume dilatancy must induce transverse tensile stresses in front of the splitting microcracks, which causes them to grow. That does not mean, however, that the bands of axial splitting cracks should grow in the direction of compression; rather these cracks form a band propagating in the inclined direction.

This mechanism is quite different from the tensile fracture mechanism, because generation of the transverse tensile stresses in front of the cracking band by volume dilatancy in the band can be a purely local mechanism that involves no significant stress and strain changes anywhere except rather near the fracture band. Therefore, the basic properties of such fracture, especially the size effect, could be quite different.

As is well known from the studies of nonlinear triaxial behavior of concrete as well as geomaterials, realistic predictions of inelastic volume dilatancy due to deviatoric stresses require a relatively sophisticated nonlinear triaxial constitutive model, covering the postpeak strain softening. Most of the constitutive models previously proposed for concrete work well only for uniaxial and biaxial stresses but not after the peak. We select for the present study the microplane model in which the normal microplane strains are split into volumetric and deviatoric components, as introduced in Bažant and Prat (1988). This model has been shown to represent quite well a very broad range of experimentally observed behavior including various types of triaxial tests, biaxial tests, biaxial and triaxial failure envelopes, softening response, etc. Furthermore, the nonlocal extension of this model has been shown to work well for tensile fracture and represent the observed size effect. A somewhat different type of extension of the previous microplane model, which can also model compression failures, has been developed by Hasegawa and Bažant (internal report, Northwestern University, 1990).

There has been extensive research into micromechanics of compressive failure of various materials (Brockenbrough and Suresh 1987; Ingraffea 1977; Kendall 1978; Miyamoto et al. 1977; Sammis and Ashby 1986; Shetty et al. 1968). Mechanisms such as the propagation of axial cracks from voids or the so-called wing-tip cracks were studied by many researchers. These studies, however, illuminated only some microstructural mechanisms but have not lead to a general macroscopic model capable of furnishing the load-displacement curves and failures states of specimens or structures.

Numerical Modeling of Compression Splitting Fracture

We analyze a rectangular concrete specimen of size 300 × 300 × 540 mm [Figs. 1(*a*) and (*b*)] uniaxially compressed between perfectly rigid platens. The specimen may be imagined to represent the cross section of a wall that is in a plane strain state. The finite element mesh is shown in Fig. 1. The material parameters of the microplane model, as defined in the previous

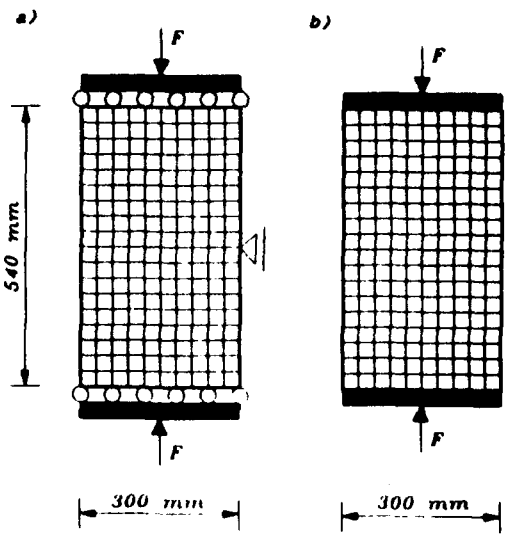

FIG. 1. Specimens Analyzed, with Finite Element Meshes

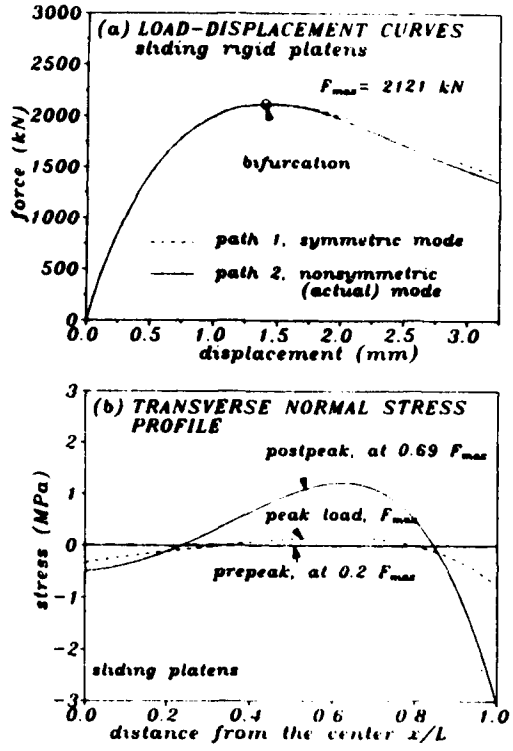

FIG. 2. (a) Calculated Curve of Load versus Axial Displacement for Specimens with Sliding Rigid Platens; and (b) Calculated Profiles of Transverse Normal Stresses Along Symmetry Axis of Specimen

study by Bažant and Prat (1988), are taken according to that study as: E_0 = 23,500 MPa (initial elastic modulus), and ν = 0.18 (Poisson ratio), a = 0.005, b = 0.043, p = 0.75, q = 2.00, e_1 = 0.00006, e_2 = 0.0015, e_3 = 0.0015, e_4 = 0., m = 1.0, n = 1.0, k = 1.0. Most of these parameters, except e_1, e_2, e_3, e_4, can be considered to have the same value for all concretes, as specified in Bažant and Prat (1988). Based on these parameter values, calculations of the uniaxial stress-strain curve for a single material point yield uniaxial compression strength 17.6 MPa and tensile strength 1.72 MPa. The maximum aggregate size is d_a = 30 mm, and the characteristic length is assumed as $l = 3d_a$.

Compared to the previous microplane model, however, a minor modification has been made; while previously the microplane shear stress and strain vectors were assumed to always be coaxial, presently they are allowed to be noncoaxial. These vectors are split in two components with respect to the rectangular in-plane coordinate axes, whose directions are chosen randomly on each microplane. (This randomness introduces a slight nonsymmetry into the model with respect to the plane of symmetry of the specimen.) The relation between the shear stress and strain components for each component direction is assumed to be the same as that between the shear stress and shear strain in the previous model.

The compression specimens are loaded through perfectly rigid platens and anlayzed both for perfectly sliding (frictionless) platens [Fig. 1(*a*)], and for bonded (nonsliding) platens [Fig. 1(*b*)]. The specimen is loaded in small steps by prescribing axial displacement increments of the top platen in each loading step. To initiate a softening damage band in the direction of compression, there must be some small initial random inhomogeneity, from which the band starts. Therefore we assume that there is a weak zone in the center of the specimen; see the shaded area in Fig. 1. The elastic modulus in the weaker zone is assumed to be 5% less than in the rest of the specimen. Isoparametric four-node quadrilaterals with four integration points are used in the calculations. All the elements are identical and their size is equal to 1/3 of the characteristic length l. For a completely symmetric situation, one may expect symmetry-breaking bifurcations of the response. As we will see, numerical results indicate that this indeed occurs for the case of the sliding boundary (but, curiously, not for the case of the boundary with perfect bond to the rigid platens, called the bonded boundary).

To determine bifurcations and stability, the tangential stiffness matrix K_t is calculated at various states by imposing $q_i = 1$, with all other $q_j = 0$; q_i are all the displacements of the structure ($i,j = 1,2, \ldots n$). Matrix $\mathbf{K}_t$ is usually nonsymmetric. Because of various possible combinations of loading and unloading at various integration points and at various microplanes at each point, there are great many matrices K_t at each stage of loading; each of them corresponding to a different sector of the space of all q_i. However, in similarity to Hill's method of linear comparison solid (Hill 1961, 1962), known from plasticity, the first bifurcation of the loading path can be determined by considering only the K_t matrix for the same unloading-loading combinations as for the previous loading steps. For the first bifurcation, this means considering matrix $K_t = K_t'$ that is calculated under the assumption that loading occurs for all q_i. Matrix K_t is in general nonsymmetric. Let $\bar{K}_t$ be its symmetric part, i.e., $\bar{K}_t = (K_t + K_t')/2$, and let λ_1 and $\bar{\lambda}_1$ be the first (i.e., minimum) eigenvalues of matrices K_t and $\bar{K}_t$. Before the first bifurcation, $\lambda_1 > 0$. At the first bifurcation $\lambda_1 = 0$, and after the first bifurcation, $\lambda_1 < 0$. Stable states are characterized by $\bar{\lambda}_1 > 0$, the limit of stability of the structure is characterized by $\bar{\lambda}_1 = 0$, and unstable states are characterized by $\bar{\lambda}_1 < 0$. The stable path is characterized by $\lambda_1 > 0$, where λ_1 is calculated from K_t for the precise loading-unloading combination for that path. According to Bromwich's theorem known from linear algebra, always $\lambda_1 \leq \bar{\lambda}_1$, i.e., the first bifurcation occurs at or before the onset of instability [for detailed explanations, see section 10.4 in Bažant and Cedolin (1991)].

The mathematical analysis of bifurcation states and postbifurcation paths can be avoided if one introduces small imperfections into the system, provided of course that these imperfections are chosen such that they excite the secondary postbifurcation path. Thus, λ_1 and $\bar{\lambda}_1$ have been calculated only for some states of the perfect system, while generally the imperfection approach has been followed, making the finite element meshes for both types of the boundary conditions slightly asymmetric. This has been done by slightly displacing four interior nodes near the center of the specimen in the lateral direction.

Results of Numerical Analysis

The results of analysis for the case of sliding boundaries are shown in Figs. 2–8. The calculated load-displacement curves for perfectly symmetric

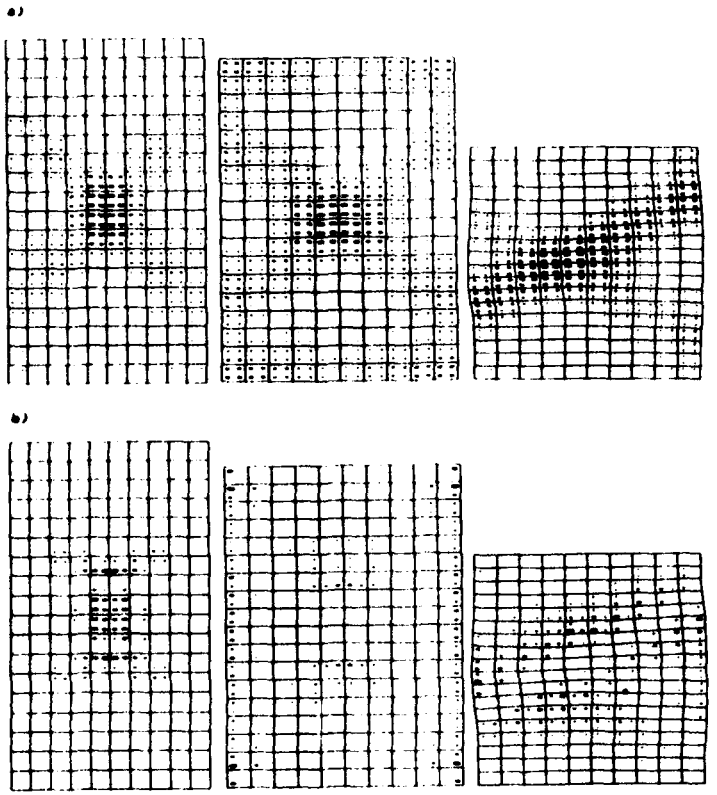

FIG. 3. Deformed Meshes (Exaggerated 50 Times) with Fields of (a) Maximum Principal Strains ε_1; and (b) Maximum Principal Stresses σ_1 (Tensile Only)—for Sliding Platens (Actual Path), at Prepeak ($0.2F_{max}$), Peak Load (F_{max}), and Postpeak ($0.84F_{max}$). (Size of Rectangles is Proportional to Magnitude and Direction of Their Long Side is ε_1-Direction)

and slightly asymmetric finite element meshes [Fig. 2(*a*)] are visually undistinguishable up to a point that lies slightly beyond the peak-load point. For the perfectly symmetric mesh, a bifurcation occurs at this point, which is revealed by singularity of the tangential stiffness matrix. The bifurcation is caused by a breakdown of symmetry in the specimen response and is a consequence of strain softening of the material. As shown in Bažant (1989a), and Bažant and Cedolin (1991, Chapter 10), for the conditions of displacement control, the path that occurs after the bifurcation point must minimize the second-order work $\delta^2 W = \delta f \delta u/2$; where δu is the prescribed displacement increment, and δf is the force reaction increment at the top of the specimen. As expected, smaller value of $\delta^2 W$ is obtained for the secondary bifurcated path that yields an asymmetric response mode. Consequently, the path that actually occurs must be the symmetry-breaking secondary path. The fact that the primary path is not the actual path is also confirmed by negativeness of the smallest eigenvalue of the tangent stiffness matrix after

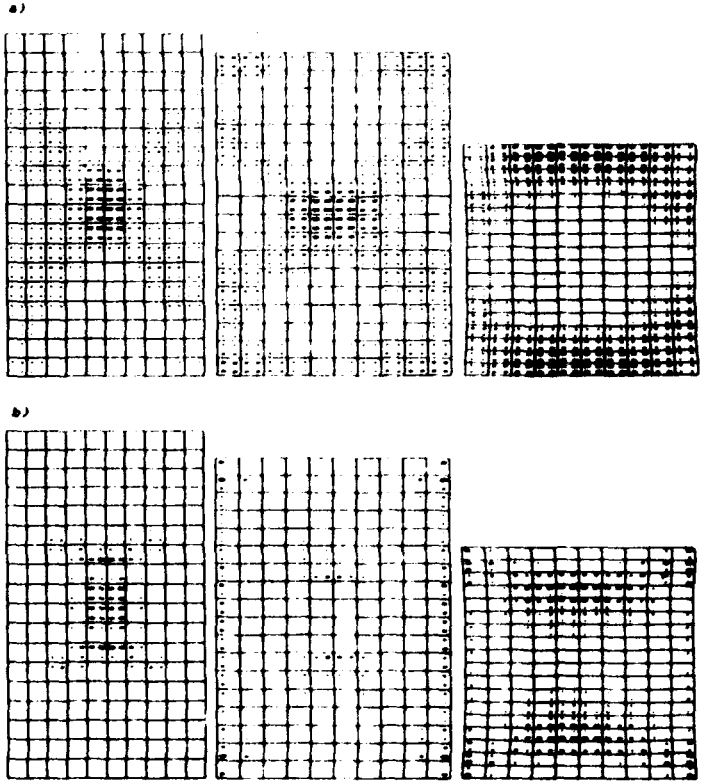

FIG. 4. Same as Fig. 3 but Symmetric Deformation Enforced (Not Actual Path), at Prepeak State ($0.2F_{max}$), Peak Load (F_{max}), and Postpeak State ($0.89F_{max}$)

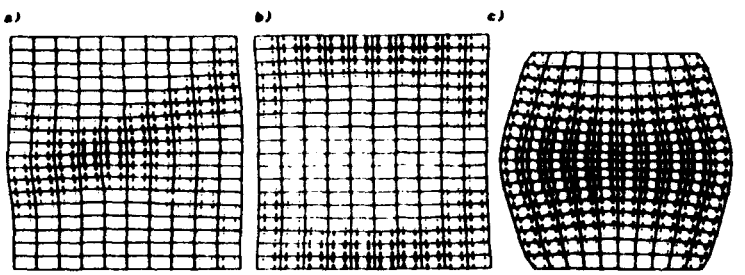

FIG. 5. Cracking Patterns Represented by Fields of Maximum Principal Inelastic Strain ε_1'' (Tensile Only), for (a) Sliding Platens (Actual Path); (b) Sliding Platens (Symmetric Deformations—Not Actual Path); and (c) Bonded Platens (Direction of Rectangles Here is Cracking Direction, Normal to ε_1'')

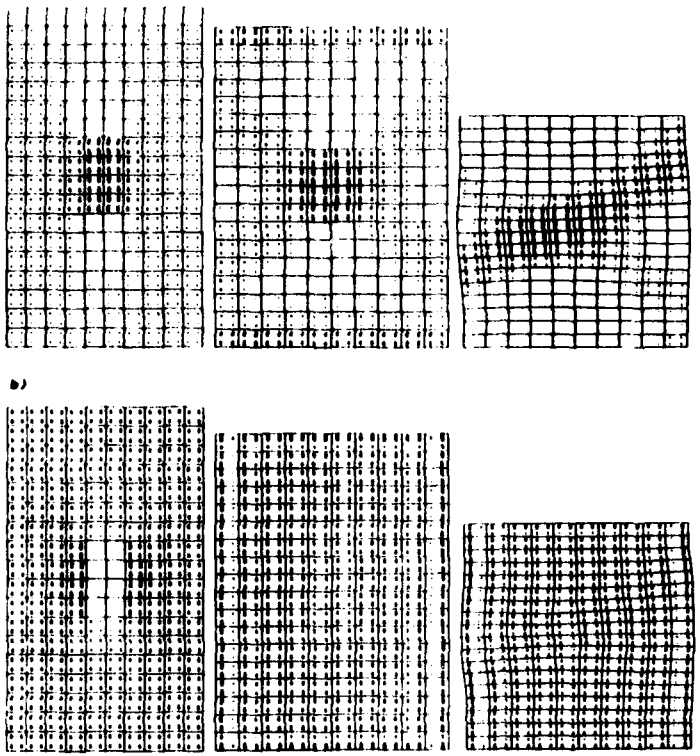

FIG. 6. Deformed Meshes with Fields of (a) Minimum Principal Strains ϵ_1; and (b) Minimum Principal Stresses σ_1 (Compressive Only)—for Sliding Platens (Actual Path)

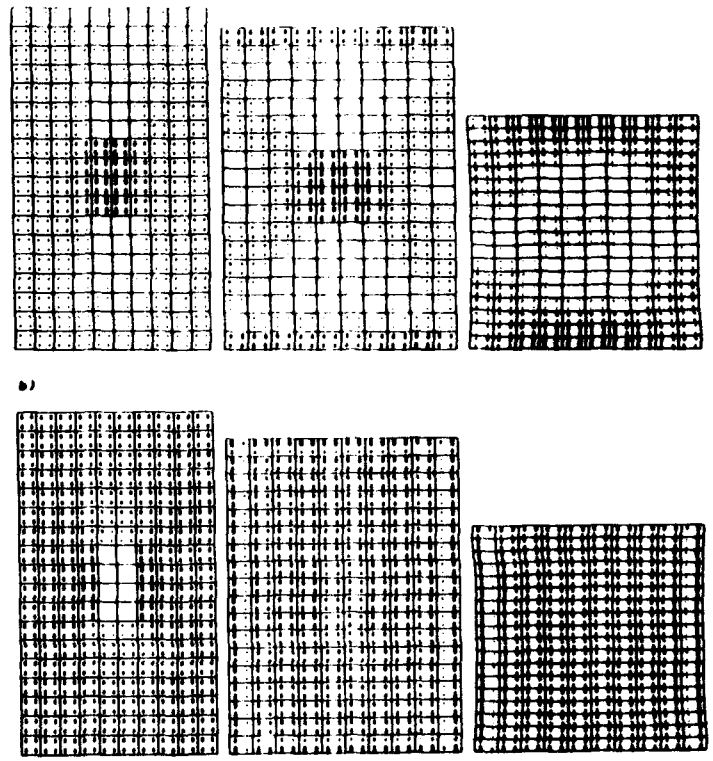

FIG. 7. Same as Fig. 6 but Symmetric Deformation Enforced (Not Actual Path)

the first bifurcation point, while for the states on the secondary path the smallest eigenvalue remains positive.

Fig. (2*b*) shows the profiles of the transverse normal stress along the specimen axis. Figs. 3(*a*) and (*b*) and 4(*a*) and (*b*) show the magnitudes and directions of the fields of the maximum principal tensile strains and stresses over the deformed specimen at various load levels, for both symmetric and asymmetric response paths. At each integration point at which the maximum principal strain or stress is positive (tension), a solid rectangle is plotted to characterize its magnitude and direction. The size (length) of each rectangle is proportional to the magnitude, and the direction of its longer side shows the principal strain or stress direction. The zones of axial splitting cracks are those in which the maximum principal stresses are negative or small positive [blank zone in Figs. 3(*b*) and 4(*b*)] while at the same time the maximum principal strains are large and positive [zone of large rectangles of Figs. 3(*a*) and 4(*a*)]. As we see, the symmetric path represents pure splitting compression failure while the inclined failure band that develops in the asymmetric path represents a combination of axial splitting with a shear band (it may also be described as a shear band that consists of axial

splitting cracks). Both modes in Figs. 3(*a*) and 4(*a*) clearly indicate a tendency toward large transverse expansions, which cause vertical (splitting) cracks. We also see that the zone of transverse expansion propagates for the symmetric mode vertically [Fig. 4(*a*)], and for the nonsymmetric mode in an inclined direction [Fig. 3(*a*)]. The driving force of the propagation appears to be the transverse expansion of the crack band front that is caused by deviatoric strains (well captured by the microplane model). Clearly this expansion must produce transverse tensile stresses ahead of the expansion zone and compressive stresses within this zone [Fig. 2(*b*)], causing the splitting cracks to close.

In a smeared, continuum representation, cracking is characterized by the smeared cracking strain ϵ_{ij}^{cr}. The inelastic strain ϵ_{ij}^{in} in general consists of the cracking strain and the plastic strain ϵ_{ij}^{p}. In the direction of the maximum principal inelastic strain ϵ_1^{in}, nearly all of it may be assumed to be due to cracking strain ϵ_1^{cr}, with a negligible contribution from plasticity. Thus, we will assume that $\epsilon_1^{cr} = \epsilon_1^{in}$. The inelastic strains are calculated as $\epsilon_{11}^{in} = \epsilon_{11} - (\sigma_{11} - \nu\sigma_{22} - \nu\sigma_{33})/E$, $\epsilon_{22}^{in} = \epsilon_{22} - (\sigma_{22} - \nu\sigma_{11} - \nu\sigma_{33})/E$, and $\epsilon_{12}^{in} = \epsilon_{12} - \sigma_{12}/2G$, where subscripts 1 and 2 refer to the coordinates x_1 and x_2 in the horizontal and vertical directions in Fig. 1; E = Young's elastic

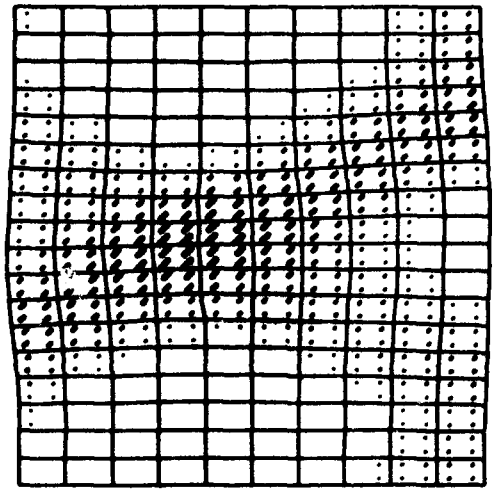

FIG. 8. Field of Maximum Shear Strains for Nonsymmetric (Actual) Deformations, Postpeak, at $0.84F_{max}$ (Size of Each Rectangle is Proportional to Magnitude, and Longer Side Indicates Stress Direction)

modulus, ν = Poisson ratio, and $G = E/2(1 + \nu)$ = elastic shear modulus. The values of ε_1'' have been calculated from ε_{11}'', ε_{22}'', and ε_{12}'' for all the integration points of all the elements. The distributions of ε_1'' for the nonsymmetric and symmetric deformation mode of a specimen with sliding platens are shown in Figs. 5(*a*) and (*b*), where the size of the rectangles is proportional to the magnitude of ε_1'', while the direction of their longer side is in this case normal (rather than parallel) to the maximum principal direction and indicates the direction of cracking. From Fig. 5(*a*) we see that cracking is essentially vertical everywhere, as expected, and that the zone of major cracking spreads in an inclined direction, thus representing a shear band. Visible cracks occur only in the areas of large ε_1'', while at locations of small ε_1'' there is only invisible microcracking.

At the peak load [Figs. 4(*a*) and (*b*), the cracking front (white area) reaches roughly to the upper and lower quarter of the specimen length. Subsequently, during postpeak softening, the cracking front (white area) propagates still further towards the loading platens. The progress of the cracking front toward the platens is also apparent from Fig. 2(*b*), which shows the distribution of the transverse normal stresses (average value for each finite element) along the specimen axis at various load stages.

Figs. 6(*a*) and (*b*) and (7*a*) and (*b*) further show the field of minimum principal (compressive) strains and stresses, which exists in the region that is blank in Figs. (3*b*) and 4(*b*) and corresponds to the field of maximum principal (tensile) strains shown in Figs. (3*a*) and 4(*a*) (the rectangles are not plotted only for the zones of negative strains or stresses).

Fig. 8 shows the maximum shear strain for the nonsymmetric failure mode. This figure clearly indicates that the inclined bands are really shear bands.

The results of the analysis for the case of nonsliding boundaries are shown in Figs. 5(*c*), and 9–11. The load-displacement curve [Fig. 9(*a*)] exhibits a slightly higher peak load than that in the case of sliding boundaries, while the descending branch is steeper. It is interesting that in this case the response of a symmetric specimen exhibits no bifurcation. This is verified by introducing a slight nonsymmetry into the computational model. The load-displacement curve remains nearly the same, and so does the failure mode for this specimen.

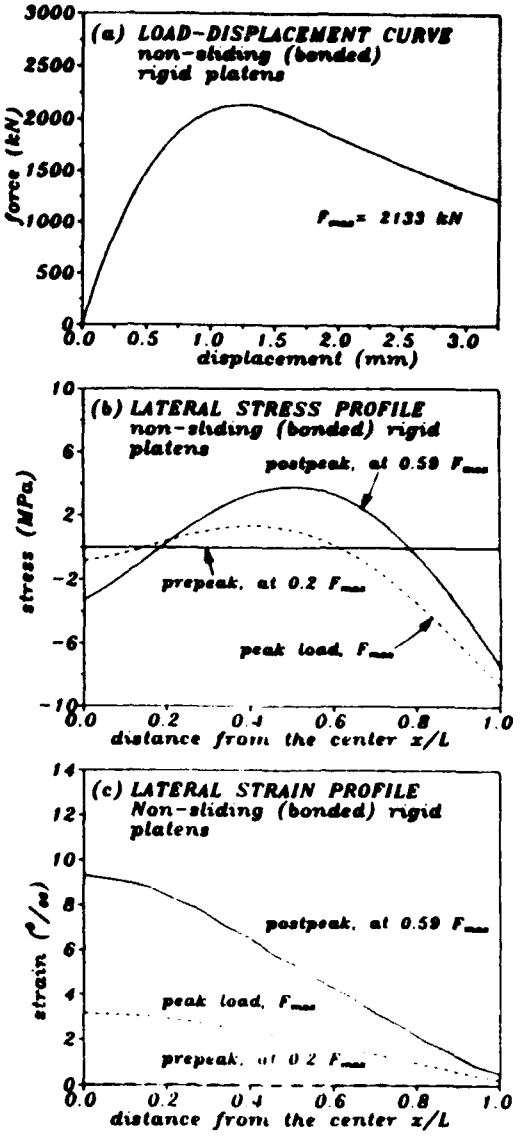

FIG. 9. (a) Load-Displacement Curve for Specimen with Bonded (Nonsliding) Platens, and Profiles of Lateral (*b*) Stress and (c) Strain for Bonded (Nonsliding) Platens

Fig. 5(*c*) shows the distribution of maximum principal cracking strain ε''

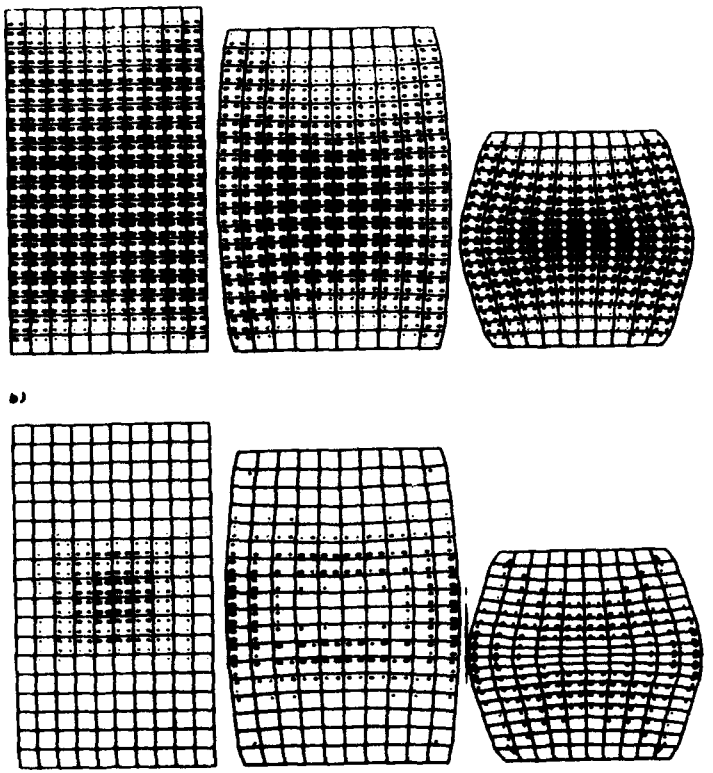

FIG. 10. Deformed Meshes (Exaggerated 50 Times) with Fields of (a) Maximum Principal Strains ε_1; and (b) Maximum Principal Stresses σ_1 (Tensile Only)—for Bonded Platens (Actual Path), at Prepeak ($0.2F_{max}$), Peak Load (F_{max}), and Postpeak ($0.59F_{max}$). (Size of Rectangle Is Proportional to Magnitude and Direction of Their Long Side Is ε_1-Direction)

[in the same manner as Fig. 5(*a*) and (*b*)]. The cracking starts to propagate vertically from the assumed weak zone at the center of the specimen, moving first towards the loading platens. Then, however, already before reaching the peak-load state, the band of vertical splitting cracks starts to propagate sideways, in two inclined directions. This happens for the present p-value while the cracking front reaches roughly to the top and bottom quarters of the specimen height. The magnitudes and directions of the fields of the maximum and minimum principal stresses and strains at various load levels are shown in Figs. 9–11. Figs. 9(*b*) and 9(*c*) show the distribution of the lateral stresses and strains along the vertical axis at various load stages.

To investigate the size effect, the aforementioned calculations for the case of a perfectly symmetric mesh have been repeated for geometrically similar specimens of three different sizes in the ratio 1:2:4, the smallest specimen having the height $h = 61 = 540$ mm. It is highly interesting, although perhaps not surprising with respect to the knowledge from experiments, that no significant size effect has been detected from the calculated results.

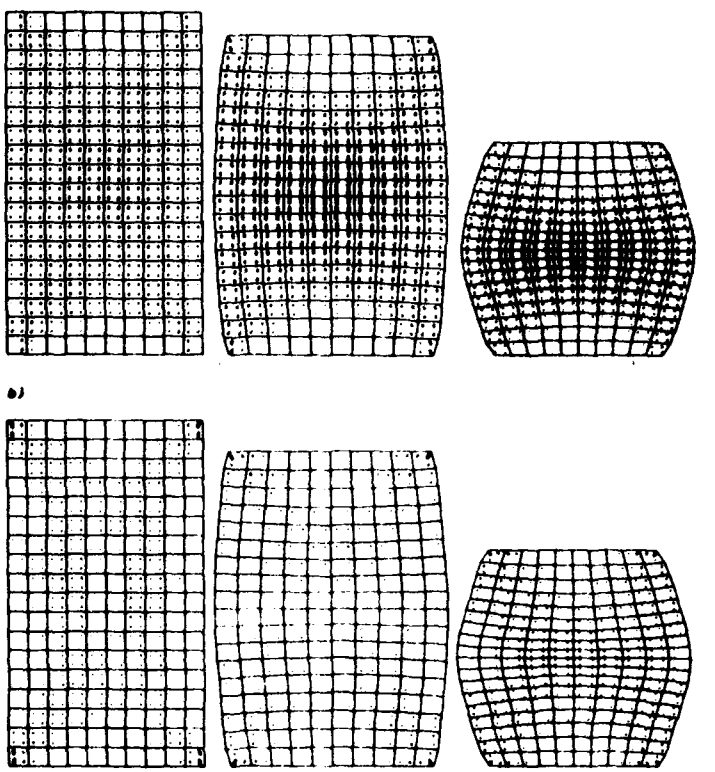

FIG. 11. Deformed Meshes with Fields of (a) Minimum Principal Strains ε_3; and (b) Minimum Principal Stresses σ_3 (Compressive Only)—for Bonded Platens (Actual Path)

that no significant size effect has been detected from the calculated results. [In compression there is, however, the size effect of specimen length on the postpeak softening slope, as shown experimentally by van Mier (1984) and modeled by Bažant (1989b); see also Bažant and Cedolin (1991), section 13.2)

The lack of size effect means that compression fracture cannot be driven by the stored elastic energy that is released globally from the entire specimen. Rather, it must be driven by a local mechanism in a region of a fixed size (depending on l but not on the specimen size) near the fracture front. This mechanism must be approximately independent of the specimen shape and boundaries, and thus involves no significant stress changes farther away from the crack band front. The length of the zone of significant transverse normal stress in Fig. 2(*b*) is approximately constant, independent of the specimen size.

It may also be noted from Fig. 3(*a*) and (*b*) that the tendency toward development of two symmetric inclined failure bands exists at the beginning of the analysis of the perfectly symmetric specimen with sliding boundaries

but is later overridden by the development of an asymmetric shear band. In the specimen with nonsliding (bonded) boundaries, on the other hand, symmetric inclined failure bands (shear bands) tend to develop also, extending toward the specimen corners. The fact that the specimen with nonsliding boundaries does not exhibit any tendency to nonsymmetric failure bands is interesting and contradicts some previous views; this fact is probably due to large transverse normal strains in the middle of the specimen. They apparently override the tendency to nonsymmetric inclined failure bands and enforce symmetric response.

Figs. 12(*a*)–(*c*) show the distribution of the relative volume change ε_V ($\varepsilon_V = \varepsilon_{kk}/3$) at the postpeak state (for both sliding and nonsliding boundaries). The circular dots are plotted only for negative ε_V and their magnitude is proportional to ε_V. It is interesting that, despite large transverse expansions, the volumetric strains are negative almost everywhere, except in the case of the nonsliding boundaries in which only slight positive volumetric strains are detected at the middle of the vertical sides.

Figs. 12(*d*)–(*f*) show the distribution of the inelastic volume change (dilatancy), defined as $\varepsilon_V'' = \varepsilon_V - \sigma_V/3K$ where $\sigma_V = \sigma_{kk}/3$ = mean stress and K = elastic bulk modulus. In contrast to Figs. 12(*a*)–(*c*), the dots are now plotted only for positive ε_V'' and their size is proportional to ε_V''. We clearly see the dilatancy to dominate in the zones of axial splitting cracks or within the shear bands. Thus, the term shear-dilatancy bands appears to be appropriate.

From the calculated strain and stress fields, the cracking pattern of the specimens with sliding and nonsliding boundaries can be reconstructed based on the analysis results shown in Figs. 5(*a*) and (*c*). The spacing of the densely

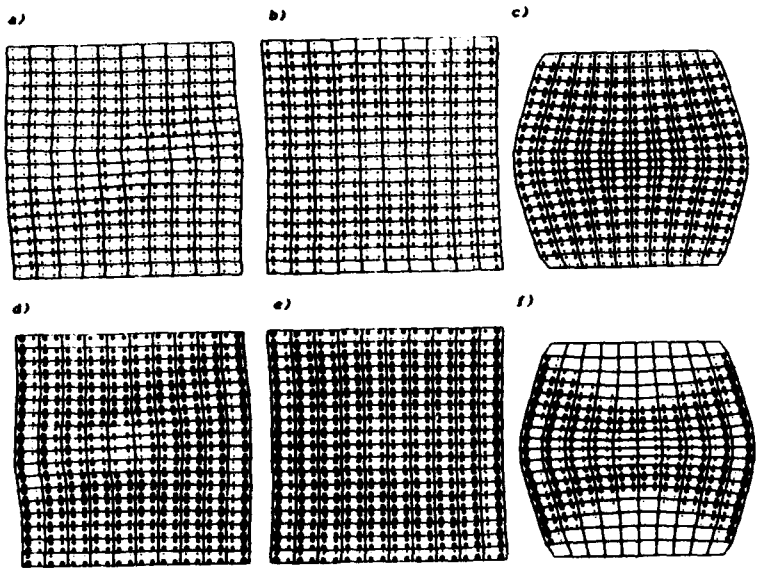

FIG. 12. Postpeak Fields of [(a), (b), (c)] Volumetric Strain ε_V (Negative Only) and [(d), (e), (f)] Inelastic Volumetric Strain (Dilatancy, Positive Only); (a), (b), (d), and (e)—Sliding Platens; (c) and (f)—Bonded Platens; (a) and (d)—Nonsymmetric (Actual) Path, (b) and (e)—Symmetric Path (Dot Diameter Is Proportional to ε_V)

distributed cracks cannot be obtained from the constitutive model. No doubt it is governed mainly by the size of the dominant inhomogeneities in the material.

The compression failure was previously investigated by a rather different constitutive model, which was not very realistic for triaxial stress states: a nonlocal version of the Drucker-Prager plasticity model with a degrading yield limit (Droz and Bažant 1988). Like in the present study, it was found that the response path of a perfectly symmetric specimen bifurcates, after which either two crossing inclined shear bands may grow (path 1) or only one band may grow while the other unloads (path 2). The asymmetric path (path 2) was found to be the actual path, for both sliding and nonsliding boundaries, and (in contrast to the present results), the difference between the symmetric and nonsymmetric responses was found more pronounced for the case of bonded platens. Due to a different (and more realistic) constitutive model, which gives a much better representation of inelastic volume dilatancy, the present analysis indicates the nonsymmetric component of the failure mode to occur only for specimens with sliding boundaries.

Conclusions

1. The previously developed nonlocal microplane model with normal microplane strains that are split into deviatoric and volumetric components appears to be capable of modeling axial splitting cracks and shear band failure of quasibrittle materials in compression.
2. The most important characteristic of compression failures in quasibrittle materials may be described in the continuum sense as tensile strain softening in the transverse direction (increase of transverse strain at decreasing transverse stress). In reality, this strain softening is manifested as damage by densely distributed axial splitting cracks. According to the present results, the axial splitting cracks appear to be caused by transverse expansion in the fracture process zone, which puts the region in front of the expansion zone into transverse tension. The axial splitting cracks organize themselves into inclined shear band propagating sideways, rather than in the direction of the cracks.
3. For specimens with perfectly sliding platens, the primary path that corresponds to symmetric deformation bifurcates, and the actual path that occurs corresponds to asymmetric deformation with one dominant inclined failure band. Bifurcation analysis can be skipped and the asymmetric deformation obtained directly if a slight asymmetry is introduced into the computational model. Without such artificial asymmetry the bifurcation is indicated by the vanishing of the smallest eigenvalue of the tangential stiffness matrix of the structure. The postbifurcation states are stable because the smallest eigenvalue of the symmetric part of the tangential stiffness matrix of the structure remains positive (under displacement-controlled loading).
4. For specimens bonded to rigid loading platens, no bifurcation is found and the failure mode involves two symmetric inclined shear bands that consist of smeared axial splitting cracks (transverse expansion with strain softening).
5. Despite large transverse expansion, the relative volume change for all the analyzed cases is negative, except for a small zone at the middle of the vertical sides in a specimen with bonded rigid platens. On the other hand, the inelastic part of the volume change (i.e., dilatancy) is positive over a large part of the specimen. The shear bands represent zones of large inelastic dilatancy, and not

only large shear strains; thus they might be more aptly called "shear-dilatancy" bands (or "shear-expansion" bands).

6. It is most interesting that the present model reveals no appreciable size effect on the nominal stress at maximum load when geometrically similar specimens of different sizes (with the same characteristic length l) are compared. This means that (1) The mechanism that drives the axial splitting must be local, coupled to the width of the shear band, which is about the same for different specimen sizes; and (2) no significant release of stored energy from the specimen as a whole into the cracking front takes place.

7. In contrast to tensile fracture, a successful modeling of compression failures apparently necessitates a constitutive model that gives not only correct shear deformations but also correct transverse expansions and volume dilatancy under complex triaxial stress states. The microplane model appears to satisfy this requirement.

Acknowledgments

Partial financial support for nonlocal analysis was received from the Air Force Office of Scientific Research (under Grant 91-0140 to Northwestern University), and for the underlying fracture studies from the Center for Advanced Cement-Based Materials at Northwestern University. Most of the paper was written during the first writer's sojourn at Lehrstuhl A für Mechanik, Technische Universität München, supported under A. von Humboldt Award of Senior U.S. Scientist.

Appendix. References

Bažant, Z. P. (1967). "Stability of continuum and compression strength." *Bulletin RILEM*, Paris, France, 39, 99–112 (in French).

Bažant, Z. P. (1989a). "Bifurcation and thermodynamic criteria of stable path of structures exhibiting plasticity and damage propagation." *Computational Plasticity* D. R. J. Owen, E. Hinton, and E. Onate, eds., Pineridge Press, Swansea, U.K., 1–25.

Bažant, Z. P., (1989b). "Identification of strain-softening constitutive relation from uniaxial tests by series coupling model for localization." *Cement and Concrete Res.*, 19, 973–977.

Bažant, Z. P., and Cedolin, L. (1991). *Stability of structures: Elastic, inelastic, fracture and damage theories*. Oxford Univ. Press, New York, N.Y.

Bažant, Z. P., and Ožbolt, J. (1990). "Nonlocal microplane model for fracture, damage, and size effect in structures." *J. Engrg. Mech.*, ASCE, 116(11), 2485–2504.

Bažant, Z. P., and Prat, P. C. (1988). "Microplane model for brittle plastic material, I. Theory and II. Verification." *J. Engrg. Mech.*, ASCE, 114, 1672–1702.

Brockenbrough, J. R., and Suresh, S. (1987). "Constitutive behavior of a microcracking brittle solid in cyclic compression." *J. Mech. Phys. Solids*, 356, 721–742.

Droz, P., and Bažant, Z. P. (1988). "Nonlocal analysis of stable states and stable paths of propagation of damage shear bands." *Cracking and damage*, J. Mazars and Z. P. Bažant, eds., Elsevier, London, England, 183–207.

Glucklich, J. (1963). "Fracture of plain concrete." *J. Engrg. Mech. Div.* ASCE, 89(6), 127–138.

Griffith, A. A. (1924). "The theory of rupture." *Proc. 1st Int. Conf. Applied Mechanics*, Delft, The Netherlands, 55–65.

Hill, R. (1961). "Bifurcation and uniqueness in non-linear elastic-plastic solids." *J. Mech. Phys. Solids*, 6, 236–249.

Hill, R. (1962). "Uniqueness criteria and extremum principles in self-adjustment problems in continuum mechanics." *J. Mech. Phys. Solids*, 10, 185–194.

Ingraffea, A. R. (1977). "Discrete fracture propagation in rocks: Laboratory tests and finite element analysis," dissertation presented to the University of Colorado, at Boulder, Colorado, in partial fulfillment of the requirements for the degree of Doctor of Philosophy.

Kendall, K. (1978). "Complexities of compression failure." *Proc. Royal Soc. of London*, A. 361, 245–263.

Lawn, B. R., and Marshal, D. B. (1978). "Indentation fracture and strength degradation in ceramics." *Fracture mechanics of ceramics*, 3, R. C. Bradt, ed., Plenum Press, 205–229.

Miyamoto, H., Fukuda, S., and Kageyama, K. (1977). "Finite element analysis of crack propagation under compression." *Fracture 1977*, Vol: 3, ICF4, Waterloo, Canada, 491–499.

Sammis, C. G., and Ashby, M. F. (1986). "The failure of brittle porous solids under compressive stress state." *Acta Metallurgica*, 34(3), 511–526.

Shetty, D. K., Rosenfield, A. R., and Duckworth, W. H. (1968). "Mixed mode fracture of ceramics in diametral compression." *J. American Ceram. Soc.*, 69(5), 437–443.

van Mier, J. G. M. (1984). "Strain-softening of concrete under multiaxial loading conditions," thesis presented to Eindhoven University of Technology, at Eindhoven, The Netherlands, in partial fulfillment of the degree of Doctor of Philosophy.